A Multipath and Thermal noise joint error characterization and exploitation for low-cost GNSS PVT estimators in urban environment

Eustachio Roberto Matera

THÈSE

En vue de l'obtention du

DOCTORAT DE L'UNIVERSITÉ DE TOULOUSE

Délivré par :

Institut National Polytechnique de Toulouse (Toulouse INP)

Discipline ou spécialité :

Informatique et Télécommunication

Présentée et soutenue par :

M. EUSTACHIO ROBERTO MATERA

le vendredi 28 janvier 2022

Titre :

A Multipath and Thermal noise joint error characterization and exploitation for low-cost GNSS PVT estimators in urban environment

---

Ecole doctorale :

Mathématiques, Informatique, Télécommunications de Toulouse (MITT)

Unité de recherche :

Laboratoire de Télécommunications (TELECOM-ENAC)

Directeur(s) de Thèse :

M. CARL MILNER

M. AXEL JAVIER GARCIA PENA

Rapporteurs :

M. KYLE O'KEEFE, UNIVERSITE DE CALGARY

MME RUI SUN, UNIVERSITE DE NANJING

Membre(s) du jury :

M. FABIO DOVIS, POLITECNICO DE TURIN, Président

M. AXEL JAVIER GARCIA PENA, ECOLE NATIONALE DE L'AVIATION CIVILE, Membre

M. BERTRAND EKAMBI, ABBIA GNSS TECHNOLOGIES, Invité(e)

M. CARL MILNER, ECOLE NATIONALE DE L'AVIATION CIVILE, Membre

A Multipath and Thermal noise joint error characterization and exploitation for low-cost GNSS PVT estimators in urban environment

written by **M. Eustachio Roberto Matera**

Ecole doctorale : **EDMITT - Ecole Doctorale Mathématiques, Informatique et Télécommunications de Toulouse**

Spécialité : **Informatique et Télécommunications**

Unité de recherche : **ENAC-LAB - Laboratoire de Recherche ENAC**

Thèse dirigée par **Carl MILNER** et **Axel Javier GARCIA PENA**

Jury **M. Kyle OKeefe**, Rapporteur **Mme Rui Sun**, Rapporteure **M. Axel Javier Garcia Pena**, Examinateur **M. Carl Milner**, Directeur de thèse

Per apprezzare

la bellezza

di un fiocco di neve

è necessario

resistere al freddo

(Aristotele)

Acknowledgements

In this paragraph I would like to dedicate a thought to the people which have played an important role during this long path toward the Ph.D. thesis defense.

Firstly, I'd like to thank Bertrand Ekambi, who always believed in this project, in my work, and in my qualities. We lived together in the project lifespan some radical changes, difficulties and the pandemic situation due to the explosion of Covid-19, and together we never gave up. I thank him for his words always comforting, decisive and his concrete support that led to the achievement of the objectives.

I want to thank my first thesis director, Olivier Julien, who was responsible for the ideas behind the project and its start-up. In the same way, I want to thank my second thesis director, Carl Milner, who accepted to manage the project in a critical time, and who always found time in his tight schedule to manage the project, always offering interesting advice.

I am also thankful to my thesis co-director Axel Garcia-Pena, who had a central and main role in this project, helping with his constant support, with numerous constructive discussions, and very long analysis of the proposed methodologies that oriented me toward efficient solutions, also during the changes of thesis directions. My professional growth has taken place thanks to his support.

I'm gratefully to Professor Kyle O'Keefe and Professor Rui Sun for reviewing my Ph.D. thesis, providing me with interesting comments and participating as jury members for the thesis defense. I would also like to thank Professor Fabio Dovis for attending the thesis defense as a president of the jury and for the provision of great advices concerning the further advancement of this research. The words he used for my proclamation moved me because they closed a cycle of my academic life, started in 2010 as a university student at the Polytechnic of Turin and closed (but not definitely) by a professor of the Polytechnic of Turin.

Infine voglio ringraziare la mia famiglia, che mi ha sempre supportato senza mai abbandonarmi, nonostante la distanza vissuta quotidianamente, e tutti gli amici e colleghi che ho incontrato in questo cammino. Spero di avervi resi orgogliosi di me.

Abstract

English

Achieving an accurate localization is a significant challenge for low-cost GNSS devices in dense urban areas. The main limitations are encountered in the urban canyons, consisting in a reduced satellite signal availability and a positioning estimation error due to the impact of Line-of-Sight and Non Line-of-Sight multipath phenomenon.

This PhD study allows to understand the impact of the multipath phenomenon on the low-cost GNSS receivers and to prove the need of accurate assessment of the multipath error model affecting the GNSS measurements, especially in urban environment. It consists in the investigation, characterization, and finally, exploitation of the multipath error components affecting the pseudorange and pseudorange-rate measurements, of a single frequency, dual constellation GNSS receiver in the urban environment, operating with GPS L1 C/A and Galileo E1 OS signals.

The first goal consists in providing a set of methodologies able to identify, isolate and characterize the multipath error components from the measurements under test. However, considering that the isolation of the multipath error is a complex operation due to the superimposed effects of multipath and thermal noise, the final method consists of isolating the joint contribution of multipath and thermal noise components. The isolated multipath and thermal noise error components are firstly classified depending the corresponding received signal C/N_0 values, and, secondly, statistically characterized by means of Probability Density Function, sample mean and sample variance. Also, the temporal and spatial correlation properties of the isolated error components are calculated by means of a methodology which estimates the temporal correlations as a function of the receiver speed.

In addition, an image processing methodology based on the application of a sky-facing fish-eye camera provides the determination of an empirical C/N_0 threshold equal to 35 dB-Hz used to qualitatively identify the Non Line-Of-Sight and Line-Of-Sight received signal reception states.

The resulting errors are characterized by a non-symmetrical, positive biased PDF for a C/N_0 lower than 35 dB-Hz, while they are characterized by a symmetrical and zero-centred PDF for a C/N_0 higher than 35 dB-Hz. Correlation times for pseudoranges are ranged from around 5s for static and very low speed dynamics to around 1s for high-speed dynamics. Correlation times for pseudorange-rates ranged from around 0.5s for static and very low speed dynamics to around 0.2s for high-speed dynamics, due to the data-rate limitations.

The second goal consists in exploiting the multipath and thermal noise error models and the LOS/NLOS received signal reception state estimation in a low-complex EKF-based architecture to improve the accuracy of the PVT estimates. This is obtained by implementing some techniques based on the measurement weighting approach to take into account the statistical properties of the error under exam and by the application of a time differenced architecture design to exploit the temporal correlation properties. Positioning performance of the tested solutions surpassed the performances of a simple EKF architecture and are comparable to the performances of a uBlox M8T receiver.

Français

Fournir une localisation précise en environnement urbain dense reste un véritable défi pour des récepteurs GNSS grand public. Les limitations principales sont rencontrées dans les zones urbaines où il existe une réduction des signaux GNSS disponibles et la formation d'erreurs d'estimation de la position créées par la présence de lignes de vue directes (LOS) et lignes de vue indirectes (NLOS), générées par le phénomène de multi-trajets.

Cette thèse de doctorat consiste en l'analyse, la caractérisation, et finalement, l'exploitation des composantes des erreurs de multi-trajets qui affectent les signaux et mesures des récepteurs GNSS grand public lors de leur utilisation dans un environnement urbain dense.

Nos travaux portent plus particulièrement sur l'identification, l'isolement et la caractérisation des erreurs de multi-trajet à partir des mesures de pseudodistances. Les données ont été captées par un récepteur GNSS monofréquence et bi-constellations, utilisant les signaux GPS L1 C/A et Galileo E1 OS. Nous avons également travaillé sur l'exploitation des erreurs de multi-trajet par un algorithme innovant basé sur une architecture de filtre de Kalman

étendu (EKF) pour améliorer la précision et la robustesse de l'estimation de la PVT en environnement urbain dense.

Considérant que l'isolement des erreurs de multi-trajet est complexe à cause de la superposition des effets causés par les multi-trajets à ceux générés par le bruit thermique du récepteur, la méthode finale que nous avons utilisée consiste à isoler la contribution conjointe des erreurs de multi-trajet de celles liées au bruit thermique. Nous avons en plus utilisé une technique de traitement des images fournies par une caméra à grand angle (vision à 360°) pour obtenir une information empirique sur le seuil de rapport signal-bruit C/N_0 déterminé pour identifier et discriminer de manière empirique les lignes de vues indirectes (NLOS) des lignes de vue directes (LOS).

Les erreurs de multi-trajet et de bruit thermique sont d'abord classées en fonction des valeurs de $C/N0$ des signaux reçus, puis elles sont statistiquement caractérisées par leur fonction de densité de probabilité (PDF) moyenne et variance d'échantillonnage. Ensuite nous estimons les propriétés des corrélations spatiales et temporelles des erreurs isolées grâce à une méthode d'estimation des corrélations temporelles en fonction de la vitesse du récepteur GNSS en mobilité urbaine.

Enfin, nous proposons un algorithme basé sur un filtre de Kalman étendu (EKF) qui exploite le modèle d'isolement des erreurs de multi-trajet et de bruit thermique, les propriétés de corrélation spatiales et temporelles, les estimations d'état de lignes de vue directes et indirectes, pour améliorer la précision de l'estimation PVT des récepteurs grand public utilisés en environnements urbains.

L'information sur la connaissance du modèle des erreurs de multi-trajet et de bruit thermique et des lignes de vue directes/indirectes est exploitée grâce à des techniques de pondération et de masquage de l'information utile/inutile. Les propriétés des corrélations temporelles et spatiales sont utilisées par une architecture de *time-differencing Kalman Filter*.

Cette étude permet de mieux comprendre l'impact des phénomènes de multi-trajet sur des récepteurs GNSS grand public, et d'apporter une meilleure prise en compte de modélisation des erreurs de multi-trajet qui affectent les mesures GNSS spécifiquement en environnement urbain.

Table of contents

List of Figures

List of Tables

List of Abbreviations

A	Amplifier
ADAS	Advanced Driver-Assistance Systems
ADC	Analog-to-Digital conversion
AGC	Automatic Gain Control
AoA	Angle of Arrival
ARNSS	Aeronautical Radio Navigation Service
Atan	Arctangent
Atan2	Four-Quadrant Arctangent
B	Body
BB	Baseband
BOC	Binary Offset Carrier
BPF	Band Pass Filter
BPSK	Binary Phase Shift Keying
C/A	Coarse/Acquisition
CBOC	Composite Binary Offset Carrier
CDF	Cumulative distribution function
CDMA	Code Division Multiple Access
CIR	Channel impulse response
CP	Cross-Product
DD	Decision directed
DDCP	Decision-directed cross-product
DGNSS	Differential GNSS
DLL	Delay Lock Loop
DOP	Dilution of precision
DP	Data Processing
DP	Dot Product
DSP	Digital Signal Processing
DS-SS	Direct Sequence Spread Spectrum
ECEF	Earth-Centered Earth-Fixed
ECI	Earth-Centered Inertial
EKF	Extended Kalman Filter
EML	Early Minus Late
EMLP	Early Minus Late Power
ESA	European Space Agency
FDMA	Frequency Division Multiple Access
FF	Flood filling
FLL	Frequency Lock Loop
FS	Frequency Synthesizer
GA	Ground Antennas
GCC	Ground Control Centre
GGPPTO	GPS to Galileo Post-Processing Time-Offset
GGTO	GPS-to-Galileo time offset
GM	Gauss-Markov
GMS	Ground Mission Segment
GNSS	Global Navigation Satellite System
GPST	GPS Time
GSS	Galileo Sensors Stations
GST	Galileo System Time

ICAO	International Civil Aviation Organization
IF	Intermediate Frequency
IFF	Intermediate Frequency Filter
IMU	Inertial Measurement Unit
ITU	International Telecommunication Union
IVS	In-Vehicle Systems
KF	Kalman Filter
LBS	Location Based Services
LN	Local Navigation
LNA	Low Noise Amplifier
LOS	Line-of-Sight
LPF	Low Pass Filter
LSE	Least Squares Estimation
MaaS	Mobility as a Service
MBOC	Multiplexed BOC
MCS	Master Control Station
MEO	Medium Earth Orbit
MN	Jointly multipath and thermal noise error
MP	Multipath
MS	Monitoring Stations
NCO	Numerically Controlled Oscillator
NLOS	Non-reception of the Line-of-Sight
NMD	Navigation Message Demodulation
OEE	Object's edge enhancement
OS	Open Service
PDF	Probability Density Function
PDP	Power Delay Profile
PLL	Phase Lock Loop
PPP	Precise Point Positioning
PRN	Pseudo-Random Noise
PSD	Power Spectral Density
PSR	Code Pseudorange
PSR-R	Doppler Pseudorange-rate
PVT	Position, Velocity and Time
PVTE	PVT estimation
RAIM	Receiver Autonomous Integrity Monitoring
RF	Radio Frequency
RFFE	Analog Radio Frequency Front-End
RHCP	Right-hand circular polarization
RNSS	Radionavigation Satellite Services
RO	Receiver Oscillator
RTK	Real Time Kinematics
SA	Standalone
SCE	Satellite Coordinates Estimation
SoL	Safety of Life
SP	Signal Processing
ST	Sidereal Time
SVN	Satellite Vehicle Number
TAI	International Atomic Time
TBS	Time Based Services
TEC	Total Electron Content
TT&C	Telemetry, Tracking and Control

TV	Time-Velocity
UAS	Unmanned Aerial System
UERE	User Equivalent Range Error
UERRE	User Equivalent Range Rate Error
UHF	ultra-high frequency
ULS	Mission Uplink Stations
UT	Universal Time
UTC	Coordinated Universal Time
WLS	Weighted Least Squares

1 Introduction

1.1 Overview

Today, people, objects and vehicles are interconnected by a network of sensors providing a multitude of location-based services (LBSs). Such services are fundamental for a large range of civilian applications, from Safety of Life (SoL) to entertainment. The localization information is often provided, at least in part, by the Global Navigation Satellite System (GNSS). Thanks to this technology, it is possible to estimate the position, velocity and time (PVT) of a user receiver. GNSS is available both as an open tariff-free service or through commercial services, ranging from standard to high accuracy positioning.

The combination of high demand and global coverage of GNSS has led to a large variety of LBSs and such opportunities for new services continue to grow through new constellations, signal modernisation and technical innovation.

At the time of writing, one of the market sectors with the largest growth are applications in the urban environment. By 2050, more than 60 percent of the world's population is expected to live in urban areas. Hence, urban mobility of people (private and public transportation) and goods is becoming an issue of great importance in today's society. The traditional mobility services are being extended through more flexible options, such as vehicle sharing, ride-hailing and micro mobility. User localization plays an essential, though often unseen role on urban mobility since, in most of the cases, this array of applications requires robust and reliable positioning and navigation [3], [4]. The large diffusion of vehicle sharing, ride-hailing and micro mobility services is opening to a new and thriving business, the so-called Mobility as a Service (MaaS) [5].

As a result of the evolution of the urbanization and the needs of the localization in the urban environement, GNSS is set to grow steadily across the next decade (2019-2029) [3],[5]. The majority of new GNSS receiver shipments is represented by mass-market receivers, where a large part is installed on smartphones and wearables, followed by GNSS receivers mainly used in either road or Unmanned Aerial System (UAS) applications. In the road sector, most revenues are generated by In-Vehicle Systems (IVS), Advanced Driver-Assistance Systems (ADAS), fleet management, and, today, micromobility services. Moreover, the current urban mobility trends and the introduction of innovative technologies are shaping the market transformation and its growth.

Among the various MaaS, this work mainly focuses on micromobility services. Micromobility is a fast-evolving sector which attempts to solve what is called the "last mile" transportation problem. Micromobility aims to transform urban mobility, and in particular short-distance routes, using lighter, less bulky and less polluting vehicles. Indeed, a proliferation of dockless, light-weight vehicles (e-bikes, e-scooters, e-motorcycles etc.) can be seen in major cities around the world, designed mainly to mitigate traffic congestion on local roads as well as providing a convenient and cleaner "last mile" solution.

Micromobility vehicles are also used as an alternative to private and public vehicle usage for urban transport and/or food and goods delivery. Commercial applications benefit greatly from micromobility and a large range of "last-mile" food and goods delivery are services are available to consumers, in an ideal case reducing the cost and waiting times for goods. A crucial role in micromobility services is covered by GNSS, supporting both users and operators to easily locate and trace vehicles across the city, and aid navigation in dense urban areas. However, to achieve the best performance in the dense urban environment, integrated localization and navigation systems are required to provide continuity and improved accuracy. Indeed, vehicle sharing applications based on micromobility vehicles require robust and reliable position estimation [3], [4] for example to provide the vehicle localization to users, to verify the correct parking of vehicles and for geofencing applications. It is clear that in the low-cost application domain of micromobility, similarly low-cost (mass-market) GNSS receivers are essential enablers [3], [4].

Unfortunately, achieving continuous accurate localization with the added benefit of robustness and reliability is a significant challenge for this growing market in dense urban areas, since GNSS devices, initially designed to work in open areas, experience significant limitations in the urban environment.

1.2 Motivations and objective of the work

Urban centres are often a high-density area of large buildings intersected by roads. Sections of the urban environment composed of a street with high elevation buildings on either side are called urban canyons. There are three main consequences of encountering urban canyons:

1. LOS multipath - the reception of the line-of-sight (LOS) signal together with one or more copies of the signal reflected off surfaces (called LOS multipath within the thesis),
2. NLOS multipath - the non-reception of the line-of-sight signal, due to obstruction, followed by the reception of the multipath reflections (called NLOS multipath within the thesis),
3. Shadowing - the total blocking of the satellite signal caused by the shadowing effect of the building on the user receiver.

Therefore, if an e-scooter or e-bike weaves its way through traffic in a metropolitan area, the positioning estimation can often be erroneous. Hence, GNSS positioning services in the urban environment are facing limitations of various natures, which can compromise the required GNSS performance for the specific localization application, in terms of accuracy, continuity and reliability.

The first limitation is the reduced satellite signal *availability*. Lack of signal availability can reduce dramatically the performance of localization services, even resulting in a total service outage. This limitation is caused by signal attenuation or blockage by objects in the line-of-sight between the emitter and the receiver resulting in decreased satellite visibility and decreased received signal strength. This limitation is especially severe in urban canyons with tall buildings.

The second limitation is the positioning estimation error due to the impact of multipath phenomenon (LOS and NLOS multipath). Multipath phenomenons are caused by the presence of high buildings and foliage which act as scatterers of the original GNSS signal, creating multiple copies of the GNSS signal.

Lastly, GNSS receivers have technology limitations depending on the costs of the equipment: unaffordable battery consumption, data communication, tracking device and PVT algorithm costs. Indeed, high-accuracy positioning services are usually provided through the use of high-cost GNSS receivers which implements high-cost equipment, such as user receiver antennas designed to reduce directly the impact of the multipath signals, and PVT solutions based on multi-frequency GNSS signal processing, external aiding through the use of sensor fusion, image processing based on real-time cameras, complex measurement error detection or Receiver Autonomous Integrity Monitoring (RAIM). The majority of the techniques previously cited cannot be fully exploited by low-cost receivers. One possible solution to cope with GNSS standalone receiver limitations, which is becoming a potential baseline platform for mass-market user devices, is to integrate an Inertial Measurement Unit (IMU) [1]. More specifically, this kind of solution increases the quality of the PVT estimations by taking advantage of the complementary nature of GNSS and the inertial systems measurements. Nevertheless, although IMU complements the weak points of GNSS in urban canyons, sensor drifts occur, which may be significant in low-cost IMU products that require correction using GNSS. Therefore, in order to obtain a reliable position estimate, it is still critical to have a robust positioning architecture and an accurate assessment of the GNSS measurement model.

This PhD was born from a collaboration between Abbia GNSS Technologies and Ecole Nationale de l'Aviation Civile (ENAC) and its objective is to overcome the previously identified GNSS mass-market receiver limitations in the urban environment, deployed for micro-mobility systems. Note that overcoming these limitations requires solutions in terms of technology, sensors and methods, and that the MaaS market for micromobility applications is looking for solutions embedded in low-cost devices to support the relative reduced costs of micromobility vehicles.

1.3 Proposed Solution

The solution proposed in this PhD thesis to reach the objective described in the previous section consists, for a low-costs GNSS receiver, firstly, in providing a consistent set of methodologies to isolate the GNSS pseudorange and pseudorange rate errors in the urban environment as a result of multipath and thermal noise (MN). Secondly, in characterizing and overbounding the joint MN error, and third and lastly, in exploiting the overbounded mathematical model in different PVT estimator architectures in order to improve the position estimation accuracy.

These three parts of the proposed solution are further described in this section after the description of the chosen low-cost receiver. Additionally, knowing the critical impact of NLOS multipath, a LOS and NLOS reception state classification methodology has also been developed as part of the proposed solution, to refine the urban environmental error characterization.

The proposed characteristics of the chosen low-cost GNSS receiver are:

- Single frequency processing;
- Signal processing based on the acquisition of basic open service GNSS signals (i.e. GPS L1 C/A, Galileo E1 OS);
- Signal processing resulting in code pseudorange and Doppler pseudorange-rate measurements;
- PVT estimation based on the basic Extended Kalman Filter (EKF) solution;

Today, the lowest-cost GNSS receivers are characterized by single frequency measurement processing. For this reason, single frequency measurement processing is addressed in this thesis. However, it should be noted that the methodology may be applied to L2C, L5, E5a and other signals and even to measurement combinations (L1/L5, E1/E5a). The low-cost GNSS receiver has been chosen to be a dual constellation receiver to handle GPS and Galileo measurements. Similarly, the work could equally be applied to other constellations and their respective signals. The choice of a dual constellation receiver is due to the inherent advantage of increasing the number of satellite measurements, which directly increases the satellite availability and improves the satellite geometry in the challenging urban environment. Therefore, the targeted low-cost receiver will be able to operate with single frequency GPS L1 C/A and Galileo E1 OS signals [6],[7],[8].

GPS has been chosen since it is the most widely used navigation satellite system across the world. Whereas the Galileo constellation, even if under deployment, is a key element of the GNSS applications deployment in the EU market area in which this PhD has been undertaken. Moreover, GPS and Galileo offer an optimized interoperability and compatibility [9], [10] due to the following elements:

- GPS L1 C/A and Galileo E1 OS modulated signals have a common centre frequency, essential for signal interoperability.
- GPS and Galileo use CDMA (Code Division Multiple Access) modulation which is essential for signal interoperability (unlike the current GLONASS system, which is Frequency Division Multiple Access - FDMA.
- Geometric Reference frame used by GPS and Galileo users have the same characteristics and are compatible.
- Timing Reference frame adopted by GPS and Galileo differs of a well-defined offset, called GPS-to-Galileo offset (GGTO), which is usually communicated or estimated by the user receivers. Once calculated, the offset could be recovered obtaining compatible measurements.

The choice of code pseudorange and Doppler frequency pseudorange-rate measurements is dictated by the urban environment limitations: the numerous loss-of-lock of GNSS signals due to masking and extreme multipath as well as an increase in cycle slips affecting the carrier phase measurements. It follows that carrier phase measurements, usually used for high-accuracy applications, are not reliable measurements in the urban environment. Therefore, code PSR measurements and Doppler frequency PSR-R measurements are collected and exploited in this work.

The proposed PVT estimator design is based on the classic EKF solution, which ensures a good level of performances and a relatively reduced complexity of the applied algorithms and thus, that make it the most applied PVT estimator in low-cost GNSS receivers. In addition to that, the basic EKF algorithms can be easily integrated by a large number of techniques which enhance its performance.

A more detailed explanation of the three parts of the proposed solution is given next. The first part of the PhD thesis proposed solution consists of providing a consistent set of methodologies to isolate the GNSS pseudorange and pseudorange rate errors from multipath and thermal noise (MN) in an urban environment, using a low-cost GNSS receiver. The proposed multipath and thermal noise error components isolation methodology consists of:

- Collecting the code pseudorange and the Doppler frequency pseudorange-rate measurements, from the low-cost GNSS receiver;
- Removing the true range and the true range-rate component from the measurements, leaving only the measurement error components;

- Removing the atmospheric and satellite clock error components through reference station corrections, leaving only the multipath and thermal noise error components;
- Isolating the multipath plus thermal noise error component from the receiver clock bias.

The second part of the PhD thesis proposed solution consists of characterizing the multipath plus thermal noise error obtained as described above. The proposed solution consists of computing the sample Probability Density Function (PDF), the sample mean, the sample variance and the temporal correlation, as a function of additional parameters (i.e. C/N_0, elevation angle, speed). This processing results in multiple plus noise error models which may be leveraged in the localisation filter in the final part of the proposed solution. Moreover, a receiver signal parameter is used to estimate if the received signal is in LOS received signal conditions after applying a LOS/NLOS discrimination methodology. This approach consists of the characterization of the environment surrounding the receiver antenna through the exploitation of fisheye camera pictures of the urban environment, simultaneously collected with the GNSS measurements, to which an image processing technique is applied to. Indeed, the images are taken from a sky-pointing fisheye camera mounted on the top of a moving platform and synchronized with a GNSS receiver.

The third part of the PhD proposed solution consists in utilising the obtained models to improve positioning performance. This is undertaken using different processing models, both standalone and differential systems. Independent data sets are used to quantify performance gains from using tailored measurement models to the urban environment. In particular, the modelling of temporal correlation has led to the use of a time differenced EKF with the empirical measurement model. Performance improvements are observed with respect to commercial software PVT solutions and a simple EKF used as benchmark.

1.4 Contributions

The main contributions made in this work are as follows:

- Development of a post-processing methodology for the isolation of the joint multipath and noise code pseudorange error;
- Development of a post-processing methodology for the isolation of the joint multipath and noise doppler pseudorange-rate error;
- Development of a post-processing methodology for the classification of LOS/NLOS received signal reception states based on an image processing and empirical C/N_0 threshold;
- Undertaking of an experimental data campaign of about 50h of low-cost receiver measurements conducted in the Toulouse urban area (France);
- Characterization of the pseudorange and pseudorange-rate statistics based on signal parameters;
- Characterization of the temporal correlation function of the error components as a function of the receiver dynamics;
- Investigation of the consistency of the proposed methodologies;
- Formulation of measurement models based on the results of the characterisations described above;
- Development of an innovative PVT estimator exploiting the models developed.

The article published along this dissertation are the followings:

1. Eustachio Roberto Matera, Axel Javier Garcia Peña, Olivier Julien, Bertrand Ekambi. Characterization Of Pseudo Range Multipath Errors In An Urban Environment. ITSNT 2018, International Technical Symposium on Navigation and Timing, Oct 2018, Toulouse, France. 10.31701/itsnt2018.22.hal-01890371
2. Matera, Eustachio Roberto, Garcia-Pena, Axel, Julien, Olivier, Milner, Carl, Ekambi, Bertrand, "Characterization of Line-of-sight and Non-line-of-sight Pseudorange Multipath Errors in Urban Environment for GPS and Galileo," Proceedings of the 2019 International Technical Meeting of The Institute of Navigation, Reston, Virginia, January 2019, pp. 177-196. https://doi.org/10.33012/2019.16687
3. Matera, Eustachio Roberto, Garcia-Pena, Axel, Milner, Carl, Ekambi, Bertrand, "Smart Exploitation of Pseudorange and Pseudorange-rate Error Characterization to Improve the PVT Solution," Proceedings of

the 32nd International Technical Meeting of the Satellite Division of The Institute of Navigation (ION GNSS+ 2019), Miami, Florida, September 2019, pp. 3959-3984. https://doi.org/10.33012/2019.17109

1.5 Organization of the dissertation

This PhD dissertation is organized as follows:

Chapter 1 introduces the context, motivations and the objective of the thesis, a description of the proposed solution to meet the objective, a list of the main contributions and a brief explanation of each chapter.

Chapter 2 contains an overview of GNSS technology. First, the fundamental GNSS operations required to calculate the user's position and velocity are introduced. These are followed by an illustration of the GNSS processing chain. GPS L1 C/A and Galileo E1 OS signal structures are described. The GNSS transmission channel is presented, including the transmitter and receiver Front End blocks and the propagation channel, with particular emphasis on the definition of the multipath environment. The transmission channel is finally exploited to define the transmitted and received signal mathematical models.

Chapter 3 presents the main characteristics of the receiver GNSS Signal Processing and Data Processing stages. Regarding the Signal Processing stage, a particular emphasis has been applied to the receiver tracking block functionalities and impairments. In the Data Processing stage, the measurement generation block, the measurement correction block and, finally, the navigation estimation block have been illustrated. The raw measurements are affected by unwanted errors where some of them are derived from the tracking stage. For this reason, the measurement correction block applies correction techniques to mitigate the impact of the errors. The final navigation estimation block contains the operations and the algorithms required for PVT estimation.

Chapter 0 establishes the impact of multipath on the receiver tracking stage, which is consequently translated in the multipath error component affecting the raw GNSS pseudorange and pseudorange rate measurements. Firstly, a simplified multipath environment model is presented. This is used to define the GNSS received signal model affected by multipath, further exploited to calculate the tracking error envelope due to the multipath error. Three different sections have been defined to describe the impact of multipath error on the Delay Lock Loop (DLL), Phase Lock Loop (PLL) and Frequency Lock Loop (FLL).

Chapter 5 addresses the multipath and thermal noise error component isolation, characterization and overbounding methodologies from GNSS pseudorange and pseudorange-rate measurements as well as the Line-of-Sight (LOS) and Non Line-of-Sight (NLOS) signal reception state classification methodology. The chapter starts with an overview of the multipath error estimation and mitigation techniques described in the state of the art. The state-of-the-art analysis is followed by the introduction of the multipath plus thermal noise isolation methodology followed by the characterization methodology, Gaussian overbounding methodology as well as the LOS and NLOS reception state classification.

Chapter 6 presents the experimental analysis conducted during this PhD work to test and to evaluate the proposed methodologies introduced in Chapter 5. The experimental work is based on a data campaign conducted during several days in the Toulouse city centre with a dynamic platform. The first section of the chapter is the data campaign description, followed by the results of the pseudorange and pseudorange-rate MN error isolation and characterization. The MN error model obtained in the previous section are exploited next to calculate the MN Gaussian error models. Finally, the pseudorange and pseudorange-rate MN error temporal correlations are calculated.

Chapter 7 addresses the innovative PVT estimator algorithms, based on the EKF structure, which exploits the models developed in the previous sections to improve the PVT estimation performance of a low-cost GNSS receiver, in the urban environment. Two different EKF structures are presented, the Standard EKF and the Time Differenced EKF structure. In the first section, the Standard EKF architecture is presented. The Standard EKF architecture exploits the MN Gaussian error Models and the LOS/NLOS discrimination threshold to provide improved PVT solutions; additionally, innovation filtering is also tested. In the second section, the Time Differenced EKF architecture is presented. Time Difference EKF architecture is a modification of the Standard EKF architecture which exploits the MN error temporal correlations to provide enhanced PVT estimations. The performances of the Standard and the Time Difference EKF are investigated in the last section.

Finally, **Chapter 8** summarizes the main comments and results obtained along this PhD thesis and lists the original contributions. Future works are then given to conclude the manuscript.

2 GNSS Architecture

In this second Chapter, a general description of the Global Navigation Satellite System (GNSS) is presented, focusing on the basic design and operations, with a particular emphasis on GPS and Galileo, for the reasons introduced in the previous Chapter. The definition of GNSS is provided by the International Civil Aviation Organization (ICAO) [11]; it refers to *a worldwide position and time determination system that includes one or more satellite constellations, aircraft receivers and system integrity monitoring, augmented as necessary to support the required navigation performance for the intended operation*. In this thesis, GNSS is used to refer to satellite navigation technology in the wider scope of all application domains, not restricted to aviation or to just one core constellation system (GPS, Galileo, GLONASS, Beidou).

GNSS core constellations have been developed by states or their governmental bodies including the United States of America (GPS), Russia (GLONASS), Europe (Galileo), China (Beidou), in accordance with the treaties set out in [11]. A satellite positioning and navigation system allows the user to determine its four-dimensional positioning and timing solution through the transmission of ranging signals by orbiting satellites, the so-called satellite constellation. To ensure the intended performance, the satellite navigation system also includes a ground control segment which communicates with the satellite constellations. As noted above, in this text, GNSS term has been used to identify uniquely the satellite navigation systems.

The core GNSS concept is based on the transmission of signals from satellite transmitters, to receivers. A receiver processes the signals emitted from multiple satellites on known trajectories to calculate the basic ranging observables and, finally, to determine the user position, velocity and time. These fundamental operations are introduced in section 2.1.

Several global satellite navigation systems are operational at the time of writing (i.e. GPS, GLONASS, Galileo, BeiDou). An overview of the GNSS infrastructure, including space, control, and user segments composition and the service description is proposed in section 2.2. In particular, this section focuses on the US and European GNSS, respectively GPS and Galileo. GPS and Galileo are the constellations used by the selected dual constellation receiver under test during the data campaign, Chapter 6.

The GNSS signal structure is described in section 2.3. Since the research work has targeted the performance of the low-cost, mass-market receivers, (Chapter 1), the analysis focuses only on standard single frequency GPS L1 Coarse/Acquisition (C/A) and Galileo E1 Open Service (OS) signals. Therefore, GPS L1 C/A and Galileo E1 OS signal architectures are briefly introduced in the same section 2.3.

Section 2.4 is devoted to the introduction of the transmission channel. The transmission channel is defined as the communication channel between transmitter and receiver; more specifically, between the digital signal generator block of the satellite and the signal processing block of the receiver. A particular emphasis has been addressed to describe the Multipath and Shadowing phenomenon, which are the cause of multipath errors focused in this work.

The mathematical model of the received GNSS signal is finally depicted in section 2.5, followed by the conclusions of the chapter in section 2.6.

2.1 GNSS Fundamentals

This first section provides an overview of the GNSS fundamental processes. In particular, two essential processes could be identified, the ranging process and the positioning process.

The ranging process generates basic ranging observables as a function of some parameters, namely the transmission and reception times (or frequencies) of the GNSS signal, resulting in the propagation time, the accumulated phase shift or the relative Doppler frequency. These basic observables are then used as inputs of a specific positioning technique to determine the user position, velocity and time.

A description of the basic ranging processes and of a simplified two-dimensional positioning technique are detailed in section 2.1.1. The positioning technique requires the definition of time and coordinate frame references as described in section 2.1.2. Finally, the mathematical models of the basic observables obtained processing GNSS transmitted signals using the ranging processes in section 2.1.1, have been introduced in section 2.1.3.

2.1.1 Ranging Process

The GNSS concept relies on determining ranging observables which provide measurements of the distance between the satellite and the receiver, albeit with the addition of a common but ambiguous clock offset due to the asynchronous nature of the clocks employed. By measuring this (pseudo)range from multiple emitters at known locations (at the determined transmission times), the receiver can finally determine its position.

In order to determine the emitter-to-receiver range, the user receiver (r) obtains the propagation time from the emitter at a known location (i). This propagation time is then multiplied by the speed of light to obtain an emitter-to-receiver distance offset by the clock bias [12] as detailed in section 2.1.1.1.

In the same way, the signal's carrier phase itself is used to obtain a measure of the distance between satellite and receiver. The phase variations of the transmitted signal during the transmission can be translated to the emitter-to-receiver distance multiplying the resulting phase measurement by the corresponding carrier wavelength. In addition to the common clock offset, such measurements also contain an additional ambiguous term which requires additional processing to resolve. The carrier phase measurement is described in section 2.1.1.2.

GNSS also provides the capability for determining user velocity. The velocity estimation is based on the calculation of the user-satellite relative velocity, projected along the line-of-sight between the user receiver and the satellite. This is usually retrieved from the relative Doppler frequency shifts, as illustrated in section 2.1.1.3.

2.1.1.1 Code-based Ranging Process

The first proposed ranging approach is based on the calculation of the transmitted signal propagation time. Supposing that the transmitter and the receiver are perfectly time-synchronized: the transmitter emits a continuous signal (modulated by the Pseudorandom noise (PRN) code as described in section 2.3) driven by the transmitter clock. The signal propagates firstly through free space and then the earth's atmosphere until being received, with a delay which is equal to the propagation time of the signal. Ideally, the range between them can be obtained by multiplying this value by the speed of the emitted electromagnetic wave (speed of light).

In the ideal case of satellite navigation with synchronization between emitters and receiver time references, at least three satellites are needed to determine the user position. However, an additional satellite is needed in the non-ideal case due to the asynchronization of satellite and receiver clocks, as explained in the following paragraphs.

A simplified example of two-dimensional (2D) positioning is now provided. The basic principle presented for the 2D case can be extended to the 3D case, where circles are generalised to spheres. Supposing the perfect synchronization between emitters and receivers, the emitter-to-receiver range defines the radius of a circle constructed around the emitter position, where the emitter is at the centre of the circle. Given two such circles, the user position will lie at one of the two intersections. This ambiguity could be removed using three emitters; the intersection between the three resultant circles identifies a unique point, which is equal to the user position, as shown in Figure 2-1. Alternatively, an approximate or previous position may be used to resolve the ambiguity. This technique is called trilateration. In the realistic 3D case, the intersection between the three spheres gives two different symmetric points, one of them close to the Earth surface, the other one in deep space. The receiver must be able to select the most realistic point.

However, GNSS is not designed to achieve synchronisation between the receiver and transmitter clocks. Therefore, the synchronisation error introduces an offset in the signal propagation time and, as a consequence, an error in the ranging measurements. In Figure 2-2 the timing offset are translated in a range error, determining a different radius represented by the dashed circle. The new radius corresponds to the emitter-to-receiver range affected by this uncertainty, which is called pseudorange (PSR), defined in section 2.1.3.1. The uncertain position estimation is represented by the area obtained connecting the points B, C and D. In effect, the system is underdetermined, the number of unknowns (four) exceeding the number of independent observables (three). This is resolved by using a minimum of four emitters.

Furthermore, the propagation delay in reality is affected by a series of additional delays, biases and errors, due to the transmitter and receiver device imperfections (section 3.2.1) and transmission channel unwanted effects (section 2.4).

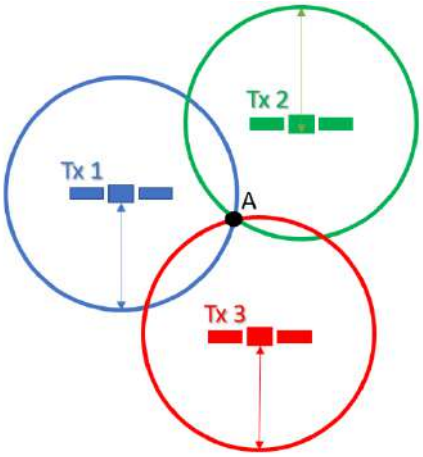

Figure 2-1 – GNSS-based Trilateration in two-dimensions

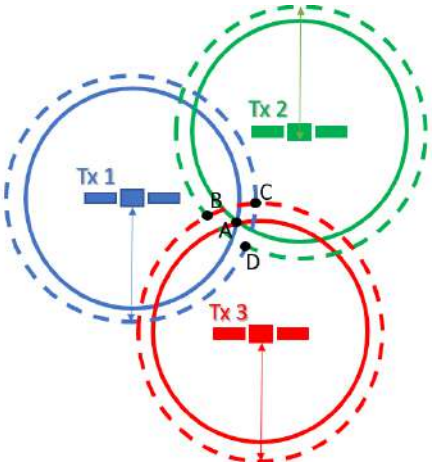

Figure 2-2 – Effect of receiver clock offset on GNSS-based Trilateration

2.1.1.2 Carrier phase-based Ranging Process

The second proposed ranging technique is based on the calculation of the transmitted carrier phase variations which can be translated in the transmitted signal propagation time. This technique is based on the calculation of the phase lag between emitter and receiver, accumulated during the signal propagation: the carrier phase being received at any instant by the receiver corresponds to the transmitted carrier phase with an additional phase lag. This lag corresponds to the propagation time because the carrier phase has linear variation with time. Hence the carrier phase and the time are proportional and can be appropriately translated to the emitter-to-receiver range. However, there exists in this measurement two type of ambiguities; the first one is related to the initial integer number of wavelengths, resulting from the fact that the receiver is only able to measure phase variations over time and not the absolute phase between satellite transmitter and receiver. The second one is related to the nature of the carrier phase measurements. Since the measurement is module 2 pi, the receiver is not able to differentiate between multiple 2 pi phase variations.

If the ambiguities can be resolved, requiring advanced techniques, the same positioning estimator described in section 2.1.1.1 can be applied to determine user position.

2.1.1.3 Doppler frequency-based Ranging-Rate Process

A method similar to 2.1.1.1 could be applied to estimate the user's velocity. Accurate velocity measurements are made by taking Doppler frequency offset measurements (derivative of carrier phase component) of the received signals. The Doppler frequency is directly a function of the relative motion between the satellite and the user receiver and can be directly translated to a velocity (or range-rate) component. Doppler frequency definition is introduced in section 2.1.3.2. Even in this case, the Doppler frequency is affected by uncertainties (synchronisation biases, atmospheric effects, multipath errors), hence, the receiver will estimate an apparent Doppler frequency, the so-called pseudorange-rate (PSR-R), derived in section 2.1.3.2.

2.1.2 Reference Frames

To ensure a consistent estimation, it is necessary to define the temporal and spatial reference frames.

The temporal reference is fundamental to GNSS, to place the satellites on the same time-scale, to compensate for the offset between the satellite clock bias and the receiver clock bias and to calculate the propagation delay, etc. A time reference is based on some periodic process able to characterize a regular time-flow. Several time references are currently in standard use, some of them are associated with periodic macro-events, like the Earth's rotation, cosmic mechanics or periodic micro-events, such as transitions between the energy levels in atomic oscillators.

The basic timing references, such as Universal Time (UT), Coordinated Universal Time (UTC) and finally the GNSS reference times, referenced to UTC, are defined in [13].

Furthermore, to formulate the mathematic models and the equations of the GNSS localization processes, it is fundamental to select a reference coordinate system in which the position of both the transmitter (satellite) and the receiver can be represented [14]. Therefore, it is typical to describe satellite and receiver dynamic states (position and velocity) in terms of position and velocity vectors measured in a Cartesian coordinate system (see Annex 10.1). The basic GNSS spatial reference frames, Eart-Centered Inertial Frame (ECI), Earth-Centred Earth-Fixed Frame (ECEF), Local Navigation Frame (LNF) and Body Frame (BF), are introduced in [15].

2.1.3 Basic Observables

This section provides the models of the ranging observables introduced in section 2.1.1. In particular, the pseudorange (PSR) measurements obtained from propagation delay and carrier phase lag are detailed in section 2.1.3.1, while the pseudorange-rate (PSR-R) measurements, obtained from the Doppler frequency measurement is depicted in section 2.1.3.2.

2.1.3.1 Range Observables

Figure 2-3 represents a simplified example of the user position and satellite position. The user's position coordinates $p_{r,x}, p_{r,y}, p_{r,z}$, defining the vector $\boldsymbol{p_r}$, are considered unknown and must be determined. The given satellite i, is located at coordinates p_x^i, p_y^i, p_z^i, corresponding to the position vector $\boldsymbol{p^i}$. The determination of $\boldsymbol{p^i}$ is usually computed in advance and considered a known parameter.

Referring to the example proposed in section 2.1.1.1, the radius of the circle in Figure 2-1 representing a given satellite-to-user vector is here referred to as $\|\boldsymbol{p_r^i}\|$. It is obtained from the vector difference between the satellite position vector, and the user position vector,

$$\boldsymbol{p_r^i}(t) = \boldsymbol{p^i}(t) - \boldsymbol{p_r}(t) \qquad 2\text{-}1$$

Thus, the amplitude of 2-1, denoted R^i, is required in order to determine the unknown $\boldsymbol{p_r}$:

$$R^i = \|\boldsymbol{p_r^i}\| = \sqrt{\left(p_x^i - p_{r,x}\right)^2 + \left(p_y^i - p_{r,y}\right)^2 + \left(p_z^i - p_{r,z}\right)^2} \qquad 2\text{-}2$$

The GNSS signal is efficiently designed to determine R^i; the signal architecture is based on three main components: the signal carrier, the navigation data, and a specific ranging code for each satellite; the details of the generic GNSS signal structure are presented in section 2.3.

The ranging code is used to derive the propagation time, in this case, we talk about code-based ranging. Also, carrier phase could be used to retrieve the propagation delay between satellite and receiver. In a similar way, we talk about carrier-based ranging.

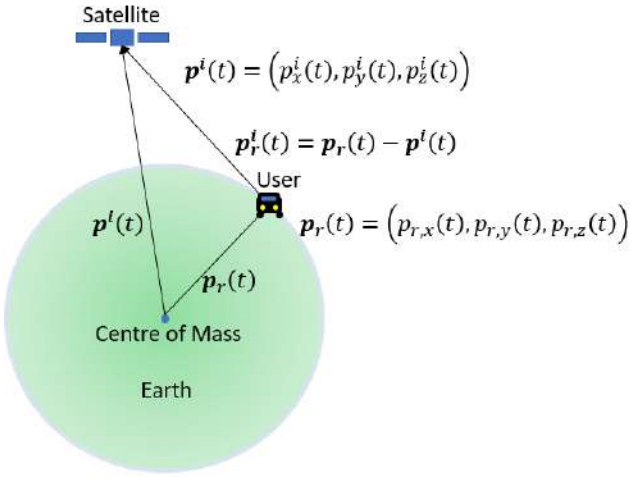

Figure 2-3 – ECI position vectors representation

The ranging codes allow the users to compute the time of arrival, t_r, while the transmitted time, t^i, is retrieved from the navigation data. The difference between t_r and t^i, gives the propagation delay, τ_r^i. Multiplying τ_r^i by the speed of light, c, the satellite-to-user pseudorange can be finally obtained:

$$R^i = (t_r - t^i) \cdot c = \tau_r^i \cdot c \tag{2-3}$$

The observables analysed so far do not take into account the unwanted errors. Indeed, in the real case, there exists a clock bias between the transmitter and the receiver $b_r^i = \Delta t \cdot c$, and the transmitted signal is subject to delays and distortions when passing through the transmission channel. The receiver range measurement is finally modelled as a pseudorange (PSR), ρ^i,

$$\rho^i = R^i + b_r^i + \varepsilon_\rho^i \tag{2-4}$$

where the PSR range error, ε_ρ^i, is equal to the overall code ranging error affecting the measurement.

Besides the code, the carrier phase is used to measure the distance between satellite and receiver [12]. However, in harsh environment, the integer ambiguity resolution can be only solved by introducing complex methodologies due to the high number of impairments, which is not in line with the scope of this project. Therefore, the carrier phase measurements will not be exploited in this work.

2.1.3.2 Doppler frequency-based range-rate

The simplified picture is illustrated in Figure 2-4. In this case, the user's velocity vector, $\dot{\boldsymbol{p}}_{\boldsymbol{r}} = \left(\dot{p}_{r,x}, \dot{p}_{r,y}, \dot{p}_{r,z}\right)$, is considered unknown, while the satellite's velocity vector, $\dot{\boldsymbol{p}}^{\boldsymbol{i}} = \left(\dot{p}_x^i, \dot{p}_y^i, \dot{p}_z^i\right)$, is computed in advance. GNSS receivers determine the user-satellite relative velocity, $\dot{\boldsymbol{p}}_{\boldsymbol{r}}^{\boldsymbol{i}}$, projected along the line-of-sight between the receiver and the satellite from the received signal by calculating the Doppler frequency. The Doppler frequency is comprised of contributions from satellite and receiver motion, and can be written in terms of transmitter and receiver velocity, (derivative of the satellite and receiver positions) as:

$$f_D(t) = \frac{1}{\lambda}\frac{d}{dt}\left|\boldsymbol{p_r}(t) - \boldsymbol{p^i}(t)\right| \tag{2-5}$$

Developing 2-5, it is obtained:

$$\frac{d}{dt}\left|\boldsymbol{p_r}(t) - \boldsymbol{p^i}(t)\right| = \\ = \frac{\left(p_{r,x}(t) - p_x^i(t)\right)\left(\dot{p}_{r,x}(t) - \dot{p}_x^i(t)\right)}{R^i} + \frac{\left(p_{r,y}(t) - p_y^i(t)\right)\left(\dot{p}_{r,y}(t) - \dot{p}_y^i(t)\right)}{R^i} + \frac{\left(p_{r,z}(t) - p_z^i(t)\right)\left(\dot{p}_{r,z}(t) - \dot{p}_z^i(t)\right)}{R^i} \tag{2-6}$$

The resulting equation is given by:

$$\left|\dot{\boldsymbol{p}}_{\boldsymbol{r}}^{\boldsymbol{i}}(t)\right| = \frac{d}{dt}\left|\boldsymbol{p_r}(t) - \boldsymbol{p^i}(t)\right| = \dot{\boldsymbol{p}}_{\boldsymbol{r}}(t) \cdot \boldsymbol{u_r^i}(t) - \dot{\boldsymbol{p}}^{\boldsymbol{i}}(t) \cdot \boldsymbol{u_r^i}(t) \tag{2-7}$$

The Doppler frequency due to the relative motion between the satellite and the receiver, f_D, could be finally written as:

$$f_D = \frac{1}{\lambda}\left(\dot{\boldsymbol{p}}_{\boldsymbol{r}}(t) \cdot \boldsymbol{u}_{\boldsymbol{r}}^{\boldsymbol{i}}(t)\right) - \frac{1}{\lambda}\left(\dot{\boldsymbol{p}}^{\boldsymbol{i}}(t) \cdot \boldsymbol{u}_{\boldsymbol{r}}^{\boldsymbol{i}}(t)\right) \quad 2\text{-}8$$

The range-rate measurement could be determined from the Doppler frequency multiplying the wavelength value:

$$\dot{R}^i = \lambda \cdot f_D \quad 2\text{-}9$$

However, the real Doppler frequency measurement is affected by satellite-to-receiver synchronization drift, $\dot{b}_r^i$,and unwanted effects of transmitted signal in the transmission channel, identified by the overall error $\varepsilon_{\dot{\rho}}$. Therefore, the real receiver measurement is the so-called pseudorange-rate measurement and is modelled as follows:

$$\dot{\rho} = \dot{R}^i + \dot{b}_r^i + \varepsilon_{\dot{\rho}} \quad 2\text{-}10$$

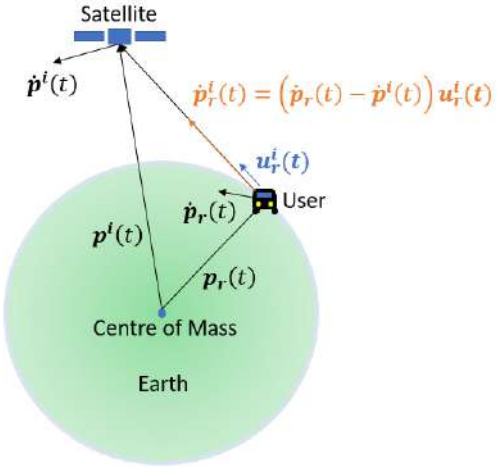

Figure 2-4 – ECI velocity vectors representation

2.2 GNSS systems overview

The GNSS technologies are composed of several components to ensure the basic processes described in the previous section. As already stated, several GNSS are operational at the time of writing, with different system design characteristics. The fully operational GNSS systems are: the Global Positioning System (GPS) developed by the USA and the Russian system Global Navigation Satellite System (GLONASS). At the time of writing, further satellite navigation systems under deployment are: the European Galileo, BeiDou, the Chinese Global Navigation system, and two Regional systems, QZSS form Japan and IRNSS from India.

The GPS (Global Positioning System) is the satellite-based navigation system developed by the U.S. Department of Defense under the NAVSTAR program launched in 1973. GPS was declared fully operational in June of 1995 [12].

The Galileo is the European Global Navigation Satellite System. It has been designed by the European Space Agency (ESA), it is under development and operated by the European Union Agency for the Space Programme (EUSPA) [12].

A typical GNSS implementation is composed of three segments, as described in Figure 2-5: the space segment, the control segment and the user segment. The space segment is made up of a constellation of satellites carrying a GNSS transmitter responsible of generating and broadcasting the ranging signal. The control segment tracks and monitors each satellite and uploads the information and the corrections to be broadcasted, in order to ensure the correct performances of the system. Finally, the user segment is composed by the GNSS receivers which exploits the transmitted GNSS signals to determine their PVT solution. The signal is transmitted from the space segment to the user/control segment through the propagation channel.

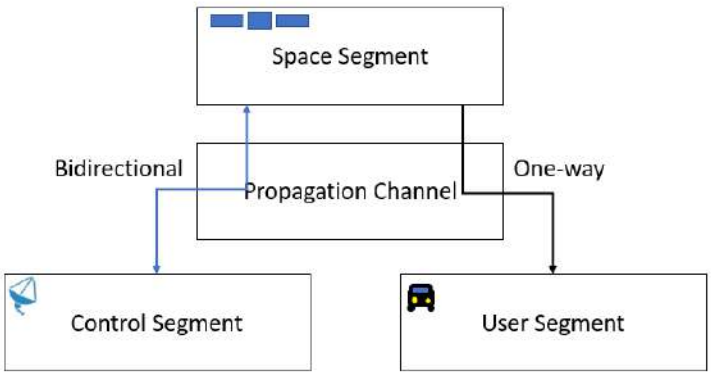

Figure 2-5 – GNSS Segments

The propagation channel includes any media and devices inside which the signal travels between the transmitter and the receiver. This is the central block of the transmission channel, as illustrated in Figure 2-6, which includes also some part of the transmitter and receiver hardware, in particular the transmitter and receiver Radio Frequency Front End and Antenna. The transmission channel is defined and applied to obtain a mathematical model of the GNSS signal transmission. More details on the transmission channel are provided in section 2.4.

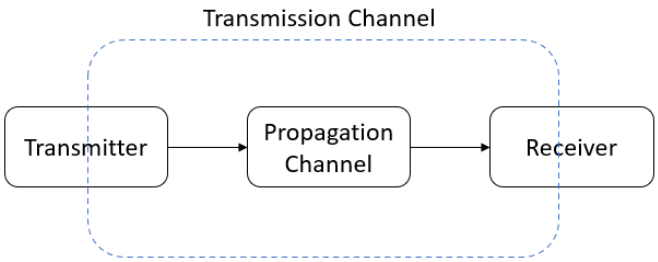

Figure 2-6 – Transmission channel decomposition relative to the perturbation effects

The Space, Control and User segments are described in 2.2.1, 2.2.2 and 2.2.3, respectively, focusing on two specific GNSS constellations, GPS and Galileo. This choice is related to the goal of this work, which is to provide advanced PVT estimation solutions for single frequency low-cost receivers in the urban environment. The low availability of satellites in the urban environment leads to the choice of operate with more than one constellation at the same time. GPS and Galileo constellations have high signal-in-space interoperability with, for example, identical centre frequencies of interoperable designed signals [9].

2.2.1 The Space Segment

The GNSS space segments of the core GNSS systems (GPS, Galileo, Beidou) are formed by satellite constellations with enough satellites to ensure that user will have at least four satellites in view simultaneously from any point on Earth's surface at any time in order to determine the user's position. The main functions of the space segment are:

- to generate and transmit code signals modulated onto the carrier wave;
- to store and broadcast (also modulated onto the carrier wave) the navigation message uploaded by the control segment.

The signal generation and transmission are carried by the transmitter, installed onboard of the satellite. An overview of the transmitter design is presented next. The structure of the transmitter is synthetized in Figure 2-7. Firstly, it generates the specific digital components, such as the ranging code, then, the digital modulated baseband signal composed by the materialization of the ranging code, the navigation data component and the carrier phase component are converted to an analog RF signal at the desired carrier frequency by the Radio Frequency Front-End. The analog RF modulated signal is then emitted via the transmitter antenna. The transmitter antenna is modelled as a source that emits the GNSS signal with a right-hand circular polarization (RHCP) [12].

The detailed model of the transmitted signal is provided in section 2.5.1, after introducing the GNSS Signal Structure in section 2.3.

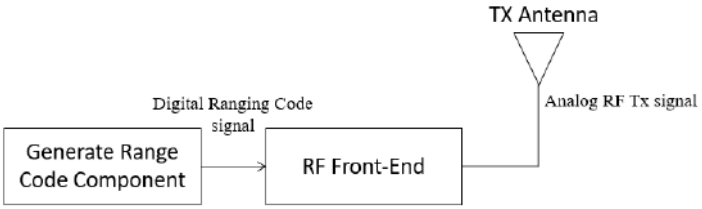

Figure 2-7 – GNSS Transmitter Structure blocks

The satellite broadcasts ultra-high frequency (UHF) signals in the L band (frequency range from 1 to 2 GHz). Firstly, the transmitter antenna is designed to completely illuminate a specific Earth hemisphere with a quasi-constant signal power [16]. Therefore, it can be assumed that the antenna would always be pointing towards the centre of the Earth and with off-boresight angles between 0 degrees, (satellite in the receiver's zenith), and roughly 14 degrees, (satellite at the receiver's horizon). These transmissions are driven by highly stable atomic clocks onboard the satellites. Moreover, all the satellites have some mechanisms to follow the required path (orbit), to communicate with the Control Segment and to broadcast the signals over the Earth [13]. The GPS constellation and Galileo Constellation details are presented in [12], [13].

2.2.2 The Control Segment

The Control Segment is based on several ground stations responsible for the monitoring and reliability of the overall constellation [12]. The Control Segment is designed and organized by the different entities in charge of the development of the different GNSS programs. Therefore, it is not possible to define a standard of the Control Segment shared by different GNSS since it should be defined individually. The text proposes to the reader the overview of GPS and Galileo Control Segments. The GPS and Galileo control segment are presented in [12], [13].

2.2.3 The User Segment

The User segment is composed of the GNSS receiver units. Their main function is to receive GNSS signals, determine observables (measurements), solve the navigation equations in order to estimate the desired states such as position, velocity or time coordinates. In some specific cases additional functions may be performed by the receiver, such as integrity monitoring, outlier rejection and/or mitigation. An overview of the basic blocks composing a generic receiver architecture for mass market receivers, focus of this PhD work, is described in section 2.2.3.1. The receiver applies mainly two types of positioning method, Standalone Positioning (SA) and Differential Positioning. Standalone Positioning provides solutions with lower accuracy with respect to receiver implementing Differential, as summarized in section 2.2.3.2.

2.2.3.1 Receiver Architecture

The GNSS receiver is the unit component composing the GNSS user segment, section 2.2.3. The GNSS receiver's goal is to receive the GNSS signals transmitted by the satellite constellations, and process them in order to determine the receiver position, velocity and time. The high-level block diagram representation of a generic GNSS receiver architecture is illustrated in Figure 2-8.

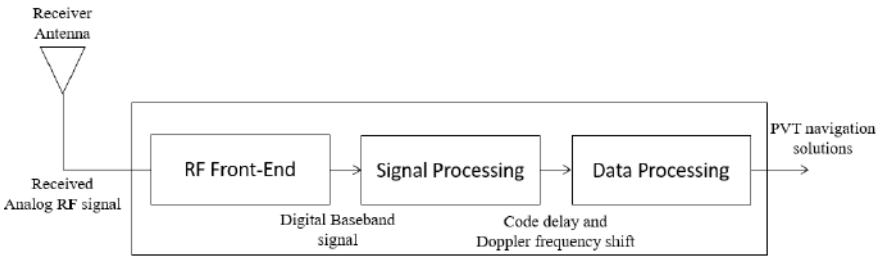

Figure 2-8 – Receiver Processing Architecture

The basic receiver's design is characterized by three sequential stages:

- the Analog Radio Frequency Front-End (RFFE), comprising also the receiver antenna, which is presented in section 2.4.2,
- the Signal Processing (SP), descried in section 3.1,
- the Data Processing (DP), depicted in section 3.2.

The RFFE is in charge of converting the L1/E1 analog signal captured from the receiver antenna, into an Intermediate Frequency (IF) digital copy of the signal. This operation allows the digital processing of the received signal, applied in the following stage.

The SP block process the digital IF by acquiring the basic observables, such as propagation time, phase shift and Doppler frequency, and by finely estimating them (tracking), as well as by demodulating the received signal to extract the navigation message. The basic observables and the demodulated navigation data are used in the next stage to compute the PSR and PSR-R measurements.

The DP block is in charge of generating the raw PSR and PSR-R measurements from the outputs of the SP block, then correcting them to obtain more accurate measurements which are finally used to compute the navigation solution.

2.2.3.2 GNSS Positioning Techniques

Standalone (SA) positioning is the standard GNSS technique. The receiver processes the single frequency transmitted signal from the available satellites from one or multiple GNSS constellations and provides an estimation of the user position, velocity and time. The low-cost receiver usually employs Standalone positioning [13].

Differential positioning is a technique which enhances the Standalone Positioning through the use of additional information, applying a differential approach. Additional information could be broadcasted by a network of ground-based reference stations, or just available information obtained from multi-frequency receivers. There are several differential GNSS techniques exploiting the information introduced above, such as the Differential GNSS (DGNSS), the Real Time Kinematics (RTK) and the Precise Point Positioning (PPP) [13].

DGNSS technique exploits only the presence of the reference stations to correct the user receiver solutions. The position of reference station position is accurately known. The reference station broadcasts corrections to the user receiver to be applied to the specific PSR measurement. The RTK technique exploits reference station corrections and, in addition, applies a difference between code and carrier phase measurements from the GNSS constellations [13]. Exploiting carrier phase measurements enables higher accuracy positioning, on the cm-level order. However, to exploit the carrier phase measurements the carrier phase ambiguity parameters must be resolved. The PPP technique exploits precise GNSS orbits and clocks broadcasted in real-time by a PPP service provider, and dual-frequency receiver measurements. If the precise satellite positions and clocks are applied for a dual-frequency GNSS receiver, PPP can provide a positioning accuracy at the centimetre/decimetre-level [13].

2.3 Signal Structure

Previous sections defined the fundamental GNSS operations and the overview of the GNSS segments. The fundamental element used by GNSS to provide the demanded services is the transmitted signal. Indeed, the transmitted signal is processed by GNSS receiver to determine first the PSR/PSR-R observables and, from them, the user PVT solution. Indeed, the GNSS signal is designed to allow the receiver to estimate the basic observables, as introduced in section 2.1.3.

GNSS satellites continuously broadcast navigation signals in several frequency sub-bands, inside the two specific bands designed for Radionavigation Satellite Services (RNSS), of the L band (from 1 to 2 GHz) allocated and coordinated by the International Telecommunication Union (ITU). Detailed information can be found in [12], [13].

The signals of interest in this work, namely GPS Coarse/Acquisition and Galileo Open Service are transmitted, respectively, in the L1 and E1 bands, which share the same central frequency, equal to 1575.42 MHz, enabling the use of the same antenna, RF front-end to simultaneously process the GPS L1C/A and Galileo E1 OS signals. GPS Coarse/Acquisition is used to provide the Standard Positioning Service as a single frequency service, transmitted only in L1. Galileo E1 OS signal modulation is used to provide an equivalent Standard Positioning Service with respect GPS, for the Galileo system.

The generic GNSS signal structure is presented in section 2.3.1. Therefore, a brief summary of the GPS L1C/A and of the Galileo E1 OS signal structure are given in section 2.3.2 and 2.3.3 respectively. A comparison between GPS L1 C/A and Galileo E1 OS is finally provided in section 2.3.4.

2.3.1 GNSS Generic signal structure

The design of GNSS signals has several goals; first of all, it is used to deliver the useful navigation message from the satellites to the user receivers sharing the same medium for transmission, with a convenient data rate; second it is used to enable accurate ranging computation for the user receivers within a range of reception conditions. Moreover, the signal design is fundamental for achieving protection against data errors, acquisition in harsh environments, mitigation of multipath, mitigation of atmospheric errors, security, anti-jamming/spoofing etc.

In order to fulfil the first requirement, the transmit signal is modulated by a navigation signal, which is used to transmit the navigation message. The components of the navigation message are described in the final part of this section. In order to transmit the navigation signals sharing the same medium of transmission, a multiple access technique is used. Two types of multiple access techniques are currently used in GNSS: Frequency Division Multiple Access (FDMA) and Code Division Multiple Access (CDMA). In FDMA, all satellites transmit the same signal in dedicated carrier frequencies, while in CDMA all satellites transmit different (dedicated) signals in the same carrier frequency, differentiated by a specific transmitted code, each one assigned to the corresponding satellite. In GPS and GALILEO, satellites transmit their signals over the same physical medium in the L-band by employing CDMA. The receiver is able to differentiate among the different satellites transmitting at the same carrier frequency. In CDMA, therefore, the number of transmitters is limited by the number of applied codes and, also, by the cross-correlation properties of the codes, which should be always close to zero. According to this technique, the signal requirements are:

- each satellite signal is composed by a carrier signal transmitted on specific carrier frequency;
- each carrier signal is modulated by a code which is independent from the transmitted data;
- each signal is also modulated by the specific data to be transmitted.

The second objective is also fulfilled by the introduction of CDMA technique which requires the implementation of Direct Sequence Spread Spectrum (DS-SS) signals. The DSSS is a spread spectrum transmission technique which spreads out the original signal bandwidth over a wider bandwidth, applying the so-called spreading codes, or Pseudorandom Noise (PRN) codes. Therefore, if the PRN codes assigned to the different users have good isolation properties among themselves (cross-correlation properties), CDMA technique can be implemented. The introduction of a PRN code means that the required navigation data signal is multiplied with the PRN code signal before being transmitted by the user. The resulting signal has thus a higher data rate than the data itself. The spreading code is a sequence of bits, or so-called chips, which are much shorter than the bits of the transmitted

data component, the so-called information bit. The modified baseband data stream is then modulated onto a carrier component.

As stated before, due to the application of DS-SS technique the overall signal is spread over a much wider bandwidth than if the initial navigation data had been simply modulated onto the carrier. This characteristic offers several advantages. It offers more accurate ranging, less interference, and increased security. However, spreading the spectral density of the signal implies a higher sampling rate at the receiver, with the consequent increase of power consumption, as well as requiring the de-spreading of the signal in order to exploit all its power, which can be difficult to achieve in harsh reception conditions.

Finally, the main signal components defining the transmitted signal are described as follows:

- The carrier component: it is a Radio Frequency sinusoidal signal generated at the desired frequency;
- PRN signal, $c(t)$: it is the materialization of the ranging code digital sequences; it allows the fine estimation of the time of arrival, t_r, (to know the pseudo range you also need information about the transmitted time, which is not provide by the PRN signal);
- The navigation data, $d(t)$: it is a data binary-coded message which goal and content have been introduced below.

The navigation component, $d(t)$, is used to transmit the navigation message. The navigation message contains the necessary information to allow users to perform positioning when this information is combined with the processing of ranging signals. In particular, it contains:

- the ephemeris parameters, needed to compute the satellite coordinates with sufficient accuracy;
- satellite health status;
- the time parameters and satellite clock corrections, which are used to estimate the satellite clock offset with respect to the GPS reference time frame;
- the service parameters and satellite health information;
- the ionosphere parameters, used to make ionosphere corrections for single-frequency receivers;
- the almanac, used to compute the position of the unacquired satellites in the constellation with a reduced accuracy with respect to the position calculated from the ephemeris, aids the signal acquisition undertaken by the receiver;
- the time of transmission.

Hence, the generic GNSS modulated signal, $s_{RF}(t)$, emitted by the satellite, transmitted in the RF band at a specific frequency f_{RF}, can be written as:

$$s_{RF}(t) = Re\{s_{l,RF}(t) \cdot e^{j(2\pi f_{RF}t)}\} = Re\{A \cdot d(t) \cdot c(t) \cdot e^{j(2\pi f_{RF}t)}\} \quad 2\text{-}11$$

$$s_{l,RF}(t) = A \cdot d(t) \cdot c(t) \quad 2\text{-}12$$

where:

- $s_{l,RF}(t)$ is the transmitted generic complex envelope GNSS signal;
- A denotes the signal amplitude;
- $c(t)$ is the ranging code component,
- $d(t)$ denotes the navigation data component;
- f_{RF} represents the signal's carrier frequency.

2.3.2 GPS L1 C/A

The design of the transmitted GPS L1 C/A signals comprise three signal components, the signal carrier, the navigation data $d(t)$ and the materialized Coarse/Acquisition (C/A) code $c_{C/A}(t)$.

The signal carrier is centred at $f_{L1} = 1575.42$ MHz and it is used to transmit the Binary Phase Shift Keying (BPSK) modulated data signal. The navigation data consist of a stream of data bits (± 1) and it is modulated over the carrier at 50 bits per second. Each bit has duration of 20 ms. The carrier signal component is also modulated by the materialized C/A code, $c_{C/A}(t)$. The C/A code is a PRN code, designed from a 37-sequences Gold code family with 1023-chip length by using feedback shift register [17]. The specific PRN codes are chosen for their autocorrelation characteristics.

The overall GPS L1 C/A signal may finally be expressed as:

$$s_{L1,C/A}(t) = \sqrt{2P_{L1,C/A}}\, c_{C/A}(t) d(t) \cos\left(2\pi f_{L_1} t\right) \quad 2\text{-}13$$

where:

- $P_{C/A} = A_{C/A}^2/2$, is the transmitted GPS C/A signal power, where the symbol $A_{C/A}$ denotes the signal amplitude;
- $c_{C/A}(t)$, is the materialized C/A PRN code sequence or PRN signal;
- $d(t)$, is the navigation data sequence;
- f_{L1} is the L1 band carrier frequency, expressed in Hz;

The C/A PRN code design is presented in [18],[19]. The overall PRN code has a period of 1023 chips transmitted at chipping frequency, f_c, equal to 1.023 Mchips/s. Therefore, the PRN period, also called PRN code period, T_{PRN}, is equal to 1 ms, which means that the code is repeated continuously every 1 ms.

From a mathematical point of view, the PRN signal could be seen as a sequence of discrete $c = \pm 1$ values, modulated by a Not Return to Zero (NRZ) rectangular shaping waveform, $m(t)$ of one chip period, T_c, as described in 2-14, and repeated continuously in time.

$$c_{C/A}(t) = \sum_{i=-\infty}^{+\infty} \left(\sum_{k=0}^{1022} c_k \cdot m(t - kT_c) \right) * \delta(t - i1023T_c) \quad 2\text{-}14$$

where:

- c_k is the discrete value of the chip;
- m is the rectangular shaping waveform;
- T_c is the chip period equal to $\frac{1}{1023}$ [ms];
- $\delta(\dots)$ is the Dirac's delta.

Additionally, $c_{C/A}(t)$ signal could also be described as the convolution between the shaping waveform and the PRN code signal before materialization, $c_I(t)$ as shown below. This mathematical modelling is very useful to calculate the autocorrelation and Power Spectral Density (PSD) of the PRN code signal (after materialization).

$$c_{C/A}(t) = c_I(t) * m(t) \quad 2\text{-}15$$

$$c_I(t) = \sum_{i=-\infty}^{+\infty} \left(\sum_{k=0}^{1022} c_k \cdot \delta(t - kT_c) \right) * \delta(t - i1023T_c) \quad 2\text{-}16$$

The autocorrelation of the PRN sequence signal (materialization of the PRN code) depends on the assumptions on the PRN code properties. The PRN code can be seen as a deterministic periodic signal with period T_{PRN} (actual signal). In this case, the correlation is, as seen earlier:

$$R_c(\tau) = \frac{1}{T} \int_T c(t) c^*(t - \tau) dt \quad 2\text{-}17$$

Assuming that the C/A code can be seen as an infinite random binary sequence with random properties, the C/A code autocorrelation should be computed as an expectation since $c_{C/A}(t)$ is seen as a random signal (PRN code can be seen as a random binary sequence with infinite length).

$$R_c(\tau) = E\{c(t) c^*(t - \tau)\} \quad 2\text{-}18$$

This assumption allows a simplification of the models. In this case, the PRN code signal autocorrelation is equal to the shaping waveform autocorrelation and does not depend on $c_I(t)$. Intuitively, in this specific case, the convolution between a square chip of duration T_c and itself is equal to a triangle large $2T_c$. and can be approximated by the triangle function expressed as:

$$R_c(\tau) = R_m(\tau) = \begin{cases} 1 - \tau/T_c & if\ -T_c \le \tau \le T_c \\ 0 & \text{elsewhere} \end{cases} \quad 2\text{-}19$$

With these simplifications, the L1 C/A PSD can be approximated as the Fourier transform of the autocorrelation function expressed in 2-19. Therefore, the GPS C/A PSD can be approximated as:

$$S_m(f) = \frac{1}{f_c}\left(\frac{\sin\left(\frac{\pi f}{f_c}\right)}{\left(\frac{\pi f}{f_c}\right)}\right)^2 \quad 2\text{-}20$$

where f_c is the chipping frequency.

In reality, the PRN code is finite and periodic. Therefore, it will be taken into account that the autocorrelation of the PRN code signal after shaping is not a perfect triangle: does not only depend on $m(t)$ but also on $c_I(t)$ as shown below. Note that customizing this expression with $R_{c_I}(\tau) = \delta(\tau)$, expression 2-21 and 2-19 become the same ($R_{c_I}(\tau)$ is only equal to $\delta(\tau)$ for infinite code length),

$$R_c(\tau) = R_{c_I}(\tau) * R_m(\tau) \quad 2\text{-}21$$

The PSD can be calculated from the Fourier transform of 2.17. The resulting PSD is a line spectrum, where the lines are separated by the inverse of the PRN code period, T_{PRN}, because $R_{c_I}(\tau)$ is periodic due to the periodic nature of the PRN code signal before materialization.

$$S_C(f) = S_{C_I}(f)S_m(f) \quad 2\text{-}22$$

The normalized approximated code autocorrelation function and PSD of the GPS L1 C/A signal are illustrated in Figure 2-9.

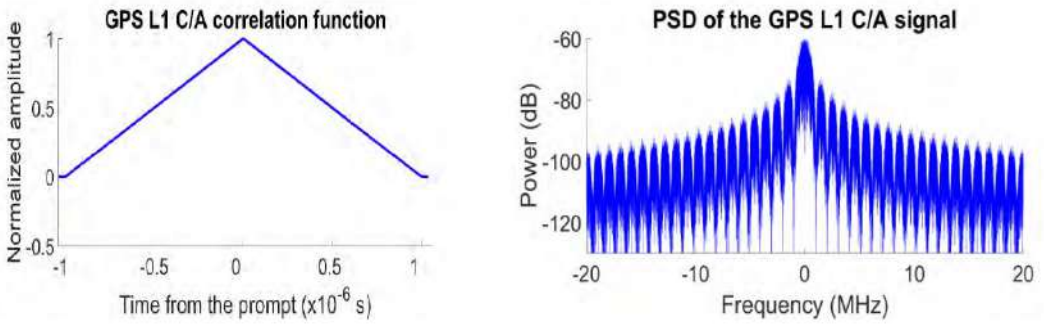

Figure 2-9 – Normalized code autocorrelation function (on the left) and normalized PSD (on the right) of the GPS L1C/A signal [20].

2.3.3 Galileo E1 OS

Galileo E1 OS signal is the Galileo counterpart of GPS L1 C/A signal. Moreover, it is designed to be compatible and interoperable with GPS L1 C/A, reducing the mutual interference between the two signals which are modulated over the same carrier frequency. Additionally, Galileo E1 OS uses a modernized signal structure in order to achieve better ranging performances with respect to GPS L1 C/A. The innovations consist of:

- *The introduction of a data-less pilot component*. This pilot component is synchronous with respect to the data component. The structure of the pilot component is similar to that of the data component; there are only the carrier component and the PRN component. Also, the PRN code used by the pilot component is orthogonal to the relative PRN code of the data component in order to minimize intra-interference.
- *The use of a different spreading code modulation*. While GPS L1 C/A uses Binary Phase Shift Key (BPSK) modulation, Galileo E1 OS uses Composite Binary Offset Carrier (CBOC) modulation. As it is

described in the following paragraphs, the Galileo PRN code is longer in terms of number of chips and thus, in terms of PRN code period since the chip rate is the same; therefore, applying the different spreading code modulation, the Galileo E1 OS signal Power Spectral Density (PSD) is different from the GPS L1 C/A PSD.

- *The use of higher data rate*, since the data bit duration is equal to the spreading code period.

The Galileo E1 OS signal is a composite signal that consists of two orthogonal different channels, the data component and the pilot component, modulating the same carrier component, centred at $f_{E1} = 1575.42$ MHz. As the name indicates, the data component is the component containing the transmitted data, $d_{E1-B}(t)$, which contains the navigation message. The time duration of a symbol is 4ms, five time smaller than the GPS L1 C/A navigation symbol duration, 20 ms, and is equal to a PRN code duration.

The E1 Open Service data component is obtained with the modulation of the navigation data and the materialized ranging code. As previously said, GPS L1 C/A and Galileo E1 signals are modulated over the same central carrier frequency, but, unlike GPS L1 C/A, Galileo E1 OS uses the so-called Binary Offset Carrier (BOC) modulation. BOC modulation can be used to minimize interference with BPSK signals sharing the same carrier frequency. It can also give better code tracking performance than a BPSK signal with the same spreading-code chipping rate. It is the result of the multiplication of the materialized squared PRN code, $c_{OS}(t)$, with a square wave sub-carrier denoted $sc_{BOC(m)}(t)$,

$$sc_{BOC(m)}(t) = \text{sign}(\sin(2\pi \cdot mf_0 \cdot t)) \qquad 2\text{-}23$$

which is mathematically obtained by taking the sign of a sine waveform of frequency mf_0, where $f_0 = 1.023$ MHz. Note that, although Galileo E1 OS uses sine waveforms to generate the square wave sub-carriers, they can also be generated from taking the sign of a cosine waveform. Galileo E1 OS signals use memory codes, which means that they cannot be obtained from a code generator algorithm and have to be stored in receiver memory. A family of 100 codes of length 4092 has been defined for Galileo.

The BOC signals are commonly referred to as $\text{BOC}(m,n)$, which is characterized by the sub-carrier frequency, f_{sc} and spreading chipping rate, f_c, where:

- m is an integer number representing the sub-carrier frequency in multiples of 1.023 MHz;
- n is an integer number representing the code chipping rate in multiples of 1.023 Mcps (Mchips per second).

Initially, the proposed Galileo E1 OS signal modulation was $\text{BOC}(1,1)$. However, following research studies an evolution of the BOC modulation that is compatible with the GPS L1 C/A signal, the so-called Multiplexed BOC modulation, $\text{MBOC}(m,1,k)$ was introduced. It is obtained by multiplexing a wideband signal, $\text{BOC}(m,1)$, with a narrow-band signal, $\text{BOC}(1,1)$, in such a way that k-th of the power is allocated, on average, to the high frequency component [21]. The actual implementation is the $\text{MBOC}(6,1,1/11)$. This modulation allows two different receiver signal processing operations:

- to process only the low-frequency component, for low-cost applications, such as the mass-market receivers;
- to use the high-frequency component, for high-accuracy applications.

There are several techniques used to obtain MBOC. The actual Galileo E1 OS signal implements a specific MBOC modulation, the Composite BOC $(\text{CBOC})(6,1,1/11)$, which adds or subtracts the $\text{BOC}(6,1)$ spreading symbols from the $\text{BOC}(1,1)$ [22].

Finally, the E1 Open Service data component is generated from the multiplexing of the navigation data, $d_{E1-B}(t)$ and the materialized squared ranging code $c_{E1-B}(t)$. Afterwards, they are modulated with the sub-carriers $sc_{E1-B,BOC(1,1)}(t)$ and $sc_{E1-B,BOC(6,1)}(t)$, respectively.

The E1 Open Service pilot component is new with respect GPS L1 C/A and corresponds to a signal component which is data-less. A data-less component is known to offer improved tracking capabilities. As a consequence, the receiver can track the pilot component while demodulating the data on the traditional data component. The pilot component is generated from the materialized squared ranging code $c_{E1-B}(t)$. Afterwards, they are modulated with the sub-carriers $sc_{E1-B,BOC(1,1)}(t)$ and $sc_{E1-B,BOC(6,1)}(t)$ in opposite phase, respectively.

Having defined the components of the Galileo E1 OS signal, the mathematical expression could be expressed:

$$s_{E1OS}(t) = \frac{1}{\sqrt{2}}[c_{E1-B}(t)d_{E1-B}(t)CBOC(6,1,1/11,'+') - c_{E1-C}(t)CBOC(6,1,1/11,'-')]\cos(2\pi f_{E1}t) \quad 2\text{-}24$$

where:

- Galileo E1 OS sub-carriers for the E1-B data and E1-C pilot channels, are respectively defined as the BOC subcarrier are equal to $sc_{BOC(X,1)} = \text{sign}\left(\sin\left(2\pi f_{sc,X}t\right)\right)$ where $f_{sc,X} = X \cdot 1.023 \cdot 10^{-6}$ chips/s;

Galileo E1 OS sub-carriers for the E1-B data and E1-C pilot channels, are respectively defined as:

- E1-B data: $\text{CBOC}(6,1,1/11,'+') = \sqrt{10/11}\, sc_{BOC(1,1)}(t) + \sqrt{1/11}\, sc_{BOC(6,1)}(t)$
- E1-C pilot: $\text{CBOC}(6,1,1/11,'-') = \sqrt{10/11}\, sc_{BOC(1,1)}(t) - \sqrt{1/11}\, sc_{BOC(6,1)}(t)$

2-25

For the E1-C (pilot) and E1-B (data) components, the $\text{CBOC}(6,1,1/11)$ autocorrelation function can be expressed by means of $\text{BOC}(1,1)$ and $\text{BOC}(6,1)$ autocorrelation and cross-correlation functions combination as [23]:

$$R_{CBOC(6,6,1/11,'+/-')}(t) = \frac{10}{11}R_{BOC(1,1)}(t) + \frac{1}{11}R_{BOC(6,1)}(t) \pm 2\,\frac{\sqrt{10}}{11}R_{BOC(1,1)/BOC(6,1)}(t) \quad 2\text{-}26$$

where the $'+/-'$ sign for the cross-correlation term refers to the E1-B (data) and E1-C (pilot) channels, respectively.

The normalized (unit power) power spectral density, neglecting the effects of band-limiting filters is equal to:

$$S_{CBOC(6,6,1/11,'+/-')}(f) = \frac{10}{11}S_{BOC(1,1)}(f) + \frac{1}{11}S_{BOC(6,1)}(f) \pm 2\,\frac{\sqrt{10}}{11}S_{BOC(1,1)/BOC(6,1)}(f) \quad 2\text{-}27$$

Figure 2-10 illustrates the normalized PSD and autocorrelation function of the Galileo E1-C signal for infinite PRN code sequences.

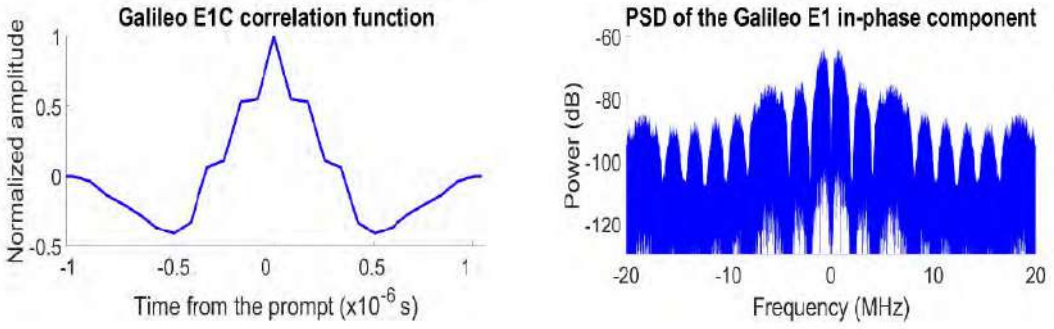

Figure 2-10 – Normalized code autocorrelation function (on the left) and normalized PSD (on the right) of the Galileo E1-C signal

2.3.4 Comparison

The comparison between the GPS L1 C/A and Galileo E1 OS normalized autocorrelation functions is provided in Figure 2-11.

It can be seen that the application of the BOC sub-carrier affects significantly the shape of the autocorrelation function of the GPS L1 C/A. In particular, the main peak of the Galileo autocorrelation function is much steeper. It can be assumed that a narrowed correlation peak can provides better tracking accuracy, therefore the modernized Galileo modulation will provide better performances.

However, a negative peak also appears at 0.5 chip, and the use of a CBOC sub-carrier creates also multiple local peaks. Therefore, the receiver acquisition/tracking operation based on the BOC signal is more sensitive to the dynamic stresses, increasing a risk of incorrect peak selection. Therefore, acquiring and tracking the correct peak can be very challenging, especially in the presence of noise and multipath [24].

The case of the correlation between a CBOC and a BOC(1,1) signal is also shown. The resulting correlation function looks like the autocorrelation function of the BOC(1,1), but with a slight reduction of the maximum amplitude equivalent to a loss of 0.41 dB in power due to the loss of the BOC(6,1) component.

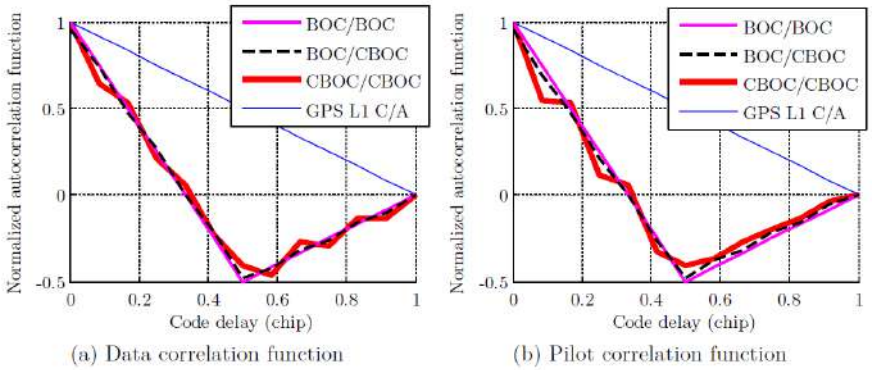

Figure 2-11 – Normalized correlation function shapes of Galileo and GPS L1 C/A ranging codes [25]

The comparison between the GPS L1 C/A and Galileo E1 OS signals PSDs is provided in Figure 2-12, including also the PSDs of BOC(1,1) and BOC(6,1) modulations. The effect of the BOC modulation is to split the spectrum of the spreading code and to create 2 main side-lobes located at $\pm mf_0$.

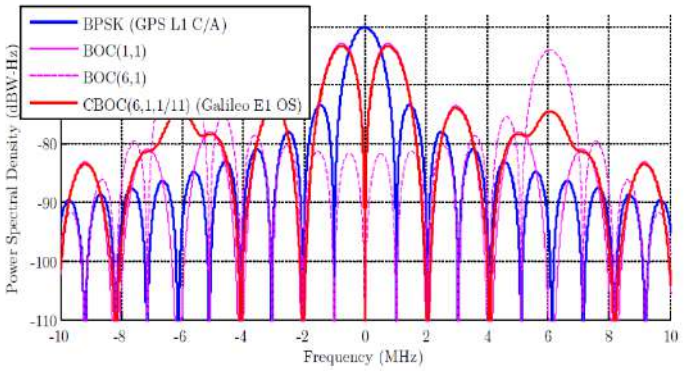

Figure 2-12 – Power Spectral Densities functions of GPS L1 C/A and Galileo E1 OS signals [25]

2.4 Transmission Channel

In this section, the transmission channel , which will be applied to define the mathematical model of the GNSS signal transmission, is described.

The transmission channel includes any media and devices inside which the signal travels between the digital signal generator block of the transmitter and the digital signal processing block of the receiver; thus, it includes the RF Front-End of the transmitter, the transmitter antenna, the propagation channel, the receiver antenna, and the RF Front-End of the receiver. Figure 2-13 illustrates the transmission channel. In the following subsections the different components of the transmission channel are described.

The transmitter model, including RF Front End (RFFE), is already introduced in section 2.2.1. It is in charge to generate the analog GNSS signal. Transmitter antenna emits the analog GNSS signal which travels through the propagation channel.

The propagation channel is the wireless propagation medium where the transmitted signal propagates in order to reach the receiver antenna (detailed in section 2.4.1). Receiver antenna captures the transmitted signal from the propagation channel and sends the resulting signal to the RFFE block. Finally, RFFE generates a digital copy of it (depicted in section 2.4.2).

The mathematical model of the transmission channel is finally presented in section 2.4.3. This is fundamental to express the received signal mathematical model, introduced in section 2.5.

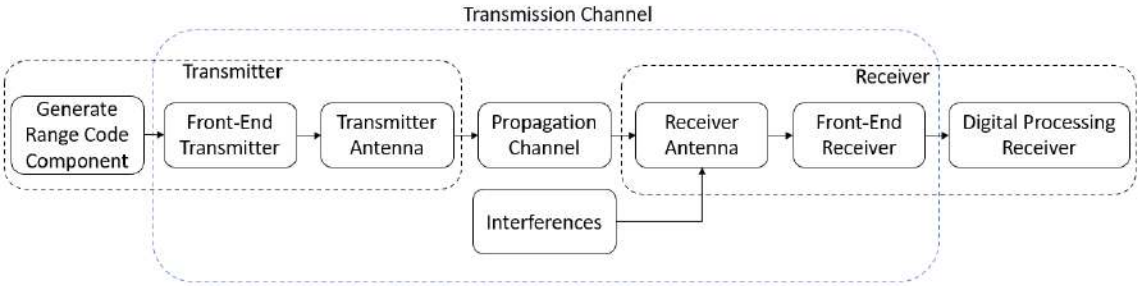

Figure 2-13 – Transmission channel decomposition relative to the perturbation effects

2.4.1 Propagation Channel

At the transmitter antenna output, from the satellite to the receiver antenna, the GNSS signal travels through a wireless medium, usually called propagation channel. The propagation channel block scheme is presented in Figure 2-14.

The transmitted signal is an electromagnetic wave which travels through the open free space before to reach the terrestrial atmosphere, composed by ionosphere, mesosphere, stratosphere and troposphere before reaching the receiver antenna. It must be pointed out that the neutral atmosphere includes the troposphere, stratosphere and mesosphere, but the dominant component is the troposphere, and therefore the name of the delay usually refers only to the troposphere, as tropospheric delay.

Once entered in the atmosphere, it is confronted with a number of natural propagation effects which may constitute sources of ranging error. Two different effects of the propagation media may be distinguished: atmospheric perturbations, and environmental perturbations due to the presence of objects around the receiver.

On one hand, concerning the atmospheric perturbations, from the point of view of signal delay, the atmosphere can be divided into two main components: the neutral atmosphere, simplified as troposphere section, which is the non-ionised and nondispersive section, and the ionosphere, which is the ionised and dispersive section, where the delay experienced by the signals depends on their frequency.

On the other hand, concerning the environmental perturbations, when the emitted signal has crossed the ionosphere and has travelled through the highest layers of troposphere, it is in the vicinity of the Earth surface. aeronautical and ground receivers now are able to capture the transmitted signal. However, before to be captured by the receiver antenna, the transmitted signal will interact with the objects surrounding it. While this interaction is reduced in the aviation receivers environment (e.g. planes, helicopters), for Ground receivers this interaction becomes one of the larger GNSS unwanted effects due to presence of a large amount of interacting objects.

In fact, when the incoming signal encounters an obstacle, the interaction between the two results in a new signal re-radiated from the obstacle. This principle is called electromagnetic scattering. Note that with this definition, scattering includes all such interaction phenomenon consisting of reflection, edge-diffraction and refraction. In the GNSS context, the fields scattered by obstacles surrounding the receiver, e.g. buildings, yield echo signals that are called multipath. As a consequence, the estimation of the propagation delay, carrier phase lag and Doppler frequency shift, between the satellite and the receiver may be degraded by these echoes. This phenomenon is called the multipath error.

The atmospheric effects are introduced in 2.4.1.1. Section 2.4.1.2 focuses on multipath phenomenon illustration. Multipath phenomenon description is largely developed being the main focus of the PhD work.

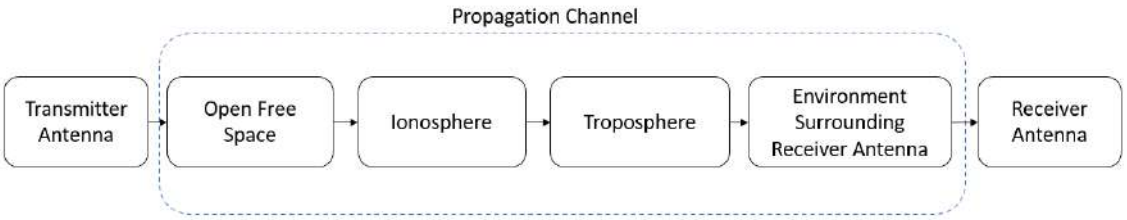

Figure 2-14 – Propagation Channel Block Scheme

2.4.1.1 Atmosphere

The first part of the section introduces the ionosphere impact, while the second part introduces the troposphere impact.

The ionosphere is the first layer of the Earth's atmosphere that the signal encounters when it is emitted by the satellite, and it goes from roughly 50 km to 1000 km above the Earth's surface. As its name implies, it is a partially ionised layer, as a result of solar X- and Extreme Ultraviolet (EUV) rays in the solar radiation and the incidence of charged particles. Therefore, the ionosphere layer is a negative ionized plasma containing free electrons for long periods of time before to be recombined with ions. The presence of free electrons depends on the gas molecules ionization due to the Sun's ultraviolet radiation. Since the number of electrons and the type of dispersion varies in time and space, the electron density in the ionosphere varies depending on these parameters. The GNSS signals propagation speed in the ionosphere depends on the electron density. The details are presented in [26]. The effect introduced by ionosphere is a signal delay in the time domain and a carrier phase advancement. These effects are caused by the introduction of a group delay on the electromagnetic wave with respect to propagation at the speed of light in a vacuum medium. The group delay is caused by the presence of free electrons in the path followed by the transmitted signal. The effects of ionosphere on the GNSS signals depend on the interval of time that the emitted signal travels into the ionosphere. The ionosphere is non-homogeneous. Its behaviour changes depending the position of the Earth's regions. Also, ionosphere behaviour changes depending on the time period (day, night, different seasons).

The troposphere is the section of the atmosphere closest to the Earth, and it goes from the surface to about 50 km. As it is in the ionosphere, the troposphere medium is refractive, but, unlike ionosphere, it is non-dispersive medium. The effect introduced by the troposphere is a signal delay in the time domain and a carrier phase delay, both delayed by the same amount. These effects are caused by the introduction of the variations in the propagation speed of the electromagnetic waves with respect to propagation at the speed of light in a vacuum medium. This is caused by the variations of temperature, pressure, and humidity in the path followed by the transmitted signal. The details are presented in [26]. The troposphere density affects the GNSS signal delay through refractions. The magnitude of the delay depends on the length of the path that the signal travels through the troposphere. The refraction effect in the troposphere depends on the density, as well as temperature, pressure and humidity of the mediums. The principal characteristic of the troposphere is that it is a non-dispersive medium (contrary to the ionosphere) for the electromagnetic signal with a frequency lower or equal to 15 GHz; therefore, the tropospheric effects are not frequency dependent for GNSS signals. Thus, the carrier phase and code measurements are affected by the same delay.

2.4.1.2 Multipath and Shadowing effects

The last part of the propagation channel is the section containing the obstacles encountered by the transmitted signal in the receiver surrounding affecting the received signal captured by the receiver antenna. In this section, in particular, two types of effects might be identified: multipath and shadowing, as represented in Figure 2-15.

The multipath (MP) phenomenon, section 2.4.1.2.1, relates to the generation of reflected and/or diffracted replicas of the direct (Line-of-Sight, LOS) signal due to the interaction between the LOS signal and the obstacles surrounding the receiver. When LOS signal and/or the unwanted MP echoes are captured by the receiver antenna, these last interfere with the LOS signal, causing a degradation of GNSS application's performances.

The shadowing effect, section 2.4.1.2.2, represents the partial or total (in this last case also known as blockage) attenuation of the direct path, typically introduced when the LOS path propagates through foliage or a structure.

The generic multipath effect influencing the GNSS receiver processing stage can be defined as a mutual combination of the shadowing and multipath phenomenon introduced above. Indeed, two different MP effect must be distinguished, the LOS MP and NLOS MP, section 2.4.1.2.3. The first is defined as the joint reception at the receiver's antenna of the satellite-to-receiver LOS transmitted signal and several MP echoes; the second is defined as the reception of the MP echoes while the LOS signal is completely attenuated.

The geometric model of the multipath environment is strictly dependent on the application of the GNSS receiver. Aeronautical, Drone, Open Space Ground, Urban Ground multipath environments are characterized by a different geometric model.

Since this work focuses on the micro mobility applications in urban environment, a detailed analysis of the geometric model of a generic urban environment, and a simplified version of it are presented in section 2.4.1.2.4 and 2.4.1.2.5.

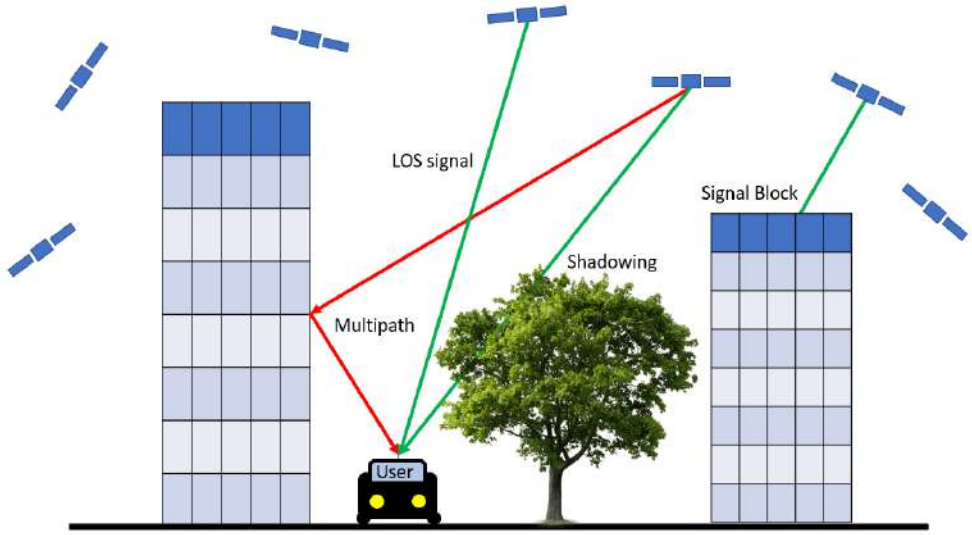

Figure 2-15 – Overview of a Reflected Multipath signal

2.4.1.2.1 Multipath effect

The multipath (MP) phenomenon is experienced in the final part of the propagation channel, where the transmitted signal usually interacts with the objects surrounding the GNSS receiver. This part of the propagation channel is usually called multipath environment. The MP phenomenon consists of the re-radiations of a distorted and delayed copy of the transmitted signal, (Line-of-Sight signal), obtained due to the electromagnetic scattering of the LOS signal when interacting with the surface of reflector's object. The multipath phenomenon is almost inevitable in most GNSS applications, since all kinds of possible reflectors surrounding the receiver are normally present, such as the earth's surface, buildings, or other objects.

The characteristics of the multipath reflections depend on two fundamental factors:

- the geometric model of the multipath environment, in which the geometric occurrence of the reflectors plays a major role;
- the physical characteristics of the electromagnetic scattering;

In this particular case, GNSS signals may be scattered by buildings, walls, vehicles, and the ground placed around the receiver's antenna, usually defining an artificial canyon for the user receivers. Moreover, glass, metal and wet surfaces, often constituting the surface of reflector objects, are particularly strong reflectors.

The physical characteristics of the MP echoes depend on the emitted signal properties and the material of the reflector object. Once the propagated signal reaches the reflector surface, different types of electromagnetic scattering can occur, depending on the material of the reflector object:

- Diffraction: this is defined as the bending of the electromagnetic signal around the corners of an obstacle.
- Refraction: this is defined as the change in direction of the electromagnetic signal passing from one medium to another or from a gradual change in the medium.

- Reflection: this is defined as the change in direction of the electromagnetic signal at an interface between two different media. Two different types of reflections can occur, depending on the material of the reflector object, the specular reflections, Figure 2-16 and diffuse reflections, Figure 2-17. In case of specular reflection, the reflection angle of reflected signal is equal to the incident angle. Diffuse reflection occurs when a ray incident on the surface is scattered at many angles rather than at just one angle as in the previous case. The power of the single specular reflected signal is higher than a single diffuse reflected one, which makes it more dangerous in the GNSS tracking stage rather than the reception of a diffuse reflection.

Figure 2-16 – Specular reflection

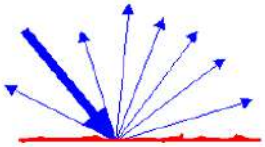

Figure 2-17 – Diffuse reflection

From the factors described above, the geometric model of the MP echo can be derived. This influences the characteristics of the multipath echo with respect to the LOS signal, which consist of:

- a power attenuation, characterized by the two factors:
  - the attenuation caused by the reflector object. To predict this effect requires knowledge about the material of the reflector, the incident angle of the reflection, and the polarization used.
  - the attenuation caused by the receiver antenna will be taken into account. It is caused by the receiver antenna gain pattern and the attenuation of signals with an orthogonal polarization [27].
- an extra code delay component: it can be stated that the MP echo will always arrive after the LOS signal because it must travel a longer propagation path, translating, therefore, in a larger propagation delay;
- an extra Doppler frequency shift: A Doppler frequency shift is introduced due to the interaction of the reflector object with the satellite and the receiver.
- a possible extra carrier phase lag: A possible carrier phase lag (positive or negative) is introduced when the LOS signal is scattered by the reflector surface.

The reception of the MP echoes at the receiver side acts as a signal interference of the LOS signal, which affect the nominal receiver tracking operations, resulting in a multipath synchronisation bias. In particular, MP echoes affects the LOS code delay tracking (section 3.1.2.2.3.2), introducing a MP tracking code delay, the LOS carrier phase tracking, introducing a MP tracking carrier phase lag, and, the LOS carrier frequency tracking, (section 3.1.2.2.3.2), introducing a MP tracking carrier frequency shift.

2.4.1.2.2 Shadowing effect

The shadowing effect is an attenuation of the LOS signal introduced when the LOS signal encounters objects through its transmission path but still manages to reach the receiver antenna; one example is given in Figure 2-18 where the LOS signal is attenuated by the tree's foliage. This kind of phenomenon can occur in outdoor situations, as showed in Figure 2-18, but also in indoor situations.

Strong shadowing effect, also called signal blockage, can attenuate the LOS signal so as to prevent the acquisition of the signal at the received side. Consequently, shadowing of the LOS signal and multipath has combined effects on the relative amplitudes of LOS path and multipaths.

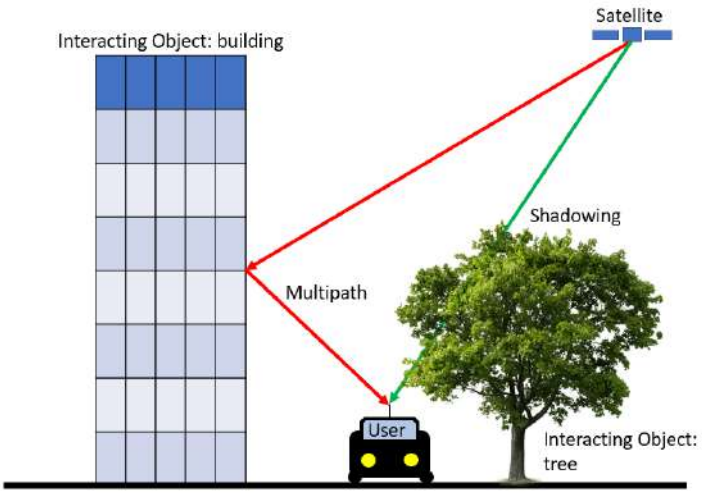

Figure 2-18 – LOS Multipath vs. LOS Shadowing effect in Outdoor multipath situation

2.4.1.2.3 LOS and NLOS MP signal reception states

Due to the combination of the shadowing and the multipath effect on the LOS signal, three received signal reception states can be defined [28]:

LOS MP reception state: The LOS multipath could be defined as the joint reception at the receiver's antenna of the satellite-to-receiver LOS transmitted signal and several delay copies of the same signal. Usually, LOS signal has a higher power compared to the received signal echoes. A picture representing the LOS multipath is presented in Figure 2-19. The LOS multipath phenomenon distorts the ideal correlation function, obtained between the LOS received signal and the local generated replica; as a consequence, the receiver tracking stage cannot properly synchronize the signal replica to the LOS received signal. Once the tracking operations are performed, the estimated tracking parameters, such as the code delay, carrier phase and Doppler frequency of the composite signal (LOS plus MP echoes) are all affected by the LOS MP tracking bias, which consists of:

- an extra code delay, equal to difference between the ideal LOS code delay estimation and the composite code delay estimation;
- an extra carrier phase lag, equal to the difference between the ideal LOS carrier phase estimation and the composite carrier phase estimation;
- and, finally, an extra Doppler frequency shift, equal to the difference between the ideal LOS Doppler frequency estimation and the Doppler frequency estimation.

NLOS MP reception state: the LOS signal does not reach the antenna with a power high enough to be processed by the GNSS receiver; however at least one powerful echo is received and can be processed by the receiver. As noted in [12], the LOS does not always exist between the receiver and transmitter, in particular for low-elevation angles. For instance, trees or buildings along a road may block signals from below a certain elevation angle. In urban environments, for example, there is high probability of signals blocked when the received signal is at elevation angle of 15º or below, and blockage of lower-elevation satellites was also not uncommon even in rural environments, due to shadowing by trees. The NLOS MP is common in dense urban areas where tall buildings block the LOS signals. Figure 2-20 illustrates the combination of these two phenomena that define the NLOS reception state. Contrarily to LOS MP, in this case the LOS correlation function is completely absent. The NLOS MP phenomenon creates a new correlation function, obtained between the most powerful MP echo and the local generated replica, and distorted by the presence of other less powerful MP echoes. As a consequence, the receiver tracking stage synchronises the local replica with this MP echo and tracks it. Once the tracking operation are performed, the estimated tracking parameters, such as the code delay, carrier phase and Doppler frequency of the received signal are all affected by the NLOS MP tracking bias, which consists of:

- an extra code delay, equal to difference between the ideal LOS code delay estimation and the NLOS MP code delay estimation;
- an extra carrier phase lag, equal to the difference between the ideal LOS carrier phase estimation and the NLOS MP carrier phase estimation;

- an extra Doppler frequency shift, equal to the difference between the ideal LOS Doppler frequency estimation and the NLOS MP Doppler frequency estimation.

NLOS MP extra code delay is always positive and it is larger than those related to the LOS MP (signals received via reflections from distant tall buildings can exhibit errors of more than a kilometre). Similarly, the estimated NLOS MP extra carrier phase lag and Doppler frequency shift are usually larger than LOS MP tracking biases.

A detailed illustration of LOS and NLOS MP error affecting the propagation time and the Doppler frequency have been presented respectively in sections 4.2 and 4.3.

BLOCKED reception state: neither the LOS nor any echoes are received with enough power by the GNSS receiver to be processed.

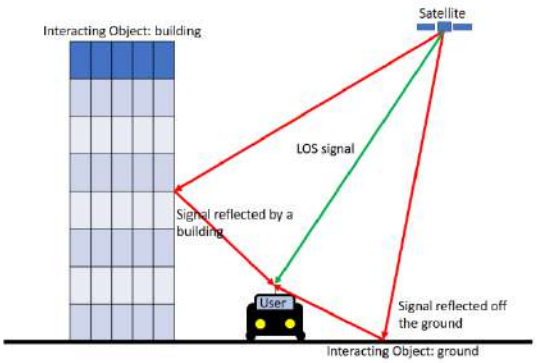

Figure 2-19 – Line-of-Sight (LOS) Multipath Interference

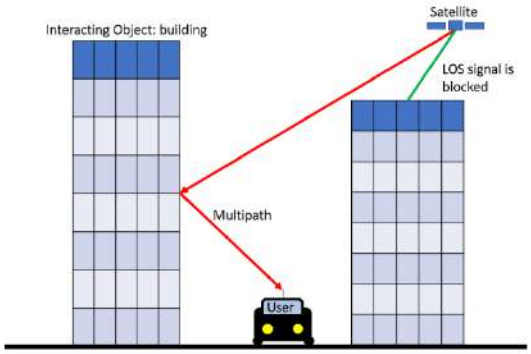

Figure 2-20 – Non Line-of-Sight (NLOS) Multipath Interference

2.4.1.2.4 Urban Environment Characteristics

This work focuses on the particular multipath environment obtained when the GNSS receiver is used in urban areas, the so-called urban environment. The urban environment is characterized by a large number of objects, buildings, cars, vegetation, etc., which the transmitted signal encounters before being captured by the receiver antenna. In this particular case, different receiver signal reception states occur depending to the relative positions of the satellites and the reflection objects and according to the physical properties of the reflected signal component, which depends also on the nature of obstacles.

The basic urban environment could be considered as the typical city street, which is defined by a set of components: roads, static obstacles (buildings, trees, poles) and dynamic obstacles (vehicles). The complexity of the city street depends on the potential number of static and dynamic obstacles and their characteristics.

Therefore, the potential multipath reflection caused by the basic city street depends on several parameters. They can be subdivided in three different groups, receiver, environment and reflector parameters, listed as follows:

Urban Environment Component	**Parameters**	**Variables**
Receiver	Receiver design	Antenna
		Front-End
	Receiver motion characteristics	
Environment	Geometry of the city street	road: width, length
		distance between the road and the buildings
		number of obstacles
		position of obstacles

	Occurrence of reflector objects	
	Satellite-to-Obstacle geometry	Position of reflection points with respect to the satellite position
		LOS's incident angle on object surface
	Obstacle-to-Receiver geometry	Position of reflection points with respect to the receiver antenna position
		MP echo incident angle on receiver antenna
Obstacle	Characteristics of reflector objects	Materials of the reflectors
		Geometric model of reflectors objects (height, length, volume, etc.)
	Obstacles motion characteristics	

Table 2-1 – Urban Environment Model Parameters

An example of the urban environment model is developed in [29], which is illustrated in Figure 2-21 and Figure 2-22.

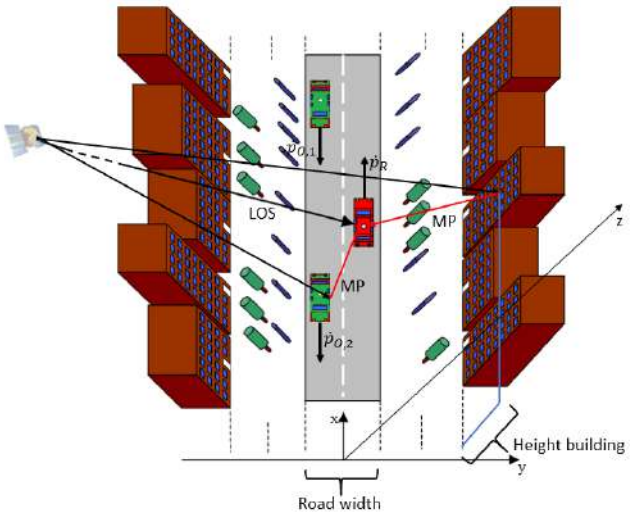

Figure 2-21 – Artificial urban scenario generated by the DLR urban propagation channel model [29]

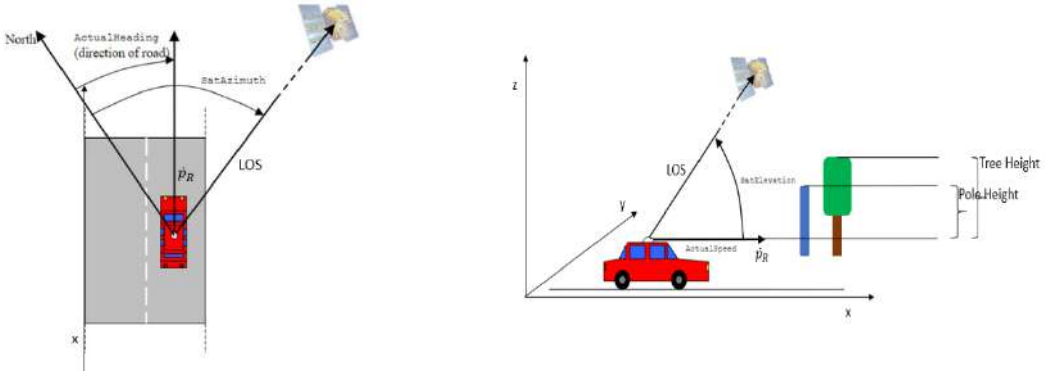

Figure 2-22 – 2D-plane visualization of the: on the left satellite azimuth and vehicle heading angles; on the right satellite elevation angel and vehicle actual speed vector [29]

2.4.1.2.5 Urban canyon

Due to the computational limitations, when considering the simulation of urban environment, a simplified model is usually applied, the so-called urban canyon, which is defined as a single section of a typical urban or suburban environment. Typical urban trenches have been modelled in several works, such as [30]–[33].

A simplified model of the urban trench, is defined by the following components: the street, two objects which act as reflectors, placed on the two sides of the street, O_1 and O_2, the GNSS satellite (transmitter) i, SV_i, the GNSS receiver, R and the reflection point, P.

The design of these components is characterized by the following parameters, portrayed in Figure 2-23 and Figure 2-24, respectively the geometric model in the x-y plane and y-z plane: the width of the street, w, the receiver position on the x-y plane, defined by $p_{r,x}$, $p_{r,y}$, the height of the objects on the two sides of the street, h_1 for $O_1$and h_2 for O_2, in the y-z plane and the length of the objects on the two sides of the street, c_1 for O_1 and c_2 for O_2, in the x-y plane.

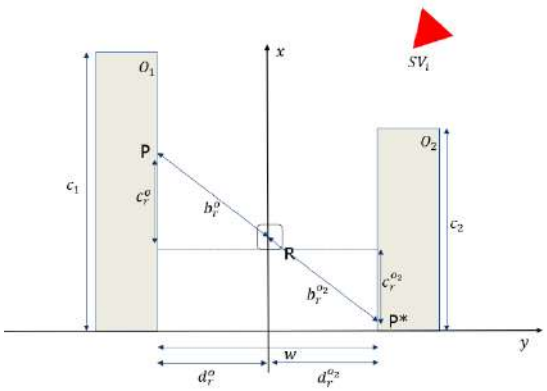

Figure 2-23 – Urban trench geometric model, x-y plane

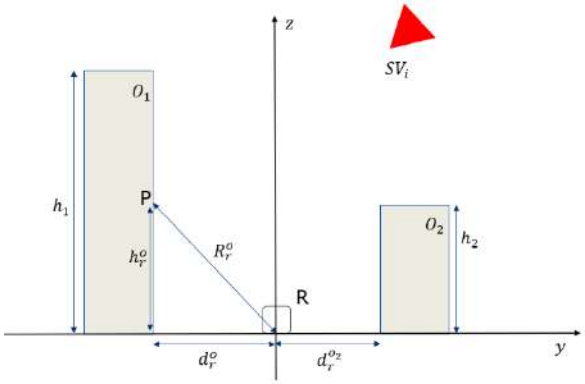

Figure 2-24 – Urban trench geometric model, y-z plane

The reflection point has been situated on the surface of the reflector O_1. The projection of P along the reflection direction on O_2 is denoted as P^*.

The distance between the receiver and the reflection point, along the y-axis, which corresponds to the distance between the receiver and the O_1surface, is denoted as d_r^o. Similarly, the distance between the receiver and the O_2 surface, along the y-axis, is denoted as $d_r^{o_2}$. The sum of d_r^o and $d_r^{o_2}$ must be equal to the width of the street, w.

The distance between the receiver and the reflection point, along the x-axis is denoted as c_r^o. The distance between the receiver and P^*, along the x-axis is denoted as $c_r^{o_2}$.

The distance between the reflection point and the receiver position in the x-y plane, b_r^o, is calculated as

$$b_r^o = \sqrt{(c_r^o)^2 + (d_r^o)^2} \quad 2\text{-}28$$

Similar calculation is conducted to define $b_r^{o_2}$.

h_r^o is the distance between the reflection point and the receiver position along z-axis. The distance between the reflection point and the receiver in the y-z plane, R_r^o, is calculated as follows:

$$R_r^o = \sqrt{(h_r^o)^2 + (b_r^o)^2} \quad 2\text{-}29$$

The relative position between the receiver and the point reflection point $P(h_r^o, b_r^o)$ can be characterized by the receiver-to-object unitary vector, $\boldsymbol{u}_r^o(\theta_r^o, \varphi_r^o)$.

Some parameters, such as road width and building's height, vary depending on the city and the specific neighbourhood. In [34] the statistical average building height and standard deviations for several cities including Toulouse, London and Berlin based on urban Digital Elevation Models are presented. An extract is showed in Table 2-2. More data could be found in [35] for Toulouse, Nantes and Paris, including the average height of the building versus average width of the roads.

	London	Toulouse	Berlin
Average of buildings height [m]	13.6	15.3	18.6
Standard deviation of building height [m]	5	3.1	4.3

Table 2-2 – Parameters of the real distribution of building heights for different cities [34]

The geometric occurrence of reflectors in the urban canyon is strictly correlated to the urban canyon geometric model. Figure 2-25 shows the likelihood distribution of reflectors in x-y plane [36]. In this figure the receiver is moving in x-direction only. It is demonstrated that the highest likelihood of receiving a reflector is when the reflector is on the right or on the left side, while the likelihood of receiving a reflector from the front is close to zero [36].

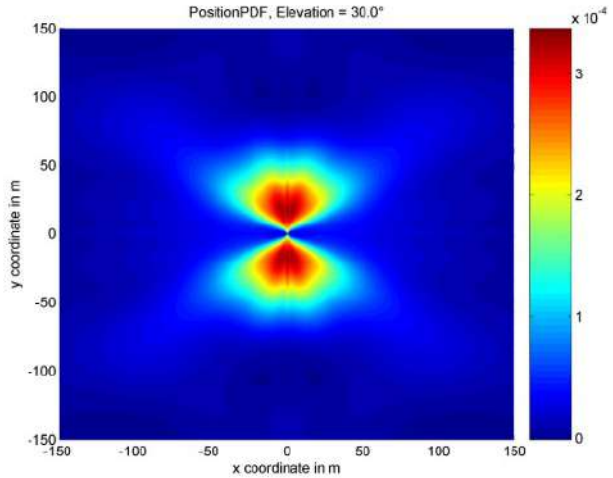

Figure 2-25 – Likelihood of reflectors being at a certain 2-D position. Moving direction of the receiver is in x-direction only [36]

Having defined the urban canyon geometric model and the physical characteristics of the reflections it is possible to design the geometric model of the reflected signal. Typically, three different geometric model are set: single, multiple and corner reflection. The simplest one is the single reflection, Figure 2-26. As the name clearly denotes, the path of the multipath signal consists of a unique echo caused by the reflection of the transmitted signal on the reflector's surface. A single reflection implies the presence of a highest-power multipath component; on the

contrary, multiple-reflected multipath components becomes negligible when the number of reflections reduces dramatically the power of the reflected signal [37]. This simplified model is the one applied during this work.

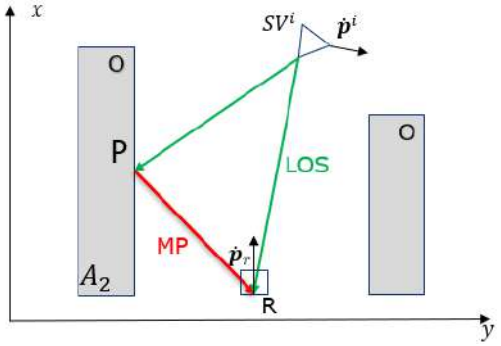

Figure 2-26 – Single reflection geometric model

2.4.2 Receiver Radio-Frequency Front-End

The Radio-Frequency Front-End (RFFE) constitutes the first stage of every RF receiver. The RFFE block comes after the receiver antenna. A generic scheme of a RFFE block is presented in Figure 2-27 [38].

The RFFE is responsible mainly for the RF received signal filtering and down-conversion to Intermediate Frequency (IF) as well as the signal analog-to-digital conversion. In further details, the purpose of the RFFE may be summarised as follows.

First, the received signal is amplified since it is received with a very low power (in this stage a first filtering of the received signal is conducted to remove noise and Out-of-Band interfering signals). Second, the amplified signal is down-converted from the central radio frequency (RF) to the Intermediate Frequency (IF) or baseband (BB), which will facilitate the signal processing operations. Third, the IF signal is filtered in order to select the signal of interest removing the interference contribution (narrower filter at IF compared to the RF filter). Finally, the IF filtered signal is digitized in order to adapt the signal to its digital process on the next receiver block, IF digital signal processing or just digital signal processing.

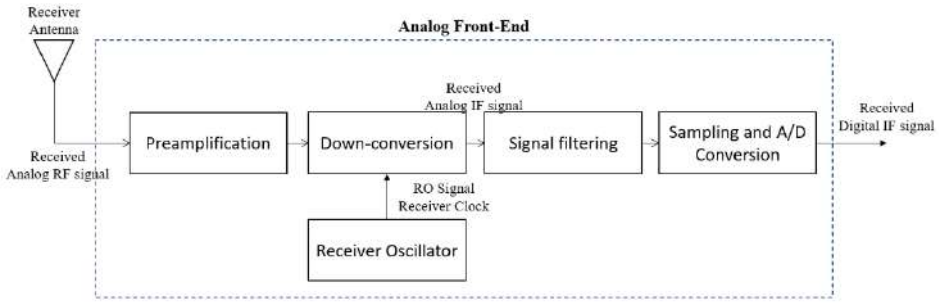

Figure 2-27 – Analog Front-end block scheme

Each block is composed by several other blocks that perform a specific operation. The detailed Front-End Scheme is deployed in [20].

One of the main component is the Receiver Oscillator Block which is used to generate local carrier signals with a specific carrier frequency value. The different local carrier signals are used to derive different process of the receivers; for example, in the RFFE block, they are used to down-convert the RF signal and to sample the IF signal (on the ADC conversion process). The RO is an electronic oscillator which is used to generate locally a monotonic signal with a specific frequency. There are several type of RO, divided in two different categories: the analog RO, which generates directly the analog signal, such as the Voltage Controlled Oscillator (VCO) and the digital oscillator, such as the Numerical Controlled Oscillators (NCO) [38]. Nowadays, the common oscillators used by GNSS receivers are the Numerical Controlled Oscillators.

2.4.3 Transmission Channel Impulse Response

The complex envelope channel impulse response (CIR), or equivalent low-pass CIR, of the transmission channel is used to model the impact of the transmission channel on the GNSS received signal. Since the antenna has some effects on the received signal depending on the direction of arrival, the receiver antenna and RF effects could be modelled as an attenuation, the model of the transfer function will thus include the effects of the propagation channel and the transmitter and receiver antennas. In the case of ground applications in urban environments, the most important factor when modelling the propagation channel is the multipath model.

The generic channel impulse response of the GNSS transmission channel $h_{TC}(t)$, can be mathematically modelled via a sum of Dirac functions representing different echoes with their own specific amplitude, frequency and phase components.

$$h_{TC}(t,\tau) = \sum_{m=0}^{M} \alpha_m(t)\delta\big(\tau - \tau_m(t)\big)e^{(j\varphi_m(t))} \qquad 2\text{-}30$$

where:

- t represent the variation in time of the CIR parameters;
- τ is a mathematical variable used to allow the convolution of a time-variant CIR with a transmitted signal in order to mathematically model the received signal;
- δ is the Dirac distribution;
- M is the number of echoes;
- $\alpha_m(t)$ is the time-variant attenuation of the m$^{\text{th}}$ echo, called Multipath-to-LOS Ratio (MLR), $\alpha_m = A_m/A_0$;
- A_0 is the amplitude of the transmitted signal;
- $\tau_m(t)$ is the time-variant propagation delay of the m$^{\text{th}}$ echo, including the delay introduced by the ionosphere and the troposphere;
- $\varphi_m(t)$ is the time-variant phase of the m$^{\text{th}}$ echo including the shift introduced by the ionosphere and the troposphere (note that over short interval of time $\varphi_m(t)$ can be approximated as an initial phase and a Doppler frequency shift $f_{D,m}$ of the m$^{\text{th}}$ echo, where $f_{D,m}$ may vary from interval to interval of time).

The power spectral density resulting from the Fourier transform is called the Doppler power spectrum of the channel, and the range of frequencies over which it is essentially nonzero is called the Doppler spread of the channel. The reciprocal of the Doppler spread is the coherence time of the channel, the time over which the multipath structure does not change much relative to the direct path, in other words, time during which parameters $\alpha_m(t)$ and $\tau_m(t)$ does not vary significantly.

The multipath profile (LOS path and reflected echoes) producing can be plotted graphically as a power-delay profile (PDP) using the relative power of the signal components and the time delay with respect to the LOS path $\{((\alpha_m)^2, \tau_m)\}_{m=1}^{M}$, as shown in Figure 2-28. The model is based on the arrivals grouped into two major components: the LOS path, a set of near echoes, characterized by a small delay, and a set of far echoes, characterized by a large delay.

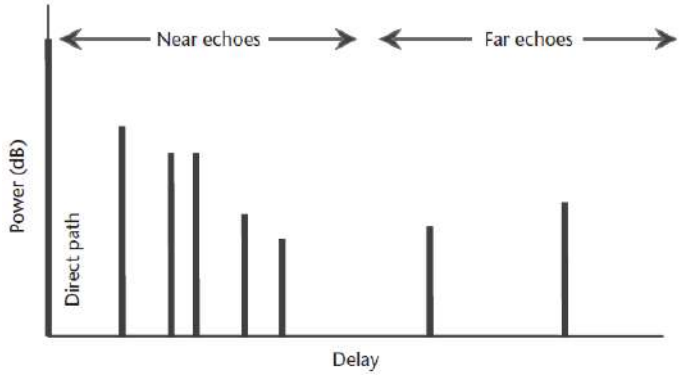

Figure 2-28 – Canonical power-delay-profile for land-mobile satellite channel [12]

Despite its limited realism, 2-30 with $N = 1$ and time-invariant parameters is widely used in theoretical assessments of multipath performance due to its ease of use. Therefore, this expression will be used in the following chapters to model received signal containing multipath.

2.5 Signal Model

Previous sections described the emitted GNSS signal and the transmission channel. These knowledges are employed here to model the received signal at the RFFE output. Firstly, the GNSS transmitted signal model is presented (2.5.1). This is finally followed by the received signal model (2.5.2).

2.5.1 GNSS Transmitted Signal Model

The generic GNSS modulated signal presented in 2-11, emitted by the satellite i, transmitted in the L1/E1 band, can be written as:

$$s_{L1}^{i}(t) = Re\{s_{l,L1}^{i}(t) \cdot e^{j(2\pi f_{L1}t)}\} = Re\{A^{i} \cdot d^{i}(t) \cdot c^{i}(t) \cdot e^{j(2\pi f_{L1}t)}\} \quad 2\text{-}31$$

where f_{L1} represents the signal's carrier frequency in the L1 and E1 band. Applying the Real operator, 2-31 could be written as:

$$s_{L1}^{i}(t) = A^{i} \cdot d^{i}(t) \cdot c^{i}(t) \cdot \cos(2\pi f_{L1}t) \quad 2\text{-}32$$

2.5.2 GNSS Received Signal Model

This subsection defines the received signal mathematical model. The received signal is modelled first at the receiver antenna input (section 2.5.2.1), and, later, at the RF front-end output (section 2.5.2.2). Moreover, the generic received signal model is derived with and without the presence of multipath components.

2.5.2.1 GNSS Received Signal Model at the Receiver Antenna input

Recalling the radio-wave signal emitted by a given satellite i, 2-31, then, according to section 2.4.3, the complex envelope of the received signal is the convolution of the complex envelope of the transmitted signal and the CIR.

$$z_{in}^{i}(t) = Re\{(s_{l,RF}(t) * h_{TC}(t,\tau)|_{\tau=t})e^{j(2\pi f_{L1}t)}\} \quad 2\text{-}33$$

Therefore, the received signal $z_{in}^{i}(t)$ at the antenna input is modelled as a sum of attenuated, time-delayed versions of $s_{L1}^{i}(t)$. Neglecting the presence of the interference component, 2-33 could be written as:

$$z_{in}^{i}(t) = Re\left\{\left(\sum_{m=0}^{M} A^{i}(t)\alpha_{m}^{i} \cdot s_{l,L1}^{i}(t - \tau_{m}^{i}(t)) \cdot e^{j\varphi_{m}^{i}(t)}\right) e^{j(2\pi f_{L1}t)}\right\} \quad 2\text{-}34$$

It is important to note that with this model, one multipath corresponds to one echo of the signal in the propagation channel. When no multipath is present, the noiseless received signal at the receiver antenna input is described as:

$$\begin{aligned} z_{in}^{i}(t) &= Re\left\{\left(A^{i}(t)\alpha_{0}^{i} \cdot s_{l,L1}^{i}\left(t - \tau_{0}^{i}(t)\right) \cdot e^{j\varphi_{0}^{i}(t)}\right) e^{j(2\pi f_{L1}t)}\right\} = \\ &= Re\left\{\left(A^{i}(t)\alpha_{0}^{i} \cdot s_{l,L1}^{i}\left(t - \tau_{0}^{i}(t)\right) \cdot e^{j\left(2\pi f_{L1}t + \varphi_{0}^{i}(t)\right)}\right)\right\} = \\ &= A^{i}(t)\alpha_{0}^{i} \cdot d^{i}\left(t - \tau_{0}^{i}(t)\right) \cdot c^{i}\left(t - \tau_{0}^{i}(t)\right) \cdot \cos\left(2\pi f_{L1}t + \varphi_{0}^{i}(t)\right) \end{aligned} \quad 2\text{-}35$$

where:

- $A^{i}(t)\alpha_{0}^{i}$ is the time-variant received signal amplitude;
- τ_0 is the time-variant satellite-receiver signal propagation time, in [sec];
- $\varphi_{0}^{i}(t)$ is the time-variant received signal phase in [rad].

A simple model for the complex envelope of a received signal with multipath, neglecting the interference contributions, at the antenna input is provided as follows:

$$z_{in}^{i}(t) = Re\left\{\left(A^{i}(t)\alpha_0^{i} \cdot s_{L1}^{i}\left(t-\tau_0^{i}(t)\right) \cdot e^{-j\varphi_0^{i}(t)} + \sum_{n=1}^{N} A^{i}(t)\alpha_n^{i} \cdot s_{L1}^{i}\left(t-\tau_n^{i}(t)\right) \cdot e^{-j\varphi_n^{i}(t)} \right) e^{j(2\pi f_{L1}t)} \right\} = \\ = A^{i}(t)\alpha_0^{i} \cdot d^{i}\left(t-\tau_0^{i}(t)\right) \cdot c^{i}\left(t-\tau_0^{i}(t)\right) \cdot \cos\left(2\pi f_{L1}t + \varphi_0^{i}(t)\right) + \sum_{n=1}^{N} A^{i}(t)\alpha_n^{i} \cdot d^{i}\left(t-\tau_n^{i}(t)\right) \cdot c^{i}\left(t-\tau_n^{i}(t)\right) \cdot \cos\left(2\pi f_{L1}t + \varphi_n^{i}(t)\right) \quad 2\text{-}36$$

where:

- N denotes the total number of received multipath echoes;
- $(A^{i}(t)\alpha_0^{i}, \tau_0(t), \varphi_0(t))$ denotes the time-variant amplitude, propagation delay, phase of the received direct path;
- $(A^{i}(t)\alpha_n^{i}, \tau_n(t), \varphi_n(t))$ denotes the time-variant amplitude, propagation delay, phase of the received multipath echoes.

2.5.2.2 GNSS Received Signal model at RF Front-end output

The transmitted GNSS signal, captured by the receiver antenna and successively processed by the front-end stage, is modified in order to be converted from an analog radio frequency signal to a digital baseband signal. During this processing stage, the active electronic elements of the receiver antenna introduce noise and distortions on the received signal.

The IF receiver signal mathematical model at the front-end output is derived in this section. First, the simple received signal mathematical model without the presence of multipath is presented in subsection 2.5.2.2.1. The received signal model including the presence of the multipath is presented in subsection 2.5.2.2.2. The received signal model will be used then, as input of the digital signal processing chain.

2.5.2.2.1 Received signal model without Multipath

The generic received noisy L1\E1 signal at the receiver antenna output from each satellite i, $z_{in}^{i}(t)$, when only the LOS signal is received is represented as next. For simplification purposes, from now on it will be assumed that the variation of the LOS amplitude, $A^{i}(t)$, as well as the LOS propagation delay, $\tau_0^{i}(t)$, evolves slowly enough to be considered as constant during the processing by the RFFE block (note that sudden changes of values, cause by sudden LOS blockages for example, are modelled).

$$z_{in}^{i}(t) = A^{i}\alpha_0^{i} \cdot d^{i}\left(t-\tau_0^{i}\right) \cdot c^{i}\left(t-\tau_0^{i}\right) \cdot \cos\left(2\pi f_{L1}t + \varphi_0^{i}(t)\right) + \zeta^{i}(t) \quad 2\text{-}37$$

where $\zeta^{i}(t)$ represents the additive thermal noise and the interference components of the transmitted signal.

2.5.2.2.1.1 Signal expression at the Front-end output

The signal is later fed to the ADC block for the sampling and quantization process. During the sampling process, a specific sampling period is used to generate the samples, T_s. The sampled signal received from satellite i at epoch n, $z_{out}^{i}(nT_s)$

$$z_{out}^{i}[n] = z_{out}^{i}(nT_s) = \\ = A^{i} \cdot d^{i}(nT_s - \tau^{i}) \cdot c_f^{i}(nT_s - \tau^{i}) \cdot \cos\left(2\pi f_{IF} nT_s + \varphi^{i}(nT_s)\right) + \eta_f^{i}(nT_s) \quad 2\text{-}38$$

where:

- T_s is the sampling period, $f_s = 1/T_s$ is the sampling frequency;
- τ^{i} is the signal transit time from satellite i to the user's receiver.

2.5.2.2.2 Received signal model in presence of Multipath

A simple model for the received signal with multipath, neglecting the noise and interference contributions, at the antenna input is provided as follows,

$$z_{in}^{i}(t) = A^{i}\alpha_{0}^{i} \cdot d^{i}\left(t-\tau_{0}^{i}\right) \cdot c^{i}\left(t-\tau_{0}^{i}\right) \cdot \cos\left(2\pi f_{L1}t + \varphi_{0}^{i}(t)\right) + \sum_{n=1}^{N} A^{i}\alpha_{n}^{i} \cdot d^{i}(t-\tau_{n}^{i}) \cdot c^{i}(t-\tau_{n}^{i}) \cdot \cos\left(2\pi f_{L1}t + \varphi_{n}^{i}(t)\right) \quad 2\text{-}39$$

2.5.2.2.2.1 Signal expression at the Front-end output

The sampled received signal from satellite i at epoch k, affected by multipath $z_{out}^{i}[k]$, applying a similar approach of the case without multipath in section 2.5.2.2.1.1 is written as:

$$z_{out}^{i}[n] = z_{out}^{i}(nT_s) = = A_{0}^{i} \cdot d^{i}\left(nT_s-\tau_{0}^{i}\right) \cdot c_{f}^{i}\left(nT_s-\tau_{0}^{i}\right) \cdot \cos\left(2\pi f_{IF}nT_s + \varphi_{0}^{i}(nT_s)\right) + \sum_{n=1}^{N} A_{n}^{i} \cdot d^{i}\left(nT_s-\tau_{n}^{i}\right) \cdot c_{f}^{i}\left(nT_s-\tau_{n}^{i}\right) \cdot \cos\left(2\pi f_{IF}nT_s + \varphi_{n}^{i}(nT_s)\right) + \eta_{f}^{i}(nT_s) \quad 2\text{-}40$$

2.6 Conclusions

In this chapter, a general overview of the GNSS has been presented. The chapter began with a description of the GNSS fundamentals, the operations necessary to calculate the user position, the reference frames as well as the definition of the basic measurements generated by the GNSS receiver to estimate the user position. An overview of the GPS and Galileo space, control and user segments, designed to ensure the correct application of the basic operations was then given.

Once the general concepts were introduced, a description of the GNSS signal structure has been proposed, focusing on GPS L1 C/A and Galileo E1 OS, since these signals are the two GNSS signals exploited in this work. The attention has been directed to the chip modulation scheme, PRN code rate and spectrum properties of the two signals of interest.

The remaining sections of the chapter have focused on the description of the transmission channel. Three different sections are used to define the transmission channel, each one focusing on one of the three main elements constituting the channel: the transmitter RF front-end block, the propagation channel and the receiver RF front-end block.

In particular, the attention has been directed to the propagation channel. The description of the propagation channel has been subdivided in three different parts: the ionosphere, the troposphere and the multipath blocks. For each part, a summary of the impairments and the relative distortion introduced on the transmitted signal is given: ionosphere and troposphere mainly introduce a code delay and a carrier phase lag; multipath phenomenon is defined as the reception of several copies of the transmitted signal, where each copy or echo is characterized by an amplitude attenuation, a code delay, with a different carrier phase lag; when the multipath echoes are captured by the receiver antenna along with the direct signal, they cause a distortion of the ideal correlation function. Due to the combination of the shadowing effect, attenuation of the direct signal, and the multipath phenomenon on the LOS signal (direct signal), two received signal reception states can be defined: LOS and NLOS received signal states. Each individual receiver reception state provides a different distortion of the ideal correlation function.

In addition to ionosphere troposphere and multipath phenomenon, two other sources of errors to the composite received signal are introduced. The interference phenomenon, defined as the different signals captured by the receiver antenna in addition to the useful GNSS signals, and the AWGN thermal noise caused by the GNSS receiver electronic components and local environment temperature. Both are approximated as additive noise components in this work.

Finally, the effects of the Transmission channel on the GNSS transmitted signal have been mathematically modelled through the definition of the Transmission Channel Impulse response and the mathematical model of the GNSS received signal at the receiver RF Front-End output is provided.

The notions described in this chapter are exploited in Chapter 3, which describes the Signal Processing and the Data Processing Blocks of a generic GNSS receiver.

3 GNSS Receiver Processing

Chapter 2 presented the general overview of the GNSS architecture, the GNSS signal structure, the transmission channel as well as the first stages of the receiver, the antenna and the radio-frequency front-end (RFFE) block. This chapter focuses on the description of the remaining stages of the receiver, denoted in this work as the Receiver Processing block, and the operations conducted by this block. After the description of the Receiver Processing block, all the state-of-the-art elements necessary to understand the principle and functioning of GNSS in nominal signal reception conditions, will have been presented. The state-of-the art receiver behaviour, specifically the signal processing part, in the presence of multipath is tackled in Chapter 0.

The Receiver Processing block is defined as the stages of the receiver which processes the GNSS signal digitized by the RFFE block, in order to determine the receiver's navigation solution. The Receiver Processing block is thus divided into two sequential blocks, as detailed in the Receiver Architecture section (section 2.2.3.1): the Signal Processing (SP) block and the Data Processing (DP) block.

The SP block receives the IF digital signal, isolates the individual signals transmitted from the different satellites and processes them in dedicated receiver channels to estimate the basic observables of each received satellite signal (signal propagation time, signal carrier phase shift, and the signal Doppler frequency, introduced in section 2.1.3) and to demodulate the respective navigation messages.

The DP block firstly determines the raw pseudorange (PSR) and raw pseudorange rate (PSR-R) measurements, whose detailed definition is given in section 2.1.3.1, from the basic observables provided by the SP block. Secondly, it corrects the raw PSR and PSR-R to obtain more precise measurements and thirdly calculates the user PVT (position, velocity, time) navigation solution from the corrected PSR and PSR-R measurements and the relevant navigation message data associated to each satellite.

The chapter is divided as follows: the SP block is detailed in section 3.1, while the DP block is presented in section 3.2. A final summary of this chapter is depicted in section 3.3. In the SP block section, the high-level structure of the GNSS receiver signal processing block (section 3.1.1) and the Digital Signal Processing Block (section 3.1.2) are described. In the DP block section, the GNSS Measurements (pseudorange and pseudorange-rate) Generation block (section 3.2.1), the GNSS Measurement Correction block (section 3.2.2), and, finally the Navigation Solution Estimation block (section 3.2.3), which exploits the corrected pseudorange and pseudorange-rate measurements to estimates the PVT solutions, are described.

3.1 GNSS Receiver Signal Processing Block

The high-level structure description of the GNSS Receiver SP block is described in section 3.1.1. Finally, this section focuses on the Digital Signal Processing Block, in section 3.1.2, which is of main interests in this PhD work.

3.1.1 High-level structure description

The Signal Processing block is illustrated in Figure 3-1. The SP block can be decomposed into two different sub-blocks: the Digital Signal Processing (DSP) and Navigation Message Demodulation (NMD).

The DSP objectives are:

- to detect the presence of the signal transmitted from a given satellite in the overall incoming IF signal (satellite-in-view detection) and to make a rough estimation of the code delay and the Doppler frequency of the received signal; this operation is known as acquisition.
- to process simultaneously the detected signals in dedicated channels to accurately estimate the unknown parameters (propagation time, carrier phase and carrier frequency) characterizing the incoming signal; this operation (for each individual signal) is known as tracking.

To cope with the goals described above, DSP performs two functions: acquisition and tracking. Acquisition is performed when the receiver must process new GNSS signals: either when switching on the receiver, when searching for new GNSS signals in addition to the ones that are currently being processed or when losing the

tracking of one signal (re-acquisition). Tracking of a GNSS signal begins once the acquisition process ends and is an iterative process performed continuously in time. Acquisition and tracking methods are based on two basic operations which are jointly executed: the signal carrier wipe-off and the PRN signal correlation, performed between the received signal and a local generated replica. The detailed analysis of DSP operations is presented in section 3.1.2.

The NMD's goal is to demodulate the transmitted navigation message of the incoming signal from the correlation operation outputs conducted by the DPS block [20]. The low-level description of the NMD block is out of the scope of this work.

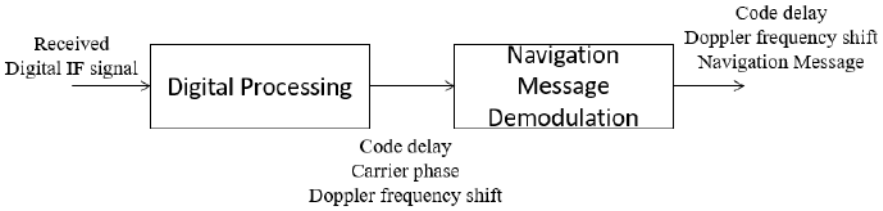

Figure 3-1 – GNSS Receiver Signal Processing block scheme

The demodulated navigation data, code delay, carrier phase shift, and Doppler frequency are finally fed into the Data Processing block.

3.1.2 GNSS Digital Signal Processing block

DSP is the first block of the Receiver Signal Processing stage whose function is the acquisition and tracking operations as introduced above and presented in Figure 3-2. These operations are performed in parallel channels, each channel dedicated to a single satellite-in-view signal.

These two processes are based on the signal carrier wipe off and the PRN signal correlation. The two are executed jointly, therefore, they are grouped for simplicity into the unique correlation process, defined in section 3.1.2.1. These operations are based on the multiplication of the incoming signal with a locally generated replica:

- The carrier wipe-off removes the carrier component from the incoming signal, when the local carrier is perfectly synchronized (in phase and in frequency) with the incoming signal carrier;
- the correlation de-spreads the spectrum of the incoming PRN signal when a perfect synchronization between the local generated and the incoming materialised code is achieved.

The correlation operation output is ideally different from zero only if the local replica is synchronized to the incoming signal and the materialised PRN codes of both signals are the same. In fact, an imperfect synchronization result implies a difference between the carrier and code components of the incoming signal and the ones of the locally generated signal, defined by a code delay, a carrier phase shift and a Doppler frequency, resulting in a significant amplitude degradation of the correlation output.

The acquisition operation detects the presence of transmitted signals and calculate a rough estimation of the code delay and the Doppler frequency shift. To do so, the acquisition process exploits the correlation principles described above. It consists in searching for the code delay and the Doppler frequency which maximizes the correlation output value. The process is characterized by a trade-off between the accuracy and the processing time. The details of acquisition processing are shown in [12]. The acquisition is performed:

- at receiver start-up,
- as a satellite moves into view of the antenna,
- following loss-of-lock.

A detailed analysis of the acquisition process is not targeted in this manuscript and can be found in several works, such as [25]. Once the acquisition process is performed, the tracking operation for each dedicated channel starts. The rough estimations provided by the acquisition block must be refined to perform the demodulation and to obtain accurate basic observables. This is achieved by an iterative closed-loop process presented in section 3.1.2.2. Different tracking loops are dedicated to the refinement of the code delay, the carrier phase shift and Doppler frequency. The loops are designed to converge to a steady state when the code delay, phase shift and Doppler frequency estimation errors are reduced to zero. In this case, the incoming signal is considered tracked.

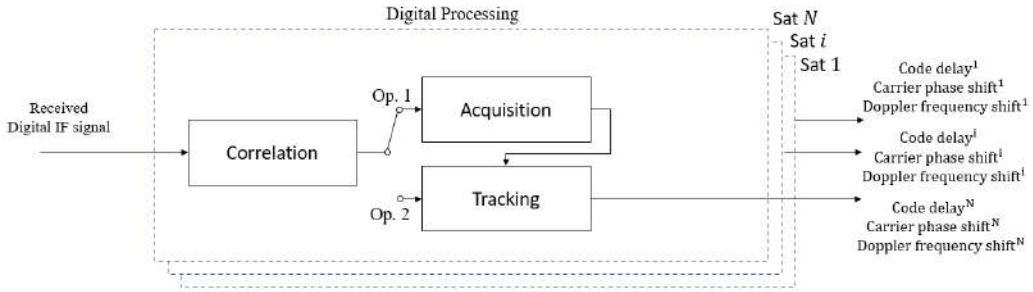

Figure 3-2 – Digital Processing block scheme

3.1.2.1 Correlation

At the RF Front-End output, the received GNSS signal is buried inside the noise, or in other words, the useful GNSS signal is not visible since the noise has a much higher power (and thus amplitude). Therefore, an operation which is able to obtain the useful GNSS from the noise-dominated incoming signal is required. The correlation exploits the properties of the PRN code modulating the GNSS signal to de-spread the PSD of the useful signal. Once the signal is de-spread, it is only composed by the data component and a residual noise component.

The correlation is obtained in three sequential steps:

- the carrier wipe-off,
- the PRN code de-spread,
- the integration of the de-spread signal obtaining the final correlator output.

The carrier wipe-off can be achieved by multiplying the incoming signal with a synchronized frequency and phase carrier replica, whereas the materialised PRN code PSD de-spreading can be achieved by multiplying the incoming signal with a time synchronized local replica of the same materialised PRN sequence.

The integration of the de-spread signal is implemented to reduce as much as possible the impact of the noise component at the correlator output since the de-spread signal has a much lower bandwidth than the spread signal. Note that an integration process is equivalent to a low-pass filter (integrator). The integration of the de-spread signal is conducted over a certain period of time, typically over an integer number, L, of full code durations, T_{PRN}, while being smaller than the duration of one data bit, T_D; this period of time is called the coherent integration time, $T_I = L \cdot T_{PRN} \leq T_D$.

Correlator outputs are generated at rates determined by the inverse of the integration time, T_I, while the incoming signal and the local replicas are available at a rate inverse to the sampling time, T_s. Consequently, the integration interval is defined as $[(k-1)T_I, kT_I]$, where the correlator outputs are available at multiples k of the integration time.

The carrier replica is synthesized using a carrier digital Receiver Oscillator, also called carrier Numerically Controlled Oscillator (NCO), and a signal generation block. The PRN code replica is generated in the same way by a code NCO and a code generating function.

The GNSS receiver applies the correlation in parallel over two different branches: in one branch the carrier wipe-off is applied using the carrier generated replica synchronized in-phase, while in the other one it is applied with a 90° phase shifted local replica (quadrature-phase synchronization). The branches are called, respectively, In-Phase (I) and Quadrature-Phase (Q) correlators.

The local replica, for satellite i, for the I and Q branches, in the discrete-time interval $[(k-1)T_I, kT_I]$, are given by:

$$\begin{aligned} r_I\left[m, \hat{\tau}_l^i, \hat{f}_{NCO}^i, \hat{\varphi}_{l,0}^i\right] &= c_l\left[mT_s - \hat{\tau}_l^i\right]\cos\left(2\pi\hat{f}_{NCO}^i(mT_s - kT_I) + \hat{\varphi}_{l,0}^i[\,kT_I]\right) \\ r_Q\left[m, \hat{\tau}_l^i, \hat{f}_{NCO}^i, \hat{\varphi}_{l,0}^i\right] &= c_l\left[mT_s - \hat{\tau}_l^i\right]\sin\left(2\pi\hat{f}_{NCO}^i(mT_s - kT_I) + \hat{\varphi}_{l,0}^i[\,kT_I]\right) \end{aligned} \quad 3\text{-}1$$

where:

- $mT_s \in [(k-1)T_I, kT_I]$;
- c_l is the PRN code replica;
- $\hat{\tau}_l^i$ is the estimated delay of the local PRN code replica, in seconds;
- $\hat{f}_{NCO}^i = f_{IF} + \hat{f}_{D,l}^i$ is the replica's carrier frequency generated by the NCO, in Hz;

- $\hat{\varphi}_{l,0}$ is the local replica phase at the beginning of the interval, expressed in radians.

The incoming signal, in nominal reception conditions (only LOS signal, without multipath), from Chapter 2, over a short time interval, such as in one integration period, T_I, can be approximated as follows:

$$z_{out}^{i}[m] = A \cdot d^{i}\left[mT_s - \tau^{i}\right] \cdot c^{i}\left[mT_s - \tau^{i}\right] \cdot \cos\left(2\pi(f_{IF} + f_{D,0}^{i})(mT_s - kT_I) + \varphi_0^{i}[kT_I]\right) + \eta^{i}[mT_s] \quad 3\text{-}2$$

where φ_0^i and $f_{D,0}^i$, are respectively the constant initial phase and the Doppler frequency signal component during the $[(k-1)T_I, kT_I]$ time interval, obtained writing the instantaneous phase component of the incoming signal as:

$$\varphi^{i}(t) = -2\pi f_{L1}\tau_p^{i}(t) \quad 3\text{-}3$$

where τ_p^i is the phase time delay introduced by the transmission channel on the transmitted signal and observed on the received signal for a given satellite i. Over the short interval T_I, the range variation can be approximated by a first order polynomial function:

$$\tau_p^{i}(t) \approx \tau_0^{i} + t\frac{d}{dt}\tau_p^{i}(t) \quad 3\text{-}4$$

It follows that inside one integration period, the phase delay varies linearly and this entails that the instantaneous phase may be written as a function of the initial phase φ_0^i and the isolated Doppler frequency $f_{D,0}^i$ as,

$$\begin{gathered}\varphi^{i}(t) \approx -2\pi f_{L1}\tau_0^{i} - 2\pi f_{L1}t\frac{d}{dt}\tau_p^{i}(t) = \varphi_0^{i} + 2\pi f_{D,0}^{i}t \\ \varphi_0^{i} = -2\pi f_{L1}\tau_0^{i} \\ f_{D,0}^{i}t = -f_{L1}\frac{d}{dt}\tau_p^{i}(t)\end{gathered} \quad 3\text{-}5$$

The resulting correlation function I for the in-phase signal branch expressed in discrete time for the k integration interval, $[kT_I, (k+1)T_I]$, is equal to:

$$I_k = \frac{A}{2} \cdot d_k \cdot R_c(\varepsilon_{\tau_k}) \cdot \cos\left(\pi\varepsilon_{f_k}T_I + \varepsilon_{\varphi_k}\right) \cdot \mathrm{sinc}(\pi\varepsilon_{f_k}T_I) + n_{I,k} \quad 3\text{-}6$$

where,

- subindex k represents the k-th integration interval;
- $R_c(\varepsilon_\tau)$ is the correlation function between the two materialized spreading codes of the local replica and the filtered received signal;
- $\varepsilon_\tau = \tau^i - \hat{\tau}_l^i$ denotes the code delay error, in seconds, between the received signal code delay induced by LOS component and the replica code delay;
- $\varepsilon_f = f_{IF} + f_{D_0}^i - \hat{f}_{NCO}^i = f_{IF} + f_{D_0}^i - f_{IF} - \hat{f}_{D,l}^i = f_{D_0}^i - \hat{f}_{D,l}^i$, denotes the Doppler frequency error, in Hertz, between the received signal Doppler frequency induced by LOS component and the replica Doppler frequency;
- $\varepsilon_\varphi = \varphi_0^i - \hat{\varphi}_{0,l}^i$ denotes the carrier phase error at the beginning of the integration interval, in radians, between the received LOS signal initial phase and the local replica initial phase;
- n_I represents the noise at the in-phase correlator output.

The quadrature component is calculated in a similar way, obtaining:

$$Q_k = \frac{A}{2} \cdot d_k \cdot R_c(\varepsilon_{\tau_k}) \cdot \sin\left(\pi\varepsilon_{f_k}T_I + \varepsilon_{\varphi_k}\right) \cdot \mathrm{sinc}(\pi\varepsilon_{f_k}T_I) + n_{Q,k} \quad 3\text{-}7$$

where n_Q represents the noise component at quadrature correlator output.

The n_I, n_Q components are modelled as independent term following a centred Gaussian distribution with zero mean and variance given by

$$\sigma_{n_I}^2 = \sigma_{n_Q}^2 = \frac{N_0}{4 \cdot T_I} \quad 3\text{-}8$$

where N_0 represents the noise PSD depending on the system noise temperature and expressed in dBW/Hz.

It can be seen that for the in-phase correlator output the useful signal component is at its maximum when ε_{τ_k}, ε_{f_k}, ε_{φ_k} are almost zero. In this case, the correlator output I contains only the navigation data message and the noise component, while Q contains only noise,

$$I_k \approx \frac{A}{2} \cdot d_k + n_{I,k}$$
$$Q_k \approx n_{Q,k} \qquad 3\text{-}9$$

This situation occurs when there is a (very) good synchronization between the incoming signal and the local replica; in this situation, the demodulation of the data component is easier to obtain. However, the presence of residual ε_{τ_k}, ε_{f_k}, ε_{φ_k} errors introduce an attenuation of the data component in the I_k branch and, as a result, the demodulation of the data component is more difficult to obtain; the data symbol is estimated with a desired low probability of error if the ratio between the signal and the noise power, the so-called Signal -to-Noise Ratio, SNR, at the correlator output is high enough,

$$SNR_{Corr} = \frac{\frac{A^2}{4}}{\frac{N_0}{4 \cdot T_I}} = 2\frac{C}{N_0}T_I \qquad 3\text{-}10$$

3.1.2.2 Tracking

The goal of the tracking process is to refine the coarse estimations of the code delay and Doppler frequency provided by the Acquisition block in addition to finely estimating the incoming signal carrier phase; in other words, its objective is to maintain the synchronization of the incoming signal over time [39]. Similar to the acquisition process, the tracking process is based on the correlation and is performed on different tracking channels, each one processing the incoming signal from a different identified satellite in view.

To maintain the synchronization of the incoming signal over time, the tracking block is designed as a closed loop module. The objective of the tracking loop is to minimize the estimation error between a targeted parameter of the incoming signal and the same parameter of the local replica (closed-loop generates the parameter value used by the local replica). Indeed, any misalignment in the replica with respect to the incoming signal should produce a nonzero phase/frequency/code delay difference so that the difference can be detected and corrected by the tracking loop. In other words, the tracking loop converges to a steady state only when the estimation error is minimized: in that case, the tracking loop is considered to be locked.

The general tracking stage is based on two fundamental modules, the Code tracking and the Carrier tracking modules. The Code tracking is used to continuously track the code delay estimation error (ε_τ) between the incoming signal's code and the local replica. The Code tracking is generally conducted using a closed feedback loop referred to as the Delay Lock Loop (DLL). The Carrier tracking is responsible to continuously tracking the Doppler frequency estimation error (ε_f) and the carrier phase estimation error (ε_φ).

The Carrier tracking module in charge of compensating only the Doppler frequency shift is a closed feedback loop called Frequency Lock Loop (FLL). Whereas, the Carrier tracking module in charge of estimating the carrier phase error and the Doppler frequency shift is a closed feedback loop called Phase Lock Loops (PLL) [39] or a PLL aided by a FLL. Carrier phase tracking is generally performed in a GNSS receiver using a Phase Lock Loop (PLL) and a Frequency Lock Loop (FLL). The objective of PLL and FLL is to keep the carrier phase alignment between the incoming signal and its local replica. However, in the case of modulated GNSS signal, a pure PLL/FLL is difficult to use because it is designed to track the carrier phase of a pure carrier, not modulated by an unknown useful data stream. As a consequence, a modified version of the ideal PLL/FLL, also called data insensitive PLL, is generally used to track a carrier modulated by data. The details of PLL are described in [12] and will not be reminded in this Chapter, since carrier phase measurements will not be treated in this PhD work because it is not very robust in case of sudden strong user's dynamics or a low C/N_0, which implies large carrier phase estimation errors. Moreover, a loss of PLL lock would translate into a drift of the local carrier with respect to the incoming carrier and correlator outputs would end up being dominated by noise (carrier wipe-off will not be conducted successfully).

The high-level scheme of the tracking stage, for a given satellite i, is presented in Figure 3-3.

The carrier frequency and code tracking loops are analysed separately in the following sub-sections. Section 3.1.2.2.2 presents the Carrier Frequency Tracking Loop, and, finally, 3.1.2.2.3 depicts the Code Tracking Loop.

The different tracking modules, code, phase and frequency, share a similar basic architecture which is introduced immediately after this preface, in order to clarify and emphasize the basic blocks before going into the explanation of the individual modules.

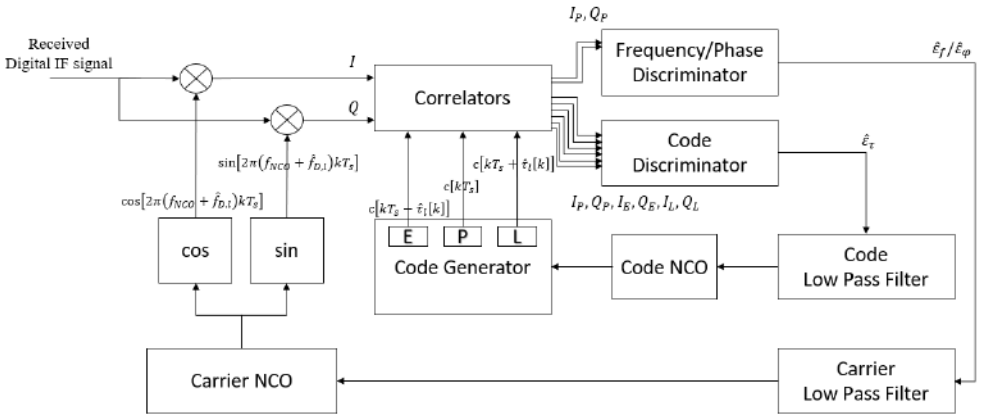

Figure 3-3 – Detailed block diagram representation of the tracking architecture

3.1.2.2.1 General Tracking Loop

The general modules constituting a tracking loop (PLL, FLL and DLL) are listed below:

- Correlator,
- Discriminator,
- Low-pass filter (LPF),
- Numerical Control Oscillator (NCO),
- Code generator,
- Carrier generator.

Basic tracking module is illustrated in Figure 3-4. First, the incoming signal is fed to the correlation block (section 3.1.2.1). The goal of this block is to correlate the incoming signal with the local replica and a 90° phase shifted local replica obtaining respectively the I and Q correlator outputs.

Once the correlation is performed, I and Q correlator outputs are used by the discriminator block (section 3.1.2.2.1.1) to calculate an estimation of the error under exam ε_x (where ε_x stays for ε_τ in case of DLL, $\varepsilon_\varphi$in case of PLL or ε_f in case of FLL and x represents the parameter to estimate). Once the discriminator output is available, it is filtered with a LPF to reduce the impact of the thermal noise, section 3.1.2.2.1.2. The filtered estimated error, $\hat{\varepsilon}_x$ is finally fed to the NCO which synthetizes a frequency used to generate a local replica correcting the targeted parameter in the next tracking loop, section 3.1.2.2.1.3. To summarize, the inherent behaviour of the closed-loop structure is to modify the targeted parameter of the local replica until the discriminator output, which should a priori provide a measurement of the estimation error under exam ε_x, is equal to 0 (since a null input will be fed to the NCO); obviously due to the effects of different sources of error on ε_x, this situation is not achieved and the closed-loop structure is constantly minimizing the discriminator output.

Within the loop structure, some signals (incoming signal, local replicas) are available at a rate inverse to the sampling time, T_s, while other signals (correlator outputs, discriminator outputs, low-pass filter outputs) are available at a rate equal to the inverse of the correlation time, T_I, or of a multiple of the correlation time. In the following, the time index k will be associated to the correlator output period, while n will be associated to the sampling period T_s.

When tracking loop converges to a locked state, the I component could be used to demodulate the navigation signal by the Signal Demodulation Block and the estimated tracking errors $\hat{\varepsilon}_x$ are used with the demodulated message to determine the basic observables (code delay, carrier phase shift and Doppler frequency shift) by the Receiver Data Processing block, section 3.2.

The accuracy of $\hat{\varepsilon}_x$ depends on several factors, such as the quality of the local oscillator, the impact of the thermal noise, the design of tracking modules, etc. A model for the errors affecting the tracking accuracy is presented in section 3.1.2.2.1.4.

The capacity of converging to the lock state and/or to maintain the lock, also called tracking sensitivity, is defined as the minimum C/N_0 necessary to achieve/maintain lock on the closed-loop. Moreover, the capacity to maintain the lock state in a closed-loop depends also on the tracking accuracy allowed to discriminate the tracking error.

In case of a large tracking error, the tracking stage might not be able to recover the error during the following epochs (the tracking error is outside the linearity region of the discriminator, described in the next section), resulting in a loss of lock. In case of a loss of lock event, the tracking process is stopped and the acquisition process should be conducted again (re-acquisition process) for that particular satellite. Once the acquisition has been successfully achieved, new rough estimation of the signals' code delay and carrier frequency, the tracking process can restart for that particular satellite.

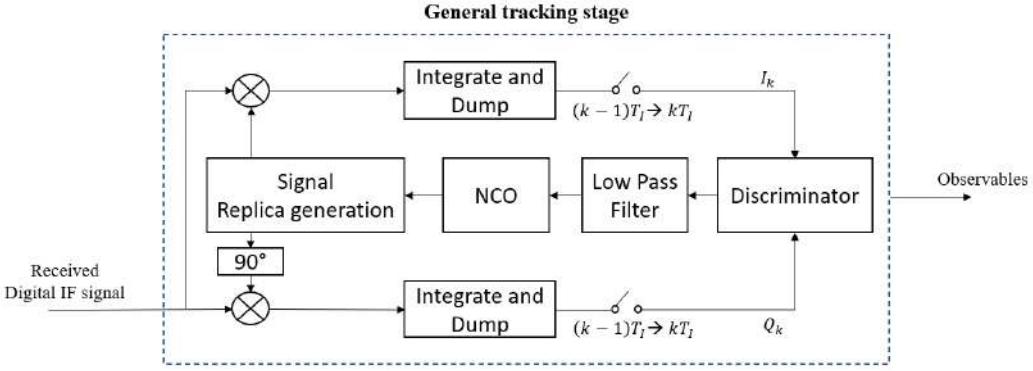

Figure 3-4 – Basic Tracking Stage module

3.1.2.2.1.1 Discriminator

The discriminator block processes the correlators' outputs to provide a measurement of the estimation error between the incoming signal and the local replica. Different discriminators are used depending on the type of tracking module (PLL, FLL, DLL) involved.

The behaviour of the discriminator output as a function of the true input error, ε_x, is called S-curve and an example is showed in Figure 3-5. The discriminator is designed to have an output proportional to the estimation error, although this objective is only achieved for ε_x values around 0. In fact, the discriminator can be approximated to a linear function for small ε_x values (close to 0) represented by the red dashed line. This means that the discriminator output, D, is a good estimation of the input error, ε_x, if ε_x value is inside this region. In this case and without loss of generality, it is possible to assume that, for a given discriminator, $D_{type,k}$ at epoch k, for a small error, the output is proportional to the real input error (already affected by some sources of error) plus thermal noise. If the discriminator is normalized, the output is equal to the real input error plus thermal noise for a small error as shown in equation 3-11. Finally, the discriminator output is successively transmitted to the Low-Pass Filter to reduce the η_x error component, described in the following section.

$$D_{type,k}(\varepsilon_x[k])\big|_{\varepsilon_x[k]\sim 0} = \varepsilon_x[k] + \eta_x[k] \qquad 3\text{-}11$$

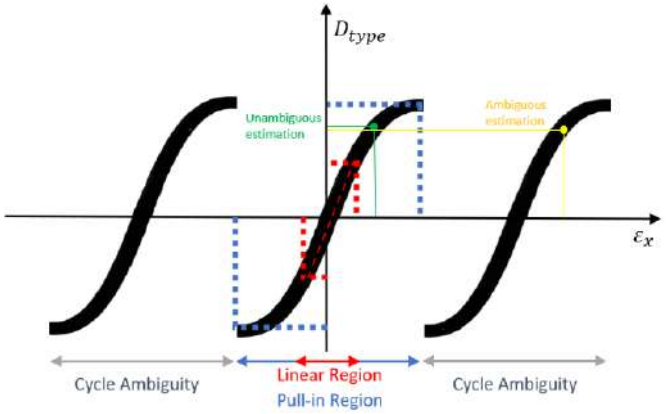

Figure 3-5 – Generic S-curve of a discriminator function

The S-curve region around the point $\varepsilon_x[k] = 0$, is the most important region of the discriminator as hinted before. The region around $\varepsilon_x[k] = 0$ where the discriminator output, D, is proportional to $\varepsilon_x[k]$ is called the linearity region and allows the optimized functioning of the tracking loop. The region around $\varepsilon_x[k] = 0$ where the inherent behaviour of the tracking loop makes the discriminator output converge towards the $\varepsilon_x[k] = 0$ point is called the pull-in region; in this region the tracking loop should only function when transitioning from a large initial or sudden estimation error to an error inside the linearity region.

Discriminator S-curve can also present other crossings across the 0 value in addition to the one corresponding to $\varepsilon_x = 0$. If the tracking loop discriminator output, through the inherent behaviour of the closed-loop, can converge towards one of these points, this point is called stable point; whereas if the tracking loop discriminator output diverges, this crossing is called instability point.

Some important remarks about the discriminator potential configurations are the following:

- The number of correlators used in a discriminator to estimate the targeted error depends on the targeted parameter and on the trade-off between complexity and accuracy.
- The choice of the discriminator also depends on the presence of the navigation data in the GNSS modulated signal. The presence of data could introduce unwanted phase shifts due to the polarity switch introduced by the bit transition [40]. In presence of data, the classic discriminator function could not be used since it is sensitive to the data bit transitions. Therefore, usually, another group of discriminators insensitive to the bit transitions are implemented.

3.1.2.2.1.2 Low Pass Filter (LPF)

The goal of the LPF is the removal of high frequency components affecting the discriminator output where the targeted effect is the reduction of the thermal noise power. The filtered estimated error, $\hat{\varepsilon}_x[k]$ or $\hat{\varepsilon}_{x_k}$ is modelled as follows:

$$\hat{\varepsilon}_x[k] = LPF\{D_{type,k}\} \quad 3\text{-}12$$

The design of the low-pass filter characterizes the receiver tracking loop and determines two of the most important performance characteristics of the tracking loop design: the capability of reducing the estimation error component generated by thermal noise and the capacity of estimating the incoming signal dynamics. Indeed, the tracking loop filter design basically is defined by two different parameters, the one-sided equivalent noise bandwidth, B_L, and the filter's order.

The design of the filter's one-sided equivalent noise bandwidth, B_L, is a critical parameter:

- for a low value, the loop significantly filters the discriminator output noise, but may not react fast enough to high signal dynamics (slow response time);
- for a high value, the loop does not significantly reduce the discriminator output noise, but may react fast enough to high signal dynamics (fast response time).

The tracking loop response, designed to correspond to the receiver dynamics and the error dynamics, depends on the filter's order. The higher the order of a filter, the faster is the rate of change of the output of the filter versus the frequency. The effects of the filter's order on the error dynamics have been summarized in section 3.1.2.2.1.4.

Once the discriminator output is filtered, it is used to drive the signal replica generation.

3.1.2.2.1.3 Numerical Controlled Oscillator (NCO)

The output of the low-pass filter, $\hat{\varepsilon}_{x_k}$, is then fed to the NCO to synthetize a frequency which is used to update the local replica; $\hat{\varepsilon}_{x_k}$ is thus the NCO command. The effect of the NCO in the targeted parameter local replica is modelled as an integrator/accumulator; for example, when estimating the incoming signal carrier phase, the NCO effect is modelled on the local replica carrier phase although strictly speaking the NCO only modifies the local replica carrier frequency (which has an impact on the local replica carrier phase observed at the correlator output). The mathematical modelling as an accumulator can be seen as a legacy effect of analog VCO (voltage control oscillator) mathematical model as well as the impact of observing the parameters at the correlator output (where the impact of the synthetized frequency is accumulated).

The NCO synthetized frequency can be modelled as shown below:

$$f_{NCO,k} = f_{nom} + \hat{\varepsilon}_{x_k} \quad 3\text{-}13$$

where f_{nom} is the nominal frequency of the NCO (when no command is present); this value is equal to f_{IF} for the PLL or FLL and equal to the nominal chip rate, f_{chip}, for the DLL.

The NCO effect on the targeted parameter $\hat{x}_k$, either code delay (DLL) or carrier phase (PLL), is modelled as shown below (note that the effect of the NCO nominal is removed):

$$\hat{x}_{k+1} = \hat{x}_k + K_{NCO}\hat{\varepsilon}_{x_k} \quad 3\text{-}14$$

where K_{NCO} is equal to $2\pi T_I$ for the PLL and T_I for the DLL. The NCO transfer function expressed in the Z domain is equal to (assuming that the input is $K_{NCO}\hat{\varepsilon}_{x_k}$)

$$T(z) = \frac{z^{-1}}{1 - z^{-1}} \quad 3\text{-}15$$

The case of the FLL is treated differently. At the LPF filter output what is obtained is a modification in seconds of the targeted parameter, for the FLL is a variation of the frequency (units s/s), for the PLL is a frequency (units rad/s) and for the DLL is a chip rate (chip/s). However, from equation 3-15, it can be seen that the NCO command is interpretated as rate modification and thus, the command must be expressed as a rate. For PLL and DLL, the command is already in the required format, but for the FLL an additional integrator must be added to obtain a rate from a rate of a rate; the extra integrator is added to mathematical model of the LPF. The consequences of adding this extra integrator is first that LPF output is no longer $\hat{\varepsilon}_f$ but directly $\hat{f}_D$; second, due to the necessity of doing this conversion, the NCO mathematical model is now different from a DLL or PLL model: the local replica carrier frequency $\hat{f}_D$ is entirely determined by the LPF filter whereas the NCO only introduces an additional constant term $f_{nom} = f_{IF}$; therefore, the transfer function in the Z domain of the NCO of a FLL can just be modelled as $T(z) = 1$. More details are given in section 3.1.2.2.2.

3.1.2.2.1.4 Error Analysis

Tracking accuracy is defined herein as the accuracy of the measurements obtained from the tracking loop considering the different sources of errors affecting the signal tracking. The disturbances affecting the tracking process are the following:

1. Thermal noise plus signal interference, $\varepsilon_{x,\eta}$;
2. Oscillator phase noise, $\varepsilon_{x,\varphi_{osc}}$;
3. Oscillator vibration, $\varepsilon_{x,v_{osc}}$;
4. Receiver dynamic error, $\varepsilon_{x,dyn}$;
5. Multipath, $\varepsilon_{x,M}$;

The *thermal noise* is generated by the environmental temperature captured by the receiver antenna and by the active elements of the RFFE block. The thermal noise in the RFFE block is modelled by an additive zero-mean white Gaussian distribution with a constant Power Spectral Density (PSD) in the frequency domain defined in [12]. Thermal noise only affects the parameter estimation.

The *oscillator phase noise* is correlated to the instabilities of the reference oscillator. The oscillator phase noise is originated by the drift of the receiver oscillator from its nominal frequency. It affects the i satellite's oscillator, generating a time variation, δt^i, w.r.t to the GPS time, and the receiver's oscillator, where the oscillator noise generates a time variation, δt_r, w.r.t to the GPS time; δt^i cannot be perfectly estimated by the tracking loop and δt_r corrupts the local replica generation and avoids the perfect estimation of the targeted parameter. Detailed analysis can be found in [12].

Another phenomenon that may cause the oscillator phase time variation phenomenon is related to the *oscillator mechanical vibrations*. In fact, the motion of the transmitter or the receiver causes mechanical movement of the associated oscillator, that may be modelled as an oscillator phase noise. In case of oscillator phase noise caused by vibration, the oscillator phase noise Power Spectral Density (PSD) can be written as in [41]. Detailed analysis can be found in [12].

Vibration and oscillator phase noise are added to the code delay and phase, and the receiver must thus also estimate them (difficulty in its estimation).

Another source of tracking performance error is the error caused by the inability of the tracking loop to estimate the targeted parameter variations generated by the *receiver dynamics*: the sudden and fast changes of the receiver's dynamics result in changes of the code propagation delay, carrier phase and frequency parameters. The tracking loop may not be prepared to estimate certain fast or high-order variations of the targeted parameters induced by the receiver dynamics; indeed, as a function of the tracking loop order, some high-order dynamics may be perfectly tracked, tracked with a bias or not tracked at all. Dynamics define the evolution of code delay and phase and depending on the evolution its tracking becomes difficult. As already introduced, the tracking loop response, designed to corresponds to the receiver dynamics and the error dynamics depends on the filter's order. A filters' order n can track:

- without bias the phase/frequency/code delay of a signal that has a dynamic of order $n-1$;
- with a bias the phase/frequency/code delay of a signal that has a dynamic of order n;
- cannot track the phase/frequency/code delay of a signal that has a dynamic of order $n+1$.

Finally, a different consideration must be made for Multipath error component: LOS and NLOS Multipath error components are described in Chapter 0.

Taking into consideration that all the error sources provided above are independent from each-other, tracking error can be computed as the linear sum of the individual error components:

$$\varepsilon_x = \varepsilon_{x,\eta} + \varepsilon_{x,M} + \varepsilon_{x,dyn} + \varepsilon_{x,\varphi_{osc}} + \varepsilon_{x,v_{osc}} \quad 3\text{-}16$$

The overall error variance is assumed equal to the sum of the variances of the independent variables.

$$\sigma_x^2 = \sigma_{x,\eta}^2 + \sigma_{x,M}^2 + \sigma_{x,dyn}^2 + \sigma_{x,\varphi_{osc}}^2 + \sigma_{x,v_{osc}}^2 \quad 3\text{-}17$$

The impact of these errors in the FLL and DLL is presented in sections 3.1.2.2.2.3 and 3.1.2.2.3.2, respectively.

3.1.2.2.1.5 Tracking Sensitivity

The tracking sensitivity is defined as the minimum C/N_0 value required by the tracking loop in order to not lose its lock (to have a tracking error falling inside the discriminator linearity region); note that the two previous definitions are accepted. Obviously, the tracking errors and tracking sensitivity are closely related because the receiver loses lock when the measurement errors exceed a certain boundary.

The tracking sensitivity is difficult and complex to be determined. However, general rules that approximate the measurement errors of the tracking loops can be used based on closed form equations to calculate the tracking sensitivity.

The general rule of thumb for the tracking threshold relates the dominant error sources presented in 3-17 to the pull-in region of the discriminators (or to the linearity region). The rule of thumb for the FLL and DLL tracking threshold are presented in section 3.1.2.2.2.3 and 3.1.2.2.3.2, respectively.

In addition to theoretical analysis of signal performance and tracking technique performance, the tracking sensitivity is used as an indicator to determine if the tracking loop is performing as a sufficient level of performance: a C/N_0 estimation is conducted and compared to the theoretical tracking sensitivity value; if the estimated C/N_0 is lower, the tracking loop is determined to have lost its lock. The block responsible for this verification is called lock detector. The combination of I and Q components is used to determine the C/N_0. Several methodologies to determine the C/N_0 are proposed in [42].

3.1.2.2.2 Carrier Frequency Tracking (Frequency Lock Loop, FLL)

All GNSS receivers include another tracking loop similar to the PLL that tracks the incoming carrier frequency mainly generated by the satellite-to-user receiver motion and the user clock drift, the so-called Frequency Lock Loop (FLL) and aims at generating a local carrier which frequency equals the frequency of the incoming carrier. The simplified block diagram representation of the carrier tracking structure is derived from Figure 3-4.

The frequency tracking operation can be seen as the differential carrier phase tracking [38]. The frequency discriminators measure the carrier phase difference over two consecutive time epochs. As a consequence, FLL needs, at least, two consecutive correlator output's pairs to compute the discriminator.

Recalling the correlators outputs in 3-6 and 3-7, the goal of the FLL is to obtain a frequency shift error close to zero, $\varepsilon_f[k] \approx 0$, in order to track with high accuracy, the received signal carrier frequency, through the local replica, $\hat{f}_{NCO}$.

The Doppler frequency discriminators are depicted in section 3.1.2.2.2.1, then, the tracking loop implementation is presented in 3.1.2.2.2.2. The FLL error analysis is provided in 3.1.2.2.2.3 and, finally, the FLL tracking sensitivity is described in 3.1.2.2.2.4.

3.1.2.2.2.1 Carrier Frequency Discriminators

The usual frequency discriminators are based on the assessment of the phase variation between two consecutive correlator outputs. There are thus two conditions to fulfil when implementing a FLL discriminator:

- The consecutive correlator outputs have to be computed with the same local carrier frequency (to have a relevant estimation). It means that the discriminator output is computed every 2, at least, consecutive correlator outputs. The loop rate and the correlation rate are thus different;
- The consecutive correlator outputs have to belong to either to the same data bit, or the discriminator has to be resistant to data bit changes [43].

The commonly used FLL discriminators are described in [12]. The cross-product (CP) and four-quadrant (Atan2) discriminators are sensitive to data bit sign changes. In this case, in-phase and quadrature branches shall be collected within the same data period. The decision-directed cross-product (DDCP) and the differential arctangent (Atan) discriminators are insensitive to bit transition [38]. The cross-product discriminator is optimal in low SNR conditions as stated in the literature [38],[12]. Therefore, this discriminator is the preferred one when designing a receiver adapted to urban environments. Moreover, it has a low computational cost.

The In-Phase and Quadrature Component in two consecutive epochs, $(k, k-1)$, assuming an integration period, T_{FLL}, equal to the half of the PLL integration period, could be written as:

$$\begin{aligned} I_{P_{k-1}} &= \frac{A}{2} R(\varepsilon_{\tau_{k-1}})\, sinc\left(\pi \varepsilon_{f_{k-1}} T_{FLL}\right) cos\left(\pi \varepsilon_{f_{k-1}} T_{FLL} + \varepsilon_{\varphi_{k-1}}\right) \\ Q_{P_{k-1}} &= \frac{A}{2} R(\varepsilon_{\tau_{k-1}})\, sinc\left(\pi \varepsilon_{f_{k-1}} T_{FLL}\right) sin\left(\pi \varepsilon_{f_{k-1}} T_{FLL} + \varepsilon_{\varphi_{k-1}}\right) \end{aligned} \quad 3\text{-}18$$

$$\begin{aligned} I_{P_k} &= \frac{A}{2} R(\varepsilon_{\tau_k})\, sinc\left(\pi \varepsilon_{f_k} T_{FLL}\right) cos\left(\pi \varepsilon_{f_k} T_{FLL} + \varepsilon_{\varphi_k}\right) \\ &= \frac{A}{2} R(\varepsilon_{\tau_k})\, sinc\left(\pi \varepsilon_{f_k} T_{FLL}\right) cos\left(\pi \varepsilon_{f_k} T_{FLL} + 2\pi \varepsilon_{f_{k-1}} T_{FLL} + \varepsilon_{\varphi_{k-1}}\right) \end{aligned} \quad 3\text{-}19$$

$$\begin{aligned} Q_{P_k} &= \frac{A}{2} R(\varepsilon_{\tau_k})\, sinc\left(\pi \varepsilon_{f_k} T_{FLL}\right) sin\left(\pi \varepsilon_{f_k} T_{FLL} + \varepsilon_{\varphi_k}\right) = \\ &= \frac{A}{2} R(\varepsilon_{\tau_k})\, sinc\left(\pi \varepsilon_{f_k} T_{FLL}\right) sin\left(\pi \varepsilon_{f_k} T_{FLL} + 2\pi \varepsilon_{f_{k-1}} T_{FLL} + \varepsilon_{\varphi_{k-1}}\right) \end{aligned}$$

where:

- ε_τ is the code delay between the received signal and the local replica; it is assumed to be constant during the two consecutive epochs when the local replica chip rate is not modified, $\varepsilon_\tau = \varepsilon_{\tau_{k-1}} = \varepsilon_{\tau_k}$;
- ε_f is the frequency error between the received signal and the local replica; it is assumed to be constant during the two consecutive epochs when the local replica carrier frequency is not modified, $\varepsilon_f = \varepsilon_{f_{k-1}} = \varepsilon_{f_k}$;
- $\varepsilon_\varphi = \varphi_0 - \hat{\varphi}_0$ is equal to the carrier phase error at the beginning of the integration interval.

3.1.2.2.2.2 FLL Tracking Loop Implementation and Key Parameters

The optimal performance of the FLL occurs when the discriminator is operating in its linear region.

$$D_{type,k}(\varepsilon_f[k])\big|_{\varepsilon_f[k]\sim 0} = \varepsilon_f[k] + \eta_d[k] \quad 3\text{-}20$$

The given discriminator output, $D_{type,k}\left(\varepsilon_{f_k}\right)$, is sent to the low-pass filter, $\hat{\varepsilon}_{f_k}$, and the NCO to produce the carrier frequency generated by the NCO taking into account the nominal carrier frequency and the Doppler frequency estimation of the received signal, $\hat{f}_{NCO}$, as described below:

$$\hat{f}_{NCO}[k+1] = f_{IF} + f_D[k+1] \quad 3\text{-}21$$

where $f_D[k+1]$ is calculated with the FLL equivalent loop model. It will be similar to that of a PLL with the use of an extra integrator as justified in section 3.1.2.2.1.3. A second order loop FLL will use a typical second order filter followed by an extra-integrator in order to generate the final equivalent loop filter; the resulting the $\hat{\varepsilon}_{f_k}$ equation [44] is:

$$f_D[k+1] = 2f_D[k] - f_D[k] + \frac{K_1 + K_2}{2\pi T_{FLL}} D_{type,k+1}\left(\varepsilon_{f_{k+1}}\right) - \frac{K_1}{2\pi T_{FLL}} D_{type,k}\left(\varepsilon_{f_k}\right) \quad 3\text{-}22$$

where the value of the coefficients K_i are:

- $K_1 = \frac{8}{3} B_{FLL} T_{FLL}$;
- $K_2 = \frac{K_1^2}{2}$;

with B_{FLL} equal to the filter bandwidth and T_{FLL} equal to the integration period.

3.1.2.2.2.3 FLL Error Analysis

The errors affecting the FLL tracking accuracy are listed in the general section 3.1.2.2.1.4. The analysis of the overall error can be found in [20]. Although the multipath effects on code tracking in delay-locked loops (DLLs), and on carrier phase tracking in phase-locked loops (PLLs) are well documented in the state of the art, [15], [18], the multipath effects on carrier frequency tracking in frequency-locked loops (FLLs) will be treated in Chapter 0.

3.1.2.2.2.4 FLL Error Sensitivity

The rule of thumb for the FLL tracking threshold is that the 99% expected carrier frequency estimation error values must not exceed one-fourth of the frequency discriminator pull-in range (where the pull-in region is determined as the inverse of the corelation integration time), stated in [12] as:

$$3\sigma_{FLL,\eta} + \varepsilon_{FLL,dyn} \leq \frac{1}{4 \cdot T_{FLL}} \quad 3\text{-}23$$

where:

- $\sigma_{FLL,\eta}$ denotes the standard deviation of the thermal noise frequency jitter;
- $\varepsilon_{FLL,dyn}$ is the dynamic stress error in the FLL tracking loop;
- T_{FLL} is the FLL loop period.

3.1.2.2.3 Code Delay Tracking (Delay Lock Loop, DLL)

The general structure of the DLL loop is illustrated in Figure 3-6.

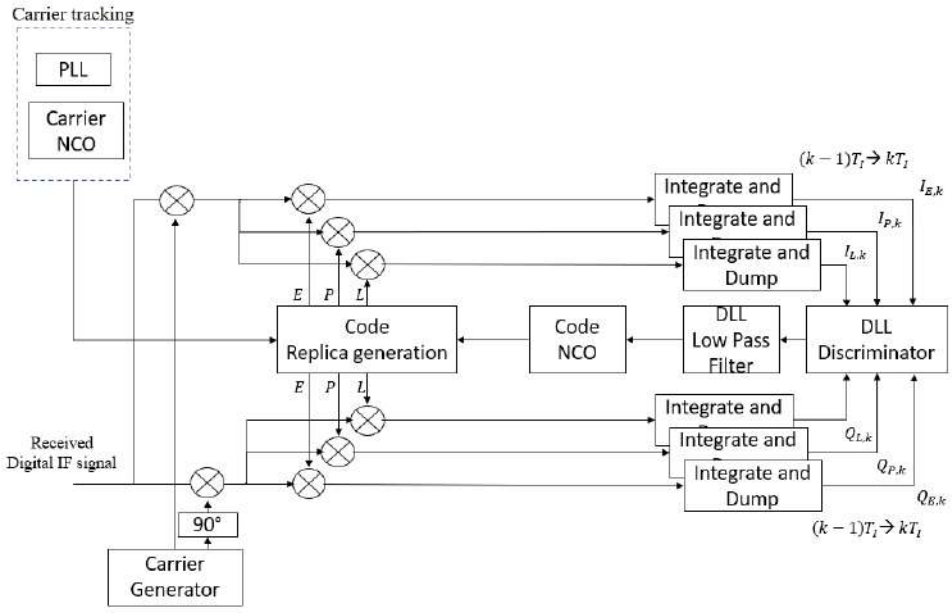

Figure 3-6 – Generic code tracking (DLL) loop

The code NCO generates three local replicas of the PRN code for the given processing channel, corresponding to the PRN code of the specific satellite in view. The three PRN copies, the so-called Early, Prompt and Late copies, are characterized by a different code delay. The prompt PRN code replica (P) is the local PRN code generated synchronously with the incoming PRN code according to the receiver (the one used by the PLL/FLL), the early PRN code replica (E) is advanced by $(d_c \cdot T_c) \,/\, 2$ with respect to the prompt PRN code and the late code replica (L) is delayed by $(d_c \cdot T_c) \,/\, 2$ with respect to the prompt PRN code, where d_c denotes the correlator early-late spacing and is expressed as the time delay between the Early and Late code replicas in units of chips.

The DLL conducts a correlation between the incoming signal and the three local replicas. The correlator output pairs result in the in-phase and quadrature signal replica components for E (I_E, Q_E), P (I_P, Q_P), and L (I_L, Q_L), as expressed by:

$$
\begin{aligned}
I_{E_k} &= \frac{A}{2} R\left(\varepsilon_{\tau_k} + \frac{d_c T_c}{2}\right) \operatorname{sinc}\left(\pi \varepsilon_{f_k} T_{DLL}\right) \cos\left(\pi \varepsilon_{f_k} T_{DLL} + \varepsilon_{\varphi_k}\right) \\
I_{P_k} &= \frac{A}{2} R\left(\varepsilon_{\tau_k}\right) \operatorname{sinc}\left(\pi \varepsilon_{f_k} T_{DLL}\right) \cos\left(\pi \varepsilon_{f_k} T_I + \varepsilon_{\varphi_k}\right) \\
I_{L_k} &= \frac{A}{2} R\left(\varepsilon_{\tau_k} - \frac{d_c T_c}{2}\right) \operatorname{sinc}\left(\pi \varepsilon_{f_k} T_{DLL}\right) \cos\left(\pi \varepsilon_{f_k} T_{DLL} + \varepsilon_{\varphi_k}\right) \\
Q_{E_k} &= \frac{A}{2} R\left(\varepsilon_{\tau_k} + \frac{d_c T_c}{2}\right) \operatorname{sinc}\left(\pi \varepsilon_{f_k} T_{DLL}\right) \sin\left(\pi \varepsilon_{f_k} T_{DLL} + \varepsilon_{\varphi_k}\right) \\
Q_{P_k} &= \frac{A}{2} R\left(\varepsilon_{\tau_k}\right) \operatorname{sinc}\left(\pi \varepsilon_{f_k} T_{DLL}\right) \sin\left(\pi \varepsilon_{f_k} T_{DLL} + \varepsilon_{\varphi_k}\right) \\
Q_{L_k} &= \frac{A}{2} R\left(\varepsilon_{\tau_k} - \frac{d_c T_c}{2}\right) \operatorname{sinc}\left(\pi \varepsilon_{f_k} T_{DLL}\right) \sin\left(\pi \varepsilon_{f_k} T_{DLL} + \varepsilon_{\varphi_k}\right)
\end{aligned}
\qquad 3\text{-}24
$$

where:

- $\left(\varepsilon_{\tau_k},\ \varepsilon_{f_k}\right)$ denotes the code delay and carrier frequency estimation errors at epoch k, expressed as the difference between the true (unknown) and the locally-estimated terms;
- $\varepsilon_{\varphi,0_k}$ denotes the carrier phase estimation error at the middle of the interval of epoch k, expressed as the difference between the true (unknown) and the locally-estimated terms;
- $d_c T_c$ refers to the E-L chip spacing with d_c representing the fraction of chip spacing and T_c denotes the code chip period.

The tracking loop implementation is presented in 3.1.2.2.3.1. Finally, the DLL error analysis is provided in 3.1.2.2.3.2.

3.1.2.2.3.1 DLL Tracking Loop Implementation

The optimal performance of the DLL occurs when the discriminator is operating in its linear region. This happens when the tracking error is low. In this case and without loss of generalities, it is possible to assume that:

$$
D_{type,k}(\varepsilon_\tau[k])\big|_{\varepsilon_\tau[k]\sim 0} = \varepsilon_\tau[k] + \eta_d[k] \qquad 3\text{-}25
$$

The discriminator output is sent to a low-pass filter to reduce the thermal noise affecting the estimation and to produce the local code delay error, $\hat{\varepsilon}_\tau[k]$.

The new local code signal is generated by chip rate frequency synthetized by NCO, where the NCO command is $\hat{\varepsilon}_\tau[k]$. The design of equivalent DLL loop is equal to the PLL one. The implementation of the low-pass filter depends as usual on several factors: filter's order n, the filter's bandwidth B_{DLL} and the integration period, T_{DLL}.

Signal dynamics have similar effects on the DLL as on the PLL. However, the DLL can be aided by the PLL (DLL-aided-PLL) so that it does not have to track the dynamics and thus, it can only focus on removing the thermal noise and mainly estimating the ionospheric delay: it is possible to reduce significantly the DLL loop bandwidth since only residual dynamics need to be tracked. Typical values of the DLL loop bandwidth when aided by the PLL/FLL are between 0.1 and 1 Hz.

For example, implementing a first order filter, the command signal is given in the equation 3-26 [44]:

$$\hat{\varepsilon}_\tau[k] = \frac{K_1}{T_I} D_{x,norm}(\varepsilon_\tau[k-1]) \quad 3\text{-}26$$

where the value of the coefficient $K_1 = 4B_{DLL}T_{DLL}$, with B_{DLL} equal to the filter bandwidth and T_{DLL} is the integration period.

3.1.2.2.3.2 DLL Error analysis

As per PLL and FLL error analysis, the main error sources affecting the DLL tracking performance are described in section 3.1.2.2.1.4. However, the receiver's oscillator noise and vibration, does not contribute significantly in the code delay error budget and thus are not presented. The detailed error analysis can be found in [12]. Multipath effects on the DLL tracking performance will be explained in the following Chapter 0. Multipath reflections impact severely the DLL process introducing a code delay resulting from the combination of the LOS component and MP components.

3.1.2.2.3.3 DLL Error Sensitivity

The conservative rule for the DLL tracking threshold is that the 3-sigma code error jitter due to the error sources given above, must not exceed the discriminator's linear region (half of the code discriminator region) as stated in [12]. Thus, the code tracking threshold for the two signals of interest is expressed as:

$$3\sigma_{DLL} = 3\sigma_{DLL,\eta} + \sigma_{DLL,dyn} \leq \frac{d_c}{2} \quad 3\text{-}27$$

where:

- $\sigma_{DLL,\eta}$ denotes the 1-sigma phase jitter due to the thermal noise;
- $\sigma_{DLL,dyn}$ is the dynamic stress error affecting the DLL tracking loop.

3.2 GNSS Receiver Data Processing

The code delay estimation, the phase lag estimation, the Doppler frequency estimation, and the demodulated navigation message, obtained through the Signal Processing Stage, are used in the Data Processing block to generate the raw measurements which are, consequently, corrected and processed to determine the receiver navigation solutions.

Figure 3-7 depicts the Data Processing chain. The first stage is the Measurement Generation (MG) block. In the MG block the output of the Digital Processing stage is used to generate the raw measurements. The raw measurements are generated at the same rate of the Digital Processing output. MG stage is further detailed in section 3.2.1.

Raw measurements are affected by several impairments which can strongly impact the accuracy of the solutions; for this reason, some of these impairments will be corrected or mitigated by the successive block, the Measurement Correction (MC), as detailed in section 3.2.2. The corrections may be applied at lower rate than the Digital Processing and MG block. This time period is denoted as data processing time, T_P, and is defined as a multiple of the integration time, $T_P = n \cdot T_I$.

Finally, the corrected measurements as well as the demodulated navigation message are processed in the Navigation Solution Estimation (NSE) block, which finally computes the receiver solutions, which are usually called Position, Velocity, and Time solutions (PVT) [12]. An introduction to the NSE stage is presented in section 3.2.3.

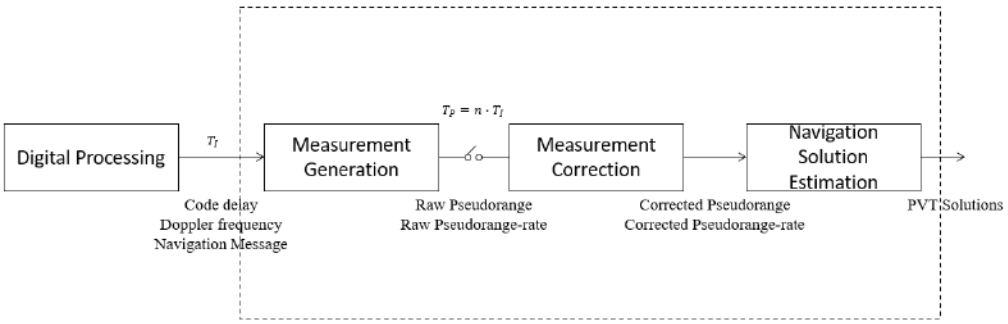

Figure 3-7 – Data Processing Block

3.2.1 Measurement Generation

The section contains a simple description of the Measurement Generation block. As described by its name, the goal of this stage is to generate the raw measurements, processing the outputs of the Digital Signal Processing block. The basic measurements include:

- Raw Pseudoranges (PSR), based on the code (or phase) delay estimation [12], representing the distance between the GNSS satellite and the receiver, as introduced in section 2.1.3.1.
- Raw Pseudorange-rates (PSR-R), based on Doppler-frequency estimation [12]. PSR-R represents relative velocities of the receiver with respect to the GNSS satellites, as depicted in section 2.1.3.1.

In this work, only code PSR are treated, whilst phase PSR may be used in some applications either through resolving ambiguities or for smoothing, they are not treated in this PhD.

This work will focus on the single frequency receiver performances in dual constellation mode. This means that the receiver is able to process two different constellations at the same time and to determine a PVT navigation solution with a higher accuracy, especially in harsh environments, where the number of visible satellites are drastically reduced. In this specific work, the GPS and Galileo constellations will be processed. In order to have a general measurement model (PSR and PSR-R) that incorporates both constellations, the bias resulting from the GPS and Galileo signal processing must be modelled. For this reason, this section will provide the model of Dual constellation (GPS and Galileo) measurement models, that will be exploited in the following sections.

The Code PSR and Doppler PSR-R models for single GNSS constellation are presented in section 3.2.1.1. Finally, the PSR and PSR-R models for Dual constellation (GPS and Galileo) are presented in section 3.2.1.2.

3.2.1.1 Single Constellation Measurement Models

In this section the raw PSR and PSR-R for a single constellation receiver are modelled and characterized. Raw PSR measurements have been obtained from the code delay observables, while PSR-R from the Doppler frequency.

The raw PSR model is introduced in section 2.1.3.1. The basic equation for the raw PSR measurement is provided in 2-4. This measurement does not take into account a detailed model of the undesired errors. Indeed, in the real case the transmitter and the receiver have synchronization biases, and the transmitted signal is subject to distortion from the transmission channel. This section provides a description of the raw PSR error model, in section 3.2.1.1.1. Similarly, the raw PSR-R model is introduced in section 2.1.3.1. The basic equation for raw PSR-R measurement is provided in 2-10. The raw PSR-R error model is introduced in the second part of section 3.2.1.1.2.

3.2.1.1.1 Pseudorange (PSR) Model

The PSR equation has been introduced in 2-4, including the error terms contributing to the total PSR error, ε_ρ. The overall error, ε_ρ, is assumed to be independent from satellite to satellite and composed by independent error variables. It can be modelled as follows:

$$\varepsilon_\rho^i = \qquad 3\text{-}28$$

$$= b_r - b^i + I^i + T^i + \xi^i + \beta_r + \beta^i + \eta^i \text{ [m]}$$

where:

- Δt^i is the satellite's clock error, in $[s]$;
- $b^i = c \cdot \Delta t^i$, is the satellite's clock error, in [m];
- I^i denotes the ionospheric error in [m];
- T^i denotes the tropospheric error in [m];
- ξ^i is the error induced by the multipath effect [m];
- β_r is the receiver hardware bias [m];
- β^i is the satellite i hardware error [m];
- η^i represents the error induced by receiver's thermal noise and the interference contribution [m];
- c is the speed of light, in [m/s].

Therefore, substituting 3-28, in 2-4, it is obtained the model of ρ, computed by the receiver for a given satellite i is equal to:

$$\rho^i = \\ = R^i + b_r - b^i + I^i + T^i + \xi^i + \beta_r + \beta^i + \eta^i \text{ [m]} \quad \text{3-29}$$

The presence of the error components in the raw PSR prevents an accurate navigation estimation. For this reason, GNSS receivers apply measurement corrections instead of processing directly the raw PSR in the NSE.

The different error sources are introduced in the following paragraphs. Detailed analysis of PSR error components could be found in [45]. In addition to that, it is also presented the ephemeris error, which is not part of measurement error model presented in 3-29. This error appears when it is needed the estimation of the satellite positions (usually for correction purposed or PVT estimation purposes), which is usually obtained applying calculating the GNSS satellite orbit through the application of the so-called ephemeris, transmitted with the satellite clock parameters in the navigation message.

The *satellite ephemeris delay* results from the mismatch between the satellite actual position and its predicted position from the satellites ephemeris broadcasted in the navigation message. The ephemeris error appears when the ephemeris has been used to estimate the satellite positions and estimates the true range. The PSR and PSR-R mathematical models including the ephemeris error components are presented in section 3.2.3.1. This term is not a part of the propagation time delay as well as error due to tracking. However, since it is relevant in the overall error model and it is usually mitigated by the application of differential measurement correction techniques, described in the following sections, it is useful to define it here. The ephemeris error is described in [12] [46].

The *satellite clock error* is caused by a deviation of the satellite oscillator from its specific frequency rate. This is caused by the oscillator phase noise and to a lesser extent oscillator vibrations. The order of magnitude of the satellite clock error depends the clock design characteristics. Neglecting the receiver clock to be estimated, in the raw measurement, the satellite clock is the dominating error source. Nominally, satellite clock errors vary slowly in time, except at navigation message changeovers. As an example, in [46] it is reported the normalized autocorrelation function for GPS satellite clock error, for a period of 30 minutes. It decorrelate significantly only over 30 minutes; Block IIR satellite clock has a correlation of 0.5. It can be assumed that the modern clocks have similar behaviour. The observables affected by satellite clock error could not be used to make PVT estimation, since satellite clock error has a large impact on the measurements (several kilometres, [47]). Thus, a satellite clock error correction is mandatory to apply the Navigation Solutions Estimation. Two different basic approach could be applied: the standalone corrections, described in section 3.2.2.1, and the DGNSS corrections, involving a reference station measurement, assuming the distance between the reference station and the receiver under exam (the so-called baseline), relatively small (under 10 km). This correction technique is detailed in section 3.2.2.2.

The ionosphere introduces a group delay on code pseudorange measurement and a phase advance of equal magnitude and opposite sign on the carrier phase measurement. The impact on the pseudorange-rate is the derivative of the phase advance error. The ionospheric error is already introduced in section 2.4.1.1. The mathematical expression for *ionospheric error* is modelled in [12]. The ionospheric error is spatially and temporally correlated. The impact of spatial correlation is a function of the distance between the two points also called the baseline length and is typically a few millimetres per kilometre for a satellite at zenith, with further details found in [48], [49]. Whereas, the magnitude of the time correlation is detailed in [46]. It could be assumed that the ionospheric error decorrelates nominally over a period larger than 30 minutes. Ionospheric error for a mass market receiver operating in an open-sky environment, could be considered the second source of error in order of magnitude, after the satellite clock error. Thus, to estimate PVT solutions with a reasonable accuracy, the

ionospheric error should be corrected, standalone and DGNSS correction techniques are briefly described in section 3.2.2.1 and 3.2.2.2, respectively.

The *tropospheric error* has been introduced in section 2.4.1.1. The effect of the troposphere on GNSS signals appears as an extra delay in the measurement of the signal traveling from the satellite to receiver, as described in [12]. The tropospheric error is temporally and spatially correlated. As per ionospheric errors, spatial correlation depends on specific baseline length with typical order of magnitude found in [48], [49]. An example of the magnitude of the tropospheric time correlation is detailed in [46]. Although the magnitude of tropospheric error is smaller than the ionospheric one, this error will have a significant effect on the accuracy of the computed positions. Thus, to estimate PVT solutions with an optimal level of accuracy, the tropospheric error should be corrected. The tropospheric standalone and DGNSS correction techniques are briefly described in section 3.2.2.1 and 3.2.2.2, respectively.

Multipath effects on GNSS signals are introduced in section 2.4.1.2. The processing of the Line-of-Sight and the replicas creates a biased discriminator output, which induces a tracking error. For both the DLL and the PLL, MP will thus create a tracking bias that will depend upon the amplitude, the phase and the delay of the multipath with the respect to the direct signal. In the case of a static GNSS receiver positioned in a MP environment, the MP errors are expected to experience higher correlation times than receivers located in an open-sky environment. Moreover, the MP error in this case becomes the dominant error source, and, therefore, most of the temporal correlation depends on the multipath error component, making the temporal correlation very dependent on the MP environment. The effect of MP on code pseudorange measurements is higher than the effect on carrier phase pseudorange measurements. However, MP in carrier phase pseudorange measurements is much harder to be mitigated due to the cycle slips events. Detailed multipath effects on the pseudorange measurement are described in Chapter 0. The multipath error correlation time depends on several factors. Firstly, the multipath error depends on the specific environment and the dynamics of the user receiver. Modelling the multipath error in the urban environment is one of the goals of this PhD research project, as illustrated in Chapter 5. The characteristics of the multipath errors, including also the time and space correlations, are described in Chapter 6.

GNSS transmitters and receivers are electronic devices which process the GNSS signals introducing some unwanted delays, usually referred to as *hardware biases*. Satellite hardware biases are mainly caused by the group delay at the transmitter RF front-end filter output. Receiver hardware biases that a single receiver experience will be different for each signal as well as different between different receivers. For signals received on the same carrier frequency, the delay introduced by hardware equipment is approximately equal. This means that the receiver RF front-end filter introduces a similar group delay for each signal received at the same carrier frequency. However, receiver hardware biases are different for each GNSS constellation, even if the signals are tracked on frequency bands that overlap between the constellations, due to differences in signal structures employed by various GNSS systems. These are commonly referred to as inter-system biases (ISBs). In the case of GPS and Galileo dual constellation, GPS L1 C/A is a BPSK(1) chip modulated signal whereas Galileo E1 OS is a CBOC(6,1,1/11) chip modulated signal. This means that the RF front-end filter introduces a different group delay for each filter that may not be corrected by the receiver before providing the pseudorange measurements without a specific tuning operation.

Thermal noise errors on the observables are induced by the receiver tracking loops. The receiver thermal noise is inevitable. It is a relatively small contributor with respect to the other errors. Ideally, it is an uncorrelated error, meaning that the noise component in two different instants of time is not statistically correlated. In the code PSR code measurements, the size of the error is related to chip width. As said, thermal noise modelled at the input of the Receiver Signal Processing is considered uncorrelated in time. On the contrary, when it is processed by the tracking blocks it could not be considered time uncorrelated due to the presence of the filter loop.

3.2.1.1.2 Pseudorange-rate (PSR-R) Model

The pseudorange-rate, $\dot{\rho}$, including the measurement errors, computed by the receiver for a given satellite i, is modelled as follows:

$$\dot{\rho}^i = \dot{R}^i + \dot{b}_r - \dot{b}^i - \dot{I}^i + \dot{T}^i + \dot{\zeta}^i + \dot{\beta}_r + \dot{\beta}^i + \dot{\nu}^i \text{ [m/s]} \qquad 3\text{-}30$$

The hardware drifts are assumed negligible with respect to the other error components for low-cost receiver in urban environment. Multipath error component in PSR-R measurements is investigated in Chapter 6.

In analogy with PSR measurements, the overall PSR-R error, $\varepsilon_{\dot{\rho}}$ is composed by several independent error components introduced randomly by the source of errors modelled in the transmission channel.

The $\varepsilon_{\dot{\rho}}$ model is equal to:

$$\varepsilon_{\dot{\rho}}^{i} = \dot{b}_r - \dot{b}^i - \dot{I}^i + \dot{T}^i + \dot{\zeta}^i + \dot{\beta}_r + \dot{\beta}^i + \dot{\nu}^i \text{ [m/s]} \quad 3\text{-}31$$

where:

- $\dot{b}^i$ is the satellite clock drift, which is equal to the derivative of the clock bias;
- $\dot{b}_r$ is the receiver clock drift, which is equal to the derivative of the clock bias;
- $\dot{I}^i$ is the ionospheric delay drift, which is equal to the derivative of the ionospheric error;
- $\dot{T}^i$ is the tropospheric delay drift, which is equal to the derivative of the tropospheric error;
- $\dot{\zeta}^i$ is the error due to the presence of the multipath;
- $\dot{\beta}_r$ is the receiver hardware error caused by receiver hardware drift, which is equal to the derivative of the receiver hardware bias;
- $\dot{\beta}^i$ is the satellite i hardware error caused by satellite hardware drift, which is equal to the derivative of the satellite hardware bias;
- $\dot{\nu}^i$ denotes the receiver's thermal noise effect on the carrier measurements;
- c is the speed of light;

3.2.1.2 Dual Constellation Measurement Models

Single constellation PSR and PSR-R measurements, for a given satellite i, are modelled in equation 3-29 and 3-31. Since this work focuses on a dual-constellation, GPS and Galileo, receiver platform, it is thus required to present the propagation delays for both GPS and Galileo constellations.

The GPS clock bias with respect to the GPS reference time is equal to:

$$\Delta t_{r,GPS} - \Delta t_{GPS}^{i} = (t_r - t_{GPS}) - (t^i - t_{GPS}) \quad 3\text{-}32$$

where:

- t_r is the receiver time corresponding to epoch k of the receiver's clock in s;
- t^i is the satellite transmission time based on the satellite clock for the reception at epoch k in s;
- t_{GPS} represents the GPS time, computed by the GPS Master Control Station in s;
- c is the speed of light, in m/s.

The GPS clock bias with respect to the GPS reference time, expressed in terms of range error is:

$$b_{r,GPS} - b_{GPS}^{i} = c \cdot \left(\Delta t_{r,GPS} - \Delta t_{GPS}^{i}\right) \quad 3\text{-}33$$

where:

- $b_{r,GPS}$ is the receiver's clock bias with respect to GPS time, expressed in [m];
- b_{GPS}^{i} is the i-th GPS satellite clock bias with respect to GPS time, expressed in [m].

The same operation could be applied for the Galileo i satellite clock term:

$$\Delta t_{r,GAL} - \Delta t_{GAL}^{i} = (t_r - t_{GAL}) - (t^i - t_{GAL}) \quad 3\text{-}34$$

with t_{GAL}^{i} and t_{GAL} representing the Galileo satellite clock time and the Galileo time, respectively. The Galileo clock bias with respect to Galileo reference time, expressed in terms of range error is:

$$b_{r,GAL} - b_{GAL}^{i} = c \cdot \left(\Delta t_{r,GAL} - \Delta t_{GAL}^{i}\right) \quad 3\text{-}35$$

where, $b_{r,GAL}$ and b_{GAL}^{i} are the receiver's clock bias and the *i-th* Galileo satellite clock bias with respect to Galileo reference time expressed in m.

However, in the approach presented in this work it has been selected only one GNSS time reference to express all the received measurements, in order to have only one receiver clock time bias to be estimated in the PVT solution. In particular it is taken GPS time as reference; therefore, expression $\Delta t_{r,GAL}$ can be modified as:

$$\Delta t_{r,GAL} = t_r - t_{GAL} = (t_r - t_{GPS}) + (t_{GPS} - t_{GAL}) = \Delta t_{r,GPS} + \Delta t_{GPS/GAL} \quad 3\text{-}36$$

where $\Delta t_{GPS/GAL}$ is the inter-constellation clock offset expressed in seconds. Therefore, in order to take into account the different time scale, in case of multi constellations use, Galileo satellites broadcast the GGTO [47] (GPS to Galileo time offset) model which consists in a first order polynomial.

$$b_{r,GAL} = c \cdot \left(\Delta t_{r,GPS} + \Delta t_{GPS/GAL}\right) = b_{r,GPS} + \delta \quad 3\text{-}37$$

where δ is the GGTO, expressed in meters.

The different time scale between GPS and Galileo PSR-R has effects on the definition of clock drift and it could be defined as follows:

$$\dot{b}_{r,GAL} = \dot{b}_{r,GPS} + \dot{\delta} \quad 3\text{-}38$$

where $\dot{\delta}$ is the time derivative of the GGTO.

In the subsection 3.2.1.2.1 the dual constellation Pseudorange model is presented, while in the subsection 3.2.1.2.2 the Pseudorange-rate model is described.

3.2.1.2.1 Dual Constellation Pseudorange Model

The code propagation delay for the i^{th} GPS satellite at epoch k, is provided by:

$$\rho^i_{GPS} = R^i + b_{r,GPS} - b^i_{GPS} + I^i + T^i + M^i + bh_{R,GPS} + bh^i_{T,GPS} + \eta^i \quad 3\text{-}39$$

The same relation also holds for the code propagation delay of the Galileo satellites, expressed as:

$$\rho^i_{GAL} = R^i + b_{r,GPS} + \delta - b^i_{GAL} + I^i + T^i + M^i + bh_{R,GAL} + bh^i_{T,GAL} + \eta^i \quad 3\text{-}40$$

3.2.1.2.2 Dual Constellation Pseudorange-rate Model

The pseudorange-rate measurement from a given constellation, for the i^{th} GPS satellite at epoch k, is provided by:

$$\dot{\rho}^i_{GPS} = \dot{R}^i + \dot{b}_{r,GPS} - \dot{b}^i_{GPS} + \dot{I}^i + \dot{T}^i + \zeta^i + \dot{\beta}_{r,GPS} + \dot{\beta}^i_{GPS} + \nu^i \ [\mathrm{m/s}] \quad 3\text{-}41$$

The same relation also holds for the pseudorange-rate measurement of the Galileo satellites, expressed as:

$$\dot{\rho}^i_{GAL} = \dot{R}^i + \dot{b}_{r,GPS} + \dot{\delta} - \dot{b}^i_{GAL} + \dot{I}^i + \dot{T}^i + \zeta^i + \dot{\beta}_{r,GAL} + \dot{\beta}^i_{GAL} + \nu^i \ [\mathrm{m/s}] \quad 3\text{-}42$$

where $\dot{b}_{r,GAL} = \dot{b}_{r,GPS} + \dot{\delta}$.

In this work, the PSR-R model is supposed not affected by the change of constellation, since the order of magnitude of the time derivative of δ is negligible with respect to the other errors.

3.2.2 Measurement Correction

As presented in section 3.2.1, some of the errors affecting the PSR measurement (errors not linked to the closed loop estimation process) could be corrected before the Navigation Solution Estimation process starts. In particular, the corrections are applied for the satellite clock, ionospheric and tropospheric errors.

The correction can be achieved either by a standalone (SA) approach or differential approach (section 2.2.3.2). The standalone approach provides less precise corrections with respect to differential corrections. SA corrections are based on the estimation of the correction terms by applying predictive models for the satellite clock error and empirical models for ionospheric and tropospheric error corrections. The estimated correction terms are finally applied to the raw measurements. This approach is applied usually by single-frequency, low-cost receivers. The SA methodology is applied in this work as a baseline measurement correction methodology for low-cost mass-market single frequency receiver. Section 3.2.2.1 presents the SA methodology.

On the contrary, the differential correction is achieved generally applying a difference between the raw measurement under test and a second measurement, under specific conditions. DGNSS correction is achieved differencing the raw measurement under exam with a measurement obtained from a reference station, used to correct ephemeris error, satellite clock, ionospheric and tropospheric errors, if the baseline between the receiver under test and the reference is small; this approach is feasible in real-time only if the receiver can acquire the measurement from the reference station; DGNSS methodology is applied in this work to provide an enhanced solution for low-cost mass-market single frequency receiver, with the hypothesis that in the future could be defined as the baseline approach for mass market receivers. DGNSS mathematical models are illustrated in section 3.2.2.2.

Dual Frequency (DF) [12] correction is a differential correction that can be applied only if the receiver is dual frequency. The receiver generates two different raw measurements depending on the specific carrier frequency

and modulation. It is applied to correct the ionospheric error. In this work, the receiver under test is single frequency, therefore, the DF could not be applied.

3.2.2.1 Standalone (SA) correction

The following subsections present the methods applied in this work to apply standalone corrections. The SA correction methodology is based on the following process:

- firstly, the satellite clock bias, ionospheric error and tropospheric error are estimated by using predictive models at the ground segment, sending of the corrections by the navigation message;
- the estimated parameters are then applied to the raw PSR and PSR-R measurements.

The predictive model used to estimate the satellite clock bias is presented in subsection 3.2.2.1.1. The empirical model used to calculate the ionospheric error is described in subsection 3.2.2.1.2, while the empirical model used to derive the tropospheric error is depicted in subsection 3.2.2.1.3. In the following part, section 3.2.2.1.4, the SA PSR and PSR-R models are described.

3.2.2.1.1 Satellite clock error correction

The satellite clock error for the GPS and Galileo constellations is modelled through three parameters $(a_{f_0}, a_{f_1}, a_{f_2})$, reflecting the clock bias, drift and drift rate retrieved from the navigation data, which are included in each satellite's navigation message together with a reference time. The GPS and Galileo Control Stations model the onboard clock deviation with respect to the GPS\Galileo reference time using a quadratic polynomial in time.

The satellite clock correction model for each satellite in view i is provided in [50] and [12]. This model may be valid for a maximum of 4 hours [50], even if GPS updates every two hours the clock parameters in the navigation message [51], while Galileo update every three hours the clock parameters [52], being valid for a 4 hours interval. The residual satellite clock error after correction results in a ranging error with a standard deviation that typically varies from 0.3 to 4 m depending on the type of the satellite and the age of the broadcasted data, according IGS and GPS SPS [53], [54].

The model is the same for both GPS and Galileo. However, they assume different time scales.

$$\widehat{\Delta t}^{i}_{GAL} = \widehat{\Delta t}^{i}_{GPS} + \widehat{\Delta t}_{GPS/GAL} \tag{3-43}$$

where $\widehat{\Delta t}_{GPS/GAL}$ is the estimated GGTO on the Navigation message.

The residual clock error in presence of SA correction is equal to:

$$\tilde{b}^{i} = c \cdot \widehat{\Delta t}^{i} = b^{i} - \hat{b}^{i} = c \cdot \left(\Delta t^{i} - \widehat{\Delta t}^{i}\right) \tag{3-44}$$

3.2.2.1.2 Ionosphere error correction

Different models are employed in the literature to estimate and thus mitigate the ionospheric delays. In standalone mode, if the receiver is a single-frequency, the only way to correct the ionospheric delay is by means of model which is able to first estimate the error. GPS uses the Klobuchar model for the ionospheric delay estimation, whose parameters are transmitted in the GPS navigation message [55]. Similarly, single-frequency Galileo receivers use the NeQuick model [56].

In this work, when SA correction method is applied, ionospheric error has been corrected using Klobuchar model in case of GPS and Nequick in case of Galileo constellation.

The residual ionospheric error is defined as the difference between the raw PSR term and the estimated ionospheric error:

$$\tilde{I} = I - \hat{I} \tag{3-45}$$

where $\hat{I}$ is the estimated ionospheric error.

3.2.2.1.3 Troposphere error correction

The effect of the troposphere on the GNSS signal appears as a delay. The tropospheric delay can be modelled as a function of the satellite elevation angle. Due to the differences between the atmospheric profiles of the dry gases and water vapour it is better to use different mapping functions in terms of the dry and wet components depending on the elevation angle. Nevertheless, simple models as [57], [2] use a common mapping for both components; for meter-level accuracy, several models can be used to mitigate the total tropospheric error, such as Hopfield, Saastamoinen or UNB3m model.

In this work, tropospheric error has been corrected using UNB3m model [58]. The residual SA tropospheric error term is defined as the difference between the raw PSR term and the estimated tropospheric error:

$$\tilde{T} = T - \hat{T} \tag{3-46}$$

where $\hat{T}$ is the estimated tropospheric error.

3.2.2.1.4 SA Measurement Models

The previous section defined the procedure used to apply the SA corrections to raw PSR measurements. This section provides then the corrected PSR model, and the derivation of the corrected PSR-R model.

Having defined in the previous subsections the estimated values of satellite clock bias $\hat{b}^i$, ionospheric error $\hat{I}$ and troposphere error $\hat{T}$, it is possible to now apply a correction to the measurement models.

The corrected pseudorange model is defined by removing the estimated bias from the raw measurement:

$$\tilde{\rho}^i = \rho^i + \hat{b}^i - \hat{I}^i - \hat{T}^i \tag{3-47}$$

Following the equation of the pseudorange model, 3-29, the corrected pseudorange model, $\tilde{\rho}^i$, is equal to:

$$\tilde{\rho}^i = R^i + b_r - \tilde{b}^i + \tilde{I}^i + \tilde{T}^i + \xi^i + \beta_r + \beta^i + \eta^i \tag{3-48}$$

Due to the superimposed effects of the thermal noise and the MP at the tracking stage level due MP and thermal noise error components will be seen as the unique and main error component in urban environment.

In this thesis, a simplified PSR-R error correction has been defined. The estimation of the satellite clock, ionosphere and troposphere drift could be calculated starting from the corresponding satellite clock, ionosphere and troposphere bias, as a difference between the actual and the previous estimations, divided by the data processing time. The resulting error models are listed as follows:

- Satellite clock drift:

$$\hat{\dot{b}}^i(t) = \frac{\hat{b}^i(t) - \hat{b}^i(t - T_P)}{T_P} = a_{f_1}^i + 2a_{f_2}^i\left(t_{GPS}^i - t_{0,c}\right) \tag{3-49}$$

- Ionosphere drift:

$$\hat{\dot{I}}^i\,(t) = \frac{\hat{I}(t) - \hat{I}(t - T_P)}{T_P} \tag{3-50}$$

- Troposphere drift:

$$\hat{\dot{T}}^i(t) = \frac{\hat{T}(t) - \hat{T}(t - T_P)}{T_P} \tag{3-51}$$

The corrected terms are equal to

- $\tilde{\dot{b}}^i = \dot{b}^i - \hat{\dot{b}}^i$ is the residual satellite's clock bias after the correction, in $[s]$;
- $\tilde{\dot{I}} = \dot{I} - \hat{\dot{I}}$ denotes the residual ionosphere error after the correction, in $[m]$;
- $\tilde{\dot{T}} = \dot{T} - \hat{\dot{T}}$ denotes the residual troposphere error after the correction, in $[m]$;

The corrected pseudorange-rate model is defined as:

$$\tilde{\dot{\rho}}^i = \dot{R}^i + \dot{b}_r - \tilde{\dot{b}}^i + \tilde{\dot{I}} + \tilde{\dot{T}} + \zeta^i + \nu^i \text{ [m/s]} \tag{3-52}$$

Same considerations of pseudorange errors in urban environment have been done, in this work, for pseudorange-rate errors.

3.2.2.2 Differential GNSS (DGNSS) correction

In this section the basic DGNSS technique used to correct the PSR and PSR-R measurements is presented. The approach consists of the difference between the raw measurements of the user and error estimates (range-free measurement) measured by a reference receiver in the vicinity of the user receiver. The choice of baseline length should depend on the spatial correlation characteristics of the error components which should be removed by DGNSS approach.

The reference station is in a fixed and known location and is used to estimate errors which are correlated spatially and temporally. However, an important drawback is that the uncorrelated errors of multipath and noise from the reference station also contaminate the corrections. Therefore, there will be an "amplification" of the uncorrelated errors in comparison to standalone processing [49]. With regards to the baseline distance: from [59] it could be assumed that ionospheric and tropospheric errors are highly spatial correlated for a baseline shorter than 10km.

The user receiver PSR ρ_r and PSR-R $\dot{\rho}_r^i$ for a given satellite i, are modelled in 3-29 and 3-30. The reference station receiver PSR ρ_{sta} and PSR-R $\dot{\rho}_{sta}^i$ for a given satellite i, are modelled as:

$$\begin{aligned} \rho_s^i &= R_s^i + b_s - b^i + I_s^i + T_s^i + \xi_s^i + \beta_s + \beta^i + \eta_s^i \\ \dot{\rho}_s^i &= \dot{R}_s^i + \dot{b}_s - \dot{b}^i + \dot{I}_s^i + \dot{T}_s^i + \zeta_s^i + \dot{\beta}_s + \dot{\beta}^i + \nu_s^i \end{aligned} \quad \text{3-53}$$

The approach is detailed in subsection 3.2.2.2.1. Once the procedure is described, the following subsection, 3.2.2.2.2, shows the DGNSS corrected PSR and PSR-R models.

3.2.2.2.1 DGNSS procedure

The DGNSS approach consists of two sequential steps:

The first step is the so called true-range removal from the reference station measurement; given the computed satellite position the range can be removed from the PSR measurements. The same approach could be used to remove the range-rate from the PSR-R measurement, given the satellite velocity. The goal is to obtain a measurement residual, also called range-free residual, which contains only the error terms. The range-free PSR residual could be computed if the location of the user and reference station antennas are known. A high precision reference trajectory is used to provide the accurate user location even in an urban environment.

$$\begin{aligned} \Delta_{\rho,s}^i &= \rho_s^i - \hat{R}_s^i \\ \Delta_{\rho,s}^i &= e_s^i + b_s - b_s^i + I_s^i + T_s^i + \xi_s^i + \beta_s + \beta_s^i + \eta_s^i \end{aligned} \quad \text{3-54}$$

For a reference receiver in a known location, $(p_{s,x}, p_{s,y}, p_{s,z})$, it is possible to precisely estimate the true range $\hat{R}_s^i$, as:

$$\hat{R}_s^i = \sqrt{\left(\hat{p}_x^i - p_{s,x}\right)^2 + \left(\hat{p}_y^i - p_{s,y}\right)^2 + \left(\hat{p}_z^i - p_{s,z}\right)^2} \quad \text{3-55}$$

where the satellite position, $(\hat{p}_x^i, \hat{p}_y^i, \hat{p}_z^i)$, is estimated from the satellite ephemeris.

Similarly, for a reference receiver, with a known velocity, $(\dot{p}_{s,x}, \dot{p}_{s,y}, \dot{p}_{s,z})$, it is possible to precisely estimate the true range-rate $\hat{\dot{R}}_s^i$, as:

$$\hat{\dot{R}}_s^i = \left(\hat{\dot{p}}_x^i - \dot{p}_{s,x}\right)\hat{u}_{s,x}^i + \left(\hat{\dot{p}}_y^i - \dot{p}_{s,y}\right)\hat{u}_{s,y}^i + \left(\hat{\dot{p}}_z^i - \dot{p}_{s,z}\right)\hat{u}_{s,z}^i \quad \text{3-56}$$

where the satellite velocity, $(\hat{\dot{p}}_x^i, \hat{\dot{p}}_y^i, \hat{\dot{p}}_z^i)$, is estimated from the satellite ephemeris, and the estimated line-of-sight vector $\hat{\boldsymbol{u}}_s^i = \left(\frac{\hat{p}_x^i - p_{s,x}}{\hat{R}_s^i}, \frac{\hat{p}_y^i - p_{s,y}}{\hat{R}_s^i}, \frac{\hat{p}_z^i - p_{s,z}}{\hat{R}_s^i}\right)$.

where e_s^i is the residual error projected in the pseudorange domain due to the satellite i position estimation error, more details are given in section 3.2.3.1.

$$e_s^i = R_s^i - \hat{R}_s^i \quad \text{3-57}$$

The range-free PSR-R residual could be computed if the speed of the user and reference station receiver are known. The reference station range-free pseudorange-rate residual (per satellite i) is equal to

$$\begin{aligned} \Delta_{\dot{\rho},s}^i &= \dot{\rho}_s^i - \hat{\dot{R}}_s^i \\ \Delta_{\dot{\rho},s}^i &= \dot{e}_s^i + \dot{b}_s - \dot{b}_s^i + \dot{I}_s^i + \dot{T}_s^i + \dot{\zeta}_s^i + \dot{\beta}_s + \dot{\beta}^i + \dot{\nu}_s^i \end{aligned} \quad \text{3-58}$$

The e_s^i is the residual error projected on the pseudorange domain due to the satellite i position estimation error.

$$\dot{e}_s^i = \dot{R}_s^i - \hat{\dot{R}}_s^i \quad \text{3-59}$$

The second step consists of the user PSR correction which is obtained by differencing the user measurements with the reference station residual measurements, obtained in the previous step. Knowing the position of the reference station, this residual can be easily determined in the case of PSR measurement by differencing the true range component (also called effective range), and the PSR measurement, and in case of PSR-R by differencing the true range-rate component, and the PSR-R measurement. The DGNSS correction is achieved differencing the user PSR, $\tilde{\rho}_r^i$, and PSR-R, $\tilde{\dot{\rho}}_r^i$, measurements with the range-free PSR residual, $\Delta_{\rho,s}^i$, and PSR-R residual, $\Delta_{\dot{\rho},s}^i$, respectively.

$$\begin{aligned} \tilde{\rho}_r^i &= \rho_r^i - \Delta_{\rho,s}^i \\ \tilde{\dot{\rho}}_r^i &= \dot{\rho}_r^i - \Delta_{\dot{\rho},s}^i \end{aligned} \quad \text{3-60}$$

3.2.2.2.2 DGNSS Measurement Models

This section follows the DGNSS correction procedure and defines the DGNSS measurement models obtained applying the methodology in section 3.2.2.2.1. The satellite clock bias and the atmospheric bias removal from pseudorange measurement is achieved by differencing the user's pseudorange measurement ρ_r^i from the reference station's range free pseudorange residual $\Delta_{\rho,s}^i$ as presented in equation .

$$\begin{aligned} \tilde{\rho}_r^i = (R^i + e_s^i) + (b^i - b_s^i) - (b_r - b_s) + (I^i - I_s^i) + (T^i - T_s^i) + (\xi^i - \xi_s^i) + (\beta_r - \beta_s) \\ + (\beta^i - \beta_s^i) + (\eta^i - \eta_s^i) \end{aligned} \quad \text{3-61}$$

Supposing the receiver under test and the reference station receiver are close enough to have a correlated atmospheric effect, 3-61 could be written as

$$\tilde{\rho}_r^i = R^i + e_s^i + \tilde{b}^i - (b_r - b_s) + (\xi^i - \xi_s^i) + (\beta_r - \beta_s) + \tilde{\beta}^i + \tilde{I}^i + \tilde{T}^i + (\eta^i - \eta_s^i) \quad \text{3-62}$$

The resulting term, $\tilde{\rho}_r^i$, is denoted as the pseudorange residual difference:

- $\tilde{b}^i = b^i - b_s^i$ denotes the residual satellite clock error after the correction, in $[m]$;
- $\tilde{I}^i = I^i - I_s^i$ denotes the residual ionosphere error after the correction, in $[m]$;
- $\tilde{T}^i = T^i - T_s^i$ denotes the residual troposphere error after the correction, in $[m]$;
- $\tilde{\beta}^i = \beta^i - \beta_s^i$ denotes the residual satellite hardware error after the correction, in $[m]$.

In this case, the residual ionospheric and tropospheric error component magnitude depends on the distance of the baseline: for short baselines, shorter than 2 km [48], the two error components are on the order of millimetres and should be negligible. For baselines shorter than 10 km, the order of magnitude is in the order of centimetre level [48].

The satellite clock bias and the atmospheric bias removal from pseudorange-rate measurement is obtained in the same way as described for pseudorange measurements. The removal is achieved by differencing the user range-free measurement $\dot{\Delta}_u^i$ from the range-free reference station pseudorange residual $\dot{\Delta}_{sta}^i$ as presented in equation 3-63.

$$\begin{aligned} \tilde{\dot{\rho}}_r^i = \dot{R}^i - \dot{e}_s^i + \left(\dot{b}_r - \dot{b}_s\right) - \left(\dot{b}^i - \dot{b}_s^i\right) + \left(\dot{I}^i - \dot{I}_s^i\right) + \left(\dot{T}^i - \dot{T}_s^i\right) + (\zeta^i - \zeta_s^i) + \left(\dot{\beta}_r - \dot{\beta}_s\right) \\ + \left(\dot{\beta}^i - \dot{\beta}_s^i\right) k(\nu^i - \nu_s^i) \end{aligned} \quad \text{3-63}$$

Supposing the receiver under test and the receiver of the reference station close enough to have the atmospheric effects space correlated, 3-63 could be written as

$$\tilde{\rho}_r^i = \dot{R}^i - \dot{e}_s^i + \left(\dot{b}_r - \dot{b}_s\right) - \tilde{\dot{b}}^i + \tilde{\dot{I}}^i + \tilde{\dot{T}}^i + \left(\zeta^i - \zeta_s^i\right) + \left(\dot{\beta}_r - \dot{\beta}_s\right) + \tilde{\dot{\beta}}^i + \left(\nu^i - \nu_s^i\right) \quad 3\text{-}64$$

The resulting term, $\dot{\epsilon}^i$, is denoted as the pseudorange-rate residual difference and is dominated by four factors:

- $\tilde{\dot{b}}^i = \dot{b}^i - \dot{b}_s^i$ denotes the residual satellite clock error after the correction, in $[\mathrm{m/s}]$;
- $\tilde{\dot{I}}^i = \dot{I}^i - \dot{I}_s^i$ denotes the residual ionosphere error after the correction, in [m/s];
- $\tilde{\dot{T}}^i = \dot{T}^i - \dot{T}_s^i$ denotes the residual troposphere error after the correction, in [m/s];
- $\tilde{\dot{\beta}}^i = \dot{\beta}^i - \dot{\beta}_s^i$ denotes the residual satellite hardware after the correction, in $[\mathrm{m/s}]$.

3.2.3 Navigation Solutions Estimation

This section describes the last block of a GNSS Receiver Processing: Navigation Solution Estimation (NSE) block. NSE processes the SA corrected measurements and the demodulate navigation data, retrieved from the Measurement Correction block, to determine the PVT solutions. The basic blocks composing RNSE are the Satellite Coordinates Estimation (SCE) and PVT estimation (PVTE). SCE block estimates the satellite's position and velocity at the transmission time. Then, PVT estimation block determines the unknown PVT solutions, processing the estimated satellite coordinates and the corrected measurements.

SCE block in a mass market receiver calculates the satellite coordinates using orbit prediction models, whose orbital parameters are extracted from the navigation message, as applied in Chapter 7. SCE is detailed in section 3.2.3.1.

Mass market PVTEs must make a trade-off between the accuracy of the estimate solutions and the complexity of the algorithms, due to the limited resources of low-cost equipment. This is often handled applying estimation methodologies based on the Linearized Least Square Error Minimization. The most common PVTEs are based on either Least Squares Estimation (LSE) or the Kalman Filter (KF). A general overview of LSE is proposed in section 3.2.3.2.2. This is followed by the description of the Extended KF (EKF) in section 3.2.3.2.3, which is the baseline methodologies applied in this work to provide the innovative PVTE, as explained in Chapter 7.

3.2.3.1 Satellite Coordinates Estimation

The satellite coordinate computation block is defined by a set of operations applied by the Receiver to estimate the position and the velocity of a given satellite i at the transmission time, t^i.

The basic methodology applied by mass-market receivers to determine GPS and Galileo satellite coordinates can be found in [60][61]. The orbit's prediction is based on the elaboration of a set of parameters, called ephemeris, extracted from the data navigation message.

GPS and Galileo ephemeris are periodically updated nominally every 2 hours for GPS, 3 hours for Galileo. The validity of the ephemeris is limited to 4 hours, beyond which the accuracy drastically decreases.

Once the estimated satellite position is determined, $\hat{\boldsymbol{p}}^i = \left(\hat{p}_x^i, \hat{p}_y^i, \hat{p}_z^i\right)$, it can be used to model the effective range as follows:

$$R^i = \hat{R}^i + e^i \quad 3\text{-}65$$

where the estimated range $\hat{R}^i$, is equal to:

$$\hat{R}^i = \sqrt{\left(\hat{p}_x^i - p_{r,x}^i\right)^2 + \left(\hat{p}_y^i - p_{r,y}^i\right)^2 + \left(\hat{p}_z^i - p_{r,z}^i\right)^2} \quad 3\text{-}66$$

and e^i is equal to the ephemeris error (section 3.2.1.1).

The SA PSR model in 3-48, applying the 3-65, could be modified as follows:

$$\tilde{\rho}^i = \hat{R}^i + e^i + b_r - \tilde{b}^i + \tilde{I}^i + \tilde{T}^i + \xi^i + \beta_r + \beta^i + \eta^i \ \ [\mathrm{m}] \quad 3\text{-}67$$

Similarly, once the satellite velocity vector is estimated, $\hat{\boldsymbol{p}}^i = \left(\hat{p}_x^i, \hat{p}_y^i, \hat{p}_z^i\right)$, the estimated range-rate $\hat{\dot{R}}^i$ can be calculated. The effective range-rate in terms of estimated $\hat{\dot{R}}^i$ is equal to:

$$\dot{R}^i = \hat{\dot{R}}^i + \dot{e}^i \quad 3\text{-}68$$

where $\dot{e}^i$ is equal to the ephemeris error due to the prediction of the satellite velocity. The modified SA PSR-R, model (3-52), becomes:

$$\tilde{\rho}^i = \hat{\dot{R}}^i + \dot{e}^i + \dot{b}_R - \tilde{\dot{b}}_T^i + \tilde{\dot{I}}^i + \tilde{\dot{T}}^i + \dot{\beta}_r + \dot{\beta}^i + \dot{\zeta}^i + \dot{v} \ \text{[m/s]} \quad 3\text{-}69$$

The DGNSS PSR and PSR-R models could be modified as follows:

$$\tilde{\rho}_r^i = R^i + e_s^i + \tilde{b}^i - (b_r - b_s) + (\xi^i - \xi_s^i) + (\beta_r - \beta_s) + \tilde{\beta}^i + \tilde{I}^i + \tilde{T}^i + (\eta^i - \eta_s^i) \ \text{[m]} \quad 3\text{-}70$$

$$\tilde{\dot{\rho}}_r^i = \dot{R}^i - \dot{e}_s^i + \left(\dot{b}_r - \dot{b}_s\right) - \tilde{\dot{b}}^i + \tilde{\dot{I}}^i + \tilde{\dot{T}}^i + (\zeta^i - \zeta_s^i) + \left(\dot{\beta}_r - \dot{\beta}_s\right) + \tilde{\dot{\beta}}^i + (v^i - v_s^i) \ \text{[m/s]} \quad 3\text{-}71$$

3.2.3.2 PVT Estimation

This section defines the fundamental mathematical models and computational steps applied by the PVTE to determine the navigation solution. The PVTE is the second block of the NSE. It processes the corrected PSR and PSR-R measurements and the satellite coordinates received from the SCE block and provides as output the estimate navigation solution. The first subsection (3.2.3.2.1) introduces the nominal PSR and PSR-R error budget models, obtained after the SA and DGNSS corrections, usually exploited in the PVT estimation design.

The second subsection (3.2.3.2.2) focuses on the PVT estimation fundamental steps, which are common to a large number of basic PVT estimators. Basic PVT Estimators apply the Least Square Error Minimization [12] to determine the navigation solutions. PVTEs could be defined in two different families, snapshot estimators, such as the Weighted Least Square estimator [12], and recursive estimators, such as Kalman Filters [15].

WLS exploits the PSR and PSR-R measurements of the current epoch to obtain the user's navigation solution at the same epoch. The main disadvantage of the snapshot navigation algorithm is that it discards useful information from previous measurements which can be used to perform the predictions, such as, the prior clock offset and drift estimates which provide a good indication of the current clock offset, and the prior position and velocity estimates providing a good indication of the current position. Hence, most of the mass market GNSS user equipment adopt a navigation filtered solution instead of a snapshot algorithm. This maintains continuous estimates of the navigation solution and uses the PSR and PSR-R measurements to correct them. As already stated, the velocity estimates are used to update the position estimates, and the clock drift is used to update the clock offset.

A navigation solution can be maintained for a limited period with only three satellites where the clock errors are well calibrated and a rough navigation solution can be maintained for a few seconds when all GNSS signals are blocked, such as in tunnels.

The commonly used navigation filter is the Kalman Filter. The Kalman filter is a Bayesian estimation technique, [62], that provides an optimal navigation estimation under certain conditions thanks to the prediction of the estimates through the use of a user dynamic model and successively correcting the predictions with the measurements [15]. The Kalman Filter is an optimal estimator in the case that the measurement errors are zero-mean Gaussian distributed random variables, but they are not necessarily identically distributed or independent.

In the final section it is introduced the so-called Extended Kalman Filter (EKF), which is the baseline PVTE from which several innovations have been introduced in this work, Chapter 7.

3.2.3.2.1 PVT Measurement Error budget

Standalone and/or differential measurements, presented respectively in section 3.2.2.1 and section 3.2.2.2 will be finally processed by the PVT algorithm to determine navigation solutions.

The PVT estimation accuracy is a function of the measurement quality and the effect of the satellite geometry with respect to the position of the receiver. The first factor will be discussed in this section while the second one is detailed in section 3.2.3.2.4, after introducing the PVT estimators.

The nominal impact of the error sources is usually quantified by a specific parameter, the so-called User-Equivalent Error, which is modelled for PSR measurements, (User Equivalent Range Error, UERE), and for PSR-R measurements, (User Equivalent Range Rate Error, UERRE). The first subsection, 3.2.3.2.1.1, introduce the UERE model, while the second subsection, 3.2.3.2.1.2, describe the UERRE model.

3.2.3.2.1.1 PSR nominal Measurement Error Model

The UERE for a given satellite is considered to be the statistical sum of the contributions from each of the error sources associated to the specific GNSS measurement, already presented in section 3.2.1, excluding the effects of the receiver clock and receiver hardware error components.

The overall error component associated to a given satellite i, is modelled as a zero-mean Gaussian random variable, where its variance is determined as the sum of the variance of each of its components. In the basic PVT estimation model, this error is usually assumed to be independent and identically distributed from satellite to satellite (a detailed description of the mathematical error model is provided in Annex 10.2.1).

Therefore, the SA UERE associated to the satellite i is defined as follows:

$$\epsilon^i_{UERE,SA} = e^i - \tilde{b}^i + \tilde{I}^i + \tilde{T}^i + \xi^i + \beta^i + \eta^i \quad 3\text{-}72$$

As a consequence, the variance of the SA UERE model, is equal to:

$$\sigma^{2^i}_{UERE,SA} = \sigma_e^{2^i} + \sigma_{\tilde{b}}^{2^i} + \sigma_{\tilde{I}}^{2^i} + \sigma_{\tilde{T}}^{2^i} + \sigma_{\xi}^{2^i} + \sigma_{\beta}^{2^i} + \sigma_{\eta}^{2^i} \quad 3\text{-}73$$

Similarly, the DGNSS UERE associated to the satellite i is defined as follows:

$$\epsilon^i_{UERE,DGNSS} = e^i_s - \tilde{b}^i + (\xi^i - \xi^i_s) + \tilde{\beta}^i + \tilde{I}^i + \tilde{T}^i + (\eta^i - \eta^i_s) \quad 3\text{-}74$$

while variance of the DGNSS UERE model, is equal to:

$$\sigma^{2^i}_{UERE,DGNSS} = \sigma_e^{2^i} + \sigma_{\tilde{b}}^{2^i} + \sigma_{\tilde{I}}^{2^i} + \sigma_{\tilde{T}}^{2^i} + \sigma_{\xi}^{2^i} + \sigma_{\xi_s}^{2^i} + \sigma_{\tilde{\beta}}^{2^i} + \sigma_{\eta}^{2^i} + \sigma_{\eta_s}^{2^i} \quad 3\text{-}75$$

The order of magnitude of $\sigma^{2^i}_{UERE,SA}$ and $\sigma^{2^i}_{UERE,DGNSS}$ could be found in Chapter 7.

3.2.3.2.1.2 PSR-R nominal Measurement Error Model

As per UERE, the overall PSR-R error is modelled as a zero mean Gaussian random variable where its variance, defined by UERRE, is determined as the sum of the variance of each of its components.

The SA UERRE associated to the satellite i is equal to:

$$\dot{\epsilon}^i_{UERRE,SA} = \dot{e}^i - \tilde{\dot{b}}^i + \tilde{\dot{I}}^i + \tilde{\dot{T}}^i + \dot{\beta}^i + \dot{\zeta}^i + \dot{\nu} \quad 3\text{-}76$$

As a consequence, the variance of the SA UERRE model, is equal to

$$\sigma^{2^i}_{UERRE,SA} = \sigma_{\tilde{b}}^{2^i} + \sigma_e^{2^i} + \sigma_{\tilde{I}}^{2^i} + \sigma_{\tilde{T}}^{2^i} + \sigma_{\zeta}^{2^i} + \sigma_{\beta}^{2^i} + \sigma_{\nu}^{2^i} \quad 3\text{-}77$$

The DGNSS UERRE associated to the satellite i is defined as follows:

$$\dot{\epsilon}^i_{UERRE,DGNSS} = \dot{e}^i_s - \tilde{\dot{b}}^i + \tilde{\dot{I}}^i + \tilde{\dot{T}}^i + (\zeta^i - \zeta^i_s) + \tilde{\dot{\beta}}^i + (\nu^i - \nu^i_s) \quad 3\text{-}78$$

Hence, the DGNSS UERRE variance is equal to:

$$\sigma^{2^i}_{UERRE,DGNSS} = \sigma_{\dot{e}_s}^{2^i} + \sigma_{\tilde{b}}^{2^i} + \sigma_{\tilde{I}}^{2^i} + \sigma_{\tilde{T}}^{2^i} + \sigma_{\zeta}^{2^i} + \sigma_{\zeta_s}^{2^i} + \sigma_{\tilde{\beta}}^{2^i} + \sigma_{\nu}^{2^i} + \sigma_{\nu_s}^{2^i} \quad 3\text{-}79$$

The order of magnitude of $\sigma^{2^i}_{UERRE,SA}$ and $\sigma^{2^i}_{UERRE,DGNSS}$ could be found in Chapter 7.

3.2.3.2.2 PVT Estimation Fundamentals

The PVT estimator's goal is the calculation of unknown parameters, collected in the so-called estimator state vector, $\boldsymbol{x}$. This is obtained solving a system of PSR and PSR-R measurements obtained from the SCE output, usually denoted measurement vector, $\boldsymbol{z}$. Due to the presence of measurement errors and an overdetermined system, it implies the mandatory application of an error reduction strategy. The common methodology applied by PVTE is based on the least square error minimization operation [12].

The generic State Model is described in section 3.2.3.2.2.1, while the Observation Model is presented in section 3.2.3.2.2.2.

3.2.3.2.2.1 State Model

The state vector of a PVT estimator is composed of the unknown receiver parameters. A generic state vector, $\boldsymbol{x}$, for a PVT estimator which process PSR and PSR-R measurements, which is appropriate for automotive kinematic applications that are characterized by moderate dynamics, is composed of the receiver position $\boldsymbol{p}_r$, velocity $\dot{\boldsymbol{p}}_r$, receiver clock bias b_r, and receiver clock drift $\dot{b}_r$. The position and receiver clock bias define the PSR state model, $\boldsymbol{x_p} = (\boldsymbol{p}_r, b_r,)$, which can be obtained solving a system of PSR measurements (at least four measurements). The receiver velocity and clock drift error define the PSR-R state model, $\boldsymbol{x_{\dot{p}}} = (\dot{\boldsymbol{p}}_r, \dot{b}_r)$, which can be obtained solving a system of PSR-R measurements. The overall state vector is composed by $\boldsymbol{x_p}$ and $\boldsymbol{x_{\dot{p}}}$. In this work it is rearranged in the following way $\widehat{\boldsymbol{x}} = (\boldsymbol{p}_r, \dot{\boldsymbol{p}}_r, b_r, \dot{b}_r)$. In the presence of ideal measurements not affected by errors, the PVT estimator should estimate directly the true state $\boldsymbol{x}$. However, measurements are usually affected by random error components; therefore, it is only able to compute an estimation of the state vector, $\widehat{\boldsymbol{x}} = \left(\widehat{\boldsymbol{p}}_r, \widehat{\dot{\boldsymbol{p}}}_r, \hat{b}_r, \hat{\dot{b}}_r\right)$.

In case of a dual constellation receiver based on GPS and Galileo measurements, it is also necessary to estimate the GGTO, δ, therefore the state vector becomes $\boldsymbol{x} = (\boldsymbol{p}_r, \dot{\boldsymbol{p}}_r, b_r, \dot{b}_r, \delta)$ with estimate $\widehat{\boldsymbol{x}} = \left(\widehat{\boldsymbol{p}}_r, \widehat{\dot{\boldsymbol{p}}}_r, \hat{b}_r, \hat{\dot{b}}_r, \hat{\delta}\right)$.

For dynamic GNSS applications, the augmentation of the state vector with the three acceleration states along each ECEF axis is also strongly advised. The accuracy of the PVT estimate is a measure of the difference between the true state and the estimated one, the estimation error, $d\boldsymbol{x}$.

$$d\boldsymbol{x} = \boldsymbol{x} - \widehat{\boldsymbol{x}} \tag{3-80}$$

3.2.3.2.2.2 Observation Model

The observation model of a PVT estimator is defined as the mathematical model which links the unknown parameters to the measurements. Using N PSR measurements, defined by the sum of N_1 GPS measurements and N_2 Galileo measurements as described in 3-81,

$$\tilde{\rho}^i = \begin{cases} \tilde{\rho}^i_{GPS} & 1 < i \leq N_1 \\ \tilde{\rho}^i_{GAL} & N_1 + 1 < i \leq N_1 + N_2 = N \end{cases} \tag{3-81}$$

the observation model for a single PSR measurement from the satellite i, is equal to:

$$\tilde{\rho}^i = R^i + b_r + \epsilon^i_{UERE} \tag{3-82}$$

where:

- R^i is the range, a non-linear function which is calculated as a function of the satellite coordinates $\boldsymbol{p}^i$ and the receiver coordinates $\boldsymbol{p}_r$;
- b_r is the clock error term;
- ϵ^i_{UERE} is the equivalent error term, expressed in 3-72 for SA, and in 3-74 for DGNSS.

To calculate the unknown state vector $\boldsymbol{x_p}$, the PVT estimator must solve a system of equations. The resulting PSR model is expressed as:

$$\tilde{\boldsymbol{z}}_p = \mathrm{h}(\widehat{\boldsymbol{p}}, \boldsymbol{x_p}) + \boldsymbol{\epsilon}^i_{UERE} \tag{3-83}$$

where:

- $\tilde{\boldsymbol{z}}_p$ is the PSR measurement vector, which is equal to $\tilde{\boldsymbol{z}}_p = (\tilde{\rho}^1, \dots, \tilde{\rho}^N)$;
- $\boldsymbol{x_p}$ denotes the state vector**;**
- $\widehat{\boldsymbol{p}}$ are the estimated satellite coordinates;
- $\mathrm{h}(\dots)$ is the non-linear function relating $\boldsymbol{x_p}$ to $\tilde{\boldsymbol{z}}_p$;
- $\boldsymbol{\epsilon}^i_{UERE} = (\epsilon^1_{UERE}, \dots, \epsilon^N_{UERE})$ is the overall PSR error vector;

Same approach is applied to define PSR-R model.

$$\tilde{\dot{\rho}}^i = \dot{R}^i + \dot{b}_r + \dot{\boldsymbol{\epsilon}}^i_{UERRE} \tag{3-84}$$

where:

- $\dot{R}^i$ is the range-rate, a non-linear function which is calculated as a function of the satellite coordinates and velocity, $\boldsymbol{p}^i$ and $\widehat{\dot{\boldsymbol{p}}}^i$, the receiver coordinates and velocity $\boldsymbol{p}_r$, $\dot{\boldsymbol{p}}_r$;

- $\dot{\boldsymbol{\epsilon}}^{i}_{UERRE}$ is the overall PSR-R noise vector, which is equal to $\dot{\boldsymbol{\epsilon}}^{i}_{UERRE} = (\dot{\epsilon}^{1}_{UERRE}, \dots, \dot{\epsilon}^{N}_{UERRE})$, where $\dot{\epsilon}^{i}_{UERRE}$ is expressed in 3-76 for SA and in 3-78 for DGNSS.

The overall measurement model, containing the PSR and PSR-R measurements is expressed as:

$$\tilde{\boldsymbol{z}} = \mathrm{h}\left(\hat{\boldsymbol{p}}^{i}, \hat{\dot{\boldsymbol{p}}}^{i}, \boldsymbol{x}\right) + \boldsymbol{\epsilon}_{eq} \tag{3-85}$$

where:

- $\tilde{\boldsymbol{z}}$ is the composed measurement vector, which is equal to $\tilde{\boldsymbol{z}} = \left(\tilde{\rho}^{1}, \dots, \tilde{\rho}^{N} | \, \tilde{\dot{\rho}}^{1}, \dots, \tilde{\dot{\rho}}^{N}\right)$;
- $\boldsymbol{x}$ denote the state vector;
- $\boldsymbol{\epsilon}_{eq}$ is equal to $\boldsymbol{\epsilon}_{eq} = (\epsilon^{1}_{UERE}, \dots, \epsilon^{N}_{UERE} | \dot{\epsilon}^{1}_{UERRE}, \dots, \dot{\epsilon}^{N}_{UERRE})$.

The dual constellation measurement vector, is based on the observation function (h_1) relating the pseudorange measurements to the state vector and the observation function (h_2) relating the pseudorange measurements to the state vector. Therefore, the measurement vector $\tilde{\boldsymbol{z}}$ includes the PSR $\tilde{\rho}^{i}$ and PSR-R $\tilde{\dot{\rho}}^{i}$, for the N GPS L1 C/A and Galileo E1 OS channels after applying the correction models, presented in 3-86:

$$\tilde{\boldsymbol{z}} = \left[h_1\left(\hat{\boldsymbol{p}}^{i}, \boldsymbol{x}_{\rho}\right) + \boldsymbol{\epsilon}^{i}_{UERE} | \; h_2\left(\hat{\boldsymbol{p}}^{i}, \hat{\dot{\boldsymbol{p}}}^{i}, \boldsymbol{x}_{\dot{\rho}}\right) + \dot{\boldsymbol{\epsilon}}^{i}_{UERRE}\right] = \left[\tilde{\rho}^{1}, \dots, \tilde{\rho}^{N} | \tilde{\dot{\rho}}^{1}, \dots, \tilde{\dot{\rho}}^{N}\right] \tag{3-86}$$

3.2.3.2.3 Extended Kalman Filter (EKF)

The Kalman Filter estimator is a PVTE which is based on the least square error minimization. The detailed derivation could be found in Annex 10.2.2. The EKF state vector, measurement vector model, and the description of the measurement error covariance matrix are detailed in Annex 10.2.3. The following sections described the Measurement error covariance matrix applied in this work (section 3.2.3.2.3.1).

3.2.3.2.3.1 Measurement error covariance matrix

The measurement noise vector $\boldsymbol{\varepsilon_l}$, at epoch l, is modelled as Gaussian noise with zero mean, $E\{\boldsymbol{v}\} = \boldsymbol{0}$, and covariance, $\boldsymbol{R_l} = E\{\boldsymbol{v_l} \cdot \boldsymbol{v_l^T}\}$. Assuming uncorrelated measurement errors between different satellites, $\boldsymbol{R_l}$ is a diagonal matrix defined as follows:

$$\boldsymbol{R}_l = \begin{pmatrix} \sigma^2_{\varepsilon^1_{\tilde{\rho}}}[l] & 0 & 0 & 0 & 0 & 0 \\ 0 & \sigma^2_{\varepsilon^2_{\tilde{\rho}}}[l] & 0 & 0 & 0 & 0 \\ \dots & \dots & \dots & \dots & \dots & \dots \\ 0 & 0 & \sigma^2_{\varepsilon^N_{\tilde{\rho}}}[l] & 0 & 0 & 0 \\ 0 & 0 & 0 & \sigma^2_{\varepsilon^1_{\tilde{\rho}}}[l] & 0 & 0 \\ 0 & 0 & 0 & 0 & \sigma^2_{\varepsilon^2_{\tilde{\rho}}}[l] & 0 \\ \dots & \dots & \dots & \dots & \dots & \dots \\ 0 & 0 & 0 & 0 & 0 & \sigma^2_{\varepsilon^N_{\tilde{\rho}}}[l] \end{pmatrix} \tag{3-87}$$

with:

$$\begin{aligned} E\{v_j \cdot v_k^T\} = 0, \text{ for all } j \text{ and } k \text{ indexes of the matrix} \\ E\{v_j \cdot v_j^T\} = \sigma_j^2, \text{ for all } j \text{ indexes of the matrix} \end{aligned} \tag{3-88}$$

Several approaches have been applied to model the variance error model. The basic approach provides a single value for the PSR and PSR-R error variances for all the measurements. This is usually equal to the UERE error model in relation to PSR measurements and UERRE model in the case of PSR-R measurements, provided in section 0:

$$\begin{aligned} {\sigma^2}^1_{\varepsilon_{\tilde{\rho}}} = {\sigma^2}^2_{\varepsilon_{\tilde{\rho}}} = \dots = {\sigma^2}^N_{\varepsilon_{\tilde{\rho}}} = \sigma^2_{UERE} \\ {\sigma^2}^1_{\varepsilon_{\tilde{\dot{\rho}}}} = {\sigma^2}^2_{\varepsilon_{\tilde{\dot{\rho}}}} = \dots = {\sigma^2}^N_{\varepsilon_{\tilde{\dot{\rho}}}} = \sigma^2_{UERRE} \end{aligned} \tag{3-89}$$

The order of magnitude of the resulting error model can be found in [63]. More complex approaches model the values of the error variances individually, applying a measurement weighting model. This consists of calculating

the error variance components applying empirical models as a function of the measured C/N_0 and elevation angle, obtained from a given satellite measurement. The empirical models are usually based on practical data, used to model the magnitudes of ionospheric, tropospheric and multipath error components as a function of the related C/N_0 and elevation angle, as proposed in [64] [65] [66], [67], [68]. Following these approaches, the statistical behaviours of the multipath plus residual thermal noise errors for low-cost receivers in urban environments have been characterised as a function of the received C/N_0. The methodology applied to isolate the multipath error from PSR and PSR-R measurements and to characterize it is presented in Chapter 5. The characterization is then applied to a large data campaign, which results are depicted in Chapter 6. These results are finally exploited to calculate the specific $\boldsymbol{R}_l$ matrix as a function of the received C/N_0, as showed in Chapter 7.

3.2.3.2.4 PVT Solution Accuracy and Satellite Geometry

The accuracy of the GNSS PVT estimation depends on the accuracy of the ranging measurements and on the received signal geometry.

Figure 3-8 illustrates this for a simple two-dimensional ranging solution. The arcs in the picture show the mean and error bounds for each ranging measurement, while the shaded areas show the uncertainty bounds for the position solution and the arrows show the line-of-sight vectors from the user to the satellites. The mutual position of the transmitters is fundamental to reduce the uncertainties as it can be seen in the central image with respect to the one on the right and the one on the left. Indeed, the overall position error for a given ranging accuracy is minimized where the line-of-sight vectors are perpendicular.

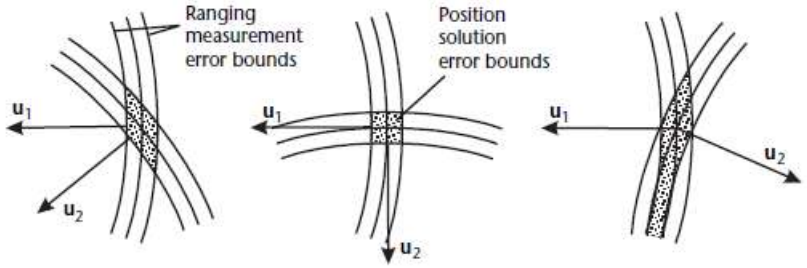

Figure 3-8 – Effect of signal geometry on the position accuracy from two-dimensional ranging [69]

Figure 3-9 illustrates a comparison between a possible good and poor signal geometry. Satellite covering a larger part of the sky could result in a better signal geometry with the respect of satellite positioned in just one portion of the sky.

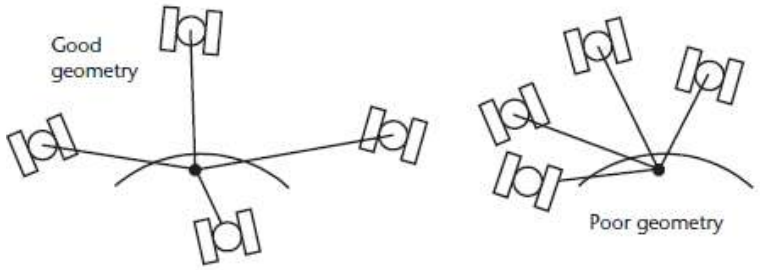

Figure 3-9 – Examples of good and poor GNSS signal geometry [15]

The effect of signal geometry on the navigation solution is quantified using the dilution of precision (DOP) concept. The DOP mixes the UERE factor, $\sigma_{\varepsilon_\rho}$, and the knowledge of signal geometry. The detailed description can be found in [15].

3.3 Summary

Chapter 3 was dedicated to the description of the GNSS Receiver processing block which follows the Radio-Frequency Front-End (RFFE) block within a GNSS receiver. A conceptual division in two main parts was made. On one hand, the Signal Processing Block conducts the receiver operations applied to the IF digital signal to acquire and to track the individual GNSS signals transmitted by the different satellites. The tracking operation estimates the received signal code delay, the phase lag and the Doppler frequency. Moreover, it also demodulates

the navigation message. On the other hand, the Data Processing Block conducts the receiver operations to generate raw measurements from the parameters previously estimated in the Signal Processing Block, to correct these raw measurements (and thus mitigating the error affecting them) and finally to process the corrected measurements to determine the receiver navigation solutions.

The Signal Processing Block is constituted of two different sub-blocks, the Digital Signal Processing (DSP), and the Navigation Message Demodulation (NMD). The DSP block conducts the following operations, the acquisition and the tracking operations. Both operations are based on two basic operations which are jointly executed: the signal carrier wipe-off and the PRN code correlation, conducted between the received signal and a local generated replica.

The acquisition operation detects the presence of the signal transmitted from a given satellite (satellite-in-view detection) and makes a rough estimation of the signal code delay and Doppler frequency. The tracking operation simultaneously process the detected signals in dedicated channels to accurately estimate all the incoming signal unknown parameters (propagation time, carrier phase and carrier frequency); three different modules are implemented to conduct the tracking process, one for each unknown parameter. First, the Phase Lock Loop (PLL) module is implemented to conduct the carrier phase tracking; the PLL ouptut is used to calculate the carrier phase pseudorange. Second, the Frequency Lock Loop (FLL) module is implemented to conduct the carrier frequency tracking; the FLL output is used to calculate the Doppler frequency pseudorange-rate. Third and last, the Code Lock Loop (DLL) module is implemented to conduct the Code Delay Tracking; the DLL output is used to calculate the code delay pseudorange.

The tracking operations are affected by different impairments which impacts the tracking loops performance and consequently the accuracy of the calculated measurements. The impairments affecting the tracking process are the thermal noise (plus signal interference), the oscillator phase noise, the oscillator vibration, the receiver dynamics and the multipath. The estimation error generated by the thermal noise, the oscillator phase noise and vibration noise are usually modelled as white Gaussian noise with a specific variance model (several models already exist in literature), whereas the estimation error resulting from the receiver dynamics is modelled as a potential bias (if the tracking loop has an order high enough to track the dynamics). The impact of the multipath on the tracking performance is one of the main goals of this thesis and will be extensively explained in the following Chapter 4. Indeed, the impact of the Multipath on the DLL, PLL and FLL tracking performance will be explained in the following Chapter 4, in order to theoretically investigate the pseudorange and the pseudorange-rate MP error components.

The Data Processing block is constituted of three different sub-blocks, the Measurement Generation Block, the Measurement Correction Block, the Navigation Solution Estimation Block. The Measurement Generation Block is in charge of the generation of the raw pseudorange (PSR) and the raw pseudorange rate (PSR-R) measurements. Two different measurement mathematical models have been defined depending on the exploitation of single constellation or the dual constellation measurements, and special attention is given to sources of errors in addition to the emitter-to-receiver range, receiver clock bias and receiver hardware delay. For single constellation measurement errors, the raw measurement error model includes the satellite's clock error, the ionospheric error, the tropospheric error, the error induced by the multipath effect (or multipath error component), the error induced by receiver's thermal noise and the interference contribution. For Dual constellation measurement errors, the raw measurement error model is equal to the single constellation error model plus an additional inter-constellation clock offset term added to one of the constellation measurements, for example for GPS L1 and Galileo E1 measurements, this term is called GGTO (GPS-to-Galileo Time Offset).

The Measurement Correction Block is in charge of applying corrections to the raw measurements in order to mitigate the different source of errors such that the resulting measurements, denoted corrected measurements, can be efficiently exploited by the Navigation Solution Estimation block to estimate the PVT solutions. The corrections are applied to the satellite clock, ionospheric tropospheric errors. The correction can be achieved basically either by Standalone (SA) approach or Differential approach. SA correction is based on the estimation of the correction terms by applying predictive models for the satellite clock error and empirical models for ionospheric and tropospheric error corrections. The resulting corrected measurements are affected by non-negligible residual measurements errors which reduce the accuracy of the PVT estimations. Standalone (SA) approach provides less precise corrections with respect to differential corrections. Differential correction is achieved generally applying a difference between the raw measurement under test and a second measurement, under specific conditions, where the correlation between the raw measurement errors and second measurement errors (or directly the errors) is

exploited. The differential correction exploited in this thesis is the DGNSS correction, which is achieved differencing the raw measurement under exam with a measurement obtained from a reference station. If the distance between the user receiver under test and the reference station receiver is lower than 10 km, the differential correction efficiently removes the corresponding errors (the residuals are in the order of centimetre level). However, an important drawback is that the multipath and noise from the reference station measurements are added to the raw measurements since these sources of error are uncorrelated. Concerning multipath error, many efforts of the scientific community are focused on developing multipath mitigation approaches, as detailed in Chapter 5.

The Receiver Navigation Solution Estimation Block is in charge of exploiting the corrected measurements to determine the PVT solutions. The Receiver Navigation Solution Estimation Block is constituted by two different sub-blocks, the Satellite Coordinates Estimation (SCE) and the PVT Estimation (PVTE). SCE is in charge of estimating the satellite's position and velocity at the transmission time. The uncertainty of the satellite position estimations leads to an additional error which is included in the PSR measurement error model; this error is called ephemeris errors and its magnitude depends on the LOS vector between the user and the satellite. PVTE is in charge of determining the unknown PVT solutions by processing the estimated satellite coordinates and the corrected measurements. At this regard, the dual-constellation (GPS L1 C/A signal and Galileo E1 OS signal) Extended Kalman Filter architecture has been presented. In particular, the fundamental operations, the mathematical models, the PVT estimation accuracy characterization as a function of the measurement errors and the satellite availability were described. The basic dual constellation EKF will be used as a starting PVT estimator architecture, to implement an improved PVT estimator solution for low-cost receivers in urban environment (Chapter 7).

4 Multipath effects on the GNSS Receiver Tracking Performances

The PVT solution accuracy is impacted by several sources of errors, satellite clock, ionosphere, troposphere, multipath and thermal noise, affecting the GNSS measurements as explained in Chapter 3. An efficient way to reduce the impact of GNSS errors is the application of measurement correction techniques. However, the efficiency and the benefit of the correction technique depends on the characteristics of the targeted error source. Indeed, due to their characteristics, satellite clock, ionosphere and troposphere errors can be efficiently corrected applying standalone or differential techniques as explained in section 3.2.2. Standard standalone techniques can mitigate these errors allowing a PVT solution accuracy at centimeter or meter level. Moreover, higher performance could be reached applying complex differential approaches, which may allow PVT solution accuracy at millimeter level. However, the complexity of the multipath errors does not allow to mitigate their impact by directly applying standalone or differential techniques to the GNSS measurements; and the multipath error can degrade the GNSS measurement accuracy, and consequently the PVT solution accuracy, from centimetre level to several meters level. This chapter focus on the multipath error impact on the receiver signal processing block to better understand its impact on the data processing block and thus, on the GNSS measurements; potential mitigation techniques at signal processing block or at data processing block level are discussed in Chapter 5.

The multipath phenomenon is caused by the reflections of the satellite signals on the surrounding obstacles of the GNSS receiver, from the ground to nearby buildings, as described in section 2.4.1.2. The scattered signals take more time to reach the receiver than the direct or LOS signal where they are captured by the receiver antenna inducing signal processing errors.

The part of the propagation channel which generates the multipath (MP) reflections/diffractions is the surroundings of the receiver and is usually called MP environment. The MP environment can be extremely complex, especially in harsh environment such as cities, due to the large number of potential reflectors, and the vast heterogeneity of the materials constituting them. Moreover, the position of the different reflectors, as well as their facets, generates a very high number of MP environment configurations since a considerable number of reflections of different nature following complex geometric paths are possible. Therefore, standalone measurement corrections based on a generic multipath environment model is unpractical. Moreover, unlike the other error sources, multipath is spatially uncorrelated between different user receiver locations at large distances and it may be loosely correlated between different user receiver locations at small distances due to the presence of large reflectors. Therefore, the differential approaches cannot be used to efficiently correct the multipath errors. As a consequence, multipath is the most significant and sometimes dominant error contributor for GNSS receiver in harsh urban environments.

Nowadays, the modernization of GNSS technologies and the application of novel techniques mitigate the impact of multipath error (a summary is presented in Chapter 5). However, the Multipath mitigation techniques are more complex than just applying standalone or differential measurements corrections as well as more resource demanding, making them challenging to be applicable in low-cost solutions. In order to evaluate potential multipath mitigation techniques for low-cost GNSS receiver, which topic is addressed in the next chapter, how the multipath phenomenon causes the presence of MP errors in the GNSS measurements must be analysed first.

As mentioned in Chapter 3, multipath reflections affect the behavior of the receiver tracking stage, inducing a distortion and/or a bias on the ideal correlation function. However, the detailed analysis has been omitted and postponed to this chapter. For this reason, this chapter aims at providing the characterization of multipath induced tracking errors on the DLL and FLL tracking modules, which directly causes the presence of MP errors in the GNSS measurements. To do this analysis, the multipath environment mathematical modelling, followed by the mathematical model of the received signal and the corresponding correlators output models must be formulated. A simplified multipath environment model based on the urban canyon has been already introduced in section 4.1. As a consequence, the urban canyon is exploited to formulate the mathematical model of the received signal and the corresponding correlators output models.

The MP effects on the DLL for GPS L1 C/A signal are widely covered in the existing literature, [1]-[70]. In addition, extended results have also been collected for the MP induced DLL tracking errors for Galileo E1 OS signal, in [71]-[72]. The code tracking error induced by MP components is theoretically derived in [1]. The mathematical expression of the coherent and non-coherent DLL discriminator errors and the resulting error envelope has been presented in [73], [74], where the term multipath error envelope specifies a positive and a negative maximum error values which bound all the possible discriminator error values. MP phenomenon affects the ideal correlation function modifying the expected correlation shape. Indeed, the composite correlation function

is equal to a delayed, attenuated and/or distorted version of the ideal correlation function, depending on the type of MP phenomenon (NLOS MP or LOS MP) affecting the composite signal. As a consequence, the presence of the composite correlation function leads to an erroneous discriminator function, which is translated in a biased tracking process. This bias will affect the PSR measurements, as introduced in section 3.1.2.2, and the final PVT solutions.

An interesting analysis of Doppler frequency variations due to MP reflections has been formulated in [75]. Moreover, [3] and [10] followed the same approach applied for the carrier tracking error model to formulate the mathematical expression of the FLL discriminator error due to the MP Doppler frequency variations. In this work, the formulation and the analysis of the frequency tracking error due to the presence of MP, inspired from the work previously cited, is further developed and completed. Doppler frequency variations due to Multipath reflections have been calculated through the simulation of a specific multipath environment configuration, reproducing in a basic way the effects of MP in the urban canyon. The resulting theoretical values have been used to calculate the theoretical PDF of the FLL tracking error due to the presence of MP and thermal noise which will be compared to the experimental results obtained in Chapter 6.

The structure of this chapter is as follows. The mathematical model of the received signal from the considered urban propagation channel as well the GNSS correlator outputs mathematical model is presented in section 4.1. A summary of the MP induced DLL tracking error is presented in section 4.2. An extensive analysis of the MP induced FLL tracking error is presented in section 4.3. Finally, the main conclusions are summarized in section 4.4.

4.1 Multipath Received Signal Model

The multipath environment can be considered as the last element of the propagation channel model, 2.4.1. It is composed by the different ground objects surrounding the GNSS receiver which reflect/refract/diffract the transmitted GNSS signal, creating several copies of the transmitted signal, characterized by a longer time delay, a carrier phase delay/advance and a different Doppler frequency due to the interaction between the satellite, the reflector and the receiver. These signals are captured by the receiver antenna, causing errors in the correlation, acquisition and tracking operations, which are finally translated in PVT solution errors.

The simplest Multipath environment model consists of the presence of a single object, O, in the vicinity of a GNSS receiver, R, as represented in Figure 4-1. A given GNSS satellite i, SV_i, transmits the signal (green arrow), which travels through the propagation channel until it enters in the multipath environment. Supposing LOS MP reception state, 2.4.1.2.3, the LOS signal is directly captured by R, while, at the same time, it hits the surface of O, in the reflection point P, which generates a signal reflection (red arrow), the so-called called Multipath (MP) component (note that this explanation is a simplified one since it does not describe the multipath scattering process in detail). The transmitted signal is modelled as a single geometric ray interacting with the objects and the receiver in a single geometric point. The satellite's dynamics are described by the vector of velocity, $\dot{\boldsymbol{p}}^i$, whereas object and receiver velocity are characterized by $\dot{\boldsymbol{p}}_o$ and $\dot{\boldsymbol{p}}_r$.

The transmitted signal interaction with O is characterized by the unit vector pointing towards the satellite from O, $\boldsymbol{u}_o^i$. The geometric distance is equal to R_o^i. Similarly, the LOS signal component is described by the unit vector pointing towards the satellite from R, $\boldsymbol{u}_r^i$, and the geometric distance R^i. Finally, the MP component is described by the unit vector pointing towards O from R, $\boldsymbol{u}_r^o$, and the geometric distance R_r^o.

Since the ground objects are relatively close with respect to the distance between any ground object and the satellite, (R_o^i, $R^i \gg R_r^o$), vector $\boldsymbol{u}_o^i$ could be considered equal to vector $\boldsymbol{u}_r^i$ without loss of precision [77].

The received signal composed by the LOS signal component and the MP reflection component (also called composite signal, or LOS MP received signal), defined with the simplified MP environment described above, has been formulated in section 4.1.1. Furthermore, the MP correlation output models, obtained modifying the DLL /FLL LOS correlation model, already introduced in Chapter 3, with the received signal affected by MP error, is introduced in section 4.1.2.

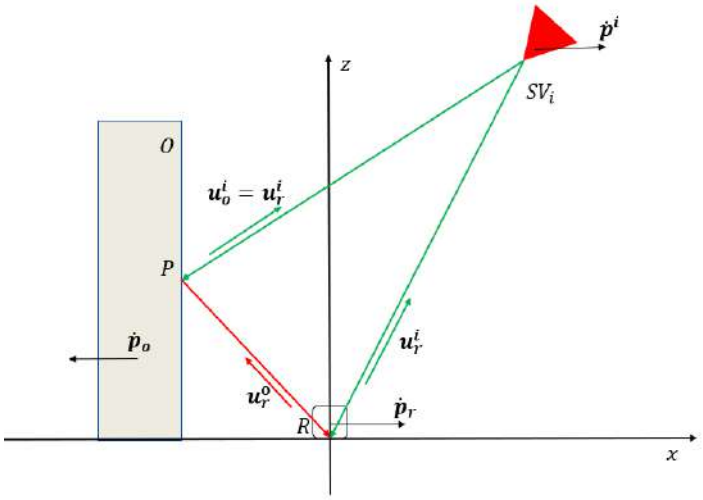

Figure 4-1 – Definition of the Multipath Environment: An object (O) acts as a reflector of the LOS signal in a single point *P* of the reflector surface (reflection point), producing the multipath component MP received by the receiver: a specular reflected signal

4.1.1 MP Signal Model

The general model of the transmitted and received signal in presence of MP have been presented in 2-36 and 2-40, respectively. The simplified model of the transmitted signal including only one reflected ray is equal to:

$$z_{in}^i(t) = A_0^i \cdot d^i(t-\tau_0^i) \cdot c^i(t-\tau_0^i) \cdot \cos\left(2\pi f_{L1} t + \varphi_0^i(t)\right) + A_1^i \cdot d^i(t-\tau_1^i) \cdot c^i(t-\tau_1^i) \cdot \cos\left(2\pi f_{L1} t + \varphi_1^i(t)\right) \quad 4\text{-}1$$

where the subscript "0" indicates the LOS component and "1" the MP one.

As a consequence, the 1-ray MP received composite signal at the RFFE output is equal to:

$$z_{out}^i(nT_s) = A_0^i \cdot d_0^i(nT_s-\tau_0^i) \cdot c_0^i(nT_s-\tau_0^i) \cdot \cos\left(2\pi f_{IF} nT_s + \varphi_0^i(nT_s)\right) + A_1^i \cdot d_1^i(nT_s-\tau_1^i) \cdot c_1^i(nT_s-\tau_1^i) \cdot \cos\left(2\pi f_{IF} nT_s + \varphi_1^i(nT_s)\right) + \eta^i(nT_s) \quad 4\text{-}2$$

where 4-2, over one integration period, T_I, could be approximated in the following way:

$$z_{out}^i(nT_s) = A_0^i \cdot d_0^i(nT_s-\tau_0^i) \cdot c_0^i(nT_s-\tau_0^i) \cdot \cos\left(2\pi(f_{IF} + f_{D,0}^i) mT_s + \varphi_0^i[kT_I]\right) + A_1^i \cdot d_1^i(nT_s-\tau_1^i) \cdot c_1^i(nT_s-\tau_1^i) \cdot \cos\left(2\pi(f_{IF} + f_{D,1}^i) mT_s + \varphi_1^i[kT_I]\right) + \eta^i(nT_s) \quad 4\text{-}3$$

where φ_1^i and $f_{D,1}^i$, are respectively the constant initial phase and the Doppler frequency MP signal component during the $[(k-1)T_I, kT_I]$ interval.

4-3 is the composite signal affected by LOS MP phenomenon (section 2.4.1.2.1). On the contrary, the composite received signal affected by NLOS MP phenomenon (section 2.4.1.2.1), is only composed by the MP signal component, since the LOS component is blocked:

$$z_{out}^i(nT_s) = A_1^i \cdot d_1^i(nT_s-\tau_1^i) \cdot c_1^i(nT_s-\tau_1^i) \cdot \cos\left(2\pi(f_{IF} + f_{D,1}^i) mT_s + \varphi_1^i[kT_I]\right) + \eta^i(nT_s) \quad 4\text{-}4$$

The composite signal is then processed by the receiver DSP block. In the absence of multipath, the receiver is able to acquire and track the direct incoming signal. However, in presence of multipath, the input of acquisition and tracking stages is the composite signal rather than the desired direct component only. In this situation, the receiver's acquisition and tracking loops performance is degraded since they were optimally designed to cope only with one received signal, although techniques exist to adapt their function to the presence of multipath components. As a consequence, the tracking error due to the MP impact affects the PVT estimation accuracy performance.

Correlator output models in presence of the composite signal, specifically used for DLL, PLL and FLL are described in section 4.1.2. Afterwards, the effects of MP component on the DLL, PLL and FLL discriminator outputs are described in the following sections.

4.1.2 MP Correlators Model

MP Correlator model used for DLL and PLL tracking loops are depicted in section 4.1.2.1. MP Correlator model used for FLL is presented in section 4.1.2.2.

4.1.2.1 DLL and PLL MP correlator outputs mathematical model

The LOS DLL correlator models are described in section 3.1.2.2.3. Neglecting the presence of data and taking into account the presence of one-reflected multipath, 4-2, the composite Early, (E), Prompt, (P), and Late, (L), correlators, at a given epoch k, are modified shown below. The PLL only uses prompt correlators whereas DLL uses Early, Prompt and Late correlator outputs.

$$\begin{aligned} I_k^E &= S_{I,k}^E + \eta_{I,k}^E = S_{I,0,k}^E + S_{I,1,k}^E + \eta_{I,k}^E \\ Q_k^E &= S_{Q,k}^E + \eta_{Q,k}^E = S_{Q,0,k}^E + S_{Q,1,k}^E + \eta_{Q,k}^E \\ I_k^P &= S_{I,k}^P + \eta_{I,k}^P = S_{I,0,k}^P + S_{I,1,k}^P + \eta_{I,k}^P \\ Q_k^P &= S_{Q,k}^P + \eta_{Q,k}^P = S_{Q,0,k}^P + S_{Q,1,k}^P + \eta_{Q,k}^P \\ I_k^L &= S_{I,k}^L + \eta_{I,k}^L = S_{I,0,k}^L + S_{I,1,k}^L + \eta_{I,k}^L \\ Q_k^L &= S_{Q,k}^L + \eta_{Q,k}^L = S_{Q,0,k}^L + S_{Q,1,k}^L + \eta_{Q,k}^L \end{aligned} \qquad 4\text{-}5$$

where:

- $S_{I,k}^E$ is the Early in-phase correlator component due to the composite signal component; it is equal to the sum of the LOS component, $S_{I,0,k}^E$, and MP component, $S_{I,1,k}^E$:

$$S_{I,0,k}^E = \frac{A_0}{2} R\left(\varepsilon_{\tau_{0,k}} + \frac{d_c T_c}{2}\right) \operatorname{sinc}\left(\pi \varepsilon_{f_{0,k}} T_I\right) \cos\left(\pi \varepsilon_{f_{0,k}} T_I + \varepsilon_{\varphi_{0,k}}\right)$$

$$S_{I,1,k}^E = \tilde{\alpha}_1 \frac{A_0}{2} R\left(\varepsilon_{\tau_{1,k}} + \frac{d_c T_c}{2}\right) \operatorname{sinc}\left(\pi \varepsilon_{f_{1,k}} T_I\right) \cos\left(\pi \varepsilon_{f_{1,k}} T_I + \varepsilon_{\varphi_{1,k}}\right)$$

- $\eta_{I,k}^E$ is the Early in-phase noise sample, generated by a white gaussian random noise process with a power equal to $\frac{N_0}{4T_I}$, (section 3.1.2.2.1.4).
- $S_{Q,k}^E$ is the Early quadrature correlator component due to the composite signal component; it is equal to the sum of the LOS component, $S_{Q,0,k}^E$, and MP component, $S_{Q,1,k}^E$:

$$S_{Q,0,k}^E = \frac{A_0}{2} R\left(\varepsilon_{\tau_{0,k}} + \frac{d_c T_c}{2}\right) \operatorname{sinc}\left(\pi \varepsilon_{f_{0,k}} T_I\right) \sin\left(\pi \varepsilon_{f_{0,k}} T_I + \varepsilon_{\varphi_{0,k}}\right)$$

$$S_{Q,1,k}^E = \tilde{\alpha}_1 \frac{A_0}{2} R\left(\varepsilon_{\tau_{1,k}} + \frac{d_c T_c}{2}\right) \operatorname{sinc}\left(\pi \varepsilon_{f_{1,k}} T_I\right) \sin\left(\pi \varepsilon_{f_{1,k}} T_I + \varepsilon_{\varphi_{1,k}}\right)$$

- $\eta_{Q,k}^E$ is the Early quadrature noise sample, generated by a white gaussian random noise process with a power equal to $\frac{N_0}{4T_I}$.
- $S_{I,k}^P$ is the Prompt in-phase correlator component due to the composite signal component; it is equal to the sum of the LOS component, $S_{I,0,k}^P$, and MP component, $S_{I,1,k}^P$:

$$S_{I,0,k}^P = \frac{A_0}{2} R\left(\varepsilon_{\tau_{0,k}}\right) \operatorname{sinc}\left(\pi \varepsilon_{f_{0,k}} T_I\right) \cos\left(\pi \varepsilon_{f_{0,k}} T_I + \varepsilon_{\varphi_{0,k}}\right)$$

$$S_{I,1,k}^P = \tilde{\alpha}_1 \frac{A_0}{2} R\left(\varepsilon_{\tau_{1,k}}\right) \operatorname{sinc}\left(\pi \varepsilon_{f_{1,k}} T_I\right) \cos\left(\pi \varepsilon_{f_{1,k}} T_I + \varepsilon_{\varphi_{1,k}}\right)$$

- $\eta_{I,k}^P$ is the Prompt in-phase noise sample, generated by a white gaussian random noise process with a power equal to $\frac{N_0}{4T_I}$.
- $S_{Q,k}^P$ is the Prompt quadrature correlator component due to the composite signal component; it is equal to the sum of the LOS component, $S_{Q,0,k}^P$, and MP component, $S_{Q,1,k}^P$:

$$S_{Q,0,k}^P = \frac{A_0}{2} R\left(\varepsilon_{\tau_{0,k}}\right) \operatorname{sinc}\left(\pi \varepsilon_{f_{0,k}} T_I\right) \sin\left(\pi \varepsilon_{f_{0,k}} T_I + \varepsilon_{\varphi_{0,k}}\right)$$

$$S_{Q,1,k}^{P} = \tilde{\alpha}_1 \frac{A_0}{2} R\left(\varepsilon_{\tau_{1,k}}\right) \operatorname{sinc}\left(\pi \varepsilon_{f_{1,k}} T_I\right) \sin\left(\pi \varepsilon_{f_{1,k}} T_I + \varepsilon_{\varphi_{1,k}}\right)$$

- $\eta_{Q,k}^{P}$ is the Prompt quadrature noise sample, generated by a white gaussian random noise process with a power equal to $\frac{N_0}{4T_I}$.
- $S_{I,k}^{L}$ is the Late in-phase correlator component due to the composite signal component; it is equal to the sum of the LOS component, $S_{I,0,k}^{P}$, and MP component, $S_{I,1,k}^{P}$:

$$S_{I,0,k}^{L} = \frac{A_0}{2} R\left(\varepsilon_{\tau_{0,k}} - \frac{d_c T_c}{2}\right) \operatorname{sinc}\left(\pi \varepsilon_{f_{0,k}} T_I\right) \cos\left(\pi \varepsilon_{f_{0,k}} T_I + \varepsilon_{\varphi_{0,k}}\right)$$

$$S_{I,1,k}^{L} = \tilde{\alpha}_1 \frac{A_0}{2} R\left(\varepsilon_{\tau_{1,k}} - \frac{d_c T_c}{2}\right) \operatorname{sinc}\left(\pi \varepsilon_{f_{1,k}} T_I\right) \cos\left(\pi \varepsilon_{f_{1,k}} T_I + \varepsilon_{\varphi_{1,k}}\right)$$

- $\eta_{I,k}^{L}$ is the Late in-phase noise sample, generated by a white gaussian random noise process with a power equal to $\frac{N_0}{4T_I}$.
- $S_{Q,k}^{L}$ is the Late quadrature correlator component due to the composite signal component; it is equal to the sum of the LOS component, $S_{Q,0,k}^{L}$, and MP component, $S_{Q,1,k}^{L}$:

$$S_{Q,0,k}^{L} = \frac{A_0}{2} R\left(\varepsilon_{\tau_{0,k}} - \frac{d_c T_c}{2}\right) \operatorname{sinc}\left(\pi \varepsilon_{f_{0,k}} T_I\right) \sin\left(\pi \varepsilon_{f_{0,k}} T_I + \varepsilon_{\varphi_{0,k}}\right)$$

$$S_{Q,1,k}^{L} = \tilde{\alpha}_1 \frac{A_0}{2} R\left(\varepsilon_{\tau_{1,k}} - \frac{d_c T_c}{2}\right) \operatorname{sinc}\left(\pi \varepsilon_{f_{1,k}} T_I\right) \sin\left(\pi \varepsilon_{f_{1,k}} T_I + \varepsilon_{\varphi_{1,k}}\right)$$

- $\eta_{Q,k}^{L}$ is the Late quadrature noise sample, generated by a white gaussian random noise process with a power equal to $\frac{N_0}{4T_I}$.
- T_I is the coherent integration time, introduced in section 3.1.2;
- T_c, is the chipping time, introduced in section 3.1.2;
- $\tilde{\alpha}_1 = A_1/A_0$, is the MLR, introduced in section 2.4.3;
- $\varepsilon_{\tau_0} = \tau_0 - \tau_l$, is the difference between LOS code delay, τ_0, and the local replica code delay, τ_l;
- $\varepsilon_{\tau_1} = \tau_1 - \tau_l$, is the difference between MP code delay, τ_1, and the local replica code delay, τ_l;
- $\varepsilon_{f_0} = f_{IF} + f_{D,0} - f_{NCO} \approx f_{D,0}$, is the difference between the LOS frequency, f_0, and the local replica frequency, f_{NCO};
- $\varepsilon_{f_{1,}} = f_{IF} + f_{D,1} - f_{NCO} \approx f_{D,1}$, is the difference between the MP frequency, f_1, and the local replica frequency, f_{NCO};
- $\varepsilon_{\varphi_0} = \varphi_0 - \varphi_{0,l}$, is the difference between the LOS initial phase, φ_0, and the initial phase of local replica, $\varphi_{0,l}$, defined at the start of the time interval;
- $\varepsilon_{\varphi_1} = \varphi_1 - \varphi_{0,l}$, is the difference between the MP initial phase, φ_1, and the initial phase of local replica, $\varphi_{0,l}$, defined at the start of the time interval.

The MP code delay, MP carrier phase shift and MP carrier frequency shift could be also written in relative terms with respect to LOS code delay, carrier phase and frequency as shown below:

$$\tau_1 = \tau_0 + \Delta\tau \quad 4\text{-}6$$

$$\varphi_1 = \varphi_0 + \Delta\varphi \quad 4\text{-}7$$

$$f_1 = f_0 + \Delta D \quad 4\text{-}8$$

where:

- $\Delta\tau$ is here defined code delay displacement;
- $\Delta\varphi$ is here defined carrier phase displacement;
- ΔD is here defined Doppler frequency displacement.

4.1.2.2 FLL MP correlator outputs mathematical model

The LOS FLL correlator models are described in section 3.1.2.2.2. Assuming that the prompt correlators, calculated for two consecutive FLL epochs, $(k-1, k)T_{FLL}$, are calculated over the same data symbol, the resulting MP in-phase and quadrature correlators, are defined as follows:

$$
\begin{aligned}
I_{k-1}^{P} &= S_{I,k-1}^{P} + \eta_{I,k-1}^{P} = S_{I,0,k-1}^{P} + S_{I,1,k-1}^{P} + \eta_{I,k-1}^{P} \\
Q_{k-1}^{P} &= S_{Q,k-1}^{P} + \eta_{Q,k-1}^{P} = S_{Q,0,k-1}^{P} + S_{Q,1,k-1}^{P} + \eta_{Q,k-1}^{P} \\
I_{k}^{P} &= S_{I,k}^{P} + \eta_{I,k}^{P} = S_{I,0,k}^{P} + S_{I,1,k}^{P} + \eta_{I,k}^{P} \\
Q_{k}^{P} &= S_{Q,k}^{P} + \eta_{Q,k}^{P} = S_{Q,0,k}^{P} + S_{Q,1,k}^{P} + \eta_{Q,k}^{P}
\end{aligned}
\qquad 4\text{-}9
$$

where:

- $S_{I,k-1}^{P}$ is the Prompt in-phase correlator component due to the composite signal component at epoch $k-1$; it is equal to the sum of the LOS component, $S_{I,0,k-1}^{P}$, and MP component, $S_{I,1,k-1}^{P}$:

$$
\begin{aligned}
S_{I,0,k-1}^{P} &= \frac{A_0}{2} R\left(\varepsilon_{\tau_{0,k-1}}\right) \operatorname{sinc}\left(\pi \varepsilon_{f_{0,k-1}} T_I\right) \cos\left(\pi \varepsilon_{f_{0,k-1}} T_I + \varepsilon_{\varphi_{0,k-1}}\right) = \\
&= \frac{A_0}{2} R\left(\varepsilon_{\tau,LOS}\right) \operatorname{sinc}\left(\pi \varepsilon_{f,LOS} T_I\right) \cos\left(\pi \varepsilon_{f,LOS} T_I + \varepsilon_{\varphi,LOS}\right) \\
S_{I,1,k-1}^{P} &= \tilde{\alpha}_1 \frac{A_0}{2} R\left(\varepsilon_{\tau_{1,k-1}}\right) \operatorname{sinc}\left(\pi \varepsilon_{f_{1,k-1}} T_I\right) \cos\left(\pi \varepsilon_{f_{1,k-1}} T_I + \varepsilon_{\varphi_{1,k-1}}\right) = \\
&= \tilde{\alpha}_1 \frac{A_0}{2} R\left(\varepsilon_{\tau,MP}\right) \operatorname{sinc}\left(\pi \varepsilon_{f,MP} T_I\right) \cos\left(\pi \varepsilon_{f,MP} T_I + \varepsilon_{\varphi,MP}\right)
\end{aligned}
$$

- $\eta_{I,k-1}^{P}$ is the Prompt in-phase noise sample at epoch $k-1$;
- $S_{Q,k-1}^{P}$ is the Prompt quadrature correlator component due to the composite signal component at epoch $k-1$; it is equal to the sum of the LOS component, $S_{Q,0,k-1}^{P}$, and MP component, $S_{Q,1,k-1}^{P}$:

$$
\begin{aligned}
S_{Q,0,k-1}^{P} &= \frac{A_0}{2} R\left(\varepsilon_{\tau_{0,k-1}}\right) \operatorname{sinc}\left(\pi \varepsilon_{f_{0,k-1}} T_I\right) \sin\left(\pi \varepsilon_{f_{0,k-1}} T_I + \varepsilon_{\varphi_{0,k-1}}\right) \\
&= \frac{A_0}{2} R\left(\varepsilon_{\tau,LOS}\right) \operatorname{sinc}\left(\pi \varepsilon_{f,LOS} T_I\right) \sin\left(\pi \varepsilon_{f,LOS} T_I + \varepsilon_{\varphi,LOS}\right) \\
S_{Q,1,k-1}^{P} &= \tilde{\alpha}_1 \frac{A_0}{2} R\left(\varepsilon_{\tau_{1,k-1}}\right) \operatorname{sinc}\left(\pi \varepsilon_{f_{1,k-1}} T_I\right) \cos\left(\pi \varepsilon_{f_{1,k-1}} T_I + \varepsilon_{\varphi_{1,k-1}}\right) = \\
&= \tilde{\alpha}_1 \frac{A_0}{2} R\left(\varepsilon_{\tau,MP}\right) \operatorname{sinc}\left(\pi \varepsilon_{f,MP} T_I\right) \sin\left(\pi \varepsilon_{f,MP} T_I + \varepsilon_{\varphi,MP}\right)
\end{aligned}
$$

- $\eta_{Q,k-1}^{P}$ is the Prompt quadrature noise sample, at epoch $k-1$;
- $S_{I,k}^{P}$ is the Prompt in-phase correlator component due to the composite signal component at epoch k; it is equal to the sum of the LOS component, $S_{I,0,k}^{P}$, and MP component, $S_{I,1,k}^{P}$:

$$
\begin{aligned}
S_{I,0,k}^{P} &= \frac{A_0}{2} R\left(\varepsilon_{\tau_{0,k}}\right) \operatorname{sinc}\left(\pi \varepsilon_{f_{0,k}} T_I\right) \cos\left(\pi \varepsilon_{f_{0,k}} T_I + \varepsilon_{\varphi_{0,k}}\right) = \\
&= \frac{A_0}{2} R\left(\varepsilon_{\tau,LOS}\right) \operatorname{sinc}\left(\pi \varepsilon_{f,LOS} T_I\right) \cos\left(3\pi \varepsilon_{f,LOS} T_I + \varepsilon_{\varphi,LOS}\right) \\
S_{I,1,k}^{P} &= \tilde{\alpha}_1 \frac{A_0}{2} R\left(\varepsilon_{\tau_{1,k}}\right) \operatorname{sinc}\left(\pi \varepsilon_{f_{1,k}} T_I\right) \cos\left(\pi \varepsilon_{f_{1,k}} T_I + \varepsilon_{\varphi_{1,k}}\right) = \\
&= \tilde{\alpha}_1 \frac{A_0}{2} R\left(\varepsilon_{\tau,MP}\right) \operatorname{sinc}\left(\pi \varepsilon_{f,MP} T_I\right) \sin\left(3\pi \varepsilon_{f,MP} T_I + \varepsilon_{\varphi,MP}\right)
\end{aligned}
$$

- $\eta_{I,k}^{P}$ is the Prompt in-phase noise sample at epoch k;
- $S_{Q,k}^{P}$ is the Prompt quadrature correlator component due to the composite signal component at epoch k; it is equal to the sum of the LOS component, $S_{Q,0,k}^{P}$, and MP component, $S_{Q,1,k}^{P}$:

$$
\begin{aligned}
S_{Q,0,k}^{P} &= \frac{A_0}{2} R\left(\varepsilon_{\tau_{0,k}}\right) \operatorname{sinc}\left(\pi \varepsilon_{f_{0,k}} T_I\right) \sin\left(\pi \varepsilon_{f_{0,k}} T_I + \varepsilon_{\varphi_{0,k}}\right) = \\
&= \frac{A_0}{2} R\left(\varepsilon_{\tau,LOS}\right) \operatorname{sinc}\left(\pi \varepsilon_{f,LOS} T_I\right) \sin\left(3\pi \varepsilon_{f,LOS} T_I + \varepsilon_{\varphi,LOS}\right) \\
S_{Q,1,k}^{P} &= \tilde{\alpha}_1 \frac{A_0}{2} R\left(\varepsilon_{\tau_{1,k}}\right) \operatorname{sinc}\left(\pi \varepsilon_{f_{1,k}} T_I\right) \cos\left(\pi \varepsilon_{f_{1,k}} T_I + \varepsilon_{\varphi_{1,k}}\right) = \\
&= \tilde{\alpha}_1 \frac{A_0}{2} R\left(\varepsilon_{\tau,MP}\right) \operatorname{sinc}\left(\pi \varepsilon_{f,MP} T_I\right) \sin\left(3\pi \varepsilon_{f,MP} T_I + \varepsilon_{\varphi,LOS}\right)
\end{aligned}
$$

- $\eta_{Q,k}^{P}$ is the Prompt quadrature noise sample, at epoch k;

- $T_I = T_{FLL}$, as introduced in section 3.1.2.2.2;
- $\varepsilon_{\tau,LOS} = \varepsilon_{\tau_{0,k-1}} = \varepsilon_{\tau_{0,k}}$, assumed constant during the $[k-1, k, k+1]T_{FLL}$ time interval;
- $\varepsilon_{f,LOS} = \varepsilon_{f_{0,k-1}} = \varepsilon_{f_{0,k}}$, assumed constant during the $[k-1, k, k+1]T_{FLL}$ time interval;
- $\varepsilon_{\tau,MP} = \varepsilon_{\tau_{1,k-1}} = \varepsilon_{\tau_{1,k}}$, assumed constant during the $[k-1, k, k+1]T_{FLL}$ time interval;
- $\varepsilon_{f,MP} = \varepsilon_{f_{1,k-1}} = \varepsilon_{f_{1,k}}$, assumed constant during the $[k-1, k, k+1]T_{FLL}$ time interval;
- $\varepsilon_{\varphi,LOS} = \varepsilon_{\varphi_{0,k-1}}$ is the phase error between the LOS initial phase at $(k-1)T_{FLL}$ and the initial phase of local replica at $(k-1)T_{FLL}$;
- $\varepsilon_{\varphi,MP} = \varepsilon_{\varphi_{1,k-1}}$ is the phase error between the MP initial phase at $(k-1)T_{FLL}$ and the initial phase of local replica at $(k-1)T_{FLL}$;
- $\varepsilon_{\varphi_{0,k}} = 2\pi\varepsilon_{f,LOS}T_I + \varepsilon_{\varphi,LOS}$, is the phase error between the LOS phase at kT_{FLL} and the phase of local replica at kT_{FLL}, calculated as a function of $\varepsilon_{\varphi,LOS}$;
- $\varepsilon_{\varphi_{1,k}} = 2\pi\varepsilon_{f,MP}T_I + \varepsilon_{\varphi,MP}$, is the phase error between the MP phase at kT_{FLL} and the phase of local replica at kT_{FLL}, calculated as a function of $\varepsilon_{\varphi,MP}$;

Herein, writing the composite correlators, 4-9, in terms of the LOS signal, and simplifying the notations, it is obtained:

$$\begin{aligned} S^P_{I,0,k-1} &= A_{LOS}\cos(LOS, k-1) \\ S^P_{I,1,k-1} &= A_{MP}\cos(MP, k-1) \\ S^P_{Q,0,k-1} &= A_{LOS}\sin(LOS, k-1) \\ S^P_{Q,1,k-1} &= A_{MP}\sin(MP, k-1) \\ S^P_{I,0,k} &= A_{LOS}\cos(LOS, k) \\ S^P_{I,1,k} &= A_{MP}\cos(MP, k) \\ S^P_{Q,0,k} &= A_{LOS}\sin(LOS, k) \\ S^P_{Q,1,k} &= A_{MP}\sin(MP, k) \end{aligned} \qquad \text{4-10}$$

where:

- $A_L = \frac{A_0}{2}R(\varepsilon_{\tau,LOS})\,\mathrm{sinc}(\pi\varepsilon_{f,LOS}T_I)$;
- $A_M = \tilde{\alpha}_1\frac{A_0}{2}R(\varepsilon_{\tau,LOS} + \Delta\tau)\,\mathrm{sinc}(\pi(\varepsilon_{f,LOS} + \Delta D)T_I)$;
- $\sin(L, k-1) = \sin(\pi\varepsilon_{f,LOS}T_I + \varepsilon_{\varphi,LOS})$;
- $\sin(M, k-1) = \sin(\pi(\varepsilon_{f,LOS} + \Delta D)T_I + \varepsilon_{\varphi,LOS} + \Delta\varphi)$;
- $\sin(L, k) = \sin(3\pi\varepsilon_{f,LOS}T_I + \varepsilon_{\varphi,LOS})$;
- $\sin(M, k) = \sin(3\pi(\varepsilon_{f,LOS} + \Delta D)T_I + \varepsilon_{\varphi,LOS} + \Delta\varphi)$;
- $\cos(L, k-1) = \cos(\pi\varepsilon_{f,LOS}T_I + \varepsilon_{\varphi,LOS})$;
- $\cos(M, k-1) = \cos(\pi(\varepsilon_{f,LOS} + \Delta D)T_I + \varepsilon_{\varphi,LOS} + \Delta\varphi)$;
- $\cos(L, k) = \cos(3\pi\varepsilon_{f,LOS}T_I + \varepsilon_{\varphi,LOS})$;
- $\cos(M, k) = \cos(3\pi(\varepsilon_{f,LOS} + \Delta D)T_I + \varepsilon_{\varphi,LOS} + \Delta\varphi)$.

This simplified notation will be useful during the calculation of the expectance and variance of the FLL discriminator output in presence of MP and the thermal noise component, in section 4.3.4.3.

4.2 MP impact on DLL

MP phenomenon affects the ideal correlation function obtained by the receiver when only the LOS signal component is received, modifying the expected correlation shape. Nevertheless, the impact of the MP reflections on the DLL tracking process must be differentiated between the effects produced by LOS MP and NLOS MP phenomenon. Indeed, the composite correlation function, resulting from the combination of the LOS and MP signal components, is equal to a delayed, attenuated and/or distorted version of the ideal correlation function, depending on the type of MP phenomenon (NLOS MP or LOS MP) affecting the composite signal.

As a consequence, the presence of the composite correlation function leads to an erroneous discriminator function, which is translated in a biased tracking process. This bias will affect the PSR measurements, as introduced in section 3.1.2.2, and the final PVT solutions.

The LOS MP impact on DLL tracking process is expressed in section 4.2.1, whereas The NLOS MP impact on DLL is detailed in section 4.2.2. The MP phenomenon under exam is the one-ray MP, introduced in section 4-5. To isolate the effects of the multipath on the code delay component, eq. 4-5 is modified applying the following assumptions:

- Perfect frequency synchronisation; the *sinc* term is approximated to 1;
- The effect of the MP on carrier phase is neglected; the cardinal *sin* term is removed.

4.2.1 LOS MP impact

The composite correlation function can be calculated from equation 4-5. A simplified equation for the composite correlation term, $\hat{R}(\varepsilon_{\tau_{0,k}})$, is proposed in equation 4-11 [12] when it is removed, for simplification purposes, the cardinal *sin* term in order to better isolate the effects of the multipath on the code delay. The composite correlation function is equal to the sum of the direct (and ideal) correlation function, $R(\varepsilon_{\tau_{0,k}})$, and a second version of the direct correlation function that is scaled in amplitude, rotated in phase and delayed in time, due to the presence of MP component, $\tilde{\alpha}_1 R(\varepsilon_{\tau_{1,k}}) \cos(\varepsilon_{\varphi_{1,k}})$.

$$\hat{R}(\varepsilon_{\tau_{0,k}}) = R(\varepsilon_{\tau_{0,k}}) + \tilde{\alpha}_1 R(\varepsilon_{\tau_{1,k}}) \cos(\varepsilon_{\varphi_{1,k}}) \qquad 4\text{-}11$$

The distortion effect introduced by the MP component on the ideal correlation function and resulting into the composite correlation function is illustrated in Figure 4-2. The figure shows the direct (dashed-point red curve), MP (dashed cyan curve) and the resulting composite correlation function (solid yellow curve), obtained for a GPS L1 C/A modulated signal, with a chip spacing of $d_c = 1$ chip and $\tilde{\alpha}_1 = 1/5$, $\Delta\tau_{1,k} = 0.25$ chips, $\Delta\varphi_{1,k} = 0$. It can be observed that the ideal correlation function symmetry is lost.

A comparison between the DLL EML discriminator S-curve of a LOS signal and the DLL EML discriminator S-curve of the composite signal described above, is illustrated in Figure 4-3. The dashed yellow line represents the LOS signal S-curve, the dashed-point red line represents the composite signal S-curve, while solid yellow line is the composite S-curve. It can be seen that the composite curve is distorted with respect to the LOS curve and shifted with respect to the zero-cross point of the LOS curve.

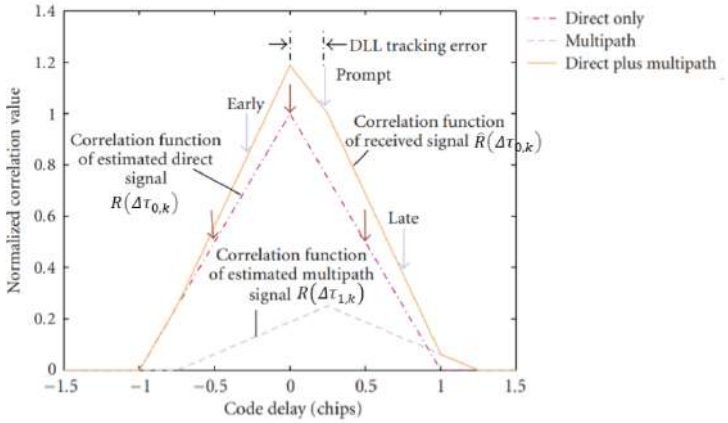

Figure 4-2 – Comparison between normalized LOS, MP and composite correlation functions, of GPS L1 C/A signal in the absence of noise and in the presence of multipath [78]

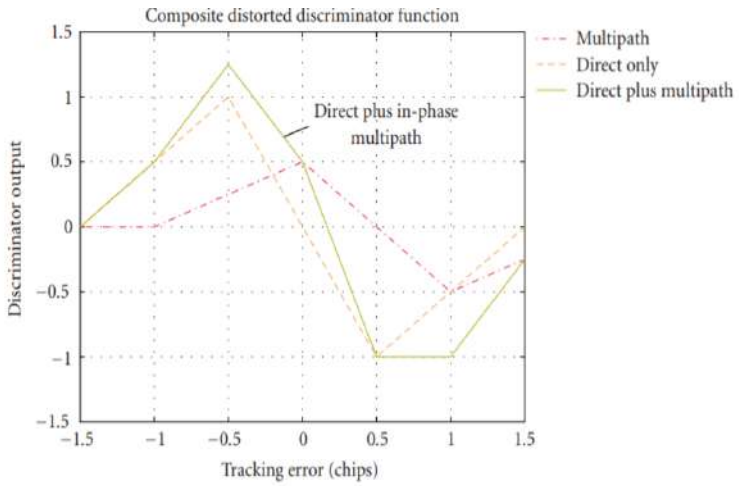

Figure 4-3 – Illustration of the S-curves for an unfiltered GPS L1 C/A signal in the absence of noise and in the presence of multipath [78]

Since the DLL inherent behavior is to drive the discriminator function to the zero value, the shifted zero-cross point of the composite signal S-curve generates a discriminator output error or bias: the discriminator out 0 crossing point does not correspond to a code delay estimation error equal to 0. Indeed, taking into account only the ideal situation, where the signal is composed only by the LOS component, the synchronization is obtained when $D_{DLL}(\varepsilon_{\tau_0}) = 0$, which is obtained for $\varepsilon_{\tau_0} = 0$. Whereas, in presence of composite signal affected by LOS MP, the discriminator output is different from zero even if the $\varepsilon_{\tau_0} = 0$ due to the presence of the composite correlation function, equation 4-11. In particular, the discriminator will be equal to zero when $\varepsilon_{\tau_0} = \delta_k$, where δ_k is the equivalent delay introduced by the multipath in the code domain, and it is a function of the code delay displacement, $\Delta\tau$, the phase displacement, $\Delta\varphi$, and the MLR, $\tilde{\alpha}_1$. An analytical solution of δ_k for EML discriminator, is developed in [70]. From the analytical solution it can be calculated the LOS MP code delay error envelope, which identifies the positive and the negative error curves, as a function of $\Delta\tau$, $\Delta\varphi$, $\tilde{\alpha}_1$, which bounds the overall LOS MP code delay error envelope.

A LOS MP code delay error envelope is portrayed in . It is obtained for a GPS L1 C/A signal and a EML discriminator, with $d_c = 1$, an RFFE equivalent filter with an infinite bandwidth, and $\tilde{\alpha}_1 = 0.5$. Code tracking error decreases for long multipath time delay and becomes zero when $\Delta\tau \geq \left(1 + \frac{d_c}{2}\right) T_c$.

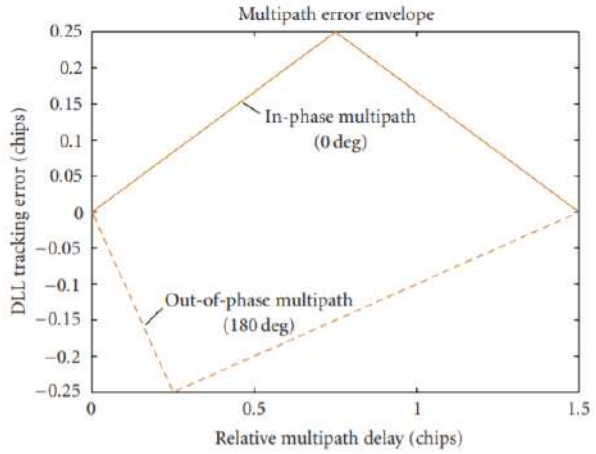

Figure 4-4 – Multipath error envelope for a conventional, one-chip early-to-late DLL receiver. Multipath component is half the strength of the direct signal [78]

The tracking error envelope is characterized by:

- The *type of modulation*: The chip modulation of a signal determines the correlation function, as presented for GPS L1 C/A and Galileo E1 OS signals in section 2.3. Figure 4-5 and Figure 4-6 introduce respectively the code tracking envelop for two different signal modulations, BPSK(1) and BOC(1,1). The BOC(1,1) tracking error envelop is smaller with respect to BPSK(1) mainly on the mid and long delay multipath.
- The *chipping rate*: it can be noticed that the code tracking errors decreases along the increase of the chipping rate. Consequently, higher chipping-rate signals, like GPS L5 or Galileo E5a are less susceptible to multipath interference.
- The *MLR*: Higher MLR implies a larger code tracking error, as illustrated in Figure 4-5.

- The *correlator spacing*: The correlator spacing, d_c, has different effects on the code tracking error. The code tracking error decreases along the decrease of the correlator spacing irrespective of the discriminator being used. An illustration of GPS L1 C/A EMLP code tracking envelope, for different correlator spacing, is presented in Figure 4-7.
- The *Front-End filter bandwidth*: The Front-End filter bandwidth also has an effect on the code tracking error. The wider Front-End filter bandwidth is, the larger the code tracking errors would be, which is independent on the type of discriminator.

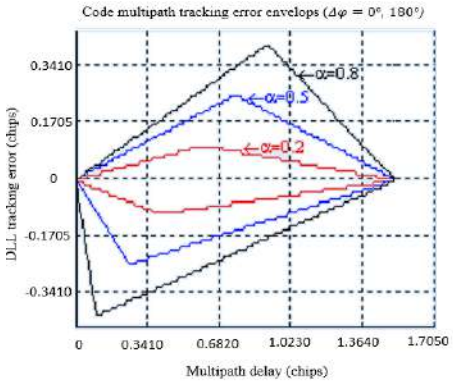

Figure 4-5 – C/A code multipath error envelope, EML discriminator, $d_c = 1$ chips [79]

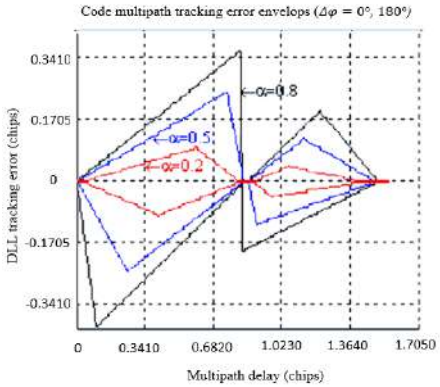

Figure 4-6 – BOC(1,1) multipath error envelope, ELM discriminator, $d_c = 1$ chips [79]

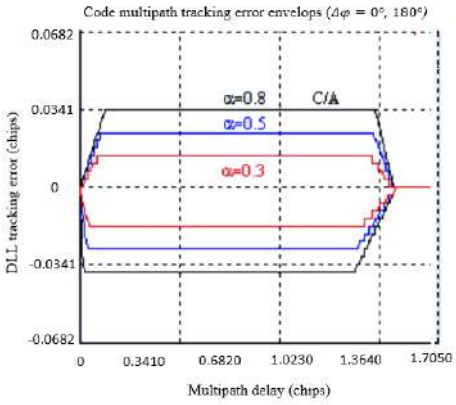

Figure 4-7 – C/A code multipath error envelope, ELM narrow correlator, $d_c = 0.2$ chips [79]

The code delay error caused by LOS MP is typically on the order of meters in open space environment [4], and on the order of tens of meters in harsh environments, depending upon the amplitude of the reflected signal and the correlator spacing used. Multipath induced error seen in urban environments tends to be a result of short delay multipath, which is problematic for the navigation application since short delay multipath is more difficult to mitigate [6].

4.2.2NLOS MP impact

In case of NLOS MP state of reception, the composite received signal is composed only by MP component, since LOS component is blocked. Therefore, the composite correlation function is only composed by the MP correlation function, which is an attenuated and delayed version of the ideal correlation function. In this case, to obtain the synchronization, the discriminator is equated to zero, $\left(D_{DLL}(\varepsilon_{\tau_1}) = 0\right)$, when $\varepsilon_{\tau_1} = 0$. The resulting error is directly proportional, therefore, to the magnitude of the code delay displacement, 4-6.

4.3 MP impact on FLL

This section aims at providing the characterization of FLL tracking error PDF generated by multipath and thermal noise in a simplified MP environment model in order to compare the derived theoretical results with the experimental results obtained in Chapter 6; this comparison is conducted in order to validate the methodology presented in Chapter 5 (and applied to collected data in Chapter 6) on isolating the multipath plus thermal noise (MN) error component of the PSR-R measurements. Nevertheless, note that the comparison will be mainly made at a qualitative level since the MP environment model considered in this chapter is simple and the exact parameters and internal structure of the low-cost receiver used in Chapter 6 are unknown.

The approach followed to derive the simplified frequency tracking error model is similar to the approach used to define the MP code delay error characterization in sections 4.2. FLL tracking error model induced by MP component depends on four main factors, the MLR, the carrier phase displacement (4-7), the code delay displacement (4-6), and the Doppler frequency displacement ΔD, (4-8), defined in section 4.1. The MP induced FLL error can also be characterized by a tracking error envelope, as already defined for DLL discriminator output error, in section 4.2.

A typical urban environment has been used in this section with the following characteristics:

- the code delay displacement is approximated to 0 (equivalently, the loss of amplitude of the LOS signal and echo individual correlation functions due to a delay displacement is assumed to be included on the MLR value);
- the MLR is arbitrarily defined as 1/2 and 1/4 to provide some numerical and graphical examples;
- the values of carrier phase displacement due to multipath reflections in urban environment are uniformly distributed between 0° and 359°,
- the Doppler frequency displacement, ΔD, values are limited to a subset which depends on the specific configuration of the urban environment, the characteristics of the multipath reflections, the GNSS receiver's dynamics and the reflector's dynamics.

From the assumptions presented above, the ΔD characterization is fundamental to develop the final FLL tracking error model. Therefore, in section 4.3.1 the Doppler frequency displacement model for a simple urban environment scenario is provided. Once the ΔD characterization have been derived, the general FLL tracking error model due to the presence of MP and thermal noise is developed in section 4.3.2; however, only the Cross-Product discriminator is inspected in this section as well as in the remaining sections since this discriminator only applies linear operations and thus facilitates the derivation of all the targeted mathematical formulas. In section 4.3.3, the focus is put on the FLL tracking error model bias and in section 4.3.4 on the FLL tracking error model variance. Finally, in section 4.3.5, the complete FLL tracking error PDF is derived; remember that this complete model will be exploited to perform a qualitative comparison with the experimental results derived in Chapter 6.

4.3.1 Doppler Frequency Displacement

The definition of Doppler frequency displacement has been provided in section 4.1.2. The mathematical model is derived in section 4.3.1.1 from the previous definition. In section 4.3.1.2, the mathematical model is exploited to characterize the Doppler frequency displacement in two specific urban environment configurations, considered as two typical urban scenarios encountered by a GNSS receiver, where the GNSS receiver is mounted on a dynamic platform. The two scenarios consist of:

1. a dynamic receiver moving along an urban canyon, represented by the street and two large static reflectors on the two sides of the street;
2. a dynamic receiver interacting with a dynamic reflector, placed in any position around the receiver and moving in a parallel direction.

The final characterization has been employed to model the FLL discriminator output tracking error in section 4.3.2.

4.3.1.1 Doppler frequency displacement model

The mathematical LOS Doppler frequency model due to the motion between a satellite and a receiver is presented in section 2.1.3.2. In this section, the LOS Doppler frequency is used to model the Doppler frequency of an echo or multipath, called MP Doppler frequency, as presented in section 4.3.1.1.1. Finally, the mathematical model of the Doppler frequency displacement, calculated as the difference between the MP component and the LOS component Doppler frequencies has been defined in section 4.3.1.1.2.

4.3.1.1.1 MP Doppler frequency mathematical model

In order to characterize the MP Doppler frequency, the first step is to define the multipath environment geometrical model. The multipath environment geometrical model used herein is a 1-ray reflection model. The reflected 1-ray is defined as the transmission of satellite i signal which interacts with the surface of a reflector object (O) placed in the vicinity of the receiver's position and that is captured by the receiver's antenna (R) as explained in section 4.1.

The Doppler shift of the received signal in the presence of an obstacle, is influenced by two different components, one induced by the relative motion between the transmitter and the obstacle; and another one induced by the relative motion between the obstacle and the receiver. Therefore, the Doppler effect depends on the composite relative motion between the receiver, the transmitter and the obstacle. The MP Doppler frequency is presented in 4-12 [80],[81]:

$$f_{D,MP} = \frac{d}{dt}|\boldsymbol{p}_r(t) - \boldsymbol{p}_o(t)|\frac{1}{\lambda} + \frac{d}{dt}\left|\boldsymbol{p}_o(t) - \boldsymbol{p}^{\boldsymbol{i}}(t)\right|\frac{1}{\lambda} \quad 4\text{-}12$$

where:

- $\boldsymbol{p}_r(t) = \left(p_{r,x}(t), p_{r,y}(t), p_{r,z}(t)\right)$ is the receiver position vector, at instant t;
- $\boldsymbol{p}_o(t) = \left(p_{o,x}(t), p_{o,y}(t), p_{o,z}(t)\right)$ is the object position vector, at instant t;
- $\boldsymbol{p}^{\boldsymbol{i}}(t) = \left(p_x^i(t), p_y^i(t), p_z^i(t)\right)$ is the transmitter position vector, at instant t;
- λ is the wavelength of the transmitted signal.

Developing the first derivative in 4-12, it is obtained

$$\frac{d}{dt}|\boldsymbol{p}_r(t) - \boldsymbol{p}_o(t)| = \\ = \frac{\left(p_{r,x}(t) - p_{o,x}(t)\right)\left(\dot{p}_{r,x}(t) - \dot{p}_{o,x}(t)\right)}{R_{ro}} + \frac{\left(p_{r,y}(t) - p_{o,y}(t)\right)\left(\dot{p}_{r,y}(t) - \dot{p}_{o,y}(t)\right)}{R_{ro}} \\ + \frac{\left(p_{r,z}(t) - p_{o,z}(t)\right)\left(\dot{p}_{r,z}(t) - \dot{p}_{o,z}(t)\right)}{R_{ro}} \quad 4\text{-}13$$

with

- $\dot{\boldsymbol{p}}_r(t) = \left(\dot{p}_{r,x}(t), \dot{p}_{r,y}(t), \dot{p}_{r,z}(t)\right)$ is the receiver velocity vector, at instant t;
- $\dot{\boldsymbol{p}}_o(t) = \left(\dot{p}_{o,x}(t), \dot{p}_{o,y}(t), \dot{p}_{o,z}(t)\right)$ is the object velocity vector, at instant t;
- $R_r^o(t) = \sqrt{\left(p_{r,x}(t) - p_{o,x}(t)\right)^2 + \left(p_{r,y}(t) - p_{o,y}(t)\right)^2 + \left(p_{r,z}(t) - p_{o,z}(t)\right)^2}$ is the receiver to object range, at instant t.

From 4-13, it could be defined:

- the vector which is the difference between the receiver's position and the object's position, $\boldsymbol{p}_{ro}(t) = \boldsymbol{p}_r(t) - \boldsymbol{p}_o(t) = \left(p_{r,x}(t) - p_{o,x}(t), p_{r,y}(t) - p_{o,y}(t),\ p_{r,z}(t) - p_{o,z}(t)\right)$;
- the unit vector pointing towards the receiver from the object $\boldsymbol{u}_r^o(t) = \left(\frac{p_{ro,x}(t)}{R_r^o(t)}, \frac{p_{ro,y}(t)}{R_r^o(t)}, \frac{p_{ro,z}(t)}{R_r^o(t)}\right)$;
- the vector which is the difference between the receiver's speed and the object's speed, $\dot{\boldsymbol{p}}_{ro} = \left(\dot{p}_{r,x}(t) - \dot{p}_{o,x}(t), \dot{p}_{r,y}(t) - \dot{p}_{o,y}(t),\ \dot{p}_{r,z}(t) - \dot{p}_{o,z}(t)\right) = \dot{\boldsymbol{p}}_r(t) - \dot{\boldsymbol{p}}_o(t)$.

Thus, the derivative in 4-13 could be rewritten as:

$$\frac{d}{dt}|\boldsymbol{p}_r(t) - \boldsymbol{p}_o(t)| = \dot{\boldsymbol{p}}_{ro}(t) \cdot \boldsymbol{u}_{ro}(t) = \dot{\boldsymbol{p}}_r(t) \cdot \boldsymbol{u}_{ro}(t) - \dot{\boldsymbol{p}}_o(t) \cdot \boldsymbol{u}_{ro}(t) \quad 4\text{-}14$$

With the same approach, the second derivative in the 4-12 is developed as

$$\frac{d}{dt}\left|\boldsymbol{p}_o(t) - \boldsymbol{p}^{\boldsymbol{i}}(t)\right| = \dot{\boldsymbol{p}}_o^i(t) \cdot \boldsymbol{u}_o^i(t) = \dot{\boldsymbol{p}}_o(t) \cdot \boldsymbol{u}_o^i(t) - \dot{\boldsymbol{p}}^i(t) \cdot \boldsymbol{u}_o^i(t) \quad 4\text{-}15$$

with

- $\boldsymbol{p}^i(t) = \left(p_x^i(t), p_y^i(t), p_z^i(t)\right)$ is the transmitter position vector, at instant t;

- $\dot{\boldsymbol{p}}^i(t) = \left(\dot{p}_x^i(t), \dot{p}_y^i(t), \dot{p}_z^i(t)\right)$ is the transmitter velocity vector, at instant t;
- the difference between the satellite's position vector and the object's position vector, $\boldsymbol{p}_o^i(t) = \boldsymbol{p}_o(t) - \boldsymbol{p}^i(t) = \left(p_{o,x}(t) - p_x^i(t), p_{o,y}(t) - p_y^i, (t)\ p_{o,z}(t) - p_z^i(t)\right)$, at instant t;
- the unit vector pointing towards the object from the transmitter $\boldsymbol{u}_o^i(t) = \left(\frac{p_{o,x}^i(t)}{R_o^i(t)}, \frac{p_{o,y}^i(t)}{R_o^i(t)}, \frac{p_{o,z}^i(t)}{R_o^i(t)}\right)$, at instant t;
- $R_o^i(t) = \sqrt{\left(p_{o,x}(t) - p_x^i(t)\right)^2 + \left(p_{o,y}(t) - p_y^i(t)\right)^2 + \left(p_{o,z}(t) - p_z^i(t)\right)^2}$ is the object to transmitter range, at instant t;
- the difference between the satellite's velocity vector and the object's velocity vector, $\dot{\boldsymbol{p}}_o^i(t) = \dot{\boldsymbol{p}}_o(t) - \dot{\boldsymbol{p}}^i(t) = \left(\dot{p}_{o,x}(t) - \dot{p}_x(t), \dot{p}_{o,y}(t) - \dot{p}_y(t),\ \dot{p}_{o,z}(t) - \dot{p}_z(t)\right)$, at instant t;

Finally, introducing 4-14 and 4-15 into 4-12, the Doppler frequency of a received multipath echo due to the presence of a reflector is equal to

$$f_{D,MP}(t) = \frac{1}{\lambda}\left(\dot{\boldsymbol{p}}_r(t) \cdot \boldsymbol{u}_{ro}(t) - \dot{\boldsymbol{p}}_o(t) \cdot \boldsymbol{u}_{ro}(t)\right) + \frac{1}{\lambda}(\dot{\boldsymbol{p}}_o(t) \cdot \boldsymbol{u}_o^i(t) - \dot{\boldsymbol{p}}^i(t) \cdot \boldsymbol{u}_o^i(t)) \quad 4\text{-}16$$

4.3.1.1.2 Doppler Frequency Displacement mathematical model

The Doppler frequency displacement could be mathematically defined as the difference between the MP Doppler Frequency and the LOS Doppler Frequency (section 4.1.2). Therefore, the Doppler Frequency Displacement is obtained as the difference between 2-8 and, 4-16:

$$\Delta D = f_{D_{LOS}} - f_{D_{MP}} = \\ = \left(\frac{1}{\lambda}(\dot{\boldsymbol{p}}_r \cdot \boldsymbol{u}_r^i) - \frac{1}{\lambda}(\dot{\boldsymbol{p}}^i \cdot \boldsymbol{u}_r^i)\right) - \left(\frac{1}{\lambda}(\dot{\boldsymbol{p}}_r \cdot \boldsymbol{u}_r^o - \dot{\boldsymbol{p}}_o \cdot \boldsymbol{u}_r^o) + \frac{1}{\lambda}(\dot{\boldsymbol{p}}_o \cdot \boldsymbol{u}_o^i - \dot{\boldsymbol{p}}^i \cdot \boldsymbol{u}_o^i)\right) \quad 4\text{-}17$$

with:

- the dot product between the receiver's velocity vector, and the transmitter-to-receiver unitary vector is equal to $\dot{\boldsymbol{p}}_r \cdot \boldsymbol{u}_r^i = \dot{p}_{r,x}u_{r,x}^i + \dot{p}_{r,y}u_{r,y}^i + \dot{p}_{r,z}u_{r,z}^i$;
- the dot product between the receiver's velocity vector, and the object-to-receiver unitary vector is equal to $\dot{\boldsymbol{p}}_r \cdot \boldsymbol{u}_r^o = \dot{p}_{r,x}u_{r,x}^o + \dot{p}_{r,y}u_{r,y}^o + \dot{p}_{r,z}u_{r,z}^o$;
- the dot product between the object's velocity vector and the object-to-receiver unitary vector, is equal to $\dot{\boldsymbol{p}}_o \cdot \boldsymbol{u}_r^o = \dot{p}_{o,x}u_{r,x}^o + \dot{p}_{o,y}u_{r,y}^o + \dot{p}_{o,z}u_{r,z}^o$;
- the dot product between the object's velocity vector and the transmitter-to-receiver unitary vector, is equal to $\dot{\boldsymbol{p}}_o \cdot \boldsymbol{u}_r^i = \dot{p}_{o,x}u_{r,x}^i + \dot{p}_{o,y}u_{r,y}^i + \dot{p}_{o,z}u_{r,z}^i$.

The transmitter-to-object vector may be approximated to the transmitter(satellite)-to-receiver vector, $\boldsymbol{u}_o^i \approx \boldsymbol{u}_r^i$ without losing accuracy since receiver and object positions are close enough with respect to the distance between the two and the satellite [75]. Applying this assumption, 4-17 becomes

$$\Delta D = \frac{1}{\lambda}(\dot{\boldsymbol{p}}_r \cdot \boldsymbol{u}_r^i - \dot{\boldsymbol{p}}_r \cdot \boldsymbol{u}_r^o + \dot{\boldsymbol{p}}_o \cdot \boldsymbol{u}_r^o - \dot{\boldsymbol{p}}_o \cdot \boldsymbol{u}_r^i) \quad 4\text{-}18$$

In order to simplify the calculation, in the following part, the scalar products in 4-18 will be expressed using the vectors in polar coordinates:

The polar expressions of $\dot{\boldsymbol{p}}_r$ and $\boldsymbol{u}_r^i$ are developed as follows:

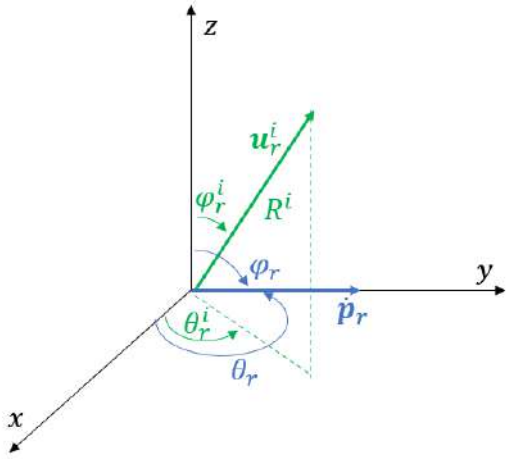

Figure 4-8 – The schematic definition of the $\dot{\boldsymbol{p}}_r$ and $\boldsymbol{u}_r^i$ vectors in polar coordinates, in the $[x, y, z]$ plane

$$\dot{p}_{r,x} = \dot{R} \sin\varphi_r \cos\theta_r$$
$$\dot{p}_{r,y} = \dot{R} \sin\varphi_r \sin\theta_r$$
$$\dot{p}_{r,y} = \dot{R} \cos\varphi_r$$

$$u_{r,x}^i = \sin\varphi_r^i \cos\theta_r^i$$
$$u_{r,y}^i = \sin\varphi_r^i \sin\theta_r^i$$
$$u_{r,z}^i = \cos\varphi_r^i$$

4-19

where:

- $\dot{R}$ is the receiver speed vector modulo;
- the direction of the receiver speed vector is defined by the polar angles: (φ_r, θ_r);
- the receiver's position with respect to the satellite position is defined by the transmitter-to-receiver polar angles $(\varphi_r^i, \theta_r^i)$;

The polar expressions of $\dot{\boldsymbol{p}}_o$ and $\boldsymbol{u}_o^i$ are developed as follows:

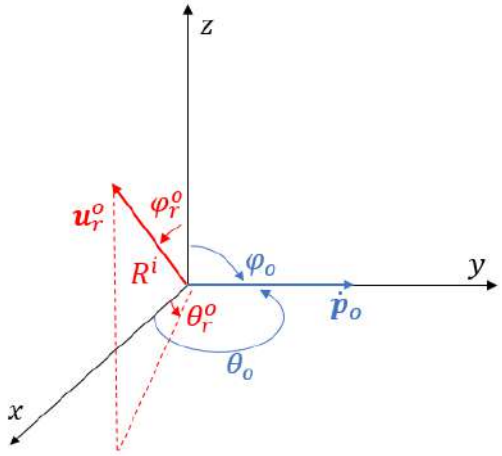

Figure 4-9 – The schematic definition of the $\dot{\boldsymbol{p}}_o$ and $\boldsymbol{u}_r^o$ vectors in polar coordinates in the $[x, y, z]$ plane

$$\dot{p}_{o,x} = \dot{R}_o \sin\varphi_o \cos\theta_o$$
$$\dot{p}_{o,y} = \dot{R}_o \sin\varphi_o \sin\theta_o$$
$$\dot{p}_{o,y} = \dot{R}_o \cos\varphi_o$$

$$u_{r,x}^o = \sin\varphi_r^o \cos\theta_r^o$$
$$u_{r,y}^o = \sin\varphi_r^o \sin\theta_r^o$$
$$u_{r,z}^o = \cos\varphi_r^o$$

4-20

where:

- $\dot{R}_o$ is the reflector speed vector modulo;
- the direction of the reflector speed vector is defined by the polar angles: (φ_o, θ_o);
- the receiver's position with respect to the satellite position is defined by the object-to-receiver polar angles $(\varphi_r^o, \theta_r^o)$.

The resulting equation is equal to:

$$\Delta D = \frac{1}{\lambda}\dot{R}\left(\sin\varphi_r \sin\varphi_r^i \cos\left(\theta_r - \theta_r^i\right) + \cos\varphi_r \cos\varphi_r^i - \sin\varphi_r \sin\varphi_r^o \cos(\theta_r - \theta_r^o) - cos\,\varphi_r\, cos\,\varphi_r^o\right)$$
$$+\frac{1}{\lambda}\dot{R}_o\left(sin\,\varphi_o\, sin\,\varphi_r^o\, cos(\theta_o - \theta_r^o) + cos\,\varphi_o\, cos\,\varphi_r^o - sin\,\varphi_o\, sin\,\varphi_r^i\, cos\left(\theta_o - \theta_r^i\right) - cos\,\varphi_o\, cos\,\varphi_r^i\right) \quad 4\text{-}21$$

whit (see Figure 4-12, Figure 4-13 and Figure 4-14):

- $\dot{R}$ is the receiver velocity vector modulo;
- $\dot{R}_o$ is the reflector velocity vector modulo;
- the direction of the receiver speed vector is defined by the polar angles: (φ_r, θ_r);
- the direction of the reflector speed vector is defined by the polar angles: (φ_o, θ_o);
- the receiver's position with respect to the satellite position is defined by the transmitter-to-receiver polar angles $(\varphi_r^i, \theta_r^i)$;
- the receiver's position with respect to the object position is defined by the object-to-receiver polar angles $(\varphi_r^o, \theta_r^o)$;

The theoretical model expressed in 4-21 can be applied to characterize the Doppler frequency displacement for a specific multipath environment configuration by just tuning the parameters in equation 4-21.

4.3.1.2 Doppler frequency displacement characterization

The goal of this section is to obtain the Doppler Frequency displacement characterization, applying the theoretical model expressed in 4-21, to a GNSS receiver mounted on a dynamic user platform in a specific urban environment configuration.

A complex urban environment model has been already introduced in section 2.4.1.2.4. However, a simplified configuration of urban environment has been modelled and exploited in this work, firstly commented in section 4.1. The description of this simplified model is detailed in section 4.3.1.2.1, including the urban environment geometric design and the multipath reflection design.

4.3.1.2.1 Multipath reflections in urban environment

Multipath environment model for a dynamic user platform can be extremely complex to simulate due to the high density of reflectors, the diversity of the environment configurations potentially encountered by the moving platform (constituting the overall urban environment), and the rate-of-change of the urban environment configurations as a function of the user platform dynamic and the reflectors dynamic.

Indeed, multipath reflections in the urban environments depend on two fundamental factors:

- The geometric model of the urban environment, section 2.4.1.2.1;
- The physical properties of the scattering phenomenon, section 2.4.1.2.1.

Therefore, due to computational limitations, when considering the simulation of an urban environment, a simplified model is usually applied, the so-called urban canyon, which is defined as a single section of a typical urban or suburban environment. Typical urban canyons have been modelled in several works, such as [30]–[33]. A simplified model of the urban canyon, applied in the simulation process, is presented in the final part of section 2.4.1.2.4.

A small summary is provided here. The proposed urban trench model is defined by the following components:

- the street,
- the GNSS satellite (transmitter) i, SV_i;
- the GNSS receiver, R, moving along the x-axis;
- two objects which act as reflectors, placed on the two sides of the street, O_1 and O_2, parallel to the movement of the GNSS receiver;
- the reflection point, P;

The design of these components is characterized by the following parameters, portrayed in Figure 2-23 and Figure 2-24, respectively the geometric model in the x-y plane and y-z plane:

- The width of the street, w;
- The receiver position on the x-y plane, defined by $p_{r,x}$, $p_{r,y}$;
- The height of the objects on the two sides of the street, h_1 for $O_1$and h_2 for O_2, in the y-z plane;
- The length of the objects on the two sides of the street, c_1 for O_1 and c_2 for O_2, in the x-y plane.

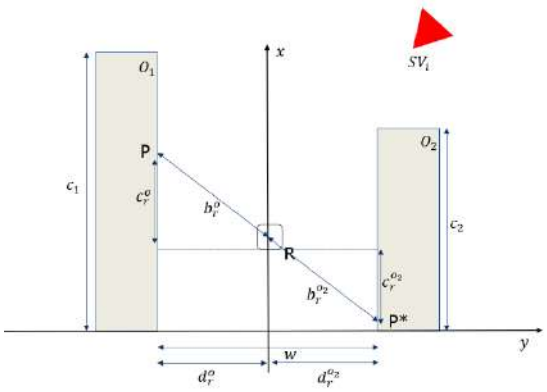

Figure 4-10 – Urban trench geometric model, x-y plane

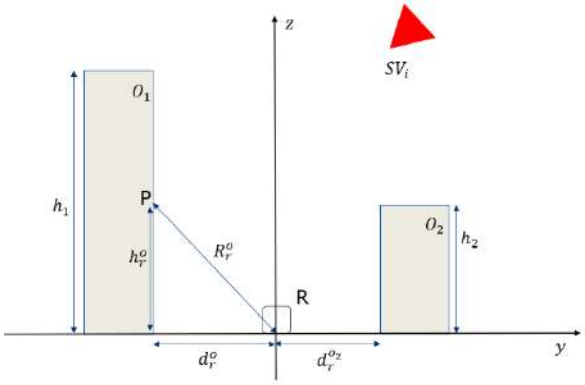

Figure 4-11 – Urban trench geometric model, y-z plane

4.3.1.2.2 Numerical Characterization of Doppler Displacement PDF

The goal of this section is to provide the characterization of the Doppler frequency displacement for a given urban environment scenario affected by multipath. The characterization consists in the calculation of the corresponding Doppler frequency displacement PDF. The characterization procedure consists of the application of two consecutive set of operations:

- Calculation of the LOS/NLOS Doppler frequency displacement vector: this first block aims to generate all the feasible Doppler frequency displacement values from all possible LOS and NLOS MP reflection situations given the model of a specific urban scenario. The details of this first block are presented in section 4.3.1.2.2.1.
- Characterization of the Doppler frequency displacement: the resulting set of LOS and NLOS Doppler frequency displacement values have been used to calculate the Doppler frequency displacement PDF, trough the calculation of the corresponding histogram. The second block is depicted in section 4.3.1.2.2.2.

The Doppler frequency displacement characterization is applied to two specific urban environment scenarios, proposed in the following sections:

- A dynamic GNSS receiver moving through the urban canyon, characterized by large static reflectors placed on the two sides of the street (such as a building, a static vehicle, etc.). The parameters and the resulting model are provided in section 4.3.1.2.2.3.
- The interaction between the GNSS dynamic receiver and a dynamic reflector moving in the same or opposite receiver's direction. The parameters and the resulting model are provided in Section 4.3.1.2.2.4.

4.3.1.2.2.1 Doppler frequency displacement calculation

The procedure used to calculate the LOS and NLOS Doppler frequency displacement consists of three different steps:

1) To generate the LOS and NLOS reflection situations.
2) To verify the feasibility of the reflection situations with respect to the urban geometric model under exam.
3) To calculate the LOS/NLOS Doppler frequency displacement, only if in presence of a feasible reflection situation.

The implemented algorithm is illustrated in Figure 4-21. Now let us see in detail the individual steps.

Step 1) To generate the LOS and NLOS reflection situations: The generation of the LOS and NLOS reflection situations implies the knowledge of:

1. The Urban canyon geometric model: it has been designed following the assumptions described in 2.4.1.2.4. The 3D model, x-y and y-z plane sections are portrayed, respectively, in Figure 4-12, Figure 4-13, Figure 4-14. The parameters applied in this simulation are summarized in Table 4-1. The width of the street, the minimum and the maximum height of the reflectors have been calculated as referred in [30], [34].

2. The Multipath reflection model: it has been designed following the assumptions described in 2.4.1.2.1. The multipath reflection model is summarized in Table 4-2.
3. The customized geometric parameters, which are tuned during the simulation:
    - The receiver velocity vector, $\dot{\boldsymbol{p}}_r(\dot{R}, \theta_r, \varphi_r)$; the receiver is modelled as always moving along the x-axis ($\theta_r \approx 90$);
    - The reflector velocity vector, $\dot{\boldsymbol{p}}_o(\dot{R}_o, \theta_o, \varphi_o)$.
    - The receiver-to-satellite unitary vector, $\boldsymbol{u}_r^i(\theta_r^i, \varphi_r^i)$. This provides the relative position of the satellite with respect to the receiver.
4. The LOS/NLOS reflection conditions: two critical elevation angles can be defined, which describe the reception state of the transmitted signal (section 2.4.1.2.3), and, as a consequence, the MP phenomenon. The used elevation angle numerical values are chosen as function of the next presented elevation angle conditions in order to simulate the targeted, LOS, NLOS or blocked reception states conditions. Graphical explanations for the interpretation and calculation of these angels are given in for each simulated scenario in sections 4.3.1.2.2.3 and 4.3.1.2.2.4
    a. *LOS reception state.* In this configuration the MP signal and the LOS are received by the receiver. 4-22 illustrates the LOS geometric reception assumption, where $\varphi_{r,LOS}^i$ is called LOS elevation angle. This angle is calculated as the minimum elevation angle providing Line of Sight between the satellite and the receiver without being blocked by a reflector.

$$\varphi_r^i \leq \varphi_{r,LOS}^i \qquad 4\text{-}22$$

    b. *NLOS reception state.* In this configuration only the MP signal is received by the receiver, while LOS is blocked by the reflector. 4-23 describes the NLOS geometric reception assumption, where $\varphi_{r,NLOS}^i$ is called NLOS elevation angle. $\varphi_{r,NLOS}^i$ is calculated as the minimum elevation angle which provides a specular reflection from one side of the urban canyon reaching the receiver without being blocked by the reflector on the opposite side of the street.

$$\varphi_{r,LOS}^i < \varphi_r^i \leq \varphi_{r,NLOS}^i \qquad 4\text{-}23$$

    c. *Blocked reception state.* In this configuration the MP signal and the LOS are blocked by the reflector. This reception state happens when:

$$\varphi_r^i > \varphi_{r,NLOS}^i \qquad 4\text{-}24$$

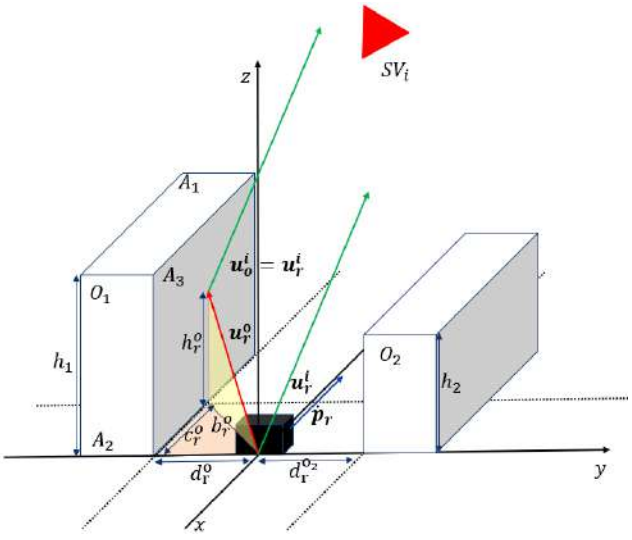

Figure 4-12 – Urban canyon geometric 3D model model

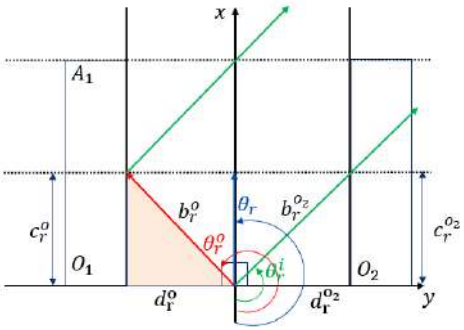

Figure 4-13 – Urban canyon geometric model, x-y plane

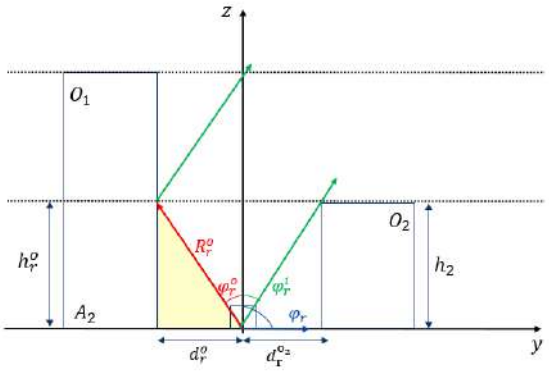

Figure 4-14 – Urban canyon geometric model, y-z plane

Knowing the urban canyon geometric model, the multipath reflection characteristics and $\boldsymbol{u}_r^i$, it is possible to define the receiver-to-object unitary vector, $\boldsymbol{u}_r^o(\theta_r^o, \varphi_r^o)$. In this simplified case, three specific assumptions have been applied:

- the simulated reflected ray is designed as a diffuse single-path reflection; this means that the incident angle and reflection angle are not equal. It is assumed that the reflecting point can only be found in front of the receiver due to the single reflection configuration (no multiple reflections are allowed).
- the reflector object is always in the opposite side of the street with respect to the position of the satellite; this guarantees the presence of a possible reflection point.
- the reflector point can be located anywhere while fulfilling the previous assumption; note that the geometrical feasibility and signal processing considerations of all locations are inspected in step 2)

Due to the assumptions formulated in the previous paragraph and imposing that the receiver is moving along the x axis ($\theta_r \approx 90°$), the range of values of the object-to-receiver unitary vector, $\boldsymbol{u}_r^o(\theta_r^o, \varphi_r^o)$ has been set as follows:

- The azimuth angle, θ_r^o, depends on the value of θ_r^i:
  - If $270° < \theta_r^i < 360°$ (see Figure 4-15), θ_r^o is uniformly distributed between 1° and 89°;
  - If $180° < \theta_r^i < 270°$ (see Figure 4-16), θ_r^o is uniformly distributed between 91° and 179°;
  - If $90° < \theta_r^i < 180°$, θ_r^o (see Figure 4-17), is uniformly distributed between 181° and 269°;
  - If $0° < \theta_r^i < 90°$, θ_r^o (see Figure 4-18), is uniformly distributed between 271° and 359°;
- The elevation angle, φ_r^o, has been simulated as uniformly distributed between 1° and 89°.

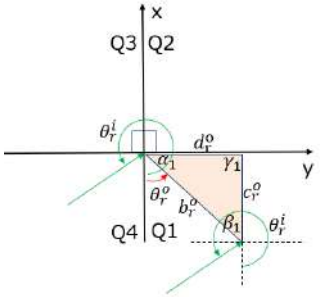

Figure 4-15 – Urban canyon geometric model, y-z plane, received signal incident to Quadrant 4

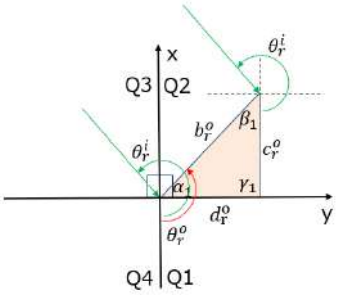

Figure 4-16 – Urban canyon geometric model, y-z plane, received signal incident to Quadrant 3

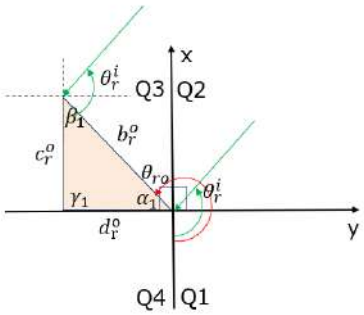

Figure 4-17 – Urban canyon geometric model, y-z plane, received signal incident to Quadrant 2

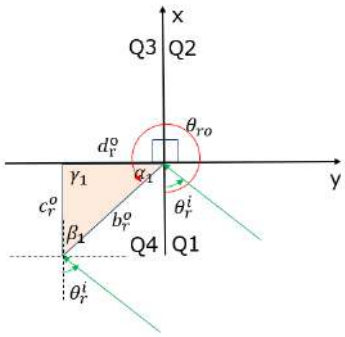

Figure 4-18 –Urban canyon geometric model, y-z plane, received signal incident to Quadrant 1

Afterwards, the receiver-to-reflector unitary vector, $\boldsymbol{u}_r^o(\theta_r^o, \varphi_r^o)$, is used to calculate the geometric variables describing the position of the reflection point, $P(c_r^o, h_r^o)$ where:

- $c_r^o = d_r^o \cot(\beta_1)$ is the distance between the receiver and the reflection point, along the x-axis, with
  - d_r^o: is the distance between the receiver and the reflector surface. It is fixed by the urban trench geometric model;
  - β_1: is the angle between the surface of the reflector and the receiver-to-object vector, in the x-y plane, Figure 4-15. It can be calculated though trigonometric operations, knowing the value of θ_r^o.
- $h_r^o = b_r^o \cot(\beta_2)$ is the distance between the reflection point and the receiver position along z-axis, with
  - b_r^o: is distance between the reflection point and the receiver position, in the x-y plane. The equation is defined in 2.4.1.2.4;
  - β_2: is the angle between the ground and the receiver-to-object vector, in the x-z plane. It can be calculated though trigonometric operations, knowing the value of φ_r^o.

Step 2) To verify the feasibility of the reflection situations with respect to the urban geometric model under exam**:** The Doppler displacement calculation is allowed only if the reflection point provides a feasible reflection; the reflection is feasible only if the reflection point is located on the surface of the reflector O_1; an example of feasible reflection is illustrated in Figure 4-19, while unfeasible reflection is portrayed in Figure 4-20. The reflection point $P(c_r^o, h_r^o)$ must respect the feasibility conditions, summarized as follows:

$$\begin{aligned} h_r^o &\leq h_{MAX} \\ R_r^o &\leq R_{MAX} \end{aligned} \qquad 4\text{-}25$$

where:

- h_{MAX} is the maximum height of the building;
- R_r^o is the distance between the reflection point and the receiver in the y-z plane, defined in section 2.4.1.2.4;
- R_{MAX} is the maximum distance between the receiver and the reflection point positions which guarantee a MP reflection affecting the DLL discriminator output. For GPS L1 C/A and a standard chip spacing equal to $d_c = 1$ chip, R_{MAX} is equal to:

$$R_{MAX} = \left[\left(1 + \frac{d_c}{2}\right) T_c\right] \cdot c = 439.88 \text{ m} \qquad 4\text{-}26$$

Note that smaller values of d_c could be used; however, smaller values of R_{MAX} will be derived leading to a more conservative Doppler displacement simulated PDF characterizations.

Step 3) To calculate the LOS/NLOS Doppler frequency displacement, only if in presence of a feasible reflection situation**:** If the reflection is feasible, the calculation of the Doppler displacement is applied, using 4-21. Once the Doppler displacement has been calculated, the algorithm starts a new iteration; the procedure is repeated for any $\boldsymbol{u}_r^i$, $\dot{\boldsymbol{p}}_o$ and $\dot{\boldsymbol{p}}_r$ allowed by simulation scenario requirements. Hence, the simulation generates a different Doppler

frequency displacement output for each value of $\dot{\boldsymbol{p}}_r(\dot{R}, \theta_r, \varphi_r)$, $\dot{\boldsymbol{p}}_o(\dot{R}_o, \theta_o, \varphi_o)$, $\boldsymbol{u}_r^i(\theta_r^i, \varphi_r^i)$ and $\boldsymbol{u}_r^o(\theta_r^o, \varphi_r^o)$, when the reflection point is feasible. The corresponding simulation's output is a discrete set of realizations, of the Doppler frequency Displacement random variable, 4-27.

$$\Delta D(\dot{R}, \theta_r, \varphi_r, \dot{R}_o, \theta_o, \varphi_o, \varphi_r^i, \theta_r^i, \varphi_r^o, \theta_r^o) \qquad 4\text{-}27$$

This is calculated separately for the LOS and NLOS MP Doppler displacement, ΔD^{LOS} and ΔD^{NLOS}, due to the application of $\varphi_{r,NLOS}^i$, and $\varphi_{r,LOS}^i$ angles condition presented above. Once the LOS and NLOS Doppler frequency displacements have been calculated, the characterization could be applied.

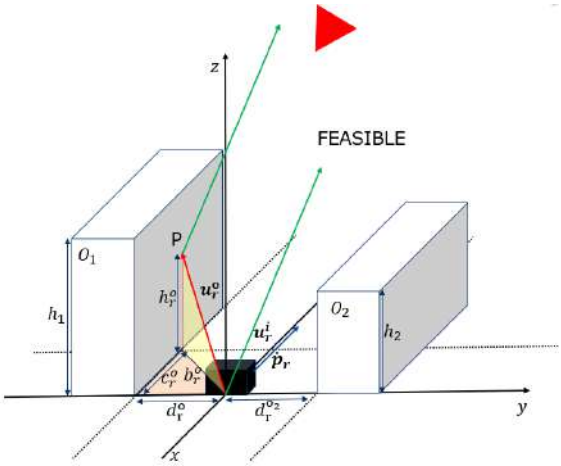

Figure 4-19 – Reflection point is on the surface of the reflector O_1, configuration of feasible reflection

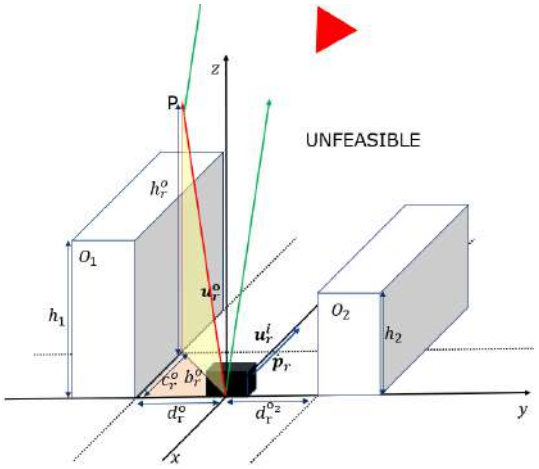

Figure 4-20 – Reflection point isn't on the surface of the reflector O_1, configuration of unfeasible reflection

Minimum height of the building, h_{min} [m]	12
Maximum height of the building, h_{MAX} [m]	18
Width of the street, w [m]	8.60

Table 4-1 – Parameters of Urban canyon geometric model

Physical reflection type	Diffuse
Geometric model of the reflection	Single reflection

Table 4-2 – Parameters of multipath reflection model

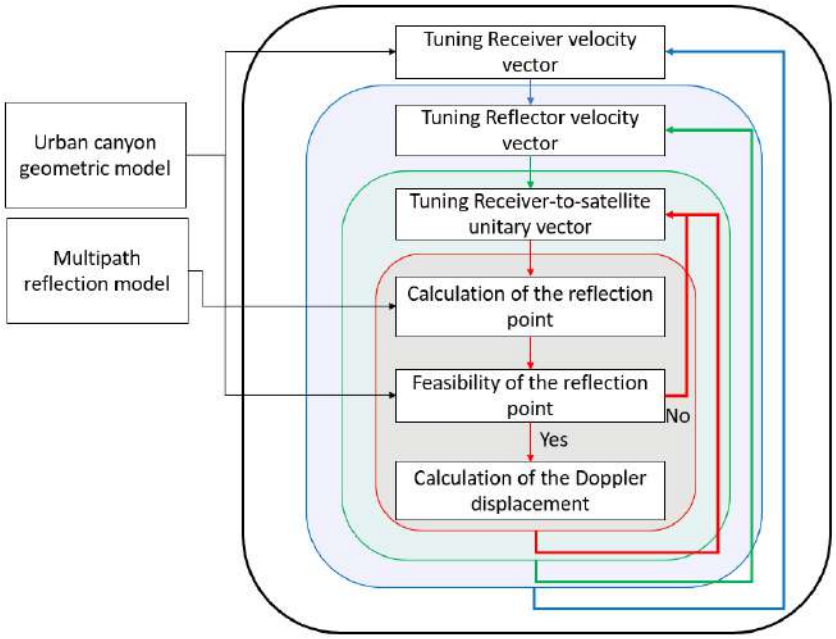

Figure 4-21 – Simulation of Doppler frequency displacement, algorithm's steps

4.3.1.2.2.2 Doppler frequency displacement characterization

Once the discrete set of realizations of the LOS and NLOS Doppler Displacement is obtained, it is possible to characterize the resulting Doppler Displacement values.

In this procedure, the characterization consists of the calculation of the so-called Doppler displacement simulated PDF. The Doppler displacement simulated PDF is based on the calculation of the Doppler frequency Displacement histogram, as a function of the receiver speed modulo, $\Delta D(\dot{R})$. As a consequence, the Doppler displacement simulated PDF is calculated in two different steps:

1) The LOS and NLOS Doppler frequency displacement set of values must be averaged with respect to all the parameter but the receiver speed modulo, obtaining $\Delta D^{LOS}(\dot{R})$ and $\Delta D^{NLOS}(\dot{R})$ values;
2) The $\Delta D^{LOS}(\dot{R})$ and $\Delta D^{NLOS}(\dot{R})$ are employed to calculate, respectively, the histogram of the LOS, $PDF_{\Delta D^{LOS}}(\dot{R})$, and the NLOS, $PDF_{\Delta D^{NLOS}}(\dot{R})$, Doppler frequency displacement, as a function of the receiver speed modulo.

4.3.1.2.2.3 Scenario 1: Dynamic receiver in the urban canyon

This scenario represents the Doppler frequency displacement obtained from a single diffuse multipath reflection caused by static reflectors in an urban canyon when a dynamic GNSS receiver is moving across the canyon. To give an impression of the common urban measurement environment simulated in Scenario 1, Figure 4-22 shows the Rue du Metz in the city centre of Toulouse.

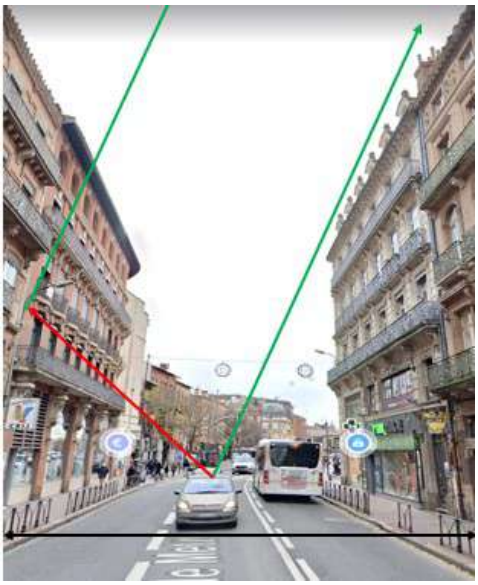

Figure 4-22 – Example of urban canyon in Toulouse city centre (Google Maps)

The static reflector geometric model, portrayed in Figure 4-23, is based on the parameters in Table 4-1. The multipath reflection model is illustrated in Table 4-2. d_r^o is fixed and is equal to the width of the street divided by 2 since, in this configuration, the receiver is exactly at the centre of the street, at the same distance between the two reflectors, $d_r^o = d_r^{o_2}$.

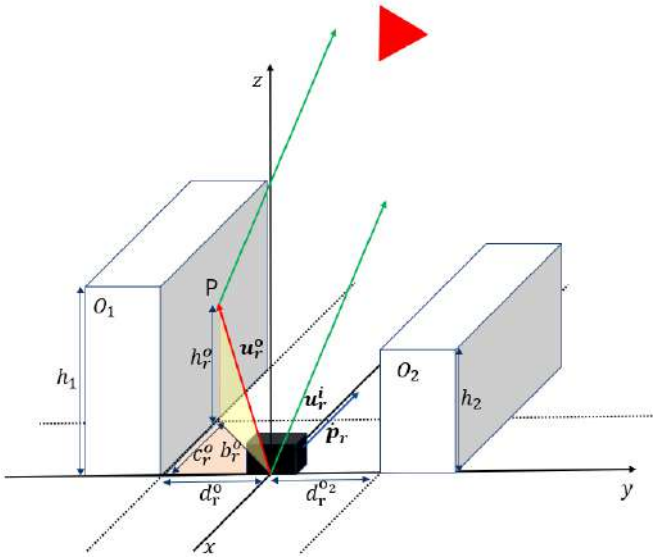

Figure 4-23 – Configuration of Urban canyon simulated in Scenario 1

The LOS and NLOS critical elevation angles, $\varphi_{r,LOS}^i$ and $\varphi_{r,NLOS}^i$ are defined as follows:

- LOS elevation angle, $\varphi_{r,LOS}^i$, Figure 4-24. It is calculated as the minimum elevation angle providing Line of Sight between the satellite and receiver without being blocked by the reflector O_2, characterized by the minimum height, $h_{2,min}$ and the fixed distance $d_r^{o_2}$ along y-axis.
- NLOS elevation angle, $\varphi_{r,NLOS}^i$, Figure 4-25. It is calculated as the minimum elevation angle which provides a specular reflection from the dynamic reflector, O_1, to the other side of the street, reaching the receiver without being blocked by the reflector on the opposite side of the street, O_2, characterized by the minimum height, $h_{2,min}$ and the fixed distance $d_r^{o_2}$ along y-axis.

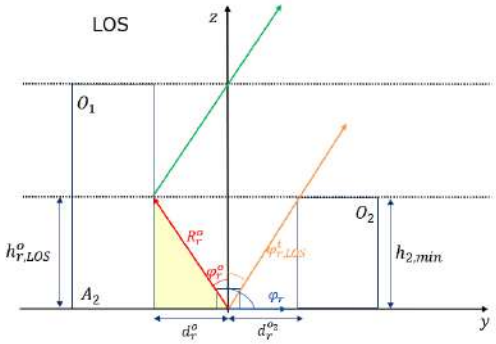

Figure 4-24 – Scenario 1, y-z plane, LOS reception state

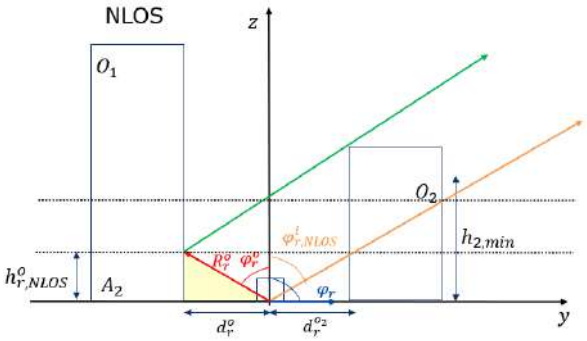

Figure 4-25 – Scenario 1, y-z plane, NLOS reception state

The values considered for the numerical evaluation of the Doppler displacement simulated PDF are given next.

First, the range of values of the receiver's dynamic is determined by the expected receiver velocity vector range of values, $\dot{\boldsymbol{p}}_r(\dot{R}, \theta_r, \varphi_r)$:

- The elevation angle, φ_r is fixed to 90°, since it is simulated a user receiver moving along the street with a ground vehicle, such as a car, a scooter or a bicycle.
- The direction of the user receiver on the x-y plane have been considered normally distributed with a mean equal to 90°, supposing that the vehicle is perfectly aligned to the street lane, and a standard deviation of 10 degrees, $\theta_r = N(\mu_{\theta_r} = 90°,\ \sigma_{\theta_r} = 10°)$.
- The speed of the vehicle, $\dot{R}$, has been chosen between the case of stopped car, 0 m/s and a maximum speed equal to 20 m/s, equal to 72 Km/h.

Second, the range of values of the reflector's dynamic is just set to a unique value, the 0 value, since the reflectors are considered static.

Third, the range of values of receiver-to-satellite unitary vector, $\boldsymbol{u}^i_r(\theta^i_r, \varphi^i_r)$ has been set as follows:

- The azimuth angle, θ^i_r, has been simulated as uniform distributed between 0 and 359 degrees. This represents the possibility to find the satellite in any position around the receiver.
- The elevation angle, φ^i_r, has been simulated as uniformly distributed between the zenith and a minimum elevation angle, $\varphi^i_{r,min}$, which depends on the urban canyon geometric design and the multipath reflection model. The minimum elevation angle is difficult to be set. In this work, two different minimum elevation angles have been selected, the $\varphi^i_{r,NLOS}$, and $\varphi^i_{r,LOS}$, which can be used respectively to simulate the Doppler frequency displacement characterization due to LOS MP and NLOS MP. These values have been calculated considering the minimum building heigh in Table 4-1, and the scenario geometry represented in Figure 4-24and Figure 4-25.

Fourth and last, the range of values of the object-to-receiver unitary vector, $\boldsymbol{u}^o_r(\theta^o_r, \varphi^o_r)$ which has been already set in section 4.3.1.2.2.1.

The parameters of LOS/NLOS Doppler displacement characterization applied to the urban Scenario 1 are summarized in Table 4-3. The $\Delta D^{LOS}(\dot{R})$ and $\Delta D^{NLOS}(\dot{R})$ characterizations are illustrated respectively in Figure 4-26 and Figure 4-27. Finally, a comparison between the ΔD^{LOS} and ΔD^{NLOS}, averaged also with respect to the receiver speed, is proposed to the reader in Figure 4-28. From these figures, it can be seen a centred PDF Doppler displacement, which is larger spread for higher receiver speeds and has a symmetric behavior for negative and positive values; moreover, it can be observed that NLOS reception state conditions also imply a larger Doppler displacement spread. Nevertheless, the Doppler displacement is mainly concentrated around the 0 Hz value.

Scenario 1			LOS classification	NLOS classification
Receiver velocity vector $\dot{\boldsymbol{p}}_r$	angle in the vertical plane	φ_r [deg]	90	90
	angle in the horizontal plane	θ_r[deg]	N(90,10)	N(90,10)
	modulo	$\dot{R}$ [m/s]	[1,5,10,15,20,]	[1,5,10,15,20,25]
Satellite to receiver vector $\boldsymbol{u}_r^i$	angle in the vertical plane	φ_r^i [deg]	$0{:}\varphi_{r,LOS}^i(\theta_r^i)$	$\varphi_{r,LOS}^i(\theta_r^i)+1{:}\varphi_{r,NLOS}^i(\theta_r^i)$
	angle in the horizontal plane	θ_r^i [deg]	0:360	0:360
receiver-to-object unitary vector $\boldsymbol{u}_r^o$	angle in the vertical plane	φ_r^o[deg]	1-89	1-89
	angle in the horizontal plane	θ_r^o[deg]	$\begin{cases} 1{:}89, \text{if } 270 < \theta_r^i < 360 \\ 91{:}179, \text{if } 180 < \theta_r^i < 270 \\ 181{:}269, \text{if } 90 < \theta_r^i < 180 \\ 271{:}359, \text{if } 0 < \theta_r^i < 90 \end{cases}$	$\begin{cases} 1{:}89, \text{if } 270 < \theta_r^i < 360 \\ 91{:}179, \text{if } 180 < \theta_r^i < 270 \\ 181{:}269, \text{if } 90 < \theta_r^i < 180 \\ 271{:}359, \text{if } 0 < \theta_r^i < 90 \end{cases}$

Table 4-3 – LOS/NLOS Doppler frequency Displacement Simulation parameters, Scenario 1

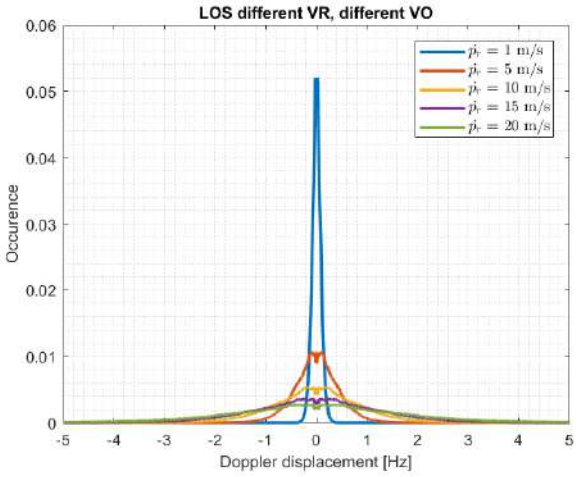

Figure 4-26 – LOS Doppler displacement simulated PDF, $PDF_{\Delta D^{LOS}}(\dot{R})$, for Scenario 1

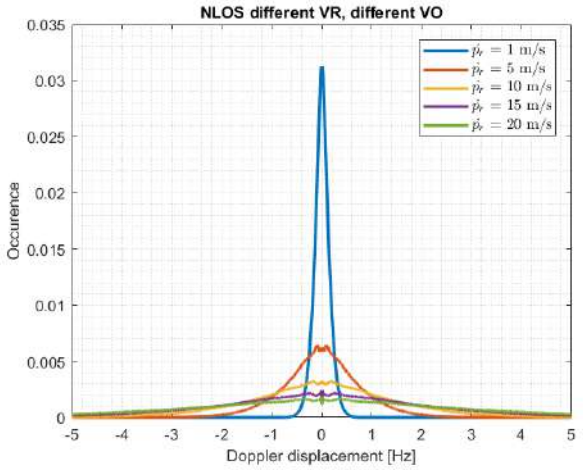

Figure 4-27 – NLOS Doppler displacement simulated PDF, $PDF_{\Delta D^{NLOS}}(\dot{R})$, for Scenario 1

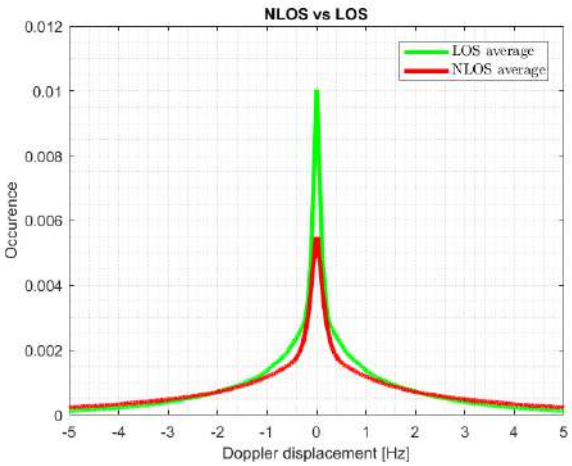

Figure 4-28 – LOS Doppler displacement simulated PDF $PDF_{\Delta D^{LOS}}$ vs NLOS Doppler displacement simulated PDF $PDF_{\Delta D^{NLOS}}$, for Scenario 1

4.3.1.2.2.4 Scenario 2: Dynamic reflectors and dynamic receiver in a urban canyon

This scenario simulates the Doppler frequency displacement pdf obtained from a single specular multipath reflection caused by dynamic reflectors (vehicles) in an urban canyon when a dynamic receiver is going across the canyon. A real example of the following scenario is illustrated in Figure 4-29.

Figure 4-29 – Example of dynamic reflectors in Toulouse city centre (Google Maps)

The dynamic reflector geometric model is based on the general parameters (common to Scenario 1) of Table 4-1 and specific parameters summarized in Table 4-4. The multipath reflection model is illustrated in Table 4-2. The scenario is illustrated in Figure 4-30. It is similar to the one defined in Section 4.3.1.2.2.3, but in this case the reflector O_1 is a dynamic reflector moving in the same or in the opposite direction of the dynamic receiver and O_2 is a building. In opposition to Scenario 1, in this case d_r^o is a variable which can be tuned to simulate the distance between the reflector and the receiver while h_r^o is fixed and is equal to the height of a vehicle.

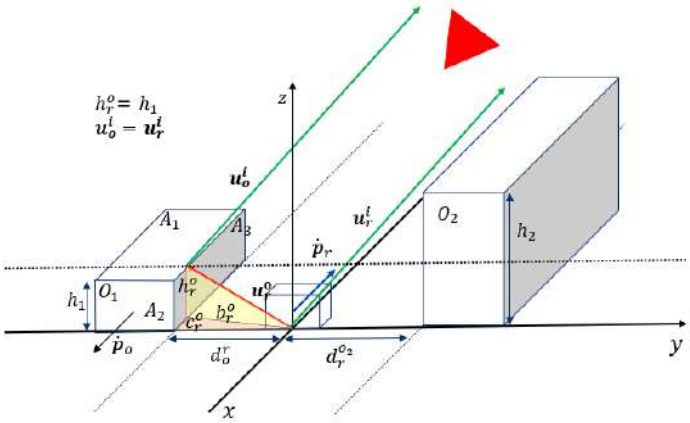

Figure 4-30 – Configuration of Urban environment simulated in Scenario 2

Once defined the urban environment configuration, in analogy with Scenario 1, it is possible to define the LOS and NLOS critical elevation angles, $\varphi_{r,LOS}^i$ and $\varphi_{r,NLOS}^i$. The critical angles have been exploited to define the two different reception state configurations, as already discussed in 4.3.1.2.2.3, LOS, (Figure 4-31), and NLOS configurations, (Figure 4-32).

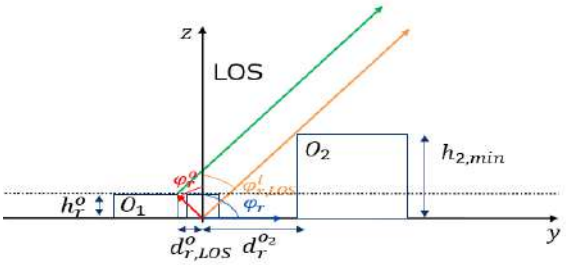

Figure 4-31 – Scenario 2, y-z plane, LOS reception state

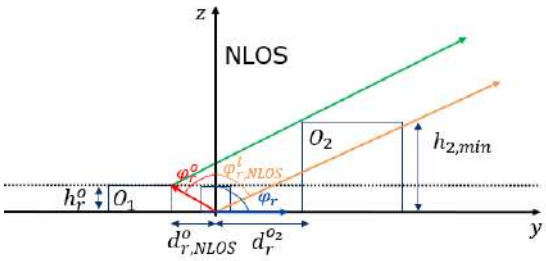

Figure 4-32– Scenario 2, y-z plane, NLOS reception state

The values considered for the numerical evaluation of the Doppler displacement simulated pdf are given next.

First, the range of values of the receiver's dynamic is determined by the expected receiver velocity vector range of values, $\dot{\boldsymbol{p}}_r(\dot{R}, \theta_r, \varphi_r)$:

- The elevation angle, φ_r is fixed to 90°, since it is simulated a user receiver moving along the street with a ground vehicle, such as a car, a scooter or a bicycle.
- The direction of the user receiver on the x-y plane have been considered normally distributed with a mean equal to 90°, supposing that the vehicle is perfectly aligned to the street lane, and a standard deviation of 10 degrees, $\theta_r = N(\mu_{\theta_r} = 90°,\ \sigma_{\theta_r} = 10°)$.
- The speed of the vehicle, $\dot{R}$, has been chosen between the case of stopped car, 0 m/s and a maximum speed equal to 20 m/s, equal to 72 Km/h.

Second, the range of values of the reflector's dynamic is determined by the expected receiver velocity vector range of values, $\dot{\boldsymbol{p}}_o(\dot{R}_o, \theta_o, \varphi_o)$: the analysis is similar to the one provided for the receiver dynamics; the only difference consists of the direction of the obstacle's motion, which can be either the same or the opposite of the receiver's direction. Therefore, the direction of the user reflector on the x-y plane have been considered in the different configurations:

- normally distributed with a mean equal to 90°, and a standard deviation of 10 degrees, $\theta_o \sim N(\mu_{\theta_o} = 90°,\ \sigma_{\theta_o} = 10°)$;
- normally distributed with a mean equal to -90°, and a standard deviation of 10 degrees, $\theta_o \sim N(\mu_{\theta_o} = 270°,\ \sigma_{\theta_o} = 10°)$;

Third, the range of values of receiver-to-satellite unitary vector, $\boldsymbol{u}_r^i(\theta_r^i, \varphi_r^i)$: A detailed analysis is already provided in 4.3.1.2.2.3.

Fourth and last, the range of values of the object-to-receiver unitary vector, $\boldsymbol{u}_r^o(\theta_r^o, \varphi_r^o)$: a detailed analysis is already provided in 4.3.1.2.2.3.

The parameters of LOS/NLOS Doppler displacement characterization applied to the urban Scenario 2 are summarized in Table 4-5. The $\Delta D^{LOS}(\dot{R})$ and $\Delta D^{NLOS}(\dot{R})$ characterizations are illustrated respectively in Figure 4-33 and Figure 4-34. Finally, a comparison between the ΔD^{LOS} and ΔD^{NLOS}, averaged also with respect to the receiver speed, is proposed to the reader in Figure 4-35. From these figures, the same trends as for the scenario 1 static case can be seen. However, dynamic reflectors appear to provide a large Doppler displacement spread.

Maximum distance between the moving vehicle and the receiver along y-axis, $d_{r,MAX}^o = w/2$ [m]	4.30
Minimum distance between the moving vehicle and the receiver along y-axis, $d_{r,min}^o = w/9$ [m]	0.96
Maximum distance between the building and the receiver along y-axis, $d_r^{o_2} = w/2$ [m]	4.30
Height of the moving vehicle, h_r^o [m]	2

Table 4-4 – Parameters of Urban environment model simulated in Scenario 2

Scenario 2			**LOS classification**	**NLOS classification**
Receiver velocity vector $\dot{\boldsymbol{p}}_r$	angle in the vertical plane	φ_r [deg]	90	90
	angle in the horizontal plane	θ_r[deg]	N(90,10)	N(90,10)
	modulo	$\dot{R}$ [m/s]	[1,5,10,15,20]	[1,5,10,15,20]
Satellite to receiver vector $\boldsymbol{u}_r^i$	angle in the vertical plane	φ_r^i [deg]	0:$\varphi_{r,LOS}^i(\theta_r^i)$	$\varphi_{r,LOS}^i(\theta_r^i)+1$:$\varphi_{r,NLOS}^i(\theta_r^i)$
	angle in the horizontal plane	θ_r^i [deg]	0:360	0:360
Reflector velocity vector $\dot{\boldsymbol{p}}_o$	angle in the vertical plane	φ_o [deg]	90	90
	angle in the horizontal plane	θ_o[deg]	N(90,10), N(270,10)	N(90,10), N(270,10)
	modulo	$\dot{R}_o$ [m/s]	[1,5,10,15,20,25]	[1,5,10,15,20,25]
receiver-to-object unitary vector $\boldsymbol{u}_r^o$	angle in the vertical plane	φ_r^o[deg]	1-89	1-89
	angle in the horizontal plane	θ_r^o[deg]	$\begin{cases} 1:89, \text{if } 270 < \theta_r^i < 360 \\ 91:179, \text{if } 180 < \theta_r^i < 270 \\ 181:269, \text{if } 90 < \theta_r^i < 180 \\ 271:359, \text{if } 0 < \theta_r^i < 90 \end{cases}$	$\begin{cases} 1:89, \text{if } 270 < \theta_r^i < 360 \\ 91:179, \text{if } 180 < \theta_r^i < 270 \\ 181:269, \text{if } 90 < \theta_r^i < 180 \\ 271:359, \text{if } 0 < \theta_r^i < 90 \end{cases}$

Table 4-5 – LOS/NLOS Doppler frequency Displacement Simulation parameters, Scenario 2

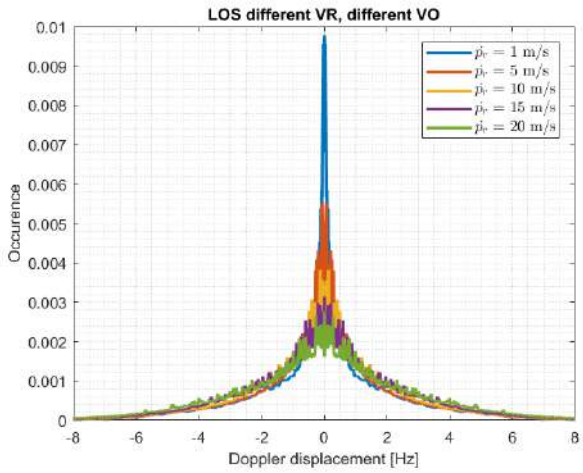

Figure 4-33 – LOS Doppler displacement simulated PDF, $PDF_{\Delta D^{LOS}}(\dot{R})$, for Scenario 2

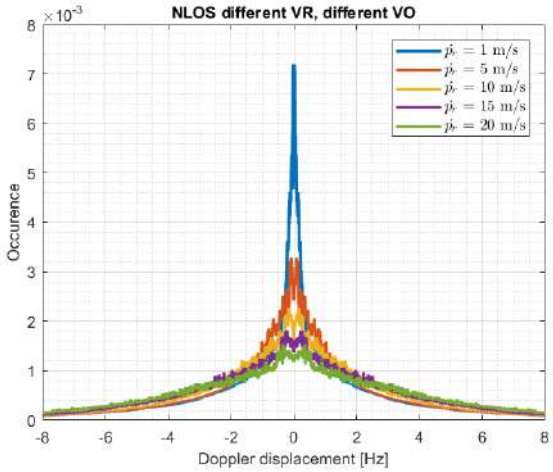

Figure 4-34 – NLOS Doppler displacement simulated PDF, $PDF_{\Delta D^{NLOS}}(\dot{R})$, for Scenario 2

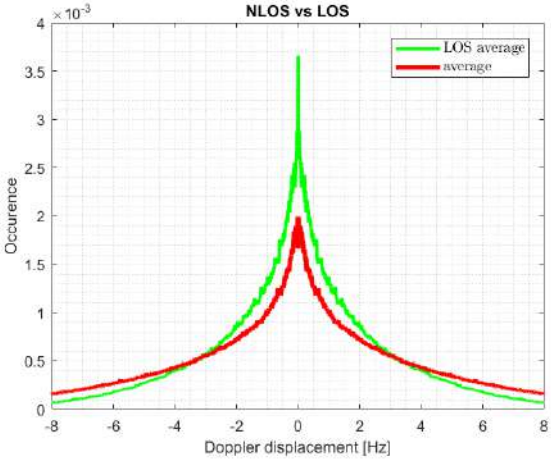

Figure 4-35 – LOS Doppler displacement simulated PDF $PDF_{\Delta D^{LOS}}$ vs NLOS Doppler displacement simulated PDF $PDF_{\Delta D^{NLOS}}$, for Scenario 2

4.3.2MP FLL tracking error model

The Doppler Frequency Displacement affects the FLL tracking stage, introducing a Doppler frequency estimation error (or FLL tracking error) due to the MP. The Doppler frequency estimation error should depend on the characteristics of the multipath, especially on the Doppler frequency displacement. In the previous section, the mathematical model Doppler Frequency Displacement was provided and a simulated characterization of Doppler Frequency Displacement PDF for two specific urban canyon configurations was conducted.

Therefore, in this section the FLL tracking error mathematical model as a function of the Doppler displacement, ΔD, and as function of the thermal noise is provided in order to allow its numerical characterization as well as the calculation of its PDF.

In this section, the mathematical model of Cross-Product FLL discriminator output is provided first in order to analyse the impact of the MP and of the thermal noise in section 4.3.2.1; note that only the Cross-Product discriminator is inspected since this discriminator only applies linear operations and thus facilitates the derivation of all the mathematical formulas as stated in the introduction of section 4.3. Second, the completely model of the FLL tracking error which uses the mathematical model of the FLL discriminator output is given in section 4.3.2.2.

4.3.2.1 General CP discrimination function

The cross-product frequency discriminator calculates the error between the received signal Doppler frequency and the estimated local replica carrier frequency, under nominal reception signal conditions. The cross-product discriminator formula [12] [9] is:

$$D_{CP,k}(\varepsilon_{f,LOS}) = \frac{CROSS}{2\pi T_I} \tag{4-28}$$

where:

$$CROSS = I_{k-1}^P Q_k^P - I_k^P Q_{k-1}^P \tag{4-29}$$

Developing further the previous expression using the $I_{k-1}^P, Q_{k-1}^P, I_k^P$ and Q_k^P mathematical models of 4.1.2.2, the CP discriminator output can be expressed as:

$$D_{CP,k} = D_{CP,k}^{noiseless} + n_{discri,k} \tag{4-30}$$

where:

- $D_{CP,k}^{no\ noise}$ is the noiseless CP discriminator output expression at epoch k;
- n_{discri} is the discriminator output noise due to thermal noise at epoch k.

Further developing the $D_{CP,k}^{noiseless}$ expression leads to:

$$D_{CP,k}^{noiseless} = \frac{S_{I,k-1}^P S_{Q,k}^P - S_{I,k}^P S_{Q,k-1}^P}{2\pi T_I} \tag{4-31}$$

Finally, n_{discri} can be expressed as:

$$n_{discri,k} = \frac{S_{I,k-1}^P \eta_{Q,k}^P + S_{Q,k}^P \eta_{I,k-1}^P + \eta_{I,k-1}^P \eta_{Q,k}^P - S_{I,k}^P \eta_{Q,k-1}^P - S_{Q,k-1}^P \eta_{I,k}^P - \eta_{I,k}^P \eta_{Q,k-1}^P}{2\pi T_I} \tag{4-32}$$

Note that equation 4-28 is not normalized but that the complete discriminator should be normalized so that $D_{CP,k}^{noiseless} \approx \varepsilon_{f,LOS}$. Next section presents the CP discriminator output mathematical expression with and without the presence of multipath.

4.3.2.1.1 CP discriminator output without multipath

In this section, the CP discriminator output expression is customized for the case when no multipath is present. $S_{I,k-1}^P, S_{Q,k-1}^P, S_{I,k}^P$ and $S_{Q,k-1}^P$ can be mathematically modelled just with the LOS term, denoted $S_{I,0,k-1}^P$, $S_{Q,0,k-1}^P$, $S_{I,0,k}^P$ and $S_{Q,0,k}^P$. Moreover, introducing the code delay estimation error effect on the amplitude factor with $R(\varepsilon_{\tau_{0,k-1}}) = R(\varepsilon_{\tau_{0,k}})$ and $A_0' = A_0 R(\varepsilon_{\tau_{0,k}})$, $S_{I,0,k-1}^P$, $S_{Q,0,k-1}^P$, $S_{I,0,k}^P$ and $S_{Q,0,k}^P$ can be modelled as given below:

$$\begin{aligned}
S_{I,0,k-1}^P &\approx \frac{A_0'}{2}\cos(\pi\varepsilon_{f,LOS}T_I + \varepsilon_{\varphi,LOS})\,\mathrm{sinc}(\pi\varepsilon_{f,LOS}T_I) \\
S_{Q,0,k-1}^P &\approx \frac{A_0'}{2}\sin(\pi\varepsilon_{f,LOS}T_I + \varepsilon_{\varphi,LOS})\,\mathrm{sinc}(\pi\varepsilon_{f,LOS}T_I) \\
S_{I,0,k}^P &\approx \frac{A_0'}{2}\cos(3\pi\varepsilon_{f,LOS}T_I + \varepsilon_{\varphi,LOS})\,\mathrm{sinc}(\pi\varepsilon_{f,LOS}T_I) \\
S_{Q,0,k}^P &\approx \frac{A_0'}{2}\sin(3\pi\varepsilon_{f,LOS}T_I + \varepsilon_{\varphi,LOS})\,\mathrm{sinc}(\pi\varepsilon_{f,LOS}T_I)
\end{aligned} \tag{4-33}$$

Therefore, the $D_{CP,k}^{noiseless}$ when no multipath is present can be expressed as:

$$D_{CP,k}^{noiseless} = \quad S_{I,0,k-1}^{P} S_{Q,0,k}^{P} - S_{I,0,k}^{P} S_{Q,0,k-1}^{P} =$$
$$= \frac{A_0'^2}{8\pi T_I} \begin{bmatrix} \cos\left(\pi\varepsilon_{f,LOS} T_I + \varepsilon_{\varphi,LOS}\right) \sin\left(3\pi\varepsilon_{f,LOS} T_I + \varepsilon_{\varphi,LOS}\right) \\ -\cos\left(3\pi\varepsilon_{f,LOS} T_I + \varepsilon_{\varphi,LOS}\right) \sin\left(\pi\varepsilon_{f,LOS} T_I + \varepsilon_{\varphi,LOS}\right) \end{bmatrix} \mathrm{sinc}^2\left(\pi\varepsilon_{f,LOS} T_I\right) \quad 4\text{-}34$$

After trigonometric manipulation, 4-34 can be written as:

$$D_{CP,k}^{noiseless} = \frac{A_0'^2}{8\pi T_I} \mathrm{sinc}^2\left(\pi\varepsilon_{f,LOS} T_I\right) \sin\left(2\pi\varepsilon_{f,LOS} T_I\right) \quad 4\text{-}35$$

Therefore, in order to obtain a final noiseless CP discriminator output equal to the LOS Doppler frequency estimation error, $D_{CP,k}^{noiseless} \approx \varepsilon_{f,LOS}$, $D_{CP,k}$ must be normalized. The normalized CP discriminator output formula is given below:

$$\widetilde{D}_{CP,k}\left(\varepsilon_{f,LOS}\right) = \frac{CROSS}{2\pi T_I \left(E\left[S_{I,k-1}^{P}\right]\right)^2 + \left(E\left[S_{Q,k-1}^{P}\right]\right)^2} \approx \varepsilon_{f,LOS} + \tilde{n}_{discri,k} \quad 4\text{-}36$$

where:

- $E[\cdot]$ is the expectation operator (usually obtained through a long accumulation int time, e.g. 1s);
- $\tilde{n}_{discri}$ is the normalised discriminator output noise due to thermal noise at epoch k.

Additionally, note that in the error analysis of the Cross Product FLL discriminator, it is usually assumed a very small frequency error $\varepsilon_{f,LOS}$, which in commercial GPS receiver means that $\varepsilon_{f,LOS} < 200\,Hz$, leading to $\mathrm{sinc}\left(\pi\varepsilon_{f,LOS} T_I\right) \sim 1$.

Finally, $2\pi T_I n_{discri}$ can be expressed as:

$$\begin{aligned} 2\pi T_I n_{discri,k} = {} & \frac{A_0'^2}{2} \cos\left(\pi\varepsilon_{f,LOS} T_I + \varepsilon_{\varphi,LOS}\right) \mathrm{sinc}\left(\pi\varepsilon_{f,LOS} T_I\right) n_{Q,k}^{P} + \\ & + \frac{A_0'^2}{2} \sin\left(3\pi\varepsilon_{f,LOS} T_I + \varepsilon_{\varphi,LOS}\right) \mathrm{sinc}\left(\pi\varepsilon_{f,LOS} T_I\right) n_{I,k-1}^{P} + n_{Q,k}^{P} n_{I,k-1}^{P} - \\ & - \frac{A_0'^2}{2} \cos\left(3\pi\varepsilon_{f,LOS} T_I + \varepsilon_{\varphi,LOS}\right) \mathrm{sinc}\left(\pi\varepsilon_{f,LOS} T_I\right) n_{Q,k-1}^{P} - \\ & \frac{A_0'^2}{2} \sin\left(\pi\varepsilon_{f,LOS} T_I + \varepsilon_{\varphi,LOS}\right) \mathrm{sinc}\left(\pi\varepsilon_{f,LOS} T_I\right) n_{I,k}^{P} - n_{Q,k-1}^{P} n_{I,k}^{P} \end{aligned} \quad 4\text{-}37$$

4.3.2.1.2 CP discrimination function with multipath

In this section, the CP discriminator output expression is customized for the case when one echo is present. Assuming that one echo is present, the $S_{I,k-1}^{P}, S_{Q,k-1}^{P}, S_{I,k}^{P}$ and $S_{Q,k-1}^{P}$ can be mathematically modelled just with the LOS and MP terms. Moreover, introducing the code delay estimation error effect on the amplitude factor with $A_0' = A_0 R\left(\varepsilon_{\tau_{0,k}}\right) = A_0 R\left(\varepsilon_{\tau_{0,k-1}}\right)$ and with $\tilde{\alpha}_1' = \tilde{\alpha}_1 R\left(\varepsilon_{\tau_{1,k}}\right) = \tilde{\alpha}_1 R\left(\varepsilon_{\tau_{1,k-1}}\right)$, the $D_{CP,k}^{noiseless}$ and the n_{discri} can be customized:

$D_{CP,k}^{noiseless}$ when one echo is present can be expressed as:

$$\begin{aligned} D_{CP,k}^{noiseless} = {} & X\left(\sin\left(\varepsilon_{\varphi_{0,k}} - \varepsilon_{\varphi_{0,k-1}}\right)\right) + Y\left(\sin\left(\varepsilon_{\varphi_{0,k}} - \varepsilon_{\varphi_{1,k-1}}\right) + \sin\left(\varepsilon_{\varphi_{1,k}} - \varepsilon_{\varphi_{0,k-1}}\right)\right) \\ & + Z\left(\sin\left(\varepsilon_{\varphi_{1,k}} - \varepsilon_{\varphi_{1,k-1}}\right)\right) \end{aligned} \quad 4\text{-}38$$

$2\pi T_I n_{discri}$ when one echo is present can be expressed as:

$$
\begin{aligned}
2\pi T_I n_{discri} = W\Big(&\big(\cos(\varepsilon_{\varphi_{0,k-1}})\cdot\eta_{Q,k}^{P}\big)+\big(\sin(\varepsilon_{\varphi_{0,k}})\cdot\eta_{I,k-1}^{P}\big)-\big(\cos(\varepsilon_{\varphi_{0,k}})\cdot\eta_{Q,k-1}^{P}\big)\\
&-\big(\sin(\varepsilon_{\varphi_{0,k-1}})\cdot\eta_{I,k}^{P}\big)\Big)\\
&+R\Big(\big(\cos(\varepsilon_{\varphi_{1,k-1}})\cdot\eta_{Q,k}^{P}\big)+\big(\sin(\varepsilon_{\varphi_{1,k}})\cdot\eta_{I,k-1}^{P}\big)-\big(\sin(\varepsilon_{\varphi_{1,k}})\cdot\eta_{Q,k-1}^{P}\big)\\
&+\big(\sin(\varepsilon_{\varphi_{1,k-1}})\cdot\eta_{I,k}^{P}\big)\Big)+\eta_{I,k-1}^{P}\cdot\eta_{Q,k}^{P}-\eta_{I,k}^{P}\cdot\eta_{Q,k-1}^{P}
\end{aligned}
\qquad 4\text{-}39
$$

where:

- $X=\frac{A_0'^2}{4}\mathrm{sinc}^2(\pi\varepsilon_{f,LOS}T_I)$;
- $Y=\tilde{\alpha}_1\frac{A_0'^2}{4}\mathrm{sinc}(\pi\varepsilon_{f,LOS}T_I)\,\mathrm{sinc}(\pi\varepsilon_{f,MP}T_I)$;
- $W=\frac{A_0'}{2}\mathrm{sinc}(\pi\varepsilon_{f,LOS}T_I)$;
- $R=\tilde{\alpha}_1'\frac{A_0}{2}\mathrm{sinc}(\pi\varepsilon_{f,MP}T_I)$;
- $\varepsilon_{\varphi_{0,k}}-\varepsilon_{\varphi_{0,k-1}}=3\pi\varepsilon_{f,LOS}T_I+\varepsilon_{\varphi,LOS}-(\pi\varepsilon_{f,LOS}T_I+\varepsilon_{\varphi,LOS})=2\pi(\varepsilon_{f,LOS})T_I$;
- $\varepsilon_{\varphi_{1,k}}-\varepsilon_{\varphi_{0,k-1}}=3\pi\varepsilon_{f,MP}T_I+\varepsilon_{\varphi,MP}-(\pi\varepsilon_{f,MP}T_I+\varepsilon_{\varphi,MP})=2\pi(f_{LOS}-f_L)T_I+3\pi\Delta DT_I+\Delta\varphi$;
- $\varepsilon_{\varphi_{0,k}}-\varepsilon_{\varphi_{1,k-1}}=3\pi\varepsilon_{f,LOS}T_I+\varepsilon_{\varphi,LOS}-(\pi\varepsilon_{f,MP}T_I+\varepsilon_{\varphi,MP})=2\pi(\varepsilon_{f,LOS})T_I-\pi\Delta DT_I-\Delta\varphi$;
- $\varepsilon_{\varphi_{1,k}}-\varepsilon_{\varphi_{1,k-1}}=3\pi\varepsilon_{f,MP}T_I+\varepsilon_{\varphi,MP}-(\pi\varepsilon_{f,MP}T_I+\varepsilon_{\varphi,MP})=2\pi(\varepsilon_{f,LOS}+\Delta D)T_I=2\pi(\varepsilon_{f,LOS})T_I+2\pi\Delta DT_I$.

4.3.2.2FLL tracking error mathematical model

In this section, the mathematical model of the FLL tracking error is analysed in the presence of multipath (and of thermal noise). The expression of this error is derived from FLL tracking error when no multipath is present. This last mathematical model in the Z-transform is obtained from the open-loop transfer function of the FLL [82] as shown below:

$$\varepsilon_f(z)=f_{LOS}(z)-f_{NCO}(z) \qquad 4\text{-}40$$

$$f_{NCO}(z)=K_0\frac{g_{FLL}(z)}{1-z^{-1}}D_{FLL}(z) \qquad 4\text{-}41$$

where:

- $g_{FLL}(z)$ is the Z-transform FLL low-pass filter (see 3.1.2.2.2.2);
- $f_{NCO}(z)$ is the estimated Doppler frequency, in LOS received signal conditions $f_{NCO}(z)=\hat{f}_{LOS}(z)$.

Modelling $D_{FLL}(z)$ as $D_{FLL}(z)=\varepsilon_f(z)+\tilde{n}_{dsicri}(z)$ (see equation 4-36), then [82]:

$$\varepsilon_f(z)=\varepsilon_r(z)+\varepsilon_n(z)=G(z)f_{LOS}(z)-H(z)\tilde{n}_{dsicri}(z) \qquad 4\text{-}42$$

where:

- $G(z)$ is the FLL open-loop transfer function;
- $H(z)$ is the FLL closed-loop transfer function.

However, assuming that multipath is present, the discriminator output can be approximated as the true Doppler frequency estimation error, plus a bias (time variant if necessary) multiplied by a coefficient, Ψ (time variant if necessary), since the discriminator output function is distorted. This approximation is valid for a $\varepsilon_f(z)$ around $\zeta(z)$. Therefore, the discriminator output can be modelled as shown below in the presence of multipath:

$$D_{FLL}(t)\cong\Psi(t)\big(\varepsilon_f(t)-\zeta(t)\big)+\tilde{n}_{dsicri}(t) \qquad 4\text{-}43$$

$$D_{FLL}(z)\cong\Psi(z)*\big(\varepsilon_f(z)-\zeta(z)\big)+\tilde{n}_{dsicri}(z) \qquad 4\text{-}44$$

where:

- $\zeta(z)$ is the bias introduced by the echo on the discriminator output with respect to the true $\varepsilon_f(z)$ term; ζ value depends on the code delay displacement, $\Delta\tau$, the phase displacement, $\Delta\varphi$, the Doppler frequency displacement, ΔD, and the MLR;

- $\Psi(z)$ represents the slope of $\varepsilon_f(z)$ around $\zeta(z)$; as well as $\zeta(z)$, it depends on $\Delta\tau$, $\Delta\varphi$, ΔD and the MLR parameters;
- $*$ is the convolution operation (usually conducted in the frequency domain with $z = e^{j2\pi f}$).

$\zeta(z)$ and $\Psi(z)$ are asummed to vary in time if the $\Delta\tau$, $\Delta\varphi$, ΔD and the MLR parameters also vary in time. A more detailed discussion about this modelling is given in section 4.3.3.1. Nevertheless, for simplification purposes it is going to be assumed that $\Psi(z)$ is constant, $\Psi(z) = \Psi$ (justification in section 4.3.3.1).

Consequently, the Z-transform FLL tracking error is now modelled as:

$$\varepsilon_f(z) = G'(z)f_{LOS}(z) + H'(z)(\Psi\zeta(z) - \tilde{n}_{dsicri}(z)) \quad 4\text{-}45$$

where:

- $G'(z)$ is the modified FLL open-loop transfer function due to the coefficient Ψ;
- $H'(z)$ is the modified FLL closed-loop transfer function due to the coefficient Ψ.

$\varepsilon_f(z)$ of equation 4-45 can now be statistically analysed/characterized. First of all, the mean of the error is obtained by applying the expectation operator (knowing that the discriminator noise is centred, see section 4.3.5.1 and that the bias behavior and value is completely deterministic if $\Delta\tau$, $\Delta\varphi$, ΔD and MLR values are known):

$$m_{\varepsilon_f} = E[\varepsilon_f(z)] = G'(z)f_{LOS}(z) + H'(z)\Psi\zeta(z) \quad 4\text{-}46$$

Moreover, assuming that the FLL is well designed and the FLL order is high enough to perfectly track the signal dynamic without any bias, the previous expression can be approximated as ($G'(z)$ is a high-pass filter which removes all the influence of $f_{LOS}(z)$ which depends on the signal dynamics):

$$m_{\varepsilon_f}(z) \approx \Psi H'(z)\zeta(z) \quad 4\text{-}47$$

Second, the variance is calculated as [83]:

$$var_{\varepsilon_f} = E\left[\left(\varepsilon_f(z) - m_{\varepsilon_f}\right)^2\right] = var[H'(z)\tilde{n}_{dsicri}(z)] = 2B_L{}'T_{update}var[\tilde{n}_{dsicri}(z)] \quad 4\text{-}48$$

where:

- $B_L{}'$ is the modified one-sided equivalent noise bandwidth;
- T_{update} is the FLL update time.

Therefore, from the previous equations, it can be seen that the multipath will induce a deterministic bias to the FLL tracking discriminator error and that the thermal noise will induce a random variation of the estimation (dependent on the C/N_0 and on the multipath characteristics, $\Delta\tau$, $\Delta\varphi$, ΔD and MLR, as will be shown in section 4.3.4).

4.3.3MP impact on FLL tracking error bias

In this section, the FLL tracking error bias introduced by the multipath, ζ, is inspected and the FLL tracking error bias PDF is calculated as a function of Doppler frequency displacement, ΔD, using the ΔD PDF calculated in section 4.3.1. Although the PDF results obtained in this section will not be used directly for the final characterization of the FLL tracking error PDF in section 4.3.5, it is still interesting to determine the FLL tracking error bias PDF. Moreover, the set of value $\varepsilon_{f,LOS}^{bias}$, defined in equation 4-52, will indeed be used for the final calculation.

This section is structured as follows. Section 4.3.3.1 presents some considerations about the FLL tracking error bias used in this analysis. Section 4.3.3.2 calculates the FLL tracking error bias numerical values as a function of the Doppler frequency displacement and the carrier phase displacement and presents how these values can be used to determine the Doppler frequency multipath error envelope. Section 4.3.3.3.1 presents the FLL tracking error bias PDF for LOS MP and NLOS MP in the two different scenarios, static and dynamic.

4.3.3.1 FLL tracking error bias definition considerations

The FLL tracking error bias defined in this work is the bias obtained assuming the steady-state regime. On the steady-state regime, the value of the mean can be calculated using the final value theorem of the Z-transform. Therefore, assuming that the sudden appearance of multipath can be modelled as the introduction of the bias multiplied by the Heaviside function, the FLL tracking error bias mean on the steady state regime, $m_{\varepsilon_f}^{ss}$, is equal to:

$$\zeta(z) = \frac{z}{z-1}\zeta_{ss} \quad \text{4-49}$$

$$m_{\varepsilon_f}^{ss} = \lim_{z\to 1}(z-1)m_{\varepsilon_f}(z) \approx \lim_{z\to 1}(z-1)\Psi H'(z)\zeta(z) = \lim_{z\to 1} z\Psi H'(z)\zeta_{ss} = \zeta_{ss} \quad \text{4-50}$$

Therefore, the FLL tracking error bias defined in this work is directly denoted as $m_{\varepsilon_f} \approx \zeta_{ss}$ and is equal to the discriminator output bias. Moreover, this assumption implies that for the steady-state regime, the FLL tracking error can be modelled as (from equations 4-45, 4-47 and 4-50):

$$\varepsilon_{f,LOS}^{ss}(z) \approx \zeta_{ss} + H'(z)\tilde{n}_{discri}(z) \quad \text{4-51}$$

In order to understand the impact of the steady-state regime and in order to understand how the ζ_{ss} value can be calculated, the inherent behavior of closed-loop, FLL in this case, must be reminded. A FLL discriminator output, irrespective of the type/structure, section 3.1.2.2.2.2, when ignoring the noise and the multipath components, is approximated as $D_{FLL}(\varepsilon_{f,LOS}) \approx \varepsilon_{f,LOS}$ in the linear region of the discriminator, where $\varepsilon_{f,LOS}$ is equal to the Doppler frequency error between the received signal f_0 ($f_0 = f_{IF} + f_{D,0}$) and the local replica $\hat{f}_{NCO}$.

The inherent behavior of any tracking loop, including thus the FLL, is to equate its discriminator output to zero; therefore, the FLL synchronizes the incoming carrier frequency with the carrier frequency of the local replica for continuous tracking in nominal conditions. In other words, the FLL reduces the error between the received signal and the generated local replica carrier frequency, $\varepsilon_{f,LOS}$, under nominal signal reception state conditions (no multipath component) section 3.1.2.2.2.2, implying $\hat{f}_{NCO} = f_0$; or equivalently $D_{FLL}(\varepsilon_{f,LOS}) \approx \varepsilon_{f,LOS} = 0$. This desired behavior is obtained in the steady-state regime after the transition phase.

In the presence of LOS MP, the inherent behavior of the FLL remains the same, but the presence of multipath component induces the bias on the Doppler frequency estimation error. Indeed, in the steady-state regime, the discriminator will still be driven to be equal to zero but, under this signal received conditions, $\varepsilon_{f,LOS} = \zeta_{ss}$ for which $D_{FLL}(\varepsilon_{f,LOS} = \zeta_{ss}) = 0$. Remember that ζ value depends on $\Delta\tau$, $\Delta\varphi$, ΔD and MLR, $\zeta_{ss}^{LOS} = f(\Delta\tau, \Delta\varphi, \Delta D, \text{MLR})$. Therefore, the steady state regime can be reached when the Doppler, carrier and code delay displacement and the MLR are fixed; if not, the correlator outputs numerical expressions vary and ζ_{ss} varies as well. Note that assuming fix values for the previous 4 parameters may be a loose assumption since the carrier phase displacement is bound to vary in time due to the Doppler frequency displacement; indeed, a constant value steady state regime may never be reached.

However, since the Doppler frequency displacement is in the order of 20Hz or lower, this assumption is considered to be sufficient to derive statistics (looser assumption for 20Hz than for 2 or 3 Hz) and to provide a final FLL tracking error PDF to conduct a qualitative comparison. Finally, note that the same approximation is made for $\Psi(\Delta\tau, \Delta\varphi, \Delta D, \text{MLR})$ in order to consider a constant value during the analysis for simplification purposes and that, as well as before, this approximation is considered sufficient to obtain a final FLL tracking error PDF for qualitative comparison purposes.

To summarize, the FLL tracking error bias for LOS MP receiver state conditions is calculated assuming a steady-state regime with a fixed $\Delta\tau, \Delta\varphi, \Delta D$ and MLR values knowing that this assumption may be loose but sufficient for statistics calculation analysis. Note that code delay multipath error envelope analysis also assumes steady-state regime and is widely used in the literature.

In case of NLOS MP, only the MP signal is captured by the antenna, and thus, the same FLL situation as for the signal reception under nominal conditions (only LOS signal is received) situation is found by changing the LOS signal parameters by the multipath component parameters; in other words, the discriminator function is equal to zero when the carrier frequency estimation error between the multipath Doppler frequency and the local replica carrier frequency is 0, $D_{FLL}(\varepsilon_{f,MP}) \approx \varepsilon_{f,MP} = 0$. In this case, $\varepsilon_{f,LOS}$ depends thus on the magnitude of the Doppler

frequency displacement and the type of discriminator (linear region) and is determined by the condition $\varepsilon_{f,MP} = 0$. Therefore, the FLL tracking error bias in steady-regime state is equal to the Doppler frequency displacement, $\zeta_{ss}^{NLOS} = \Delta D$.

4.3.3.2 FLL tracking error bias envelope analysis

The FLL tracking error bias or discriminator output bias have been obtained by numerically searching the $\varepsilon_{f,LOS}$ value which equates to 0 the FLL discriminator output defined in equation 4-28 for a given range of Doppler displacement values and a given range of carrier phase displacement values. The numerical evaluation is based on the parameters defined in Table 4-6:

- the code delay displacement is considered equal to 0, and the correlation function is simplified to one;
- the range of carrier phase displacement values is between 0° and 359°;
- the range of Doppler frequency displacement values is between -200 Hz and 200 Hz;
- two different MLR are evaluated, $\tilde{\alpha}_1 = 1/2$ and $\tilde{\alpha}_1 = 1/4$;
- the FLL correlation integration time is equal to 10 ms, corresponding to the classic GPS L1 C/A FLL design;
- the Filter bandwidth is considered infinite.

MP-to-LOS power ratio	$\tilde{\alpha}_1$	$1/2, 1/4$
Multipath phase displacement	$\Delta\varphi$ [deg]	0:359
Multipath Doppler Frequency displacement	ΔD [Hz]	-200:200
Integration Time	T_{FLL} [ms]	10

Table 4-6 – Open-loop frequency error due to Doppler displacement simulation parameters

The results of the numerical evaluation of mathematical model presented in equation 4-28 are illustrated in Figure 4-36 for LOS MP receiver state conditions. The upper and lower limits of the red curve is the Doppler frequency multipath error envelope with $\tilde{\alpha}_1 = 1/2$, while the upper and lower limits of green curve is the one where $\tilde{\alpha}_1 = 1/4$. Note that a similar figure is not given for the NLOS MP receiver state conditions case, since the bias is equal to the Doppler frequency displacement.

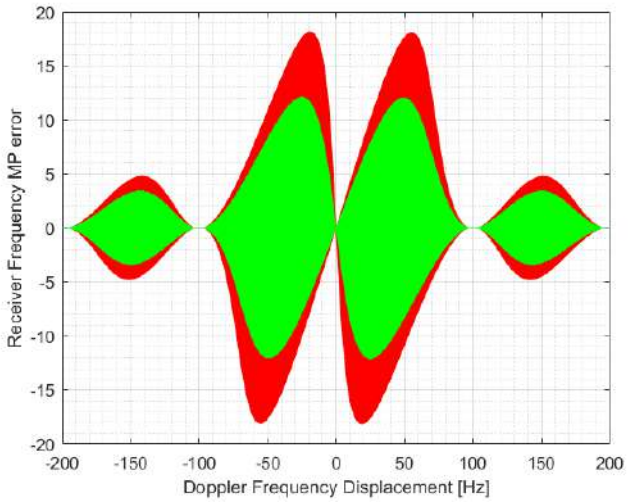

Figure 4-36 – Behavior of the Doppler frequency multipath error envelope (output of the FLL discriminator) affected by the presence of multipath ray, described by the MP-to-LOS power ration, α_1, the Doppler Frequency Displacement ΔD, and the Initial Phase Displacement $\Delta\varphi$.

Finally, the outputs set of the FLL tracking error bias or discriminator output bias, denoted as $\boldsymbol{\zeta}_{ss}^{LOS}$ or $\varepsilon_{f,LOS}^{bias}$, numerical evaluation in the steady-state regime are denoted as follows:

$$\boldsymbol{\zeta}_{ss}^{LOS} = \left[\zeta_{ss}^{LOS,1,1,1}(\Delta\varphi_1, \Delta D_1, \alpha_1), \dots, \zeta_{ss}^{LOS,i,j,k}(\Delta\varphi_i, \Delta D_j, \alpha_k), \dots, \zeta_{ss}^{LOS,I,J,K}(\Delta\varphi_I, \Delta D_J, \alpha_K)\right] \quad 4\text{-}52$$

with:

- $i = 1, \dots, I$ number of evaluated $\Delta\varphi$ values; N_I is the number of different evaluated $\Delta\varphi$ values
- $j = 1, \dots, J$ number of evaluated ΔD values; N_j is the number of different evaluated ΔD values
- $k = 1, \dots, K$ number of evaluated α values.

4.3.3.3FLL tracking error bias PDF

Once the FLL tracking error bias as a function of the Doppler frequency displacement and the carrier phase displacement is determined, the FLL tracking error bias PDF, or equivalently $P_{\zeta_{ss}^{LOS}}$, can be calculated as follows.

In case of LOS MP, for each set of values corresponding to a given α_K in equation 4-51, the FLL tracking error bias PDF is constructed as the histogram of the $\boldsymbol{\zeta}_{ss}^{LOS}$ set considering the independence of ΔD and $\Delta\varphi$ random variables, modelling $\Delta\varphi$ as a uniform random variable $[0,2\pi)$ and modelling ΔD as a random variable with a specific PDF. Indeed, not all ΔD values have the same probability of appearing; in fact, as shown in section 4.3.1, the ΔD simulated PDF, $P_{\Delta D}$, is not uniform and depends on the specific MP environment configuration. $P_{\Delta D}$ is provided in Figure 4-28 (static scenario) and in Figure 4-35 (dynamic scenario).

Therefore, the FLL tracking error bias PDF can be calculated applying the results obtained with $\tilde{\alpha}_1 = 1/2$ and the Doppler displacement characterization, obtained for the two different urban environment scenarios. The results are presented in 4.3.3.3.1.

In case of NLOS MP, the FLL tracking error bias PDF is directly equal to the Doppler frequency displacement PDF, as defined in section 4.3.2. Thus, the FLL tracking error bias PDF is equal to the NLOS Doppler displacement characterization, obtained for the two different urban environment scenarios, static and dynamic. The results are presented in 4.3.3.3.2.

4.3.3.3.1 FLL tracking error bias PDF conditioned by LOS MP

The resulting FLL tracking error bias PDF, provided for the static and dynamic LOS Doppler displacement characterizations, is illustrated in Figure 4-37. Both static and dynamic receiver scenarios are characterized by a zero-centred and symmetric simulated PDF shape. Static simulated PDF curve (red) is higher for the receiver velocity absolute error range equal to $|\varepsilon_{f,LOS}| = [0,1.5]$ m/s, whereas dynamic simulated PDF curve (blue) becomes slightly higher than the static one for receiver velocity error range higher than 1.5 m/s and lower than -1.5 m/s.

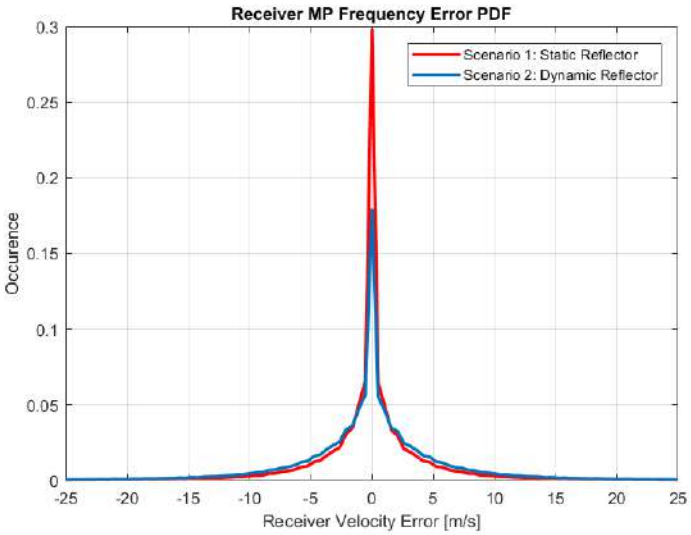

Figure 4-37 – Doppler frequency multipath error PDF at the FLL discriminator output error as a function of the LOS MP Doppler displacement characterization

4.3.3.3.2 FLL tracking error bias PDF conditioned by NLOS MP

The resulting FLL tracking error bias PDF, provided for the static and dynamic NLOS Doppler displacement characterizations, is illustrated in Figure 4-38. Both static and dynamic receiver scenarios are characterized by a zero-centred and symmetric simulated PDF shape. Static simulated PDF curve (red) is higher for the receiver velocity absolute error range equal to $|\varepsilon_{f,LOS}| = [0,10.5]$ m/s, whereas dynamic simulated PDF curve (blue) becomes slightly higher than the static one for receiver velocity error range higher than 10.5 m/s and lower than -10.5 m/s.

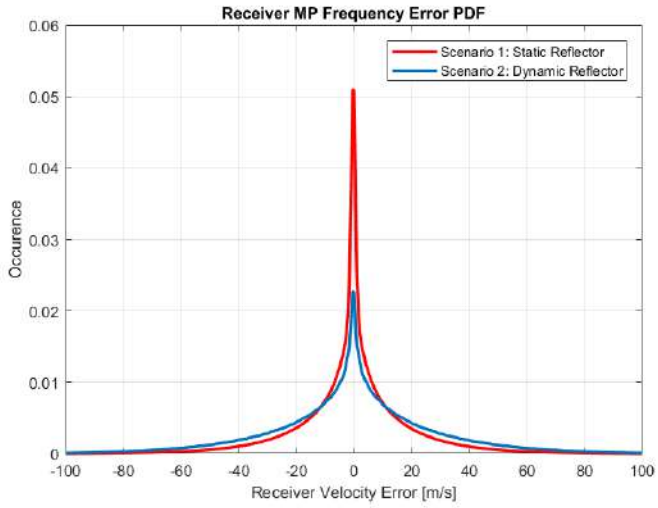

Figure 4-38 – Doppler frequency multipath error PDF at the FLL discriminator output error as a function of the NLOS MP Doppler displacement characterization

4.3.4 MP and Noise impact on FLL tracking error variance

In this section, the FLL tracking error variance introduced by the thermal noise is calculated as a function of Doppler frequency displacement, ΔD, using the ΔD PDF calculated in section 4.3.1. Note that in the presence of MP NLOS received conditions, the FLL tracking error variance is the same as the FLL tracking error variance in LOS signal conditions without the presence of multipath since the 1-echo is tracked by the FLL as if it was the LOS signal.

The FLL tracking error variance can be calculated from the discriminator output variance as shown in equation 4-48; and the discriminator output variance is equal to the variance of the normalized discriminator noise, $\tilde{n}_{discri}$, defined in equation 4-32 (without the normalization factor). Using this notion, a generic FLL tracking error variance is given in section 4.3.4.1. One the generic formula is defined, it is applied to derive the open-loop FLL tracking error variance (or discriminator output error variance) without the presence of multipath in section 4.3.4.2 (which can also be used for MP NLOS received signal conditions) and in the presence of multipath in section 4.3.4.3 (which is used for MP LOS received signal conditions).

4.3.4.1 Generic open loop variance model of the FLL CP Discriminator

In this section, the general formulas used to calculate the Open Loop frequency error variance (or discriminator output error variance) of the Cross-Product discriminator are given. These formulas are valid for any type of received signal conditions, LOS or LOS with MP.

The non-normalized discriminator output error variance due to thermal noise is modelled as (see Annex 10.3.3 for details):

$$var\left(D_{CP,k}\right) = E\left[\left(D_{CP,k}\right)^2\right] - \left(E\left[D_{CP,k}\right]\right)^2 = var[n_{discri}] = E[(n_{discri})^2] \quad 4\text{-}53$$

Considering the definition of n_{discri}, in equation 4-32, considering the independence of $\eta^P_{I,k-1}, \eta^P_{Q,k-1}, \eta^P_{I,k}$ and $\eta^P_{Q,k}$, considering that each noise component is a Gaussian variable with 0 mean and σ^2 variance, $N(0,\sigma^2)$ $var\left(D_{CP,k}\right)$ is equal to:

$$var\left(D_{CP,k}\right) = E[(n_{discri})^2] \quad 4\text{-}54$$

and

$$var\left(D_{CP,k}\right) = \sigma^2\left(\left(S^P_{I,k-1}\right)^2 + \left(S^P_{Q,k-1}\right)^2 + \left(S^P_{I,k}\right)^2 + \left(S^P_{Q,k}\right)^2\right) + 2\sigma^4 \quad 4\text{-}55$$

Therefore, the application of equation 4-55 with the corresponding customization of $S^P_{I,k-1}$, $S^P_{Q,k-1}$, $S^P_{I,k}$ and $S^P_{Q,k}$ to the targeted received signal conditions allows to calculate to the CP discriminator output error variance in these conditions.

4.3.4.2 Open loop variance model of the FLL CP Discriminator without the presence of MP

The goal of this section is to derive a mathematical model of the Open Loop frequency error variance (or discriminator output error variance) when affected by the presence of thermal noise only; no multipath component is present. This derivation is used to verify the validity of the derived methodology and applied formulas; for this purpose, the theoretical derivation is compared to results obtained from Monte-Carlo simulations. Moreover, note that these formulae can also be used as the FLL tracking error variance in the case of MP NLOS received signal conditions.

The normalized CP discriminator error variance is computed by customizing $S^P_{I,k-1}$, $S^P_{Q,k-1}$, $S^P_{I,k}$ and $S^P_{Q,k}$ in LOS conditions as given in equation 4-33. The CP discriminator error variance is given below. For simplification purposes, it has been assumed $R\left(\varepsilon_{\tau_{0,k}}\right) = R\left(\varepsilon_{\tau_{0,k-1}}\right) \approx 1$.

$$\sigma^2_{CP,theoretical} = var\left(\widetilde{D}_{CP,k}\right) = \frac{var\left(D_{CP,k}\right)}{\left[2\pi T_I\left(\left(E\left[S^P_{I,k-1}\right]\right)^2 + \left(E\left[S^P_{Q,k-1}\right]\right)^2\right)\right]^2}$$

$$= \frac{E[(n_{discri})^2]}{\pi^2 T_I^2 C \mathrm{sinc}^4\left(\pi\varepsilon_{f,LOS}T_I\right)} = \frac{1 + \frac{1}{2T_I\frac{C}{N_0}}}{4\pi^2 T_I^3 \frac{C}{N_0}} \quad 4\text{-}56$$

where:

- $\left(E[S^P_{I,k-1}]\right)^2 + \left(E[S^P_{Q,k-1}]\right)^2 = \frac{A_0^2}{4}\mathrm{sinc}^2\left(\pi\varepsilon_{f,LOS}T_I\right) = \frac{1}{2}C\mathrm{sinc}^2\left(\pi\varepsilon_{f,LOS}T_I\right)$;
- for BPSK, $C = \frac{A_0^2}{2}$.

A simulation of the CP discriminator output using different $\mathrm{C/N_0}$ is performed, and the CP discriminator output error variance results are compared to the values obtained from the equation in 4-56.

The CP discriminator output is simulated by implementing equation 4-36. The impact of noise is simulated generating the random noise samples, η_l, for the In-phase, $\eta_{I,l}$, and Quadrature, $\eta_{Q,l}$, components, corresponding to a specific Carrier-to-Noise ratio, C/N_0. A high number of runs are implemented to have a Monte Carlo simulation.

The simulated CP discriminator output values are thus considered as a set of realizations of the random variable D_{CP}, characterized by the simulated C/N_{0_k} and, finally, the noise component value, η_l (used to simulate the different Monte-Carlo simulations):

$$\mathbf{D}_{CP} = \left[D_{CP}^{1,1}\left(C/N_{0_1}, \eta_1\right), \ldots, D_{CP}^{k,l}\left(C/N_{0_k}, \eta_l\right)\right] \quad 4\text{-}57$$

where:

- $k = 1, \ldots, K$ whit K equal to the number of simulated C/N_0 values;
- $l = 1, \ldots, L$ whit L number of Monte Carlo runs.
- η_l determines the l outcome of a Gaussian variable (with independency between outcomes)

The variance of the simulated D_{CP} values characterized by a given C/N_{0_k} are be calculated as follows:

- Simulated Variance: The simulated variance of the CP discriminator output values of 4-61, characterized by a specific set of $\Delta D_j, C/N_{0_k}$ values is equal to:

$$\sigma_{CP}^{2\ k,l}\left(D_{CP}^{k,l}\right) = \frac{1}{L}\sum_{l=1}^{L}\left(D_{CP}^{k,l}\left(C/N_{0_k}, \eta_l\right) - m_{CP}^{k,l}\right)^2 \quad 4\text{-}58$$

where $m_{CP}^{k,l}$ is the mean of the discriminator output as a function of the number of Monte Carlo runs:

$$m_{CP}^{k,l} = \frac{1}{L}\sum_{l=1}^{L} D_{CP}^{k,l}\left(C/N_{0_k}, \eta_l\right) \quad 4\text{-}59$$

The parameters numerical values are given in Table 4-7.

The simulated LOS-to-MP power ratio	$\tilde{\alpha}_1$	$1/2$
LOS Carrier-to-Noise ratio	$\frac{C}{N_0}$ [dB-Hz]	[50, 47, 44, …, 32]
Monte Carlo runs	L	10^6

Table 4-7 – CP discriminator output error due to thermal noise, simulation parameters

The results are showed in Figure 4-39. From this figure, it can be observed a perfect match between the proposed FLL tracking error variance formula in LOS received signal conditions and the simulated results. Therefore, the proposed formula is validated in LOS received signal conditions.

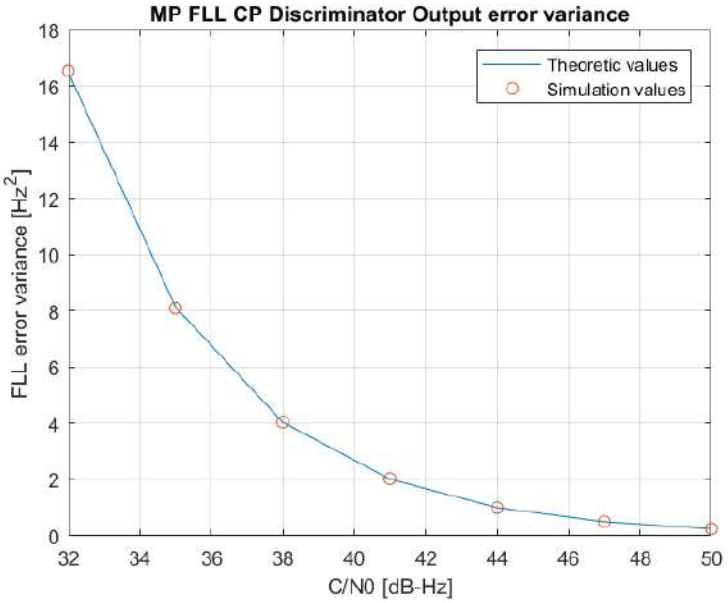

Figure 4-39 – FLL Open Loop Variance Error Doppler Displacement and thermal noise, Cross Product Discriminator

4.3.4.3Open loop variance model of the FLL CP Discriminator in presence of MP

Similarly to section 4.3.4.1, the goal of this section is first to derive a mathematical model of the Open Loop frequency estimation error variance (or discriminator output error variance), when affected jointly by the thermal noise and the 1-ray multipath component; and second, to validate the derived formula by comparing it with simulated results.

The normalized CP discriminator error variance is computed by customizing $S_{I,k-1}^{P}$, $S_{Q,k-1}^{P}$, $S_{I,k}^{P}$ and $S_{Q,k}^{P}$ in LOS MP conditions as given in equation 4-9. The derivation of the theoretical normalized CP discriminator output error variance in presence of Multipath and thermal noise is presented in Annex 10.3.2. The final equation, expressed in Hz^2, is given by:

$$\sigma_{CP,theoretical}^{2} = var\left(\tilde{D}_{CP,k}\right) = \frac{\begin{bmatrix} sinc^2\left(\pi\varepsilon_{f,LOS}T_I\right) + \tilde{\alpha}_1^2\, sinc^2\left(\pi\left(\varepsilon_{f,LOS}+\Delta D\right)T_I\right) + \tilde{\alpha}_1\, sinc\left(\pi\varepsilon_{f,LOS}T_I\right) sinc\left(\pi\left(\varepsilon_{f,LOS}+\Delta D\right)T_I\right) \\ \left[cos(3\pi(-\Delta D)T_I - \Delta\varphi) + cos(\pi(-\Delta D)T_I - \Delta\varphi)\right] \end{bmatrix} + \frac{1}{2T_I\frac{C}{N_0}}}{16\pi^2 T_I^3 \frac{C}{N_0}\begin{bmatrix} \frac{1}{2}\mathrm{sinc}^2\left(\pi\varepsilon_{f,LOS}T_I\right) + \frac{\tilde{\alpha}_1^2}{2}\mathrm{sinc}^2\left(\pi\left(\varepsilon_{f,LOS}+\Delta D\right)T_I\right) \\ +\tilde{\alpha}_1\,\mathrm{sinc}\left(\pi\varepsilon_{f,LOS}T_I\right)\mathrm{sinc}\left(\pi\left(\varepsilon_{f,LOS}+\Delta D\right)T_I\right)\left[\cos(\pi(-\Delta D)T_I - \Delta\varphi)\right] \end{bmatrix}^2} \quad 4\text{-}60$$

Note that in this work, since the inspected case is the steady-state regime, $\varepsilon_{f,LOS}$ equal to the steady-state regime bias, $\varepsilon_{f,LOS} = \zeta_{ss}^{LOS}$ which depends on ΔD and on $\Delta\varphi$. Moreover, note that the normalization is make assuming that the 1-ray echo is present for a long time and thus affects the normalization result. Another possible assumption is to have the normalization factor average out all potential multipath effects; this alternative option was not considered and thus, if the reader wants to consider it, equation 4-60 denominator should be modified.

The mathematical model of equation 4-60 is then compared to the simulated results of a software-implemented CP open-loop FLL in order to validate the derived formulas. The comparison is conducted in two steps, the first step is the *Simulation of CP discriminator output values* and the second step is the *Calculation of statistics and theoretical values*.

Step 1) Simulation of CP discriminator output values: The CP discriminator output is simulated by implementing equation 4-36. The impact of multipath error is simulated tuning the initial carrier phase displacement $\Delta\varphi$ and the Doppler frequency displacement, ΔD, terms; moreover, due to the steady state regime assumption, the $\varepsilon_{f,LOS}$ equal to the bias term $\zeta_{ss}^{LOS}(\Delta D, \Delta\varphi)$ which is also determined by ΔD and $\Delta\varphi$. The impact of noise is simulated generating the random noise samples, η_l, for the In-phase, $\eta_{I,l}$, and Quadrature, $\eta_{Q,l}$, components, corresponding to a specific Carrier-to-Noise ratio, C/N_0. A high number of runs are implemented to have a Monte Carlo simulation.

The simulated CP discriminator output values are thus considered as a set of realizations of the random variable D_{CP}, characterized by the simulated carrier phase displacement, $\Delta\varphi_i$, the Doppler frequency displacement ΔD_j the C/N_{0_k} and, finally, the noise component value, η_l (used to simulate the different Monte-Carlo simulations):

$$\mathbf{D}_{CP} = \left[D_{CP}^{1,1,1,1}\left(\Delta\varphi_1, \Delta D_1, C/N_{0_1}, \eta_1\right), \ldots, D_{CP}^{i,j,k,l}\left(\Delta\varphi_i, \Delta D_j, C/N_{0_k}, \eta_l\right)\right] \quad 4\text{-}61$$

where:

- $i = 1, \ldots, I$ whit I equal to the number of simulated carrier phase displacement values;
- $j = 1, \ldots, J$ whit J equal to the number of simulated Doppler frequency displacement values;
- $k = 1, \ldots, K$ whit K equal to the number of simulated C/N_0 values;
- $l = 1, \ldots, L$ whit L number of Monte Carlo runs.
- η_l determines the l outcome of a Gaussian variable (with independency between outcomes)

Step 2) Calculation of statistics and comparison with theoretical values: The variance of the simulated D_{CP} values characterized by a given set of $\Delta\varphi_i, \Delta D_j, C/N_{0_k}$ are be calculated as follows:

- Simulated Variance: The simulated variance of the CP discriminator output values of 4-61, characterized by a specific set of $\Delta D_j, C/N_{0_k}$ values is equal to:

$$\sigma_{CP}^{2\ j,k}\left(D_{CP}^{j,k}\right) = \frac{1}{I}\frac{1}{L}\sum_{i=1}^{I}\sum_{l=1}^{L}\left(D_{CP}^{i,j,k,l}\left(\Delta\varphi_i, \Delta D_j, C/N_{0_k}, \eta_l\right) - m_{CP}^{i,j,k}\right)^2 \quad 4\text{-}62$$

where $m_{CP}^{i,j,k}$ is the mean of the discriminator output as a function of the number of Monte Carlo runs:

$$m_{CP}^{i,j,k} = \frac{1}{L}\sum_{l=1}^{L} D_{CP}^{i,j,k,l}\left(\Delta\varphi_i, \Delta D_j, C/N_{0_k}, \eta_l\right) \quad 4\text{-}63$$

Moreover, as verified in section 4.3.5.1, the simulated mean result is equal to 0.

The simulated values are compared to the theoretical values:

- Theoretical Variance: The theoretical variance is calculated from equation 4-60, by averaging all values of σ_{CP}^2 as a function of $\Delta\varphi_i$ assuming a uniform random variable $[0,2\pi]$ for the carrier phase displacement.

$$\sigma_{CP,theor}^{2\ j,k} = \frac{1}{I}\sum_{i=1}^{I}\sigma_{CP,theor}^{2\ i,j,k}\left(\Delta\varphi_i, \Delta D_j, C/N_{0_k}\right) \quad 4\text{-}64$$

The simulated variance and the theoretical variance are compared as a function of ΔD and C/N_0 in order to validate the theoretical CP discriminator output error variance.

Comparison: The parameters used in the simulation process are defined in the methodology step 1 in addition to other fixed value parameters such as the MLR and code delay displacement. The parameters numerical values are given in Table 4-8.

The simulated LOS-to-MP power ratio	$\tilde{\alpha}_1$	$1/2$
LOS Carrier-to-Noise ratio	$\frac{C}{N_0}$ [dB-Hz]	[50, 47, 44, …, 32]
Code delay displacement	$\Delta\tau$ [s]	0
Initial phase Multipath Displacement	$\Delta\varphi$ [deg]	[0, 1, 2, …, 359]
Doppler Frequency Displacement	ΔD [Hz]	[-50, -30, -25, …, 50]
CP Discriminator output bias in steady-state regime	ζ_{SS}^{LOS} [Hz]	Select corresponding value of $\boldsymbol{\zeta}_{SS}^{LOS}$ as a function of ΔD and on $\Delta\varphi$
Monte Carlo runs	L	10^6

Table 4-8 – CP discriminator output error due to Doppler displacement and thermal noise, simulation parameters

Figure 4-40 compares the theoretical normalized CP discriminator output variance obtained from 4-64 to the simulated values obtained from equation 4-62. As seen in Figure 4-40, theoretical values match the simulated results confirming the validity of the theoretical model presented in equation 4-60. Finally, as a reminder, the normalized CP discriminator output error variance is equivalent to the variance of the normalized discriminator noise as indicated in equation 4-54.

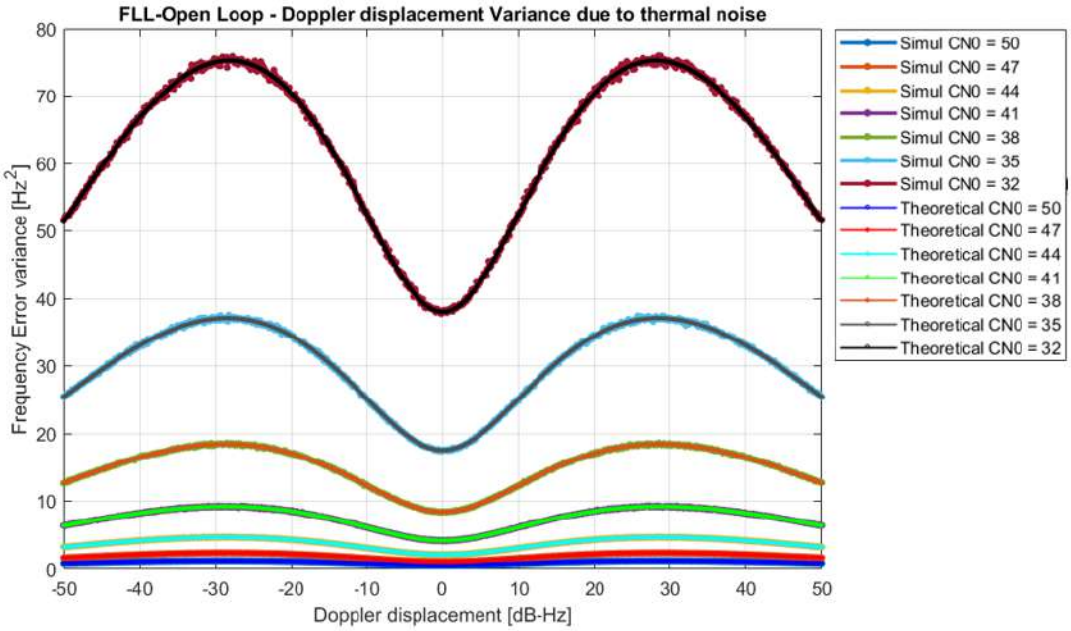

Figure 4-40 –FLL discriminator output error variance in presence of Multipath, theoretical values vs. experimental values. Discriminator: Cross Product

4.3.5Complete FLL tracking error PDF

In this section, the complete FLL tracking error PDF due to MN plus thermal noise (MN) is finally derived in the steady-state regime for MP LOS received signal conditions and for a 1-ray echo propagation channel model with a static reflector;

For simplification purposes, the calculation for MP NLOS received signal conditions is not tackled. Similarly, the FLL tracking error PDF due to MN plus thermal noise (MN) is derived in the dynamic regime has not been calculated.

The derived complete FLL tracking error PDF is used to make a qualitative comparison with the multipath plus noise (MN) error component of the PSR-R measurement isolated in Chapter 6. The comparison is made in in order to validate the isolation methodology described in Chapter 5 and applied to collected data in Chapter 6. The comparison is qualitative since the MP environment, just 1-ray echo, is a simple modelling of the true urban canyon. Therefore, the MLR, set to 1/2, and the code delay, carrier phase and Doppler frequency displacement are fixed values or calculated from this simple model and thus, they derive from their true values.

The complete FLL tracking error PDF calculation is made in two steps. First, in section 4.3.5.1, the PDF of the $\tilde{n}_{discri}$ is approximated. Second, in section 4.3.5.2, using the FLL tacking error model of equation 4-51, using the discriminator output error bias of Figure 4-36, using the FLL tracking error variance of equation 4-48 and the $\tilde{n}_{discri}$ PDF when assuming a constant $\Delta\tau, \Delta\varphi, \Delta D$ and MLR parameter values, the complete FLL tracking error PDF is calculated.

4.3.5.1 Discriminator noise PDF derivation

In this section, the normalized discriminator noise, $\tilde{n}_{discri}$, PDF is approximated when assuming constant $\Delta\tau, \Delta\varphi, \Delta D$ and MLR parameter values.

The PDF of $\tilde{n}_{discri}$ can be approximated from the no-normalized n_{discri} expression given in equation 4-32. In this equation, n_{discri} is the sum of 4 centred and independent gaussian variables plus the multiplication of two of pairs of them. Assuming a moderate to high C/N_0 value, the multiplication of Gaussian variables is going to have a negligeable contribution to the n_{discri} with respect to the 4 Gaussian variables which are multiplied by the useful signal contribution. Therefore, since the normalization factor will just influence the variance numerical value but

no the noise PDF, the noise PDF can be approximated as centered Gaussian variable with variance defined in equation 4-48.

In order to verify this analysis, a Monte-Carlo simulation has been run. Figure 4-41 shows the probability density function of the discriminator output when using $\varepsilon_{f,LOS} = \zeta_{ss}^{LOS}$ (useful signal contribution is thus removed); the PDF is obtained by exploiting 10^6 Monte-Carlo runs with $C/N_0 = 50$ dB-Hz, $\Delta\varphi = 0°$ and $\Delta D = -50$ Hz. It can be observed that the PDF corresponds to a zero-biased gaussian shape, which confirms the additive gaussian properties of the thermal noise component affecting the CP FLL discriminator output.

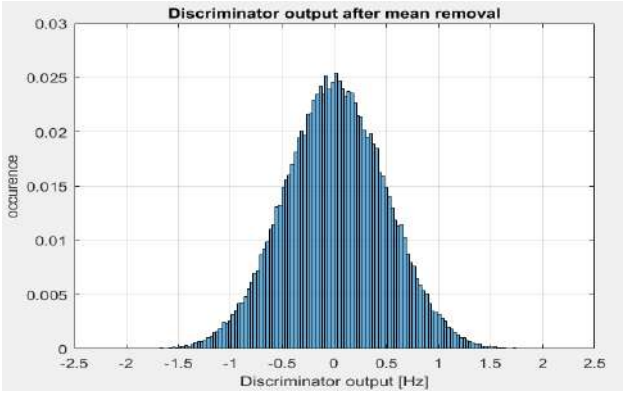

Figure 4-41 – PDF of the FLL discriminator output in presence of Multipath and thermal noise component, obtained with $C/N_0 = 50$ dB-Hz, $\Delta\varphi = 0°$ and $\Delta D = -50$ Hz

4.3.5.2Complete FLL tracking error PDF calculation

In this section, the complete FLL tacking error PDF due to MN plus thermal noise (MN) in the steady-state regime for MP LOS received signal conditions and for a 1-ray echo propagation channel model with a static reflector is calculated.

The FLL tacking error PDF is calculated using as basis FLL tacking error model derived in equation 4-51. From this equation, a given PDF is generated from a set of parameter values, $C/N_0, \Delta\tau, \Delta\varphi, \Delta D$ and MLR, denoted as $P_{\varepsilon_{f,LOS}}(C/N_0, \Delta\tau, \Delta\varphi, \Delta D, \text{MLR})$. The set of parameters values generated PDF is then weigthed by the probability of appearance of each of the values to obtain the complete PDF; or in other words, the total law probability theorem is used when considering independence of the parameters. In this work, the PDF is calculated for a fixed value of MLR, equal to 1/2, and for a fixed value of code delay displacement $\Delta\tau$, equal to 0 or equivalently to be accounted for in the MLR parameter. Therefore, the complete FLL tracking error PDF is calculated as shown below as a function of the received signal C/N_0:

$$P_{\varepsilon_{f,LOS}}\left(C/N_0, \Delta\tau = 0, \text{MLR} = \frac{1}{2}\right) = \\ = \int_{<\Delta D>} \int_{<\Delta\varphi>} P_{\varepsilon_{f,LOS}}\left(C/N_0, \Delta\tau = 0, \text{MLR} = \frac{1}{2} \middle| \Delta\varphi_i, \Delta D_j\right) P_{\Delta D}(\Delta D) P_{\Delta\varphi}(\Delta\varphi) d\Delta D d\Delta\varphi \quad \text{4-65}$$

Where $P_{\Delta D}(\Delta D)$ is given in Figure 4-28 for a static reflector and $\Delta\varphi$ is modelled as a unfirom random variable with $[0,2\pi)$. Note that the weighting operation of equation 4-65 is an approximation to the real parameter values time variation behavior; as specified in section 4.3.3.1, $\Delta\varphi$ and ΔD will vary in time and thus a constant value state-steady regime will probably not be attained. Therefore, the weighting operation approximates the statistics of the parameters time variation per the statistics of the steady-state regime assuming convergence and fixed initial conditions (with all possible initial conditions); note that this approximation is similar to assuming an ergodic process.

Each $P_{\varepsilon_{f,LOS}}(\Delta\tau, \Delta\varphi, \Delta D, \text{MLR})$ is modelled as the addition of a constant term, the FLL tracking error bias in steady-state regime ζ_{ss}^{LOS}, and the a centred Gaussian variable with variance equal to the variance of the normalized

discriminator output, $var[\tilde{n}_{discri}]$, multiplied by $2B'_L T_{update}$, as stated in equation 4-48. Therefore, the resulting $P_{\varepsilon_{f,LOS}}(C/N_0, \Delta\tau, \Delta\varphi, \Delta D, \text{MLR})$ is a Gaussian variable with mean equal to ζ_{ss}^{LOS} and variance equal to $2B'_L T_{update} var[\tilde{n}_{discri}]$, $\sim N(\zeta_{ss}^{LOS}, 2B'_L T_{update} var[\tilde{n}_{discri}])$.

The ζ_{ss}^{LOS} value is recovered from the set of ouputs $\boldsymbol{\zeta}_{ss}^{LOS}$ used to generate Figure 4-36. The $var[\tilde{n}_{discri}]$ is calculated from equation 4-60. Finally, the $2B'_L T_{update}$ term is assumed to be equal to the chosen by design $2B_L T_{update}$. This assumption implies that the slope coefficient, Ψ, does not impact the closed-loop transfer function zeroes and poles which is not true. Indeed, it can be seen that the introduction of Ψ as a multiplying factor on $\varepsilon_{f,LOS}$ does modify the zeroes and poles and thus changes B'_L. Nevertheless, for simplification purposes and reminding that the final comparison can only be done in a qualitative manner, in this work, $B'_L \approx B_L$.

Figure 4-42 presents the complete FLL tracking error PDF due to MN plus thermal noise (MN) in the steady-state regime for MP LOS received signal conditions and for a 1-ray echo propagation channel model with a static reflector, for 30, 35, 40 and 45 dB-Hz of C/N_0 values and with $\Delta\tau = 0$ and $MLR = 1/2$. Figure 4-42 was elaborated applying equation 4-65 and approximating $\Delta\varphi$ and ΔD with discrete variables; $\Delta\varphi$ sampling step has been set to 1° and ΔD sampling step has been set to 0.1Hz.

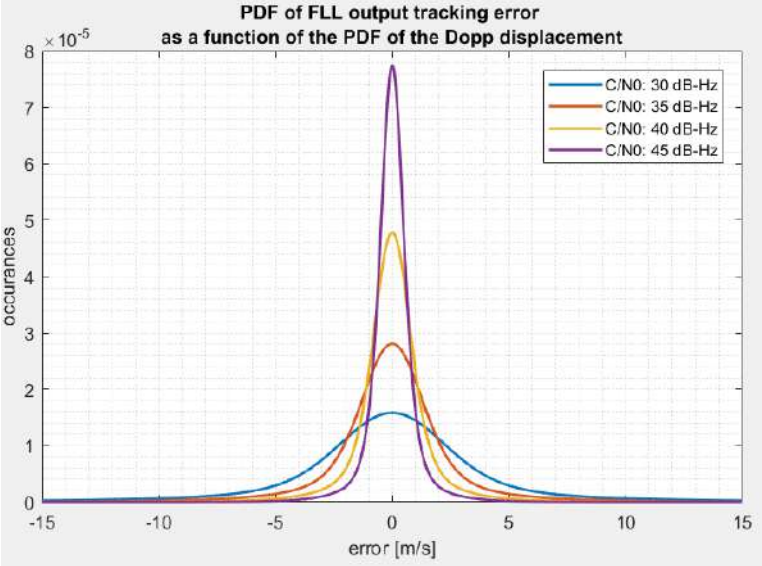

Figure 4-42 – Complete FLL tracking error PDF in the steady-state regime for MP LOS received signal conditions and for a 1-ray echo propagation channel model with a static reflector, for 30, 35, 40 and 45 dB-Hz of C/N_0 values and with $\Delta\tau = 0$ and $MLR = 1/2$

From Figure 4-42, it can be seen that the FLL tracking error even for low C/N_0 values seldomly larger than +/-10Hz. Indeed, the PDF is clearly conditioned by the FLL tracking error bias which, in its turn, is conditioned by the Doppler frequency displacement: in Figure 4-28, the Doppler frequency displacement was seldomly larger than +/-5Hz and in Figure 4-36, the FLL tracking error bias absolute value was always smaller than 20Hz. Moreover, as expected, it can be observed that lower C/N_0 values imply a large variance.

Finally, in order to observe if the complete FLL tracking error PDF is a Gaussian variable, Figure 4-43 presents the CDF calculation for the previous defined case for C/N_0 values equal to 30 and 45dB-Hz (in blue). These dereived CDF are compared to Gaussian variable CDF with the same mean and variance as the derived CDF; note that this methodology ahs been chosen to be coherent with Chapter 6 overbouding methodology figures to allow an easier comparison between theoretically derived CDF and data collected CDF. From Figure 4-43, it can be observed that the theoretically derived CDF are below the Gaussian approximated CDF below 0 Hz and above the Gaussian approximated CDF above 0 Hz. Therefore, it can be concluded that the theoretically derived FLL tracking error PDF is more concentrated around the 0 Hz than the Gaussian approximated CDF; it has a more prominent peak. This characteristic is probably due to the Doppler frequency displacement which is concentrated

among the 0 Hz values. Finally, no trend/shape difference appears to be as a function of the C/N_0 since both figures are similar (in shape not in absolute values).

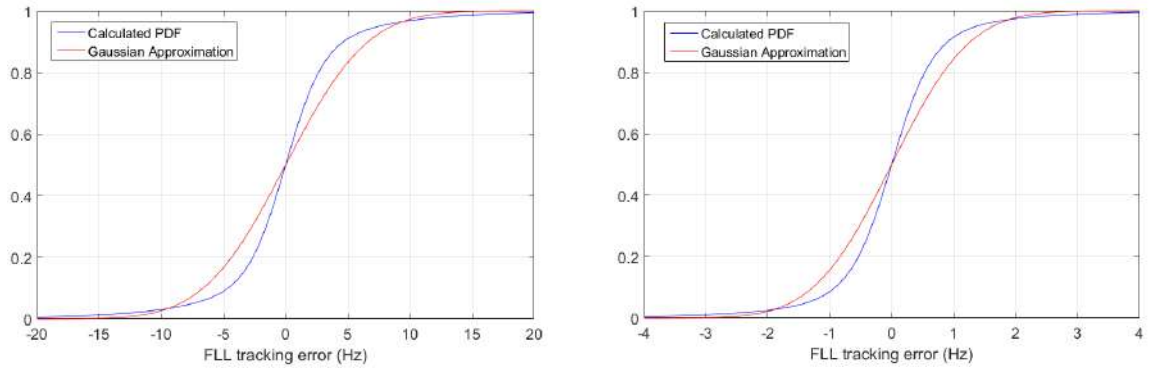

Figure 4-43 – Complete FLL tracking error CDF for 30 and 45 dB-Hz of C/N_0 values and with $\Delta\tau = 0$ and $MLR = 1/2$ compared to a Gaussian variable CDF with the same mean and variance

4.4 Conclusions

Chapter 0 was dedicated to the theoretical characterization of the GNSS measurements error components caused by the presence of multipath on the received signal. The characterization was conducted by deriving the multipath induced tracking errors on the DLL and FLL modules since, as shown in Chapter 0, the DLL module is used to derive GNSS pseudo-range (PSR) measurements and the FLL module is used to derive GNSS pseudo-range rate (PR-R) measurements. Therefore, the DLL and FLL multipath induced tracking errors are directly assumed to be equal to the GNSS PSR and PSR-R measurements multipath error component. The objective of the theoretical characterization of the GNSS PSR and PSR-R measurements multipath error component was to validate the multipath plus thermal noise (MN) error component isolation methodology developed in Chapter 5 and applied to collected data in Chapter 6.

The theoretical DLL and FLL multipath induced tracking error models were developed considering a simple propagation channel which consists of the potential reception of the LOS signal and the reception of one multipath signal or echo. The reception or the lack of reception of the LOS signal defined to different cases to analyze; LOS reception state, where the received signal is constituted of the LOS and the MP signal components, and the NLOS reception state, where the received signal is only constituted of the MP signal component. The MP signal component is defined by the MP-to-LOS amplitude (or power ratio), MLR, the code delay displacement, $\Delta\tau$, the carrier phase displacement, $\Delta\varphi$, and the Doppler frequency Displacement, ΔD. The code delay displacement is defined as the code delay difference between the LOS signal and the MP signal with analogous definitions for the carrier phase and the Doppler frequency displacements.

The traditional tracking module MP error characterization consists of the calculation of the DLL and FLL multipath tracking error envelope: the calculation of the DLL and FLL discriminator output error as function of the code delay displacement and the Doppler frequency displacement, respectively. The discriminator output error, which affects the tracking loop performance, appears due to the degradation of the ideal correlation function. Indeed, a new correlation function, denoted as composite correlation function, is obtained as the sum of the LOS (and ideal) correlation function and the correlation function of the echo. Therefore, since the composite correlation function differs from the ideal correlation function, the DLL and FLL discriminators do not function as designed leading to biased tracking estimations. The composite correlation function depends on the multipath defining parameters, MLR, $\Delta\tau$, $\Delta\varphi$, and ΔD. Moreover, note that in NLOS reception state, the composite correlation function is equal to the MP correlation function and the discriminator output is directly equal (and thus the bias is equal) to the code delay or Doppler frequency displacement (depending on the tracked parameter).

The impact of LOS reception state on the DLL tracking process has been analyzed through a literature review in this chapter. As stated before, it induces the presence of a code delay estimation bias which value depends on the code delay displacement, the phase displacement, and the MLR; code delay multipath error envelope. The code delay estimation bias can never be larger than $1+C_s/2$, where C_s is the early-late spacing, and it can be either positive or negative depending on the carrier phase displacement; this characteristic implies that the multipath error components of PSR measurements generated from code delay measurements in LOS reception state conditions should be centered; the addition of the thermal noise component will only add a Gaussian shape to the MN error component PDF. Moreover, Galileo E1 OS signal should present smaller code delay error bias with

respect to GPS L1 C/A signal for medium to long code delay displacements due to the chip modulation, CBOC vs BOC(1) modulation. Concerning NLOS reception state, the generated code delay bias due to multipath-only should always be positive since the emitter-to-receiver echo path is always longer than the emitter-to-receiver LOS signal path. Therefore, in NLOS reception state, the multipath plus thermal noise (MN) error component PDF of PSR measurements generated from code delay measurements should be positive skewed.

The impact of LOS and NLOS reception state on the FLL tracking process has been theoretically analyzed in this chapter. The characterization is conducted in 4 steps: Doppler frequency displacement characterization, FLL tracking error bias characterization, FLL discriminator output error characterization and complete FLL tracking error PDF characterization. The FLL tracking error PDF was derived in the steady-state regime implying fixed MLR, $\Delta\tau$, $\Delta\varphi$, and ΔD values which may not correspond to the reality. However, for small Doppler displacement values, for qualitive comparison purposes (with Chapter 6 collected data results) and knowing that the same assumption is used in the literature for code delay multipath error envelope analysis, this assumption is considered sufficient in this work.

The Doppler frequency displacement was derived from two specific urban environment scenarios: a dynamic GNSS receiver moving through the urban canyon, characterized by large static reflectors placed on the two sides of the street (such as a building, a static vehicle, etc.) and the interaction between the GNSS dynamic receiver and a dynamic reflector moving in the same or opposite receiver's direction. The characterization was conducted assuming only 1 potential diffuse reflection for several receiver speeds. For both scenarios, the LOS and NLOS receiver state Doppler frequency displacement PDFs are symmetric and zero-centred distributions, with high concentrations of values around the 0 Hz frequency. For any speed value and any receiver state, the PDF values are marginal for values higher than 10 Hz and NLOS receiver state Doppler frequency displacement PDF is spreader than for LOS receiver state conditions.

The FLL tracking error model for LOS receiver state conditions in the steady-state regime was determined to be equal to a constant FLL tracking error bias plus the normalized discriminator noise multiplied by the closed-loop transfer function in the Z-transform domain. FLL tracking error bias depends on the Doppler frequency displacement and on the carrier phase displacement and is the value which makes the FLL discriminator equal to 0. In this work the, Cross-Product (CP) discriminator was analyzed. The absolute value of the FLL tracking error bias for a MLR = ½ is never larger than 20Hz and for a MLR = ¼ is never larger than 12Hz for any Doppler frequency displacement value; the bias becomes 0 every multiple of the inverse of the correlation time and is not symmetric with respect to 0.

The CP discriminator error variance has been theoretically derived in this chapter. The error variance depends on the thermal noise and its value depends on the received signal C/N_0 as well as on the carrier phase and on the Doppler frequency displacements. Irrespective of the C/N_0, it presents minima at multiples of the inverse of the correlation time and maxima at the Doppler frequency displacement values equally placed between two minima. Its value goes from few Hz^2 for 50dB-Hz to about 80 Hz^2 for 30dB-Hz.

The complete FLL tracking error PDF has been calculated from the Doppler displacement PDF, FLL tracking error bias and CP discriminator output error variance. The calculation has been approximated by assuming that the closed-loop transfer function in presence of multipath is not modified with respect to the function when no multipath is present. Future work will tackle this impact. The derived FLL tracking error PDF is similar to a Gaussian PDF but with a higher concentration of values around the 0 Hz frequency as seen from the calculated CDF functions. This concentration around the 0 Hz frequencies is probably due to the Doppler frequency displacement PDF. The derived FLL tracking error PDF is concentrated in small values even for low C/N_0, such as 30 dB-Hz where at +/-10 Hz the PDF value is very small.

Finally, the FLL tracking error PDF for NLOS receiver state conditions has not been numerically determined. However, during this chapter its expected shape has been discussed. The FLL tracking error bias is expected to be equal to the Doppler frequency displacement since only the multipath signal is received, and the FLL tracking error variance is expected to be created by the normalized discriminator noise. Therefore, the complete FLL tracking error PDF is expected to be generated by the weighted average of Gaussian PDFs with mean equal to the Doppler frequency displacement and variance equal to the normalized discriminator noise variance multiplied by 2 times the FLL update time, T_{update}, and the one-sided equivalent noise bandwidth, B_L.

5 Multipath Characterization Methodologies

Positioning errors may be dominated by multipath (MP) ranging errors both under conditions where the Line-Of-Sight (LOS) signal is received, defined previously as LOS MP, and under conditions where the LOS is blocked, defined previously as NLOS MP (Non Line-of-sight) (section 2.4.1.2.3). Multipath affects the GNSS receiver tracking operation, as described in Chapter 0, inducing an error on the pseudorange (PSR) and pseudorange-rate (PSR-R) measurements, which is finally translated into PVT errors, as described in Chapter 0.

Multipath induced errors depend on the characteristics of the MP environment and the receiver dynamics. Indeed, the MP effect is influenced by the number of reflectors, the geometry of the surroundings, the reflectors' materials, the reflector's facets and the rate of change of the MP environment configuration due to the receiver dynamics, as described in Chapter 0. The main parameters influencing the magnitude of the induced error are the MP-to-LOS amplitude ratio, the code delay displacement, the carrier phase displacement as well as the Doppler frequency displacement, as discussed in Chapter 0.

MP in harsh environments, such as urban canyons, is often the most significant source of error and has the greatest impact on low-cost navigation applications in urban environments. As a consequence, the LOS and NLOS MP impact on PSR and PSR-R measurements should be characterized, if possible detected, and mitigated in order to handle the poor performance of GNSS in densely urban environments [84]. For this purpose, a large range of strategies have been studied and developed in the literature. A summary of these methodologies is provided in section 5.1.

In this PhD, the selected approach is to first characterise precisely the distributions of MP errors on PSR and PSR-R measurements before addressing mitigation strategies in Chapter 7 at positioning estimation level. The isolation methodology of the MP errors from PSR and PSR-R measurements of a single frequency low-cost GNSS receiver is given in section 5.2. However, considering that the isolation of the MP error is a complex operation due to the superimposed effects of MP and thermal noise, the final method consists of isolating the joint contribution of MP and thermal noise components. In addition, the methodology provides the classification of the isolated errors with respect to NLOS (direct signal not received) and LOS (direct signal received) received signal reception states if a fish-eye camera is also used.

Once isolated, the urban LOS/NLOS isolated multipath plus thermal noise (MN) errors on PSR and PSR-R can be characterized. The characterization adopted in this work is based on the development of MN error statistical models and the characterization of the temporal and spatial correlations of the MN errors. The statistical characterization is fundamental to further investigate the nature of MN errors and to develop PVT estimation algorithms able to mitigate the impact of MN errors and, consequently, to improve the PVT solution accuracy. The details are provided in section 5.3.

The MN isolation methodology and the MN statistical characterization have been further applied to a large experimental data campaign, whose results are proposed in Chapter 6. Moreover, the results of Chapter 6 have been exploited to design a new KF-based PVT estimator presented in Chapter 7.

5.1 LOS and NLOS MP Mitigation strategies

The urban environment presents three major impairments to the GNSS signal reception, which lead to severe degradation of PVT accuracy:

1) *Availability*: Signal availability is the primary limiting factor of the PVT accuracy. Satellites are blocked from view by buildings and the only satellites that the receiver is able to track continuously are those at high elevation. Some tests based on real measurements collected in Toulouse city area performed during this work showed an average between 6 and 7 visible satellites for GPS and 5 for Galileo, during the data campaign, section 6.2.6.
2) *Geometrical distribution*: Even with good signal availability, the position solution can suffer because of relatively poor geometrical distribution of the satellites which are tracked.

3) *Multipath*: The proximity of obstacles to the GNSS receiver in the urban environment generates close reflections (Chapter 0), that have a large impact on GNSS signal processing. Moreover, the absence of the direct LOS signal in NLOS circumstances can lead to gross errors and increased performance degradation.

The first two impairments can be partially mitigated by the employment of multi-constellation receivers: as is shown in Chapter 6, the uses of several constellations increase the satellite availability in urban environments, improving, as a consequence, also the satellite geometrical distribution.

For the third impairment, the mitigation of LOS and NLOS MP in urban environment is essential. A list of possible LOS MP and NLOS MP mitigation strategies adopted in literature are summarized, respectively, in section 5.1.1 and 5.1.2.

5.1.1 LOS MP mitigation strategies

This section summarizes the state-of-the-art GNSS LOS MP mitigation strategies. Such mitigation strategies may be split into the following groups; **signal structure design**, **antenna design**, **signal processing** and **data processing**. An extract of possible mitigation strategies, based on [85] and [86], is presented in the next paragraphs. A summary of the presented approaches is illustrated in Table 5-1.

Signal structure design, as described in Chapter 0, has an impact on the receiver MP tracking error envelope; in particular, the chip modulation characteristics (correlation function and chipping rate) can be modified to reduce the MP error. Indeed, new modulations (such as BOC modulations) have been proposed [87],[72] for modernized GNSS systems. Moreover, higher chip rates than the chip rate of GPS L1 C/A have been proposed for Galileo E5 and GPS L5 signals [87].

Antenna design is one of the most impactful approaches to reduce MP. Some examples are:

- *Polarization-sensitive antennas*: knowing that MP reflections arrive at the antenna as LHCP signals and knowing that GNSS signals are RHCP signals, to design antennas which are able to reduce the magnitude of LHCP signals is a very straightforward and effective solution to limit multipath interference.
- *Choke rings antennas*: the design is based on a series of concentric rings, mounted on a ground plane around the antenna element, to attenuate the signals with low and negative elevation, knowing that low elevation angles usually refer to reflected signals (GNSS signals come from satellites in the sky). However, this provides little protection against higher elevation reflected signals.
- *Adjustable Gain pattern antennas*: These antennas can modify in real-time the antenna gain pattern to minimise the gain in the direction of interference sources, and/or maximise the gain in the direction of the direct signal.
- *Antenna arrays*: The GNSS antenna array can be used to measure the angle of arrival (AOA) of the received signals. Where the orientation of the antenna is known, LOS and NLOS signals may be distinguished simply by comparing the direction of the measured LOS with the direction determined from the satellite ephemeris.
- *Multiple antennas*: This solution can be applied for large vehicles. Multiple GNSS antennas may be deployed on different parts of the vehicle. NLOS MP and LOS MP signals may be identified verifying the differences and the inconsistencies in the measurements which are derived from the different antennas.

Signal processing stage techniques mitigate the effects of multipath interference by modifying the discriminator design, or modifying the tracking stage structures:

- *DLL discriminator design*: this solution consists of increasing the resolution of the receiver's code discriminator, enabling the direct and reflected signal components to be separated.
- *DLL EML approach*: this solution consists of modifying the EML approach based on the comparation of the amplitude variation of the early and late correlator outputs. Where multipath interference is present, the late correlator amplitude will fluctuate more as the interference varies between constructive and destructive, due to the carrier phase variations, as presented in section 4.2.
- *FLL discriminator design*: an approach similar to DLL discriminator design could be applied to separate out the different signal components by Doppler shift, when the receiver is moving with respect to the reflectors.
- *Vector tracking:* it is a hybrid technique which combines signal tracking and position determination into a single process and can reduce the impact of multipath interference [88].

Data processing stage approaches mitigate the effects of multipath interference by modifying the PVT estimator architecture. Four different classes can be distinguished:

The first class consists of low-complexity methodologies based on the modification of basic PVT estimators:

- *Carrier smoothing*: a way to reduce the impact of multipath is the so-called carrier smoothing technique. Multipath errors in the code domain can be mitigated by filtering the code measurements with time-differenced carrier measurements or integrated Doppler-shift measurements.
- *Measurement masking*: Multipath reception may be mitigated simply by selecting a parameter screening threshold, under which the satellite measurements are automatically discarded. This is usually done selecting a threshold based on a specific elevation angle or a C/N_0 parameters; measurements at low C/N_0 or elevation angles are more susceptible to multipath. Tests in a dense urban environment have shown that C/N_0-based weighting of measurements in the navigation solution provides a more accurate position solution, on average, than elevation-based weighting [85]. These results have been confirmed by two independent experiments made during this PhD, whose results can be found in Chapter 6. However, low C/N_0 can also occur because of signal attenuation, which can be due to foliage, object masking or a null in the antenna gain pattern. On the contrary, abnormally high C/N_0 can be due to signals reflected from glass, metal, and wet surfaces which can be almost as strong as direct signals. These impairments limit the accuracy obtained with this technique.
- *Measurement weighting*: this approach consists of modifying the KF-based PVT measurement model by implementing a de-weighting strategy of the received measurements affected by multipath. This can be achieved in several ways. A first approach consists of analysing some particular received signal parameters, like the measured C/N_0 and the satellite elevation angle. The C/N_0 is normally lower for LOS MP signals. Similarly, signals from low-elevation satellites are more vulnerable to a variety of ranging errors, including LOS MP interference.

The second class consists of the design of basic PVT estimators, such as EKF, integrating other navigation technologies, based on different sensors, usually not affected by MP; this is called PVT sensor fusion:

- *Inertial Measurements Units (IMU) integration*: Inertial Units, usually composed by accelerometers and gyroscopes, are used for dead reckoning navigation. This type of devices does not suffer of atmospheric errors or signal propagation errors; therefore, INS could be integrated with GNSS to reduce the impact of MP errors.
- *Camera integration*: as per IMU integration, the real time image processing could reduce the impact of MP in urban environments since image-based navigation is not impacted by signal propagation errors.

Third class consists of mitigation techniques based on the family of Consistency Checking Techniques.

- *Consistency Checking:* consists of exploiting the KF to identify inconsistent measurements, testing different received signal combinations at the current epoch. With this technique should be possible to finally detect and exclude satellites affected by major errors. Consistency Checking could be used to identify MP reflections: if the position solutions are computed using combinations of signals from different satellites, those obtained using only the LOS MP-free signals should have a better accuracy than those that include multipath and LOS MP measurements.
- *Integrity Monitoring*: It is the same methodology that is applied for the fault detection in the Receiver Autonomous Integrity Monitoring (RAIM).
- *Innovation Filtering*: This technique operates on the same principle as consistency checking. The key difference being that the consistency of current measurements and previous measurements is checked. It is used to compare new measurements against predictions of those measurements from the time-propagated navigation solution. Measurements that are inconsistent with their predicted values are rejected.

The last class of techniques is based on the substitution of the basic PVT estimators with more complex and innovative estimation techniques. GNSS positioning problems are usually solved using the estimation methodologies based on LSE and KF techniques, see section 3.2.3.2.2. These two types of estimators are optimal only if the measurement error components can be accurately modelled as Gaussian random variables [89] and assuming state and measurement linear models. The assumption of Gaussianity could not fit perfectly the nature of the real measurement errors; this is the case for MP errors. Therefore, classic KF might be substituted by others estimators, which handle non-linearities and non-Gaussian distributions, in order to exploit directly the statistical knowledges of multipath errors. Two examples are:

- *Sigma Point Kalman Filter (SPKF)*: can provide better approximation to the nonlinearities and handle generic error distributions (with limitations) through deterministically selected sigma points; the most famous is the Unscented Kalman Filter;
- *Particle Filter* (PF): can better handle both the system nonlinearities and the state vector posterior density assumption through the truly random sample particles.

Processing Stage	Approach	Technique
Signal architecture	Chip modulation Design	BOC
		Increase of chipping rate
Hardware	Antenna Design	Dual polarization
		Choke Rings
		Adjustable Gain pattern antennas
		Angle of Arrival (AOA) measurements
		Multiple Antennas
Signal Processing	Receiver Processing Design	Code Discriminator Design
		Early-Late Correlator Comparison
		FLL discriminator design
		Vector Tracking
Data Processing	PVT Weighting Model	C/N_0 based weighting model
		Satellite elevation-based weighting model
		Doppler Domain Multipath Mitigation
		Carrier Smoothing
	PVT Sensor Fusion	PVT aided by Inertial Measurement Unit and/or other sensors
		PVT aided by Cameras
	Consistency checking	RAIM
		KF-based innovation filtering
	Statistical Approaches	Sigma Point Kalman Filter
		Particle Filter

Table 5-1 – Classification of the GNSS Multipath Mitigation Approaches

5.1.2 NLOS estimation and mitigation strategies

Some of the MP mitigation techniques presented in section 5.1.1 may only be effective in the case of LOS MP where the direct signal is received. Another important step to improve the PVT solution accuracy in urban environments is the ability to detect the NLOS condition. Once NLOS is detected, it may also be possible to correct NLOS MP error. Recently, several works in the literature have treated the detection and the correction of NLOS in urban environment, [90]-[91]. Two different groups can be identified:

The first group consists of the detection of NLOS signals and the consequent exclusion from the position computation. Ignoring NLOS satellites can improve positioning accuracy. Unfortunately, excluding satellites

degrades the geometrical configuration, commonly represented by the DOP, leading to a less accurate position estimation. In addition, if the number of satellites used in the PVT computation is too limited, the PVT estimation becomes unavailable.

Therefore, the second group consists of the detection of NLOS signals and the consequent correction and exploitation in the PVT estimator algorithms to improve the solution's accuracy.

The most influential techniques are summarised in Table 5-2 and introduced in the next paragraphs.

- **Antenna design** [90]: antennas that have the capacity to measure the angle of arrival of signal components allow NLOS and direct-LOS signals to be distinguished simply by comparing the measured lines of sight with those determined from the satellite ephemeris data. The PVT estimators can exploit this information to discriminate LOS and NLOS and exclude the last signal.
- **Data processing stage:**
    - A low-complexity method in [92] is based on a LOS\NLOS discrimination through the application of a C/N_0 threshold chosen according to empirical models. This method can guarantee only an approximated classification of NLOS and LOS.
    - More complex techniques are based on the use of 3D city models. For example, in [93], to determine and exclude NLOS signals it is exploited a 3D data model of the environment based on cartography and elevation maps in order to identify NLOS signals by ray-tracing.
    - Consistency checking mechanisms may be used to detect NLOS measurements, although their success depends upon the number of NLOS measurements. Techniques such as RAIM rely on the assumption that a low number of measurements are biased.
- **Sensor fusion:**
    - In [92] a vision-based method is applied. This consists of using a panoramic camera able to generate a picture of the environment surrounding the receiver and a real-time image processing able to detect obstacles and determine LOS and NLOS state of receptions.
    - Recent works have substituted a panoramic camera with a fisheye camera. Therefore, NLOS discrimination is based on the application of image processing techniques able to verify the presence of the direct path between the satellite and the receiver looking for the satellite and potential blocking obstacles. Different image processing algorithms have been developed, based on the segmentation of the pictures depending on specific characteristics:
        - In [94] colour image obtained from the fish-eye camera is segmented, in order to detect sky and obstacle areas. To distinguish the pixel associated to the sky elements and the pixel associated to non-sky elements, they measure in parallel a theoretical C/N_0 for LOS signals in open-sky environment. They apply a strategy of NLOS satellite rejection for the final localization.
        - In [95], a grey-scale sky-pointing fisheye camera and the C/N_0 receiver estimation is used to determine LOS/NLOS satellites. This method is based on the so-called canny edge segmentation and a flood fill operation to detect the sky area in the pictures, jointly to a C/N_0 threshold, above which the signal is estimated as LOS satellite with higher probability.
        - Authors of [96] evaluate different picture segmentation methods for detecting sky and non-sky areas in sky-facing images. They use a colour ultra-wide-angle camera with a 90° field of view. The methodology applied in this work is similar to the one proposed in the previous works. The satellites positions are projected into the images in order to determine the LOS/NLOS receiver reception state through an image processing methodology.

NLOS exploitation:

Authors of [97] and [98] use a measurement de-weighting approach within the KF PVT algorithm to improve the position estimation, taking into account LOS or NLOS status of the signals. The LOS/NLOS satellites are determines using the fisheye real-time image processing method presented in [99]. On the contrary, authors in [100] weight the contribution of NLOS signals in the position computation according to the C/N_0, identified using the fisheye vision-based method of [99].

A more complex approach is presented in in [91]. It is called the Shadow Matching technique. The technique consists in testing a set of different possible likelihood positions around the initial GNSS position that is computed. Therefore, for each received signal, the goal is to use the 3D model and ray-tracing to describe areas where the satellite might be LOS, NLOS or Blocked. The test is done by correlating the reception state of each satellite

estimated from the model with real C/N_0 measurements. The candidate position with the best score is considered as the final estimated position.

Goal	Processing Stage	Technique
NLOS estimation	Antenna Design	AoA estimation [90]
	Data Processing	C/N_0-based threshold [92]
		Elev. angle-based threshold [92]
		Ray tracing with 3D Models [93]
	Sensor Fusion	Real time Camera Image processing [92], [94], [95], [96]
		Ray trancing with 3D Maps [93]
NLOS exploitation	Data Processing	KF LOS/NLOS-based weighting models [97], [98]
		Shadow Matching [91]

Table 5-2 – Classification of the GNSS NLOS Multipath Mitigation Approaches

5.2 LOS/NLOS MP plus Noise (MN) Isolation

The spread of the low-cost GNSS receiver market and the necessity of localization/navigation applications in urban environment in recent years, necessitates methodologies which can effectively handle the MP reflection problems of the urban environment, without increasing the costs unsuitable for the mentioned market segment. At the time of this PhD writing, many of the MP mitigation strategies summarised in section 5.1 are too expensive for low-cost applications. This is the motivation to develop a methodology for the isolation of MN error statistics for PSR and PSR-R (in post-processing mode) to firstly understand better the source of error, its dependencies and correlation properties. The detailed motivations behind this methodology have been further developed in section 5.2.1. The multipath plus noise (MN) error isolation, from PSR and PSR-R is described in section 5.2.2. Finally, the proposed LOS/NLOS MN discrimination strategy is explained in section 5.2.3.

5.2.1 Motivations

Recent years have seen a large contribution in the scientific community of the development of MP error estimation, characterization and mitigation strategies, predominantly developed for high-accuracy GNSS applications, and tuned for specific configurations of MP environment and GNSS receiver dynamics. A summary has been proposed to the reader in section 5.1.1. The application of a large range of these strategies could not be exploited for low-cost navigation applications in urban environment based on the use of mass-market receivers, for several reasons:

- The designed hardware is expensive for low-cost applications;
- The designed software is resource-demanding, which limits its applicability to mass-market receivers;
- The developed strategy is targeted to a certain kind of MP environment and does not perform accurately in other environments, which limits the benefits of such a methodology in the urban environment;
- The developed strategy has remarkable results if applied to receiver with well-known dynamics (i.e. static, airplanes, boats), yet underperforms in case of a dynamic receiver, in urban environment, usually characterized by a large range of dynamics.

Some considerations can be made for the MP mitigation methodologies presented in section 5.1.1:

Chip Modulation: The treatment of modernized chip modulations is already a standard feature of professional grade GNSS receivers. Simple BOC(1,1) chip modulation have been already introduced in the low-cost GNSS receivers. A reduction in production costs could result in the integration of receiver signal processing channels dedicated to the reception and the elaboration of the modernized signals in mass-market receivers in the following years.

Antenna design: GNSS applications employing mass market receivers usually do not exploit complex antenna designs or antenna arrays, since the cost and size are prohibitive. The polarization-sensitive antennas are the standard equipment for the professional GNSS receivers; the patch antennas, usually used for low-cost applications, such as micromobility vehicle navigation have a limited polarization sensitivity; finally, the antenna used for smartphone and wearable devices are linearly polarized, so are equally sensitive to direct and reflected signals (RHCP and LHCP signals). Also, choke-ring antennas are too large for most dynamic positioning applications. Adjustable Gain pattern and AoA antenna systems are, nowadays, relatively large and expensive.

Signal processing: Multipath-resistant code discriminator designs are already a standard feature of professional grade GNSS receivers. However, to implement them on consumer-grade receivers would increase the manufacturing cost and power consumption. The same considerations are applicable to Doppler Domain Multipath Mitigation and Vector tracking, which require a much more complex receiver design, increasing the cost and power consumption.

Data processing: Carrier smoothing is difficult to be applied in urban environment due to the frequent occurrence of cycle slips, which affects the carrier measurements.

Measurement masking is already a standard feature of consumer-grade receivers due to the low complexity implementation. Moreover, measurement de-weighting is largely applied to low-cost receiver PVT estimators. However, the efficiency of such solutions depends on the appropriateness of the measurement error models. Regarding the MP error models, usually empirical models have been developed for specific MP environment configurations (i.e. static receiver in open area environment, applied for geomatic applications). This is a limiting factor if the PVT estimator should be applied on a variable MP environment, such as urban environment. Hence, to increase the accuracy of PVT solutions it is necessary to accurately model the measurement error distributions.

Moreover, consumer-grade receivers integrating at least an inertial measurement unit (IMU) and GNSS signal processing units are becoming the fundamental baseline platforms. Due to low availability in urban/indoor scenarios as well as poor GNSS measurement performance in urban canyons due to multipath phenomenon, these hybrid systems still rely on GNSS measurements for correcting IMU errors; in other words, even in this case the necessity to model accurately the measurement error distributions is fundamental to reaching high positioning accuracy.

Measurement masking, de-weighting and PVT hybridization can be applied together to reach a better PVT accuracy level and are becoming standard feature of consumer-grade receivers as explained along this section. However, these three techniques require GNSS error characterization to be conducted or to be conducted with high accuracy. Hence, properly characterizing the GNSS position errors is essential to improve accuracy of navigation solutions in the urban environment.

In light of the above, the objective of the proposed approach in section 5.2.2 is to provide a post-processing methodology to derive highly realistic model of the Multipath errors in an urban and sub-urban environment based on measurement error modelling approach (in particular regarding the PSR and PSR-R measurements). Unfortunately, the proposed isolation approach is not able to differentiate MP error from thermal noise error. Therefore, the resulting output is a joint MP and thermal noise (MN) isolated error.

The main advantage of the proposed approach comes from the possibility to characterize MN errors in urban environments as a function of some basic parameters, such as C/N_0 and/or satellite elevation angle which can be directly integrated and exploited by the PVT estimator with a negligible increase of algorithm complexity. Details about the error characterization and PVT error model integration are provided, respectively, in section 5.3 and Chapter 7.

A limitation of the MN characterization process is the difficulty in obtaining perfect discrimination between LOS MP and NLOS MP characterization. In the ideal case, the LOS reception and NLOS reception conditions should be treated differently within the PVT algorithm, since the characteristics of the resulting errors are different, as defined in Chapter 0. Introducing different assumptions for the two conditions within the positioning algorithm results could improve the accuracy of the PVT solutions [85]. Therefore, the fish-eye camera-based techniques described in section 5.1.2, have inspired in this PhD an efficient post-processing methodology used to classify the PSR and PSR-R multipath error components, with respect to the LOS and NLOS received signal conditions.

Real-time LOS/NLOS discriminators proposed in the literature are resource-demanding and must be integrated in complex PVT estimators, which make them inaccessible to low-cost systems. On the contrary, post-processing discrimination could help to classify the LOS/NLOS signal reception states and further characterize them by

specific received signal parameter values, which can be directly exploited in a simple standalone PVT estimator architecture. This method can guarantee a better classification of NLOS and LOS and improved MP characterization accuracy with respect the low-cost approach presented in [92].

The proposed LOS/NLOS discriminator methodology belongs to the measurement domain error models family. It is composed by three sequential blocks, as described in Figure 5-1 [101]. First, the MN error isolation method is applied. The MN error is isolated from L1 band dual constellation (GPS\Galileo) PSR and PSR-R measurements. Second, a MN error classification based on the LOS/NLOS characterization of the MN error component is adopted. The classification algorithm consists in an upward-looking fish-eye camera and specific image-processing software allowing to separate the satellite signals received in LOS and NLOS conditions. Finally, a MN error characterization process is conducted based on the statistical approach, assuming that both MP and thermal noise error components are generated by an ergodic random process.

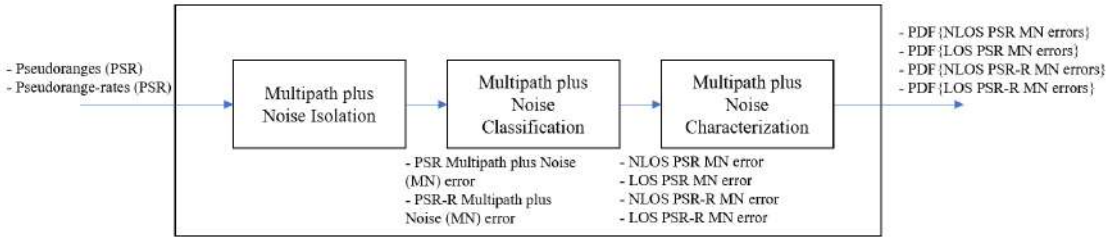

Figure 5-1 – Statistical Multipath and Noise Isolated Characterization

5.2.2 MN Error Isolation

This section presents the theoretical fundamentals of the MN error isolation methodology. The raw PSR measurement obtained by a user receiver from satellite i has been modelled in 3-30 as:

$$\rho^i = R^i + b_r - b^i + I^i + T^i + \xi^i + \beta_r + \beta^i + \eta^i$$

Similarly, the raw PSR-R measurement, computed by the receiver for a given satellite i, has been modelled in 3-31 as:

$$\dot{\rho}^i = \dot{R}^i + \dot{b}_r - \dot{b}^i + \dot{I}^i + \dot{T}^i + \zeta^i + \dot{\beta}_r + \dot{\beta}^i + \nu^i$$

The proposed method consists in isolating, as best as possible, the multipath error components, ξ^i and ζ^i, from the other measurement error terms. However, the estimator cannot discriminate multipath error component from residual thermal noise, η^i and ν^i; therefore, the isolation method consists of the joint multipath and thermal noise estimation errors, called multipath plus thermal noise error component (MN). This methodology has been inspired from the DGNSS correction approach, described in section 3.2.2.2. An alternative approach based on the use of the code-minus-carrier observable was rejected due to the need to remove the mean error value and thus an inability to identify NLOS errors.

This procedure can be applied individually to GPS and Galileo constellation without any particular modification. However, the proposed methodology can be also adapted for dual constellation applications. In this thesis, single constellation GPS L1 C/A and Galileo E1 OS and, consequently, dual constellations multipath isolation is performed.

The main interest in using measurements from different constellations is to improve the clock bias estimation by increasing the availability of good-quality measurements (see Chapter 6). This improvement is significant in urban environments where the reception of NLOS signals is considerable and the number of observed LOS satellites is reduced. This is particularly relevant for Galileo, since the number of healthy satellites is lower than GPS (at the time of data collection, the Galileo constellation was still under deployment). In fact, taking only into account the Galileo constellation, there are often no LOS satellites available for a given time epoch, as was observed during the conducted data campaign. Therefore, it is impossible to obtain a precise and continuous clock bias estimate using Galileo only measurements.

However, there is an additional issue to be considered: the presence of receiver processing differences between GPS and Galileo which lead to inconsistency between the GPS and Galileo PSR and PSR-R measurements. This inconsistency does not allow the direct application of the same MP isolation methodology for the two constellations. Indeed, the difference between GPS and Galileo measurements introduced by the different receiver signal processing stages as well as the difference between the clock bias terms must be estimated and removed. Once it is removed, the GPS and Galileo measurements are consistent and can be jointly processed.

The section is structured as follows. First, the single constellation MN error isolation, individually applicable to both GPS and Galileo measurements, is depicted in section 5.2.2.1. Second, in the subsection 5.2.2.2 the method to adapt the isolation multipath methodology from single constellation to dual constellation is presented.

5.2.2.1 Single constellation MN Error Isolation method

The procedures employed for the removal of the different error terms are depicted in Figure 5-2. The different steps are commented here briefly and a more detailed explanation, as well as the mathematical modelling and the objective, are provided in the following subsections. First of all, the satellite-to-receiver range, R^i, can be easily subtracted if the receiver and satellite position are known. The range should be estimated and then removed from the PSR measurement. The same approach could be used to remove the satellite-to-receiver range-rate, $\dot{R}^i$, from the PSR-R measurement if the receiver and satellite velocity are known. This operation is performed computing the true geometrical range and range-rate and removing the estimated range from the PSR and PSR-R measurements. This step is called True Range component removal.

The second step is the removal of all atmospheric and satellite-dependent elements. It can be obtained by differencing the measurements with the measurements of a nearby reference station, since the atmospheric effects are highly spatially (and temporal) correlated and the satellite clock error is satellite dependent, whereas the MN error is not. To apply this differential operation, initially the PSR and PSR-R reference station errors should be isolated from the true measurements applying the same operation, true range/range-rate removal, applied above for the user receiver. The result of the differencing block is called PSR/PSR-R differential residuals.

Finally, the receiver clock and hardware biases/drifts can be estimated and removed from the differential residual components in order to isolate the multipath error component. This is possible since clock and hardware biases are characterized by strong temporal correlation, (section 3.2.1.1.1), much longer than the time correlation of the MN error component.

The section is structured as follows. The satellite-to-receiver range removal is described in subsection 5.2.2.1.1. The differential approach, between the user receiver measurements and the reference station measurement is presented in 5.2.2.1.2. Afterward, the estimation of clock error component and isolation from multipath and residual thermal noise are described in 5.2.2.1.3.

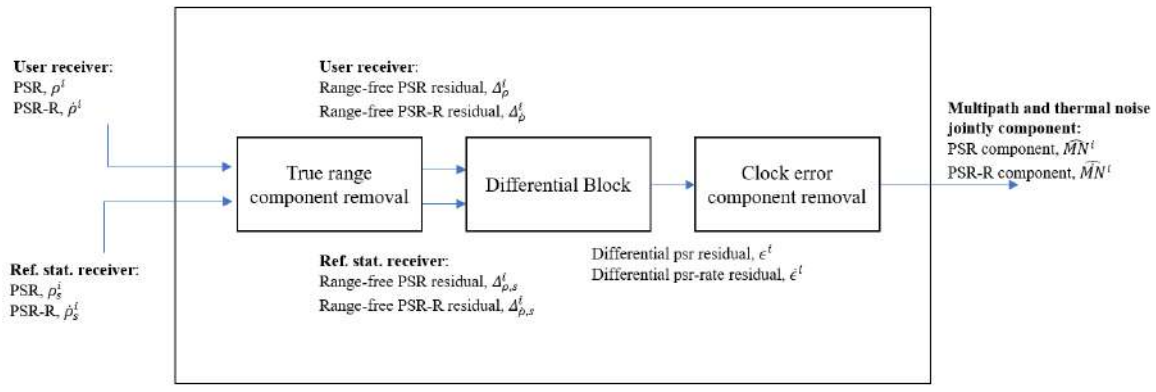

Figure 5-2 – Single Constellation MN Isolation Block

5.2.2.1.1 True component removal

The first block of the multipath error component isolation method is the true range component removal. The goal is to obtain measurement residuals which contain only the measurement error terms, also called range-free residual (per satellite).

This residual can be easily determined in the case of PSR measurement by differencing the true receiver-to-satellite range component (also called effective range), and the PSR measurement, as described in 5.2.2.1.1.1, and in the case of PSR-R measurement by differencing the true receiver-to-satellite range-rate component and the PSR-R measurement, as described in 5.2.2.1.1.2.

5.2.2.1.1.1 Range-free PSR Residual

The Range-free PSR residual may be obtained from the user and reference station antenna phase centre positions. This is relatively straightforward for the reference station. In the case of the receiver a high precision system to provide the accurate user location even in an urban environment is used in this work as while be detailed later on for the data collection.

For a receiver in a known location, $[p_x, p_y, p_z]$, it is possible to precisely estimate the true receiver-to-satellite i range as:

$$\begin{aligned} \Delta_{\rho}^{i} &= \rho^{i} - \hat{R}^{i} \\ \Delta_{\rho}^{i} &= e^{i} + b_r - b^{i} + I^{i} + T^{i} + \xi^{i} + \beta_r + \beta^{i} + \eta^{i} \end{aligned} \quad \text{5-1}$$

where e^i is the residual error projected in the PSR domain due to the satellite i position estimation error, as already introduced in section 3.2.2.2.2.

The same can be done to obtain range-free reference station PSR residuals (see equation 5-2):

$$\begin{aligned} \Delta_{\rho,s}^{i} &= \rho_{s}^{i} - \hat{R}_{s}^{i} \\ \Delta_{\rho,s}^{i} &= e_{s}^{i} + b_s - b_{s}^{i} + I_{s}^{i} + T_{s}^{i} + \xi_{s}^{i} + \beta_s + \beta_{s}^{i} + \eta_{s}^{i} \end{aligned} \quad \text{5-2}$$

5.2.2.1.1.2 Range-free PSR-R Residual

True range component removal, is also applied to the user's range rate-free PSR-R residual (per satellite i). It is equal to:

$$\begin{aligned} \Delta_{\dot{\rho}}^{i} &= \dot{\rho}^{i} - \hat{\dot{R}}^{i} \\ \Delta_{\dot{\rho}}^{i} &= \dot{e}^{i} + \dot{b}_r - \dot{b}^{i} + \dot{I}^{i} + \dot{T}^{i} + \zeta^{i} + \dot{\beta}_r + \dot{\beta}^{i} + \nu^{i} \end{aligned} \quad \text{5-3}$$

where $\dot{e}^i$ is the residual error projected on the PSR domain due to the satellite i velocity estimation error.

The same approach can be applied to obtain reference station's range rate-free PSR-R residuals (see equation 5-2):

$$\begin{aligned} \Delta_{\dot{\rho},s}^{i} &= \dot{\rho}_{s}^{i} - \hat{\dot{R}}_{s}^{i} \\ \Delta_{\dot{\rho},s}^{i} &= \dot{e}_{s}^{i} + \dot{b}_s - \dot{b}_{s}^{i} + \dot{I}_{s}^{i} + \dot{T}_{s}^{i} + \zeta_{s}^{i} + \dot{\beta}_s + \dot{\beta}^{i} + \nu_{s}^{i} \end{aligned} \quad \text{5-4}$$

5.2.2.1.2 Measurement Differential Block

The second step of the proposed method consists in removing the impairments from the vehicle receiver PSR/PSR-R residual which are common to the reference station ones:

- satellite clock error;
- satellite hardware bias;
- ionospheric error;
- tropospheric error.

This is exactly the same approach applied during the DGNSS correction, section 3.2.2.2.1.

The PSR differential residual is presented in section 5.2.2.1.2.1. The PSR-R differential residual is illustrated in section 5.2.2.1.2.2.

5.2.2.1.2.1 PSR measurement

The satellite clock bias and the atmospheric effect biases removal from PSR measurement is achieved by differencing the user's range-free PSR residual, Δ^i, from the reference station's range-free PSR residual, Δ_s^i, as presented in equation 3-63.

$$\epsilon^i = \Delta^i - \Delta_s^i = \\ = (b_r - b_s) + (e^i - e_s^i) + (\xi^i - \xi_s^i) + (\beta_r - \beta_s) + (I^i - I_s^i) + (T^i - T_s^i) + (\eta^i - \eta_s^i) \quad \text{5-5}$$

The resulting term, ϵ^i, is denoted as the differential PSR residual and is composed by seven components:

- the vehicle-reference station receiver clock difference, $(b_r - b_s)$;
- the residual error due to the satellite position estimation error, induced by the broadcast ephemeris, projected on the PSR domain, $(e^i - e_s^i)$;
- the difference of the user receiver and the reference station multipath error component, $(\xi^i - \xi_s^i)$;
- the difference of the receivers' bias hardware terms, $(\beta_r - \beta_s)$;
- the residual ionospheric error, $(I^i - I_s^i)$;
- the residual tropospheric error, $(T^i - T_s^i)$;
- the difference of the user receiver noise, η^i and the reference station receiver noise, η_s^i.

The multipath error component experienced by the test receiver, ξ^i, is much greater than that experienced by the reference receiver, ξ_s^i, due to the signal reception environment and the receiver quality. Therefore, the PSR multipath component residual difference can be considered to be dominated by the receiver multipath component error.

Similarly, the thermal noise component experienced by the reference receiver, η_s^i, could be considered negligible with respect to the multipath and noise experienced by the test receiver, η^i; reference station should use a high-end receiver (large RFFE equivalent bandwidth, small correlator chip spacing, d_c, double delta discriminator) whereas the user is assumed to use a low-cost receiver (smaller RFFE equivalent bandwidth, larger correlator spacing, d_c, EMLP discriminator).

The residual ephemeris errors difference, $e^i - e_s^i$, are negligible with respect to the multipath error experienced by low-cost receiver in urban environment.

The receiver and satellite hardware bias varies slowly during the measurement campaign and are removed by a detrending approach. Moreover, the vehicle-reference station receiver clock difference, $b_r - b_s$, and the receivers' bias hardware term, $\beta_r - \beta_s$ are estimated together as a unique term called the clock bias term, bh_r^s.

Ionospheric and tropospheric residual errors could be considered negligible providing that the distance between the user receiver and the reference station is lower than 10 Km [45].

Applying the assumptions described above, equation 3-63 can be simplified into:

$$\epsilon^i \approx bh_r^s + \xi^i + \eta^i = bh_r^s + MN^i \quad \text{5-6}$$

where the MP component error and the thermal noise component error on the PSR measurement have been jointly described by MN^i.

5.2.2.1.2.2 PSR-R measurement

The satellite clock bias and the atmospheric bias removal from PSR-R measurement is obtained in the same way as described in 5.2.2.1.2.1 for PSR measurements. The removal is achieved by differencing the user range rate-free measurement $\dot{\Delta}^i$ from the range rate-free reference station PSR-R residual $\dot{\Delta}_s^i$ as presented in equation 3-63.

$$\dot{\epsilon}^i = \dot{\Delta}^i - \dot{\Delta}_s^i = \\ = \left(\dot{b}_r - \dot{b}_s\right) + (\dot{e}_r^i - \dot{e}_s^i) + \left(\dot{I}_r^i - \dot{I}_s^i\right) + \left(\dot{T}_r^i - \dot{T}_s^i\right) + (\zeta^i - \zeta_s^i) + \left(\dot{\beta}_r - \dot{\beta}_s\right) + (\nu^i - \nu_s^i) \quad \text{5-7}$$

The resulting term, $\dot{\epsilon}^i$, is denoted as the differential PSR-R residual and is dominated by seven factors:

- the vehicle-reference station receiver clock drift difference, $\left(\dot{b}_r - \dot{b}_s\right)$;
- the residual error due to the satellite velocity estimation error, induced by the broadcast ephemeris, projected in the PSR-R domain, $(\dot{e}_r^i - \dot{e}_s^i)$;
- the residual ionospheric drift, $\left(\dot{I}_r^i - \dot{I}_s^i\right)$;

- the residual tropospheric drift, $\left(\dot{T}_r^i - \dot{T}_s^i\right)$;
- the difference of the user receiver and the reference station multipath rate error component, $(\dot{\zeta}^i - \dot{\zeta}_s^i)$;
- the difference of the receivers' hardware drift terms, $\left(\dot{\beta}_r - \dot{\beta}_s\right)$;
- the difference of the user receiver noise, $\dot{v}^i$ and the reference station receiver noise, $\dot{v}_s^i$.

In the case of PSR-R residual difference it is assumed that:

- the multipath rate error of the test receiver is much greater than of the reference receiver (due to the signal reception environment and the receiver quality), thus, the PSR-R residual difference can be considered to be dominated by the receiver multipath component error;
- the residual ephemeris errors difference is negligible relative to the receiver multipath error;
- the vehicle-reference station receiver clock drift difference, $\dot{b}_r - \dot{b}_s$, and the receivers' hardware drift term, $\dot{\beta}_r - \dot{\beta}_s$, are estimated together as a unique term called clock bias term, $\dot{bh}_r^s$;
- the receiver hardware drift can be considered negligible during the measurement campaign;

The differential PSR-R residual can be simplified into (5-8) as justified in [1]:

$$\dot{\epsilon}^i \approx \dot{bh}_r^s + \dot{\zeta}^i + \dot{v}^i = \dot{bh}_r^s + \dot{MN}^i \qquad 5\text{-}8$$

where the MP component error and the thermal noise component error on the PSR-R measurement have been jointly described by $\dot{MN}^i$.

5.2.2.1.3 Receiver Clock error removal

The last step of the proposed multipath error component isolation method consists in isolating each individual multipath and thermal noise component, MN^ior $\dot{MN}^i$, inside the residual difference term, ϵ^i or $\dot{\epsilon}^i$, from the clock bias\drift terms, bh_r^s or $\dot{bh}_r^s$. The isolation process is conducted by estimating the clock error term from the residual difference terms and finally removing the estimated clock bias term, from each PSR\PSR-R residual difference.

The process of isolation from PSR differential residual is described in section 5.2.2.1.3.1, while the process of isolation from PSR-R differential residual is described in section 5.2.2.1.3.2.

5.2.2.1.3.1 PSR MN isolation

The isolation process is an iterative process which consists of two macro stages:

1. To estimate bh_r^s from the PSR residual difference terms;
2. To remove (subtracting) the estimated clock bias term, $\widehat{bh_r^s}$, from each PSR residual difference, ϵ^i, to finally estimate the multipath and noise component, $\widehat{MN}^i$.

The final residuals, $\widehat{MN}^i$, are re-processed in order to refine the final output, until the estimated clock bias term, $\widehat{bh_r^s} \approx 0$. The detailed block-diagram of the isolation process is summarized in Figure 5-3.

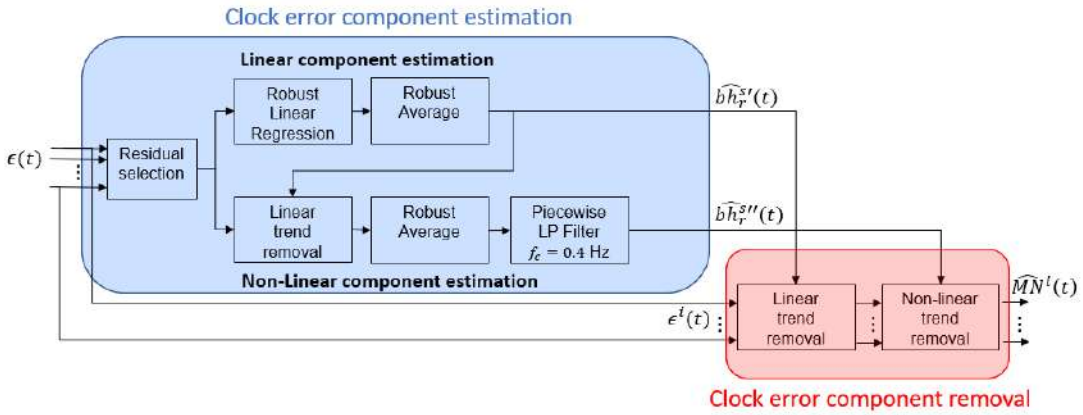

Figure 5-3 – Schematic of PSR MP error isolation from the residual containing MP error, clock bias term and thermal noise term

The first block consists in the estimation of clock error term. First of all, it is fundamental to define the clock error component model as:

$$bh_r^s(t) = bh_r^{s\prime}(t) + bh_r^{s\prime\prime}(t) \quad 5\text{-}9$$

where:

- $bh_r^{s\prime}$ is the linear component, due to the slow variations, relative to bh_r^s;
- $bh_r^{s\prime\prime}$ is the non-linear component, due to the fast variations, relative to bh_r^s.

Considering the presented decomposition, the proposed estimation process consists thus of two sequential processes; first, the estimation of the linear component and afterwards, the estimation of the non-linear one. Both estimation processes are performed only on a subset of the overall calculated residual differences which are designated by a selection process. The motivation behind only using a residual difference subset is presented next. The receiver clock error component is a receiver-dependent error and thus, it has the same value in all PSR residual difference terms at the same epoch t, $\boldsymbol{\epsilon}(t)$; on the contrary, the multipath error and thermal noise components are satellite dependent. Therefore, in order to reduce the impact of the receiver noise and multipath error components, mainly NLOS signals, on the clock bias term estimate, only "good-quality" satellite measurements must be used to estimate the clock error component. This "good-quality" satellite measurements identification is achieved in this work by selecting only healthy and LOS satellites, where such a chosen subset is characterized by a high level of C/N_0; experimental results in Chapter 6 demonstrates a correlation between high C/N_0 and LOS reception state.

For this reason, the residual difference selection method consists in selecting satellite signals fulfilling the following characteristics: satellite i signal characterized by a C/N_0 higher than 35 dB-Hz (section 6.2.5), and constantly present over a 20 seconds sliding window.

Afterwards, the selected PSR residual differences are exploited to make the individual estimation of the linear (section 5.2.2.1.3.1.1) and non-linear (section 5.2.2.1.3.1.2) bh_r^s components.

5.2.2.1.3.1.1 Linear component estimation

The bh_r^s linear component estimation is based on two sequential processes: individual linear estimation and averaging process. This approach is based on the assumption that the linear component of residual difference, $\epsilon'(t)|_i$, of any satellite i can be directly approximated to $bh_r^{s\prime}$, since bh_r^s has slow variations in time with respect to the MN error component.

Individual Linear component estimation: It consists of individually estimating the linear components, $\widehat{bh_r^{s\prime}}(t)\big|_i$, from the selected residual difference error, $\boldsymbol{\epsilon}^i$, of satellite i. Individual linear components are estimated applying a linear regression to any time epochs. The linear regression is obtained by estimating $b_0 b_1 \epsilon^i(t)\ \hat{\epsilon}'(t)|_i$

$$\hat{\epsilon}'(t)|_i = b_0 + b_1 x(t) \approx \epsilon'(t)|_i \quad 5\text{-}10$$

where $x(t)$ is the vector of the time epochs. Hence, the estimated $\widehat{bh_r^s}'(t)\big|_i = \hat{\epsilon}'(t)|_i$.

Averaging process: Since the bh_r^s error component is common to all the selected residual differences, in order to reduce the impact of the receiver noise and multipath error components on the clock bias term estimate, a robust average of the selected residual differences, $\widehat{bh_r^s}'(t)\big|_i$is performed. This is obtained removing 50% of the outliers at each time epoch, similar to taking the median of the residual set:

$$\widehat{bh_r^s}'(t) = \frac{1}{N(t)} \sum_{i \neq outliers(t)} \widehat{bh_r^s}'(t)\big|_i \quad 5\text{-}11$$

where $N(t)$ in this case is the number of residuals exploited after outlier's removal.

5.2.2.1.3.1.2 Non-Linear component estimation

Once the linear component of the clock term has been estimated, the non-linear component can be estimated. This is obtained applying the three following steps:

Linear trend removal: the first step is the linear trend removal from the selected measurements. This is obtained differencing the selected residuals with the linear component estimation, $\widehat{bh_r^s}'(t)$. The result is the estimation of the clock term non-linear component of each satellite i, $\widehat{bh_r^s}''(t)\big|_i$:

$$\widehat{bh_r^s}''(t)\big|_i \approx bh_r^s{}'(t) + bh_r^s{}''(t) - \widehat{bh_r^s}'(t) + MN^i(t) = \widetilde{bh_r^s}'(t) + bh_r^s{}''(t) + MN^i(t) \quad 5\text{-}12$$

where $\widetilde{bh_r^s}'$ is the residual linear component clock term resulting from the linear trend removal. If the linear estimation is accurate, $\widetilde{bh_r^s}'$ can be approximated to 0.

Averaging process: The second step consists of averaging the estimated second order residuals, $\widehat{bh_r^s}''(t)\big|_i$, applying a robust linear estimation to any time epochs, as already adopted for the linear estimation, 5-11.

$$\widehat{bh_r^s}''(t) = \frac{1}{N(t)} \sum_{i \neq outliers(t)} \widehat{bh_r^s}''(t)\big|_i \quad 5\text{-}13$$

This raw estimation, however, cannot be a representative estimation of the non-linear clock term, $\widehat{bh_r^s}''(t)$, because of the following issues:

- The averaging process is subject to the time-variant number of measurements processed after measurement selection. If a satellite measurement is suddenly selected or filtered out by the selection process for that specific time window, then the averaging process can present an unwanted bias in correspondence of that time window.
- In urban environment, the set of selected residuals usually consists of a limited number of measurements. For this reason, if a non-outlier residual, which has been processed by the averaging process, presents a non-negligible bias with respect to the average of the other selected measurements due to a higher MN error component, this residual can influence further the accuracy of the final average estimation than it would in the case that more measurements were available.

An example of non-linear estimated clock term is provided in Figure 5-4. The black curves are the selected residuals after the linear trend removal, $\widehat{bh_r^s}''(t)\big|_i$, before the averaging process. The blue curve represents the non-linear clock term estimation applying the average as expressed above, $\widehat{bh_r^s}''(t)$. The red curve is the non-linear estimated clock term estimated by U-Blox M8T receiver used to make this test. The average presents some unwanted peaks which differs from the estimation provided by U-Blox receiver.

Low-pass filtering: To avoid the issues presented above, the averaged term, $\widehat{bh_r^s}''(t)$ has been split into piecewise continuous sections of 10 seconds and consequently it has been applied a low-pass filtering operation to any sections, with a frequency cut-off empirically selected at 0.4 Hz (Figure 5-5). The split in continuous section has been applied to reduce the impact of discontinuities due to the outlier rejection. The filtering process is applied to

reduce the unwanted impact of MN error components on the estimation, assuming that non-linear clock error component has slower variations than MN errors.

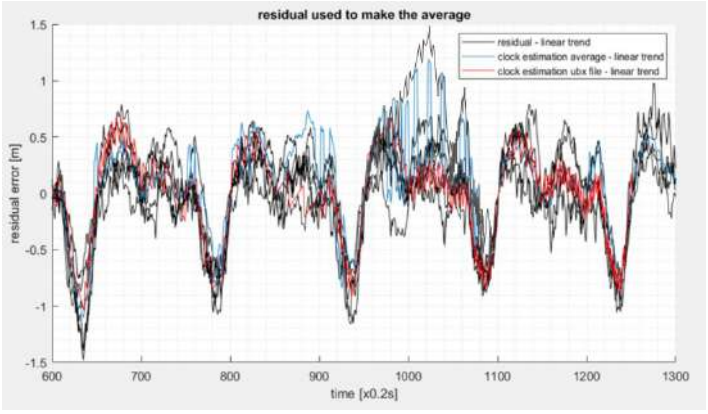

Figure 5-4 – Comparison between non-linear estimated clock term applying averaging process and U-Blox M8T non-linear clock term estimation

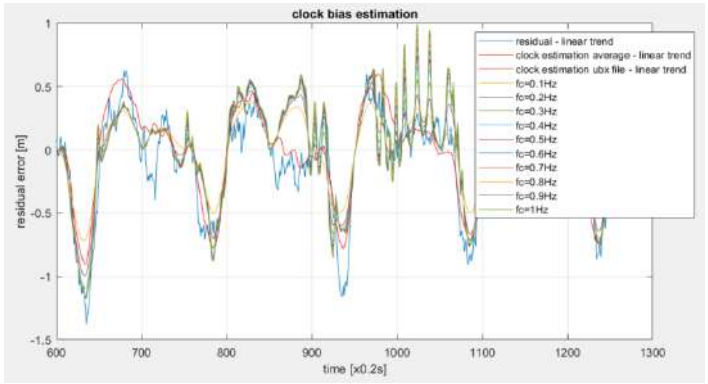

Figure 5-5 – Comparison between non-linear estimated clock term after low-pass filtering process and U-Blox M8T non-linear clock term estimation

5.2.2.1.3.1.3 Clock error removal

Once the linear and non-linear clock error estimations have been determined, the resulting clock error estimation, $\widehat{bh_r^s}(t) = \widehat{bh_r^s}'(t) + \widehat{bh_r^s}''(t)$, is removed from the residual, $\epsilon^i(t)$, in order to estimate the MN residual errors, $\widehat{MN}^i$. The resulting equation is:

$$\widehat{MN}^i(t) = \epsilon^i(t) - \widehat{bh_r^s}(t) = \widetilde{bh_r^s}'(t) + \widetilde{bh_r^s}''(t) + MN^i(t) \qquad 5\text{-}14$$

where $\widetilde{bh_r^s}''$ is the residual non-linear component clock term resulting from the non-linear trend removal.

5.2.2.1.3.2 PSR-R MN isolation

The exact same approach described in section 5.2.2.1.3.1 for PSR residuals can be applied to jointly isolate each individual multipath error plus thermal noise components, $\widehat{MN}^i$ [102] inside the differential residual term, $\dot{\epsilon}^i$ from the clock drift term, $\dot{bh}_r^s$. The isolation process is conducted by:

1. Estimating $\dot{bh}_r^s$ from the PSR-R residual difference terms, $\widehat{\dot{bh}_r^s}$;
2. Removing (subtracting) the estimated clock drift term, $\widehat{\dot{bh}_r^s}$, from each PSR-R residual difference, $\dot{\epsilon}^i$, to estimate each $\widehat{MN}^i$.

The block-diagram of isolation process is summarized in Figure 5-6. The lowpass filter has a cutoff frequency equal to 0.04 Hz.

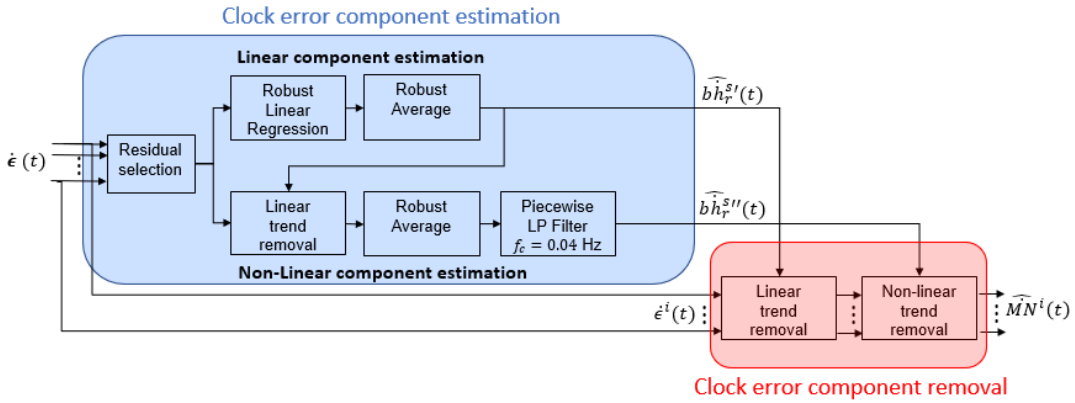

Figure 5-6 – Isolation of multipath and thermal noise error component from clock drift component

5.2.2.2 Dual Constellation MN Error Isolation

In this section, the methodology proposed to isolate the PSR and PSR-R multipath error component from satellites of two different GNSS constellations broadcasting in the L1 band, GPS and Galileo, is provided. In fact, the procedure to individually estimate the multipath error plus the thermal noise components for Galileo is identical to the method proposed for GPS.

On the contrary, the dual constellation MN error isolation method presents some additional issues to be considered. As already said in 5.2.2, the main one consists of the differences between GPS and Galileo signals receiver processing, leading to measurement inconsistency due to constellation signal processing differences between the GPS and Galileo PSR and PSR-R measurements.

Regarding PSR measurements, the main complication is the difference between the clock bias term values between the GPS signals, $bh_r^s(t)|_{GPS}$, and the Galileo signal, $bh_r^s(t)|_{GPS}$; this term will be called from now on GPS to Galileo Post-Processing Time-Offset (GGPPTO), $\delta_{GGPPTO}(t)$, which include also the GGTO term.

From the detailed analysis of GGPPTO, presented in section 5.2.2.2.1.1, it has been demonstrated that GGPPTO is an important bias and must be removed from the Galileo measurements before applying the clock error component removal. Indeed, once the GGPPTO is removed, the GPS and Galileo measurements are consistent and can be jointly processed to estimate a common clock bias term, $\widehat{bh_r^s}(t)$. The Dual constellation Isolation scheme is presented in Figure 5-7.

Regarding PSR-R measurement, the effect of the difference between the clock and hardware drift between GPS and Galileo can be considered negligible with respect to the clock drift terms.

The PSR and PSR-R Dual constellation MP isolation method is presented in section 5.2.2.2.1.2.

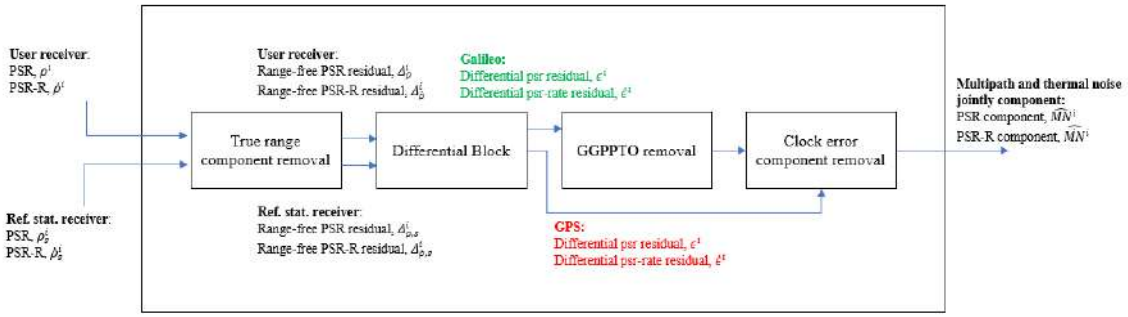

Figure 5-7 – Dual Constellation MN Isolation Block

5.2.2.2.1.1 GPS to Galileo post-processing time-offset (GGPPTO)

This section is devoted to the GGPPTO term analysis. Different reasons explain the GGPPTO term:

- *GPS-Galileo-Time-Offset* (GGTO): There is an inherent time difference between the two constellation reference time systems, section 3.2.1.2, whose influence cannot be neglected. It could be stated that a clock offset term called GGTO is introduced to Galileo measurements when processing GPS and Galileo measurements at the same time and when using GPS time as the clock receiver time frame reference.
- *GPS-Galileo hardware bias*: there is no guarantee that the reference station hardware used for processing GPS L1 C/A signal is the same as the one used for processing Galileo E1 OS signal; this means that an additional bias reference station dependent could be introduced. This phenomenon has been observed as shown in section 5.2.2.2.1.1.2.
- *GPS-Galileo processing bias*: The two signals have implemented a different chip modulation. Therefore, there is no information about the processing conducted by the user receiver or the reference station on these two signals. And this means that there is an additional time uncertainty between the processing of the two signals which could appear on the PSR measurements of each signal.

To investigate the presence of the GGPPTO term and to inspect its relevance, the GGPPTO should be firstly isolated and estimated. The GGPPTO estimation methodology method consists in three different steps:

1) The GPS L1 C/A clock bias is estimated, $\widehat{bh}_r^s(t)\big|_{GPS}$, as described in 5.2.2.1.3.1.3, using only GPS L1 C/A satellite measurements for a static receiver in open-sky signal conditions with an antenna which is able to reduce the impact of the multipath; in this way the impact of the multipath is negligible and the methodology can estimate with an higher accuracy the clock bias term.
2) The same operation should be done estimating the Galileo E1 OS clock bias term, $\widehat{bh}_r^s(t)\big|_{GAL}$, using only Galileo E1 OS satellite.
3) The raw estimation of the GGPPTO, $\hat{\delta}_{GGPPTO}(t)$, is obtained as a difference of the estimated GPS and the Galileo clock bias terms:

$$\hat{\delta}_{GGPPTO}(t) = \widehat{bh}_r^s(t)\big|_{GPS} - \widehat{bh}_r^s(t)\big|_{GAL} \qquad 5\text{-}15$$

The theoretical model of 5-15 has been derived is section 5.2.2.2.1.1.1. The importance and order of magnitude of the GGPPTO is provided through different tests in section 5.2.2.2.1.1.2. Successively, a detailed study of the different component affecting the GGPPTO is presented (5.2.2.2.1.1.3). Finally, a possible GPS to Galileo offset removal technique is presented (5.2.2.2.1.2).

5.2.2.2.1.1.1 GGPPTO model

Recalling equation 5-15:

- the GPS estimated clock bias term could be modelled as

$$\widehat{bh}_r^s(t)\big|_{GPS} \approx \text{LPF}\left\{\begin{matrix}(b_r(t)|_{GPS} + \beta_r(t)|_{GPS} + \zeta^{avg}(t)|_{GPS} + \nu^{avg}(t)|_{GPS}) \\ -\left(b_s(t)|_{GPS} + \beta_s(t)|_{GPS} + \zeta_s^{avg}(t)\big|_{GPS} + \nu_s^{avg}(t)\big|_{GPS}\right)\end{matrix}\right\}$$

- the Galileo estimated clock bias term is equal to

$$\widehat{bh}_r^s(t)\big|_{GAL} \approx \text{LPF}\left\{\begin{matrix}\left(b_r(t)|_{GPS} + \beta_r(t)|_{GAL} + \zeta^{avg}(t)|_{GAL} + \nu^{avg}(t)|_{GAL} + \delta_r(t)\right) \\ -\left(b_s(t)|_{GPS} + \beta_s(t)|_{GAL} + \zeta_s^{avg}(t)\big|_{GAL} + \nu_s^{avg}(t)\big|_{GAL} + \delta_s(t)\right)\end{matrix}\right\}$$

- the $LPF\{...\}$ notation represents the lowpass filtering process presented in section 5.2.2.1.3.

Therefore, the offset could be modelled as showed in 5-16:

$$\hat{\delta}_{GGPPTO}(t) = \text{LPF}\left\{\begin{matrix}(\beta_r(t)|_{GPS} - \beta_r(t)|_{GAL}) - (\beta_s(t)|_{GPS} - \beta_s(t)|_{GAL}) + \\ (\zeta^{avg}(t)|_{GPS} - \zeta^{avg}(t)|_{GAL}) - \left(\zeta_s^{avg}(t)\big|_{GPS} - \zeta_s^{avg}(t)\big|_{GAL}\right) + \\ (\nu^{avg}(t)|_{GPS} - \nu^{avg}(t)|_{GAL}) - \left(\nu_s^{avg}(t)\big|_{GPS} - \nu_s^{avg}(t)\big|_{GAL}\right) + \\ (\delta_r(t) - \delta_s(t))\end{matrix}\right\} = \qquad 5\text{-}16$$

$$= \delta_{\beta_r}^f(t) - \delta_{\beta_s}^f(t) + \delta_{\zeta^{avg}}^f(t) - \delta_{\zeta_s^{avg}}^f(t) + \delta_{\nu^{avg}}^f(t) - \delta_{\nu^{avg}}^f(t) + \delta_{GGTO}^f(t)$$

The resulting term is composed by:

- The filtered difference of the averaged receiver under test's multipath error component between GPS and Galileo measurements, LPF$\{(\zeta^{avg}(t)|_{GPS} - \zeta^{avg}(t)|_{GAL})\} = \delta^{f}_{\zeta^{avg}}(t)$;
- The filtered difference of the averaged reference station' multipath error component between GPS and Galileo measurements, $LPF\left\{\left(\zeta_s^{avg}(t)\big|_{GPS} - \zeta_s^{avg}(t)\big|_{GAL}\right)\right\} = \delta^{f}_{\zeta_s^{avg}}(t)$, which is no longer negligible with respect to the receiver under test multipath if the user receiver is in open sky environment;
- The filtered difference of the averaged receiver under test' thermal noise error between GPS and Galileo measurements, $LPF\{(\nu^{avg}(t)|_{GPS} - \nu^{avg}(t)|_{GAL})\} = \delta^{f}_{\nu^{avg}}(t)$;
- The filtered difference of the averaged reference station's thermal noise error between GPS and Galileo estimation,$LPF\left\{\left(\nu_s^{avg}(t)\big|_{GPS} - \nu_s^{avg}(t)\big|_{GAL}\right)\right\} = \delta^{f}_{\nu_s^{avg}}(t)$;
- The filtered GPS L1 C/A to Galileo E1 OS receiver under test hardware/processing bias difference, $LPF\{(\beta_r(t)|_{GPS} - \beta_r(t)|_{GAL})\} = \delta^{f}_{\beta_r}(t)$;
- The filtered GPS L1 C/A to Galileo E1 OS reference station hardware/processing bias difference, $LPF\{(\beta_s(t)|_{GPS} - \beta_s(t)|_{GAL})\} = \delta^{f}_{\beta_s}(t)$;
- Filtered difference between the user receiver GGTO and the reference station' GGTO, $LPF\{(\delta_r(t) - \delta_s(t))\} = \delta^{f}_{GGTO}(t)$, also called residual GGTO.

Given the open sky environment, the averaging and low-pass filtering processes, the resulting equation can be expressed as:

$$\hat{\delta}_{GGPPTO}(t) \approx \delta^{f}_{\beta_r}(t) - \delta^{f}_{\beta_s}(t) + \delta^{f}_{GGTO}(t) + res \qquad 5\text{-}17$$

Where the term res groups all the a priori negligible terms commented before.

5.2.2.2.1.1.2 GGPPTO relevance analysis

To test the presence and the relevance of the GGPPTO, a static test in open-sky received signal conditions is done at ENAC to estimate the raw GGPPTO, δ_{GGPPTO}. A simultaneous data collection is performed with:

- High-quality receiver, Novatel Propak 6, with a dish antenna on the SIGNAV building rooftop (position, x:1346688.317, y:4877242.133, h:205.375).
- A Mass-market receiver, U-Blox M8T (a), using a patch antenna.
- Another Mass-market receiver, U-Blox M8T (b), sharing the same antenna of Novatel receiver.

And two different reference stations are used to apply the multipath isolation method:

- The Reference station TLSE (position, x:4627852.066 m, y:119639.756 m, z:4372993.324 m in RGF93 coordinates);
- The Reference station TLSG (position, x:4628685.106 m, y:119996.725 m z:4372110.023 m in RGF93 coordinates).

The collected data is then processed applying the GGPPTO estimation method presented in section 5.2.2.2.1.1.1. Once the GGPPTO term is estimated, $\hat{\delta}_{GGPPTO}(t)$, it is characterized by calculating the average, $\hat{m}_{GGPPTO}$, and the standard variation $\hat{\sigma}_{GGPPTO}$.

The $\hat{\delta}_{GGPPTO}$ estimation results obtained using the reference station TLSE are shown in Figure 5-8. As can be seen, a significant offset is present, between 1.4 and 2.2 meters, which is far from being negligible, in each of the three different cases. Table 5-3 summarizes the mean and the standard deviation of the resulting GPS to Galileo offsets. The time fluctuations are not negligible; however, the overall term does not present any type of temporal trend, therefore the average can be considered constant in time.

For TLSG results, the three different receiver presents an offset which is close to 0 but not enough to be considered negligible due to the standard deviation's values. Therefore, the GGPPTO should be considered as a non-negligible offset which is also time-variant. Therefore, the only way to apply a GPS and Galileo joint multipath error isolation is removing the GGPPTO from the Galileo measurements before the isolation process.

In the next section the nature of the GGPPTO term is investigated, focusing on the different influence of the user receiver and the reference station's receiver.

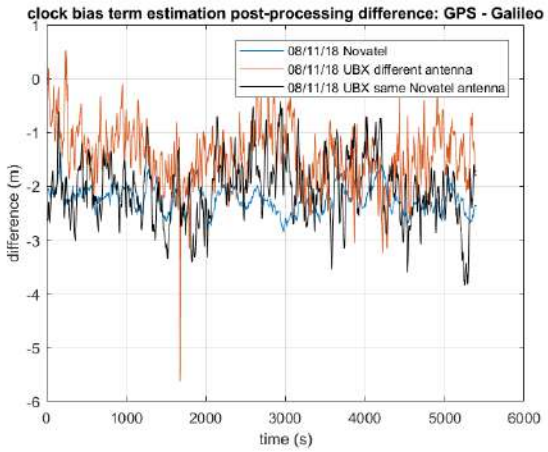

Figure 5-8 – The picture contains the GPS to Galileo offset obtained from three different receivers, NoVatel, U-Blox M8T b which share the same antenna of Novatel and U-Blox M8T which uses a different antenna. The used reference station is TLSE

Ref. Stat.	Receiver	Mean(m)	Std(m)
TLSE	Novatel	-2.23	0.24
	Ubx-a	-1.41	0.54
	Ubx-b	-2.06	0.57
TLSG	Novatel	-0.29	0.25
	Ubx-a	0.44	0.53
	Ubx-b	-0.13	0.56

Table 5-3 – Table containing the mean and the standard deviation of the $\hat{\delta}_{GGPPTO}$ estimation obtained from three different receivers, NoVatel, U-Blox M8T b which shares the same antenna of Novatel and U-Blox M8T a which uses a different antenna. The used reference station are: 1) TLSE, 2) TLSG.

5.2.2.2.1.1.3 GGPPTO estimation analysis

In this section, the nature of the GGPPTO term is analyzed to determine the most suitable method to estimate its value: whether it is more adapted to just assume a constant value with an uncertainty estimation factor or whether the GGPPTO time-evolution can be estimated. To reach such a conclusion, several tests are conducted. The nature of the GGPPTO term has been analyzed, investigating the influence of the receiver under test and the reference station.

Three different tests have been implemented:

1. To investigate the influence of the receiver under test and the reference station on the $\hat{\delta}_{GGPPTO}$.
2. To observe the influence of the receiver under test on the $\hat{\delta}_{GGPPTO}$.
3. To observe the influence of the reference station on the $\hat{\delta}_{GGPPTO}$.
4. To observe the influence of the receiver under test in slow and fast time variations of the $\hat{\delta}_{GGPPTO}$.

Test 1: the first analysis can be conducted from the results presented in Figure 5-8 and Table 5-3. The first parameter to be analyzed is the magnitude of the $\hat{\delta}_{GGPPTO}$ average:

- *TLSE*: Novatel and Ubx-b, have a similar mean offset, the difference is equal to 0.17 m whereas the difference between the Novatel and Ubx-a is equal to 0.82 m.
- *TLSG*: The difference between the Novatel and Ubx-b is equal to 0.16 m whereas the difference between the Novatel and Ubx-a is equal to 0.73 m.
- The difference between the Novatel-TLSE and Novatel-TLSG is equal to 1.94 m; the difference between the Ubx-b-TLSE and Ubx-b-TLSG is equal to -1.79 m; finally, the difference between the Ubx-a-TLSE and Ubx-a -TLSG is equal to -1.93 m. Therefore, the difference between the TLSE and TLSG offsets, for any user receiver, is important and denotes a dependency from the reference station receiver.
- Comparing the difference between the receivers under test between TLSE and TLSG, (first and second bullets), it can be noticed similar results; the difference between Novatel and Ubx-b receivers, is almost equal for the two cases (-0.17 m vs. -0.16 m), whereas the difference between Novatel and Ubx-a have offsets with the same order of magnitude, (-0.82 m vs. -0.73 m).

First, the influence of the receiver under test on the $\hat{\delta}_{GGPPTO}$ has been investigated. To verify its influence, the following test has been conducted. From this analysis, it could be stated that the influence of the receiver under test is not negligible. However, it has a minor impact with respect to the reference station' receiver. In addition, the antenna design also plays a role in the estimation methodology, probably due to the presence of residual MP reflections.

The second parameter to be analyzed is the $\hat{\delta}_{GGPPTO}$ standard deviation:

- *TLSE*: Ubx-a and Ubx-b have similar time variation trends, certified by the values of the standard deviation, 0.54 m vs. 0.57 m. On the contrary, Novatel receiver GGPPTO is more stable, presents smaller time fluctuations; the standard deviation is equal to 0.24 m.
- *TLSG*: It presents similar results with respect TLSE case. The standard deviations for the Ubx-a and Ubx-b are, respectively, 0.53 m and 0.56 m. Novatel receiver presents again smaller time fluctuations and a smaller standard deviation, equal to 0.25 m.
- The difference between the Novatel-TLSE and Novatel-TLSG is equal to 0.01 m. Similar results can be obtained differencing the TLSE Ubx-b and Ubx-a with the correspondent values in TLSG Ubx-b and Ubx-a values.
- Comparing the TLSE and TLSG results, it can be noticed similar trends Indeed, the difference between Novatel and Ubx-b from TLSE and TLSG is almost constant (-0.33 m vs -0.31 m). Similarly, the difference between Novatel and Ubx-a from TLSE and TLSG is almost constant (-0.30 m vs -0.28 m).

From this analysis, it can be assumed that the standard deviation of the GGPPTO term is, mainly, user receiver dependent. The reference station receiver has a minor impact which can be considered negligible. To verify this assumption, a new GGPPTO estimation analysis is made in *Test 2*.

Test 2: GGPPTO estimation is calculated from the two U-Blox receivers, connected to different antennas, in an open sky environment and performed with the TLSE refence station. In addition to the classical estimation depicted in 5-17, a 1st order low-pass filtering operation is applied, with cutting frequency equal to 0.01 Hz. This is used to better observe the $\hat{\delta}_{GGPPTO}$ mean and the slow variations, assuming that slow variations are linked to GGPPTO residual error while fast variations are more linked to any lingering multipath or noise contributions. The results are presented in Figure 5-9 and the estimated statistics in Table 5-4. It can be observed that although the time evolution is different, which means that even the slow time variations are different, the statistics are quite similar. Therefore, from this first analysis it can be concluded the important influence of the receiver under test on the time variations of final $\hat{\delta}_{GGPPTO}$.

Test 3*:* The second parameter to be investigated is the influence of the reference station on the $\hat{\delta}_{GGPPTO}$. This analysis is conducted by performing a test which avoids the use of the receiver under test (Novatel or U-Blox): the same MN isolation method proposed in the previous tests is now applied but using the TLSE reference station receiver as a receiver under test and TLSG as the reference station. Therefore, if the reference station has only a minor impact on the $\hat{\delta}_{GGPPTO}$, the estimated value should be almost zero. The $\hat{\delta}_{GGPPTO}$ for this test are presented below:

$$E\{\hat{\delta}_{GGPPTO}[l]\} = -1.85 \text{ m}$$
$$\sigma\{\hat{\delta}_{GGPPTO}[l]\} = 0.16 \text{ m}$$

The resulting mean is not zero and thus, it can be assumed that the reference stations introduce an offset which is an important contribution of the $\hat{\delta}_{GGPPTO}$ constant offset. This offset could be generated by the GPS-to-Galileo hardware/processing bias difference, $\delta_{bh,sta}$, and/or the residual GGTO, δ_{GGTO}.

Moreover, the obtained standard deviation, which should be a contribution of both reference stations sources of error (hardware/processing bias, residual GGTO, filtered multipath and noise), is lower than the standard deviation obtained for the three receivers under test (Novatel and U-Blox) cases (see Table 5-3), even if these values still have the same order of magnitude. Therefore, it can be concluded that the dominant term generating the GGPPTO time variation is the receiver under test rather than the reference station.

Test 4: To verify the consideration presented in *Test 3*, and to show that even low variations are receiver under test dependent, an additional test has been conducted: similar procedure applied in *Test 2* is now applied to estimate the $\hat{\delta}_{GGPPTO}$ using Novatel receiver and the two reference stations, TLSE and TLSG. Figure 5-10 presents the GGPPTO time evolution for TLSE and TLSG cases. From this figure, it can be seen the high resemblance (plus and offset) between the two cases. Table 5-5 contains the statistics. The TLSE and TLSG standard deviations are almost equal.

Table 5-6 summarizes the influence of the user receiver under test, the reference station's receiver and the tye of antenna on the GGPPTO estimated term.

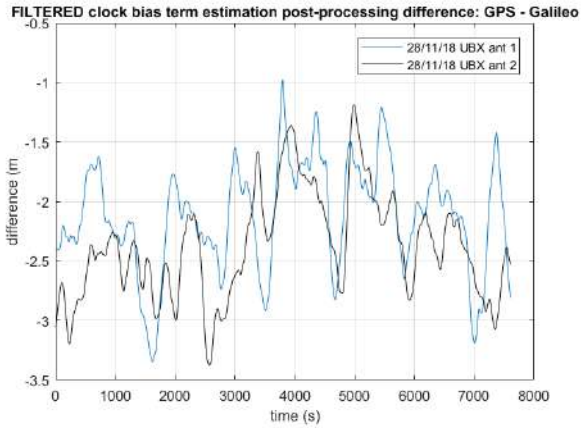

Figure 5-9 – The picture contains the GPS to Galileo offset obtained from two different U-Blox M8T receivers, which use different antennas. The used reference station is TLSE

Ref. Stat.	Receiver	Mean (m)	Std (m)
TLSE	U-Blox a	-2.12	0.4
	U-Blox b	-2.37	0.38

Table 5-4 – Table containing the mean and the standard deviation of GPS to Galileo offset of Figure 5-9

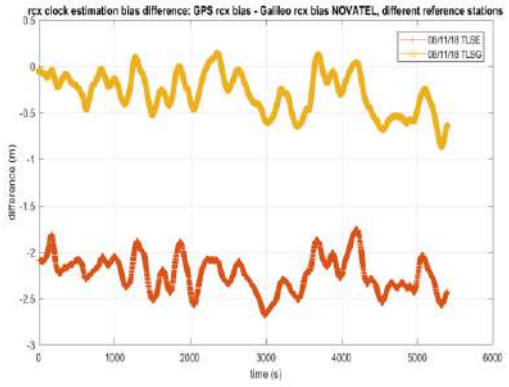

Figure 5-10 – Comparison of GGPPTO obtained used NovAtel and 1) TLSE, 2) TLSG

Ref. Stat.	Receiver	Mean (m)	Std (m)
TLSE	Novatel	-2.23	0.19
TLSG	Novatel	-0.29	0.2

Table 5-5 – Table containing the mean and the standard deviation of GPS to Galileo offset, comparisons between TLSE and TLSG reference stations

GGPPTO influence	**Antenna design**	**User receiver**	**Reference station receiver**
Offset's magnitude	Medium Influence	Low Influence	High Influence
Time variations	Low influence	High influence	Low influence

Table 5-6 – The influence of the user receiver under test, the reference station's receiver and the type of antenna on the GGPPTO estimated term

5.2.2.2.1.2 Proposed Dual constellation MN error isolation methodology

From the estimation analysis presented in Section 5.2.2.2.1.1.3, the following conclusions are extracted. The reference station introduces a non-negligible constant bias to the $\hat{\delta}_{GGPPTO}$; the time variations of the GGPPTO term are driven by the contribution of the receiver under test; indeed, fast and slow time-variations created by the receiver under test are receiver-dependent.

Therefore, to apply the multipath isolation method with two type of constellation measurements, GPS L1 C/A and Galileo E1 OS, the following operations should be added to the clock error component estimation block of the multipath isolation method presented for measurements of only one constellation, see section 5.2.2.1:

1) The expected GGPPTO term, $\hat{\delta}_{GGPPTO}$ must be estimated, and the estimation must be performed on the overall observation window.
2) The Galileo E1 OS PSR measurements are modified by subtracting the GGPPTO term;

$$\epsilon^i_{GAL}(t) = \epsilon^i_{GAL}(t) - \hat{\delta}_{GGPPTO} \qquad 5\text{-}18$$

The structure of the clock error component estimation and removal blocks are illustrated in Figure 5-11.

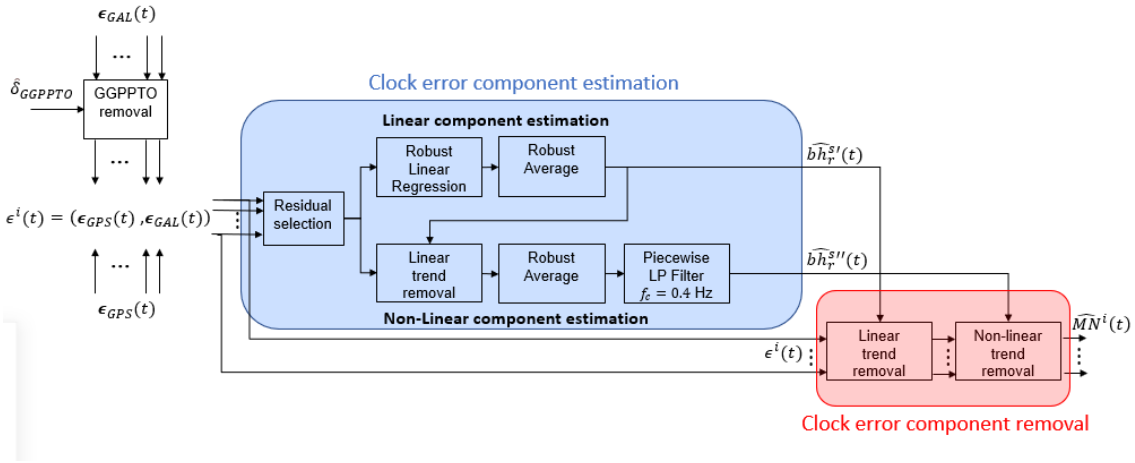

Figure 5-11 – Dual constellation Multipath isolation Scheme

In this work, it has been decided that the estimation of the GGPPTO term will be made over the full observation window; the estimation will consist in providing a constant value, $\hat{\delta}_{GGPPTO}$, plus an indication of the uncertainty of this estimation, $\sigma_{\hat{\delta}_{GGPPTO}}$, since the time evolution component of $\hat{\delta}_{GGPPTO}$ cannot be reliably predicted. Therefore, the GGPPTO estimation process proposed in this work is the following. First, the GGPPTO term is estimated as a function of time, $\hat{\delta}_{GGPPTO}(t)$, applying directly eq. 5-19 to the dataset collected for the receiver under test. In this case it is sufficient to estimate the GGPPTO as a difference of the first-order GPS and Galileo clock terms, as detailed in Figure 5-12.

$$\hat{\delta}_{GGPPTO}(t) = \widehat{bh}^{s\prime}_r(t)\big|_{GPS} - \widehat{bh}^{s\prime}_r(t)\big|_{GAL} \qquad 5\text{-}19$$

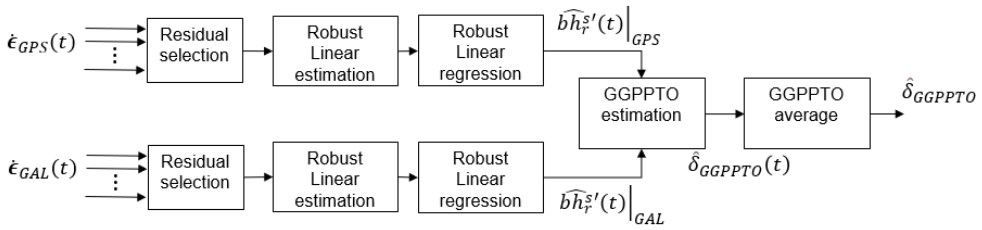

Figure 5-12 – GGPPTO estimation process using only user receiver data measurements

Second, the final estimate of the GGPPTO, $\hat{\delta}_{GGPPTO}$, is obtained as the mean of the raw GGPPTO, $\hat{\delta}_{GGPPTO}(t)$.

5.2.3 LOS/NLOS MN Classification

In this study, an efficient post-processing approach for automatic LOS and NLOS reception state classification is proposed. Detailed analysis of the decision process is illustrated in section 5.2.3.1. This approach has been proposed in order to benefit from the following fundamental advantages as further detailed at the beginning of this chapter:

- The first one is the possibility to characterize separately the impact of LOS and NLOS MP errors, since, as will be seen in Chapter 6, MP reflections have different impacts on the measurement domain of the multipath error component, depending on whether the satellite LOS signal is received or not. A different characterization for both situations should provide two different mathematical models/statistics which could be used to improve further the PVT calculation accuracy and reliability, allowing low-complex NLOS estimation.
- The second is a consequence of the first; if the PVT estimator is able to estimate LOS and NLOS MP receiver states as a function of some specific parameters, the receiver could decide to directly exclude or further de-weight NLOS measurements, without the introduction of external aiding, such as fish-eye cameras, 3D maps etc (section 5.1.2); indeed, this operation is a low-complexity NLOS exclusion/exploitation operation.

Following the work proposed in [95], the core of the discrimination process is the image processing. Indeed, real-time LOS\NLOS discriminators based on the image processing techniques applied to fisheye camera pictures of the urban environment, section 5.1.2, have been used. Hence, the images are taken from a sky-pointing grey-scale fisheye camera mounted on the top of a moving platform and synchronized with a GNSS receiver.

The image processing techniques determine which regions of the image are sky regions or non-sky regions (buildings, bridges, trees, or any kind of obstacle). Basically, the satellite positions are projected into the images, determining a snapshot configuration of the instantaneous multipath environment. These pictures are consequently processed to understand whether or not the direct path between satellite and receiver is obstructed. The proposed algorithm must also be effective with the type of images taken by the camera being used during the test campaign: grayscale with a JPEG compression; an output picture is shown in Figure 5-14. The image processing technique used in this work is detailed in section 5.2.3.2.

The principle of the camera selected in this PhD consists in capturing wavelengths in the visible region. This means that the acquired image is greatly affected by luminosity changes and weather conditions, particularly the presence of clouds, which disrupt the process of extracting the obstacle region and identifying NLOS satellites. In fact, most of the conventional image segmentation algorithms initially developed for different purposes than outdoor navigation will produce poor results. Best results could be obtained in some specific circumstances (i.e. complete cloudy sky conditions) which could be exploited.

For this reason, the image processing decision is double-checked by an LOS\NLOS reception state decision based on the estimation of a received signal parameter. Practically, aligning this work to the previous approaches, [95] [28], in order to increase the accuracy of the estimate, the image processing estimation is checked by a C/N_0 threshold, considered as a good indicator of received signal reception state, as described in [85] and confirmed by experimental results in Chapter 6.

The section is divided as follows. Subsection 5.2.3.1 presents the overall LOS\NLOS discrimination methodology. Section 5.2.3.2 depicts the image processing techniques used to classify LOS\NLOS signal reception state. Section 5.2.3.3 highlights the difficulties related to the image processing approach. Finally, in the section 5.2.3.4 is presented the final approach, including the image processing estimator coupled with a Parameter decision based on $C\backslash N_0$ threshold.

5.2.3.1 LOS/NLOS decision algorithm

The LOS/NLOS decision algorithm architecture is described in Figure 5-13. This is based on a mutual image processing and received signal parameter estimation, based on the following inputs:

1. Fish-eye camera output pictures, $\boldsymbol{F}(t)$.
2. The satellites i position at given epoch t with the respect to the receiver antenna, $\boldsymbol{p}^i(t)$.
3. Carrier to noise ratio of the satellite i at given time t, $C/N_0^i(t)$.

The decision process is based on three stages:

1) the satellite position projection into the fish-eye camera pictures;
2) the LOS/NLOS Reception State decision for a given satellite i, $\hat{S}^i$ based on image processing characterization;
3) the reception state refinement based on a received signal $C/N_0^i(t)$.

These three stages are defined in the next paragraphs.

Satellite projection: The position of the satellites at a given time epoch, $\boldsymbol{p}^i(t)$, must be projected into the relative picture, $\boldsymbol{F}(t)$. Once projected, the satellite position will correspond to a specific pixel of the picture under exam. However, the lens of the fisheye camera is orthographic; therefore, an orthogonal projection must be applied. The detailed approaches are described in [103],[104]. The inputs of the satellite projection block are the internal parameters of the fish-eye camera and $\boldsymbol{p}^i(t)$. The internal parameters of the fish-eye camera were estimated applying a fish-eye camera calibration Toolbox for MATLAB [105].

Following the projection, the picture, $\boldsymbol{F}(t)$, and the projected satellite position, $\boldsymbol{p}_F^i(t)$, are used by the image processing tool to estimate the received signal Reception State, $\hat{S}^i(t)$.

LOS/NLOS Reception State decision based on Image processing: The image processing technique is able to discriminate between blocked and direct satellite-to-receiver direct path at given time epoch, t, processing the projected satellite position, $\boldsymbol{p}_F^i(t)$ and the relative fisheye pictures, $\boldsymbol{F}(t)$. The detailed algorithm is presented in section 5.2.3.2. Basically, the estimator segments the picture into sky and non-sky regions. Then, it analyses the value of the image's pixel in which the satellite is projected [2]. Note that, if the pixel's value corresponds to a sky area, the reception state of the received signal corresponding to that satellite is estimated as LOS, $\hat{S}^i(t) = LOS$, otherwise it is estimated as NLOS, $\hat{S}^i(t) = NLOS$. However, the image processing methodology suffers from several issues, presented in section 5.2.3.3, which degrade its performances. A standalone image processing decision is thus not recommended.

Reception State refinement decision based on a received signal C/N_0: A possible way to improve the accuracy of the image processing classification is using a double-check decision with an external signal processing tool. This is obtained checking the image processing estimation, $\hat{S}^i(t)$ of satellite i, with its corresponding received signal C/N_0^i. The proposed algorithm is detailed in section 5.2.3.4.

Once the state of reception is classified, these reception states can be associated to observable error distributions. As a consequence, $\widehat{MN}^i(t)$ and $\widehat{MN}^i(t)$ errors associated to $\hat{S}^i(t) = LOS$, are considered LOS and identified by $\widehat{MN}_{LOS}^i(t), \widehat{MN}_{LOS}^i(t)$. On the contrary MN errors associated to $\hat{S}^i(t) = NLOS$, are considered NLOS and identified by $\widehat{MN}_{NLOS}^i(t), \widehat{MN}_{NLOS}^i(t)$.

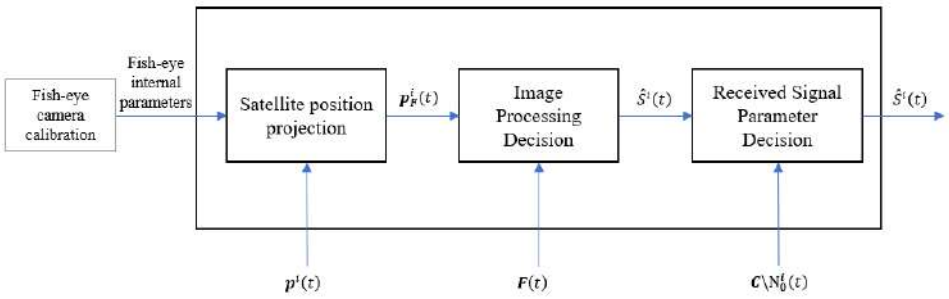

Figure 5-13 – Detailed sections of the proposed LOS and NLOS decision algorithm

5.2.3.2 LOS/NLOS Image processing-based decision

The Image processing tool is defined by two different stages:

- Image sky and non-sky region determination
- Satellite reception state discrimination

Image sky and non-sky region determination: In the first stage, the original fish-eye input picture, $\boldsymbol{F}(t)$, is processed in order to define the sky and non-sky image segments. The proposed method consists of an object's edge enhancement (OEE) approach followed by a flood filling algorithm. The goal of OEE is the enrichment of all the object's borders contained in the original picture, so that the processed picture, $\boldsymbol{F}_{OEE}(t)$, should be characterized by a sharp distinction between open areas and borders lines. The aim of flood filling (FF) algorithm is to process the OEE picture in order to discriminate between sky and non-sky areas. The segmented output picture, $\boldsymbol{F}_{FF}(t)$, is characterized by three different colors, from which black and white pixels correspond to non-sky areas whereas grey pixels correspond to sky-area.

The OEE is achieved in two different steps:

- Reduction of the presence of light variations modifying the luminance features of the original picture. The picture is modified in order to average and reduce the sparkles due to sunlight. The resulting picture is a modified grey-scale picture.
- Application of a canny edge detector. Similar to the binarization of the image, the method detects the edges in the picture and differentiates between them and non-edges. The resulting picture is a black and white (b/w) picture where the edges are white. Figure 5-15 is the result of applying the detector to Figure 5-14.

The FF process can be summarized in the four following steps:

- Orthogonal projection of the satellite positions at a given time epoch t, $\boldsymbol{p}_F^i(t)$, is placed into the OEE picture [104], corresponding to a pixel of $\boldsymbol{F}_{OEE}(t)$;
- The pixel corresponding to the location of the satellite with the highest carrier-to-noise ratio (C/N_0^{max}) is assumed to be a sky region.
- From that projected point, the surrounding area is also considered as a sky region until, in every possible direction, an edge is reached. A simple description is proposed in Figure 5-16.
- The final picture, $\boldsymbol{F}_{FF}(t)$, is illustrated in Figure 5-17. The color of the pixels corresponding to the detected sky-region has changed to grey. On the contrary, any area beyond these edges is assumed to be a non-sky region. Therefore, the remaining black and white areas are considered obstacles (non-sky) areas.

Satellite reception state discrimination: The second stage consists of the received signal reception state discrimination, based on the segmented $\boldsymbol{F}_{FF}(t)$ and the projected satellite positions. The reception state discrimination, for a given received signal corresponding to a satellite i is estimated as follows:

- If the projected satellite position, $\boldsymbol{p}_F^i(t)$, corresponds to a pixel of a non-sky region (black or white pixel, see Figure 5-17), the estimated reception state is NLOS, $\hat{S}^i(t) = NLOS$;
- If the projected satellite position, $\boldsymbol{p}_F^i(t)$, corresponds to a pixel of a sky region (grey pixel, see Figure 5-17), the estimated reception state is NLOS, $\hat{S}^i(t) = NLOS$;

Figure 5-18 shows the results of the image processing sky-area estimation: the green points are considered in the sky-area, the red points are considered to be obstructed by obstacles.

Figure 5-14 – Fish-eye camera output picture, $\boldsymbol{F}(t)$

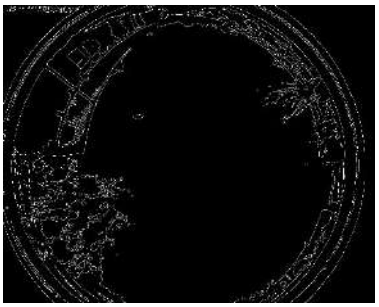

Figure 5-15 – Resulting picture from OEE, $\boldsymbol{F}_{OEE}(t)$

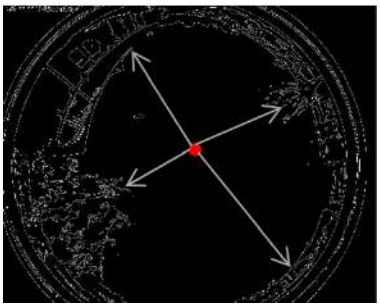

Figure 5-16 – Flood-filling approach. The red point is the projection of the satellite position with higher C/N_0. The grey arrows are the direction of the flood-filling operation.

Figure 5-17– Resulting picture from flood-filling algorithm, $\boldsymbol{F}_{FF}(t)$

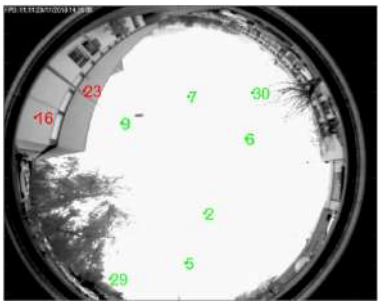

Figure 5-18 – Possible image processing sky-area estimation: the green points are considered in the sky-area, the red points are considered to be obstructed by obstacles

5.2.3.3Image Processing Drawbacks

The standalone image processing decision is not reliable due to several limitations which prevent a correct border detection during the OEE and FF processes, and, consequently, LOS/NLOS discrimination.

The border detection errors can be summarized as follows:

- the color of the reflector object is similar to the sky area color; in this case the object is not perfectly recognized, consequently, the borders are not highlighted;
- the presence of a sun glare flashes a specific area of the picture containing a reflector object; similar to the previous case, the reflector object is not recognized, consequently, the borders are not highlighted;
- the presence of a sun glare flashes a portion of the sky area of the picture; the sun glare artifact in the picture is recognized as an object, consequently, the borders of this artificial object are highlighted;
- the dimension of the reflector object is too small; the object is not perfectly recognized, consequently, the borders are not highlighted;
- dynamic reflectors are distorted in the picture; in this case the borders of the distorted object shape are magnified;
- the undefined shape of a certain type of reflectors, such as a bunch of trees, cannot be perfectly recognized, therefore, edges enhancement could not be accurately performed.

Moreover, LOS\NLOS discrimination error during Satellite reception state discrimination step occurs also in case of invalid NLOS decision due to the presence of the trees. Trees are usually detected as an obstacle, blocking the LOS between satellite and receiver if the satellite position is placed on the trees area. However, the signal covered by trees cannot be always considered NLOS: the LOS can still reach the receiver. Figure 5-19 and Figure 5-20 show respectively the projection of GPS 6 in time in the fish-eye picture with the respect of a static position and the relative C/N_0. It could be assumed that the satellite is in open sky region and the relative C/N_0 assumes values between the 52 and 42 dB-Hz.

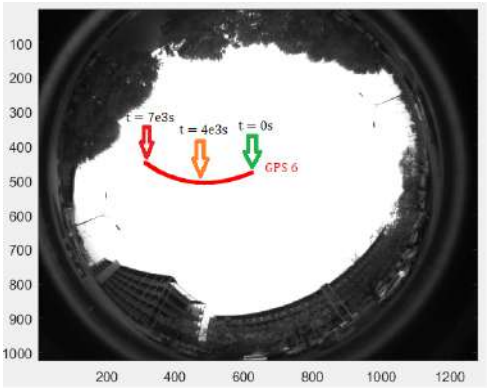

Figure 5-19 – Projection of GPS 6 in time in the fish-eye picture with the respect of a static position

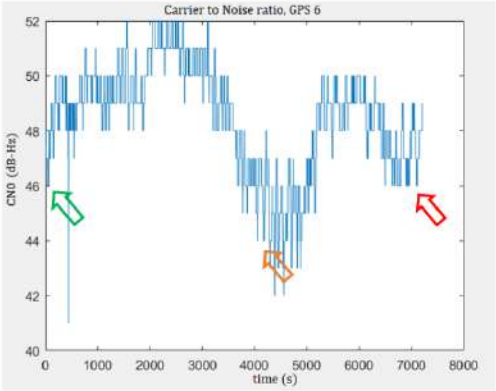

Figure 5-20 – C/N_0 time evolution of GPS 6

Figure 5-21 and Figure 5-22 show respectively the projection of GPS 9 in time in the fish-eye picture with respect to a static position and its estimated C/N_0. It can be observed that the satellite is in the first part in open sky region at the start of the observation interval, then it is covered by a bunch of trees between 2e3s and 4e3s and, lastly, it is blocked by a building starting from 4e3s until the end of the observation interval. The estimated C/N_0 values are around 45/40 dB-Hz when the satellite is in open sky or blocked by trees; this means that the trees do not introduce a heavy obstruction to the LOS signal. When the signal starts to be blocked by the building, the C/N_0 drops from 40/35 dB-Hz to 10 dB-Hz. The building introduces a high obstruction.

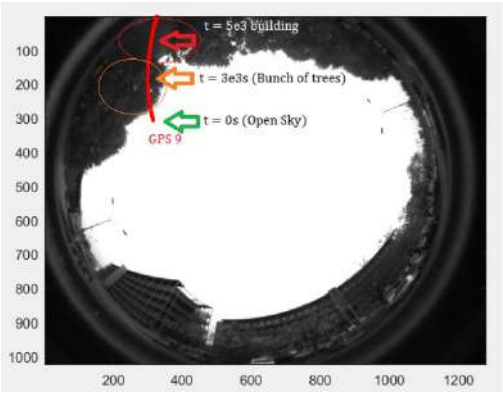

Figure 5-21– Projection of GPS 9 in time in the fish-eye picture with the respect of a static position

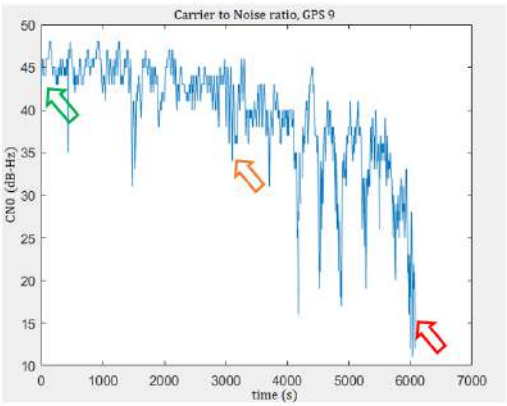

Figure 5-22– C/N_0 time evolution of GPS 9

Therefore, from previous figures, it is assumed that trees do not introduce NLOS obstruction since it is assumed that a high enough C/N_0 value means that the LOS signal is successfully processed by the receiver. However, the borders of the trees are identified and enhanced by the image processing algorithm, in this way the flood-filling algorithm will not fill the area related to the trees and therefore this area will be identified as an obstruction area which implies NLOS reception. As an example, Figure 5-23 shows the image processing estimation of the GPS satellite (identified by 1000 + PRN number) and Galileo satellites (4000 + PRN number). The respective GPS L1 C\A and Galileo E1 OS received C/N_0 are summarized in Table 5-7 and Table 5-8. The green color corresponds to a LOS estimation while the red color corresponds to a NLOS estimation.

It can be seen that the satellites in open sky are considered as LOS receiver reception state, the satellites covered by buildings (ex. 1003) are considered NLOS receptions as well as the satellite which are obstructed by trees when they should not be. These estimation errors affect systematically the image processing algorithm, which could not be used without any external aiding to perform the LOS/NLOS signal classification.

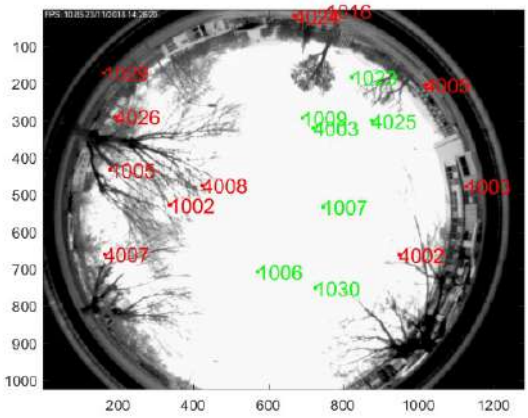

Figure 5-23 – Possible image processing NLOS/LOS estimation: the green points are considered in the sky-area, the red points are considered to be obstructed by obstacles

Modulation	PRN	C/N_0 [dB-Hz]
GPS L1 C/A	2	39
	3	15
	5	26
	6	48
	7	50
	9	45
	16	13
	23	38
	29	10
	30	47

Table 5-7 – C/N_0 values of the received signals from different GPS L1 C/A satellite at a given epoch, corresponding to the configuration of Figure 5-23

Modulation	PRN	C/N_0 [dB-Hz]
Galileo E1 OS	2	36
	3	49
	5	18
	7	25
	8	45
	24	20
	26	30

Table 5-8 – C/N_0 values of the received signals from different Galileo E1 OS satellite at a given epoch, corresponding to the configuration of Figure 5-23

5.2.3.4 LOS/NLOS estimation based on Parameter decision

The limitations of the image processing classification (section 5.2.3.3) undermine its decision process reliability.

For this reason, $\hat{S}^i(t)$ is checked by a received signal parameter threshold. The most indicative parameters are elevation angle or C/N_0. However, elevation angle is not the best indicator of LOS/NLOS reception state in an urban environment. The urban environment is a complex and obstacle-dense environment where the knowledge of the elevation angle between the satellite and the receiver is only a partial indicator of possible obstructions of the LOS signal, as described in Chapter 6. Indeed, the use of elevation angle is incomplete, if not followed by other indicators, such as the relative azimuth or the power of the received signal. A superior indicator is the C/N_0 as clearly justified in Chapter 6.

Therefore, the image processing estimation is checked by a C/N_0 threshold. Based on [95] and [28], and validated by the results in section 6.2.4 and 6.2.5, it can be seen that in order to have a LOS/NLOS characterization less affected by image processing errors, a C/N_0 threshold equal to 35 dB-Hz it should be used with the following exclusion rules: once the image processing estimates $\hat{S}^i(t)$, the corresponding $C/N_0^i(t)$ is verified:

- In case of image processing LOS estimation:

- If $C/N_0^i > 35$ dB-Hz, the post-processing approach estimation is set as LOS estimation, $\hat{S}^i(t) = LOS$;
- If $C/N_0^i < 35$ dB-Hz, the image processing estimation is considered wrong, probably due to image processing errors. Corresponding measurement is not used for the Multipath error LOS\NLOS characterization process.

- In case of image processing NLOS estimation:
  - If $C/N_0^i > 35$ dB-Hz, the image processing estimation is considered to be uncertain, probably due to trees error classification. Corresponding measurement is not used for the Multipath error LOS\NLOS characterization process;
  - If $C/N_0^i < 35$ dB-Hz, the post-processing approach estimation is set as NLOS estimation, $\hat{S}^i(t) = NLOS$.

5.3 MN error modelling

In the previous sections a Multipath error characterization methodology and, successively, a new LOS\NLOS MN error isolation methodology were proposed. The proposed post-processing isolation method has been designed in a larger framework, which the main objective is the improvement of low-cost PVT estimators for automotive applications in urban environment. As a consequence, the isolation of MN errors is just the first fundamental step to obtain a reliable and accurate MN error model in urban environment, which can be exploited by innovative PVT architecture solutions.

Hence, the subject of this last section is the PSR\PSR-R MN error characterization and overbounding process. The MN characterization and overbounding's goal is to obtain a mathematical model which overbounds the PSR and PSR-R MN errors' statistical behavior. This is obtained by first calculating the MN error empirical PDF and its moments and second, by finding Gaussian distributions which overbound the empirical PDFs with a set criterion. The detailed statistical characterization is described in section 5.3.1.

Moreover, another characteristic of great interest which is used to refine the model of MN error characterization is the error temporal correlation. Indeed, multipath errors are environment-dependent (thus, spatially correlated) and temporally correlated. Moreover, spatial and temporal correlation are conditioned by the receivers' dynamics, since the MN urban canyon configuration varies as a function of the receiver velocity vector. A temporal correlation methodology, as a function of the receiver speed dynamic, is thus proposed in section 5.3.2 to characterize the correlation properties of MN error components.

5.3.1 MN Error Statistical characterization and overbounding

MN error statistical characterization is based on the calculation of the empirical PDF, the sample mean and variance from the isolated PSR\PSR-R MN error components. These statistics are only representative if the true process is ergodic.

Thermal noise components may be modelled as a White Gaussian ergodic random process with zero mean. Regarding the MP error component, it can be possible to assume that MP random process is an ergodic random process only if the number of collected data is sufficiently large to be representative of MP error component in an urban environment.

The MN error statistical characterization process is based on the two sequential operations:

- *MN error classification*: the PSR\PSR-R MN error components, at different time epochs and from different satellites, are grouped depending on a specific received signal parameter. Two types of classifications are considered in this work, C/N_0, and satellite elevation angle [101];
- *MN error PDF computation:* The empirical PDF is determined for each bin of MN errors (previous step definition); it is obtained by calculating the normalized MN error histograms along with the corresponding sample average, and the sample standard deviation.

The characterization process described above could be applied separately to:

- general MN isolated components, $\left(\widehat{MN}^i, \widehat{MN}^i\right)$, after the MN error isolation (section 5.2.2) and before LOS\NLOS classification, as described in section 5.3.1.1;
- LOS and NLOS MN components after LOS/NLOS classification, (section 5.2.3), $\left(\widehat{MN}^i_{LOS}, \widehat{MN}^i_{LOS}\right)$, and $\left(\widehat{MN}^i_{NLOS}, \widehat{MN}^i_{NLOS}\right)$.

The MN error statistical overbounding is the pre-process necessary to exploit the resulting characterized MN PDFs by modified PVT estimators to ensure accurate PVT solutions. Indeed, complex PVT architectures, such as a particle filter, could exploit directly the characterized non-Gaussian MN PDFs, but PVT architecture based on a KF model requires Gaussian error models. Therefore, in this latter case which is the option pursued in this PhD work, to cope with this limitation, a possible solution is to calculate the Gaussian PDF which overbounds the generic MN PDFs applying a set criterion. The Gaussian overbounding process and the chosen cirterion applied to the experimental results (section 6.3) is proposed in section 5.3.1.3.

5.3.1.1 General MN error characterization

Once the PSR/PSR-R MN errors have been estimated, a first general (non-discriminated by LOS/NLOS reception state) characterization of the MN statistical properties can be elaborated.

MN error classification: The general MN error components, at different time epochs and from different satellites, are grouped depending on a specific signal reception parameter, P, such as the C/N_0 or the satellite elevation angle, associated to the isolated MN error [101].

The classification process is defined as follows. Considering a generic signal reception parameter P, representing either C/N_0 or the satellite elevation angle, the P-based MN error classification is conducted in two steps:

1) To define the signal parameter classification bins, b_j in which the different MN errors should be grouped. The bins determination is conducted as follows by uniformly dividing the potential output range of P in N bins, of the specific bin size, d_P:

P bins	
b_1	$0 \leq P < d_P$
b_2	$d_P \leq P < 2d_P$
b_3	$2d_P \leq P < 3d_P$
b_4	$3d_P \leq P < 4d_P$
…	…
b_N	$(N-1)d_P \leq P < Nd_P$

Table 5-9 - Definition of the generic signal parameter classification bins, with respect to the dimension of the specific bin size, d_P

2) To classify the MN error components into the corresponding P bins. PSR and PSR-R measurement classification is exactly the same, thus the PSR procedure will be taken as an example. A given $\widehat{MN}^i(t)$ error at epoch t, associated to the signal reception parameter $P^i(t)$, can be grouped into the set of MN errors corresponding to the specific bin b_j, $\widehat{\boldsymbol{MN}}_{P,b_j}$, if the corresponding $P^i(t)$ parameter belongs to b_j:

$$\widehat{MN}^i(t) \in \widehat{\boldsymbol{MN}}_{P,b_j} : P^i(t) \in b_j \qquad 5\text{-}20$$

MN error PDF computation: Each different MN error group must be statistically characterized; to do so, the empirical probability density function, $PDF\left(\widehat{\boldsymbol{MN}}_{P,b_j}\right)$ is calculated as well as the sample mean $\mu_{\widehat{\boldsymbol{MN}}_{P,b_j}}$ and the sample standard deviation, $\sigma_{\widehat{\boldsymbol{MN}}_{P,b_j}}$.

Characterization Result: The summary of the general PSR MN error characterization is illustrated in Table *5-10*. The same table could be derived for PSR-R MN errors, just substituting the $\widehat{\boldsymbol{MN}}_{P,b_j}$ with $\widehat{\boldsymbol{MN}}_{P,b_j}$.

P bins	MN error sets	Statistical Characterization	Sample mean [m]	Sample Standard deviation [m]
b_1	$\widehat{\boldsymbol{MN}}_{P,b_1}$	$PDF\left(\widehat{\boldsymbol{MN}}_{P,b_1}\right)$	$\mu_{\widehat{\boldsymbol{MN}}_{P,b_1}}$	$\sigma_{\widehat{\boldsymbol{MN}}_{P,b_1}}$
b_2	$\widehat{\boldsymbol{MN}}_{P,b_2}$	$PDF\left(\widehat{\boldsymbol{MN}}_{P,b_2}\right)$	$\mu_{\widehat{\boldsymbol{MN}}_{P,b_2}}$	$\sigma_{\widehat{\boldsymbol{MN}}_{P,b_2}}$
b_3	$\widehat{\boldsymbol{MN}}_{P,b_3}$	$PDF\left(\widehat{\boldsymbol{MN}}_{P,b_3}\right)$	$\mu_{\widehat{\boldsymbol{MN}}_{P,b_3}}$	$\sigma_{\widehat{\boldsymbol{MN}}_{P,b_3}}$
b_4	$\widehat{\boldsymbol{MN}}_{P,b_4}$	$PDF\left(\widehat{\boldsymbol{MN}}_{P,b_4}\right)$	$\mu_{\widehat{\boldsymbol{MN}}_{P,b_4}}$	$\sigma_{\widehat{\boldsymbol{MN}}_{P,b_4}}$
…	…	…	…	…
b_N	$\widehat{\boldsymbol{MN}}_{P,b_j}$	$PDF\left(\widehat{\boldsymbol{MN}}_{P,b_N}\right)$	$\mu_{\widehat{\boldsymbol{MN}}_{P,b_N}}$	$\sigma_{\widehat{\boldsymbol{MN}}_{P,b_N}}$

Table 5-10 – General MN error component characterization based on the classification of MN error components with respect to the generic signal reception parameter P

The results can be found in Chapter 6, where it has been tested and compared two different signal reception parameters, (C/N_0 and elevation angle), and different bin size, d_P.

5.3.1.2 LOS/NLOS MN error characterization

The same approach described above for general MN error characterization could be applied to LOS and NLOS MN error components. The only difference is found during the classification step where an additional parameter is used to further divide the MN measurements classification, the receiver state condition $\hat{S}^i(t)$ equal to LOS or NLOS.

The PDF characterization step remains the same. For each LOS and NLOS MN bin the empirical probability density function, the sample mean, and the sample standard deviation are thus determined. The summary of the LOS PSR MN error characterization is illustrated in Table 5-11, whereas NLOS PSR MN error characterization is illustrated in Table 5-12. The same table could be derived for PSR-R MN errors.

P bins	MN error sets	Statistical Characterization	Sample mean [m]	Sample Standard deviation [m]
b_1	$\widehat{\boldsymbol{MN}}_{LOS,P,b_1}$	$PDF\left(\widehat{\boldsymbol{MN}}_{LOS,P,b_1}\right)$	$\mu_{\widehat{\boldsymbol{MN}}_{LOS,P,b_1}}$	$\sigma_{\widehat{\boldsymbol{MN}}_{LOS,P,b_1}}$
b_2	$\widehat{\boldsymbol{MN}}_{LOS,P,b_2}$	$PDF\left(\widehat{\boldsymbol{MN}}_{LOS,P,b_2}\right)$	$\mu_{\widehat{\boldsymbol{MN}}_{LOS,P,b_2}}$	$\sigma_{\widehat{\boldsymbol{MN}}_{LOS,P,b_2}}$
b_3	$\widehat{\boldsymbol{MN}}_{LOS,P,b_3}$	$PDF\left(\widehat{\boldsymbol{MN}}_{LOS,P,b_3}\right)$	$\mu_{\widehat{\boldsymbol{MN}}_{LOS,P,b_3}}$	$\sigma_{\widehat{\boldsymbol{MN}}_{LOS,P,b_3}}$
b_4	$\widehat{\boldsymbol{MN}}_{LOS,P,b_4}$	$PDF\left(\widehat{\boldsymbol{MN}}_{LOS,P,b_4}\right)$	$\mu_{\widehat{\boldsymbol{MN}}_{LOS,P,b_4}}$	$\sigma_{\widehat{\boldsymbol{MN}}_{LOS,P,b_4}}$
…	…	…	…	…
b_N	$\widehat{\boldsymbol{MN}}_{LOS,P,b_N}$	$PDF\left(\widehat{\boldsymbol{MN}}_{LOS,P,b_N}\right)$	$\mu_{\widehat{\boldsymbol{MN}}_{LOS,P,b_N}}$	$\sigma_{\widehat{\boldsymbol{MN}}_{LOS,P,b_N}}$

Table 5-11 – LOS MN error component characterization based on the classification of MN error components with respect to the generic signal reception parameter P

P bins	MN error sets	Statistical Characterization	Sample mean [m]	Sample Standard deviation [m]
b_1	$\widehat{\boldsymbol{MN}}_{NLOS,P,b_1}$	$PDF\left(\widehat{\boldsymbol{MN}}_{NLOS,P,b_1}\right)$	$\mu_{\widehat{\boldsymbol{MN}}_{NLOS,P,b_1}}$	$\sigma_{\widehat{\boldsymbol{MN}}_{NLOS,P,b_1}}$
b_2	$\widehat{\boldsymbol{MN}}_{NLOS,P,b_2}$	$PDF\left(\widehat{\boldsymbol{MN}}_{NLOS,P,b_2}\right)$	$\mu_{\widehat{\boldsymbol{MN}}_{NLOS,P,b_2}}$	$\sigma_{\widehat{\boldsymbol{MN}}_{NLOS,P,b_2}}$
b_3	$\widehat{\boldsymbol{MN}}_{NLOS,P,b_3}$	$PDF\left(\widehat{\boldsymbol{MN}}_{NLOS,P,b_3}\right)$	$\mu_{\widehat{\boldsymbol{MN}}_{NLOS,P,b_3}}$	$\sigma_{\widehat{\boldsymbol{MN}}_{NLOS,P,b_3}}$
b_4	$\widehat{\boldsymbol{MN}}_{NLOS,P,b_4}$	$PDF\left(\widehat{\boldsymbol{MN}}_{NLOS,P,b_4}\right)$	$\mu_{\widehat{\boldsymbol{MN}}_{NLOS,P,b_4}}$	$\sigma_{\widehat{\boldsymbol{MN}}_{NLOS,P,b_4}}$
…	…	…	…	…
b_N	$\widehat{\boldsymbol{MN}}_{NLOS,P,b_N}$	$PDF\left(\widehat{\boldsymbol{MN}}_{NLOS,P,b_N}\right)$	$\mu_{\widehat{\boldsymbol{MN}}_{NLOS,P,b_N}}$	$\sigma_{\widehat{\boldsymbol{MN}}_{NLOS,P,b_N}}$

Table 5-12 – NLOS MN error component characterization based on the classification of MN error components with respect to the generic signal reception parameter P

5.3.1.3 Gaussian overbounding

This section describes the Gaussian overbounding technique applied to the MN statistical error models characterized in the previous sections. The overbounding method can be applied to Gaussian but more importantly to non-Gaussian distribution as well, i.e., to replace the non-Gaussian MN error distribution with a standard Gaussian distribution.

Several overbounding strategies have been proposed in the literature. In [106], a review of the classic methods is presented to the reader. The basic principle of the overbounding method consists of determining an inflated sigma such that the inflated Gaussian distribution is more conservative than the empirical, Gaussian or non-Gaussian, distribution being treated.

There are two groups of overbounding methods:

1. Probability density function (PDF) overbounding.
2. Cumulative distribution function (CDF) overbounding, in which the single CDF overbounding and the paired-overbounding (PB) are two typical implementations.

It is important to remark that the PDF-based overbounding and Single CDF overbounding present important issues. These methodologies require that the distributions of the error under exam should be zero-mean, unimodal and symmetric. However, the strong limitations of PDF and Single CDF overbounding impact only applications with demanding requirements on the overbound in terms of integrity such as safety critical applications including RAIM. This is not the case for the MN Gaussian overbounding for PVT estimators in the applications addressed in this thesis. In this case, the fundamental requirement is to model a Gaussian distribution which could be representative of the nominal MN error model.

Two different approaches are considered:

1. *Standard Gaussian CDF overbounding*: The zero-centered CDF overbound of the error distribution is used as the initial value prior to an empirically inflation process. The goal of the inflation process consists of overbounding the 95th-percentile nominal MN error distributions, taking into account both left and right tails (2.5% from left tail and 2.5% from the right tail).
2. *Gaussian CDF overbounding with mean removal*: The nominal MN error distribution is first centered to zero removing the empirical mean of the distribution (derived from the statistical model presented in the previous sections); second, the *Standard Gaussian CDF overbounding* approach is applied.

The fundamental criteria implemented in the Gaussian overbounding method proposed in this work are the following:

- The CDF obtained from Gaussian overbounding must be always zero mean.
- Gaussian inflation must guarantee an overbound of the original CDF between the 2.5% and 30% for the left tail and between 70% and 97.5% for the right tail.

- Gaussian inflation does not guarantee the overbound of the original CDF between 30% and 70% of the original CDF.
- The two previous criteria are defined with the following mathematical equations:

$$CDF_o(x) \geq CDF_{X,b_j}(x) \quad \forall\, x_{inf} \leq x < x_{lb}$$
$$CDF_o(x) \leq CDF_{X,b_j}(x) \quad \forall\, x_{hb} \geq x > x_{sup} \qquad 5\text{-}21$$

where the bound limits are chosen respecting the assumptions presented in the previous paragraphs:

$$x_{inf} \rightarrow CDF_{X,b_j}(x_{inf}) = 0.015, \text{ corresponding to 1.5\% of the nominal } CDF_{X,b_j}$$
$$x_{sup} \rightarrow CDF_{X,b_j}(x_{sup}) = 0.975, \text{ corresponding to 98.5\% of the nominal } CDF_{X,b_j}$$
$$x_{lb} \rightarrow CDF_{X,b_j}(x_{lb}) = 0.3, \text{ corresponding to 30\% of the nominal } CDF_{X,b_j} \qquad 5\text{-}22$$
$$x_{hb} \rightarrow CDF_{X,b_j}(x_{hb}) = 0.7, \text{ corresponding to 70\% of the nominal } CDF_{X,b_j}$$

The proposed procedure can be applied either to PSR or PSR-R. Therefore, the PSR case is taken as an example. The zero-centered CDF overbound method is an iterative process which calculates the overbounding Gaussian CDF applying the following steps:

1. *Empirical CDF calculation:* To calculate the Cumulative Distribution Function of a specific MN error set, $\widehat{\boldsymbol{MN}}_{P,b_j}$, belonging to the bin b_j, classified by the generic signal reception parameter P:

$$\widehat{\boldsymbol{MN}}_{P,b_j} \rightarrow CDF_{\widehat{\boldsymbol{MN}}_{P,b_j}}(x) \qquad 5\text{-}23$$

where x is the error magnitude.

2. *Gaussian distribution candidate generation:* To generate a specific Gaussian distribution candidate characterized by zero mean and the σ_o^2 -variance candidate. The Cumulative Distribution Function, $CDF_o(x)$, of the candidate distribution is calculated.

$$N(0, \sigma_o^2) \rightarrow CDF_o(x) \qquad 5\text{-}24$$

3. *Gaussian ovebounding distribution test*: the goal of this step is to test if the Gaussian distribution candidate overbounds the specific MN error CDF by fulfilling the criteria defined in equations 5-21 and 5-22:
   - If the test distribution does not fulfill the criteria presented in 5-21, the current Gaussian distribution candidate is discarded and the *Gaussian distribution candidate generation* step is conducted again with a higher value of σ_o^2 variance candidate.
   - If the test distribution fulfills the criteria, the process stops and the Gaussian distribution candidate is selected as the Gaussian overbounding distribution.
   - Additionally, if the inflated σ_o^2 becomes too large to be representative of the nominal MN error model, the process stops and no candidate is retained.

An example of overbounding of 97-th percentile right and left tail MN error Gaussian overbounding process is portrayed in Figure 5-24. The blue curve represents the original $CDF_{\widehat{\boldsymbol{MN}}_{P,b_j}}(x)$ of PSR measurement dataset. The red curve represents the CDF of the selected Gaussian distribution candidate overbounds, $CDF_o(x)$.

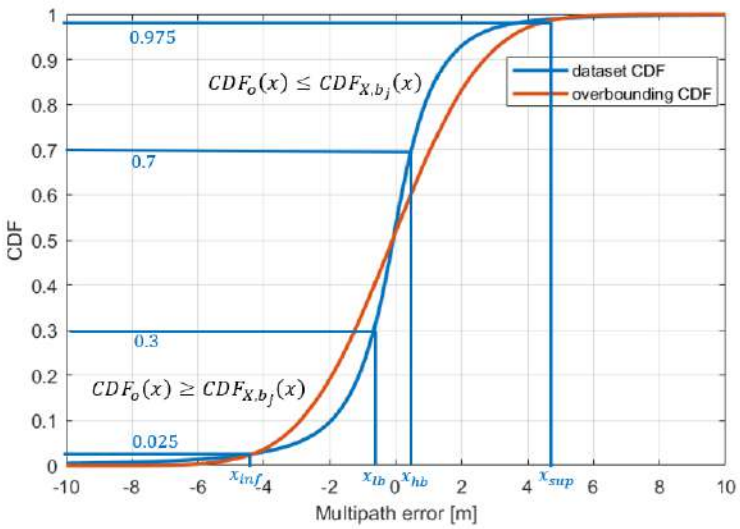

Figure 5-24 – Example of 97-th percentile right and left tail MN error Gaussian overbounding process

The Gaussian overbounding methodology has been applied to the MN error statistic models derived from a large data collection which is part of an experimental data campaign which has been conducted during the experimental phase of this PhD. These results can be found in section 6.3. These results have been finally used to test an innovative low-cost KF-based PVT estimator algorithm designed to reach good performances in presence of urban environment. The details are provided in Chapter 7.

5.3.2 MN Correlation Model

In addition to the probability distribution function and its moments, there are other fundamental characteristics of the multipath error in the urban environment which must be examined: the temporal and spatial correlation.

The temporal correlation of GNSS measurements is widely recognized. Indeed, some attempts to model it are found in [107], [108], [109], [110], while its effect on the positioning results is investigated in other works, [111], [112], [113]. Spatial correlation of GNSS atmospheric errors has been investigated in differential-based positioning approaches, [45], [49].

Concerning MP correlation errors, MP temporal and spatial error correlation are difficult to analyze; some attempts to model the temporal MP error correlation for static receiver configurations are given in [114]. Other works modelled the temporal MP error correlation for airplanes, in open sky environments [115]. However, to the knowledge of the author, the investigation of MP correlation errors for dynamic receivers, in urban environment is marginal, due to the high complexity of the MP environment (i.e. geometry of the reflectors, number of reflectors, etc.) and the fast variations of MP urban geometry due to receiver's dynamics. Indeed, the environment which is surrounding the receiver changes either smoothly or suddenly depending on the receiver dynamics and on the environment elements, and thus, as a function of the travelled space and observation time. This statement implies that to be representative of the real error correlation, the MP correlation error analysis in urban environments should be conducted studying a very large amount of measurement data collected in the urban environment from a dynamic receiver.

In this particular case, temporal correlation, which can potentially be exploited in a KF-based architecture [1], [2], only partially describes the correlation nature of the MP error. Thus, a more complete way consists of jointly characterizing the temporal correlation and the spatial correlation of MP error components.

Therefore, an efficient characterization of the MN error temporal correlation as a function of the receiver test velocity (mutual temporal-spatial correlation) is proposed in this final section of Chapter 5. For the sake of simplicity, the isolated dual constellation multipath plus noise error samples, obtained applying the methodology in section 5.2.1, are from now on termed MN error samples. The MN error samples are characterized by a given time epoch and are associated to the receiver speed, receiver position and the received signal C/N_0.

The temporal and spatial correlation of the MN error samples can be characterized in two different ways:

- A complex approach exploiting the time and receiver position associated to the MN error samples to perform the correlation (Time-Space (TS) correlation method); the outputs of the TS correlator are the temporal correlation functions associated to individual and different receiver paths.
- A simplified approach exploiting the time and the receiver speed information associated to the MN error samples to perform the correlation (Time-Velocity (TV) correlation method); MN error correlation is calculated only between MN error samples associated to the same receiver test speed. The outputs of the TV correlator are the temporal correlation functions associated to a specific receiver speed value.

The first method is more accurate and provides a better resolution of error correlation characteristics. However, introduction of the TS correlation into a PVT estimator introduces further difficulties. The correlation time could be estimated only if the receiver path is known since only in this case the corresponding temporal correlation function can be selected. This is impractical for low-cost PVT estimators, since it is not possible to access in real-time the "history" of the trajectory covered by the receiver.

Therefore, the simplified TV correlation method has been preferred. Section 5.3.2.1 is devoted to the mathematical model of the Time-Velocity Correlation model.

5.3.2.1 Time-Velocity Correlation Model

The methodology proposed in this work to characterize the temporal and spatial correlation of the isolated MN error components is the called Time-Velocity correlation technique. The goal of this technique is the characterization of the temporal correlation of MN error samples as a function of the receiver velocity. In particular, the approach consists of calculating the MN error temporal correlation from the set of MN error components, among all collected MN error components, associated to the same receiver speed bin.

The MN error samples isolated from PSR and PSR-R measurement of satellite i, for a given time epoch t could be also characterized by the user receiver speed, evaluated in the same time epoch, $\dot{R}$:

$$\widehat{MN}^i(t,\dot{R}),\ \widehat{MN}^i(t,\dot{R}) \qquad 5\text{-}25$$

From now on the TV correlation process will be described only for PSR MN errors. The same operation can be applied for PSR-R MN errors.

Firstly, the classic temporal correlation applied to the MN error samples is presented in section 5.3.2.1.1. Consequently, the temporal correlation of MN error samples as a function of the receiver speed is presented in section 5.3.2.1.2.

5.3.2.1.1 Temporal correlation

If the receiver speed is not taken into account, the temporal correlation of a set of consecutive $\widehat{MN}^i$variables (from $t = 0$ to $t = K$, where K is the number of collected measurements), is calculated as follows [109]:

$$r^i(l) = \frac{1}{K}\sum_{k=1}^{K} r_k^i(l) \qquad 5\text{-}26$$

with

- $l = 0,1,\dots,L$ equal to the time lag between the MN error samples;
- L is the maximum time lag;
- $r_k^i(l)$ is called the **correlation coefficient**, calculated independently for each satellite, i, at time epoch k. Applying the definition of correlation to $r_k^i(l)$, the correlation coefficient may be written as:

$$r_k^i(l) = \frac{\left(\widehat{MN}^i(k) - \mu_{\widehat{MN}^i(k)}\right)\cdot\left(\widehat{MN}^i(k+l) - \mu_{\widehat{MN}^i(k+l)}\right)}{\sigma_{\widehat{MN}^i(k)}\sigma_{\widehat{MN}^i(k+l)}} \qquad 5\text{-}27$$

where:

- $\mu_{\widehat{MN}^i(k)}$ and $\sigma_{\widehat{MN}^i(k)}$ are the sample mean and the sample standard deviation associated to the random process from which the random variable $\widehat{MN}^i(k)$ is a sample. These are equal to the values already calculated in section 5.3.1, given the corresponding C/N_0^i.
- $\mu_{\widehat{MN}^i(k+l)}$, and $\sigma_{\widehat{MN}^i(k+l)}$ are the sample mean and the sample standard deviation associated to the random process from which the random variable $\widehat{MN}^i(k+l)$. Again, these are equal to the values already calculated in section 5.3.1, given the corresponding C/N_0^i.
- $k = 0, \dots, K-1$ is the time epoch, where K is the number of time epochs inside the dataset.

To simplify the calculation, the correlation coefficients are computed only on a specific temporal sliding window, called **correlation window**:

$$\boldsymbol{W}_k^i = \left[r_k^i(0), \dots, r_k^i(L)\right] \quad 5\text{-}28$$

where k is the initial time epoch characterizing the subset of data and L is the maximum time lag, corresponding to the maximum number of samples inside the window.

The presence of a selective window is needed due to the extensive computational cost of the correlation applied to the whole dataset and the non-necessity to calculate the correlation factors where the correlation is theoretically irrelevant. The temporal window associated to the specific velocity bin is limited to 60 seconds; MN error samples separated by more than 60 seconds are assumed to be uncorrelated assuming that the minimum receiver speed is 5 Km/h: the receiver travels around 83 meters over 60s, which means that the MP environment configuration is likely greatly different from the initial configuration, and the error correlation should be negligible. Therefore, N_w is chosen in order to limit the temporal window to a maximum value of 60 s (depending on the sampling rate).

As a consequence, after the introduction of the correlation window, the temporal correlation is calculated in two different steps:

Firstly, the correlation coefficients are calculated independently for each sliding window $\boldsymbol{W}_k^i$. Those characterized by the same time lag, l, have been collected in the same set, $\boldsymbol{S}_l$, as follows:

$$\boldsymbol{S}_l = [\boldsymbol{W}_0^0(l), \dots, \boldsymbol{W}_{K-1}^0(l), \dots, \boldsymbol{W}_0^I(l), \dots, \boldsymbol{W}_{K-1}^I(l)] \quad 5\text{-}29$$

where I is the number of the visible satellites.

The time lag, l, as a consequence, is limited to the dimension of the sliding window. Secondly, the temporal correlation, at the time lag l, is obtained calculating the average of the correlation coefficients composing $\boldsymbol{S}_l$:

$$S_l = \frac{1}{N_s}\sum_{n=1}^{N_s} \boldsymbol{S}_l[n] \quad 5\text{-}30$$

where N_s is the number of correlation coefficients in $\boldsymbol{S}_l$. Finally, the correlation function corresponds to the correlation values S_l for the different values of the time lag $(0, \dots, L)$:

$$\boldsymbol{S} = [S_0, \dots, S_K] \quad 5\text{-}31$$

However, 5-30 cannot be directly applied due to two different issues related to the MN error samples under exam:

- Firstly, as seen in the MN statistical models, the MN average for some C/N_0 bins (especially for C/N_0 bins lower than 37 dB-Hz) are different from zero. This translates into a systematic bias in 5-27; $r_k^i(l)$ might be different from zero even if the lag between the two residual samples under exam is consistent. This presents the application of the direct application of the average operation. To remove the systematic bias, the corresponding mean must be removed from the MN residual components.
- Secondly, this correlation set doesn't contain homogeneous terms, since it contains correlation factors calculated for different instant of times, from different MN error components and different satellites, each one characterized by a different value of C/N_0. It can be shown that each factor depends on the product between the standard deviations of the corresponding MN statistical model associated to the tested MN error components. If the C/N_0^i values associated to the different MN error samples correspond to different C/N_0 bins of the MN characterization model, the values of the associated variance will be different. In this case, the correlation coefficients are not homogeneous. Thus, any type of operations, such as average or normalization, cannot be applied.

Therefore, three different steps can be applied to calculate the temporal correlation function:

1. The systematic bias removal, described in section 5.3.2.1.1.1.
2. MN error samples homogenization process, depicted in section 5.3.2.1.1.2.

3. Temporal correlation function calculation, defined in section 5.3.2.1.1.3.

5.3.2.1.1.1 Systematic bias removals

The sample average values corresponding to $\widehat{MN}_j^i(k)$ and $\widehat{MN}_j^i(k+l)$, are firstly derived from the MN statistical models described in section 5.3.1, knowing the corresponding C/N_0^i values associated to the two residual components, and successively removed. The corrected MN residual components are used to calculate the correlation coefficient:

$$\begin{aligned}\widetilde{MN}^i(k) &= \widehat{MN}^i(k) - \mu_{\widehat{MN}^i(k)} \\ \widetilde{MN}^i(k+l) &= \widehat{MN}^i(k+l) - \mu_{\widehat{MN}^i(k+l)}\end{aligned} \quad 5\text{-}32$$

The corrected correlation coefficient is equal to:

$$\tilde{r}_k^i(l) = \frac{\widetilde{MN}^i(k) \cdot \widetilde{MN}^i(k+l)}{\sigma_{\widehat{MN}^i(k)}\sigma_{\widehat{MN}^i(k+l)}} \quad 5\text{-}33$$

5.3.2.1.1.2 MN error samples homogenization process

This issue could be avoided selecting the MN error samples of the same correlation window such that the C/N_0 does not change significantly between the two epochs under exam. In particular, only the MN residuals of the correlation window having a C/N_0 difference lower than 2.5 dB-Hz with respect to the first residual of the window must be accepted.

The resulting correlation window for a specific satellite i, $\widetilde{\boldsymbol{W}}_l^i$, can be written as follows:

$$\widetilde{\boldsymbol{W}}_k^i = \left[\tilde{r}_k^i(0), \dots, \tilde{r}_k^i(L)\right] \quad 5\text{-}34$$

where:

$$\tilde{r}_k^i(l) \in \widetilde{\boldsymbol{W}}_k^i : C/N_0\left(\widehat{MN}^i(k+l)\right) - C/N_0\left(\widehat{MN}^i(k+l)\right) \leq 2.5 \text{ dB-Hz}$$

With this assumption, the resulting correlation factors will be homogeneous and the normalization can be applied, as shown in 5-35:

$$\widehat{\boldsymbol{W}}_k^i = \widetilde{\boldsymbol{W}}_k^i \cdot \sigma^2_{\widehat{MN}^i(0)} \quad 5\text{-}35$$

where the normalization factor is equal to the product of the standard deviations associated to the MN error components of the first correlation coefficient of the window, $\sigma^2_{\widehat{MN}^i(0)}$.

The proposed approach reduces the impact of the reflection's discontinuity in time: residual errors isolated from measurements that have a high variation of the C/N_0 from one epoch to the next are probably characterized by a sudden change of reflectors or a change between LOS and NLOS reception states.

The correlation coefficients are calculated independently for each sliding window $\widehat{\boldsymbol{W}}_k^i$. Those characterized by the same time lag, l, have been collected in the same set, $\widehat{\boldsymbol{S}}_l$, as follows:

$$\widehat{\boldsymbol{S}}_l = \left[\widehat{\boldsymbol{W}}_0^0(l), \dots, \widehat{\boldsymbol{W}}_{K-1}^0(l), \dots, \widehat{\boldsymbol{W}}_0^I(l), \dots, \widehat{\boldsymbol{W}}_{K-1}^I(l)\right] \quad 5\text{-}36$$

5.3.2.1.1.3 Temporal correlation function

The correlation is finally obtained calculating the average of the correlation factors which compose $\widehat{\boldsymbol{S}}_l$:

$$\hat{S}_l = \frac{1}{N_s}\sum_{n=1}^{N_s} \widehat{\boldsymbol{S}}_l[n] \quad 5\text{-}37$$

where N_s is the number of correlation coefficients in $\widehat{\boldsymbol{S}}_l$.

5.3.2.1.2 Temporal correlation as a function of the receiver speed

If the receiver speed is considered in the calculation, then, the temporal correlation is calculated only for a subset of consecutive $\widehat{MN}^i$variables of the correlation window, for which the associated received speed values meet, at the same time, two fundamental requirements:

Homogeneous receiver speed requirement: $\widehat{MN}^i$ are selected if the associated received speed values belong to the same receiver speed bin, which is defined as follows: the potential receiver speed dynamic, v, is uniformly divided into M different bins, of the specific bin size, $d_v = 5$ Km/h:

v bins	
v_1	$0 \leq v < d_v$
v_2	$d_v \leq v < 2d_v$
v_3	$2d_v \leq v < 3d_v$
v_4	$3d_v \leq v < 4d_v$
…	…
v_M	$(M-1)d_v \leq v < Md_v$

Table 5-13 – Definition of the receiver speed bins

Therefore, a given MN error, $\widehat{MN}^i(t, v)$, can be selected into the set of MN error samples corresponding to the specific bin v_j, $\widehat{\boldsymbol{MN}}_j$, if the corresponding receiver speed parameter belongs to v_j:

$$\widehat{MN}^i(t, v) \in \widehat{\boldsymbol{MN}}_j : v(t) \in v_j \quad 5\text{-}38$$

where $\widehat{\boldsymbol{MN}}_j$ is a subset of the general MN error components containing only the N_j error components belonging to the v_j, $\widehat{MN}_j^i$.

Constant receiver speed dynamics requirement: $\widehat{MN}_j^i(t)$ residual components must be selected only if they belong to the same receiver speed bin v_j, in consecutive time epochs of the data collection. In other words, the assumption is that the correlation factors are calculated only for constant speed dynamics and continuous time. The final subset is defined as follows:

$$\boldsymbol{W}_{k,j}^i = \left[r_{k,j}^i(0), \dots, r_{k,j}^i(N_v)\right] \quad 5\text{-}39$$

where:

- k is the initial time epoch characterizing the subset of data associated to the same velocity bin v_j;
- $N_v \leq L$ is the number of consecutive epochs where the receiver speed belongs to the velocity bin v_j, where L value is chosen in order to limit the temporal window to a maximum value of 60 s (depending on the sampling rate) (section 5.3.2.1.1).

The correlation coefficients are calculated independently for each satellite i and each sliding window $\boldsymbol{W}_{k,j}$. Those characterized by the same time lag, l, have been collected in the same set, $S_{j,l}$, as follows:

$$\boldsymbol{S}_{j,l} = \left\{\boldsymbol{W}_{0,j}^0(l), \dots, \boldsymbol{W}_{K-1,j}^0(l), \dots, \boldsymbol{W}_{0,j}^I(l), \dots, \boldsymbol{W}_{K-1,j}^I(l)\right\} \quad 5\text{-}40$$

The characteristics of the correlation factors, already presented in section 5.3.2.1.1, hold also for $r_{k,j}^i$. Therefore, systematic bias removal (5.3.2.1.1.1) and MN error samples homogenization process (5.3.2.1.1.2) should be applied before to calculate the temporal correlation as a function of the receiver speed:

As described in section 5.3.2.1.1.1, the MN error samples corresponding to $\widehat{MN}_j^i(k)$ and $\widehat{MN}_j^i(k+l)$, are firstly derived from the MN statistical models described in section 5.3.1, knowing the corresponding C/N_0^i values associated to the two residual components, and successively removed. The corrected MN residual components are used to calculate the correlation coefficient:

$$\tilde{r}_{k,j}^i(l) = \frac{\widehat{MN}_j^i(k) \cdot \widehat{MN}_j^i(k+l)}{\sigma_{\widehat{MN}_j^i(k)} \sigma_{\widehat{MN}_j^i(k+l)}} \quad 5\text{-}41$$

Consequently, the resulting correlation factor set, $\widehat{\boldsymbol{S}}_{j,l}$, is calculated applying the MN error samples homogenization process, section 5.3.2.1.1.2. The TV correlation is finally obtained calculating the average of the correlation factors which compose $\widehat{\boldsymbol{S}}_{j,l}$, as described in 5.3.2.1.1.3:

$$\hat{S}_{j,l} = \frac{1}{N}\sum_{n=1}^{N} \hat{S}_{j,l}\,[n] \qquad 5\text{-}42$$

The final correlation function is, therefore, a 2D function of the time lag, l, and receiver speed bin, j, $\hat{S}_{j,l}$, as illustrated in Figure 5-25. Each line of the 2D matrix, corresponds to the time correlation function for a specific receiver speed bin.

The TV Correlation has been applied to a large data campaign conducted during the experimental phase of this PhD. The experimental results are illustrated in section 6.4. The TV correlation functions characterized with this methodology can be easily exploited by a given PVT estimator to improve the PVT estimation solutions, in an urban environment. The corresponding TV correlation function, at a given epoch, could be selected by the PVT estimator given the estimated receiver speed at the specific epoch. Successively, from the TS correlation function the correlation time can be derived which can be directly exploited in a modified PVT estimator. The proposed solution will be investigated in the final part of the thesis, Chapter 7.

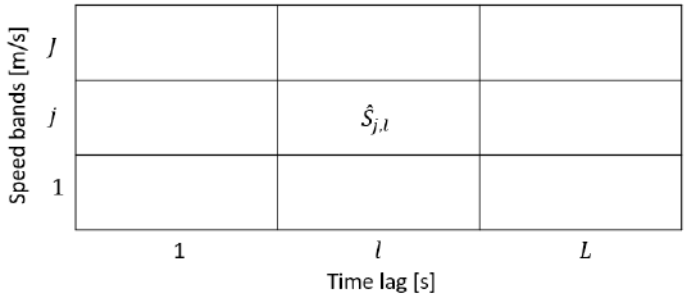

Figure 5-25 – Time-Velocity correlation 2D matrix model

5.4 Conclusions

This chapter has described the methodology for isolating and characterizing the MP and thermal noise error components from the PSR and PSR-R measurements of a low-cost GNSS receiver in an urban environment, before exploiting this knowledge to improve the PVT estimator, in Chapter 7.

The growth of the low-cost GNSS receiver market and the necessity of localization/navigation applications in urban environment in recent years, necessitates methodologies that can efficiently handle the MP effect of the urban environment without increasing the GNSS receiver costs; an unsuitable option for the mentioned market segment. However, many of the MP mitigation strategies adopted in the literature are too expensive for low-cost applications. For this reason, measurement weighting and masking techniques are widely applied to low-cost receiver PVT estimators. Nevertheless, the efficiency of such solutions depends on the appropriateness of the multipath error models. Hence, it is concluded that the **use of measurement modelling to properly characterize the MP error** in the urban environment is the approach to be taken.

Different processing strategies have been proposed in the literature; in this work it is concluded to determine the **differential observed-minus-computed range** measure to estimate the combined multipath and noise error component, thereby removing the signal is space errors and atmospheric delays. The receiver clock remained a nuisance parameter within the multipath and noise estimates and a method for **detrending and filtering the receiver clock** was selected with a **0.4Hz frequency determined as optimal filter threshold** for the type of receiver and clock under test. Finally, to apply the methodology for a dual constellation receiver, an **inter-constellation channel bias was detected** and verified through additional offline tests: regarding PSR measurements, the **main complication** is the difference between the clock bias term values between the GPS signals and the Galileo signal, **the so-called GPS to Galileo Post-Processing Time-Offset (GGPPTO) term**. It has been demonstrated that GGPPTO must be removed from the Galileo measurements before applying the clock error component removal, since is value has an average of roughly 2m and a variance of roughly 0.2m and,

therefore, it is non-negligible and prevent the used of dual constellation methodology if not mitigated. The concluded methodology is applied in Chapter 6.

Further work was undertaken regarding a methodology to discriminate between LOS and NLOS signal reception conditions. A camera image processing technique exploiting fish-eye camera pictures was tested. However, it was **concluded that the image processing suffers from a number of inaccuracies** and is not recommended to be directly used in the employed configuration. Indeed, the final methodology configuration combines the use of the fish-eye camara pictures with received signal C/N_0 threshold verification, although a significant number of measurements are set as unusable as a result. Nevertheless, this complete configuration is not adopted in the following of this work since the positioning platform defined in Chapter 1 does not include a fish-eye camera to keep a low-cost solution. Rather, this methodology was used to validate the use of a $\boldsymbol{C/N_0}$ **threshold as an approximate NLOS detection** method and to determine the C/N_0 threshold numerical value (equal to 35dB-Hz and justified in Chapter 6).

Refinement of the modelling and characterization of MN errors **led to a choice of C/N0 bin size** and the use **of core CDF overbounding at the 95% level**. The final conclusions in this chapter relate to the modelling of error temporal correlation (analysed in full in Chapter 6 and employed in Chapter 7). It was concluded that **temporal correlation alone is insufficient** to capture the true behaviour of error correlation due to the stop start nature of the vehicle dynamics. A **comparison of Time-Space and Time-Velocity correlation models was made**, concluding in the **selection of Time-Velocity for its practicality** in real-time applications.

6 Multipath Characterization Results

In Chapter 5, methodologies for deriving mathematical models of the multipath plus noise (MN) error component were derived for pseudorange (PSR) and pseudorange-rate (PSR-R) measurements. In this chapter, theses methodologies are applied, in order to isolate and characterize such errors and derive the models which will be critical to the PVT architectures studied in Chapter 7. Therefore, a substantial data collection, composed of several datasets from multiple data collection runs, has been built, employing a low-cost GNSS receiver mounted on a vehicle following a predetermined route in Toulouse city centre.

The applied isolation methodology consisted of removing all the other error components present on the PSR and PSR-R measurements, by exploiting their spatial and temporal correlation properties. The applied statistical characterization methodology consisted of calculating the empirical PDFs from the isolated MN error component and calculating its associated sample mean and sample standard deviation as a function of the satellite elevation angle and the received signal C/N_0. The applied overbounding process consisted of finding a Gaussian distribution which overbounds the MN error component empirical PDF fulfilling specific criteria. Moreover, in addition to the three previous commented methodologies, a method to estimate the temporal and spatial correlation of isolated MN components as well as a method to classify the isolated MN components with respect to LOS and NLOS reception states, both presented in section 5.3, have also been applied to the collected data. The application of both methods targeted a more detailed/complete mathematical modelling of the MN error component.

Considering the motivation and general goal of this chapter, eight objectives have been set:

1) To test the single constellation PSR and PSR-R MN error isolation methodology, comparing the experimental results with the theoretical assumptions made in section 4.4.
2) To test the dual constellation PSR and PSR-R MN error isolation methodology, comparing the experimental results with the theoretical assumptions made in section 4.4.
3) To determine, from the collected data, the most suitable observable (or receiver signal) parameter allowing to discriminate/estimate the received signal conditions, LOS or NLOS.
4) To determine the value, or threshold, of the previously identified observable parameter to be used to estimate if the received signal is in LOS received signal conditions, when the observable value is above the threshold, or in NLOS signal received conditions, when the observable value is below the threshold; note that this threshold must not be interpreted as a certainty but as an estimation since it is guaranteed that for LOS received signal conditions the observable value can be below the threshold (and the opposite for NLOS); nevertheless, the threshold is chosen to minimize the probability of making a wrong estimation when only using the observable value as a decision metric.
5) To investigate the satellite availabilities in the urban environment to determine whether the use of measurements from two constellations are needed for isolating and removing the receiver clock bias.
6) To obtain a reliable GPS L1 C/A and Galileo E1 OS PSR and PSR-R MN error component statistical models from the collected PSR and PSR-R measurements as a function of observable (or receiver signal) parameters; the statistical error models are based on the derivation of the empirical PDF, assuming that the MN error component can be modelled as an ergodic random variable for a given value range of the selected observable parameter, as proposed in section 5.3;
7) To obtain the MN error mathematical model from the collected PSR and PSR-R measurements which can be exploited by a KF-based PVT estimator architecture; this mathematical model is obtained by calculating the Gaussian overbounding models of the MN error component empirical PDFs derived in the previous point, as described in section 5.3.1.3;
8) to obtain the estimation of the MN error temporal correlations as a function of user receiver speed from collected PSR and PSR-R measurements, obtained by an innovative Time-Velocity correlation approach proposed in section 5.3.2.

The description of the equipment, setup and the features of the data collections is given in Section 6.1. The results of the PSR and PSR-R MN error isolation, characterization and LOS/NLOS classification methodologies, applied to real measurements, are presented in section 6.2. The results of the PSR/PSR-R MN error Gaussian model, obtained through the application of the Gaussian overbounding processes, are illustrated in section 6.3. The results of the PSR/PSR-R MN error temporal correlation as a function of the receiver under test speed are detailed in Section 6.4. Finally, the conclusions of the chapter are summarized in section 6.5.

6.1 Data Campaign description

To isolate and to characterize the MN error components from true PSR and PSR-R measurements of a GNSS receiver, a data collection campaign has been conducted during this work. The goal of the data campaign is to collect single frequency, dual constellation (GPS, Galileo) PSR and PSR-R measurements with a dynamic low-cost receiver in an urban environment. A single frequency, low-cost receiver has been chosen to collect the PSR and PSR-R measurements in urban environment representing a range of GNSS receivers which could be mounted on vehicles, such as scooters, bicycles and cars.

Recall that the choice of a dual constellation receiver is due to the inherent advantage of increasing the number of satellite measurements, which directly increases the satellite availability and improves the satellite geometry. Moreover, Galileo E1 OS signal is a compatible and interoperable with GPS L1 C/A signal, which means that GNSS receiver manufactures can enable the implementation of dual GPS\Galileo RFFE filtering and signal processing on their receivers with a minimum increase in production and final product costs.

Recall also that the choice of PSR and PSR-R measurements is dictated by the urban environment limitations: the numerous loss-of-lock of GNSS signals due to masking and extreme multipath as well as an increase in cycle slips affecting the carrier phase measurements. It follows that carrier phase measurements, usually used for high-accuracy applications, are not reliable measurements in a urban environment. Therefore, code PSR measurements and Doppler frequency PSR-R measurements are collected and exploited in this work.

The MP environment chosen to collect the data is the Toulouse city center area. The data collection campaign is composed of several datasets which have been employed for different purposes:

- to provide initial results and to verify the efficiency of the methodology,
- to tune the characterization parameters with respect the specific MP environment configuration of Toulouse city area,
- to investigate the LOS\NLOS reception state classification,
- to provide a large number of isolated MN error component values used to elaborates the MN statistical models.
- To test PVT navigation filers exploiting the derived MN error components overbounded Gaussian models as well as the derived Time-Velocity correlation (Chapter 7)

Despite the total amount of data collected during the data campaign exceeding 50 hours, the characterization obtained from the data campaign under exam might still be considered to not be a highly accurate description of the statistical model of the multipath error component in the case of a large MP environment, like an urban area. Similarly, LOS\NLOS classification performance may also be limited by the number of post-processed data. For this reason, the results shown in this chapter may have a potentially limited numerical validity. An even larger data campaign is thus highly recommended.

The elements constituting the data collection campaign are described in the following subsections. The list of the equipment used to perform the data campaign is provided in section 6.1.1. The hardware setup description is proposed in section 6.1.2. The MN isolation methodology proposed in Chapter 5 requires external inputs, which are detailed in section 6.1.3. The reference trajectory used for the data collections is presented in section 6.1.4.

6.1.1 Data Collections Equipment

The data collection campaign is conducted collecting simultaneously the pictures of the environment from a fisheye camera and the GNSS measurements from two different receivers: a low-cost receiver and a high-accuracy GNSS receiver combined with an Inertial Measurement Unit (IMU), both mounted in a dynamic platform moving in the urban area. The list of the equipment used during the data campaign is summarized in Table 6-1.

The first receiver is the designated low-cost “mass-market” receiver, working in the L1 frequency band, which collects the data to be analyzed containing the MN errors component to be isolated. The chosen receiver is a single-frequency multi-constellation U-Blox EVK-M8T [116], manufactured in 2015, mounting an active ANN-MS patch antenna, [117]. The receiver configuration is illustrated in Figure 6-1.

The role of the high-accuracy GNSS\IMU integrated receiver is to obtain a very precise PVT solution of the car during the data collection campaign, considered as the reference (true) position of the receiver at any instant of time, which will be used to remove the true range component from the PSR and PSR-R measurements (section 5.2). Moreover, this receiver is also responsible for providing the vehicle heading information and speed information which can be extrapolated to the test receiver antenna using the known level-arm between the IMU and the antenna. The selected high-accuracy GNSS\IMU integrated receiver is a Novatel GNSS\INS tightly-

coupled solution, called SPAN (Synchronous Position, Attitude and Navigation), using a Novatel Propak 6 GNSS receiver [118], and a tactical grade U-IMU-LCI [119]. The SPAN receiver accuracy is at the decimetre-level or better, depending on the surrounding environment [120]. In an urban environment, the SPAN receiver accuracy can be generally expected to be at sub-decimeter level accuracy on the beltway and at sub-meter level accuracy in the most severe urban canyons [65]. Moreover, although the lever arm between the SPAN antenna and the receiver under test antenna was measured carefully, errors of a few centimeters can be expected on the reference trajectory even when the Novatel SPAN ambiguities are fixed due to lever-arm distance and orientation error [65]. The receiver configuration is illustrated in Figure 6-2.

The role of the fish-eye camera consists in taking pictures of the sky-environment of the vehicle in synchronization with the U-Blox estimated time. The fish-eye camera used in this study consists of a fish-eye lens [121] connected to an IDS digital camera of the CMOS sensor family [122]. With this configuration, the camera can capture pictures with a field angle greater than 180° (~185°) which allow the full coverage of the perimeter surrounding the receiver antenna, with an elevation angle range going from 0° to 90°. The captured images are in a greyscale and have a resolution of 1280 × 1024 pixels. The internal parameters of the fish-eye camera have been estimated with the Omnidirectional Calibration Toolbox for MATLAB [105]. The fisheye camera equipment is described in Figure 6-3.

Finally, the GNSS measurements of the low-cost receiver under test have been collected on a Laptop through a USB connection. At the same time, the fish-eye camera pictures have been independently collected on another Laptop, through a USB connection.

Device	Model	Year	Role	References
Low-cost GNSS Receiver	U-Blox M8T	2015	GPS/Galileo L1 receiver dynamic data collection	Figure 6-1
Low-cost GNSS Antenna	U-Blox Patch Antenna		GPS/Galileo L1 receiver dynamic measurement acquisition	Figure 6-1
Integrated GNSS and IMU receiver	Novatel & Span	2015	GPS/GLONASS L1 L2 Reference trajectory data collection	Figure 6-2
High-accuracy GNSS Antenna	703GGG		GPS/GLONASS L1 L2 Reference trajectory measurement acquisition	Figure 6-2
Video Camera	IDS uEye Camera UI-3240CP	2017	Acquiring pictures of environment surrounding dynamic receiver antenna	Figure 6-3
Fish-eye Lens	Fujitsu FE185C057HA-1		Allow to capture pictures with a field angle of ~185°	Figure 6-3
Laptop (PC-RAW)			Collect raw GNSS measurements	
Laptop (PC-IA)			Collect fisheye pictures	

Table 6-1 – Equipment description

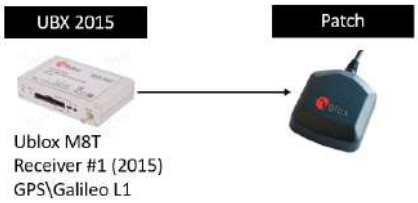

Figure 6-1 – GNSS receiver and antenna used for the data collection

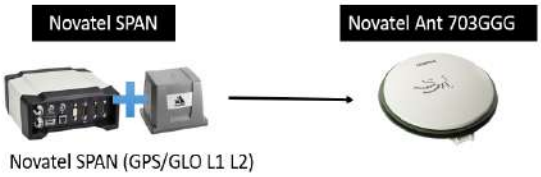

Figure 6-2 – GNSS receiver and antenna used for estimates precise reference trajectory

Figure 6-3 – Left: IDS uEye UI-3240CP camera, Center: Right: Fish-eye Lens Fujistu FE185C057HA-1, Right: Fish-eye Lens mounted on uEye camera

6.1.2 Hardware Setup

In this section, the hardware setup of the equipment used to perform the data campaign is described. The first part is devoted to the hardware setup installed on the dynamic platform. The second part consists of the description of the hardware connections.

The receiver under test, represented as already mentioned by the U-Blox EVK-MT8 2015, have been installed in a van: a Citroen Jumpy furnished by ENAC, (Toulouse, France). The picture of the van is presented in Figure 6-4. The van is prepared to contain a laboratory equipped with a battery, and some platforms used to install the equipment. On the roof of the van, a platform is mounted where the antennas and the fisheye camera are installed.

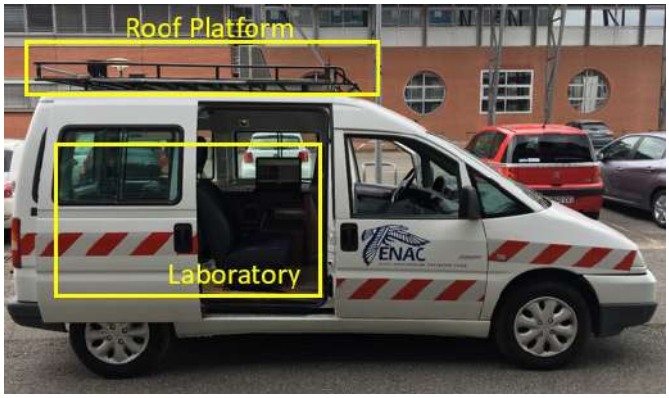

Figure 6-4 – Renault Jumpy used to make the Data Campaign

In the van's laboratory, the IMU, the Novatel receiver, the U-Blox M8T 2015 receiver and the laptop are set up as shown in Figure 6-5. The equipment is fed by an internal battery as presented in Figure 6-6. Finally, the antennas are mounted on the roof platform as showed in Figure 6-7. To facilitate this operation, an antenna support is already installed and fixed where the antenna will be screwed.

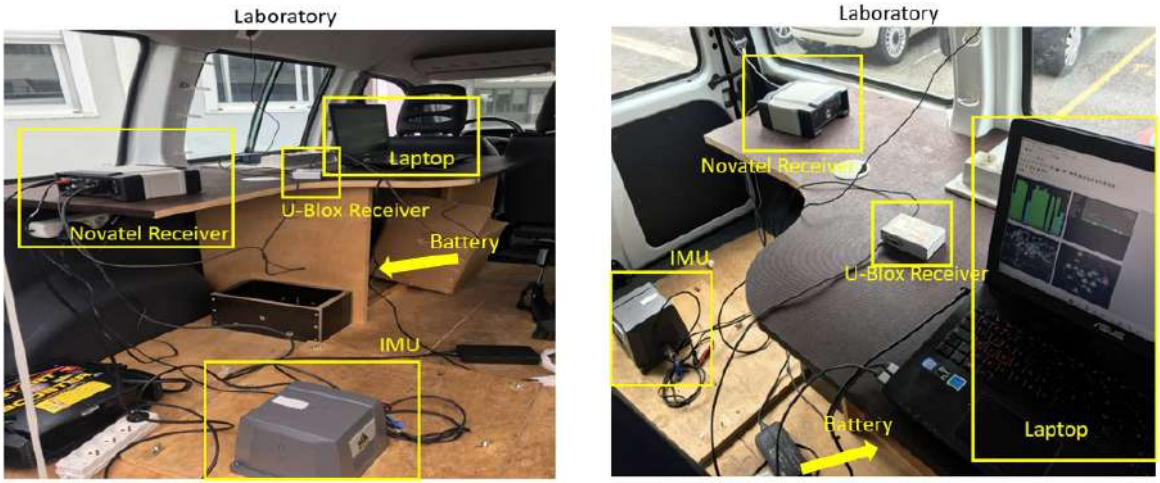

Figure 6-5 – Laboratory of the Renault Jumpy

Figure 6-6 – Power supply for the set-up (battery and inverter)

Figure 6-7 – Roof Platform of the Renault Jumpy

In Figure 6-8, the Dynamic Platform hardware setup is portrayed, considering approximately the base of the IMU device and the phase center of the antennas. The U-Blox M8T 2015 antenna, Novatel antenna and the fisheye camera are installed on the roof of the ENAC test vehiclse. The Novatel module, the IMU sensors, the U-Blox receiver as well as the computers, which records the GNSS data and pictures, are inside the vehicle.

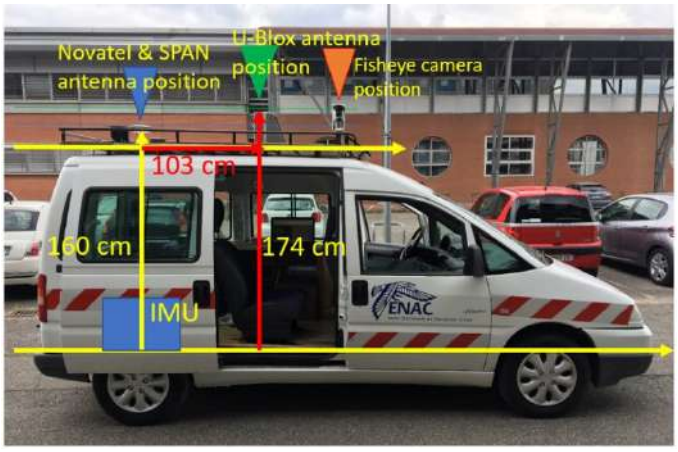

Figure 6-8 – Experiment Data Campaign Setup

The camera has been aligned with the SPAN orientation used for the dynamic data collection, as presented in Figure 6-9.

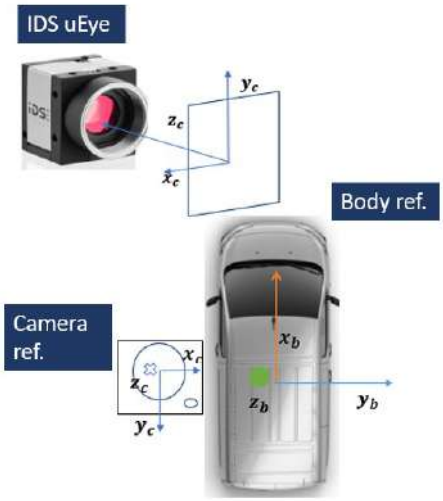

Figure 6-9 – Camera reference vs. Body reference

Once the hardware setup has been presented, the hardware connection configuration is now described for the two "dynamic" receivers, low-cost and high-accuracy receivers. Afterwards, the configuration between the receiver under test and the fisheye camera is described.

The configuration of the U-Blox EVK-M8T 2015 and Novatel SPAN is illustrated in Figure 6-10. The data from the U-Blox EVK-M8T 2015 and Novatel SPAN are collected independently. This means that U-Blox, and Novatel are not directly connected for example via a master/slave configuration. Collected data synchronization will thus be achieved in the post-processing stage exploiting the independent GPS time-tag by which the receivers identify the collected data. These time estimations are supposed to be sufficiently accurate with respect to the data collection rate to provide a robust enough post-processing time synchronization between the independent collected data. Moreover, to ensure time synchronization, the individual data collection never exceeds 4 hours, avoiding potential large time drift between the two receivers. The U-Blox receiver is connected to a Laptop (PC-RAW) by a USB link; hence, U-Blox data collection is controlled and saved in the internal memory of the Laptop. Novatel SPAN uses its internal memory to save the data measurements, as seen in Figure 6-10, which means that it is not directly connected to the laptop.

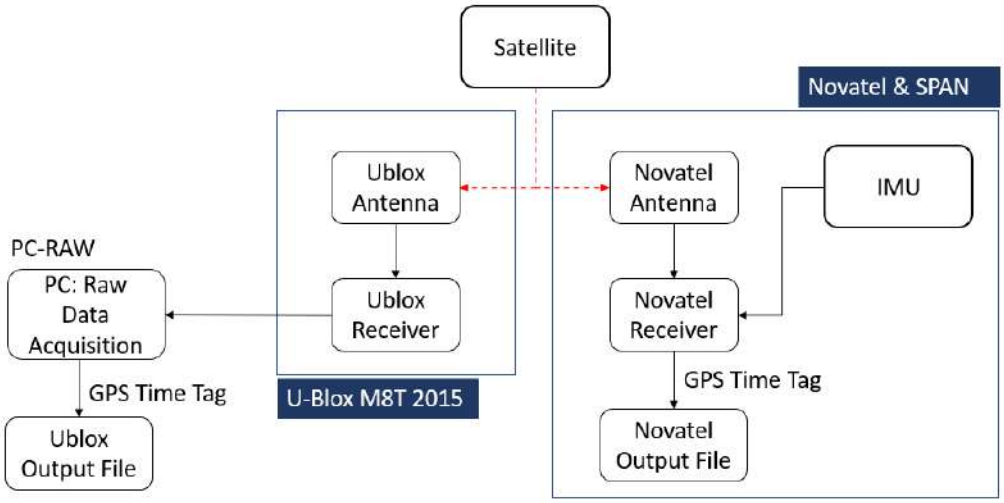

Figure 6-10 – U-Blox and NovAtel synchronization setup.

The configuration of the U-Blox EVK-M8T 2015 and fisheye camera is illustrated in Figure 6-11. The hardware configuration is based on a master/slave solution where the U-Blox receiver is used to trigger the camera. U-Blox generates time-pulses which are synchronized to the GPS Time Tag of the collected measurements; U-Blox and fisheye camera have a wired connection, as a consequence, the camera shot is triggered by the U-Blox generated

impulse. In addition, the camera is connected to the PC which is used to save the pictures each time the camera is triggered. A photo of the setup connections is presented in Figure 6-12.

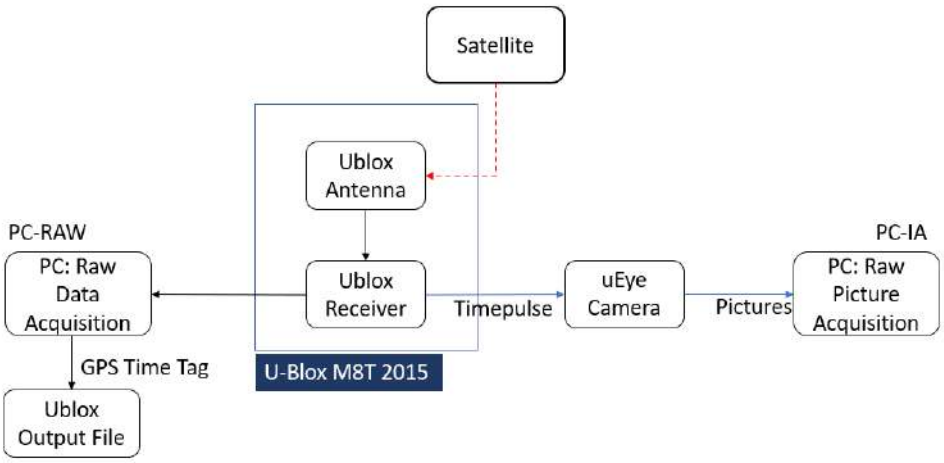

Figure 6-11 – U-Blox and Ueye camera synchronization setup.

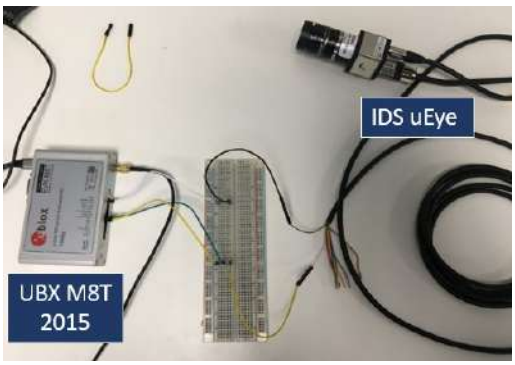

Figure 6-12 – UBX M8T and IDS Ueye Connection

6.1.3 External inputs

A high-quality static receiver of a reference station in the Toulouse region is used to collect a static dataset of PSR and PSR-R measurements, which have been used to correct common satellite and atmospheric errors (section 5.2) [123]. The used reference station was TLSG from the RGP network. The receiver position is portrayed in Figure 6-13-Figure 6-14.

Figure 6-13 – CNES Reference station on Toulouse map (Google Maps)

Figure 6-14 - CNES Reference station antenna on building (Google Maps)

6.1.4 Trajectory used for data collections

The selected location for the data collection campaign was the Toulouse urban area. The location was chosen in order to have a representation of different types of obstacles and different LOS\NLOS scenarios. The trajectory followed in the Toulouse urban area is presented in Figure 6-15. The trajectory covered during the data collection is representative of an urban environment scenario containing three types of situations:

- a suburban environment corresponding to areas of low buildings;
- a dense urban environment corresponding to urban canyons and significant masking;
- open areas.

Some pictures from the trajectory are portrayed in Table 6-2.

The first part of the trajectory connects ENAC headquarters to the city centre (black line in Figure 6-15). The second part of the trajectory starts in the city centre and is based on several loops in the most challenging canyons of the city (blue line in in Figure 6-15). Therefore, the same path has been covered in different time epochs to collect the measurements with different satellite positions in the sky. Finally, the last part of the trajectory connects the city centre to ENAC headquarters.

The reference trajectory was obtained by post-processing both IMU and GPS L1/L2 data from the Novatel SPAN module. Data was post-processed using Inertial Explorer 8.40, in tight integration mode and using multi-pass processing. The maximum baseline distance between the dynamic receiver and the reference station is 8.9 Km.

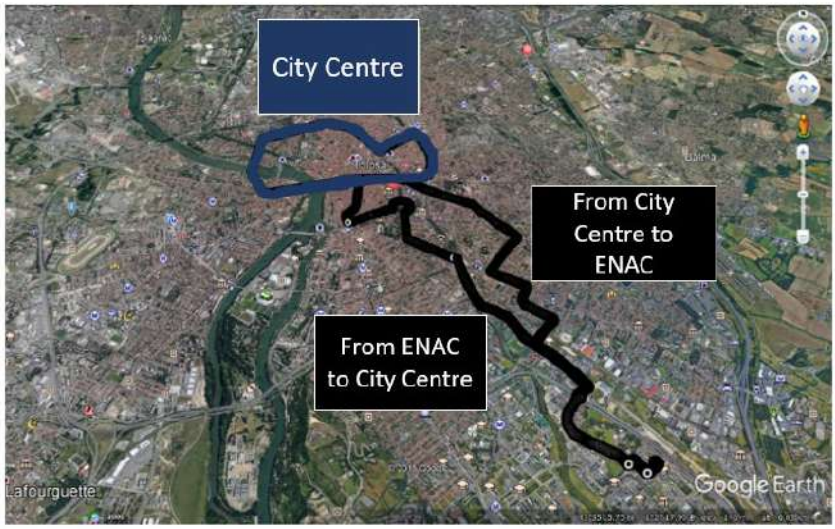

Figure 6-15 – Trajectory of the data collection experiment.

Traj.	Suburban environment	Dense urban environment	Open Sky Area
Pictures			
			

Table 6-2 – Photos from Data campaign trajectory

6.2 MN Isolation and Characterization results

The MN error isolation and characterization methodologies proposed in Chapter 5 have been applied to the datasets collected during the data collection campaign described in the previous section. Six main objectives are targeted:

Objective 1: The first objective allows to understand if the mathematical Isolation Methodology proposed in Chapter 5 for single constellation PSR and PSR-R measurements (GPS L1 C/A) can be exploited to obtain a reliable MN error components characterization.

Objective 2: The second objective allows to understand if the mathematical Isolation Methodology proposed in Chapter 5 for dual constellation PSR and PSR-R measurements (GPS L1 C/A and Galileo E1 OS) can be exploited to obtain a reliable MN error components characterization.

Objective 3: The third objective consists of the determination of the most suitable receiver signal parameter or observable which allows the discrimination/estimation of the received signal conditions, to be either LOS or NLOS.

Objective 4: The fourth objective allows the definition of an empirical threshold of the previous identified observable (received signal) parameter, able to estimate LOS and NLOS receiver reception states. This empirical threshold can be easily exploited in a standalone PVT estimator. New PVT estimation techniques can take advantage of the LOS/NLOS discrimination to improve the PVT estimation accuracy, as described in Chapter 7.

Objective 5: The fifth objective proposed in this section consists of determining whether the use of dual constellation measurements for isolating and removing the receiver clock bias is necessary when considering the increased complexity and uncertainty brought by dual constellation algorithm and GGPPTO term (see section 5.2.2.2).

Objective 6: The last objective targets a reliable PSR and PSR-R MN error component characterization which can be exploited by a PVT estimator to develop new PVT estimation algorithms in order to improve the accuracy of the PVT estimations.

Different tests have been performed to tackle the objectives previously presented. The test's description, configuration and the relative results are presented in the following sections:

- The tests performed to meet the requirements of Objective 1 is described in section 6.2.2.
- The tests performed to meet the requirements of Objective 2 is described in section 6.2.3.
- The tests performed to meet the requirements of Objective 3 is described in section 6.2.4.
- The tests performed to meet the requirements of Objective 4 is described in section 6.2.5.
- The tests performed to meet the requirements of Objective 5 is described in section 6.2.6.
- The tests performed to meet the requirements of Objective 6 is described in section 6.2.7.

The description of the datasets applied in the following tests is illustrated in section 6.2.1.

6.2.1 Datasets description

Three different Data Collections have been exploited to conduct the different tests (section 6.2). The characteristics are summarized in the following paragraphs.

The characteristics of *Data collection 1* are depicted in Table 6-3. This is a dual constellation dataset (GPS L1 C/A, Galileo E1 OS) of short duration, roughly 2 hours and 90 minutes, where the data-rate is equal to 5 Hz.

Data collection 1: *parameters*		
Date		23/07/2018
Length		2 hours and 90 minutes
Receiver under test	Data Rate	5 Hz
	Evaluated constellation	GPS L1 C/A, Galileo E1 OS
Reference receiver	Data Rate	200 Hz
	Evaluated constellation	GPS, GLONASS

Table 6-3 – Summary of the characteristics of the Dataset 1

The characteristics of the *Data collection 2* are described in Table 6-4. This dual constellation dataset has a length of about 4 hours and 30 minutes. The dataset is composed of the GNSS raw measurements and the fisheye pictures. The receiver under test data-rate is equal to 5 Hz, therefore fisheye camera rate is also equal to 5 Hz.

Data collection 2: *parameters*		
Date		23/11/2018
Length		4 hours and 30 minutes
Receiver under test	Data Rate	5 Hz
	Evaluated constellation	GPS L1 C/A, Galileo E1 OS
Reference receiver	Data Rate	200 Hz
	Evaluated constellation	GPS, GLONASS
Fisheye Camera	Data Rate	5 Hz

Table 6-4 – Summary of the characteristics of the Dataset 2

The characteristics of the *Data collection 3* are presented in Table 6-5. The data collection is based on 48 hours of data, collected in several days, for up to 3 hours per day. *Data collection* 3 is composed by GNSS raw measurements and fisheye pictures. The receiver under test data-rate and the fisheye camera rate are equal to 5 Hz.

Data collection 3: *parameters*		
Date		from 23/10/2019 to 20/11/2019
Length		48 hours
Receiver under test	Data Rate	5 Hz
	Evaluated constellation	GPS L1 C/A, Galileo E1 OS
Reference receiver	Data Rate	200 Hz
	Evaluated constellation	GPS, GLONASS
Fisheye Camera	Data Rate	5 Hz

Table 6-5 – Summary of the characteristics of the Dataset 3

6.2.2 Objective 1: Validation of MN isolation Methodology for single constellation measurements

The description of the test conducted to validate the Single constellation measurements MN Isolation Methodology, is presented in section 6.2.2.1. The expected theoretical Multipath and Thermal Noise error model, isolated from PSR and PSR-R measurements, illustrated in Chapter 0, are summarized in section 6.2.2.2. The results of the test are provided in section 6.2.2.3. Finally, section 6.2.2.4 presents the conclusions.

6.2.2.1 Test description

In this test, the capacity of the methodology proposed in Chapter 5, to isolate a Single Constellation Multipath and thermal Noise (MN) errors from PSR and PSR-R measurements, is analyzed. The test consists in calculating a preliminary statistical characterization of the GPS L1 C/A MN error components (PDFs), and in comparing the real data PDFs results with the theoretical expected PDFs (expressed in Chapter 0). The resulting calculated PDFs are modelled as a function of two different observable parameter, the received signal C/N_0 and the satellite elevation angle. The theoretical expected model, derived from Chapter 0, classified for LOS and NLOS reception state, are summarized in section 6.2.2.1.

Two different analyses are conducted:

- **Analysis 1**: To characterize the PSR/PSR-R MN error components, as a function of the C/N_0 and compare them with the theoretical expected models. The Dataset applied in this case is Data collection 1. For this preliminary evaluation, the measurement output data rate has been limited to 1 Hz.
- **Analysis 2**: To characterize the PSR/PSR-R MN error components, as a function of the elevation angle and compare them with the theoretical expected models. The Dataset applied in this case is Data collection 1. For this preliminary evaluation, the measurement output data rate has been limited to 1 Hz.

The choice of the C/N_0 bin size depends on the number of samples used to characterize the residual errors in that specific bin. The optimal choice is to choose a small bin size, resulting in a higher fidelity model. Such a choice will reduce dramatically the number of MN samples included in the different bins, affecting the reliability of the final statistics. Knowing that the dataset under exam is too small to apply a reduced bin size, the selected bin size was 5 dB-Hz. The same applies to the elevation angle bin size; in that case, 10 degrees bin size has been selected.

The configuration of the executed analyses is summarized in Table 6-6.

Objective	Analysis	Constellation	Measurements	Reception State	C/N_0 Bin size [dB-Hz]	El angle Bin size [degrees]	Statistic model	Data Set
To test the MN isolation and characterization methodology for single constellation measurements	**Analysis 1**: MN error characterization as a function of C/N_0	GPS	PSR, PSR-R	LOS + NLOS	5	---	PDF, Main peak, average, variance	Data Collection 1
	Analysis 2: MN error characterization as a function of elevation angle	GPS	PSR, PSR-R	LOS + NLOS	---	10	PDF, Main peak, average, variance	Data Collection 1

Table 6-6 – Description of the Analysis developed for Objective 1

6.2.2.2 Theoretical expected Multipath plus noise characterization

The theoretical PSR MN error model is described in section 6.2.2.2.1. The theoretical PSR-R MN error model is presented in section 6.2.2.2.2.

6.2.2.2.1 Theoretical results of PSR LOS\NLOS MN

Theoretical results of LOS/NLOS MN reflection affecting PSR measurements have been presented in section 4.4. They can be summarized as follows:

- LOS MN: The estimated MN error PDF obtained from LOS MP error should theoretically be close to a centered Gaussian distribution: this result comes from the combination of
    - the presence of LOS signal, which implies the absence of a systematic bias in case of MP effected measurements;
    - the presence of the residual MP component, smaller or comparable to thermal noise errors, which can create either zero-mean positive or negative errors, evolving in time (similar to thermal noise);
    - the presence of thermal noise, which is centered Gaussian distributed.
- NLOS MN: The estimated MN error PDF obtained from NLOS MP error should theoretically be a positive-biased and non-symmetrical distribution, and should tend to have a very heavy positive tail: this result comes from the combination of
    - the absence of LOS signal, which should always introduce a positive bias since the receiver only tracks the NLOS signal(s).
    - the presence of residual MP components (smaller than thermal noise error), which can create either zero-mean positive or negative errors, evolving in time, with a variance equal or smaller than the one of the thermal noise components.
    - the presence of significant MP components (bigger than thermal noise error), which can create either zero-mean positive or negative errors, evolving in time, with a variance higher than the one of the thermal noise components.
    - the presence of thermal noise, which is centered Gaussian distributed.

6.2.2.2.2 Theoretical results of PSR-R LOS/NLOS MN

Theoretical results of LOS\NLOS MN reflection affecting PSR-R measurements have been presented in 4.4. They can be summarized as follows:

- LOS MN: Doppler frequency variations due to LOS MP reflections distorts the FLL Discriminator output with respect to the ideal LOS discriminator output producing a FLL tracking error. This variation could be positive or negative, depending to the geometry of MP environment and direction of motion of user receiver and dynamic reflectors. The error magnitude depends on the direct-to-reflected relative receive signal power, the magnitude of the Doppler displacement and the phase displacement. The expected PDF is symmetric and zero-biased. The variance depends on the joint effect of the thermal noise components and the MP components.
- NLOS MN: Doppler frequency values due to NLOS MP reflections are directly tracked by the FLL Discriminator output, in the absence of direct received signal components. This variation, as described before, could be positive or negative, depending to the geometry of the MP environment and direction of motion of user receiver as well as dynamic reflectors. The expected PDF when aggregating all data is symmetric and zero-biased. Also in this case, the variance depends on the joint effect of the thermal noise components and the MP components.

6.2.2.3 Test Results

The results of analysis 1 are presented in section 6.2.2.3.1, while the results of analysis 2 are depicted in section 6.2.2.3.2.

6.2.2.3.1 Analysis 1: MN characterization with C/N_0 classification

The Single Constellation PSR and PSR-R MN error characterization results are depicted, respectively, in sections 6.2.2.3.1.1 and 6.2.2.3.1.2 as follows. First, a list of specific MN error PDFs related to a given $\mathrm{C/N_0}$ bin size is illustrated and commented. Second, the complete MN error model is presented in the form of a table containing the main peak, the sample mean and the sample standard deviation subdivided by different $\mathrm{C/N_0}$ bins values. Third

and last, these preliminary results have been then compared to the theoretical MN error behavior, expressed in section 6.2.2.2.1.

6.2.2.3.1.1 PSR MN errors statistical characterization

This section illustrates the Single Constellation PSR MN error characterization as a function of the C/N_0.

A list of specific MN error PDFs related to a given C/N_0 bin size is illustrated. Figure 6-16 corresponds to the PSR MN PDF in the 45-50 dB-Hz C/N_0 bin, Figure 6-17 corresponds to the PSR MN PDF in the 35-40 dB-Hz C/N_0 bin, Figure 6-18 corresponds to the PSR MN PDF in the 25-30 dB-Hz C/N_0 bin and Figure 6-19 corresponds to the PSR MN PDF in the 15-20 dB -Hz C/N_0 bin.

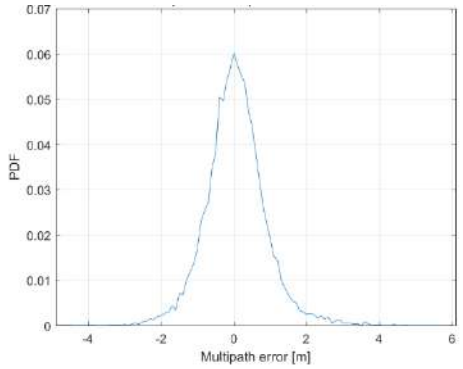

Figure 6-16 – GPS L1 C/A PSR MN PDF in the 45-50 dB-Hz C/N_0 bin

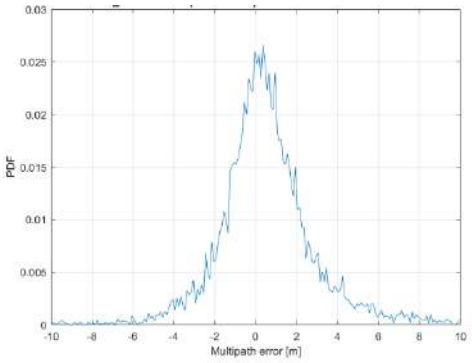

Figure 6-17 – GPS L1 C/A PSR MN PDF in the 35-40 dB-Hz C/N_0 bin

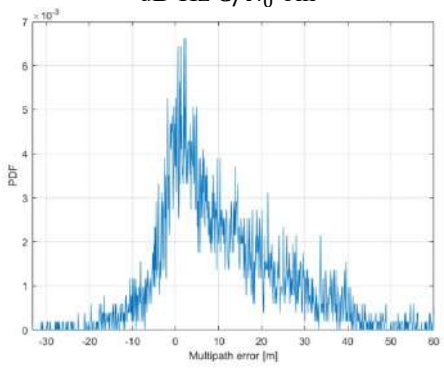

Figure 6-18 – GPS L1 C/A PSR MN PDF in the 25-30 dB-Hz C/N_0 bin

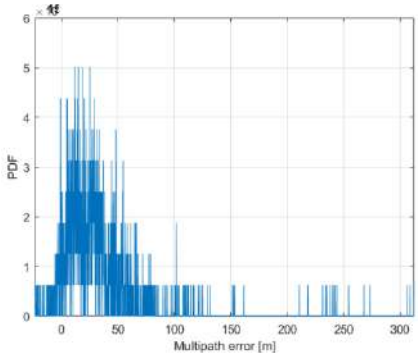

Figure 6-19 – GPS L1 C/A PSR MN PDF in the 15-20 dB-Hz C/N_0 bin

Table 6-7 presents the main peak, the sample mean and the sample standard deviation of the PSR MN error as a function of C/N_0 bin values.

C/N_0 bins [dB-Hz]	Main Peak [m]	$\mu(\widehat{MN}_u^i)$ [m]	$\sigma(\widehat{MN}_u^i)$ [m]	N samples
0 – 5	-	-	-	0
5 – 10	19.68	56.67	72.70	62
10 – 15	15.12	40.60	47.54	834
15 – 20	11.50	29.78	33.78	1352
20 – 25	7.79	19.94	22.24	17131
25 – 30	2.04	11.48	16.69	38745
30 – 35	-0.04	4.93	11.54	51027
35 – 40	0.35	0.91	5.18	73011
40 – 45	0.12	0.26	1.72	90521
45 – 50	0.01	0.05	0.82	109839
50 – 55	-0.01	-0.10	0.71	3981

Table 6-7 – PSR Multipath plus Noise (MN) error PDF's characteristics per different C/N_0 bins

The PSR MN PDF in the 45-50 dB-Hz C/N_0 bin (Figure 6-16) has a symmetric shape centered in 0 and a standard deviation of 0.82 meters. The PDF symmetry implies that the multipath error is mainly generated from LOS signals measurements, as stated in section 6.2.2.2.1. It could be stated that the resulting PDF has a zero-biased Gaussian-like shape.

The PSR MN PDF in the 35-40 dB-Hz C/N_0 bin (Figure 6-17) is slightly non-symmetrical: the PDF's values corresponding to the positive multipath errors seem to be higher than the negative part. This phenomenon is probably due to the presence of signals received in NLOS conditions that result in positive biases as stated in section 6.2.2.2.2. The presence of these biases means that, in this C/N_0 bin, there begins to be a not so negligible presence of MN errors components generated by NLOS satellites as in higher value C/N_0 bins.

The effect of NLOS situations can be clearly seen in the PSR MN PDF in the 25-30 dB-Hz C/N_0 bin (Figure 6-18). The PDF main peak is located at around 2 meters. The mean is located at 11.48 meters. As well as before, the PDF positive error part is higher than the negative error part. The MN error component seems thus to be dominated by NLOS satellites.

The PSR MN PDF in the 15-20 dB-Hz C/N_0 bin (Figure 6-19) is definitely non-symmetrical. The magnitude of the MN error increases significantly with respect to higher C/N_0 values. The PDF dispersion is larger, and it seems highly biased in the positive part. The MN error component is clearly dominated by NLOS satellites.

From Table 6-7, it can be observed that from 30-35 dB-Hz and below, the main peak has a significant difference with respect to the mean value. Moreover, the mean is significantly non-zero. Therefore, it can be observed that from the 30-35 dB-Hz range, a significant number of NLOS signals are received.

The resulting MN error characterization satisfy the expected theoretical model, section 6.2.2.2.1.

6.2.2.3.1.2 PSR-R MN error statistical characterization

This section illustrates the Single Constellation PSR-R MN error characterization as a function of the C/N_0.

Similar to section 6.2.2.3.1.1, some MN PDFs have been illustrated in the following paragraphs, and compared to the theoretical behavior expressed in section 6.2.2.2.2. Figure 6-20 corresponds to the MN PDF in the 45-50 dB-Hz C/N_0 bin, Figure 6-21 corresponds to the MN PDF in the 35-40 dB-Hz C/N_0 bin, Figure 6-22, corresponds to the MN PDF in the 25-30 dB-Hz C/N_0 bin and Figure 6-23, corresponds to the MN PDF in the 15-20 dB -Hz C/N_0 bin.

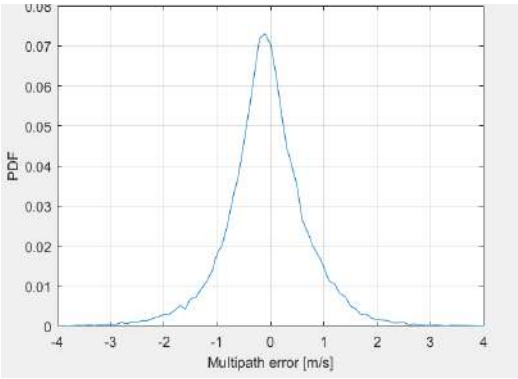

Figure 6-20 – GPS L1 C/A PSR-R MN PDF in the 45-50 dB-Hz C/N_0 bin

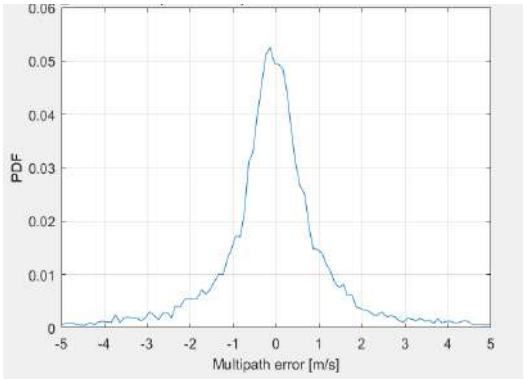

Figure 6-21 – GPS L1 C/A PSR-R MN PDF in the 35-40 dB-Hz C/N_0 bin

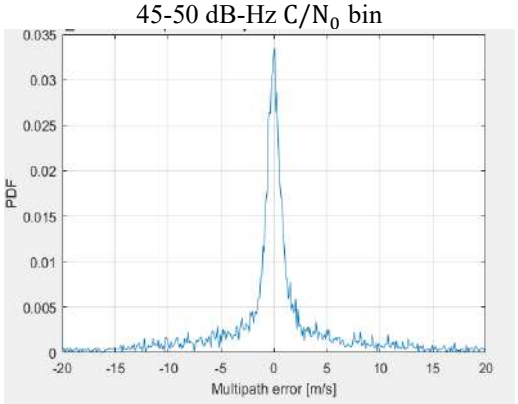

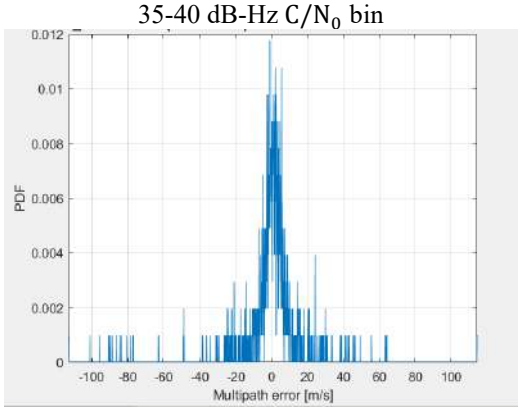

Figure 6-22 – GPS L1 C/A PSR-R MN PDF in the 25-30 dB-Hz C/N_0 bin

Figure 6-23 – GPS L1 C/A PSR-R MN PDF in the 15-20 dB-Hz C/N_0 bin

Table 6-8 presents the main peak, the sample mean and the sample standard deviation of the PSR-R MN error as a function of $\mathrm{C/N_0}$ bin values..

C/N_0 bins (dB-Hz)	$\mu\left(\widehat{MN}_u^i\right)$ [m/s]	$\sigma\left(\widehat{MN}_u^i\right)$ [m/s]	N samples
0 – 5	No value	No value	0
5 – 10	No value	No value	62
10 – 15	-2.42	17.5	834
15 – 20	0.2	15.97	1352
20 – 25	0.05	11.84	17131
25 – 30	0.38	10.02	38745
30 – 35	0.39	6.64	51027
35 – 40	0.019	3.35	73011
40 – 45	-0.04	1.23	90521
45 – 50	-0.08	0.81	109839
50 – 55	-0.07	0.79	3981

Table 6-8 – PSR-R Multipath plus Noise (MN) error PDF's characteristics per different C/N_0 bins

The PSR-R MN PDF in the 45-50 dB-Hz $\mathrm{C/N_0}$ bin (Figure 6-20) has a symmetric shape centered at 0 and a standard deviation of 0.81 m/s.

The PSR-R MN PDFs in the 35-40, 25-30 and 15-20 dB-Hz $\mathrm{C/N_0}$ bin, (respectively, Figure 6-21 Figure 6-22 and Figure 6-23) are symmetric and centered also for lower $\mathrm{C/N_0}$ bins.

Therefore, it may be concluded that the NLOS residual error components do not affect the final shape of PDF as significantly as was observed in the PSR case. This phenomenon agrees with the theoretical model expressed in section 6.2.2.2.2. In addition to that, the standard deviation of the statistical models increases as the C/N_0 descreases. This corresponds to the theoretical analysis conducted in Chapter 0. This phenomenon is probably due to the presence of Doppler spreading and, mainly, due to a higher level of thermal noise and a higher number of multipath rays. Therefore, the resulting MN error characterization satisfy the expected theoretical models, section 6.2.2.2.2.

6.2.2.3.2 Analyses 2: MN characterization with elevation angle classification

The residual error characterization performed by isolating the MN error components from the PSR and PSR-R measurements has also been conducted as a function of the satellite elevation angle. The relative results are depicted in sections 6.2.2.3.2.1 and 6.2.2.3.2.2.

The results are presented as follows. First, a list of specific MN error PDFs related to a given elevation angle bin value is illustrated and commented. Second, the complete MN error model is presented in form of a table containing the sample mean and the sample standard deviation subdivided by different elevation angle bins. These results have been then compared to the theoretical MN error behavior, expressed in section 6.2.2.1.

6.2.2.3.2.1 PSR MN errors statistical characterization

This section illustrates the Single Constellation PSR MN error characterization as a function of the satellite elevation angle.

A list of specific MN error PDFs related to a given elevation angle bin size is illustrated and commented. Figure 6-24 corresponds to the PSR MN PDF in the 70-80° elevation angle range, Figure 6-25 corresponds to the PSR MN PDF in the 30-40° elevation angle range, Figure 6-26 corresponds to the PSR MN PDF in the 10-20° elevation angle range.

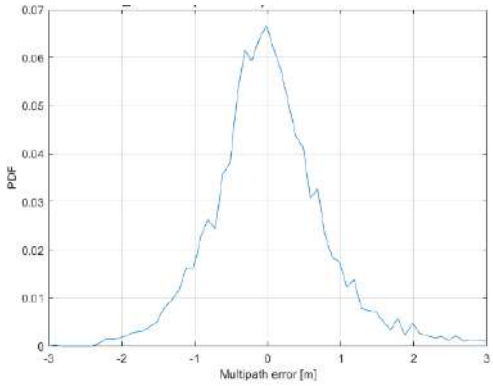

Figure 6-24 – GPS L1 C/A PSR MN PDF in the 70-80° elevation angle bin. GPS constellation case

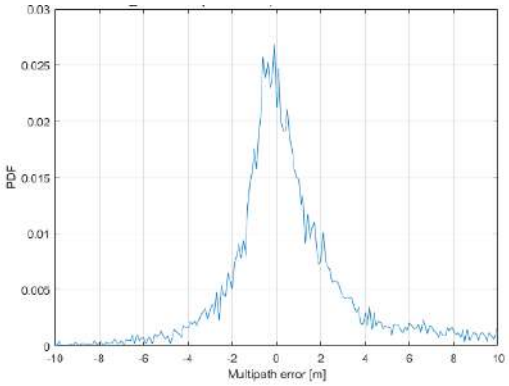

Figure 6-25 – GPS L1 C/A PSR MN PDF in the 30-40° elevation angle bin

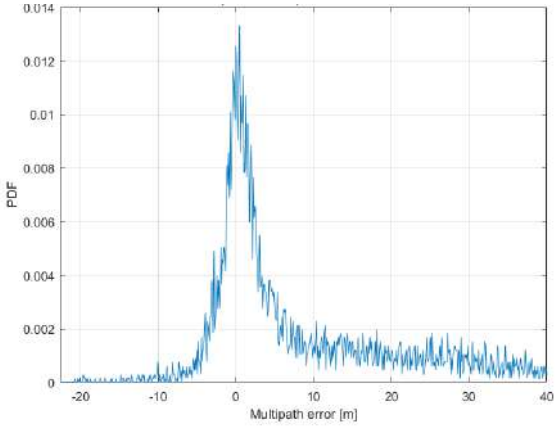

Figure 6-26 – GPS L1 C/A PSR MN PDF in the 10-20° elevation angle bin

Table 6-9 presents the main peak, the sample mean and the sample standard deviation of the PSR-R MN error as a function of satellite elevation angle bin values.

Elevation angle bins [degrees]	$\boldsymbol{\mu(\widehat{MN}_u^i)}$ **[m]**	$\boldsymbol{\sigma(\widehat{MN}_u^i)}$ **[m]**	**N samples**
0 – 10	17.77	31.62	0
10 – 20	12.89	23.67	91
20 – 30	7.19	13.86	1022
30 – 40	2.45	8.93	2251
40 – 50	2.13	7.93	89758
50 – 60	0.72	4.18	97136
60 – 70	0.20	1.56	99254
70 – 80	0.01	0.82	85471
80 – 90	-0.27	0.84	10520

Table 6-9 – PSR Multipath plus Noise (MN) error PDF's characteristics per different elevation angle bins

The PSR MN PDF in the 70-80° elevation angle bin (Figure 6-24) has a symmetric shape centered at 0 and a standard deviation of 0.82m. The PDF symmetry implies that the MN error is mainly generated from LOS MP signals measurements as stated in section 6.2.2.2.1. Similar results are faced for the PSR MN PDF in 45-50 dB-Hz C/N_0 bin (Figure 6-16). A connection between the two results could be seen: higher C/N_0 are usually related to the satellites with higher elevation angle. In this case, the MN error component has a very low impact on the PSR measurement.

The PSR MN PDF in the 30-40° elevation angle (Figure 6-25) bin has a slightly non-symmetric, positive biased shape, with a mean value of 2.45 meters. It could be stated that the lower elevation angle is masking the LOS signals. Therefore, this phenomenon is probably due to the presence of NLOS conditions that result in positive biases as stated in section 6.2.2.2.1.

The PSR MN PDF in the 10-20° elevation angle bin (Figure 6-26) is mostly positive biased; the mean is equal to 12.89 meters. As before, the PDF positive error part contains more data than the negative possibly due to the presence of many NLOS errors.

From Table 6-9 it can be observed that from range 40-50° the mean value is non-zero. Therefore, it can be observed that from the 40-50° range, a significant number of NLOS signals are received. Moreover, the sample mean is slightly different from 0 (mostly positive biased) even in 50-60° and 60-70° bins, hence, it seems that the elevation angle characterization performs a worst LOS/NLOS discrimination with respect to the C/N_0 observable parameter and does not completely satisfy the expected theoretical model, section 6.2.2.2.1.

6.2.2.3.2.2 PSR-R MN error statistical characterization

This section illustrates the Single Constellation PSR-R MN error characterization as a function of the satellite elevation angle. Table 6-10 contains the PDF's mean and standard deviation for each different PDF characterized by a different elevation angle range.

Elevation angle bins [degrees]	$\mu(\widehat{MN}_u^i)$ **[m/s]**	$\sigma(\widehat{MN}_u^i)$ **[m/s]**	**N samples**
0 – 10	-6.52	21.05	0
10 – 20	8.69	32.77	91
20 – 30	-2.42	10.84	1022
30 – 40	0.2	12.04	2251
40 – 50	0.5	7.63	89758
50 – 60	0.38	3.26	97136
60 – 70	0.6	1.56	99254
70 – 80	-0.19	0.79	85471
80 – 90	-0.6	0.55	10520

Table 6-10 – PSR-R Multipath plus Noise (MN) error PDF's characteristics per different elevation angle bins

In this case the sample mean is always different from 0, especially for low elevation angle bins. The standard deviation decreases proportionally with the elevation angle. Standard deviation results are similar to the results obtained with C/N_0 classification, whereas the sample mean results are slightly different from the expected results. Hence, the resulting MN error characterization does not satisfy the expected theoretical models, summarized in section 6.2.2.2.2.

6.2.2.4 Conclusion

The analysis applied to test the capacity of the methodology proposed in Chapter 5, to isolate a Single Constellation Multipath and thermal Noise (MN) errors from PSR and PSR-R measurements, validates the reliability of the proposed methodology.

6.2.3 Objective 2: Validation of MN isolation Methodology for dual constellation measurements

The description of the test conducted to validate the Dual constellation measurements MN Isolation Methodology, is presented in section 6.2.3.1. The results of the test are provided in section 6.2.2.3. Finally, the conclusions are presented in section 6.2.3.3.

6.2.3.1 Test description

In this test the capacity of the methodology proposed in Chapter 5, to isolate a Dual Constellation Multipath and thermal Noise (MN) errors from PSR and PSR-R measurements, is analyzed. The test consists in calculating a preliminary statistical characterization of the GPS L1 C/A MN + Galileo E1 OS MN error components (PDFs)

and in comparing the real data PDFs results with the theoretical expected PDFs (expressed in Chapter 0). The resulting PDFs are modelled as a function of two different observable parameter, the C/N_0 and the elevation angle. The theoretical expected model, derived from Chapter 0, classified for LOS and NLOS reception state, are summarized in section 6.2.2.1.

The proposed analyses are developed to meet the specific goal:

- **Analysis 1**: To characterize the PSR MN error components, as a function of the received signal C/N_0. Data Collection 2 has been exploited to conduct this test.
- **Analysis 2**: To characterize the PSR MN error components, as a function of the satellite elevation angle. Data Collection 2 has been exploited to conduct this test.

Similar to section 6.2.2.1 for Single constellation, the Dual constellation MN error statistical characterization consists of the calculation of the empirical PDFs, calculated from the MN samples collected in the different C/N_0 and elevation angle bins. From the empirical PDFs, the sample average and the sample variance have been extracted.

As described in section 6.2.2, the choice of the C/N_0 bin size depends on the number of samples used to characterize the residual errors in that specific bin. The optimal choice is to choose a small bin size, resulting in a higher fidelity model. Such a choice will reduce dramatically the number of MN samples included in the different bins, affecting the reliability of the final statistics. Knowing that the dataset under exam is too small to apply a reduced bin size, the selected bin size was 5 dB-Hz. The same applies to the elevation angle bin size; hence, 10 degrees has been selected.

The correct functioning of the MN methodology is achieved by comparing the applied methodology results to the expected results, and thus to the theoretical behaviour described in Chapter 0. The theoretical expected model, derived from Chapter 0, classified for LOS and NLOS reception state, are summarized in section 6.2.2.1.

The configuration of the executed analyses is summarized in Table 6-11.

Objective	Analysis	Constellation	Measurements	Reception State	C/N_0 Bin size [dB-Hz]	El angle Bin size [degrees]	Statistic model	Data Set
To test the MN isolation and characterization methodology for dual constellation measurements	**Analysis 1**: MN error characterization as a function of C/N_0	GPS + GAL	PSR	LOS + NLOS	5	---	PDF, Main peak, average, variance	Data Collection 2
	Analysis 2: MN error characterization as a function of elevation angle	GPS + GAL	PSR	LOS + NLOS	---	10	PDF, Main peak, average, variance	Data Collection 2

Table 6-11 – Description of the Analysis developed for Objective 2

6.2.3.2 Test results

The results of analysis 1 are presented in section 6.2.3.2.1. The results of analysis 2 are depicted in section 6.2.3.2.2.

6.2.3.2.1 Analysis 1: PSR MN characterization with C/N_0 classification

This section illustrates the Dual Constellation PSR MN error characterization as a function of the C/N_0.

A list of specific MN error PDFs related to a given C/N_0 bin size is illustrated below. Figure 6-27 corresponds to the PSR MN PDF in the 45-50 dB-Hz C/N_0 bin and Figure 6-28 corresponds to the PSR MN PDF in the 35-40 dB-Hz C/N_0 bin.

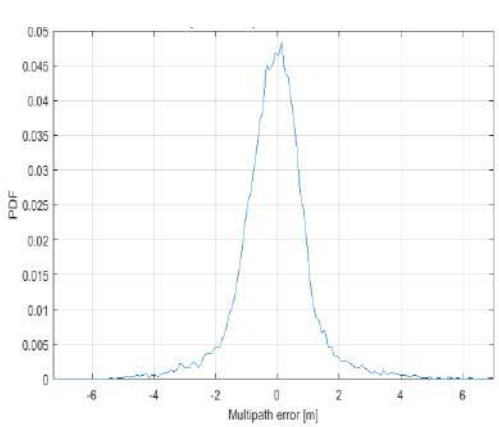

Figure 6-27 – GPS L1 C/A + GAL E1 OS PSR MN PDF in the 45-50 dB-Hz C/N_0 bin

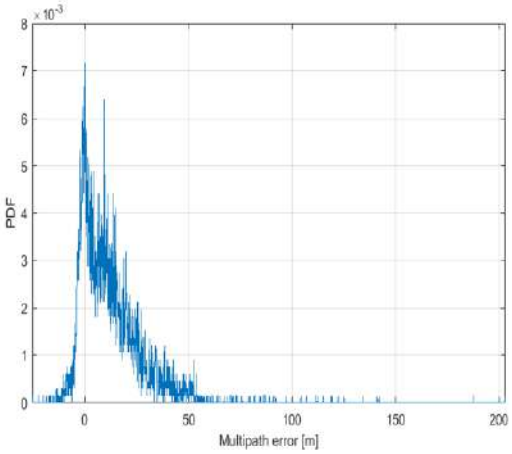

Figure 6-28 – GPS L1 C/A + GAL E1 OS PSR MN PDF in the 25-30 dB-Hz C/N_0 bin

Table 6-12 presents the sample mean and the sample standard deviation of the PSR MN error component as a function of the C/N_0 bins values.

C/N_0 bins [dB-Hz]	$\mu(\widehat{MN}_u^i)$ [m]	$\sigma(\widehat{MN}_u^i)$ [m]	N Samples
0 – 5	-	-	0
5 – 10	25.96	14.03	83
10 – 15	14.30	24.09	1880
15 – 20	34.54	24.40	10328
20 – 25	21.31	18.27	28434
25 – 30	12.15	14.53	49895
30 – 35	6.50	8.49	61304
35 – 40	2.20	5.52	93082
40 – 45	1.40	3.35	150694
45 – 50	0.75	1.65	149910
50 – 55	0.02	0.74	40441
55-60	0.94	0.94	23

Table 6-12 – Dual Constellation PSR Multipath plus Noise (MN) error PDF's characteristics per different C/N_0 bins

The PSR MN PDF in the 45-50 dB-Hz C/N_0 range (Figure 6-27) has a symmetric bell shape, centred at 0, and a standard deviation of 1.65 meters. The PDF symmetry implies that the multipath error is mainly generated from LOS signals measurements. The PDF features are consistent with the results obtained in section 6.2.2.

Similarly, the PSR MN PDF in the 25-30 dB-Hz C/N_0 range seems to be an asymmetrical distribution. The PSR MN PDF is clearly affected by the presence of NLOS satellites. As a consequence, the comparison between the Single Constellation and Dual Constellation MN error models, validates the Dual Constellation Isolation Methodology which meets the expected theoretical hypothesis formulated in section 6.2.2.2.1.

6.2.3.2.2 Analysis 2: PSR MN characterization with satellite elevation angle classification

This section illustrates the Dual Constellation PSR MN error characterization as a function of the elevation angle.

A list of specific MN error PDFs related to a given elevation angle bin size is illustrated below and commented. Figure 6-29 corresponds to the PSR MN PDF in the 70-80° elevation angle bin. Figure 6-30 corresponds to the PSR MN PDF in the 30-40° elevation angle bin.

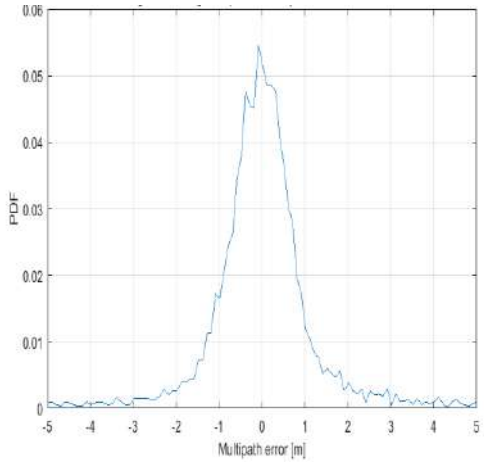

Figure 6-29 – GPS L1 C/A + GAL E1 OS PSR MN PDF in the 70-80° elevation angle bin

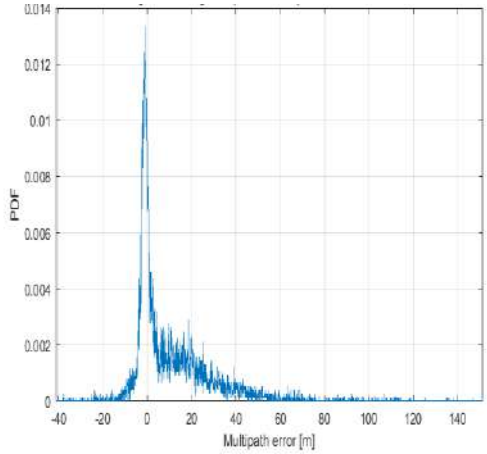

Figure 6-30 – GPS L1 C/A + GAL E1 OS PSR MN PDF in the 10-20° elevation angle bin

Table 6-13 presents the sample mean and the sample standard deviation of the Dual Constellation PSR MN error component as a function of the elevation angle bin values.

Elevation angle bins [degrees]	$\mu(\widehat{MN}_u^i)$ **[m]**	$\sigma(\widehat{MN}_u^i)$ **[m]**	**N Samples**
0 – 10	9.70	14.11	14338
10 – 20	3.31	9.22	25448
20 – 30	4.18	5.83	76458
30 – 40	2.32	5.77	78911
40 – 50	3.39	5.52	216842
50 – 60	1.2	6.12	51782
60 – 70	0.45	3.18	65131
70 – 80	0.2	1.22	56146
80 – 90	0.01	0.84	1018

Table 6-13 – Dual Constellation PSR Multipath plus Noise (MN) error PDF's characteristics per different elevation angle bins

The PSR MN PDF in the 70-80° elevation angle bin (Figure 6-29) has a symmetric shape centred at 0. The PDF symmetry implies that the MN error is mainly generated from LOS signals measurements and has a similar shape with respect to the MN model provided by the section 6.2.2.

The PSR MN PDF in the 10-20° elevation angle bin (Figure 6-30) is asymmetric and mostly positive biased. As well as before, The PDF features are consistent with the results obtained in section 6.2.2.

From Table 6-13 it can be observed that from range 40-50° the mean value is non-zero. Therefore, it can be observed that from the 40-50° range, a significant number of NLOS signals are received, as defined in Test 1, section 6.2.2.3. Also, the sample mean is slightly different from 0 (mostly positive biased) even in 50-60° and 60-70° bins, hence, the elevation angle characterization performs a worst LOS/NLOS discrimination with respect to the C/N_0 observable parameter and does not completely satisfy the expected theoretical model, section 6.2.2.2.1, even in the case of Dual constellation MN error characterization.

Finally, the comparison between the Single Constellation and Dual Constellation MN error models validates the application of Dual Constellation Isolation Methodology.

6.2.3.3 Conclusion

The analysis applied to test the capacity of the methodology proposed in Chapter 5, to isolate a Dual Constellation Multipath and thermal Noise (MN) errors from PSR and PSR-R measurements, validates the reliability of the proposed methodology.

6.2.4 Objective 3: Determination of most suitable observable for NLOS/LOS received signal conditions estimation

The test proposed to fulfill the objective of this section is presented in section 6.2.4.1. The results of the test are described in section 6.2.4.2. Finally, the conclusions are depicted in section 6.2.4.3.

6.2.4.1 Test description

The proposed test has been applied to investigate and select the observable parameter (C/N_0 or elevation angle) which allows for a better discrimination between LOS and NLOS receiver reception state. The test consists of

first express the received signal $\mathrm{C/N_0}$ as a function of the corresponding satellite elevation angle, and second, of comparing the influence of C/N_0 characterization and elevation angle characterization of a preliminary statistical characterization of the GPS L1 C/A MN + Galileo E1 OS MN error components with respect to the theoretical behaviour, expressed in Chapter 0. The theoretical expected model, derived from Chapter 0, classified for LOS and NLOS reception state, are summarized in section 6.2.2.1.

Therefore, the proposed test is divided in two analyses:

- **Analysis 1**: To evaluate the $\mathrm{C/N_0}$ associated to the respective MN error samples as a function of the corresponding satellite elevation angle.

This investigation is applied to the Data Collection 1 and the Data Collection 3. However, since the Data Collection 3 is larger (roughly 48 times the dimension of the first Data Collection), the results related to Data Collection 3 are considered more reliable and are showed in the corresponding Test results section. The results related to Data Collection 1 can be found in the Annex 10.4.1.

- **Analysis 2**: To characterize the PSR/PSR-R MN error components, as a joint function of the C/N_0 and the elevation angle.

The configuration of the executed Analyses 2 is described in Table 6-14. Instead of dividing the MN residual error components in specific sets characterized by received signal C/N_0 or satellite elevation angle, they have been divided in different sets characterized by both C/N_0 and elevation angle, being aware that with this kind of subdivision the number of samples belonging to the same subset is highly reduced, impacting on the reliability of the resulting statistical models.

The configuration of the executed analyses is summarized in Table 6-14.

Goal	Analyses	Constellation	Measurements	Reception State	C/N_0 Bin size [dB-Hz]	El angle Bin size [deg]	Statistic model	Data Set
Goal 2: To select the LOS\NLOS discrimination parameter	**Analyses 1:** $\mathrm{C/N_0}$ vs. elevation angle	GPS	C/N0 estimations	LOS + NLOS	-	-	-	Data Collection 3
	Analyses 2: MN error characterization as a function of C/N_0 and elevation angle	GPS, GAL	PSR	LOS + NLOS	5	10	PDF, Main peak, average, variance	Data Collection 2

Table 6-14 – Description of the Analysis developed for Objective 3

6.2.4.2 Test Results

The results of analysis 1 are presented in section 6.2.4.2.1. The results of analysis 2 are depicted in section 6.2.4.2.2.

6.2.4.2.1 Analysis 1: C/N_0 vs elevation angle characterization accuracy

This section evaluates the statistics of the available received measurements C/N_0 as a function of the elevation angle of the corresponding satellites. In particular, the evaluations are provided for:

Data Collection 1: The results and the comments are presented in Annex 10.4.1.

Data Collection 3: Figure 6-31, Figure 6-32, Figure 6-33 are 2D plots showing the occurrence of a specific couple elevation angle- C/N_0 for, respectively, the GAP+Galileo, GPS and Galileo constellation.

As it can be seen from the Figure 6-31, red and yellow points (higher number of occurrences) are centered around 45 dB-Hz – 45°, meaning that the highest measurement availabilities have been centred in this section. From this figure, it can be observed that for low elevation angle values, the C/N_0 has a large variation which goes from 10 dB-Hz to 45 dB-Hz (vertical axis): a lot of possible C/N_0 situations/received signal conditions, even quite high C/N_0 values, are allowed. On the contrary, for low C/N_0 values, the elevation angle values are less spread and more concentrated in the low values (horizontal axis): only a reduced number of situations/received signal conditions are allowed.

The first conclusion that can be extracted is that there is not a direct correlation between received signal C/N_0 and satellite elevation angle. The second conclusion is that, considering the 1st conclusion and since (as s already observed in *Test 1*, section 6.2.2.3.1) the expected LOS/NLOS theoretical identification is better met by C/N_0 classification than by elevation angle classification, the selected observable to discriminate between LOS/NLOS receiver conditions is the received signal C/N_0 parameter.

From the comparison between GPS (Figure 6-32) and Galileo (Figure 6-33) it is observed that the envelopes follow a similar behavior, however there are interesting differences between the two constellations. GPS C/N_0 values are more concentrated in two different regions, (45-50 dB-Hz)\(65°-70°) and (45-50 dB-Hz)\(50°-45°) whereas Galileo C/N_0 values are more uniformly spread with a larger incidence in (40-45 dB-Hz)\(37°-45°). Moreover, it can be noticed in the Galileo plot the presence of a larger number of low C/N_0 values corresponding to low elevation angle values, in the region (35-20 dB-Hz)\(10°-35°), with a much higher incidence than GPS.

From these analysis, it can be deduced that the (35-20 dB-Hz)\(10°-35°) region of dual constellation statistics is mainly occupied by Galileo signals.

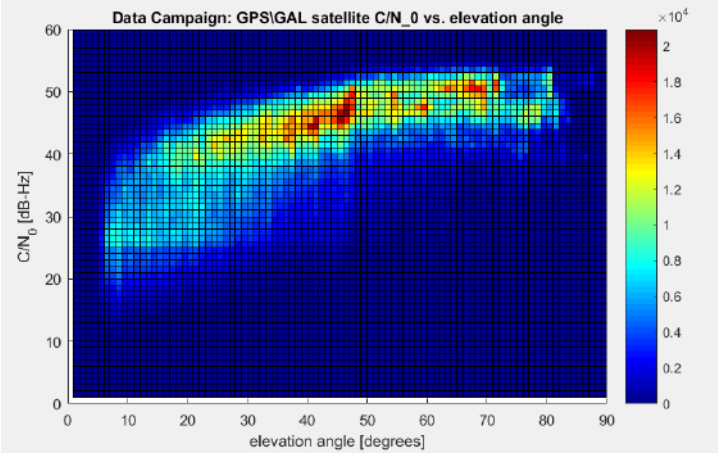

Figure 6-31 – Link between the elevation angle of the satellites and the respective received signal C/N_0 for dual constellation dataset

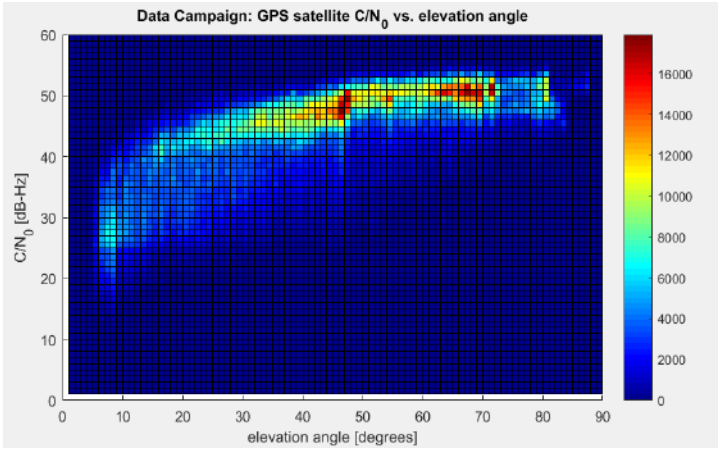

Figure 6-32 – Link between the elevation angle of the satellites and the respective received signal C/N_0 for GPS L1 C/A constellation dataset

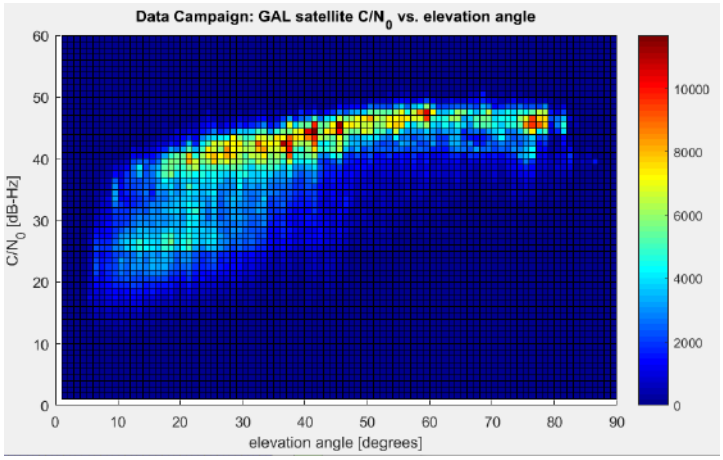

Figure 6-33 – Link between the elevation angle of the satellites and the respective received signal C/N_0 for Galileo E1 OS constellation dataset

6.2.4.2.2 Analysis 2: PSR MN characterization with respect to C/N_0 and elevation angle classification

This section illustrates the Dual Constellation PSR MN error characterization as a joint function of the elevation angle and the C/N_0.

Table 6-15 contains the PSR MN error PDF sample mean and sample standard deviation, divided in different sets, characterized by elevation angle and C/N_0, while Table 6-16 contains the corresponding number of samples. On the one hand, considering the received signal C/N_0, from Table 6-15, it can be observed that from range 30-35 dB-Hz to lower values, the mean is far from being equal to 0. Therefore, it can be deduced that a significant number of NLOS signals are received in the 30-35 dB-Hz range. However, for C/N_0 bin values above 35-40 dB-Hz range, the mean is usually below 1m. Moreover, it can be observed that the PSR error mean is usually quite constant for a given C/N_0 bin value irrespective of the satellite elevation angle value (although some exceptions can be found), where these constant values are an indicator of the same multipath situation (presence a higher amount of LOS or of NLOS receiver conditions). On the other hand, considering the satellite elevation angle,

it can be observed that the mean and the standard deviations vary significantly for a given bin value as a function of the received signal C/N_0, which indicates a mix of LOS and NLOS receiver conditions for the same satellite elevation angle bin. Therefore, it can be concluded that received signal C/N_0 parameter is a better observable than satellite elevation angle to discriminate between LOS and NLOS receiver conditions.

	Elevation angle range (degrees)											
	0 - 10		**10 - 20**		**20 - 30**		**30 - 40**		**40 - 50**		**> 50**	
C/N_0 bins [dB-Hz]	μ [m]	σ [m]	μ [m]	σ [m]	μ [m]	σ [m]	μ [m]	σ [m]	μ [m]	σ [m]	μ [m]	σ [m]
0 – 5	-	-	-	-	-	-	-	-	-	-	-	-
5 – 10	-9,41	24,42	6,72	52,48	0	0	28,62	17,78	51,69	0	0	0
10 – 15	-22,94	31,63	22	29,24	30,39	34,89	22,18	27,41	34,78	28,03	37,67	1,96
15 – 20	30,63	43,95	27,87	21,69	24,92	25,22	24,37	21,57	34,5	16,65	58,35	43,34
20 – 25	23,66	24,88	20,54	20,51	20	19,95	19,37	23,88	20,11	13,72	7,68	24,32
25 – 30	20,85	24,29	15,72	19,76	14,29	15,98	10,9	16,62	12,12	15,57	10,19	11,73
30 – 35	8,82	18,11	7,43	16,2	7,72	12,97	5,1	10,81	2,77	7,68	4,47	10,87

35 – 40	1,25	17	7,03	9,58	1,06	10,02	0,8	6,28	0,71	6,06	-0,66	4,53
40 – 45	5	18	3,24	10,41	4,44	2,66	-0,38	2,9	-0,36	2,37	-0,43	1,9
45 – 50	15	7	-2,73	3,49	1,26	2,21	-0,55	1,62	-0,19	1,21	0,07	1,12
50 – 55	0	0	0	0	-0,84	1,13	0,07	1,04	-0,09	0,95	0,24	0,8
55 – 60	0	0	0	0	0	0	0	0	0	0	0,93	0,94

Table 6-15 – Table containing the PSR MN error component PDF's mean values and standard deviations characterized by a different elevation angle range and C/N_0 range

	Elevation angle range (degrees)					
	0 - 10	**10 - 20**	**20 - 30**	**30 - 40**	**40 - 50**	**> 50**
C/N_0 bins [dB-Hz]	**N**	**N**	**N**	**N**	**N**	**N**
0 – 5	-	-	-	-	-	-
5 – 10	6	7	8	12	15	**-**
10 – 15	175	121	175	167	339	677
15 – 20	78	276	1181	1457	3925	3271
20 – 25	276	650	2296	1606	10052	7245
25 – 30	382	741	2341	1780	16545	17748
30 – 35	212	1557	5120	6812	22184	19341
35 – 40	151	2485	8574	9927	31555	18625
40 – 45	4324	7252	19385	18832	46896	37999
45 – 50	5251	8612	17165	17515	49511	35021
50 – 55	**-**	**-**	5458	7494	8341	8991
55 – 60	**-**	**-**	**-**	**-**	-	21

Table 6-16 – Table containing the PSR MN error component PDF's mean values and standard deviations characterized by a different elevation angle range and C/N_0 range

6.2.4.3 Conclusions

From the results proposed in the previous sections, it can be stated that it is preferred to differentiate between LOS and NLOS situations using the received signal C/N_0 than the satellite elevation angle. Indeed, even for the Dual Constellation MN error characterization (GPS L1 C/A and Galileo E1 OS), the C/N_0 received signal parameter allows for a better classification of the multipath error component received signal conditions (LOS/NLOS). Moreover, C/N_0 characterization is preferred since it could bring to a better LOS/NLOS MN error modelling exploitable in the PVT estimation (quite constant mean and sigma irrespective of the satellite elevation angle). The value of the C/N_0 threshold will be finally selected from the results of the following section, 6.2.5.

Additionally, a better refinement with joint elevation angle and C/N_0 or elevation angle and azimuth angle characterization could also be pursued but, to perform such characterization, a larger data collection would be required. In other words, the use of elevation angle parameter as classification parameter is only recommended if accompanied by an additional parameter.

As a last conclusion, the results of this section show a tendency of the PSR MN PDF to be dominated by the MN residuals corresponding to a receiver measurement considered in NLOS reception state for C/N_0 values below or equal to 35 dB-Hz. On the contrary, above 35 dB-Hz there is a higher chance to collect MN residuals corresponding to a receiver measurement in LOS reception state. However, this analysis is not sufficient to define an empirical C/N_0 threshold able to estimate between MN residual errors in LOS and in NLOS receiver signal reception state. This will be the objective of the analyses proposed in section 6.2.5.

6.2.5 Objective 4: Determination of most suitable observable threshold for NLOS/LOS received signal conditions estimation

The test proposed to fulfill the objective of this section is presented in section 6.2.5.1. The results of the test are described in section 6.2.5.2. Finally, the conclusions are depicted in section 6.2.5.3.

6.2.5.1 Test description

The objective of this test is to determine the most suitable receiver signal parameter threshold which allows the discrimination/estimation of the received signal conditions, LOS or NLOS. This test consists in analyzing the performances of the NLOS/LOS MN classification using the fish-eye camera (Chapter 5), and, in selecting the better empirical C/N_0 threshold able to classify LOS/NLOS reception conditions without the aid of external sensors. Note that the selected threshold can be exploited in the PVT estimator structures, Chapter 7.

More specifically, the proposed test consists in the following analysis:

- **Analysis 1**: To test LOS/NLOS image processing algorithm and in particular, to calculate the number of samples discarded after the application of Signal Processing refinement, due to the application of a specific C/N_0 threshold. The C/N_0 threshold generating the lower number of discarded samples will b chosen as the most suitable empirical threshold.

The configuration of the executed analysis is described in Table 6-17. The image processing methodology is applied to the Data collection 2.

Moreover, an additional analysis a little outside the general objectives of the thesis can be conducted for completeness's sake:

- **Analysis 2**: To characterize the PSR MN error components, as a function of the C/N_0, using the MN error components selected with the NLOS/LOS MN classification method of section 5.2.3 (using fish-eye camera and the C/N_0 threshold selected in analysis 1). Note that since this characterization requires the use of the fish-eye camera in addition to the C/N_0 threshold, it cannot be used by receiver which does not include a fish-eye camera for NLOS/LOS receiver state discrimination.

The MN error statistical characterization consists of the calculation of the empirical PDFs, calculated from the MN samples collected in the different C/N_0. In addition to the empirical PDFs, have been extracted the sample average, the sample variance and the value of the main peak. The C/N_0 bin size depends on the number of samples used to characterize the residual errors in that specific bin. Knowing that the dataset under exam is too small to apply a reduced bin size, the selected bin size was 5 dB-Hz. The results are depicted in section 6.2.5.2.2.

The configuration of the executed analyses is described in Table 6-17.

Goal	Analyses	Constellation	Measurements	Reception State	C/N_0 Bin size [dB-Hz]	El angle Bin size [degrees]	Statistic model
Goal 1: To test LOS/NLOS image processing algorithm	**Analyses 1**: To experimentally choose the LOS/NLOS signal parameter discriminator threshold	GPS + GAL	PSR	LOS + NLOS	---	----	----
	Analyses 2: MN error characterization when applying NLOS/LOS methodology as a function of C/N_0	GPS + GAL	PSR	LOS + NLOS	5	----	PDF, Main peak, average, variance

Table 6-17 – Description of the tests developed for the Objective 4

6.2.5.2 Test Results

The results of analysis 1 are presented in section 6.2.5.2.1. The results of analysis 2 are depicted in section 6.2.5.2.2.

6.2.5.2.1 Analysis 1: LOS/NLOS MN error characterization

The analysis consists of the evaluation of different C/N_0 threshold values applied to the LOS/NLOS image processing algorithm and signal processing refinement (defined in section 5.2.3) and of selecting the most suitable empirical C/N_0 threshold able to classify LOS/NLOS reception conditions.

This subsection is separated in 4 parts. The first part explains the fundamental idea, the second part discusses some considerations about the fundamental ideal and the method proposed to implement it, the third part presents the exact metholodogy used to implement the fundamental idea and the last part presents the results.

6.2.5.2.1.1 Fundamental idea

The fundamental idea is to compare the number of measurements classified as LOS and NLOS by the image processing part of the LOS/NLOS characterization process to the number of measurements classified as LOS and NLOS by the signal processing part (which uses the tested C/N_0 threshold). The threshold providing the highest number of matched decisions is selected as the best threshold to estimate between LOS and NLOS receiver conditions.

In order to implement this fundamental idea, it is necessary first to make a quick reminder of the LOS/NLOS characterization process methodology. The LOS/NLOS characterization process methodology is based on two sequential blocks. The first one is the Image Processing (IP) estimation, based on the image processing algorithm applied to the collected fisheye pictures. The second block consists of the verification of the IP decision through the application of a Signal Processing (SP) estimation.

In the first block, at a given epoch, the IP block estimates the LOS/NLOS reception state as described in section 5.2.3. However, the picture is processed only if the fisheye picture has been collected, is synchronized to the corresponding GNSS measurements, is not corrupted, can be read by the IP algorithm, does not present errors not allowing the correct application of the IP algorithm and if the resulting picture after application of the IP algorithm does not present any processing error. Due to these assumptions, the number of samples which can be exploited by the overall LOS/NLOS classification algorithm is just a subset of the collected data. An example of the resulting number of samples, applied to the Data Collection 2, is detailed in the Annex section 10.4.2.

In the second block, the SP block, the estimation of the IP algorithm is compared to the corresponding C/N_0 at the given epoch. The comparison rules are summarized below (section 5.2.3).

- In case of IP LOS estimation:
  - If C/N_0^i is higher than the selected threshold, the post-processing approach estimation is set as LOS estimation;
  - If C/N_0^i is lower than the selected threshold, the image processing estimation is considered wrong. Corresponding measurement is discarded from the Multipath error LOS\NLOS characterization process.
- In case of IP NLOS estimation:
  - If C/N_0^i is higher than the selected threshold, the image processing estimation is considered to be uncertain (for example due to trees). Corresponding measurement is discarded from the Multipath error LOS/NLOS characterization process;
  - If C/N_0^i is lower than the selected threshold, the post-processing approach estimation is set as NLOS estimation.

From this reminder, it can be seen that the knowledge of the number of discarded measurements due to the application of the C/N_0 threshold is equivalent to the match decision between the IP and SP blocks. Therefore, the number of discarded samples can be exploited to investigate the LOS/NLOS reception state estimations and the reliability of the corresponding tested C/N_0 threshold. Indeed, the tested threshold providing a lower number of discarded samples (while verifying that this number if lower than 50%) will be selected as the most suitable threshold.

6.2.5.2.1.2 Discarded simples considerations

Some considerations must be made about the discarded samples. Different reasons/sources can be identified for measurements/pictures to fall in the previous discarding cases and, unfortunately, not all of them correspond to the NLOS/LOS classification as a function of the signal C/N_0. Note that only the IP exploitable measurements can be discarded.

The identified reasons/sources are given below.

- Image processing errors:
  - Estimation errors due to wrong Border detection;
  - Estimation errors due to wrong flood filling operation;
- Signal processing errors:
  - Wrong C/N_0 value assigned to the corresponding MN error sample;
- Limitations of Signal Processing refinement due to the application of the C/N_0:
  - It has been observed that sometimes MN error components associated to NLOS reception are characterized by a C/N_0 higher than the selected C/N_0 threshold; viceversa MN error components associated to LOS reception are characterized by a C/N_0 lower than the selected C/N_0 threshold.

The discarded measurements due to "Limitations of Signal Processing refinement due to the application of the C/N_0" are indeed the main source of error to be minimized by the suitable selection of the C/N_0 threshold; in other words, ideally, the discarded measurements should only happen due to this source allowing then the optimal selection of the C/N_0 threshold. However, the presence of the other two sources of errors may affect this ideal selection. In any case, as justified in the following paragraph, the LOS/NLOS characterization process (as defined in Chapter 5) has been considered enough to determine the most suitable C/N_0 threshold. Moreover, even when assuming this ideal case, if the number of discarded samples is always higher than 50% irrespective of the C/N_0 threshold, it will mean that the C/N_0 threshold is not a good or sufficient indicator to discriminate between LOS and NLOS receiver state conditions, and a new observable should be investigated.

The justification of why LOS/NLOS characterization process is considered enough to determine the most suitable C/N_0 threshold is given below by further analysis the other two sources of discarded measurements:

- Signal processing errors: There is no mean to correct/identify them since U-blox receiver does not allow access to the signal processing data (correlator outputs, etc). However, they are assumed to be infrequent and are considered to have a negligible impact.
- Image processing errors: The number of discarded samples due to this source is higher than the number of discarded samples due to signal processing errors. Their complete automatic detection implies a highly advanced IP algorithm (a more advanced refinement than the one implemented during this thesis even able to detect any potential outlier) which was out of the scope of this thesis, while an individual inspection of each picture is not feasible due to the large number of collected measurements. IP LOS estimation coupled with an estimated C/N_0 below threshold tends to favor a selection of low C/N_0 threshold values, whereas IP NLOS estimation coupled with an estimated C/N_0 above threshold tends to favor a selection of high C/N_0 threshold values. Therefore, although the number of discarded samples by this source of error is not negligible, this source of error is considered to have a neutral impact on the C/N_0 threshold selection process.

6.2.5.2.1.3 Methodology

In this section, the exact methodology applied to select the the most suitable C/N_0 threshold, which allows the discrimination/estimation of the received signal conditions, is described.

1) C/N_0 threshold under test, Th, is set as candidate.
2) Th is used by the Signal Processing refinement approach to estimates the LOS/NLOS receiver reception state.
3) The resulting measurement samples, after the Signal Processing refinement, are grouped with respect to the corresponding C/N_0 in different bins of 5 dB-Hz.
4) Two specifics C/N_0 bins are selected:
   - *Th bin NLOS*: C/N_0 bin from $(Th - 5)$ dB-Hz to Th dB-Hz. If Th is correctly defined, the *Th bin NLOS* must contain mainly NLOS samples.
   - *Th bin LOS*: C/N_0 bin from Th dB-Hz to $(Th + 5)$ dB-Hz. If Th is correctly defined, the *Th bin LOS* must contain mainly LOS samples.
5) Verification of the number of discarded data after the Signal Processing refinement in *Th bin NLOS*. If the percentage of discarded data with respect to the original dataset in *Th Bin NLOS* is higher than 50%, Th is flagged.
6) Verification of the number of discarded data after the Signal Processing refinement in *Th bin LOS*. If the percentage of discarded data with respect to the original dataset in *Th bin LOS* is higher than 50%, Th is flagged.

7) If the $Th\ bin\ NLOS$ and $Th\ bin\ LOS$ are not flagged, the C/N_0 threshold under test, Th, is marked as a final candidate solution.
8) Go back to step 1) to test remaining Th candidates
9) If more than one C/N_0 threshold, Th, is marked as final candidate, then, the final candidate C/N_0 threshold which minimize the number of discarded samples is selected as the most suitable C/N_0 threshold.

6.2.5.2.1.4 Results

The methodology presented in the previous section has been applied to the Data Collection 2 to test three different thresholds, 30, 35, and 40 dB-Hz. Table 6-18 shows the number of the samples of the dataset available after the image processing block, and the number of samples after the application of signal processing algorithm with the three different previous thresholds. The number of samples are given C/N_0 bins of 5 dB-Hz. Table 6-18 also shows the percentage of discarded data due to the signal processing application. As it can be seen from Table 6-18, the percentage of the discarded data varies with respect to the selected threshold, in particular in 30-35 and 35-40 dB-Hz bins.

C/N_0 bins [dB-Hz]	***N* samples after Image Processing**	***N* samples after Reception State refinement with Th: 30 dB-Hz**	**% Samples Discarded Th: 30 dB-Hz**	***N* samples after Reception State refinement with Th: 35 dB-Hz**	**% Samples Discarded Th: 35 dB-Hz**	***N* samples after Reception State refinement with Th: 40 dB-Hz**	**% Samples Discarded Th: 40 dB-Hz**
0 – 5	-	-	-	-	-	-	-
5 – 10	48	48	0	48	0	48	0
10 – 15	1654	1529	7.55	1529	7.55	1529	7.55
15 – 20	10188	10102	0.84	10102	0.84	10102	0.84
20 – 25	22125	22034	0.41	22034	0.41	22034	0.41
25 – 30	39537	36469	**7.76**	36469	**7.76**	36469	**7.76**
30 – 35	55226	15516	**71.90**	39710	**28.09**	39710	**28.09**
35 – 40	71317	59123	**17.09**	59123	**17.09**	12194	**82.90**
40 – 45	134688	133566	**0.83**	133566	**0.83**	133566	**0.83**
45 – 50	133075	132987	0.06	132987	0.06	132987	0.06
50 – 55	30284	30257	0.09	30257	0.09	30257	0.09
55-60	21	19	9.52	19	9.52	19	9.52
TOT	498163	441650	**11.34**	465844	**6.48**	418915	**15.90**

Table 6-18 – PSR MN Samples after Image processing and after Reception State Refinement with different choice of empirical C/N_0 thresholds, per different C/N_0 bins

Several observations can be made from Table 6-18 as a function of the C/N_0 threshold.

- $\underline{Th = 30\ \text{dB-Hz}}$:
  - The percentage of discarded data in Th NLOS (25-30 dB-Hz) is 7.76%; the percentage of discarded values is acceptable.
  - The percentage of discarded data in Th LOS (30-35 dB-Hz) is 71.90%, this means there are more chances to have NLOS samples with a C/N_0 higher than 30 dB-Hz than having LOS samples; the percentage of discarded values is not acceptable.
  - 30 dB-Hz C/N_0 threshold does not fulfill the requirements.
- $\underline{Th = 35\ \text{dB-Hz}}$:
  - The percentage of discarded data in Th NLOS (30-35 dB-Hz) is 28.09%, the percentage of discarded values is acceptable.
  - The percentage of discarded data in Th LOS (35-40 dB-Hz) is 17.09%, the percentage of discarded values is acceptable.
  - 35 dB-Hz C/N_0 threshold fulfills the requirements.
- $\underline{Th = 40\ \text{dB-Hz}}$:

- The percentage of discarded data in Th NLOS (35-40 dB-Hz) is 82.90%, this means there are more chances to have LOS samples with a C/N_0 lower than 40 dB-Hz than having NLOS samples; the percentage of discarded values is not acceptable.
- The percentage of discarded data in Test Th LOS (40-45 dB-Hz) is 0.83%; the percentage of discarded values is acceptable.
- 40 dB-Hz C/N_0 threshold does not fulfill the requirements.

The previous results can also be observed on the total percentage of discarded samples equal to 11.34% for 30 dB-Hz threshold, 6.48% for 35 dB-Hz threshold and 15.9% for 40 dB-Hz threshold. Therefore, from Table 6-18 results, the C/N_0 equal to 35 dB-Hz is finally selected as the LOS/NLOS classification threshold.

One final important observation to make is about the percentage of discarded data when $Th = 35$dB-Hz, which is equal to 28.09% in *Th NLOS* (30-35 dB-Hz) and equal to 17.09% in *Th LOS* (35-40 dB-Hz). These numbers are non-negligible and shown two limitations. The first one is the use of the C/N_0 threshold as the unique LOS/NLOS receiver state discriminator; the combination of several observables could potentially provide a better discrimination. The second one is the potential impact of Image processing errors which unfortunately, cannot be discriminated from the wrong LOS/NLOS receiver state estimations.

6.2.5.2.2 Analysis 2: Definition of the Empirical LOS/NLOS characterization threshold

Once the signal observable parameter has been selected and the experimental LOS/NLOS discriminator threshold defined, the completed LOS/NLOS classification approach using Image processing classification and Signal Processing refinement can be applied and the PSR and PSR-R characterization can be conducted to the classified measurements. Nevertheless, note that this characterization should only be applied in PVT solution where the positioning platform integrates a fish-eye camera to conduct the LOS/NLOS classification in real time. If the positioning platform does not contain a fish-eye camera, the PSR and PSR-R characterization to be used is the one presented in section 6.2.7 (as in this work) since the positioning platform could not conduct the LOS/NLOS classification; which means that the PSR and PSR-R statistics are better represented by section 6.2.7 results than by the results presented in this section where significant part of the samples have been removed (see Table 6-18 for C/N_0=35 dB-Hz). However, it is interesting to evaluate them since it can be directly compared to the expected LOS/NLOS MN error discrimination to evaluate the impact of the selected threshold on the LOS/NLOS MN error characterization.

In this section, the PSR and PSR-R data collections are thus subdivided in two different subsets classified by the LOS/NLOS receiver signal reception state used to obtain the LOS/NLOS MN error statistical models. Table 6-19 shows the Dual Constellation LOS/NLOS PSR MN error characterization as a function of the C/N_0, calculated from the Data Collection 2, containing, the sample mean, the sample standard deviation and the number of samples subdivided by different C/N_0 bins. C/N_0 threshold being used is equal to 35 dB-Hz as identified in analysis 1.

C/N_0 bins [dB-Hz]	**Receiver reception State**	**$\mu(\widehat{MN}_u^i)$ [m]**	**$\sigma(\widehat{MN}_u^i)$ [m]**	**N**
0 – 5	NLOS Reception State	-	-	0
5 – 10		42.78	39.48	48
10 – 15		41.79	29.81	1529
15 – 20		38.03	31.86	10102
20 – 25		25.82	24.63	22034
25 – 30		20.59	24.82	30469
30 – 35		10.79	18.70	39710
35 – 40	LOS Reception State	1.72	10.83	55123
40 – 45		0,44	5.16	133566
45 – 50		-0,59	2.02	132987
50 – 55		-0,01	0.70	30257
55-60		0,02	0.23	19

Table 6-19 – Dual constellation LOS/NLOS PSR Multipath plus Noise (MN) error PDF's characteristics per different C/N_0 bins

Several observations can be made from Table 6-19. The PSR LOS MN model is defined from the 35-40 dB-Hz bin to the 55-60 dB-Hz bin. It is characterized by a zero-mean, symmetrical distribution, with the standard deviation which decreases with the C/N_0 increase. The PSR NLOS MN model is defined from the 0-5 dB-Hz bin to the 30-35 dB-Hz bin. It is characterized by a positive biased, non-symmetrical distribution. The sample mean is always positive and decreases from 42.78 m to 10.79 m with the C/N_0 increase. The standard deviation is always higher than the corresponding values of PSR LOS MN model and also decreases with the C/N_0 increase.

Moreover, it can be seen that even if the sample mean between 30-35 dB-Hz bin and 35-40 dB-Hz bin decreases from 10.79 to 1.72 m, it is still difficult to clearly and unambiguously set the separation between NLOS and LOS reception state at C/N_0 = 35 dB-Hz in these results. Indeed, the value of the sample mean in 35-40 dB-Hz bin, which is different from zero, shows that NLOS measurements have not been completely filtered out (even after Image processing selection); remember that in average only NLOS receiver state can generate a non-zero mean.

6.2.5.3 Conclusions

Due to the C/N_0 threshold determination in the previous sections, the final characterization methodology may now be formalized and applied in order to obtain a reliable and refined PSR and PSR-R MN error characterization.

The refined MN statistical characterization process will be based only on C/N_0 characterization since, in this work, no fish-eye camera is assumed to be included in the positioning platform. To provide a better LOS/NLOS classification, the C/N_0 bin size, previously equal to 5 dB-Hz, could be reduced: ideally, the optimal value should be equal to the resolution of the receiver C/N_0 estimator; however, a bin size of 1 dB-Hz will reduce dramatically the number of collected data belonging to a specific C/N_0 bin and, in its turn, will affect the characterization process (not enough samples to calculate representative statistics). A practical bin size of 2 or 3 dB-Hz can be eventually used, as a function of the data collection length.

A C/N_0 threshold equal to 35 dB-Hz is finally selected as the LOS\NLOS classification threshold in this work. A PSR MN error LOS/NLOS reception state model is formalized with respect to the knowledges acquired in the previous sections. The results are classified in four different sections depending on the LOS/NLOS received signal conditions, as shown in Table 6-20.

For below 30 dB-Hz C/N_0 bins, the resulting error distributions are obtained by MN error samples with a higher chance to be in NLOS received signal reception state since only 7.76% of the samples were discarded. For above 40 dB-Hz C/N_0 bins, the resulting error distributions are obtained by MN error samples with a higher chance to be in LOS received signal reception state since only .0.83% of the samples were discarded.

However, bins values going from 30 to 40 dB-Hz are difficult to discriminate. The percentage of discarded samples, even if lower than 50%, cannot be neglected, 28.09% for 30-35 dB-Hz bin and 17.09 for 35-40 dB-Hz bin. Although some of the discarded data should be caused by the image processing errors, there is still an intrinsic uncertainty in the LOS and NLOS signal reception state discrimination as a function of the C/N_0 threshold: a LOS receiver state could have a 34 dB-Hz as true C/N_0 value and or a NLOS receiver state could have a 36 dB-Hz as true C/N_0 value leading to a wrong estimation by the use of the C/N_0 threshold as unique indicator. Therefore, in this work, it is assumed that in the 30-35 dB-Hz bin the resulting MN error distributions are obtained by MN error samples with a moderate to higher chance to be in NLOS received signal reception state, whereas in the 35-40 dB-Hz bin the resulting MN error distributions are obtained by MN error samples with a moderate to higher chance to be in LOS received signal reception state. It should be noted that the split is not intended or expected to be perfect but that the general behavior within the C/N_0 ranges is indicative.

C/N_0 Threshold [dB-Hz]	μ [m]	RX signal condition
$C/N_0 < 30$	$\mu \gg 1$	Higher chances of NLOS conditions
$30 \leq C/N_0 < 35$	$\mu > 1$	Moderate to higher chance of NLOS conditions
$35 \leq C/N_0 < 40$	$\mu > 1$	Moderate to higher chance of LOS conditions

$C/N_0 > 40$	$\mu \leq 1$	Higher chances of LOS conditions

Table 6-20 – Classification of Receiver signal reception with respect to the C/N_0

6.2.6 Objective 5: Measurement Availability Statistics

The Test proposed to fulfill the objective of this section is presented in section 6.2.6.1. The results of the test are described in section 6.2.6.2. Finally, the conclusions are given in section 6.2.6.3.

6.2.6.1 Test description

The objective of this test is the investigation of the satellite availabilities in the urban environment in order to determine whether the use of dual constellation measurements for isolating and removing the receiver clock bias is necessary when considering the increased complexity and uncertainty brought by dual constellation algorithm and GGPPTO term (see section X chapter 5). The proposed analysis is the following:

- **Analysis**: to evaluate the GPS, Galileo and GPS plus Galileo satellite availabilities, in a urban environment, which consists of the calculation of the number of available satellites histograms during the data collection. Different histograms have been calculated for the satellites belonging to single GPS, Galileo and GPS plus Galileo.

The Dataset applied for this Test is Data Collection 3. The Test description is summarized in Table 6-21.

Goal	Analysis	Constellation	Measurements	Reception State	C/N_0 Bin size [dB-Hz]	Statistical model	Data set
To investigate of the satellite availabilities in the urban environment	To characterize GPS, Galileo and Dual Constellation satellite availabilities	GPS, Gal, GPS + Gal	PSR	LOS + NLOS	----	Histograms	Data Collection 3

Table 6-21 – Description of the tests developed for Objective 5

6.2.6.2 Test Results

Figure 6-34 and Figure 6-35 illustrate the C/N_0 histogram and satellite availabilities histogram of GPS plus Galileo constellation satellites in urban environment. Same results are illustrated for standalone Galileo statistics (Figure 6-36, Figure 6-37) and standalone GPS statistics (Figure 6-38, Figure 6-39).

The number of the available GPS satellites in urban environment is higher than Galileo satellites; where a maximum number of 8 available GPS satellites with respect to 5 available Galileo satellites. Therefore, dual constellation measurements definitely improve, and is even mandatory for Galileo measurements, the MN isolation methodology accuracy due to the higher satellite availabilities allowing a better receiver clock estimation and isolation (see section 5.2.2.2). This statement has been confirmed through numerical analysis although it is not presented in this thesis.

The C/N_0 histograms allow to make an analysis of:

- the comparison between GPS and Galileo received signals characteristics;
- the characteristics of LOS\NLOS received signal reception states, in urban environment.

Comparing GPS and Galileo figures, it could be stated that GPS satellites reach higher C/N_0 values with respect to Galileo satellite: the peak of GPS C/N_0 histogram is around 48-50 dB-Hz while the peak of Galileo C/N_0 histogram is around 43-45 dB-Hz. It can be also notice that GPS and Galileo histograms have a similar shape; this is due to the MP environment surrounding the tested receiver which affects the C/N_0 statistics.

NLOS reception state, corresponding to the C/N_0 values below 35 dB-Hz (section 6.2.5.3), is a non-negligible part of the histograms. For this reason, the NLOS estimation approach and, consequently, Exclusion\Exploitation methodologies, become fundamental in order to develop such an improved PVT estimation algorithm, applied in urban environment.

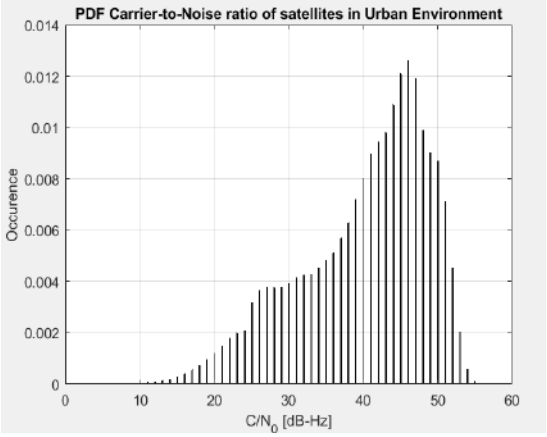

Figure 6-34 – Statistics of C/N_0 for dual constellation dataset

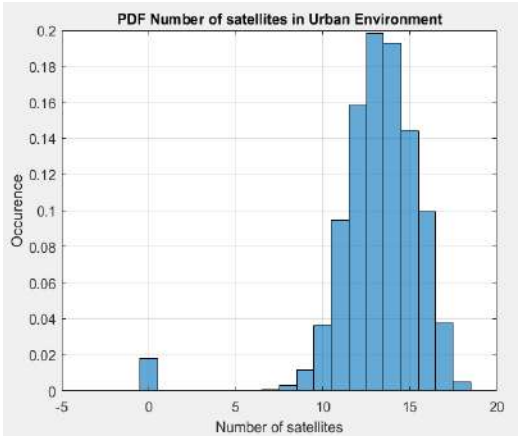

Figure 6-35– Statistics of satellite availabilities for dual constellation dataset

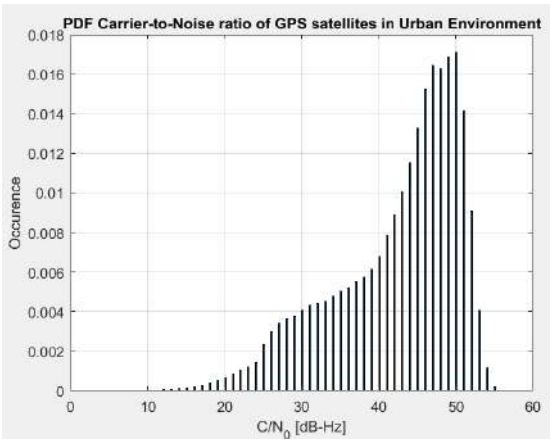

Figure 6-36 – Statistics of C/N_0 for GPS L1 C/A dataset

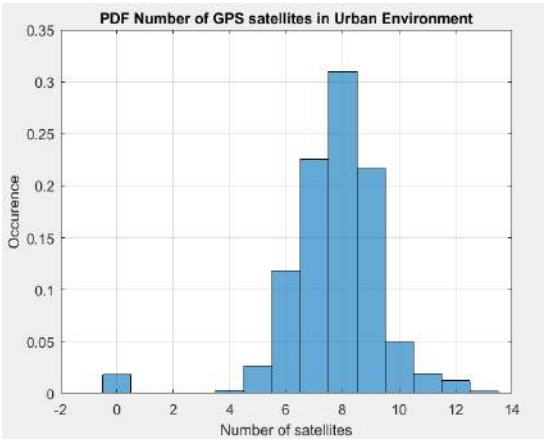

Figure 6-37 – Statistics of satellite availabilities for GPS L1 C/A dataset

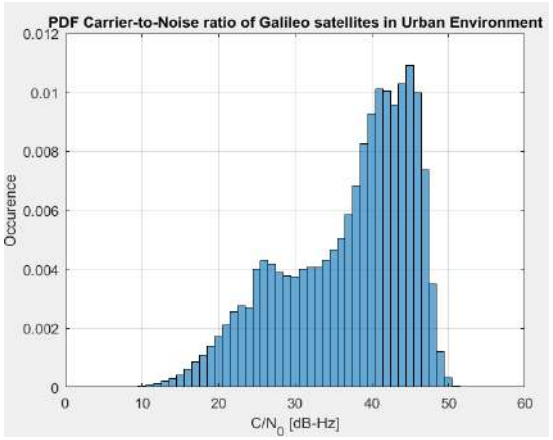

Figure 6-38 – Statistics of C/N_0 for Galileo E1 OS dataset

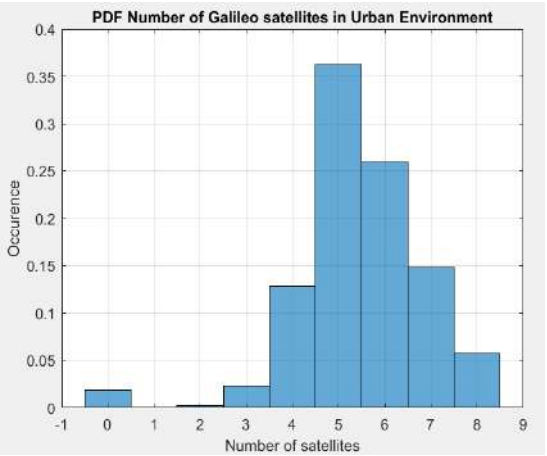

Figure 6-39 – Statistics of satellite availabilities for Galileo E1 OS dataset

6.2.6.3 Conclusions

As already known, the use of dual constellation receivers increases the number of available PSR and PSR-R in comparison to single constellation receivers; indeed, this availability can be quite low for standalone Galileo constellation in urban environment. As a consequence, the use of dual constellation measurements becomes mandatory for achieving a high accuracy on the receiver clock bias estimation part of the MN error component isolation methodology accuracy despite the extra complexity and the uncertainty brough by the GGPPTO term. Therefore, in the final characterization of the PSR and PSR-R MN error component derived in section 6.2.7, the

MN error component isolation methodology will use dual constellation measurement to estimate the receiver clock bias.

Additionally, since NLOS reception state, estimated to be mostly found at C/N_0 values below 35 dB-Hz, is a non-negligible part of the histograms, it can be concluded that exclusion\exploitation methodologies become fundamental in order to develop improved PVT estimation algorithms with improved accuracy in urban environment. Such an improved algorithm is described in section 7.1.2.

6.2.7 Objective 6: MN characterization

The test proposed to fulfill the objective of this section is presented in section 6.2.7.1. The results of the test are described in section 6.2.7.2. Finally, the conclusions are depicted in section 6.2.7.3.

6.2.7.1 Test description

The objective of this test is to obtain a reliable multipath and noise statistical error models exploitable in the PVT Estimation Algorithms, proposed in Chapter 7. For this reason, the MN error isolation and characterization methodologies are applied to a large data collection, Data Collection 3.

The proposed analyses are the following:

- **Analysis 1**: To calculate the statistical characterization of the GPS L1 C/A, Galileo E1 OS, and Dual constellation PSR MN errors as a function of the C/N_0.
- **Analysis 2**: To calculate the statistical characterization of the GPS L1 C/A, Galileo E1 OS, and Dual constellation PSR-R MN errors as a function of the C/N_0.

The MN error statistical characterization consists of the calculation of the empirical PDFs, calculated from the MN samples collected in the different C/N_0 bins. In addition to the empirical PDFs, the sample average, the sample variance and the number of samples used to calculate the statistics have been extracted. The choice of the C/N_0 bin size depends on the number of samples used to characterize the residual errors in that specific bin. To provide a better characterization, the C/N_0 bin size, previously equal to 5 dB-Hz, could be reduced as stated before (see section 6.2.5.3). A practical bin size of 2.5 dB-Hz can be eventually used, as a function of the data collection length (48 hours of data).

The configuration of the executed analyses is described in Table 6-22.

Goal	Analyses	Constellation	Measurements	Reception State	C/N_0 Bin size [dB-Hz]	Statistical model	Data set
To obtain a reliable multipath and noise statistical error models exploitable in the PVT Estimation Algorithms	To characterize PSR MN errors	GPS, Gal, GPS + Gal	PSR	LOS + NLOS	2.5	PDF, average, variance	Data Collection 3
	To characterize PSR MN errors	GPS, Gal, GPS + Gal	PSR-R	LOS + NLOS	2.5	PDF, average, variance	Data Collection 3

Table 6-22 – Description of the tests developed for the Objective 6

6.2.7.2 Test Results

The results of analysis 1 are presented in section 6.2.7.2.1. The results of analysis 2 are depicted in section 6.2.7.2.2.

6.2.7.2.1 Analysis 1: PSR MN Residual Errors characterization

The combined, GPS and Galileo MN isolated PSR MN errors are summarized in Table 6-23. Table 6-23 contains the sample mean, standard deviation and the number of samples. The PDF figures may be found in Annex 10.4.3.

PSR MN	GPS+GAL			GPS			GAL		
C/N_0 Bins [dB-Hz]	μ [m]	σ [m]	N	μ [m]	σ [m]	N	μ [m]	σ [m]	N
0-2.5	-	-	0	-	-	0			0
2.5-5	-	-	0	-	-	0			0
5-7.5	22.26	50.38	150	7.37	28.85	40	27.75	55.27	110
7.5-10	30.76	42.54	2111	37.92	51.15	477	28.66	39.45	1633
10-12.5	33.22	41.20	6622	46.33	54.76	1386	29.74	35.99	5235
12.5-15	32.65	37.07	26560	46.38	48.94	5720	28.88	32.06	20839
15-17.5	31.29	34.63	42151	44.17	42.83	8754	27.91	31.27	33396
17.5-20	28.35	29.99	128712	37.49	35.91	29760	25.61	27.33	98951
20-22.5	24.27	25.87	147326	30.93	29.31	37110	22.03	24.20	110215
22.5-25-	20.44	23.98	329256	27.40	28.26	106810	17.10	20.82	222445
25-27.5	16.96	21.31	339691	22.29	25.02	142217	12.66	19.01	197473
27.5-30	12.56	19.29	527064	17.97	20.91	260783	7.27	15.85	266280
30-32.5	9.18	17.44	394142	14.37	19.22	204800	3.56	13.14	189341
32.5-35	5.36	13.57	642049	9.47	14.87	338403	0.78	10.15	303644
35-37.5	2.12	9.49	507367	5.28	11.22	253679	-1.03	5.84	253687
37.5-40	0.31	5.95	1007841	1.99	7.60	444491	-1.01	3.71	563349
40-42.5	-0.39	3.66	870299	0.01	4.17	404745	-0.76	3.09	465552
42.5-45	-0.24	2.67	1551139	0.07	2.55	830668	-0.45	2.79	720470
45-47.5	-0.12	2.14	1115185	0.005	1.75	737787	-0.38	2.73	377397
47.5-50	0.03	1.65	1286115	0.07	1.40	1174541	-0.50	3.22	111573
50-52.5	0.022	1.15	532500	0.02	1.14	531360	-1.28	3.59	1139
52.5-55	0.038	1.16	115923	0.038	1.16	115908	1.2	1.98	14
55-57.5	0.7	1.08	371	0.67	1.08	369	-	-	0
57.5-60	0.37	0.94	8	0.37	0.94	8	-	-	0

Table 6-23 – PSR MN error PDF's characteristics per different C/N_0 range.

6.2.7.2.2 Analysis 2: PSR-R MN Residual Errors characterization

The combined, GPS and Galileo MN isolated PSR-R MN errors are summarized inTable 6-24. As for PSR MN characterization, Table 6-24 contains the sample mean, standard deviation and the number of samples. The PDFs figures may be found in Annex 10.4.3.

PSR-R MN	GPS+GAL			GPS			GAL		
C/N_0 Bins [dB-Hz]	μ [m/s]	σ [m/s]	N	μ [m/s]	σ [m/s]	N	μ [m/s]	σ [m/s]	N
0-2.5	-	-	0	-	-	0	-	-	0
2.5-5	-	-	0	-	-	0	-	-	0
5-7.5	0.045	0.37	48	0.02	0.39	12	0.05	0.37	35
7.5-10	0.49	6.52	1279	0.001	4.45	289	0.64	7.01	989
10-12.5	0.51	7.53	5347	0.25	5.56	1004	0.57	7.92	4342
12.5-15	0.39	7.51	24740	0.38	6.25	4906	0.39	7.79	19833
15-17.5	0.38	7.71	40490	0.45	6.89	7843	0.36	7.90	32646
17.5-20	0.21	7.81	124753	0.23	7.38	26872	0.21	7.92	97880
20-22.5	0.14	7.86	143589	0.17	7.79	33829	0.13	7.88	109759
22.5-25-	0.08	7.38	311361	0.07	7.26	92628	0.09	7.43	218732
25-27.5	0.005	6.36	312906	0.002	6.48	119111	0.008	6.29	193794
27.5-30	0.055	5.24	485421	0.05	5.88	223057	0.06	4.64	262363

30-32.5	0.06	4.48	368003	0.06	5.35	180333	0.06	3.45	187669
32.5-35	0.03	3.64	612854	0.02	4.41	311011	0.05	2.61	301842
35-37.51	0.02	2.79	494830	0.02	3.45	241676	0.02	1.98	253153
37.5-40	0.01	2.05	994484	0.016	2.63	433318	0.009	1.45	561165
40-42.5	0.01	1.54	866687	0.02	1.89	400333	0.01	1.16	466353
42.5-45	0.007	1.20	1544410	0.007	1.41	825877	0.006	0.92	718532
45-47.5	0.001	0.97	1114077	0.002	1.05	735384	0.001	0.82	378692
47.5-50	0.004	0.83	1284487	0.004	0.82	1173472	0.002	0.89	111014
50-52.5	0.001	0.66	531160	0.001	0.66	530000	0.08	0.89	1159
52.5-55	0.001	0.67	115896	0.001	0.67	115883	0.60	1.30	12
55-57.5	0.04	0.83	356	0.05	0.83	355	0.54	0.74	1
57.5-60	0.07	0.06	9	0.07	0.06	9	-	-	0

Table 6-24 – PSR-R MN error component PDF's characteristics per different C/N_0 range

6.2.7.3 Conclusion

This section contains the reliable PSR/PSR-R MN error characterizations, obtained by applying the MN error isolation methodology and characterization process described in Chapter 5. The results obtained in this section are exploited in the PVT Estimation Algorithms, developed in Chapter 7.

6.3 MN error Gaussian Overbounding Model

The PSR and PSR-R MN error statistical models presented in section 6.2.7 can be exploited in a PVT estimation algorithm to provide better performances in terms of accuracy of the PVT estimates. Complex PVT algorithms, such as Particle Filters, could exploit directly the MN error models, while simple solutions based on the EKF algorithms require zero-centred Gaussian measurement errors models (Chapter 5). For this reason, a PSR and PSR-R MN Gaussian error model are derived from the original PSR and PSR-R Mn error models. This is obtained applying the Gaussian overbounding approach, described in Chapter 5.

In section 6.3.1 the Gaussian overbounding of PSR MN statistics is presented, while in section 6.3.2 the Gaussian overbounding of PSR-R MN statistics is depicted. The overall PDFs figures may be found in Annex 10.4.3.

6.3.1 Pseudorange Residual Errors Gaussian overbounding

Once the MN characteristics have been derived, the successive step is to define a MN error mathematical model which can be exploited by the PVT estimator in order to improve the PVT estimation performances. Since the targeted PVT design is the EKF estimator (Chapter 7), the targeted mathematical model is a MN Gaussian error model, in order to allow EKF estimator as PVT solution exploiting the MN characteristics. The MN error Gaussian model is obtained applying the two different Gaussian overbounding strategies defined in Chapter 5.

This section summarizes the results of the PSR MN Gaussian error model obtained with the Gaussian overbounding process described in Chapter 5, applied to the MN error model presented in section 6.2.7.

Table 6-25 shows the standard deviations of the centered Gaussian overbounding models obtained with the two methodologies proposed in Chapter 5. For the first methodology, the overbounding process is applied directly to MN PDFs, whereas in the second methodology, the overbounding process is applied after the mean removal. The number of MN samples used to calculate the MN statistical models is also provided, where a higher number of samples implies a more reliable Gaussian overbounding model. The overbounding process is applied only if the number of samples is higher than 5000.

PSR MN	**GPS+GAL**			**GPS**			**GAL**		
C/N_0 Bins [dB-Hz]	**σ Standard [m]**	**σ Mean removal [m]**	**N**	**σ Standard [m]**	**σ Mean removal [m]**	**N**	**σ Standard [m]**	**σ Mean removal [m]**	**N**
0-2.5	-	-	0	-	-	0	-	-	0
2.5-5	-	-	0	-	-	0	-	-	0

5-7.5	-	-	150	-	-	40	-	-	110
7.5-10	-	-	2111	-	-	477	-	-	1633
10-12.5	80.39	61.69	6622	-	-	1386	66.83	51.03	5235
12.5-15	72.71	54.81	26560	106.46	65.96	5720	60.42	45.82	20839
15-17.5	68.29	51.89	42151	85.51	57.51	8754	59.94	46.43	33396
17.5-20	56.18	42.28	128712	66.69	47.89	29760	50.26	37.56	98951
20-22.5	45.06	33.26	147326	51.38	35.08	37110	42.49	31.49	110215
22.5-25-	40.57	30.37	329256	48.85	35.05	106810	33.91	25.01	222445
25-27.5	36.50	27.90	339691	42.41	30.91	142217	29.60	23.01	197473
27.5-30	30.18	23.98	527064	36.10	26.90	260783	23.26	19.46	266280
30-32.5	25.92	21.22	394142	31.60	24.30	204800	18.03	16.23	189341
32.5-35	21.065	18.36	642049	25.25	20.55	338403	12.23	11.93	303644
35-37.5	14.27	13.17	507367	18.31	15.70	253679	5.93	5.93	253687
37.5-40	7.049	6.942	1007841	11.19	10.19	444491	3.80	3.80	563349
40-42.5	3.75	3.75	870299	5.16	5.16	404745	3.19	3.19	465552
42.5-45	2.77	2.77	1551139	3.14	3.14	830668	2.88	2.88	720470
45-47.5	2.24	2.24	1115185	1.94	1.84	737787	2.83	2.83	377397
47.5-50	1.74	1.74	1286115	1.70	1.60	1174541	3.32	3.31	111573
50-52.5	1.35	1.25	532500	1.34	1.24	531360	-	-	1139
52.5-55	1.46	1.26	115923	1.46	1.26	115908	-	-	14
55-57.5	-	-	371	-	-	369	-	-	0
57.5-60	-	-	8	-	-	8	-	-	0

Table 6-25 – Dual constellation, GPSL1 C/A, Galileo E1 OS, PSR MN Error Gaussian Overbounding model, per C/N_0 bins

6.3.2 Pseudorange-Rate Residual Errors Gaussian overbounding

Similar to PSR MN errors overbounding process shown in section 6.3.1, this section illustrates the Gaussian overbounding model applied to the PSR-R MN error PDFs derived in section 6.2.7. The results are summarized in Table 6-26.

PSR-R MN	**GPS+GAL**			**GPS**			**GAL**		
C/N_0 Bins [dB-Hz]	**σ Standard [m]**	**σ Mean removal [m]**	**N**	**σ Standard [m]**	**σ Mean removal [m]**	**N**	**σ Standard [m]**	**σ Mean removal [m]**	**N**
0-2.5	-	-	0	-	-	0	-	-	0
2.5-5	-	-	0	-	-	0	-	-	0
5-7.5	-	-	48	-	-	12	-	-	110
7.5-10	-	-	1279	-	-	289	-	-	1633
10-12.5	10.28	10.08	5347	-	-	1004	9.56	9.27	5235
12.5-15	9.69	9.49	24740	9.52	9.33	4906	9.78	9.58	20839
15-17.5	9.60	9.50	40490	9.35	9.15	7843	9.68	9.58	33396
17.5-20	9.30	9.30	124753	8.65	8.55	26872	9.42	9.32	98951
20-22.5	9.35	9.26	143589	9.27	9.17	33829	9.38	9.28	110215
22.5-25-	8.77	8.67	311361	8.55	8.55	92628	8.82	8.72	222445
25-27.5	7.35	7.36	312906	7.27	7.27	119111	7.38	7.48	197473
27.5-30	5.74	5.74	485421	6.37	6.37	223057	5.13	5.23	266280
30-32.5	4.77	4.87	368003	5.84	5.84	180333	3.74	3.74	189341
32.5-35	3.93	3.93	612854	4.90	5.001	311011	2.71	2.71	303644
35-37.5	2.89	2.89	494830	3.84	3.84	241676	2.07	2.07	253687
37.5-40	2.15	2.15	994484	2.83	2.83	433318	1.54	1.54	563349
40-42.5	1.64	1.64	866687	1.99	1.99	400333	1.25	1.25	465552
42.5-45	1.30	1.30	1544410	1.50	1.50	825877	1.01	1.01	720470

45-47.5	1.07	1.07	1114077	1.14	1.14	735384	0.91	0.91	377397
47.5-50	0.92	0.92	1284487	0.91	0.91	1173472	0.98	0.98	111573
50-52.5	0.76	0.76	531160	0.75	0.75	530000	-	-	1139
52.5-55	0.76	0.76	115896	0.76	0.76	115883	-	-	14
55-57.5	-	-	356	-	-	355	-	-	0
57.5-60	-	-	9	-	-	9	-	-	0

Table 6-26 – Dual constellation, GPSL1 C/A, Galileo E1 OS, PSR-R MN Error Gaussian Overbounding model, per C/N_0 bins

6.4 MN error Time-Velocity Correlation characterization

The MN error components cannot be really modelled as white noise. In particular, MP errors are temporally and spatially correlated, since they depend on the environment surrounding the receiver antenna. Moreover, MP error component correlation should depend on the receiver dynamics: theoretically, a static receiver should exhibit a longer time correlation than a dynamic receiver since its surroundings are changing at lower rate (even if the receiver is static, other obstacles, such as vehicles, are not). In addition, the presence of thermal noise should also produce a temporal correlated error component when processed by the receiver DLL\FLL, due to the effects of the DLL\FLL equivalent filters.

To improve the MN error component characterization, this work has proposed to assess the temporal correlation as a function of receiver velocity, presented in section 5.3.2.1. The goal of the Time-Velocity (TV) correlation models is first to provide a model as a function of the receiver speed bins, and second, to extract the corresponding correlation time of each speed bin.

The final aim is thus to obtain a correlated in-time mathematical model of the MN error which should be more reliable with respect to the real MN error process than assuming only a gaussian process with independent samples. This is obtained by modelling the MN error as a 1st order Gaussian Markov process. Therefore, the correlation time has been derived; it is directly exploited in the PVT estimation model proposed in Chapter 7.

The TV correlation model have been calculated from the Data Collection 3, described in section 6.2.1, and used to obtain the reliable PSR and PSR-R MN error characterization in section 6.2.7.

Section 6.4.1 presents the TV correlation results obtained from the PSR MN error components Section 6.4.2 shows the TV correlation results obtained from the PSR-R MN error components.

6.4.1 PSR MN errors Time-Velocity Characterization

The correlation is performed for MN error components belonging to the same receiver speed bins, as explained in section 5.3.2.1. The receiver speed bins have a size of 5 Km/h and cover a velocity range going from 0 to 60 Km/h. The time correlation value is chosen to be the $1/e$ time correlation crossing point [124].

Figure 6-40 to Figure 6-44 presents the temporal correlation of the PSR MN error components isolated from the Data Collection 3 and obtained with the assistance of the sample mean and sample standard deviation calculated in section 6.2.7. In particular, Figure 6-40 shows the results for GPS measurements, Figure 6-42 for Galileo measurements whereas in Figure 6-44, the dual-constellation (GPS + Galileo) temporal correlation functions is presented. The resulting time correlation values are summarized in Table 6-27.

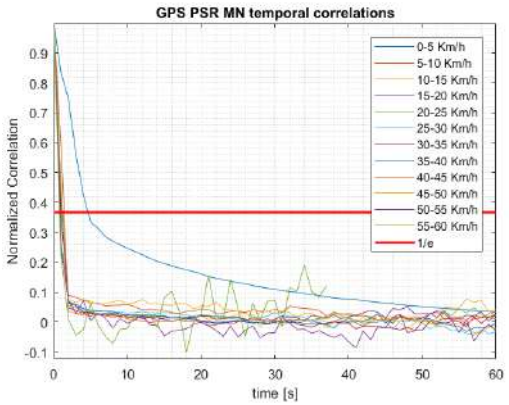

Figure 6-40 – One-dimension Time-Velocity Correlation of GPS PSR MN error residuals

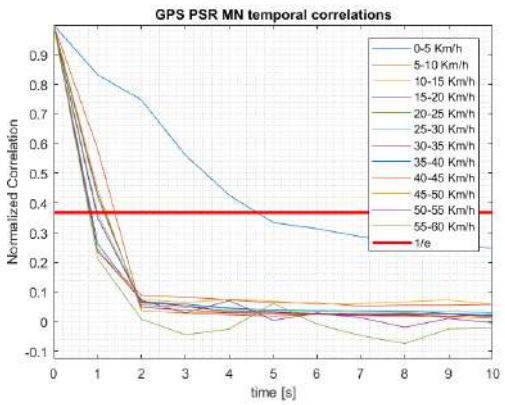

Figure 6-41 – Zoom of Figure 6-40 around 1/e cross-point

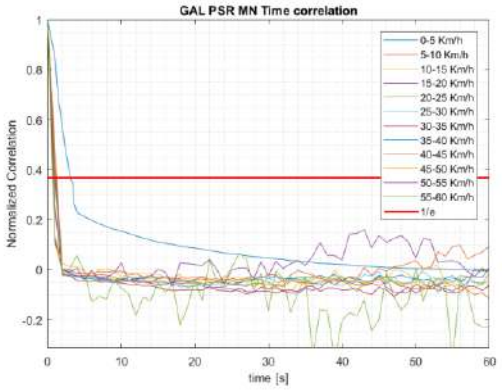

Figure 6-42 – One-dimension Time-Velocity Correlation of Galileo PSR MN error residuals

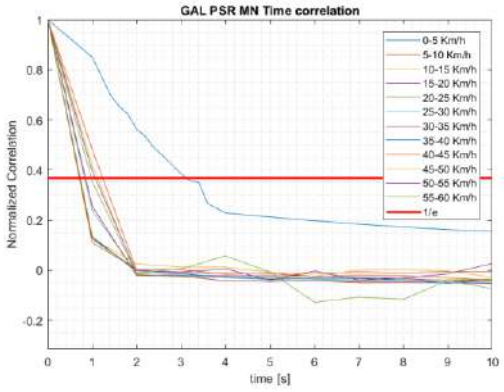

Figure 6-43 – Zoom of Figure 6-42 around 1/e cross-point

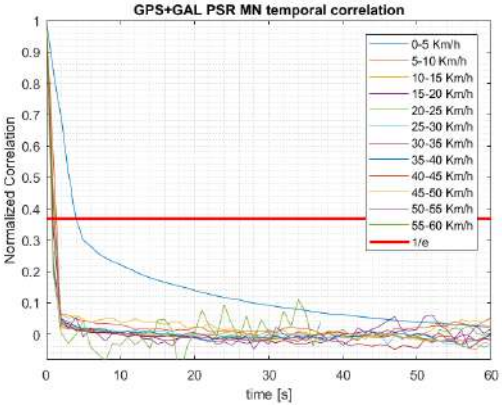

Figure 6-44 – One-dimension Time-Velocity Correlation of GPS + Galileo PSR MN error residuals

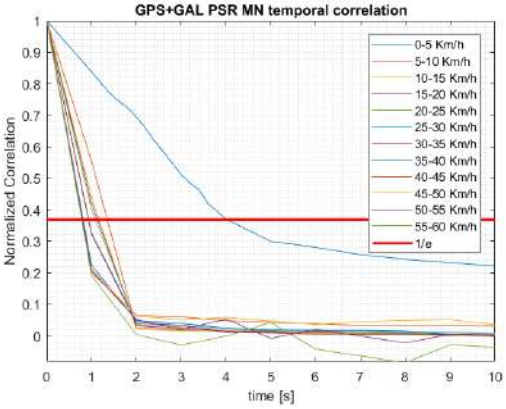

Figure 6-45 – Zoom of Figure 6-44 around 1/e cross-point

The time correlation is larger for MN error components obtained from static or low receiver speeds and decreases as the receiver speed grows. It is important to note that the correlation is always non-zero even in the case of high dynamics: since the MN error component is composed of multipath and thermal noise residual components, even if the multipath error correlation has a tendency to be null for high receiver speed (spatially uncorrelated errors), due to the DLL/FLL equivalent loop filters, the MN error components will still be time correlated. The magnitude of the thermal noise correlation depends on the design of the DLL equivalent loop filter bandwidth. Supposing that the DLL equivalent loop filter bandwidth is equal to 1 Hz, the resulting correlation should be assumed to be around 1s, as observed in Table 6-27.

GPS and Galileo MN error components have similar temporal-velocity correlation behaviour, with only minor differences. Notably GPS has higher correlation times for static and low receiver speed values. One potential explanation could be the difference in chip modulation, BPSK(1) for GPS L1 C/A and CBOC(6, 1/11, +/-) for Galileo E1 OS, which generates a different multipath error envelope (see section 4.2). Nevertheless, the single constellation analyses have limited accuracy due to the restricted number of data, especially for Galileo (section 6.2.7).

	GPS	**Galileo**	**GPS + Galileo**
Speed Bin [Km/h]	**Time correlation [s]**	**Time correlation [s]**	**Time correlation [s]**
0-5	4.6	3.2	4
5-10	1.4	1.4	1.4
10-15	1.2	1.2	1.2
15-20	1.2	1.2	1.2
20-25	1.2	1	1.2
25-30	1	1	1
30-35	1	0.8	0.8
35-40	0.8	0.8	0.8
40-45	0.8	0.6	0.8
45-50	0.8	0.6	0.8
50-55	0.8	0.6	0.8
55-60	0.8	0.6	0.8

Table 6-27 – Time-Velocity Correlation values of PSR MN error residuals

To verify if most of MN error components are time correlated, even in high receiver dynamics situations, an additional verification analysis is performed. The analysis consists of the calculation of the temporal correlation function for each satellite measurement belonging to each different daily data collections (length limited to roughly 3 hours) belonging to the Data Collection 3. There is a total of 121 MN satellite/daily measurements. The different correlation functions are all plotted together. From the different temporal correlation functions is calculated the correlation time. Moreover, the 5th, 50th and 90th percentiles are calculated for each lag time. If the different correlation functions show a correlation time which is generally different from 0, it can be stated that most of the MN error components are time correlated.

The temporal correlation function of the MN error component of a single satellite measurement during a single daily dataset, defined as $\boldsymbol{R}_m^i$, where i corresponds to the specific satellite and m corresponds to the specific daily dataset belonging to Data Collection 3, is calculated as follows:

$$\boldsymbol{R}_m^i = [R_m^i(0), \dots, R_m^i(l), \dots, R_m^i(N_m - 1)]$$
$$R_m^i(l) = \sum_{t=0}^{N_m - l - 1} \widehat{MN}^i(t)\widehat{MN}^i(t + l) \qquad 6\text{-}1$$

where l corresponds to the lag between the MN error components and N_m represents the total number of data belonging to the satellite i measurements for the specific daily dataset m.

Each temporal correlation function, is plotted in Figure 6-46. Moreover, the 5th, 50th and 90th percentiles are calculated for each lag time. The corresponding Table 6-28 depicts the results of the percentile functions. It can be noted that the behavior of the time correlations is different from zero for the majority of the cases, as can be also verified from the values of 5th, 50th and 90th percentile. This behavior confirms the fact that the error residuals are always correlated.

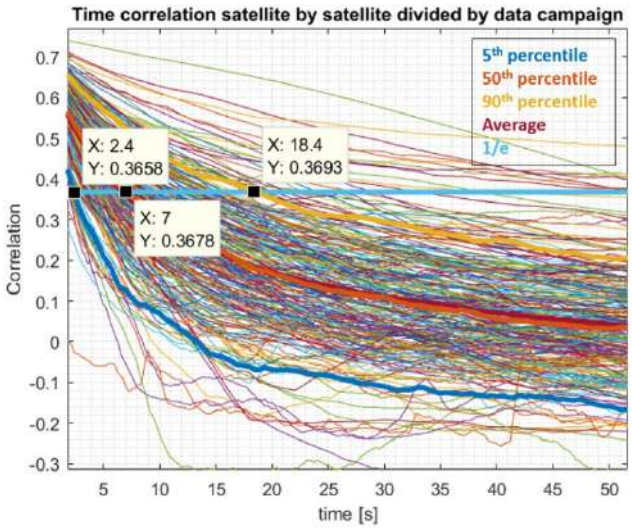

Figure 6-46 – Time correlation obtained processing each residual error component satellite by satellite, versus the 5th, 50th, 90th and the mean of the resulting correlation values.

	Time correlation [s]
5th percentile	2.4
50th percentile	7
90th percentile	18.4
Mean	7.2

Table 6-28 – Time correlation of 5th, 50th, 90th and the mean of the correlation functions

6.4.2PSR-R MN errors Time-Velocity Characterization

The same approach illustrated in Section 6.4.1 is used to obtain PSR-R MN residual error TV correlation results. In particular, Figure 6-47 shows the results for GPS measurements, Figure 6-49 for Galileo measurements whereas in Figure 6-51 the dual-constellation (GPS + Galileo) temporal correlation functions are shown. The resulting time correlation values are summarized in Table 6-29.

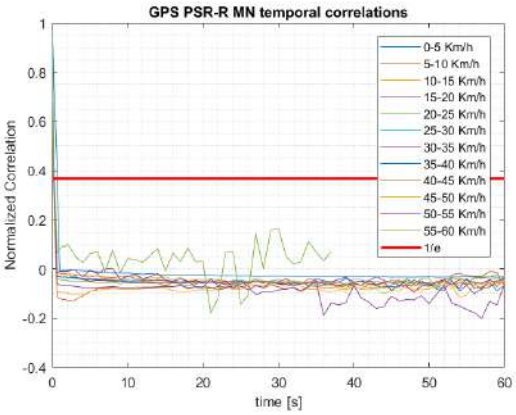

Figure 6-47 – One-dimension Time-Velocity Correlation of GPS PSR-R MN residual error

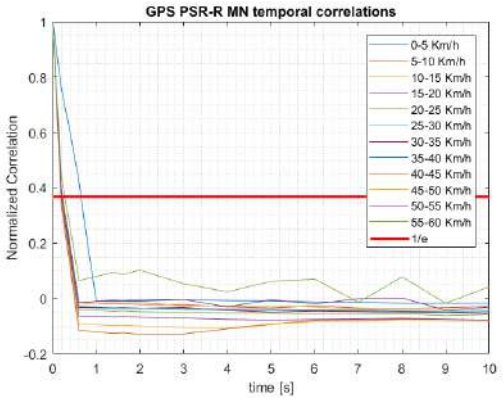

Figure 6-48 – Zoom of Figure 6-47 around 1/e cross-point

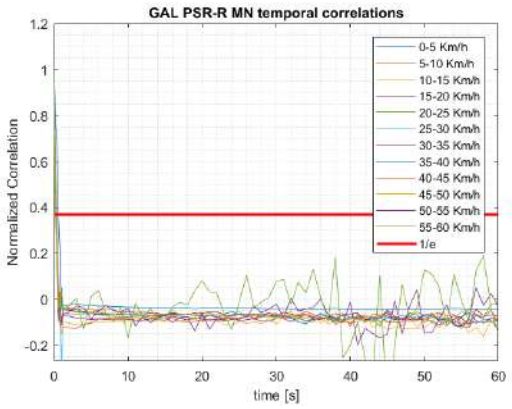

Figure 6-49 – One-dimension Time-Velocity Correlation of Galileo PSR-R MN residual error

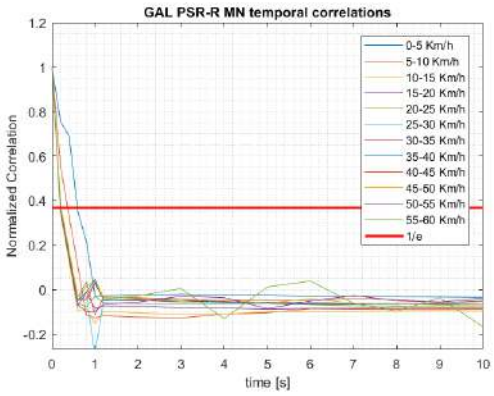

Figure 6-50 – Zoom of Figure 6-49 around 1/e cross-point

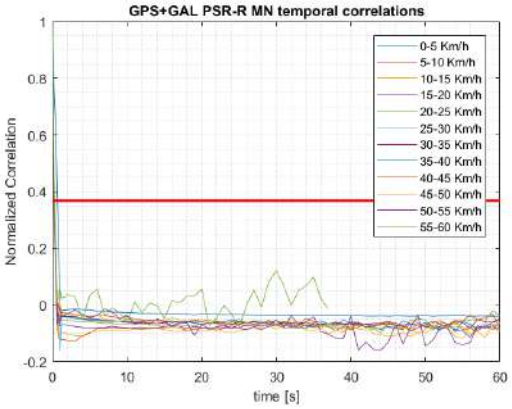

Figure 6-51 – One-dimension Time-Velocity Correlation of GPS + Galileo PSR-R MN residual error

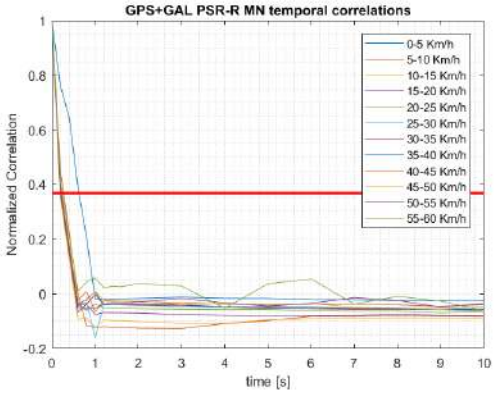

Figure 6-52 – Zoom of Figure 6-51 around 1/e cross-point

The PSR-R MN residual error could be considered temporally and spatially correlated when the receiver is static, due to the joint effect of multipath and thermal noise. As can be seen from the table, the correlation time is always 0.2s, even for higher receiver speed. The value of the correlation time is probably limited by the sampling interval.

For example, if it is assumed that, for higher receiver speed, the MP error components are uncorrelated, the correlation time only depends on the correlated thermal noise components, which depends on the design of the FLL equivalent loop filter bandwidth. If it is assumed a bandwidth of 10 Hz, the corresponding value of the thermal noise time correlation will be around 0.1s. However, since the sampling interval is limited to 0.2s, it can be possible that all the values lower than 0.2s are approximated to 0.2s.

In any case, the difference between 0.1s and 0.2s in the time correlation model only results in a slightly different and less precise approximation of the time correlation model, which can be exploited by a PVT algorithm.

	GPS	**Galileo**	**GPS + Galileo**
Speed Bin [Km/h]	**Time correlation [s]**	**Time correlation [s]**	**Time correlation [s]**
0-5	0.64	0.6	0.61
5-10	0.2	0.4	0.4
10-15	0.2	0.2	0.2
15-20	0.2	0.2	0.2
20-25	0.2	0.2	0.2

25-30	0.2	0.2	0.2
30-35	0.2	0.2	0.2
35-40	0.2	0.2	0.2
40-45	0.2	0.2	0.2
45-50	0.2	0.2	0.2
50-55	0.2	0.2	0.2
55-60	0.2	0.2	0.2

Table 6-29 – Time-Velocity Correlation values of Doppler MN error residuals

6.5 Conclusion

Chapter 6 has characterized the multipath plus noise errors. The evaluation is obtained through the application of the MN error isolation and characterization methodologies, proposed in Chapter 5, to real PSR and PSR-R measurements, collected from a low-cost GNSS receiver (U-Blox M8T), in an urban environment (Toulouse city centre). A large data campaign (roughly 50 hours of measurements) has been conducted, the collected data have been exploited and conclusions on the following issues have been extracted:

1) To test the validity of the proposed single constellation PSR/PSR-R MN isolation methodology: from the experimental analyses, it could be stated that the proposed methodology is a **valid tool able to isolate MN error components** from PSR and PSR-R measurements.
2) To test the validity of the proposed dual constellation PSR/PSR-R MN isolation methodology: from the experimental analyses, it could be stated that the proposed methodology is a **valid tool able to isolate the dual constellation (GPS L1 C/A and Galileo E1 OS) MN error components** from PSR and PSR-R measurements.
3) To investigate and select the observable parameter (C/N_0 or elevation angle) applied into the MN error characterization process, which allows for a better discrimination between LOS and NLOS receiver reception state: It is **preferred to differentiate between LOS and NLOS situations using the received signal $\boldsymbol{C/N_0}$** than the satellite elevation angle. Moreover, a better refinement with joint elevation angle and azimuth angle or joint elevation angle and C/N_0 characterization could also be pursued. However, to perform such a characterization, a larger data collection would be required. C/N_0 characterization is also preferred since it enables a better LOS/NLOS MN error modelling exploitable in the PVT estimation.
4) To determine the most suitable C/N_0 threshold which allows the discrimination/estimation of the received signal conditions, LOS or NLOS. The **$\boldsymbol{C/N_0}$ value equal to 35 dB-Hz** is finally selected as the LOS\NLOS classification threshold. Moreover, a LOS/NLOS reception state model is formalized with respect to the conclusions made in the previous sections. The results are classified in three to four different sections depending on the LOS\NLOS received signal conditions, below 30 dB-Hz, from 30 to 40 dB-Hz and above 40dB-Hz.
    a. For below 30 dB-Hz C/N_0 bins, the MN error samples have with a higher chance to be in the NLOS received signal reception state. The resulting MN error **PSR distributions are positive-biased, non-Gaussian and asymmetric**, featured by high standard deviations, which are inversely related to the C/N_0.
    b. For higher than 40 dB-Hz C/N_0 bins, the MN errors samples have a higher chance to be in LOS received signal reception state. The resulting **MN PSR error distributions are zero-mean, Gaussian-like and with a standard deviation inversely related to $\boldsymbol{C/N_0}$**.
    c. For C/N_0 bins from 30 to 40 dB-Hz, the MN errors samples are usually mixed between LOS and NLOS received signal states, with a higher influence of LOS or NLOS samples depending on how close the C/N_0 bin is to 30 or 40 dB-Hz. The resulting MN error distributions are a mix of the previously described ones. In the 30 to 40 dB-Hz region, the percentage of discarded samples by the signal processing refinement of the LOS/NLOS classification process (see section 5.2.3.2), even if lower than 50%, cannot be neglected. Although some of the discarded data should depend on the image processing errors, there still is an intrinsic uncertainty in the LOS and NLOS signal reception state discrimination in the LOS and NLOS signal reception state discrimination as a function of the C/N_0 threshold. Therefore, it is assumed that in the 30-35 dB-Hz bin the resulting error distributions are obtained by MN error samples with a moderate to higher chance to be in NLOS received signal reception state, whereas in the 35-40 dB-Hz bin the resulting error distributions are obtained by MN error samples with a moderate to higher chance to be in LOS received signal reception state. The **PSR-R MN error characterization is not affected by the LOS/NLOS signal reception state**, since the corresponding **PDFs are**

always centered, Gaussian-like distributions. Finally, it should be noted that the split is not intended or expected to be perfect but that the general behaviour within the C/N_0 ranges is indicative. This approximation is exploited to define the PVT estimator architecture proposed in Chapter 7.

5) To investigate the satellite availabilities in the urban environment to determine whether the use of measurements from two constellations are needed for isolating and removing the receiver clock bias. This is of significance considering the increased complexity and uncertainty brought by the dual constellation algorithm and the GGPPTO term: it was verified that due to low Galileo measurements availability, it was **mandatory to use GPS and Galileo (equivalently two constellations) measurements** to conduct the MN error component isolation methodology. This statement was corroborated by numerical analysis not presented in this PhD. Moreover, since NLOS reception state, estimated to be mostly found at C/N_0 values below 35 dB-Hz is a non-negligible part of the histograms, it can be concluded that exclusion\exploitation methodologies, become fundamental in order to develop improved PVT estimation algorithms with improved accuracy in urban environment.
6) To obtain a reliable GPS L1 C/A and Galileo E1 OS PSR/PSR-R MN error statistical characterization. A reliable **PSR/PSR-R MN error characterization has been obtained** applying the MN error isolation and characterization to a **data collection of 48 hours**. The MN error models are obtained for GPS L1 C/A, Galileo E1 OS and the two constellations together:
    a. Dual constellation MN error model:
        i. PSR MN error model is characterized by:
            1. sample average:
                a. between 0.37m and – 0.12m for the C/N_0 values higher than 40 dB-Hz
                b. between 0.39m and 2m for $40 \leq C/N_0 < 35$ dB-Hz,
                c. progressively increasing as a function of the C/N_0 decrease, for $C/N_0 < 35$ dB-Hz (between 2m and 30m).
            2. sample standard deviation:
                a. between 0.9m and 4m for the C/N_0 values higher than 40 dB-Hz,
                b. between 4m and 14m for $40 \leq C/N_0 < 35$ dB-Hz,
                c. progressively increasing as a function of the C/N_0 decrease, for $C/N_0 < 35$ dB-Hz (between 14m and 50m).
            3. The **experimental results** are **comparable to** the **theoretical assumptions** formulated in section 4.4.
        ii. PSR-R MN error model is characterized by:
            1. sample average:
                a. around 0m/s for all the C/N_0 values.
            2. sample standard deviation:
                a. progressively increasing as a function of the C/N_0 decrease: from 0.06m/s for $57.5 \leq C/N_0 < 60$ dB-Hz to 6.52m/s for $7.5 \leq C/N_0 < 10$.
            3. The **experimental results** are **comparable to** the **theoretical assumptions** formulated in section 4.4.
    b. The GPS PSR/PSR-R MN error models are almost similar to the Dual constellation MN error model, since the number of GPS MN error samples is higher than Galileo MN error samples, providing a major impact on the dual constellation characterization.
        i. PSR MN error model is characterized by:
            1. sample average:
                a. around 0m for the C/N_0 values higher than 40 dB-Hz,
                b. between 0.01m and 5.28m for $40 \leq C/N_0 < 35$ dB-Hz,
                c. progressively increasing as a function of the C/N_0 decrease, for $C/N_0 < 35$ dB-Hz (between 5.28m and 40m).
            2. sample standard deviation
                a. between 0.94m and 4.17m for the C/N_0 values higher than 40 dB-Hz,
                b. between 4m and 15m for $40 \leq C/N_0 < 35$ dB-Hz,
                c. progressively increasing as a function of the C/N_0 decrease, for $C/N_0 < 35$ dB-Hz (between 15m and 50m).
            3. The **experimental results** are **comparable to** the **theoretical assumptions** formulated in section 4.4.
        ii. PSR-R MN error model is characterized by:

1. sample average:
    a. around 0m/s for all the C/N_0 values.
2. sample standard deviation:
    a. progressively increasing as a function of the C/N_0 decrease; from 0.06m/s for $57.5 \leq C/N_0 < 60$ dB-Hz to 5m/s for $7.5 \leq C/N_0 < 10$.
3. The **experimental results** are **comparable to** the **theoretical assumptions** formulated in section 4.4.

c. Galileo PSR/PSR MN characterization are less reliable than GPS PSR/PSR-R MN error models since the number of isolated Galileo MN errors is smaller than the corresponding GPS MN errors. However, it is assumed that the corresponding MN error model is reliable when the number of samples used to derive the statistical properties is higher than 5000. In these cases, it can be shown that the sample mean and standard deviation of Galileo MN error models is always lower than the corresponding GPS MN error values:
    i. PSR MN error model is characterized by:
        1. sample average:
            a. between 0.50m and 1m for the C/N_0 values higher than 40 dB-Hz (higher than GPS, but less reliable since the lower number of samples used to make the calculation),
            b. around 1m for $40 \leq C/N_0 < 35$ dB-Hz,
            c. progressively increasing as a function of the C/N_0 decrease, for $C/N_0 < 35$ dB-Hz (between 1m and 50m), but always lower than the corresponding value of GPS MN model.
        2. sample standard deviation:
            a. between 2m and 3m for the C/N_0 values higher than 40 dB-Hz,
            b. between 3m and 6m for $40 \leq C/N_0 < 35$ dB-Hz,
            c. progressively increasing as a function of the C/N_0 decrease, for $C/N_0 < 35$ dB-Hz (between 5m and 50m), but always lower than the corresponding value of GPS MN model.
        3. The **experimental results** are **comparable to** the **theoretical assumptions** formulated in section 4.4.
    ii. PSR-R MN error model is characterized by:
        1. sample average:
            a. around 0m/s (0m/s to 0.64m/s) for all the C/N_0 values.
        2. sample standard deviation:
            a. progressively increasing as a function of the C/N_0 decrease: from 0.08m/s for $50 \leq C/N_0 < 52.5$ dB-Hz to 7m/s for $7.5 \leq C/N_0 < 10$.
        3. The **experimental results** are **comparable to** the **theoretical assumptions** formulated in section 4.4.

7) To obtain a reliable multipath and noise statistical error models exploitable in the PVT estimation algorithms, proposed in Chapter 7: since the targeted PVT design is the EKF estimator (Chapter 7), the MN error mathematical model must be a Gaussian error model, in order to allow EKF estimator as PVT solution exploiting the MN characteristics. The **MN error Gaussian model is obtained applying the two different Gaussian overbounding strategies** defined in Chapter 5. Therefore, a PSR/PSR-R MN error Gaussian characterization has been derived.
8) To refine the MN error mathematical model which can be exploited by the PVT estimator in order to improve the PVT estimation performance: the MN error components are temporally and spatially correlated, since they depend on the environment surrounding the receiver antenna and due to the influence of DLL\FLL equivalent filters. Therefore, a correlated in-time mathematical model of the MN error which is more reliable with respect to the real MN error process than assuming only a gaussian process with independent samples has been derived. The **Temporal-Velocity correlation functions are calculated** with the methodology presented in section 5.3.2.1 **used to model the MN error as a 1st order Gaussian Markov process**. These values can be directly exploited in the PVT estimation model proposed in Chapter 7. As verified by the investigations, the estimated PSR and PSR-R MN correlation time corresponding to the different received speed bins, is always different from zero. As expected, for static and low-speed receiver dynamic, this value is higher and corresponds to roughly 4s for GPS/Galileo PSR MN errors and 0.6s for GPS/Galileo PSR MN errors in $5 \leq \dot{p} < 0$ Km/h bin. It abruptly decreases in $10 \leq \dot{p} < 5$ Km/h bin, reaching roughly 1.2/1.4s for GPS/Galileo PSR MN errors and 0.2/0.4s for GPS/Galileo PSR MN errors. However, this value decreases to 0.8/0.6s for GPS/Galileo PSR MN errors

and 0.2s for GPS/Galileo PSR MN errors for higher receiver speed bins never becoming 0. This is probably due to the effects of the DLL/FLL tracking operations which correlates the estimated parameters. Therefore, even if the multipath error correlation has a tendency to be null for high receiver speed (spatially uncorrelated errors), due to the DLL/FLL equivalent loop filters, the MN error components will still be time correlated. The magnitude of the thermal noise correlation depends on the design of the DLL equivalent loop filter bandwidth. Supposing that the DLL equivalent loop filter bandwidth is equal to 1 Hz, the resulting correlation should be assumed to be around 1s. Since the PSR-R MN correlation time is always 0.2s, even for higher receiver speed it has been assumed that value of the correlation time is probably limited by the sampling interval.

7 Proposed Extended Kalman Filter Algorithm

In the previous chapters, the investigation into the impact of Multipath and thermal noise on dual constellation (GPS L1 C/A, Galileo E1 OS) low-cost GNSS receiver measurements collected in an urban environment has been presented culminating in a modelling methodology (Chapter 5) and an empirical model (Chapter 6). The model is expressed in terms of variances of a CDF overbound, as a function of the C/N_0, and the temporal correlation constant as a function of speed. Furthermore, discrimination between LOS and NLOS signal reception states is achieved using a C/N_0 cutoff threshold of 35 dB-Hz.

In this chapter, the outputs of that work are employed to aid the design of a low-cost GNSS PVT estimator, for GNSS-based micromobility applications in the urban environment both in standalone and DGNSS modes. The family of techniques pertaining to the Data Processing Stage are investigated, as outlined in Chapter 5, in particular measurement masking, weighting and consistency checking (section 5.1). The benefits of these techniques are the following:

- low complexity, since based on predefined mathematical models;
- low impact on the receiver memory;
- low cost, without need for additional sensors.

However, there are some limitations:

- too generic to take into account the dynamic urban environment;
- only through partial detection of NLOS conditions.

In light of the above, the solution proposed in this PhD attempts to enhance the benefits of the basic masking and weighting techniques through the testing of different configurations and architectures e.g. standard vs. time differenced (see below), standalone vs. differential. The description of the proposed techniques, which culminates with the design of the proposed Standard EKF estimator, is depicted in section 7.1.

The proposed estimator will include the evaluation of the temporal and spatial correlations of the errors. The MN error components are temporally and spatially correlated as shown in chapter 6. Some attempts to model it are found in [107],[108],[109],[110] while its effect on the positioning results is investigated in other works, [111]–[113]. Since the EKF assumes independence between the measurement errors and the state prediction errors, correlation leads to a contravention of this assumption and a sub-optimal estimation.

Correlated noise cannot be modelled as white noise, the assumed input to an EKF; but as colored noise. Colored noise can be efficiently modelled as a Gauss-Markov process (GMP) or a first-order autoregressive model driven by white Gaussian noise. If these quantities are subsequently processed by a KF, the correlation should be appropriately addressed through modifying the conventional KF [1], [2], [110]. The approaches that remedy the KF to address the colored measurement noise can be roughly categorized into two types: the state-augmentation approach, and the measurement time-difference approach [1].

Even if the temporal correlation in GNSS measurements is widely recognized, it is challenging to address. The environment which is surrounding the receiver may change smoothly or suddenly depending on the receiver dynamics, and thus as a function of the travelled distance. One means to address this, is proposed in section 7.2 below. The proposed EKF design is based on the EKF-TC solution proposed in [1], [2] incorporating the work of Chapters 5 and Chapter 6, and is presented in section 7.2.

Following these theoretical elaborations, results relating to each solution are presented in section 7.3 and conclusions on the analyses have been made in section 7.4.

7.1 Standard EKF based on MN statistics

This section provides a description of the dual-constellation PVT estimator proposed in this work, exploiting the knowledge of *a priori* PSR and PSR-R MN error distributions and LOS/NLOS discrimination.

The proposed PVT estimator is an evolution based on a trivial EKF, presented in section 3.2.3.2.3, also defined as the **benchmark** PVT estimator for low-cost single frequency GNSS receivers applied in micromobility applications. It implements a multipath error mitigation solution, which consists of the two following blocks:

- the **Baseline** block, whose solution pertains to the family of measurement weighting techniques;
- the **Improvement** block, whose proposed techniques are based on the family of the measurement masking techniques.

The Baseline block is applied between the EKF prediction block and the innovation block, as illustrated in Figure 7-1, and consists of calculating the Measurement Error Covariance Matrix based on the exploitation of the PSR/PSR-R MN error distributions. In the **benchmark EKF**, the PSR and PSR-R measurement error variance associated to the different received signals are equal for all the satellites in view, and **constant** in time. On the contrary, in the proposed solution, the PSR and PSR-R measurement error variances associated to the different received signals will be different for each satellite in view, and time variant, depending on the value of C/N_0 corresponding to the received signal. As a consequence, the Measurement Error Covariance Matrix becomes time-variant, where the diagonal terms correspond to variance of the MN errors previously introduced. The Baseline block is presented in section 7.1.1.

The Improvement Block is applied before the Baseline Block and consists of selecting measurements using the LOS/NLOS discrimination and MN error statistics derived in Chapter 6. Therefore, the refined measurement vector is sent to the Baseline block to calculate the corresponding Measurement Error Covariance Matrix. The reasons which lead to the proposition of the Improvement Block, are briefly presented in the following paragraph:

The precision of the EKF estimations depends on two different factors:

- the precision of the state propagation model and,
- the precision of the measurement innovation model.

First, the precision of the state propagation model is necessary to better model the dynamics of the state under estimation; second, the precision of the measurement vector is important to reduce the possible impairments introduced by the use of real measurements.

In fact, even with a well-designed model of the propagation states, the estimation uncertainties will grow in time if the a-priori estimations are not corrected by the measurements. However, the measurement precision degrades significantly in the urban environment, leading to a lack of PVT estimation accuracy. Focusing on the PVT performances of a low-cost receiver in the urban environment, it is fundamental to analyse how the errors affect the measurements and to explore some innovative low-complex solutions to reduce the impact of the measurement errors. The impact of the so-called “bad” satellites (low-quality measurements) should be reduced to increase the accuracy of the PVT solution. A way to reduce their impact is based on the reliable knowledges of the measurement errors, as obtained applying the Baseline Block. However, Baseline Block is not able to select/exclude satellite measurements exploiting any different criteria. Therefore, the PVT solution will be estimated by leans of all the possible satellite measurements, weighted with respect to the a-priori knowledges of the measurement error model.

The PVT estimation accuracy of the measurement innovation vector is based on two different criteria:

- The quality of the satellite measurement, which could be classified a-priori by the C/N_0 of the received signal and the elevation angle of the satellite, and the NLOS/LOS received signal conditions. A satellite measurement featured by low C/N_0 and/or low elevation angle and/or NLOS received signal conditions, could be a-priori defined as “bad” satellite in the measurement vector. The presence of “bad” satellites leads to a certain level of estimates accuracy degradation. This problematic could be reduced by the realistic knowledges of the measurement errors in the given environment, as focused in the first part of the actual work.
- The geometry of the set of satellites used to make the innovation of the state. A poor signal-geometry, reduces the accuracy of the estimates. Usually, in the urban environments, the number of satellites in view is reduced and these satellites are mostly positioned to similar sky portion, reducing systematically the signal-geometry.

A solution could be afforded if the Signal processing module has additional knowledges of the measurement errors. It could be possible to select only the satellite measurements determined to be useful measurement in order to

improve the PVT solutions. This is a Measurement Masking-based technique called Satellite Measurement Exclusion. Two different Satellite Measurement Exclusion techniques are described in section 7.1.2.

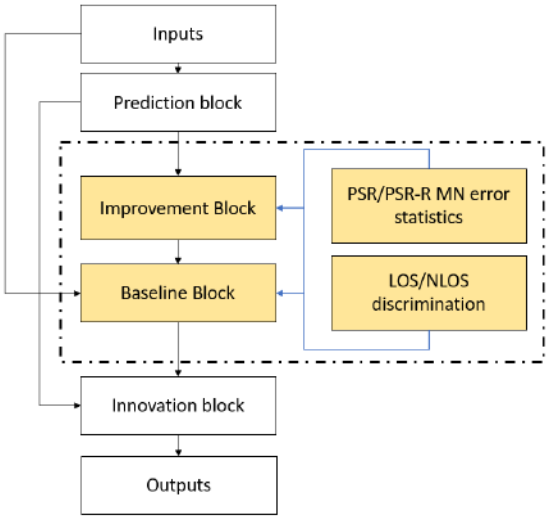

Figure 7-1 – Structure of the Standard EKF based on MN Statistics

7.1.1 Baseline Block: Measurement Weighting Solution based on MN Statistics

The Baseline Block consists on the calculation of the Measurement Error Covariance Matrix by the exploitation of the MN error statistics. Two different variants of PVT estimators have been designed, depending on the implemented positioning technique, the SA EKF and the DGNSS EKF. Hence, two different Measurement Error Covariance Matrix have been designed, the SA and the DGNSS Measurement Covariance Matrix.

On one hand, The SA EKF is a low-complexity PVT estimator, but, in this case, the presence of non-negligible satellite clock error, ionospheric and tropospheric errors reduce the benefits of the MN error model exploitation. On the other hand, the DGNSS EKF model is more complex but reduces the impact of the satellite clock error, ionospheric and tropospheric errors, which usually become negligible with respect to the MN error components in urban environment. For this reason, the MN error component characterization have theoretically a larger impact on the estimation accuracy. The mathematic model of the SA and DGNSS Measurement Error Covariance Matrix, are presented in section 7.1.1.1.

7.1.1.1 Mathematical model

The benchmark EKF estimator mathematical models and computational steps have been introduced in section 0. In the EKF, the GNSS measurements have a key role in the Innovation block, since are used to generate a correction of the predicted estimations, which finally lead to a corrected state estimation and a corrected state covariance matrix. This is obtained through the applications of the Kalman Gain and the vector estimate update. The Kalman gain requires as input the Measurement Noise Covariance Matrix, $\boldsymbol{R}$, which standard definition applied to the **benchmark** EKF is described in 3-89, while the vector estimate update requires as input the measurement vector, $\boldsymbol{z}$, which is defined in 3-86.

The measurements vector of a dual constellation EKF is composed by the GPS and Galileo PSR and PSR-R measurements, processed by the GNSS receiver at a given epoch is equal to:

$$\tilde{\mathbf{z}}_l = \left(\tilde{\rho}^1_{l,GPS}, \dots, \tilde{\rho}^N_{l,GAL}, \tilde{\dot{\rho}}^1_{l,GPS}, \dots, \tilde{\dot{\rho}}^N_{l,GAL}\right) \quad 7\text{-}1$$

Depending on the positioning technique (SA/DGNSS) applied by the PVT estimator, the PSR and PSR-R measurements, $\tilde{\rho}^i_l$, $\tilde{\dot{\rho}}^i_l$, are different:

- For the Stand Alone (SA) PVT estimator, the PSR and PSR-R measurements are corrected through the application of error correction models (section 3.2.2.1). After the application of the error correction models, ionospheric, tropospheric and satellite clock residuals, non-negligible with respect to the multipath and thermal noise error components, appear in the measurements.
- In the differential (DGNSS) case, the reference station measurements are used to remove the satellite clock bias, ionosphere and troposphere biases from the user measurements (section 3.2.2.2). After the application of the differential correction, the GPS and Galileo PSR and PSR-R corrected measurements present a small ionospheric and tropospheric residual, depending on the length of the baseline between the receiver under process and the reference station receiver. In urban environment, ionospheric and tropospheric residual errors can be assumed negligible with respect to the multipath and thermal noise error components. Moreover, the overall MP and thermal noise components are composed by a combination of the MP and thermal noise errors deriving from the two receivers.

The variance and the covariance of the overall error component affecting the different received PSR and PSR-R measurements are modelled in the Measurement error Covariance Matrix (section 3.2.3.2.3.1). In the benchmark EKF approach the overall error components are usually modelled as additive zero-mean Gaussian variable and considered independent and identically distributed for all the satellites, therefore:

- the covariance values are usually equal to 0 for all the combination of the PSR and PSR-R measurements;
- the variance of the PSR measurements is different from 0 and is a unique and equal value for all the measurements; similarly, the variance of the PSR-R measurements is different from 0 and is unique and equal value for all the measurements. The PSR and PSR-R error variance are defined by the UERE and UERRE error model (section 3.2.3.2.1).

The design of the Measurement Error Covariance Matrix depends on the model of the UERE/UERRE associated to the GNSS measurements. The UERE and UERRE model of the different received measurements depend on the type of positioning technique applied to the PVT estimator. The classic UERE and UERRE error models defined in literature satisfy the PVT requirements of the aviation navigation. However, the use of these classical error models does not yield the required performances in the urban user environment: this is a consequence of the mismatch between the estimated UERE multipath error and the urban user environment, which results in overly estimation of UERE, which ultimately contribute to the further degradation of the navigation system performances in urban environment. In order to improve the PVT estimation performances in urban environment, a possible solution is to estimate reliable UERE/UERRE error models relying on more sophisticated and more realistic error models in urban environment, especially for MP error component. For this reason, in this work, the reliable characterization of MN error components isolated from PSR and PSR-R measurements of a low-cost GNSS receiver in an urban environment has been exploited to design a reliable UERE/UERRE models. The mathematical models are presented in section 7.1.1.1.1.

The design of the Measurement Covariance Matrix, based on the application of the proposed SA and DGNSS UERE/UERRE models, is defined in section 7.1.1.1.2.

The application of the proposed UERE/UERRE models in the original Measurement Error Covariance Matrix is equivalent to the application of a Measurement Weighting Technique, where, the PSR and PSR-R measurement errors are characterized by a different reliable weight derived from the MN error characterization. The MN error characterization takes into account the severity of the MP and the thermal noise errors and the LOS/NLOS reception state conditions, as a function of the corresponding C/N_0 parameter calculated by the GNSS receiver. With this model the measurement covariance matrix remains diagonal but UERE/UERRE variance values are different for each PSR and PSR-R measurements, and time-dependent. The steps followed by the proposed solution are:

- Firstly, the PVT estimator selects separately the corresponding GPS and Galileo PSR and PSR-R MN error variance from the look-up tables implemented directly in the memory of the GNSS receiver, as a function of the corresponding C/N_0^i parameter, estimated by the GNSS receiver.
- Consequently, the PVT estimator exploit the GPS and Galileo PSR and PSR-R MN error variance calculated in the previous step, to calculate the corresponding $\sigma^2_{UERE^i}$ and $\sigma^2_{UERRE^i}$;
- Finally, the resulting $\sigma^2_{UERE^i}$ and $\sigma^2_{UERRE^i}$ are used to obtain the new Measurement Error Covariance Matrix.

The proposed SA and DGNSS Measurement Error Covariance Matrix, are presented in section 7.1.1.1.2.

It must be pointed out that the basic EKF is an optimal estimator with the assumption that the measurement errors are modelled as white zero-mean Gaussian distributions. However, as showed in section 6.2.5.3, the PSR MN error distribution is assumed to be divided in three different sections depending on the received signal C/N_0 and the LOS/NLOS received signal conditions. It is stated that for $C/N_0 > 40$ dB-Hz, when the distribution is obtained by MN isolated errors coming from signal with higher chance to be defined in LOS reception state, the error model is Gaussian-like and zero-mean, while for $C/N_0 < 35$ dB-Hz, when the distribution is obtained by MN isolated errors coming from signal with higher chance to be defined in NLOS receiver reception state, the distribution is non-Gaussian, non-symmetric and positive biased. Therefore, to handle the non-Gaussian, non-symmetric and positive biased MN error models, two possible Measurement Models can be applied (section 5.3):

- ***Measurement Model 1***: The first possibility is to calculate the MN Gaussian error model directly applying the zero-mean Gaussian overbounding to the MN error characterizations, section 6.3.1. In this case, the $\sigma^2_{\widehat{MN_u^l}}$ values applied to the GPS and Galileo Measurements have been extracted from Table 6-25.
- ***Measurement Model 2:*** The second possibility is to calculate the MN Gaussian error model in two different steps; firstly, the mean of the LOS and NLOS MN error characterizations is removed. Consequently, the zero-mean Gaussian overbounding is applied to the resulting LOS and NLOS MN error characterizations, section 6.3.1. In this case, the $\sigma^2_{\widehat{MN_u^l}}$ values applied to the GPS and Galileo Measurements have been extracted thus, from Table 6-25.

To apply the first solution, the standard measurement vector, does not need any modification. On the contrary, the standard measurement vector can't be directly applied with the second solution, since it must be taken into account the mean removal applied to calculate the resulting MN error variance. The measurement vector, applied at a given epoch l, is modified as proposed in 7-2. However, this solution involves specific assumptions which may be not representative or at best suboptimal of the received measurement models and could not be formally a universal solution, but more specific to the dataset under test.

$$\tilde{\mathbf{z}}_l = \left(\tilde{\rho}^1_{l,GPS} - \mu\left(\widehat{MN}_l^1\right), \dots, \tilde{\rho}^N_{l,GAL} - \mu\left(\widehat{MN}_l^1\right), \tilde{\rho}^1_{l,GPS}, \dots, \tilde{\rho}^N_{l,GAL}\right) \qquad 7\text{-}2$$

The block scheme of the Baseline Solution is portrayed in Figure 7-2.

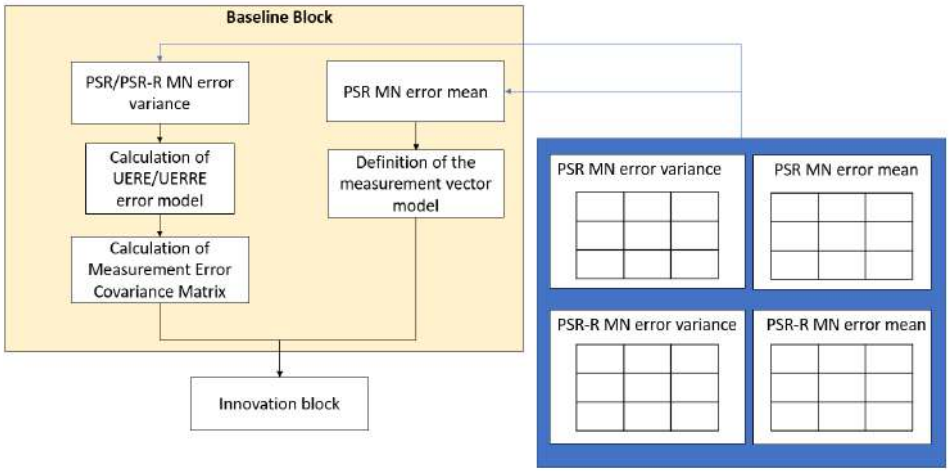

Figure 7-2 – Scheme of the Baseline Block applied in Standard EKF based on MN statistics

7.1.1.1.1 Proposed UERE and UERRE models

The UERE and UERRE models, mainly developed for civil aviation positioning applications, are equally applicable to the urban environment with the side effect of the underestimation or overestimation of the MP error component [9]:

- On one hand UERE/UERRE models applied for receivers in open-sky LOS receiver reception state can efficiently model the overall error component.
- On the other hand, UERE/UERRE models applied for receivers in constrained environment with a high chance of NLOS receiver reception state cannot be able to efficiently model the MP error component, impacting the performances of the PVT estimator.

The proposed mathematical model of SA and DGNSS UERE/UERRE models applied for GNSS receiver, in urban environment, are depicted, respectively, in section 7.1.1.1.1.1 and 7.1.1.1.1.2.

7.1.1.1.1.1 Proposed SA UERE/UERRE models

Some GPS and Galileo SA UERE error models already exist in literature, [12], [125]. The models applied to estimate the variance of the Satellite clock and Ephemeris error, Ionospheric error, Tropospheric error and Thermal noise error can be applied for both aviation domain and the urban context, such as:

- Satellite clock and Ephemeris error:
  - GPS: the Satellite clock and ephemeris residual error standard deviation is generally referred to as user range accuracy (URA) [10]. The URA is provided to the users within the navigation message.
  - Galileo: The SISA (Signal in Space Accuracy) is the predicted minimum standard deviation of a Gaussian distribution that overbounds the error distribution [125]. The SISA is provided to the users within the navigation message.
- Ionospheric error:
  - GPS: GPS single frequency receivers estimate the ionospheric delay using the Klobuchar model (section 3.2.2.1.2). From the Klobuchar correction model, it is possible to compute the residual error standard deviation [45].
  - Galileo: Similarly to GPS, Galileo single frequency receivers estimate the ionospheric delay using the NeQuick model (section 3.2.2.1.2). The residual error specifications, defined by the calculation of the standard deviation, can be derived directly from the NeQuick algorithm [45].
- Tropospheric error:
  - Tropospheric corrections are calculated applying the UNB3 model and do not differ for GPS and Galileo constellations (section 3.2.2.1.3). The residual error specifications, defined by the calculation of the standard deviation, are summarized in [45].
- Thermal noise error:
  - GPS: PSR error due to thermal noise at the receiver's front-end input depends on the signal modulation and on the receiver design. It has been widely studied and its error model is well known [12].
  - Galileo: Galileo E1 OS noise error variance have been formulated in [13].

However, the model for the multipath error cannot be applied directly in urban framework since the local effects are completely different from that of the aviation applications, Chapter 0:

- the variance of MP error can be estimated by empirical models, Chapter 5, which accuracy is limited by the complexity and the reliability of the empirical models;
- the variance of MP error can be estimated by sophisticated models, Chapter 5, based on the application of sensor fusion, 3D mapping, ray tracing etc.

The variance of the SA UERE model, is therefore, modelled as follows:

$$\begin{aligned}\sigma^{2^i}_{UERE,SA} &= \sigma^{2^i}_{e} + \sigma^{2^i}_{\tilde{b}} + \sigma^{2^i}_{I} + \sigma^{2^i}_{T} + \sigma^{2^i}_{\xi} + \sigma^{2^i}_{\eta} \\ &= \sigma^{2^i}_{e,\tilde{b}} + \sigma^{2^i}_{\tilde{I}} + \sigma^{2^i}_{\tilde{T}} + \sigma^{2^i}_{\xi} + \sigma^{2^i}_{\eta}\end{aligned} \quad \text{7-3}$$

where:

- $\sigma^{2^i}_{e,\tilde{b}} = \sigma^{2^i}_{e} + \sigma^{2^i}_{\tilde{b}}$ is the equivalent model of the satellite clock error and ephemeris error;
- $\sigma^{2^i}_{\tilde{I}}$ is the model of the residual ionospheric error variance;
- $\sigma^{2^i}_{\tilde{T}}$ is the model of the residual tropospheric error variance;
- $\sigma^{2^i}_{\xi}$ is the model of the MP error variance;
- $\sigma^{2^i}_{\eta}$ is the model of the thermal noise error variance.

Similarly, the variance of the SA UERRE model is equal to:

$$\sigma^{2^i}_{UERRE,SA} = \sigma^{2^i}_{\dot{e},\tilde{b}} + \sigma^{2^i}_{\tilde{I}} + \sigma^{2^i}_{\tilde{T}} + \sigma^{2^i}_{\zeta} + \sigma^{2^i}_{\nu} \quad \text{7-4}$$

where:

- $\sigma^{2^i}_{\dot{e},\tilde{b}}$ is the equivalent model of the satellite clock drift error and ephemeris drift error variance, which is assumed to be on the order of millimeter, and is negligible with respect to the thermal noise and multipath error variances;
- $\sigma^{2^i}_{\tilde{I}}$ is the model of the residual ionospheric drift error variance, which is assumed to be on the order of millimeter, and is negligible with respect to the thermal noise and multipath error variances;
- $\sigma^{2^i}_{\tilde{T}}$ is the model of the residual tropospheric drift error variance, which is assumed to be on the order of millimeter, and is negligible with respect to the thermal noise and multipath error variances;
- $\sigma^{2^i}_{\zeta}$ is the model of the MP error variance, which is defined in section 4.3.3;
- $\sigma^{2^i}_{v}$ is the model of the thermal noise error variance, which is modelled by the FLL tracking error model in section [20].

The variance of the thermal noise error component and the multipath error component, for the SA UERE and UERRE model, can be jointly defined by the equivalent MP and noise error variance, $\sigma^{2^i}_{MN}$ and $\sigma^{2^i}_{\dot{M}N}$ as follows:

$$\sigma^{2^i}_{MN} = \sigma^{2^i}_{\xi} + \sigma^{2^i}_{\eta} \quad 7\text{-}5$$

$$\sigma^{2^i}_{\dot{M}N} = \sigma^{2^i}_{\zeta} + \sigma^{2^i}_{v} \quad 7\text{-}6$$

As a consequence, the PSR and PSR-R MN error models described in Chapter 6, can be exploited to model directly the equivalent MP and noise error variance. Therefore, 7-5 and 7-6 can be directly substituted by the realistic PSR and PSR-R multipath plus noise joint error distribution variances obtained through 7-7 and 7-8, $\sigma_{\widehat{MN}^i_u}$ and $\sigma_{\widehat{\dot{M}N}^i_u}$:

$$\sigma^{2^i}_{MN} = \sigma^2_{\widehat{MN}^i_u}\left(C/N^i_0\right) \quad 7\text{-}7$$

$$\sigma^{2^i}_{\dot{M}N} = \sigma^2_{\widehat{\dot{M}N}^i_u}\left(C/N^i_0\right) \quad 7\text{-}8$$

where $\sigma^2_{\widehat{MN}}$ and $\sigma^2_{\widehat{MN}^i_u}$ are the variance of the isolated GPS and Galileo pseudorange and pseudorange-rate MN Gaussian error models, derived respectively in 6.3.1 and 6.3.2. The values of the variance are characterized by the corresponding C/N^i_0, estimated by the GNSS receiver.

The final equation of the SA UERE variance, obtained applying the PSR MN error model is:

$$\sigma^2_{UERE^i} = \sigma^{2^i}_{e,\tilde{b}} + \sigma^2_{I^i} + \sigma^2_{T^i} + \sigma^2_{\widehat{MN}^i_u}\left(C/N^i_0\right) \quad 7\text{-}9$$

while the final equation of the SA UERRE variance, obtained applying the PSR-R MN error model is:

$$\sigma^2_{UERRE^i} = \sigma^{2^i}_{\tilde{I}} + \sigma^{2^i}_{\tilde{T}} + \sigma^2_{\widehat{\dot{M}N}^i_u} \approx \sigma^2_{\widehat{\dot{M}N}^i_u}\left(C/N^i_0\right) \quad 7\text{-}10$$

where it is assumed that in case of low-cost receivers in urban environment the satellite clock error, ephemeris error, ionospheric error and tropospheric error are negligible with respect to the MN error component.

7.1.1.1.1.2 Proposed DGNSS UERE/UERRE models

The DGNSS UERE/UERRE error models [45], [125] depend on one fundamental factor, the distance between the user receiver and the reference station receiver. If the baseline is shorter than 10 Km [45]:

- The Satellite clock error and ephemeris errors are in the order or centimetres;
- The ionospheric errors, typically, does not exceed the 2 m.
- The tropospheric errors, typically, does not exceed the 1.5 m.
- The thermal noise error component is composed by the combination of the thermal noise error of the reference station (usually small contribution) and the thermal noise error of the receiver under test (usually the main error component). Therefore, the variance of thermal noise error can be approximated to the value calculated for the SA thermal noise component. In case of open-sky and LOS receiver reception state, the thermal noise error component is the main error.
- The multipath error component is composed by the combination of the multipath error of the reference station (usually small contribution) and the multipath error of the receiver under test (usually the main error component). In case of constrained environment, the multipath error component becomes the main error.

The variance of the DGNSS UERE model, is therefore, equal to:

$$\begin{aligned}\sigma^{2^i}_{UERE,DGNSS} &= \sigma^{2^i}_{e} + \sigma^{2^i}_{\tilde{b}} + \sigma^{2^i}_{\tilde{I}} + \sigma^{2^i}_{\tilde{T}} + \sigma^{2^i}_{\xi} + \sigma^{2^i}_{\xi_s} + \sigma^{2^i}_{\eta} + \sigma^{2^i}_{\eta_s} \\ &\cong \sigma^{2^i}_{\tilde{I}} + \sigma^{2^i}_{\tilde{T}} + \sigma^{2^i}_{\xi_{eq}} + \sigma^{2^i}_{\eta_{eq}}\end{aligned} \quad 7\text{-}11$$

where:

- $\sigma^{2^i}_{e}$ is considered negligible with respect to the other errors;
- $\sigma^{2^i}_{\tilde{b}}$ is considered negligible with respect to the other errors;
- $\sigma^{2^i}_{\xi_{eq}} = \sigma^{2^i}_{\xi} + \sigma^{2^i}_{\xi_s}$ is the equivalent MP error component variance;
- $\sigma^{2^i}_{\eta_{eq}} = \sigma^{2^i}_{\eta} + \sigma^{2^i}_{\eta_s}$ is the equivalent thermal noise error component variance.

The variance of the DGNSS UERRE model is equal to:

$$\begin{aligned}\sigma^{2^i}_{UERRE,DGNSS} &= \sigma^{2^i}_{\dot{e}} + \sigma^{2^i}_{\dot{\tilde{b}}} + \sigma^{2^i}_{\tilde{I}} + \sigma^{2^i}_{\tilde{T}} + \sigma^{2^i}_{\zeta_{eq}} + \sigma^{2^i}_{\nu_{eq}} \\ &= \sigma^{2^i}_{\tilde{I}} + \sigma^{2^i}_{\tilde{T}} + \sigma^{2^i}_{\zeta_{eq}} + \sigma^{2^i}_{\nu_{eq}}\end{aligned} \quad 7\text{-}12$$

where:

- $\sigma^{2^i}_{\dot{e}}$ is considered negligible with respect to the other errors;
- $\sigma^{2^i}_{\dot{\tilde{b}}}$ is considered negligible with respect to the other errors;
- $\sigma^{2^i}_{\zeta_{eq}} = \sigma^{2^i}_{\zeta} + \sigma^{2^i}_{\zeta_s}$ is the equivalent MP error component variance.
- $\sigma^{2^i}_{\nu_{eq}} = \sigma^{2^i}_{\nu} + \sigma^{2^i}_{\nu_s}$ is the equivalent thermal noise error component variance.

The variance of the thermal noise error component and the multipath error component for the DGNSS UERE and UERRE model, can be jointly defined in 7-13 and 7-14 by the equivalent MP and noise error variance, $\sigma^{2^i}_{MN,eq}$ and $\sigma^{2^i}_{\dot{M}N,eq}$ as follows:

$$\sigma^{2^i}_{MN,eq} = \sigma^{2^i}_{\xi_{eq}} + \sigma^{2^i}_{\eta_{eq}} \quad 7\text{-}13$$

$$\sigma^{2^i}_{\dot{M}N,eq} = \sigma^{2^i}_{\zeta_{eq}} + \sigma^{2^i}_{\nu_{eq}} \quad 7\text{-}14$$

It is assumed that the reference station receiver error components are negligible with respect to the user receiver error components when the user receiver is low-cost and applied in the urban environment, therefore, the 7-13 and 7-14 can be simplified as follows:

$$\sigma^{2^i}_{MN,eq} = \sigma^{2^i}_{MN} \quad 7\text{-}15$$

$$\sigma^{2^i}_{\dot{M}N,eq} = \sigma^{2^i}_{\dot{M}N} \quad 7\text{-}16$$

where

- $\sigma^{2^i}_{MN}$ is the GPS or Galileo variance of the user receiver multipath plus noise equivalent PSR error component, defined in 7-7;
- $\sigma^{2^i}_{\dot{M}N}$ is the GPS or Galileo variance of the user receiver multipath plus noise equivalent PSR-R error component, defined in 7-8.

The final equations for the variance of the DGNSS UERE model is:

$$\sigma^{2^i}_{UERE,DGNSS} = \sigma^{2^i}_{\tilde{I}} + \sigma^{2^i}_{\tilde{T}} + \sigma^{2^i}_{MN,eq} \approx \sigma^{2^i}_{MN,eq} \quad 7\text{-}17$$

where $\sigma^{2^i}_{\tilde{I}}$ and $\sigma^{2^i}_{\tilde{T}}$ are considered negligible with respect to the thermal noise error and multipath error components.

Similarly, the final equations for the variance of the DGNSS UERRE model is:

$$\sigma^{2^i}_{UERRE,DGNSS} = \sigma^{2^i}_{\tilde{I}} + \sigma^{2^i}_{\tilde{T}} + \sigma^{2^i}_{\dot{M}N,eq} \approx \sigma^{2^i}_{\dot{M}N,eq} \quad 7\text{-}18$$

7.1.1.1.2 Design of Measurement Error Covariance Matrix

In this section the design of the proposed time-variant Measurement Error Covariance Matrix is presented.

The Measurement Noise Covariance Matrix, $\boldsymbol{R}_l$, at a given epoch l, is defined as follows:

$$\boldsymbol{R}_l = \mathrm{diag}\left(\begin{matrix} \left\{\left(\sigma^2_{UERE^1}[l], \dots, \sigma^2_{UERE^i}[l], \dots, \sigma^2_{UERE^{N_{GPS}}}[l]\right)^{GPS}, \left(\sigma^2_{UERE^1}[l], \dots, \sigma^2_{UERE^j}[l], \dots, \sigma^2_{UERE^{N_{GAL}}}[l]\right)^{GAL}\right\}^{PSR} \\ , \left\{\left(\sigma^2_{UERRE^1}, \dots, \sigma^2_{UERRE^i}[l], \dots, , \sigma^2_{UERRE^{N_{GPS}}}[l]\right)^{GPS}, \left(\sigma^2_{UERRE^1}[l], \dots, \sigma^2_{UERRE^j}[l], \dots, \sigma^2_{UERRE^{N_{GAL}}}[l]\right)^{GAL}\right\}^{PSR-R} \end{matrix} \right)$$

7-19

where:

- $\left\{\left(\sigma^2_{UERE^1}[l], \dots, \sigma^2_{UERE^i}[l], \dots, \sigma^2_{UERE^{N_{GPS}}}[l]\right)^{GPS}, \left(\sigma^2_{UERE^1}[l], \dots, \sigma^2_{UERE^j}[l], \dots, \sigma^2_{UERE^{N_{GAL}}}[l]\right)^{GAL}\right\}^{PSR}$ defines the overall UERE error variances of the $N_{GPS} + N_{GAL}$ received PSR measurements;
- $\left(\sigma^2_{UERE^1}[l], \dots, \sigma^2_{UERE^i}[l], \dots, \sigma^2_{UERE^{N_{GPS}}}[l]\right)^{GPS}$ defines the GPS L1 C/A UERE error variances of the N_{GPS} received PSR measurements;
- $\sigma^2_{UERE^i}[l]$ is the value of the UERE variance associated to the GPS satellite i;
- $\left(\sigma^2_{UERE^1}[l], \dots, \sigma^2_{UERE^j}[l], \dots, \sigma^2_{UERE^{N_{GAL}}}[l]\right)^{GAL}$ defines the Galileo E1 OS UERE error variances of the N_{GAL} received PSR measurements;
- $\sigma^2_{UERE^j}[l]$ is the value of the UERE variance associated to the Galileo satellite j;
- $\left\{\left(\sigma^2_{UERRE^1}, \dots, \sigma^2_{UERRE^i}[l], \dots, , \sigma^2_{UERRE^{N_{GPS}}}[l]\right)^{GPS}, \left(\sigma^2_{UERRE^1}[l], \dots, \sigma^2_{UERRE^j}[l], \dots, \sigma^2_{UERRE^{N_{GAL}}}[l]\right)^{GAL}\right\}^{PSR-R}$ defines the overall UERRE error variances of the $N_{GPS} + N_{GAL}$ received PSR-R measurements;
- $\left(\sigma^2_{UERRE^1}, \dots, \sigma^2_{UERRE^i}[l], \dots, , \sigma^2_{UERRE^{N_{GPS}}}[l]\right)^{GPS}$ defines the GPS L1 C/A UERRE error variances of the N_{GPS} received PSR measurements;
- $\sigma^2_{UERRE^i}[l]$ is the value of the UERRE variance associated to the GPS satellite i;
- $\left(\sigma^2_{UERRE^1}[l], \dots, \sigma^2_{UERRE^j}[l], \dots, \sigma^2_{UERRE^{N_{GAL}}}[l]\right)^{GAL}$ defines the Galileo E1 OS UERRE error variances of the N_{GAL} received PSR measurements;
- $\sigma^2_{UERRE^j}[l]$ is the value of the UERRE variance associated to the Galileo satellite j;

7.1.2 Improvement Block: Measurement Masking and MN Statistics

The knowledges acquired from the PSR/PSR-R MN error statistics and the LOS/NLOS receiver reception state classification have been also exploited, implementing three different solutions, with the intent of improving the performances of the proposed EKF algorithm, excluding the low-quality measurements.

These techniques are based on the application of a Measurement Masking approach, which consists on the selection of the good-quality measurements through the application of a conditional threshold:

- The PSR and PSR-R measurements are selected by the Measurement Masking block through a specified selection condition;
- The selected measurements are sent then to the MW block to define the Measurement Error Covariance Matrix.

The proposed solutions are based on the application of the following techniques:

NLOS Satellite Measurement Exclusion. This is a low-complex technique which exploits the empirical C/N_0 LOS/NLOS discrimination threshold, defined in Chapter 6, to exclude the NLOS measurements (Figure 7-3): every measurement below the empirical threshold is excluded by default. The major drawback of the NLOS Satellite Exclusion is the reliability of the LOS/NLOS discrimination, based on an empirical parameter. This simplified approach can't provide an effective solution for the "outliers" measurement errors: i.e. a measurement affected by a large MP error, but characterized by a C/N_0 higher than the LOS/NLOS threshold, isn't removed and, therefore, has an impact on the final PVT estimations.

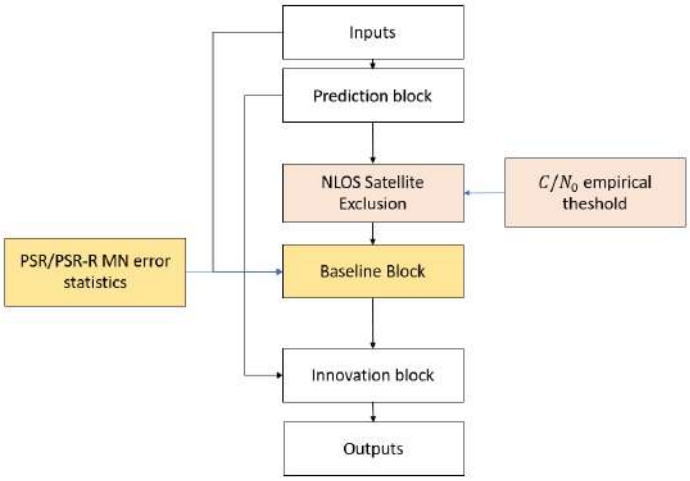

Figure 7-3 – Standard EKF including Baseline Block and NLOS Satellite Exclusion

Innovation Filtering. This technique exploits a measurement quality threshold based on the PSR and PSR-R MN error characterization to exclude the low-quality measurements (Figure 7-4). The innovation filtering consists on the comparison between the absolute value of the PSR/PSR-R measurement residuals (10-20), $\left|d\tilde{\rho}^i\right|$ and $\left|d\tilde{\dot{\rho}}^i\right|$, with respect to the PSR/PSR-R the measurement quality thresholds, defined as follows:

- PSR measurement quality threshold: three times the PSR MN standard deviation calculated for the corresponding C/N_0 bin:

$$d\rho^i\big|_{IF} = 3 \cdot \sigma_{\widehat{MN}}\left(C/N_0^i\right) \quad 7\text{-}20$$

- PSR-R measurement quality threshold: three times the PSR-R MN standard deviation calculated for the corresponding C/N_0 bin:

$$d\dot{\rho}^i\big|_{IF} = 3 \cdot \sigma_{\widehat{\dot{M}N}}\left(C/N_0^i\right) \quad 7\text{-}21$$

Therefore, the PSR measurement is selected only if the absolute value of the corresponding PSR measurement residual, is lower than the PSR measurement quality threshold, 7-20:

$$\left|d\tilde{\rho}^i\right| < d\rho^i\big|_{IF} \quad 7\text{-}22$$

Similarly, the PSR-R measurement is selected only if the absolute value of the corresponding PSR-R measurement residual, is lower than the PSR-R measurement quality threshold, 7-21:

$$\left|d\tilde{\dot{\rho}}^i\right| < d\dot{\rho}^i\big|_{IF} \quad 7\text{-}23$$

The measurement which does not satisfy the established criteria, is excluded from the measurement vector. This methodology should be less affected by the "outlier" measurements, since the MN error characterization is more reliable than the LOS/NLOS discrimination based on a single parameter (C/N_0)

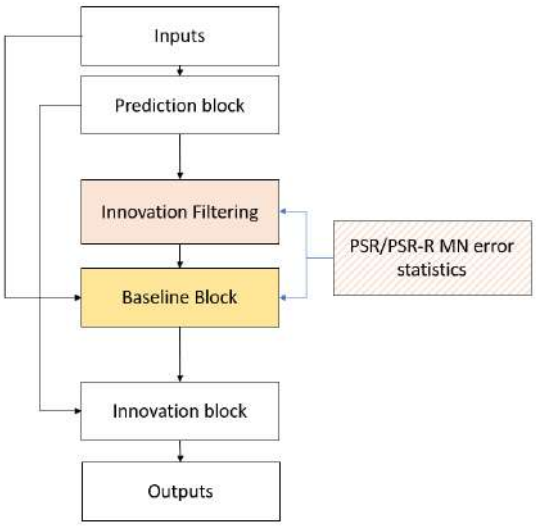

Figure 7-4 – Standard EKF including Baseline Block and Satellite Exclusion based on MN error statistics

Finally, the two techniques can be also applied together to exploit simultaneously the MN error statistics and the LOS/NLOS C/N_0 threshold Figure 7-5.

The techniques are summarized in Table 7-1. However, the Satellite Exclusion techniques are just sub-optimal approaches since they do not take into account the satellite availabilities and the overall satellite-geometry factor: as already stated in section 6.2.6, in the urban environment the number of satellites in the LOS visibility usually is reduced with the respect of open-sky environment. Sometimes only few satellites are in view, therefore the satellite measurement innovation vector is usually affected by poor geometry. Removing a-priori satellite measurements could not be an optimal solution: a smaller set of satellite is going to be used to make the innovation, decreasing the quality of the signal geometry. The related PVT solution might be worst even if the estimator is excluding all the NLOS satellites. It is suggested, therefore, in future works, to develop Satellite Exclusion methodologies which take into account also the geometrical factors.

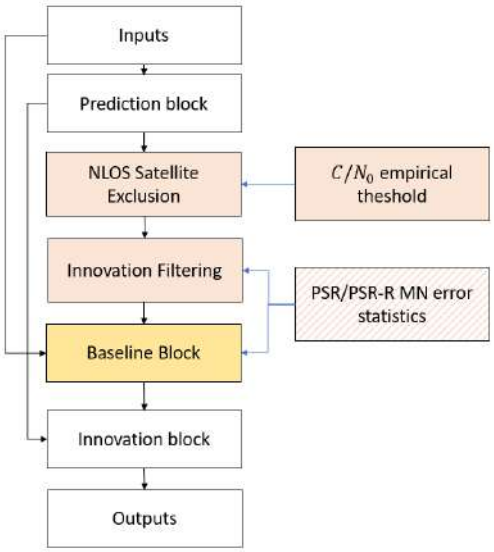

Figure 7-5 – Standard EKF including Baseline Block, NLOS Satellite Exclusion followed by the Innovation Filtering

Satellite Measurement Selection	Parameter	Criteria

NLOS Satellite Exclusion (NLOS SE)	Empirical C/N_0Threshold: $C/N_0\|_{SE}$	PSR and PSR-R Measurement excluded if: $C/N_0^i < C/N_0\|_{SE}$
Innovation Filtering (IF)	PSR MN error variance-based threshold: $d\rho^i\|_{IF} = 3 \cdot \sigma_{\widehat{MN}}(C/N_0^i)$	PSR Measurement excluded if: $\left\|d\tilde{\rho}^i\right\| > d\rho^i\|_{IF}$
	PSR-R MN error variance-based threshold: $d\dot{\rho}^i\|_{IF} = 3 \cdot \sigma_{\widehat{MN}}(C/N_0^i)$	PSR-R Measurement excluded if: $\left\|d\tilde{\rho}^i\right\| > d\dot{\rho}^i\|_{IF}$
NLOS SE + IF	$C/N_0\|_{SE}$, $d\rho^i\|_{IF}$	PSR Measurement excluded if: $C/N_0 < C/N_0\|_{SE}$, and $\left\|d\rho^i\right\| > d\rho^i\|_{IF}$
	$C/N_0\|_{SE}$, $d\dot{\rho}^i\|_{IF}$	PSR-R Measurement excluded if: $C/N_0 < C/N_0\|_{SE}$, and $\left\|d\tilde{\rho}^i\right\| > d\dot{\rho}^i\|_{IF}$

Table 7-1 –Summary of the techniques which can be applied in the Improved Block

7.2 Time differenced EKF based on MN statistics

The Standard EKF model, proposed in section 7.1, as well as the benchmark EKF model are modelled with the assumption that the measurement errors are uncorrelated. In this work, it is confirmed that the PSR and PSR-R MN errors are correlated in time as a function of the speed of the car (environment dependent). Moreover, the PSR/PSR-R residual errors due to the presence of multipath and thermal noise are systematically time correlated because of the DLL/FLL processing stage. Colored noise can be efficiently modelled as a Gauss-Markov process (GMP) or a first-order autoregressive model driven by white Gaussian noise.

When colored noise is subsequently processed by a Kalman filter (KF) inaccuracies result due to the correlation of the new measurements and the predicted states, thereby contradicting the assumptions employed in developing the KF. The KF must be modified to account for such inputs [110], [1]. Therefore, it is feasible to improve the EKF performance by exploiting models of the (speed dependent) temporal correlation derived in chapter 6. The method is proposed in [1] using simulated data and assuming a single correlated noise component. In this thesis the approach follows that method described in [1] but through application in considering real data and its artefacts. It exploits the measurement differencing over time to remove the time-correlated component of the measurement errors. Therefore, the PVT estimator applied in this work consists in an EKF algorithm based on the time-differenced Kalman Filter in [1],[2], adapted to the MN residual error time-velocity correlation characterization proposed in section 6.4. The mathematical model is depicted in section 7.2.1.

Moreover, the techniques defined in the Improvement Block of the Standard EKF (section 7.1.2), are also exploited in the Time Differenced EKF.

7.2.1 Mathematical model

The state and covariance propagation equations of a Standard EKF (section 7.1) are given by and , respectively. If the measurements are not considered correlated in time, the measurement vector $\boldsymbol{z}_l$ is related to the state vector by , where $\boldsymbol{H}_l$ is the design matrix of the original process (derived in section 10.2.2.2), $\boldsymbol{v}_l$ is the original measurement noise vector, and $\boldsymbol{R}_l$ is Measurement Covariance Matrix defined in 7-19.

Now consider the case of measurements, $\boldsymbol{l}_l$, with time-correlated errors [1]:

$$\boldsymbol{l}_l = \boldsymbol{H}_l \cdot \boldsymbol{x}_l + \boldsymbol{u}_l + \boldsymbol{n}_l \qquad 7\text{-}24$$

where:

- $\boldsymbol{H}_l$ is, now, the design matrix of the time-correlated measurements;
- $\boldsymbol{x}_l$ is the state vector;
- $\boldsymbol{u}_l$ is the new colored noise vector;
- $\boldsymbol{n}_l$ is the white noise vector.

The time-correlated errors are expressed by 7-25,

$$\boldsymbol{u}_{l+1} = \boldsymbol{S}_{l+1} \cdot \boldsymbol{u}_l + \boldsymbol{\varepsilon}_l \tag{7-25}$$

where:

- $\boldsymbol{S}_l$ is the transition matrix for the time-correlated measurement errors;
- $\boldsymbol{\varepsilon}_l$ is the driving noise vector for the correlated measurement error process, assumed to be composed of white Gaussian noise.

The driving noise vector is modelled as follows:

$$\boldsymbol{\varepsilon}_l = \left[\boldsymbol{\varepsilon}_{PSR,l}, \boldsymbol{\varepsilon}_{PSRR,l}\right] = \left[\varepsilon^1_{PSR,l}, \dots, \varepsilon^N_{PSR,l} \mid \varepsilon^1_{PSRR,l}, \dots, \varepsilon^N_{PSRR,l}\right] \tag{7-26}$$

where:

- $\boldsymbol{\varepsilon}_{PSR,l}$ is the PSR process noise vector corresponding to the N PSR measurements;
- $\boldsymbol{\varepsilon}_{PSRR,l}$ is the PSR-R process noise vector corresponding to the N PSR-R measurements;

The PSR and PSR-R driving noise terms, $\varepsilon_{PSR,l}$ and $\varepsilon_{PSRR,l}$, of a given satellite i, are normally distributed random variables, 7-27, with a standard deviations equal to 7-28:

$$\begin{aligned} \varepsilon^i_{PSR,l} &\sim N\left(0, \sigma^i_{\varepsilon,PSR,l}\right) \\ \varepsilon^i_{PSRR,l} &\sim N\left(0, \sigma^i_{\varepsilon,PSRR,l}\right) \end{aligned} \tag{7-27}$$

$$\begin{aligned} \sigma^i_{\varepsilon,PSR,l} &= \sigma_{\widehat{MN}}\left(C/N^i_{0_l}\right)\sqrt{1 - e^{-2T_P/\tau_{PSR,l}}} \\ \sigma^i_{\varepsilon,PSRR,l} &= \sigma_{\widehat{MN}}\left(C/N^i_{0_l}\right)\sqrt{1 - e^{-2T_P/\tau_{PSRR,l}}} \end{aligned} \tag{7-28}$$

where:

- the reference standard deviation is chosen to be $\sigma_{\widehat{MN}^i_l}$ in the case of PSR measurements and $\sigma_{\widehat{MN}^i_l}$ in case of PSR-R measurements. These standard deviations relate to the chosen GPS and Galileo MN error models, illustrated in section 6.3, selecting the corresponding C/N_0 band with the C/N_0 of the specific measurement i.
- the values of the correlation times for GPS/Galileo PSR and PSR-R residual errors, respectively $\tau_{PSR,l}$ and $\tau_{PSRR,l}$, are chosen from the results of section 6.4, taking into account the speed of the car estimated by the EKF, at given epoch l.

The time correlated error may be modelled as a first-order Gauss-Markov process [1] where $\boldsymbol{u}_{l+1}$ is the first order Gauss-Markov process being generated, t_l and t_{l-1} are the times of consecutive epochs, at intervals of T_P (7-29), τ is the time constant of the process, and $\boldsymbol{\varepsilon}_l$ is the driving noise.

$$\boldsymbol{u}_{l+1} = \boldsymbol{u}_l e^{-\left(\frac{t_l - t_{l-1}}{\tau}\right)} + \boldsymbol{\varepsilon}_l \tag{7-29}$$

Since the Gauss-Markov process is a time-continuous process, in this work it is assumed that the MN error component is always continuous in time, whose variation, $\sigma_{\widehat{MN}}\left(C/N^i_{0_l}\right)$ or $\sigma_{\widehat{MN}}\left(C/N^i_{0_l}\right)$, has been calculated from the statistics. Unfortunately, assuming continuity of the MN random process is just an approximation and assumption. The MN errors result from the sum of all reflector contributors, including time epochs where the MN residuals are characterized by sudden change of reflectors, or change of the NLOS/LOS reception state; in this case the multipath component can suddenly jump in value. In these situations, the statistical variation characterized by the standard deviation could not be representative of the temporal variation. This could turn out a limitation of the TD EKF model that probably should be investigated in future works.

Finally, the model of the transition matrix for the time-correlated PSR and PSR-R MN errors are presented in 7-30 and 7-31, respectively.

$$\begin{bmatrix} u_l^1 \\ u_l^2 \\ \dots \\ u_l^N \end{bmatrix}^{PSR} = \begin{bmatrix} e^{-\left(\frac{T_P}{\tau^1_{PSR,l}}\right)} & 0 & 0 & 0 \\ 0 & e^{-\left(\frac{T_P}{\tau^2_{PSR,l}}\right)} & 0 & 0 \\ 0 & 0 & \dots & 0 \\ 0 & 0 & 0 & e^{-\left(\frac{T_P}{\tau^N_{PSR,l}}\right)} \end{bmatrix}^{PSR} \cdot \begin{bmatrix} u_{l-1}^1 \\ u_{l-1}^2 \\ \dots \\ u_{l-1}^N \end{bmatrix}^{PSR} + \begin{bmatrix} \varepsilon_{PSR,l}^1 \\ \varepsilon_{PSR,l}^2 \\ \dots \\ \varepsilon_{PSR,l}^N \end{bmatrix}^{PSR} \quad 7\text{-}30$$

$$\begin{bmatrix} u_l^{N+1} \\ u_l^{N+2} \\ \dots \\ u_l^{2N} \end{bmatrix}^{PSR-R} = \begin{bmatrix} e^{-\left(\frac{T_P}{\tau^1_{PSRR,l}}\right)} & 0 & 0 & 0 \\ 0 & e^{-\left(\frac{T_P}{\tau^2_{PSRR,l}}\right)} & 0 & 0 \\ 0 & 0 & \dots & 0 \\ 0 & 0 & 0 & e^{-\left(\frac{T_P}{\tau^N_{PSRR,l}}\right)} \end{bmatrix}^{PSR-R} \cdot \begin{bmatrix} u_{l-1}^{N+1} \\ u_{l-1}^{N+2} \\ \dots \\ u_{l-1}^{2N} \end{bmatrix}^{PSR-R} + \begin{bmatrix} \varepsilon_{PSRR,l}^1 \\ \varepsilon_{PSRR,l}^2 \\ \dots \\ \varepsilon_{PSRR,l}^N \end{bmatrix}^{PSR-R} \quad 7\text{-}31$$

Applying the time-differencing approach [1] yields a new measurement, $\boldsymbol{z}_l^*$, with the following form:

$$\begin{gathered} \boldsymbol{z}_l^* = \boldsymbol{l}_l - \boldsymbol{S}_l \boldsymbol{l}_{l-1} = \boldsymbol{H}_l \cdot \boldsymbol{x}_l + \boldsymbol{u}_l + \boldsymbol{n}_l - S_l(\boldsymbol{H}_{l-1} \cdot \boldsymbol{x}_{l-1} + \boldsymbol{u}_{l-1} + \boldsymbol{n}_{l-1}) = \\ = \boldsymbol{H}_l \cdot \boldsymbol{x}_l + \boldsymbol{u}_l + \boldsymbol{n}_l - \boldsymbol{S}_l(\boldsymbol{H}_{l-1} \cdot \boldsymbol{x}_{l-1}) - \boldsymbol{S}_l(\boldsymbol{u}_{l-1}) - \boldsymbol{S}_l(\boldsymbol{n}_{l-1}) = \end{gathered} \quad 7\text{-}32$$

applying 7-25 into 7-32, it is obtained

$$\begin{gathered} \boldsymbol{z}_l^* = \boldsymbol{H}_l \cdot \boldsymbol{x}_l + \boldsymbol{S}_l \cdot \boldsymbol{u}_{l-1} + \boldsymbol{\varepsilon}_{l-1} + \boldsymbol{n}_l - \boldsymbol{S}_l(\boldsymbol{H}_{l-1} \cdot \boldsymbol{x}_{l-1}) - \boldsymbol{S}_l(\boldsymbol{u}_{l-1}) - \boldsymbol{S}_l(\boldsymbol{n}_{l-1}) = \\ = \boldsymbol{H}_l \cdot \boldsymbol{x}_l + \boldsymbol{\varepsilon}_{l-1} + \boldsymbol{n}_l - \boldsymbol{S}_l(\boldsymbol{H}_{l-1} \cdot \boldsymbol{x}_{l-1}) - \boldsymbol{S}_l(\boldsymbol{n}_{l-1}) \end{gathered} \quad 7\text{-}33$$

Further, as proposed in [1], 7-33 can be simplified assuming that $\boldsymbol{x}_{l-1} = \boldsymbol{\Phi}_{l-1,l}^{-1}(\boldsymbol{x}_l - \boldsymbol{w}_{l-1})$, obtaining

$$\boldsymbol{z}_l^* = \left(\boldsymbol{H}_l - \boldsymbol{S}_l \cdot \boldsymbol{H}_{l-1} \cdot \boldsymbol{\Phi}_{l-1,l}^{-1}\right)\boldsymbol{x}_l + \boldsymbol{\varepsilon}_{l-1} + \boldsymbol{n}_l + \boldsymbol{S}_l \cdot \boldsymbol{H}_{l-1} \cdot \boldsymbol{\Phi}_{l-1,l}^{-1}(\boldsymbol{w}_{l-1}) - \boldsymbol{S}_l \cdot \boldsymbol{n}_{l-1} \quad 7\text{-}34$$

where:

- $\boldsymbol{\Phi}_{l-1,l}^{-1}$ is the inverse of the original state transition matrix;
- $\boldsymbol{w}_{l-1}$ is the state vector process noise of the original system, at epoch $l-1$.

Equation 7-34 can then be rewritten more compactly as:

$$\boldsymbol{z}_l^* = \boldsymbol{H}_l^* \cdot \boldsymbol{x}_l + \boldsymbol{v}_l^* \quad 7\text{-}35$$

where the new differential design matrix and the noise vector are 7-36 and 7-37, respectively.

$$\boldsymbol{H}_l^* = \boldsymbol{H}_l - \boldsymbol{S}_l \cdot \boldsymbol{H}_{l-1} \cdot \boldsymbol{\Phi}_{l-1,l}^{-1} \quad 7\text{-}36$$

$$\boldsymbol{v}_l^* = \mathbf{S}_l \cdot \boldsymbol{H}_{l-1} \cdot \boldsymbol{\Phi}_{l-1,l}^{-1}(\boldsymbol{w}_{l-1}) + \boldsymbol{\varepsilon}_{l-1} + \boldsymbol{n}_l - \mathbf{S}_l \cdot \boldsymbol{n}_{l-1} \quad 7\text{-}37$$

The noise components $\boldsymbol{w}_{l-1}$, $\boldsymbol{\varepsilon}_{l-1}$, $\boldsymbol{n}_l$ and $\boldsymbol{n}_{l-1}$ are all assumed to be white and mutually uncorrelated. However, the uncorrelated measurement noise terms, $\boldsymbol{n}_l$ and $\boldsymbol{n}_{l-1}$, are from adjacent epochs, therefore, the differenced measurement noise, is correlated between adjacent epochs since they contain a common term.

Mathematically, the differenced measurement noise at adjacent epochs l and $l+1$ can be written as:

$$\boldsymbol{v}_l^* = \mathbf{S}_l \cdot \boldsymbol{H}_{l-1} \cdot \boldsymbol{\Phi}_{l-1,l}^{-1}(\boldsymbol{w}_{l-1}) + \boldsymbol{\varepsilon}_{l-1} + \boldsymbol{n}_l - \mathbf{S}_l \cdot \boldsymbol{n}_{l-1}$$

$$\boldsymbol{v}_{l+1}^* = \mathbf{S}_{l+1} \cdot \boldsymbol{H}_l \cdot \boldsymbol{\Phi}_{l,l+1}^{-1}(\boldsymbol{w}_l) + \boldsymbol{\varepsilon}_l + \boldsymbol{n}_{l+1} - \mathbf{S}_{l+1} \cdot \boldsymbol{n}_l$$

The correlation between the differenced measurement noise vectors can be mathematically expressed as follows:

$$E\left\{\boldsymbol{v}_l^* \boldsymbol{v}_{l+1}^{*T}\right\} = E\{\boldsymbol{n}_l \boldsymbol{n}_l^T \boldsymbol{S}_{l+1}^T\} = \boldsymbol{N}_l \boldsymbol{S}_{l+1}^T \quad 7\text{-}38$$

where $\boldsymbol{N}_l$ is the covariance matrix of $\boldsymbol{n}_l$, which in this work it is equal to the Measurement Error Covariance Matrix described in the Standard EKF Baseline Block, 7-19.

However, since correlation only exists between measurement differences sharing a common epoch (i.e., not between differenced measurements separated by more than one epoch), it can be avoided by simply differencing every other pair of measurements [2], (e.g., difference measurement at epoch 0 and 1, 2 and 3, etc.).

In order to address this, two solutions are feasible. Either, the state prediction is performed over two epochs or a combination of a standard EKF update and a time-differenced EKF update are used. The second approach is taken in this work to avoid the growth in state prediction error from the longer prediction in light of the moderate dynamics. A comparison of the two approaches should be treated in future work.

Therefore, the proposed methodology, called the EKF-Temporally Correlated (EKF-TC) consists of two different blocks:

- The application of a Standard EKF (section 7.1);
- The application of the Time Differenced EKF, depicted in this section.

The single-epoch EKF must be used in the initialization epoch, $l = 0$, and in the "even" time epochs (i.e. 2,4,6,8 etc.). The Time Differenced EKF must be used for the "odd" time epochs (i.e. 1,3,5,7 etc.), as portrayed in the Figure 7-6.

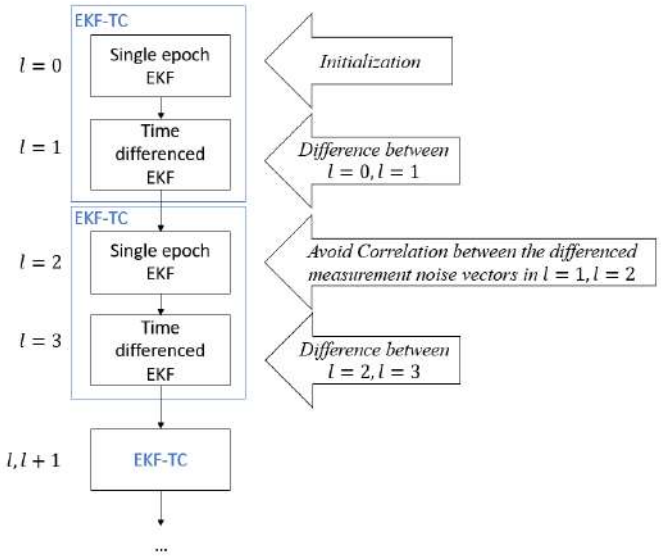

Figure 7-6 – Scheme of the EKF Temporally Correlated (EKF-TC) Model, implementing the Standard EKF (section 7.1) and the Time Differenced EKF

Therefore, applying the differential strategy proposed above, the new measurement vector, $\boldsymbol{v}_l^*$, is also white and thus uncorrelated over time.

Since the measurement error vector is now an explicit function of w_{l-1}, the measurement and process noise vectors are now correlated according to,

$$\boldsymbol{C}_l = E\{\boldsymbol{w}_{l-1}\boldsymbol{v}_l^{*T}\} = \boldsymbol{Q}_{l-1}\boldsymbol{\Phi}_{l-1,l}^{-1\ T}\boldsymbol{H}_{l-1}^T\boldsymbol{S}_l^T \quad 7\text{-}39$$

Because of this correlation, the original update equations are not applicable and they must instead be written as 7-40 and 7-41:

$$\hat{\boldsymbol{x}}_l^+ = \hat{\boldsymbol{x}}_l^- + \boldsymbol{K}_l^*\boldsymbol{z}_l^* \quad 7\text{-}40$$

$$\boldsymbol{P}_l^+ = \boldsymbol{P}_l^- - \boldsymbol{K}_l^*(\boldsymbol{H}_l^*\boldsymbol{P}_l^-\boldsymbol{H}_l^{*T} + \boldsymbol{R}_l^* + \boldsymbol{H}_l^*\boldsymbol{C}_l + \boldsymbol{C}_l^T\boldsymbol{H}_l^{*T})\boldsymbol{K}_l^{*T} \quad 7\text{-}41$$

where the Kalman gain is written as

$$\boldsymbol{K}_l^* = (\boldsymbol{P}_l^-\boldsymbol{H}_l^{*T} + \boldsymbol{C}_l)(\boldsymbol{H}_l^*\boldsymbol{P}_l^-\boldsymbol{H}_l^{*T} + \boldsymbol{R}_l^* + \boldsymbol{H}_l^*\boldsymbol{C}_l + \boldsymbol{C}_l^T\boldsymbol{H}_l^{*T})^{-1} \quad 7\text{-}42$$

Finally, the covariance matrix of the measurement noise now is given by

$$\boldsymbol{R}_l^* = E\{\boldsymbol{v}_l^*\boldsymbol{v}_l^{*T}\} = \boldsymbol{M}_{l-1} + \boldsymbol{N}_l + \boldsymbol{S}_l\boldsymbol{N}_{l-1}\boldsymbol{S}_l^T + \boldsymbol{S}_l\boldsymbol{H}_{l-1}\boldsymbol{\Phi}_{l-1,l}^{-1}\boldsymbol{Q}_{l-1}\boldsymbol{\Phi}_{l-1,l}^{-T}\boldsymbol{H}_{l-1}^T\boldsymbol{S}_l^T \quad 7\text{-}43$$

where $\boldsymbol{M}$ is the covariance matrix of $\boldsymbol{\varepsilon}_l$, and $\boldsymbol{N}$ is the covariance matrix of $\boldsymbol{n}_l$. In particular $\boldsymbol{n}_l$ is the white noise measurements vector and $\boldsymbol{\varepsilon}_l$ is the process noise vector use for the correlated measurement error.

Therefore, to model matrices $\boldsymbol{M}$ and $\boldsymbol{N}$, the standard deviation of n_l and ε_l for each measurement residual error at given epoch l is required. In this work, the standard deviation of the measurement residual error model is simply that of the MN model. Such a residual error model accounts for all the multipath and noise contributors including white noise and a range of colored noise components. In particular, the sigma derived from the model is the resulting standard deviation of a mix between correlated and uncorrelated components.

However, some assumptions could be considered to simplify the mathematical model and apply the equations to the MN statistical model. In section 6.4, it has been highlighted that the PSR and PSR-R MN residual errors are always correlated. Thus, it has been stated that if the time correlation value, extracted from section 6.4, is different from zero, then the overall residual errors characterizing the specific MN statistical model in the specific C/N_0 band are considered correlated. On the contrary, if the time correlation value is equal to zero, the overall residual errors are considered uncorrelated. Note that if one component dominates, the temporal correlation of the total error will be close to the value for this dominating component.

In this work, the assumptions previously introduced have been exploited for simplification purposes; the residual errors are therefore considered to contain only correlated or uncorrelated components:

- when the C/N_0 jumps by at least 2.5 dB-Hz the noise component is considered uncorrelated, the n_l is non-zero whereas $\boldsymbol{\varepsilon}_l$ and $\boldsymbol{S}_l$ are equal to zero; It transpires that the $\boldsymbol{N}$ matrix corresponds to the 7-19 matrix if the whole measurements are uncorrelated. In this case, the matrix $\boldsymbol{S}$ becomes a zero matrix.
- otherwise, the noise component is considered purely correlated, the $\boldsymbol{\varepsilon}_l$ and $\boldsymbol{S}_l$ are different from zero whereas $\boldsymbol{n}_l$ and $\boldsymbol{N}_l$ are equal to zero.

The justification for this is as follows. In nominal dynamics and tracking conditions, i.e. when the C/N_0 changes slightly, the error is dominated by relatively slowly varying multipath and filtered noise. However, at sudden changes in C/N_0, it may be reasoned that there is a change in environment and the potential for error decorrelation is high.

The measurement innovations are modified taking into account the differential method. They are rewritten in the following form,

$$d\boldsymbol{z}_l^* = \boldsymbol{z}_l^* - h^*(\hat{\boldsymbol{x}}_l^-) \tag{7-44}$$

where the differential predicted PSR and PSR-R measurements can be written as

$$\boldsymbol{h}^*(\hat{\boldsymbol{x}}_l^-) = \left(\hat{\rho}^{*1}_l, \hat{\rho}^{*2}_l, \hat{\rho}^{*3}_l, \dots, \hat{\rho}^{*N}_l | \hat{\dot{\rho}}^{*1}_l, \hat{\dot{\rho}}^{*2}_l, \hat{\dot{\rho}}^{*3}_l, \dots, \hat{\dot{\rho}}^{*N}_l\right) \tag{7-45}$$

with,

- $\hat{\rho}^{*i}_l = \hat{\rho}^i_l - \boldsymbol{S}_l \hat{\rho}^i_{l-1}$ is the differential predicted range;
- $\hat{\dot{\rho}}^{*i}_l = \hat{\dot{\rho}}^i_l - \boldsymbol{S}_l \hat{\dot{\rho}}^i_{l-1}$ is the differential predicted range-rate.

7.3 Results

In this section, the performance of the PVT estimators based on the MN error characteristics from (Chapter 6) are presented. It is structured as follows. In the first section 7.3.1, the objectives of the proposed analyses and the methodologies applied to calculate the performances are presented. Successively, in section 7.3.2, the results of the SA/DGNSS Benchmark EKF, which has been used to design the proposed PVT estimators, are depicted. Hence, the results of the SA/DGNSS Standard EKF (7.1), based on the Baseline Block (7.1.1) and Improvement Block (section 7.1.2) are presented and compared to the Benchmark EKF and other commercial PVT estimators, in section 7.3.3. Finally, in section 7.3.4, the results of the SA/DGNSS Temporally Correlated EKF (7.2), are presented and investigated.

7.3.1 Objectives

The results section is composed of three different subsections.

In section 7.3.2 the calculation of the SA and DGNSS **Benchmark EKF** performances are provided. The objectives of this section are:

- to calculate the PVT estimation error to be used as a Benchmark solution for the performance comparison with the proposed solutions;
- to identify the causes of the estimation errors and to provide suggestions to mitigate the impact of these errors, corresponding to the methodologies proposed in this chapter.

In section 7.3.3, the performance of the proposed **Standard EKF** is shown. Firstly, in section 7.3.3.2 the proposed **Standard EKF** with the application of the ***Baseline Block*** is provided. The evaluation is conducted accomplishing the following objectives:

- to determine the optimal ***Baseline Block*** configuration by refining the receiver clock model (section 7.3.3.2.1) and selecting the Baseline Measurement Model (section 7.3.3.2.2);
- to analyze the performance of SA and DGNSS Standard EKF implementing the ***Baseline Block*** configuration derived and comparing with the Benchmark EKF (section 7.3.3.2.3) and commercial PVT estimators (section 7.3.3.2.4).

Secondly, in section 7.3.3.3 the performance of the proposed **Standard EKF** applying the ***Baseline Block*** and the ***Improvement Block*** is shown. The evaluation is conducted accomplishing the following objectives:

- to determine the optimal ***Improvement Block*** configuration through selection of the empirical C/N_0 threshold for NLOS Satellite Exclusion (section 7.3.3.3.1) and selecting the optimal configuration of NLOS SE, Innovations Filtering (IF) (section 7.3.3.3.2);
- to analyses the performances of SA and DGNSS Standard EKF implementing the Improvement Block derived and comparing with the Benchmark EKF (section 7.3.3.3.3) and commercial PVT estimators (section 7.3.3.3.4).

In section 7.3.4 the performance of the proposed EKF-TC (as outlined in section 7.2.1) is addressed. Firstly, by analyzing the SA TD EKF (section 7.3.4.2) whose objectives are:

- to compare the performance with and without the ***Improvement Block*** (section 7.3.4.2.1)
- to compare with the Standard EKF (section 7.3.4.2.2) and commercial PVT estimators (7.3.4.2.3).

Secondly in section 7.3.4.3 by analyzing the DGNSS EKF-TC whose objectives are:

- to compare the performance with and without the ***Improvement Block*** (section 7.3.4.3.1);
- to compare with the Standard EKF (section 7.3.4.3.2) and commercial PVT estimators (7.3.4.3.3).

The proposed PVT estimators have been designed and simulated in MATLAB, applying two different Datasets collected during the data Campaign, Data Collection 1 and Data Collection 2 (section 6.2.1).

The PVT estimation accuracy have been calculated in the following way: firstly, the position estimation error vector, $\boldsymbol{e}_{p,l}$, at a given epoch l is computed. This vector is equal to the difference between the PVT estimated position, $\widehat{\boldsymbol{p}}_l$ and the SPAN reference position estimations, $\boldsymbol{p}_{SPAN,l}$:

$$\boldsymbol{e}_{p,l} = \widehat{\boldsymbol{p}}_l - \boldsymbol{p}_{SPAN,l} \tag{7-46}$$

From $\boldsymbol{e}_{p,l}$ the norm $e_{p,l}$, is determined and the resulting Root Mean Square Error (RMSE), $\mathrm{RMSE}(e_{p,l})$, which is used as a metric to compare the various solutions. The accuracy of the Standard EKF and the EKF-TC have been tested and compared to the performance of commercial SA/DGNSS PVT estimators, employing the same datasets.

The commercial solutions tested are:

- Inertial Explorer PVT algorithm, [126].
- U-blox M8T receiver PVT algorithm, [116], [127].

7.3.2 Benchmark EKF

This section analyses the performance of the SA and the DGNSS Benchmark EKF, presented in section 0.

In the first section, 7.3.2.1, the EKF's configuration parameters applied to calculate the PVT estimations are presented. Successively, in section 7.3.2.2, the SA and DGNSS absolute position errors and the corresponding RMSE values are illustrated and analyzed. Furthermore, the causes of the estimation errors have been identified and consequently, some suggestions have been proposed to mitigate the impact of these errors.

7.3.2.1 EKF Parameter's Configuration

In the EKF State Model, the process noise of the acceleration, receiver clock bias, clock drift and inter-constellation bias between GPS and Galileo are modelled as white noise random processes characterized by the following variances:

- σ_a^2 is the acceleration process noise variance resolved about the axes of ECEF frame, which depends on the dynamic of the application. A suitable value used for the car tested in the data campaign under exam [15] is 1 $m^2 s^{-3}$;
- σ_b^2 is the clock bias process noise variance: this parameter depends on the oscillator characteristics. Regarding the receiver under test, the oscillator is unknown, therefore is selected typical value for a TCXO equal to 0.01 $m^2 s^{-1}$ [15];
- σ_b^2 is the clock drift process noise variance: as for the clock bias, typical value for a TCXO is 0.001 $m^2 s^{-3}$ [15];
- σ_δ^2 is the inter-constellation GPS-to-Galileo variance: it is considered small compared to the $S_{ck,\phi}$; the value chose is equal to 0.0001 $m^2 s^{-1}$ [128];
- σ_{MN}^2 is the PSR error variance: it is assumed to be equal to 25 m^2 [15];
- $\sigma_{\dot{M}N}^2$ is the PSR-R error variance: it is assumed to be equal to 0.25 m^2/s^2[15].

7.3.2.2 Results

Figure 7-7 and Figure 7-8 illustrate the norm of the position error estimation and the RMSE of the SA Benchmark EKF, applied to the Data Collection 1 and Data Collection 2. The corresponding RMSE values are 20.26 m and 22.86 m.

Figure 7-9 and Figure 7-10 illustrate the norm of the position error estimation and the RMSE of the DGNSS Benchmark EKF, applied to the Data Collection 1 and Data Collection 2. The corresponding RMSE values are 15.62 m and 19.92 m.

The RMSE values are summarized in Table 7-2.

Position Estimation Error: RMSE [m]	**SA Benchmark EKF**	**DGNSS Benchmark EKF**
Data Collection 1	20.26	15.62
Data Collection 2	22.86	19.92

Table 7-2 – Summary of the SA and DGNSS Benchmark RMSE

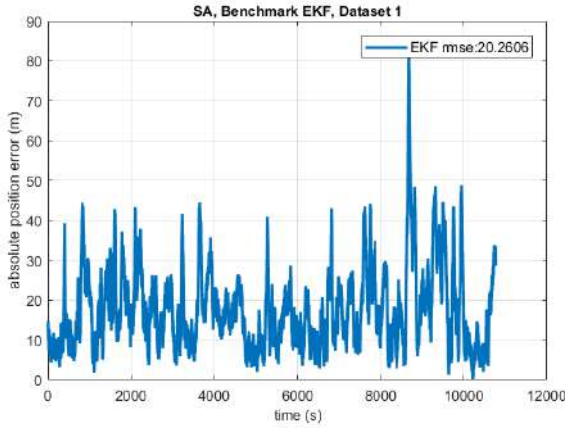

Figure 7-7 – Absolute Position estimation error with the corresponding RMSE: Dataset 1, SA Benchmark EKF

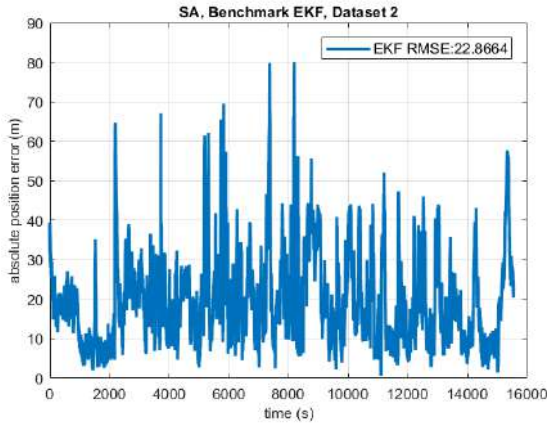

Figure 7-8 – Absolute Position estimation error with the corresponding RMSE: Dataset 2, SA Benchmark EKF

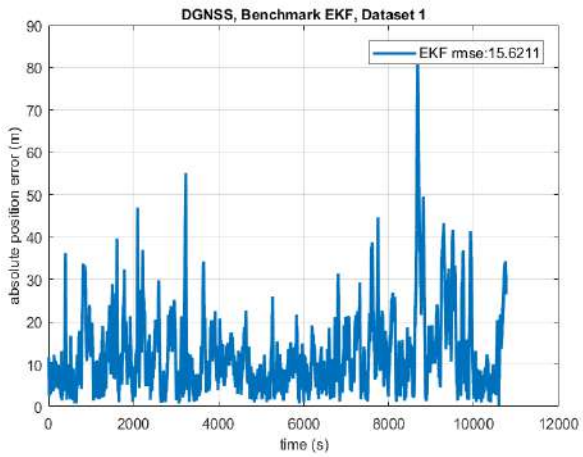

Figure 7-9 – Absolute Position estimation error with the corresponding RMSE: Dataset 1, DGNSS Benchmark EKF

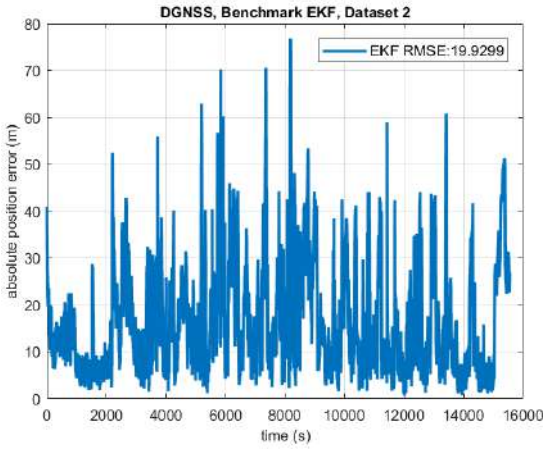

Figure 7-10 – Absolute Position estimation error with the corresponding RMSE: Dataset 2, DGNSS Benchmark EKF

The norm of the position estimation error is, as expected, higher for SA EKF with respect to the DGNSS EKF. However, the difference is not as high as one might expect. From this, it can be deduced that estimation errors are largely caused by the presence of multipath. For this reason, it can be assumed that the MN error mitigation introduced by the application of the Baseline Block, can have a positive impact on the PVT estimations, improving the general performance. In particular, further improvements should be expected for DGNSS estimators, since satellite clock, ionospheric and tropospheric residual errors are negligible with respect to the MN errors, and, therefore, the mitigation of the MN errors should have a major impact.

Moreover, from the investigations of the presented figures, it can be observed that the position error estimation norm shows some punctual high errors causing an increase of the overall RMSE error. An example is presented in the case of the DGNSS Benchmark EKF applied to Data Collection 1 (Figure 7-9), which presents the highest error peak between 8650 and 8750 seconds, as isolated in Figure 7-11.

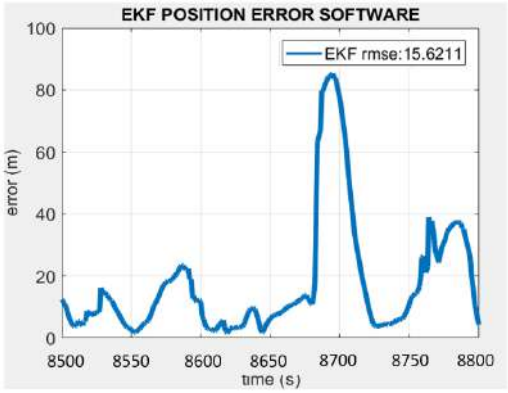

Figure 7-11 – Dataset 1, DGNSS PVT solutions: Zoom of around the highest error peak

To investigate the nature of this highest error peak, Figure 7-12 shows the PSR reference innovations, calculated as follows:

- Firstly, the reference range are calculated, using the estimated satellite positions and the reference SPAN position.
- Consequently, the predicted reference PSR are calculated, using the reference range, calculated previously, and the estimated clock bias.
- Finally, the PSR reference innovation is calculated as the difference between the real PSR measurements and the predicted reference PSR measurement.

To prove the impact of the bias on the EKF performance, Figure 7-13 shows the difference between the real innovations, calculated using the Benchmark EKF estimations and the reference innovations.

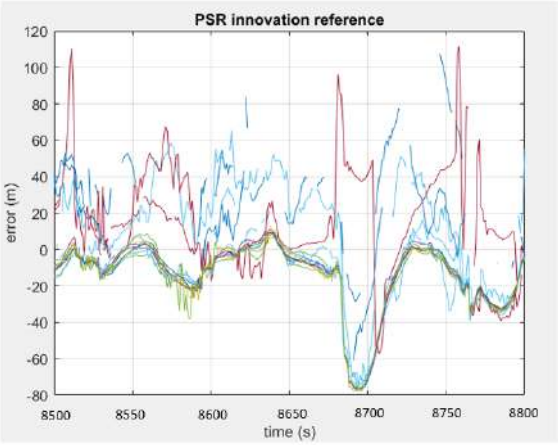

Figure 7-12 – Dataset 1, DGNSS Benchmark EKF: PSR Innovation values obtained using reference SPAN positions

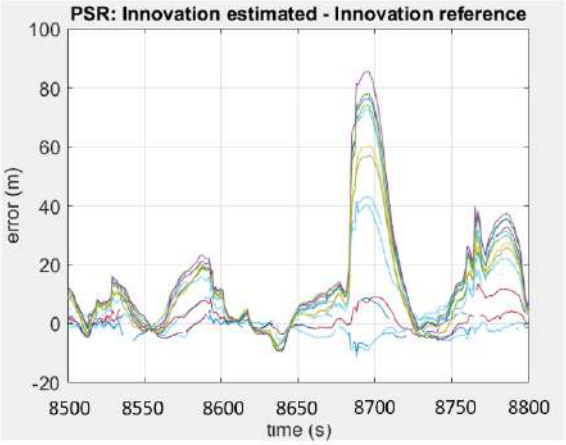

Figure 7-13 – Dataset 1, DGNSS Benchmark EKF: Difference between PSR EKF Innovations and PSR Innovations obtained using reference SPAN positions

It can be clearly seen that the innovations are biased by a common factor. This bias is probably introduced by a bad satellite geometry and/or the presence of the large MP error components, which are translated in:

- a position estimation error;
- a receiver clock bias estimation error.

Consequently, the hypothesis taken into account to reduce the impact of the bias due to the higher error peaks are the following:

- To improve the EKF state model:
  - to improve the position estimation error; to modify the state model with a model more adapted to vehicle dynamics;
  - to improve the receiver clock bias estimation error; to modify the state model with one more suited to the receiver clock model.
- To reduce the impact of the measurements affected by Multipath error components

To verify the impact of the satellite geometry, the Position DOP values and the number of satellites corresponding to the temporal section showed in Figure 7-11, have been calculated. The results are portrayed in Figure 7-14 and Figure 7-15. Further, to investigate the impact of the MP error components, the isolated MN error temporal vectors, for each different satellites, are illustrated in Figure 7-16.

The PDOP does not show a significant increase in correspondence of the peaks presented in Figure 7-11; moreover, the number of satellites, even showing a decrease between 8700s and 8770s is still high (9 satellites in the worst case). On the contrary, the majorities of the satellite's PSR MN errors increases with a similar tendency in correspondence of the peaks presented in Figure 7-11. It follows that the main impairment is the effect of MP errors on the PVT estimations.

In the light of above, the mitigation of the impact of the measurements affected by Multipath error components is fundamental to obtain better results, hence, this work focused more in this second option at the expense of the first.

However, it has been proposed a first improvement based on the refinement of the receiver clock EKF estimation model with a more precise model of the receiver clock used to collect the Data collection 1 and 2. This is a complex operation since presupposes the knowledges of the characteristics of the receiver clock under test. The sub-optimal solution proposed in this work, is the application of the receiver clock EKF model tuning based on the dataset collected during the data campaign. However, these datasets are collected in urban environment, therefore, the measurements are affected by MP errors. The refinement obtained applying this technique should be very limited.

The main improvement proposed in this work solution consists therefore, in the application of the techniques implemented in the Improvement Block, (section 7.1.2).

The results obtained applying the proposed solutions are presented, respectively in section 7.3.3.2.1 and 7.3.3.3.

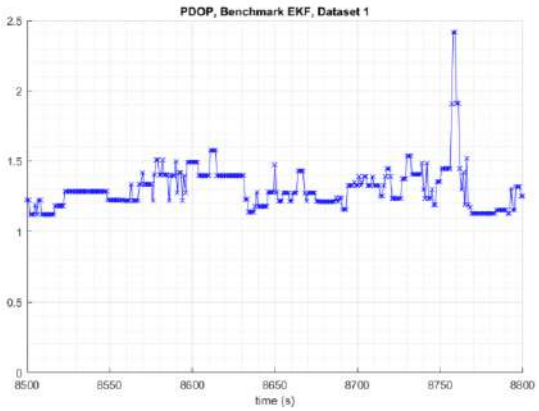

Figure 7-14 – PDOP values of DGNSS Benchmark EKF, applied to Data Collection 1, in the temporal section presented in Figure 7-11

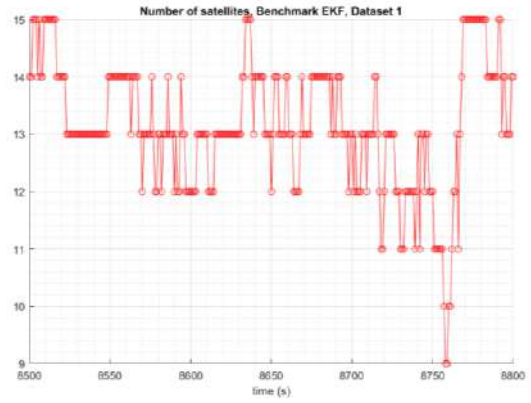

Figure 7-15 – Number of satellites used by DGNSS Benchmark EKF, applied to Data Collection 1, in the temporal section presented in Figure 7-11

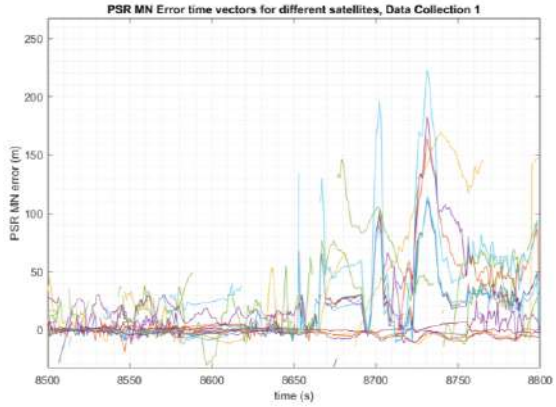

Figure 7-16 – Satellite's PSR MN error vectors isolated from the Data Collection 1, in the temporal section presented in Figure 7-11

7.3.3 Standard EKF Results

This section contains the results of the investigations proposed for the Standard EKF model. In the first section, 7.3.3.1, the EKF's configuration parameters are presented. Section 7.3.3.2 shows the results of the Standard EKF applying Baseline Block. Finally, section 7.3.3.3 presents the results of the Standard EKF applying the Baseline Block, and the Improvement Block.

7.3.3.1 EKF Parameter's Configuration

The Standard EKF parameters configuration is the same one applied for the Benchmark EKF estimator, described in section 7.3.2.1, with the following differences:

- σ_{MN}^2 is the PSR MN error variance: is derived from the PSR MN error statistics, defined in section 6.3.1. GPS and Galileo PSR MN error variances are selected separately from the GPS and Galileo MN error characterizations.

- σ^2_{MN} is the PSR-R MN error variance: is derived from the PSR-R MN error statistics, defined in section 6.3.2. GPS and Galileo PSR-R MN error variances are selected separately from the GPS and Galileo MN error characterizations.
- σ^2_b, $\sigma^2_{\dot{b}}$ and σ^2_δ are calculated by the application of the receiver clock model tuning, described in section 7.3.3.2.1:
    - the clock bias noise variance, σ^2_b: 0.03 m^2s^{-1}.
    - the clock drift noise variance, $\sigma^2_{\dot{b}}$: 0.003 m^2s^{-3}.
    - the inter-constellation GPS-to-Galileo variance, σ^2_δ: 0.0001 m^2s^{-1}.

7.3.3.2 Application of Baseline Block

This section summarizes the results of the Standard EKF applying the Baseline Block.

The first goal of the section is to determine the optimal Baseline Block configuration. This is obtained firstly by calculating a refined receiver clock EKF model (section 7.3.3.2.1) and subsequently selecting the optimal Baseline Measurement Model (section 7.3.3.2.2).

The second goal of the section is to assess the performance of the SA and DGNSS Standard EKF, implementing the Baseline Block configuration derived above, with respect to the Benchmark EKF (section 7.3.3.2.3) and commercial PVT estimators (section 7.3.3.2.4). Some final considerations are summarized in section 7.3.3.2.5.

7.3.3.2.1 Receiver clock model tuning

During the Benchmark EKF performance analysis (see section 7.3.2), it was suggested that the receiver clock bias estimation error may lead to further performance degradations. Therefore, in this section tuning of the receiver clock EKF model is undertaken in order to:

- improves the performances of the related PVT estimator
- verify the improvements introduced by the MN error statistics whose impact is greater once other issues are resolved

This is a complex operation which ideally would benefit from information regarding the *a priori* physical properties of the receiver clock. If these characteristics are unknown, a sub-optimal receiver clock EKF model must be derived empirically.

Therefore, in this section, the clock model tuning is undertaken based on the measurements collected in the dataset 1. Tuning undertaken using dataset 2 were almost identical and partially verify that they are driven by the clock behavior and not by the data. Whilst, from the point of view of data independence this is not ideal, due to the limitations in the number of datasets, it was chosen as the practical way forward. In future work, an independent data set wild ideally be used in open sky conditions to meet this goal. Ultimately, the solution should present a fair test in relation to the U-Blox solution which is based on internal proprietary information.

The refined receiver clock EKF model consists of the selection of the σ^2_b, $\sigma^2_{\dot{b}}$, σ^2_δ parameters which minimize the $\mathrm{RMSE}(e_p)$ of the DGNSS Benchmark EKF model configuration:

$$[\hat{\sigma}^2_b, \hat{\sigma}^2_{\dot{b}}, \hat{\sigma}^2_\delta] = \underset{\sigma^2_b, \sigma^2_{\dot{b}}, \sigma^2_\delta}{\operatorname{argmin}} [\mathrm{RMSE}(e_p)] \qquad 7\text{-}47$$

The procedure has been applied to the DGNSS Benchmark EKF (for the reasons illustrated in section 7.3.3.2.1) with Data Collection 1. The parameters which have been iteratively tested are the following:

- the clock bias noise variance, σ^2_b: from 0.01 m^2s^{-1} to 0.06 m^2s^{-1}, with a step of 0.01 m^2s^{-1}.
- the clock drift noise variance, $\sigma^2_{\dot{b}}$: from 0.001 m^2s^{-1} to 0.005 m^2s^{-1}, with a step of 0.001 m^2s^{-1}.
- the inter-constellation GPS-to-Galileo variance, $\sigma^2_{\delta C}$: from 0.0001 m^2s^{-1} to 0.0004 m^2s^{-1}, with a step of 0.0001 m^2s^{-1}.

Therefore, the parameters which minimize the $\mathrm{RMSE}(\boldsymbol{e}_{p,l})$, as described in Figure 7-17, are

- the clock bias noise variance, σ_b^2: 0.03 $m^2 s^{-1}$.
- the clock drift noise variance, $\sigma_{\dot{b}}^2$: 0.003 $m^2 s^{-3}$.
- the inter-constellation GPS-to-Galileo variance, σ_δ^2: 0.0001 $m^2 s^{-1}$.

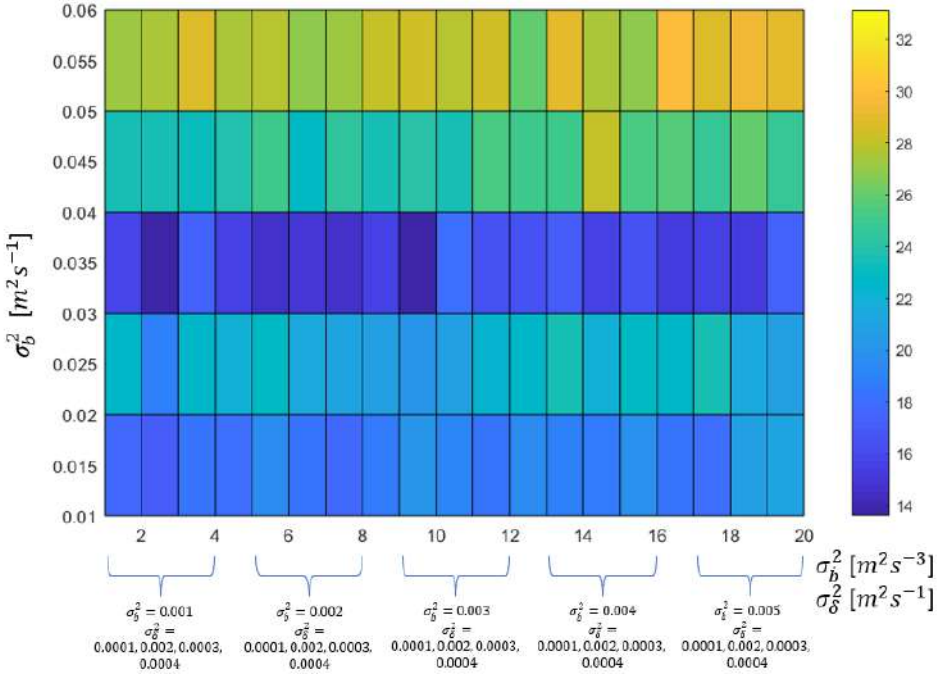

Figure 7-17 – RMSE of the DGNSS Benchmark EKF as a function of the receiver clock EKF model

The comparison between the norm of the estimated position error before and after the application of the refinement receiver clock model and the corresponding RMSE are shown in Figure 7-20 showing a slight improvement due to the refined clock model application. The RMSE decreases from 15.62 m to 13.66, with an improvement of 12.54%. The same receiver clock parameters have been therefore applied to the DGNSS Benchmark EKF with Data Collection 2 (Figure 7-21), with an improvement of 10.05%, the SA Benchmark EKF with Data Collection 1 (Figure 7-18), with an improvement of 9.72%, and the SA Benchmark EKF with Data Collection 2 (Figure 7-19), with an improvement of 8.35%. The resulting RMSE and the corresponding improvements are summarized in Table 7-3. Despite this change, the bias affecting the estimated position is not removed since the error peaks are not removed. Therefore, the refinement of receiver clock is ineffective against the highest error peaks.

Finally, it is also pointed out that the application of a refined receiver clock EKF model allows for a more reliable comparison between the PVT estimator under test and the commercial U-blox M8T, since the dataset applied to analyses the performances of the proposed PVT estimators have been collected by the same U-blox M8T receiver. Therefore, the refined receiver clock EKF model should be more similar to the refined receiver clock U-blox model.

	SA			**DGNSS**		
Position Estimation Error: RMSE [m]	Benchmark EKF, no clock ref	Benchmark EKF, yes clock ref	**Improv. [%]**	Benchmark EKF, no clock ref	Benchmark EKF, yes clock ref	**Improv. [%]**
Data Collection 1	20.26	18.29	**9.72**	15.62	13.66	**12.54**
Data Collection 2	22.86	20.95	**8.35**	19.92	18.10	**10.05**

Table 7-3 – Comparison between the SA and DGNSS Benchmark RMSE without the refined receiver clock model and with the refined receiver clock model

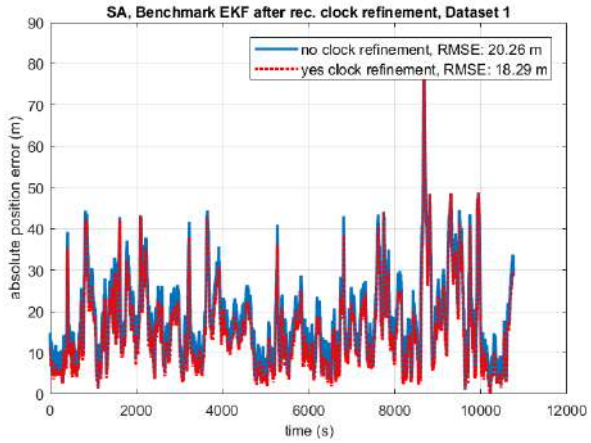

Figure 7-18 – Absolute Position estimation error with the corresponding RMSE: Dataset 1, SA Benchmark EKF, without refined receiver clock model (blue line) vs. with refined receiver clock model (red line)

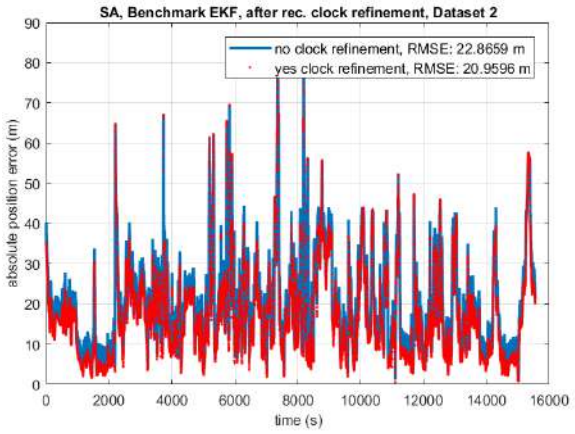

Figure 7-19 – Absolute Position estimation error with the corresponding RMSE: Dataset 2, SA Benchmark EKF, without refined receiver clock model (blue line) vs. with refined receiver clock model (red line)

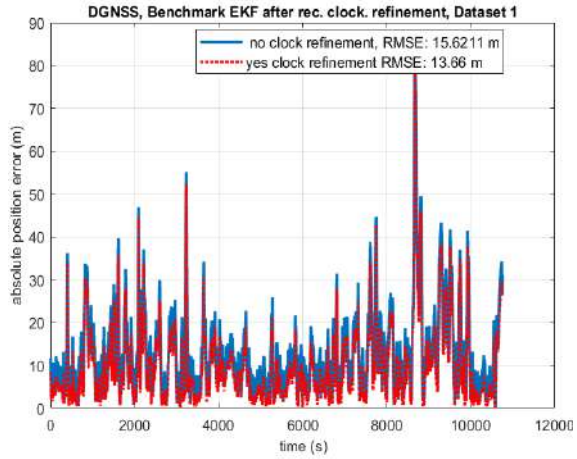

Figure 7-20 – Absolute Position estimation error with the corresponding RMSE: Dataset 1, DGNSS Benchmark EKF, without refined receiver clock model (blue line) vs. with refined receiver clock model (red line)

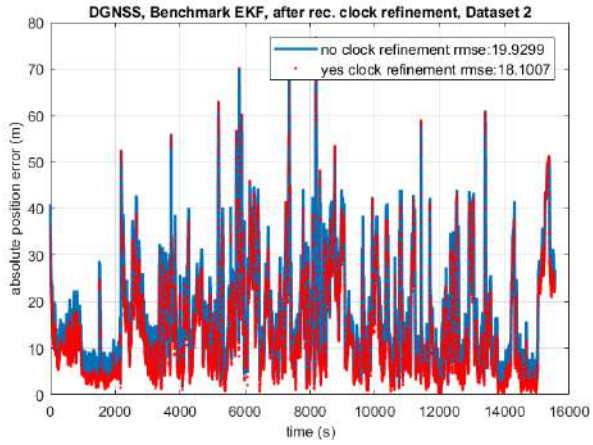

Figure 7-21 – Absolute Position estimation error with the corresponding RMSE: Dataset 2, DGNSS Benchmark EKF, without refined receiver clock model (blue line) vs. with refined receiver clock model (red line)

7.3.3.2.2 Selection of the Baseline Measurement Model

The second evaluation applied to determine the best Baseline Block configuration is the Baseline Measurement Model selection. In this section the results of SA and DGNSS Standard EKF are compared applying the refined receiver clock EKF model with the Baseline Measurement Model 1 and the Baseline Measurement Model 2, in order to select the Measurement Model which guarantees higher performances.

In the first part, the SA Standard EKF performance have been investigated. The results have been divided with respect to the two different Data Collections.

The norm of the position error estimation and the corresponding RMSE of the SA Benchmark EKF, SA Standard EKF with Baseline Measurement Model 1 and Measurement Model 2 applied to Data Collection 1 are portrayed in Figure 7-22

The norm of the position error estimation and the corresponding RMSE of the DGNSS Benchmark EKF, DGNSS Standard EKF with Baseline Measurement Model 1 and Measurement Model 2 applied to Data Collection 1 are portrayed in Figure 7-23.

The norm of the position error estimation and the corresponding RMSE of the SA Benchmark EKF, SA Standard EKF with Baseline Measurement Model 1 and Measurement Model 2 applied to Data Collection 2 are portrayed in Figure 10-213, in Annex 10.5.

The norm of the position error estimation and the corresponding RMSE of the DGNSS Benchmark EKF, DGNSS Standard EKF with Baseline Measurement Model 1 and Measurement Model 2 applied to Data Collection 2 are portrayed in Figure 10-214, in Annex 10.5.

- Results of Data Collection 1:
  - Baseline Measurement Model 1 (Figure 7-22): the RMSE is equal to 12.63 m.
  - Baseline Measurement Model 2 (Figure 7-22): the RMSE is equal to 14.08 m.
- Results of Data Collection 2:
  - Baseline Measurement Model 1 (Figure 10-213): the RMSE is equal to 14.61 m.
  - Baseline Measurement Model 2 (Figure 10-213): the RMSE is equal to 15.73 m.

Hence, in the case of SA Standard EKF, the Baseline Measurement Model 1 have better performances.

In the second part the DGNSS Standard EKF performances have been investigated:

- Results of Data Collection 1:
  - Baseline Measurement Model 1 (Figure 7-23): the RMSE is equal to 8.37 m.
  - Baseline Measurement Model 2 (Figure 7-23): the RMSE is equal to 8.45 m.
- Results of Data Collection 2:
  - Baseline Measurement Model 1 (Figure 10-214): the RMSE is equal to 9.62 m.
  - Baseline Measurement Model 2 (Figure 10-214), the RMSE is equal to 9.80 m.

Thus, in the case of DGNSS Standard EKF, the Baseline Measurement Model 1 and Measurement Model 2 have similar results. The corresponding RMSE values are summarized in Table 7-4.

From the results shown in the previous paragraphs, the two Baseline Measurement Models provides similar results. Therefore, the Measurement Model 2 which is based on the application of MN Gaussian error model derived from the application of the mean removal and the Gaussian overbounding, section 6.3, does not introduce any significant advantages. Therefore, it is assumed that the simpler Measurement Model 1 should be adopted as standard Measurement Model in the Baseline Block, while the Measurement Model 2 is discarded. This is preferred since it is difficult to justify the use of a mean error as being representative of the *population* mean when the reality is that the real error distribution is not ergodic.

Position Estimation Error: **RMSE [m]**	**SA Standard EKF**		**DGNSS Standard EKF**	
	Baseline Model 1	Baseline Model 2	Baseline Model 1	Baseline Model 2
Data Collection 1	12.63	14.08	8.37	8.45
Data Collection 2	14.61	15.73	9.62	9.80

Table 7-4 – Comparison between the SA/DGNSS Benchmark RMSE and the SA/DGNSS Standard EKF with Baseline Measurement Model 1 and 2

7.3.3.2.3 Comparison with Benchmark EKF

In this section the results of the SA/DGNSS Standard EKF with Baseline Measurement Model 1 and the SA/DGNSS Benchmark EKF are compared.

In the first part the results concerning the SA Standard EKF are presented:

- Data collection 1 (Figure 7-22): the application of the Baseline Block provides an improvement with respect to the Benchmark EKF (RMSE equal to 12.63m against 18.29m) of 30.94%.
- Data collection 2 (Figure 10-213): the application of the Baseline Block provides an improvement with respect to the Benchmark EKF (RMSE equal to 14.61m against 20.95m) of 30.26%.

Therefore, the application of the proposed Baseline Block increases the performances of the corresponding SA PVT estimators with respect to the SA Benchmark solution of 30%.

In the second part the results concerning the DGNSS Standard EKF are presented:

- Data Collection 1 (Figure 7-23): the application of the Baseline Block provides an improvement with respect to the Benchmark EKF (RMSE equal to 8.37m against 13.66m) of 38.72%.
- Data Collection 2 (Figure 10-214): the application of the Baseline Block provides an improvement with respect to the Benchmark EKF (RMSE equal to 9.62m against 18.10m) of 46.80%.

Therefore, the application of the proposed Baseline Block improves the performance of the corresponding DGNSS PVT estimators with respect to the DGNSS Benchmark solution by 40%. As expected, the improvements introduced by the application of the Baseline Solution are higher for DGNSS PVT estimators (between 38% and 46%) than SA PVT estimators (between 23% and 31%).

The RMSE values of the SA and DGNSS Benchmark EKF, the RMSE values of the SA and DGNSS Standard EKF and the relative improvements are summarized in Table 7-5.

	SA			**DGNSS**		
Position Estimation Error: RMSE [m]	Benchmark EKF	Standard EKF Baseline	**Improv. [%]**	Benchmark EKF	Standard EKF Baseline	**Improv. [%]**
Data Collection 1	18.29	12.63	**30.94**	13.66	8.37	**38.72**
Data Collection 2	20.95	14.61	**30.26**	18.10	9.62	**46.80**

Table 7-5 – Comparison between the SA/DGNSS Benchmark RMSE and the SA/DGNSS Standard EKF with Baseline Measurement Block

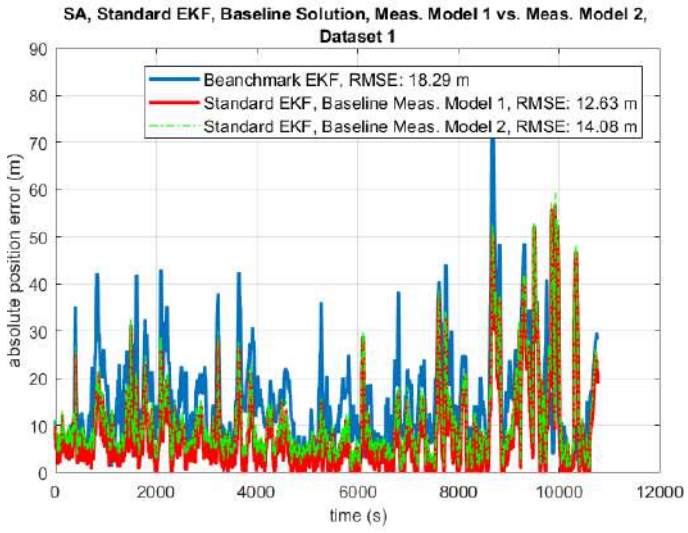

Figure 7-22 – Absolute Position estimation error with the corresponding RMSE: Dataset 1, SA Benchmark EKF (blue line) vs. Standard EKF with Baseline Block Measurement Model 1 (red line) vs. Measurement Model 2 (green line).

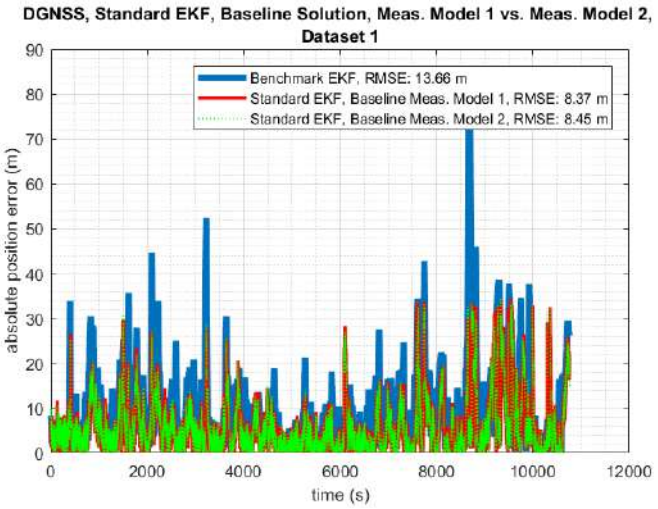

Figure 7-23 – Absolute Position estimation error with the corresponding RMSE: Dataset 1, DGNSS Benchmark EKF (blue line) vs. Standard EKF with Baseline Block Measurement Model 1 (red line) vs. Measurement Model 2 (green line)

7.3.3.2.4 Comparison with commercial PVT estimators

In this section the results of the SA/DGNSS Standard EKF with Baseline Measurement Model 1 are compared with the SA/DGNSS commercial PVT estimators, presented in section 7.3.1.

The norm of the position error estimation and the corresponding RMSE of the SA Standard EKF with Baseline Measurement Model 1, of the SA Inertial Explorer and of the U-blox M8T, applied to Data Collection 1, are portrayed in Figure 7-24

The norm of the position error estimation and the corresponding RMSE of the SA Standard EKF with Baseline Measurement Model 1, of the SA Inertial Explorer and of the U-blox M8T, applied to Data Collection 1, are portrayed in Figure 7-25.

The norm of the position error estimation and the corresponding RMSE of the SA Standard EKF with Baseline Measurement Model 1, of the SA Inertial Explorer and of the U-blox M8T, applied to Data Collection 2, are portrayed in Figure 10-215, in Annex 10.5.2.

The norm of the position error estimation and the corresponding RMSE of the DGNSS Benchmark EKF, DGNSS Standard EKF with Baseline Measurement Model 1 and Measurement Model 2 applied to Data Collection 2 are portrayed in Figure 10-216, in Annex 10.5.2.

In the first part the results concerning the SA Standard EKF are analysed:

- Data collection 1 (Figure 7-24):
  - The RMSE of the Standard EKF with Baseline Solution is lower than the RMSE of the SA IE estimations: 14.08 m vs. 24.44 m;
  - The RMSE of the Standard EKF with Baseline Solution is much higher than the RMSE of the U-blox M8T estimations: 14.08 m vs. 6.73 m
- Data collection 2 (Figure 10-215):
  - The RMSE of the Standard EKF with Baseline Solution is lower than the RMSE of the SA IE estimations: 15.73 m vs. 22.96;
  - The RMSE of the Standard EKF with Baseline Solution is much higher than the RMSE of the U-blox M8T estimations: 15.73 m vs. 5.73 m

In the second part the results concerning the DGNSS Standard EKF are analysed:

- Data collection 1 (Figure 7-25):
  - The RMSE of the Standard EKF with Baseline Solution is comparable to the RMSE of the DGNSS IE estimations: 8.37 m vs. 9.75 m;
  - The RMSE of the Standard EKF with Baseline Solution is, even in DGNSS mode, is still higher than the RMSE of the U-blox M8T estimations: 8.37 m vs. 6.75 m
- Data collection 2 (Figure 10-216):
  - The RMSE of the Standard EKF with Baseline Solution is comparable to the RMSE of the DGNSS IE estimations: 9.62 m vs. 9.66 m;

- The RMSE of the Standard EKF with Baseline Solution is, even in DGNSS mode, is still higher than the RMSE of the U-blox M8T estimations: 9.62 m vs. 5.73 m

The results are summarized in Table *7-6*. In conclusion:

- the proposed SA PVT estimator have better performances with respect to the SA IE commercial software solution, however, it has worst performances with respect to the SA U-blox M8T receiver solutions.
- the proposed DGNSS PVT estimator have similar performances with respect to the DGNSS IE commercial software solution, however, it has worst performances with respect to the SA U-blox M8T receiver solutions.

Position Estimation Error: RMSE [m]	**SA**			**DGNSS**	
	U-blox M8T	Inertial Explorer	Baseline	Inertial Explorer	Baseline
Data Collection 1	6.73	24.44	12.63	9.75	8.37
Data Collection 2	5.73	22.96	14.61	9.66	9.62

Table 7-6 – RMSE of the Proposed SA/DGNSS Standard EKF with Baseline Measurement Model 1, compared to commercial SA/DGNSS PVT estimators

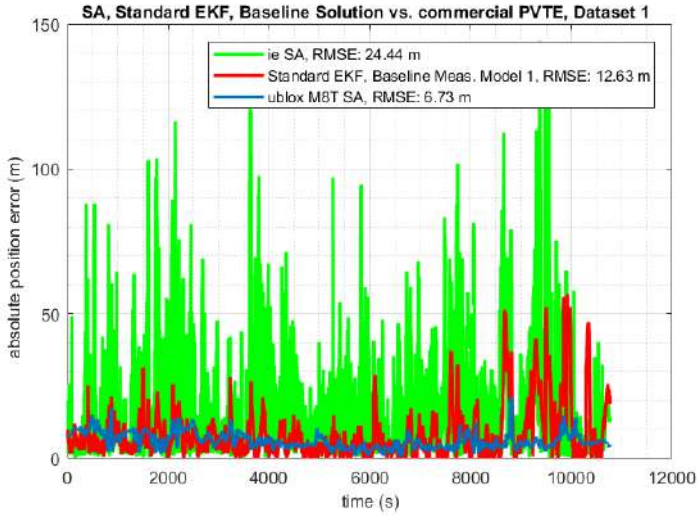

Figure 7-24 – Absolute Position estimation error with the corresponding RMSE: Dataset 1, SA Standard EKF with Baseline Measurement Model 1 (red line) vs. SA Inertial Explorer (green line) vs. SA U-Blox M8T(blue line)

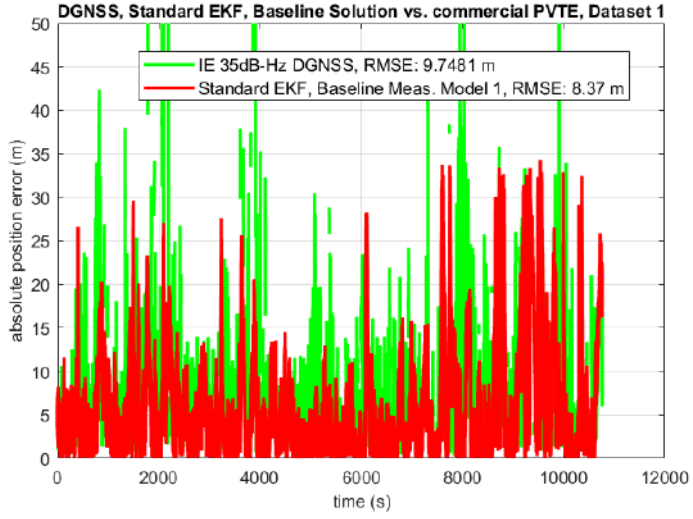

Figure 7-25 – Absolute Position estimation error with the corresponding RMSE: Dataset 1, DGNSS Standard EKF with Baseline Measurement Model 1 (red line) vs. DGNSS Inertial Explorer (green line)

7.3.3.2.5 Conclusions

In this section the performance of the SA and DGNSS Standard EKF with Baseline Solution have been illustrated and investigated.

The first goal of the section was the determination of the best Baseline Block configuration. This is obtained firstly calculating a refined receiver clock EKF model (section 7.3.3.2.1) and, consequently, selecting the Baseline Measurement Model which ensure higher improvements (section 7.3.3.2.2).

The refined receiver clock EKF model has been calculated applying a receiver clock model tuning consisting of the selection of the receiver clock EKF parameters which minimize the RMSE$(\boldsymbol{e}_p)$ of the DGNSS Benchmark EKF model configuration applied to the Data Collection. It is noted that a slight improvement is seen due to the refined clock model application of roughly 10% with respect the application of the generic receiver clock EKF model. Despite this change, the common bias affecting the EKF innovations is not removed, since the error peaks are not removed. Therefore, the refinement of receiver clock is ineffective against the highest error peaks.

The Baseline Measurement Model selection has been accomplished by comparing the SA and DGNSS Standard EKF performances applying the Baseline Measurement Model 1 and the Baseline Measurement Model 2. The application of the two different models provides similar performances. Therefore, the application of the mean removal before the Gaussian overbounding in the MN Gaussian error model does not provide any improvement. Therefore, it has been selected the simplest Baseline Measurement Model 1 as standard Measurement Model applied in the Baseline Block.

The second goal of the section is the investigation of the performance of SA and DGNSS Standard EKF, implementing the Baseline Block configuration derived in the previous points. In particular, the performances of the proposed SA and DGNSS Standard EKF are compared firstly to the Benchmark EKF (section 7.3.3.2.3) and, successively, the commercial PVT estimators (section 7.3.3.2.4).

Firstly, the SA Standard EKF has been compared to the SA Benchmark EKF. It provides an improvement of 30.94% for Data Collection 1 and 30.26% for Data Collection 2. Therefore, the application of the proposed Baseline Solution improves the performance of the corresponding PVT estimators with respect to the Benchmark solution.

Secondly, the DGNSS Standard EKF has been compared to the DGNSS Benchmark EKF. It provides an improvement of 38.72% for Data Collection 1 and 46.80% for Data Collection 2. Therefore, the application of the proposed Baseline Solution increases the performances of the corresponding PVT estimators with respect to the Benchmark solutions. As expected, the improvements introduced by the application of the Baseline Solution are higher for DGNSS PVT estimators (between 38% and 46%) than SA PVT estimators (between 23% and 31%).

Thirdly, the SA Standard EKF has been compared to the SA Inertial Explorer and SA U-blox M8T. It provides better results with respect to SA IE, while the performances are worse than U-blox solutions, 14.08 m against 6.73 m for data collection 1, 15.73 m against 5.73 m for data collection 2.

Finally, the DGNSS Standard EKF has been compared to the DGNSS Inertial Explorer and SA U-blox M8T error performances. It provides comparable performances with respect to DGNSS IE, while the performances are worse than SA U-blox solutions, 8.37 m against 6.73 m for data collection 1, 9.62 m against 5.73 m for data collection 2.

7.3.3.3 Application of Improvement Block

This section summarizes the results of the Standard EKF applying the Baseline Block and the Improvement Block.

The first goal of the section is the determination of the best Improvement Block configuration. This is obtained firstly determining the empirical C/N_0 threshold for NLOS Satellite Exclusion (section 7.3.3.3.1), and, consequently, selecting the technique (NLOS SE, IF or the combination of the two) which ensures higher performance (section 7.3.3.3.2).

The second goal of the section is the investigation of the performances of SA and DGNSS Standard EKF, implementing the Baseline Block and the Improvement Block configuration derived in the previous points. In particular, the performances of the proposed SA and DGNSS Standard EKF are compared firstly to the Benchmark EKF (section 7.3.3.3.3) and, successively, the other commercial PVT estimators (section 7.3.3.3.4). Some final considerations are summarized in section 7.3.3.3.5.

7.3.3.3.1 NLOS Satellite Exclusion C/N_0 Threshold Selection

The section evaluates the performance of the NLOS Satellite Exclusion applying five different C/N_0 LOS/NLOS discrimination thresholds: 30, 32.5, 35, 37.5, 40 dB-Hz.

The performance of the NLOS Satellite Exclusion will depend on the trade-off between the quality of the excluded measurements and the total number of the selected measurements used to calculate the PVT estimation: a lower C/N_0 threshold will exclude a smaller number of "bad" measurements privileging a better satellite availability, while a higher C/N_0 threshold will exclude a larger number of "bad" measurements, privileging a better NLOS Satellite Exclusion, with the cost of reducing the satellite availability.

The evaluation is performed for the SA and DGNSS Standard EKF with Baseline Measurement Model 1 applied to the Data Collection 1 and Data Collection 2. The RMSE values are summarized in Table 7-7. The 30, 37.5 and 40 dB-Hz thresholds have worst impact with respect to 32.5 and 35 dB-Hz. Therefore, the thresholds which allow better performances are 32.5 and 35 dB-Hz.

In the first part the results concerning the SA Standard EKF are analysed:

- Data collection 1:
  - the application of NLOS SE with 32.5 and 35 dB-Hz have comparable results: RMSE is 9.52 m (32.5 dB-Hz) vs. 9.62 m (35 dB-Hz);
- Data collection 2:
  - the application of NLOS SE with 35 have better performance with respect to 32.5 dB-Hz: the RMSE is 10.9 m (35 dB-Hz) vs. 11.37 m (32.5 dB-Hz);

In the second part the results concerning the DGNSS Standard EKF are analysed:

- Data collection 1:
  - the application of NLOS SE with 32.5 and 35 dB-Hz have comparable results: RMSE is 7.42 m (32.5 dB-Hz) vs. 7.64 m (35 dB-Hz);
- Data collection 2:
  - the application of NLOS SE with 35 have better performance with respect to 32.5 dB-Hz: the RMSE is 7.85 m (35 dB-Hz) vs. 8.20 m (32.5 dB-Hz);

The results are summarized in Table 7-7.

It can be assumed that the threshold which allows better performances is $C/N_0 = 35$ dB-Hz. This value is applied as standard C/N_0 LOS/NLOS discrimination thresholds when the NLOS Satellite Exclusion has been used.

Position estimation error, RMSE [m]		**NLOS Satellite Exclusion**				
Data Collection	**Positioning Technique**	*30 dB-Hz*	*32.5 dB-Hz*	*35 dB-Hz*	*37.5 dB-Hz*	*40 dB-Hz*
Dataset 1	SA	10.80	9.52	9.62	9.91	9.93
	DGNSS	8.75	7.42	7.64	7.84	7.90
Dataset 2	SA	14.19	11.37	10.69	10.84	12.22
	DGNSS	8.83	8.20	7.85	7.93	7.88

Table 7-7 – The Table summarize the RMSE obtained applying the Standard EKF with Baseline Block and the NLOS Satellite Exclusion applied with different C/N_0 thresholds

7.3.3.3.2 Comparison between different Satellite Exclusion Techniques

This section evaluates the performance of the SA and DGNSS Standard EKF with Baseline Block and the different techniques of the Improvement Block.

The different techniques under test are:

- NLOS Satellite Exclusion (NLOS SE), with C/N_0 threhsold equal to 35 dB-Hz (as provided in section 7.3.3.3.1);
- Innovation Filtering (IF);
- The application of NLOS SE followed by IF (NLOS SE + IF).

The norm of the position error estimation and the corresponding RMSE of the SA Standard EKF with Baseline Measurement Model 1 and the different techniques applied in the Improvement Block (NLOS SE, IF, NLOS SE + IF), applied to Data Collection 1, are portrayed in Figure 7-26.

The norm of the position error estimation and the corresponding RMSE of the DGNSS Standard EKF with Baseline Measurement Model 1 and the different techniques applied in the Improvement Block (NLOS SE, IF, NLOS SE + IF), applied to Data Collection 1, are portrayed in Figure 7-27.

The norm of the position error estimation and the corresponding RMSE of the SA Standard EKF with Baseline Measurement Model 1 and the different techniques applied in the Improvement Block (NLOS SE, IF, NLOS SE + IF), applied to Data Collection 2, are portrayed in Figure 10-217, in Annex 10.5.2.

The norm of the position error estimation and the corresponding RMSE of the DGNSS Standard EKF with Baseline Measurement Model 1 and the different techniques applied in the Improvement Block (NLOS SE, IF, NLOS SE + IF), applied to Data Collection 2, are portrayed in Figure 10-218, in Annex 10.5.2.

In the first part the results concerning the SA Standard EKF are analyzed:

- Data Collection 1 (Figure 7-26):
  - with NLOS Satellite Exclusion, the RMSE is equal to 9.58 m, providing an improvement of 24.14% with respect to the Standard EKF with Baseline Model (RMSE: 12.63 m);
  - with Innovation Filtering, the RMSE is equal to 11.70 m, providing an improvement of 7.36% with respect to the Standard EKF with Baseline Model;
  - with NLOS Satellite Exclusion + Innovation Filtering, the RMSE is equal to 8.26 m, providing an improvement of 34.60% with respect to the Standard EKF with Baseline Model.
- Data Collection 2 (Figure 10-217):
  - with NLOS Satellite Exclusion, the RMSE is equal to 10.69 m, providing an improvement of 26.83% with respect to the Standard EKF with Baseline Model (14.61 m);
  - with Innovation Filtering, the RMSE is equal to 13.80 m, providing an improvement of 5.54% with respect to the Standard EKF with Baseline Model;
  - with NLOS Satellite Exclusion + Innovation Filtering, the RMSE is equal to 13.80 m, providing an improvement of 39.08% with respect to the Standard EKF with Baseline Model.

The highest improvement is obtained by applying the NLOS SE + IF, while the lowest is obtained with the IF.

In the second part the results concerning the DGNSS Standard EKF are analyzed:

- Data Collection 1 (Figure 7-27):
  - with NLOS Satellite Exclusion, the RMSE is equal to 7.58 m, providing an improvement of 8.45% with respect to the Standard EKF with Baseline Model (RMSE: 8.28 m);
  - with Innovation Filtering, the RMSE is equal to 6.32 m, providing an improvement of 23.67% with respect to the Standard EKF with Baseline Model;
  - with NLOS Satellite Exclusion + Innovation Filtering, the RMSE is equal to 4.75 m, providing an improvement of 42.62% with respect to the Standard EKF with Baseline Model.
- Data Collection 2 (Figure 10-218):
  - with NLOS Satellite Exclusion, the RMSE is equal to 7.85 m, providing an improvement of 18.40% with respect to the Standard EKF with Baseline Model (RMSE: 9.62 m);
  - with Innovation Filtering, the RMSE is equal to 8.95 m, providing an improvement of 6.96% with respect to the Standard EKF with Baseline Model;
  - with NLOS Satellite Exclusion + Innovation Filtering, the RMSE is equal to 5.68 m, providing an improvement of 40.95% with respect to the Standard EKF with Baseline Model.

The corresponding RMSE values and the relative improvements are summarized in Table 7-8.

The highest improvement is obtained by applying the NLOS SE + IF, while the lowest is obtained with the IF.

Position Estimation Error:	**Improvement Block techniques**

RMSE [m]								
	Data Collection	Baseline	NLOS SE	**Improv. [%]**	IF	**Improv. [%]**	NLOS SE + IF	**Improv. [%]**
SA	**Dataset 1**	12.63	9.58	**24.14**	11.70	**7.36**	8.26	**34.60**
	Dataset 2	14.61	10.69	**26.83**	13.80	**5.54**	8.90	**39.08**
DGNSS	**Dataset 1**	8.28	7.58	**8.45**	6.32	**23.67**	4.75	**42.62**
	Dataset 2	9.62	7.85	**18.40**	8.95	**6.96**	5.68	**40.95**

Table 7-8 – Comparison between the SA/DGNSS Standard EKF with Baseline Measurement Model 1 and SA/DGNSS Standard EKF with Improved Solution

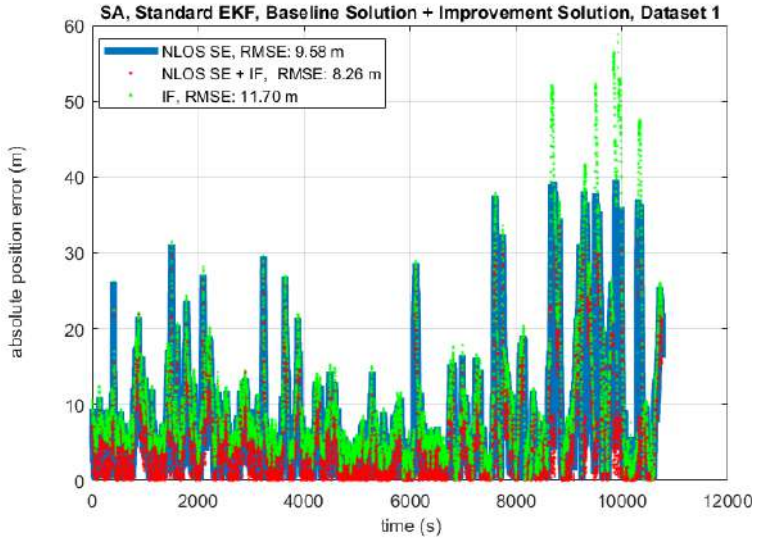

Figure 7-26 – Absolute Position estimation error with the corresponding RMSE: Dataset 1, SA Standard EKF with Improvement Block: NLOS SE (blue line) vs. IF (green-dot line) vs. NLOS SE + IF (red-dot line)

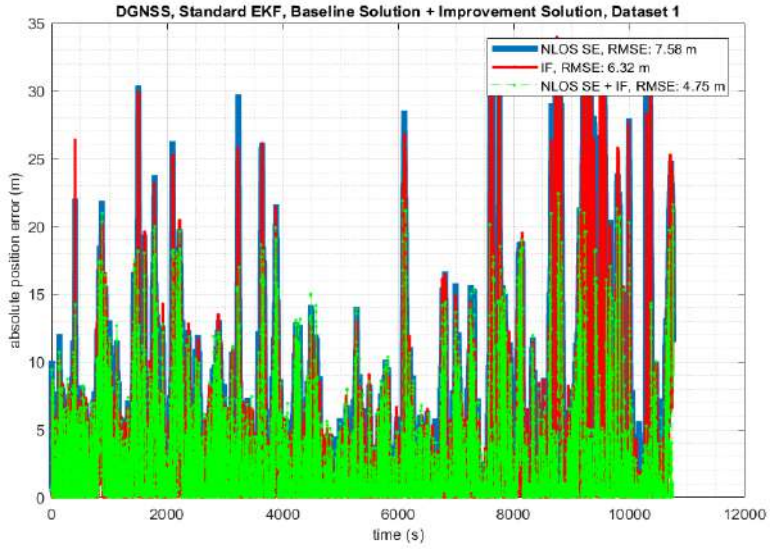

Figure 7-27 – Absolute Position estimation error with the corresponding RMSE: Dataset 1, DGNSS Standard EKF with Improvement Block: NLOS SE (blue curve) vs. IF (red curve) vs. NLOS SE + IF (green-dashed curve)

Moreover, it has also been verified if the application of these methodologies improves the performance of the related PVT estimators mitigating the impact of the measurements strongly affected by MP error components, as supposed in section 7.3.2. Therefore, in analogy with section 7.3.2, the reference innovations, and the difference between the real EKF innovations and the reference one of the DGNSS Standard EKF applying the Innovation Filtering to the Data Collection 1. The reference innovations in the time window 8500-8800 s are plotted in Figure 7-28, in correspondence of the high error peak of the DGNSS Benchmark EKF showed in Figure 7-12. Consequently, the difference between the real EKF innovations and the reference innovations, in the same time window, are plotted in Figure 7-29. According to the results portrayed in the pictures, the common large biases affecting the innovations in Figure 7-12 have been removed. Therefore, the application of the Improvement Block

attenuates the effects of the measurements affected by MP error components introducing an improvement of the receiver clock bias estimation accuracy.

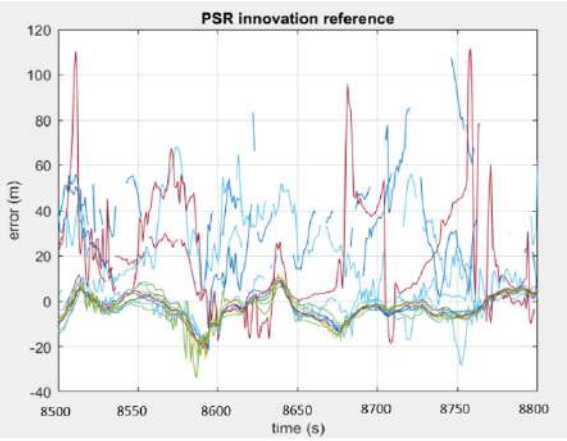

Figure 7-28 – Dataset 1, DGNSS PVT solutions: Pseudorange Innovation values obtained using reference SPAN positions, applying IF method

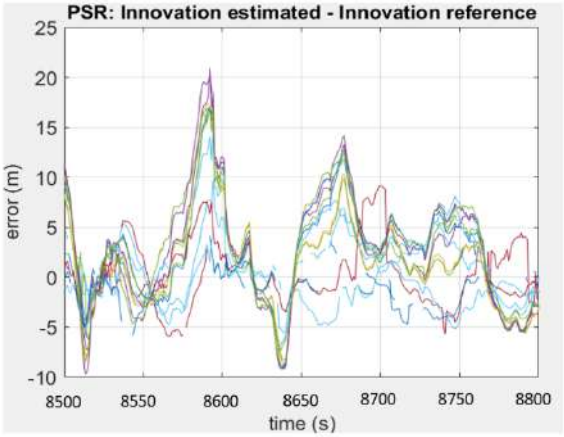

Figure 7-29 – Dataset 1, DGNSS PVT solutions: Difference between Pseudorange EKF Innovations and Pseudorange Innovations obtained using reference SPAN positions, applying IF method

7.3.3.3.3 Comparison with Benchmark EKF

This section presents the results of the SA/DGNSS Standard EKF with Baseline Measurement Model 1 and the NLOS SE + IF improvement Block and the SA/DGNSS Benchmark EKF.

In the first part the results concerning the SA Standard EKF are compared:

- Data collection 1: the application of the proposed solution provides an improvement with respect to the Benchmark EKF (RMSE equal to 8.26m against 18.29m) of 54.83%.
- Data collection 2: the application of the Baseline Block provides an improvement with respect to the Benchmark EKF (RMSE equal to 8.90m against 20.95m) of 57.51%.

Therefore, the application of the proposed solution increases the performance of the corresponding SA PVT estimators with respect to the SA Benchmark solution of around 55%.

In the second part the results concerning the DGNSS Standard EKF are compared:

- Data Collection 1: the application of the Baseline Block provides an improvement with respect to the Benchmark EKF (RMSE equal to 4.75m against 13.66m) of 65.22%.
- Data Collection 2: the application of the Baseline Block provides an improvement with respect to the Benchmark EKF (RMSE equal to 5.68m against 18.10m) of 68.62%.

Therefore, the application of the proposed solution increases the performances of the corresponding DGNSS PVT estimators with respect to the DGNSS Benchmark solution of around 66%. As expected, the improvements introduced by the application of the Baseline Solution are higher for DGNSS PVT than SA PVT estimators.

The RMSE values of the SA and DGNSS Benchmark EKF, the RMSE values of the SA and DGNSS Standard EKF and the relative improvements are summarized in Table 7-9.

Position Estimation Error RMSE [m]	**SA**			**DGNSS**		
	Benchmark EKF	Standard EKF Baseline + Improvement Blocks	**Improv. [%]**	Benchmark EKF	Standard EKF Baseline + Improvement Blocks	**Improv. [%]**

Data Collection 1	18.29	8.26	**54.83**	13.66	4.75	**65.22**
Data Collection 2	20.95	8.90	**57.51**	18.10	5.68	**68.62**

Table 7-9 – Comparison between the SA/DGNSS Benchmark RMSE and the SA/DGNSS Standard EKF with Baseline + Improvement Blocks

7.3.3.3.4 Comparison with commercial PVT estimators

This section compares the results of SA/DGNSS Standard EKF with Baseline Measurement Model 1 followed by the NLO SE + IF Improvement Block, and the SA/DGNSS commercial PVT estimators, presented in section 7.3.1.

In the first part the results concerning the SA Standard EKF are analysed:

- Data collection 1:
  - The RMSE of the proposed solution is much lower than the RMSE of the SA IE estimations: 8.26 m vs. 24.44 m;
  - The RMSE of the Standard EKF with Baseline Solution is higher than the RMSE of the U-blox M8T estimations of roughly 1 m: 8.26 m vs. 6.73 m
- Data collection 2:
  - The RMSE of the Standard EKF with Baseline Solution is much lower than the RMSE of the SA IE estimations: 8.90 m vs. 22.96 m;
  - The RMSE of the Standard EKF with Baseline Solution is higher than the RMSE of the U-blox M8T estimations of about 2m: 8.90 m vs. 5.73 m.

In the second part the results concerning the DGNSS Standard EKF are analysed:

- Data collection 1:
  - The RMSE of the Standard EKF with Baseline Solution is 5m lower than the RMSE of the DGNSS IE estimations: 4.75 m vs. 9.75 m;
  - The RMSE of the Standard EKF with Baseline Solution is 2m lower than the RMSE of the SA U-blox M8T estimations: 4.75 m vs. 6.75 m
- Data collection 2:
  - The RMSE of the Standard EKF with Baseline Solution is 4m lower than the RMSE of the DGNSS IE estimations: 5.68 m vs. 9.66 m;
  - The RMSE of the Standard EKF with Baseline Solution is comparable to the RMSE of the U-blox M8T estimations: 5.68 m vs. 5.73 m.

The results are summarized in Table *7-10*.

In conclusion:

- the proposed SA PVT estimator has better performance with respect to the SA IE commercial software solution, however, it has worst performance (2-3 meters higher RMSE) with respect to the SA U-blox M8T receiver solutions.
- the proposed DGNSS PVT estimator have better performance with respect to the DGNSS IE commercial software solution, and, it has comparable performances with respect to the SA U-blox M8T receiver solutions.

Position Estimation Error: RMSE [m]	**SA**			**DGNSS**	
	U-blox M8T	Inertial Explorer	Baseline +NLOS SE + IF	Inertial Explorer	Baseline +NLOS SE + IF
Data Collection 1	6.73	24.44	8.26	9.75	4.75

Data Collection 2	5.73	22.96	8.90	9.66	5.68

Table 7-10 – RMSE of the Proposed SA/DGNSS Standard EKF with Baseline and Improvement Blocks, compared to SA/DGNSS commercial PVT estimators

7.3.3.3.5 Conclusions

In this section the performance of the SA and DGNSS Standard EKF with Baseline Block and the Improvement Block have been illustrated and investigated.

The first goal of the section was the determination of the best Improvement Block configuration. This is obtained firstly determining the empirical C/N_0 threshold for NLOS Satellite Exclusion (section 7.3.3.3.1), and, consequently, selecting the technique (NLOS SE, IF or the combination of the two) for best performance (section 7.3.3.3.2).

Firstly, the performance of the NLOS Satellite Exclusion applying five different C/N_0 thresholds (30, 32.5, 35, 37.5, 40 dB-Hz) have been evaluated. The threshold which gives the best performance on the data addressed is $C/N_0 = 35$ dB-Hz. Secondly, the performance of the SA and DGNSS Standard EKF with Baseline Block and the different techniques of the Improvement Block (NLOS Satellite Exclusion, Innovation Filtering and NLOS Satellite Exclusion followed by Innovation Filtering) have been analysed, in order to select the technique which provides the best performance. Regarding the SA solution, the highest improvement is obtained by applying the NLOS SE + IF, providing an improvement of 34.60% applying the Data Collection 1, and an improvement of 39.08% applying the Data Collection 2. Regarding the DGNSS solution, the highest improvement is obtained by applying the NLOS SE + IF, providing an improvement of 42.62% applying the Data Collection 1, and an improvement of 40.95% applying the Data Collection 2.

The second goal of the section was the investigation of the performances of SA and DGNSS Standard EKF, implementing the Baseline Block and the Improvement Block configuration derived in the previous points. In particular, the performances of the proposed SA and DGNSS Standard EKF are compared firstly to the Benchmark EKF (section 7.3.3.3.3) and, successively, the other commercial PVT estimators (section 7.3.3.3.4).

Firstly, the SA Standard EKF has been compared to the SA Benchmark EKF. It provides an improvement of the 54.83% for Data Collection 1 and 57.51% for Data Collection 2. Therefore, the application of the proposed NLOS SE + IF Solution increases the performances of the corresponding PVT estimators with respect to the Benchmark solution.

Secondly, the DGNSS Standard EKF has been compared to the DGNSS Benchmark EKF. It provides an improvement of the 65.22% for Data Collection 1 and 68.62% for Data Collection 2. Therefore, the application of the proposed solution increases the performances of the corresponding PVT estimators with respect to the Benchmark solutions. As expected, the improvements introduced by the application of the Baseline Solution are higher for DGNSS PVT estimator than SA PVT estimator.

Thirdly, the SA Standard EKF has been compared to the SA Inertial Explorer and SA U-blox M8T. The proposed SA PVT estimator has better performances with respect to the SA IE commercial software solution, however, it has worst performances (2-3 meters higher RMSE) with respect to the SA U-blox M8T receiver solutions.

Finally, the DGNSS Standard EKF has been compared to the DGNSS Inertial Explorer and SA U-blox M8T error performances. The proposed DGNSS PVT estimator have higher performances with respect to the DGNSS IE commercial software solution, and, it has comparable performances with respect to the SA U-blox M8T receiver solutions.

7.3.4Temporally Correlated EKF (EKF-TC) Results

The section contains the results of the investigations proposed for the EKF-TC model incorporating the Time-Differenced EKF (TD EKF), presented in section 7.2. In the first section, 7.3.4.1, the EKF's configuration parameters applied to calculate the PVT estimations are presented. Section 7.3.4.2 provides the investigation of the SA EKF-TC model. Afterwards, Section 7.3.4.3 provides the evaluation of the DGNSS EKF-TC model.

7.3.4.1 EKF Parameter's Configuration

The EKF-TC parameters configuration is the same one applied for the Standard EKF estimator, described in section 7.3.3.1 with the addition of:

- $\tau_{PSR,l}$ is the GPS/Galileo PSR MN error temporal correlation as defined in section 6.4.1 and expressed as a function of speed;
- $\tau_{PSRR,l}$ is the GPS/Galileo PSR-R MN error temporal correlation as defined in section 6.4.2 and expressed as a function of speed.

7.3.4.2 SA EKF Results

This section summarizes the results of the proposed SA EKF-TC model.

The first goal of the section is the performances comparison between the SA EKF-TC estimator implementing the Baseline solution and the one implementing the Improvement Solution (section 7.3.4.2.1).

The second goal of the section is the performances comparison of the SA EKF-TC with the SA Standard EKF (section 7.3.4.2.2). The third goal is the comparison of the performances between the SA EKF-TC and the other commercial PVT estimators (section 7.3.3.2.4). Some final considerations are summarized in section 7.3.3.2.5.

7.3.4.2.1 Baseline Solution vs. Improvement Solution

This section analyses the performance of the SA EKF-TC with the application of Baseline Block and with or without the Improvement Block:

- Regarding the Data Collection 1:
  - The RMSE of EKF-TC with Baseline Block is equal to 13.53;
  - The application of NLOS Satellite Exclusion provides an improvement with respect to the Baseline Solution of 22.80%;
  - The application of Innovation Filtering provides slightly deterioration of the performances with respect to the Baseline Solution;
  - The application of NLOS Satellite Exclusion + Innovation Filtering provides an improvement with respect to the Baseline Solution of 18.91%.
- Regarding the Data Collection 2:
  - The RMSE of EKF-TC with Baseline Block is equal to 9.78m;
  - The application of NLOS Satellite Exclusion provides an improvement with respect to the Baseline Solution of 13.01%;
  - The application of Innovation Filtering provides slightly provides an improvement with respect to the Baseline Solution of 15.74%;
  - The application of NLOS Satellite Exclusion + Innovation Filtering provides an improvement with respect to the Baseline Solution of 31.04%.

The corresponding RMSE values and the relative improvements are summarized in Table 7-11.

Similarly, to the Standard EKF, the highest improvement is obtained by applying the NLOS SE + IF, while the lowest is obtained with the IF.

Position Error Estimation RMSE [m]	**SA EKF-TC**						
	Baseline	NLOS SE	**Impr. [%]**	IF	**Impr. [%]**	NLOS SE + IF	**Impr. [%]**
Data Collection 1	9.78	7.55	**22.80**	9.97	**---**	7.93	**18.91**
Data Collection 2	13.53	11.77	**13.01**	11.40	**15.74**	9.33	**31.04**

Table 7-11 – SA EKF-TC, Baseline Block performances vs. Improvement Block performances

7.3.4.2.2 Standard EKF vs EKF-TC

The Standard EKF and EKF-TC performances have been compared through the evaluation of the corresponding RMSE of the position error estimation calculated for the Data Collection 1 and Data Collection 2:

- Regarding Data Collection 1:
  - The RMSE of EKF-TC with Baseline Block is equal to 9.78 m against 12.63 m of the Standard EKF, providing an improvement of 22.5%.
  - The RMSE of EKF-TC with Baseline Block and NLOS SE is equal to 7.55 m, against 9.58 m of the Standard EKF, providing an improvement of 21.18%.
  - The RMSE of EKF-TC with Baseline Block and IF is equal to 9.97 m, against 11.70 m of the Standard EKF, providing an improvement of 14.78%.
  - The RMSE of EKF-TC with Baseline Block and NLOS SE + IF is equal to 7.93 m, against 8.26 of the Standard EKF, providing an improvement of 3.99%.
- Data Collection 2:
  - The RMSE of EKF-TC with Baseline Block is equal to 13.53 m against 14.61 m of the Standard EKF providing an improvement of 7.39%.
  - The RMSE of EKF-TC with Baseline Block and NLOS SE is equal to 11.77 m, against 10.69 m of the Standard EKF, providing a deterioration of the performances.
  - The RMSE of EKF-TC with Baseline Block and IF is equal to 11.40 m, against 11.70 m of the Standard EKF, providing an improvement of 2.56%.
  - w The RMSE of EKF-TC with Baseline Block and NLOS SE + IF is equal to 9.33 m, against 8.26 m of the Standard EKF, providing a slightly deterioration of the performances.

The corresponding RMSE values and the relative improvements are summarized in Table 7-12 for Data Collection 1 and Table 7-13 for Data Collection 2.

Another performances comparison can be obtained analyzing the residual belonging to the innovation vector of the Kalman filters in the two different configurations (Standard and TC) using Baseline Block, NLOS SE + IF.

The complexity of the Standard model is too limited to handle with the time correlated errors presented before. This is verified by the presence of structured residuals characterized by non-zero mean (different from white noise). An example is proposed in Figure 7-30 for the innovation vector obtained applying the Standard EKF on Dataset 1. The figure shows the behavior of the residuals obtained from the different satellite-in-view measurements, between 50s and 400s. The color of the lines is the same in order to focus on the general behavior and general characteristics. It is possible to notice a bias between the different residual, due to the presence of time correlated residual errors. The same analysis is applied in Figure 7-31 for the Time Correlated KF applied to Dataset 1. The residual in this case has similar behavior with respect to the previous case. The innovation vectors obtained for the whole dataset are depicted in Annex 10.5.1.

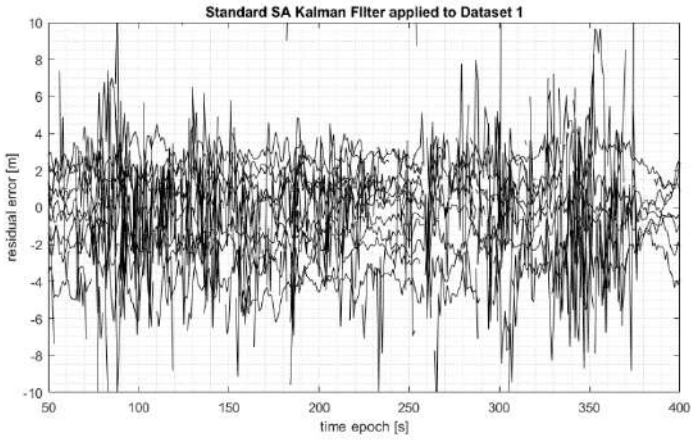

Figure 7-30 – Innovation residuals obtained for all satellite-in-view measurements applying the Stand Alone Standard EKF on Dataset 1

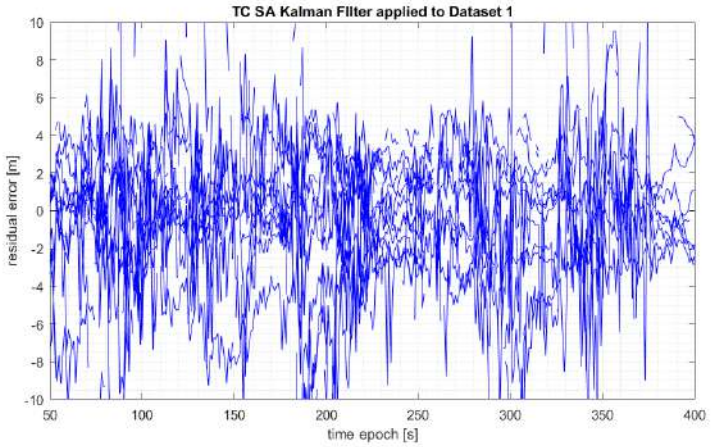

Figure 7-31 – Innovation residuals obtained for all satellite-in-view measurements applying the Stand Alone TC EKF on Dataset 1

Even though a slight improvement can be observed for Data Collection 1, this in not observed for Data Collection 2, therefore, it can be assumed that the application of EKF-TC in the configuration tested is not effective for SA PVT estimators and the improvements observed for Data Collection 1 are not due to the exploitation of the MN temporal characterization. The possible reason is that the presence of the satellite clock, ionospheric, and tropospheric errors, which are characterized by a larger temporal correlation than MN errors and are not spatially correlated on a small scale (the multipath environment), makes that the temporal correlation model based on MN characterization not suitable for SA measurements. Therefore, the application of the MN correlation time does not match a reliable model.

Another possible reason is related to the application of the Standard EKF every two epochs (see section 7.2.1), which does not take into account the correlation of the errors at this interval. Further works will compare the performances of the EKF-TC proposed in this work and the Time Differenced EKF obtained applying a propagation of the state predictions over two epochs.

Position Error Estimation RMSE [m]	**SA EKF-TC**			
	Data Collection 1			
	Baseline	NLOS SE	IF	NLOS SE + IF
Standard	12.63	9.58	11.70	8.26
Time Differenced	9.78	7.55	9.97	7.93
Improvements [%]	**22.5**	**21.18**	**14.78**	**3.99**

Table 7-12 – Comparison between the SA Standard EKF and EKF-TC, applied to Data collection 1

Position Error Estimation RMSE [m]	**SA EKF-TC**			
	Data Collection 2			
	Baseline	NLOS SE	IF	NLOS SE + IF
Standard	14.61	10.69	11.70	8.90

Time Differenced	13.53	11.77	11.40	9.33
Improvements [%]	**7.39**	**-**	**2.56**	**-**

Table 7-13 – Comparison between the SA Standard EKF and EKF-TC, applied to Data collection 2

7.3.4.2.3 Comparison with commercial PVT estimators

In this section are compared the results of SA EKF-TC with Baseline Measurement Model 1 followed by the NLO SE + IF Improvement Block, and the SA commercial PVT estimators, presented in section 7.3.1:

- Regarding Data collection 1:
  - The RMSE of the proposed solution is much lower than the RMSE of the SA IE estimations: 7.93 m vs. 24.44 m;
  - The RMSE of the Standard EKF with Baseline Solution is higher than the RMSE of the U-blox M8T estimations of roughly 1 m: 7.93 m vs. 6.73 m
- Regarding Data collection 2:
  - The RMSE of the Standard EKF with Baseline Solution is much lower than the RMSE of the SA IE estimations: 9.33 m vs. 22.96 m;
  - The RMSE of the Standard EKF with Baseline Solution is higher than the RMSE of the U-blox M8T estimations of about 3m: 8.90 m vs. 5.73 m.

The results are summarized in *Table 7-14*.

In conclusion, the proposed SA PVT estimator has better performances with respect to the SA IE commercial software solution, however, it has worst performances (2-3 meters higher RMSE) with respect to the SA U-blox M8T receiver solutions. The application of the Time Differenced technique and the MN temporal correlations do not provide any improvement on the performances of the proposed PVT estimator.

Position Estimation Error: RMSE [m]	**SA**		
	U-blox M8T	Inertial Explorer	Baseline +NLOS SE + IF
Data Collection 1	6.73	24.44	7.93
Data Collection 2	5.73	22.96	9.33

Table 7-14 – RMSE of the Proposed SA EKF-TC with Baseline + Improvement Blocks, compared to existing SA PVT estimators

7.3.4.2.4 Conclusions

In this section the performance of the SA EKF-TC with Baseline Block and the Improvement Block have been illustrated and investigated.

The first goal of the section was the performance comparison between the SA TD EKF estimator implementing the Baseline solution and the one implementing the Improvement Solution (section 7.3.4.2.1). Similar to the case of the Standard EKF, the highest improvement is obtained by applying the NLOS SE + IF.

The second goal of the section was the performance comparison of the SA TD EKF with the SA Standard EKF. Even though a slight improvement can be observed for Data Collection 1, this in not observed for Data Collection 2, therefore, it can be assumed that the application of EKF-TC is not effective for SA PVT estimators and the improvements observed for Data Collection 1 are not due to the exploitation of the MN temporal characterization. The possible reason is that the presence of the satellite clock, ionospheric, and tropospheric errors, which are characterized by a larger temporal correlation than MN errors and are not spatially correlated on a small scale (the

multipath environment), makes that the temporal correlation model based on MN characterization not suitable for SA measurements. Therefore, the application of the MN correlation time does not match a reliable model.

The third goal was the comparison of the performance between the SA TD EKF and the commercial PVT estimators (section 7.3.3.2.4). Some final considerations are summarized in section 7.3.3.2.5. The proposed SA PVT estimator has better performances with respect to the SA IE commercial software solution, however, it has worst performances (2-3 meters higher RMSE) with respect to the SA U-blox M8T receiver solutions. The application of the Time Differenced technique and the MN temporal correlations do not provide any improvement on the performances of the proposed PVT estimator.

7.3.4.3 DGNSS EKF Results

This section summarizes the results of the proposed DGNSS EKF-TC model.

The first goal of the section is the performances comparison between the DGNSS TD EKF estimator implementing the Baseline solution and the one implementing the Improvement Solution (section 7.3.4.2.1). The second goal of the section is the performances comparison of the DGNSS TD EKF with the DGNSS Standard EKF (section 7.3.4.3.2). The third goal is the comparison of the performances between the DGNSS TD EKF and the other commercial PVT estimators (section 7.3.3.2.4). Some final considerations are summarized in section 7.3.3.2.5.

7.3.4.3.1 Baseline Solution vs. Improvements Solution

The section analyses the performances of the DGNSS TD EKF with the application of Baseline Block and Baseline Block followed by the Improvement Block:

- Regarding the Data Collection 1:
  - The RMSE of TD EKF with Baseline Block is equal to 6.91 m;
  - The application of NLOS Satellite Exclusion provides an improvement with respect to the Baseline Solution of 20.40%;
  - The application of Innovation Filtering provides an improvement with respect to the Baseline Solution of 2.89%;
  - The application of NLOS Satellite Exclusion + Innovation Filtering provides an improvement with respect to the Baseline Solution of 49.20%.
- Regarding the Data Collection 2:
  - The RMSE of TD EKF with Baseline Block is equal to 8.03 m;
  - The application of NLOS Satellite Exclusion provides an improvement with respect to the Baseline Solution of 20.42%;
  - The application of Innovation Filtering provides an improvement with respect to the Baseline Solution of 13.45%;
  - The application of NLOS Satellite Exclusion + Innovation Filtering provides an improvement with respect to the Baseline Solution of 42.59%.

The corresponding RMSE values and the relative improvements are summarized in Table 7-15.

The highest improvement is obtained by applying the NLOS SE + IF, while the lowest is obtained with the IF.

Position Error Estimation RMSE [m]	**DGNSS EKF-TC**						
	Baseline	NLOS SE	**Impr. [%]**	IF	**Impr. [%]**	NLOS SE + IF	**Impr. [%]**
Data Collection 1	6.91	5.50	**20.40**	6.71	**2.89**	3.51	**49.20**

Data Collection 2	8.03	6.39	**20.42**	6.95	**13.45**	4.61	**42.59**

Table 7-15 – DGNSS EKF-TC, Baseline Block performances vs. Improvement Block performances

7.3.4.3.2 Standard EKF vs EKF-TC

The Standard EKF and EKF-TC performances have been compared through the evaluation of the corresponding RMSE of the position error estimation calculated for the Data Collection 1 and Data Collection 2:

- Regarding Data Collection 1:
  - The RMSE of TD EKF with Baseline Block is equal to 6.91 m against 8.28 m of the Standard EKF providing an improvement of 16.54%;
  - The RMSE of TD EKF with Baseline Block and NLOS SE is equal to 5.50 m, against 7.58 m of the Standard EKF, providing an improvement of 27.44%;
  - The RMSE of TD EKF with Baseline Block and IF is equal to 6.71 m, against 6.32 m of the Standard EKF, providing a slightly deterioration of the performances;
  - The RMSE of TD EKF with Baseline Block and NLOS SE + IF is equal to 3.51 m, against 4.75 m of the Standard EKF, providing an improvement of 26.10%.
- Regarding Data Collection 2:
  - The RMSE of TD EKF with Baseline Block is equal to 8.03 m against 9.62 m of the Standard EKF providing an improvement of 16.53%;
  - The RMSE of TD EKF with Baseline Block and NLOS SE is equal to 7.85 m, against 6.39 m of the Standard EKF, providing an improvement of 18.60%;
  - The RMSE of TD EKF with Baseline Block and IF is equal to 6.95 m, against 8.95 m of the Standard EKF, providing an improvement of 22.35%;
  - w The RMSE of TD EKF with Baseline Block and NLOS SE + IF is equal to 4.61 m, against 5.68 m of the Standard EKF, providing an improvement of 18.84%

The corresponding RMSE values and the relative improvements are summarized in Table 7-16 f or Data Collection 1 and Table 7-17 for Data Collection 2.

The measurement residuals obtained from the innovation vector for Standard and TC Kalman Filter suing Baseline Block, NLOS SE + IF, applied to Dataset 1, have been analyzed in the next paragraph.

Figure 7-32 depicts the innovations for Standard KF (red lines) and TC KF (green lines), between 50s and 400s (results for a larger period are presented in Annex 10.5.1). Contrarily to the SA case, in this case the TC residuals are more zero-centred and less spreader than the corresponding Standard results.

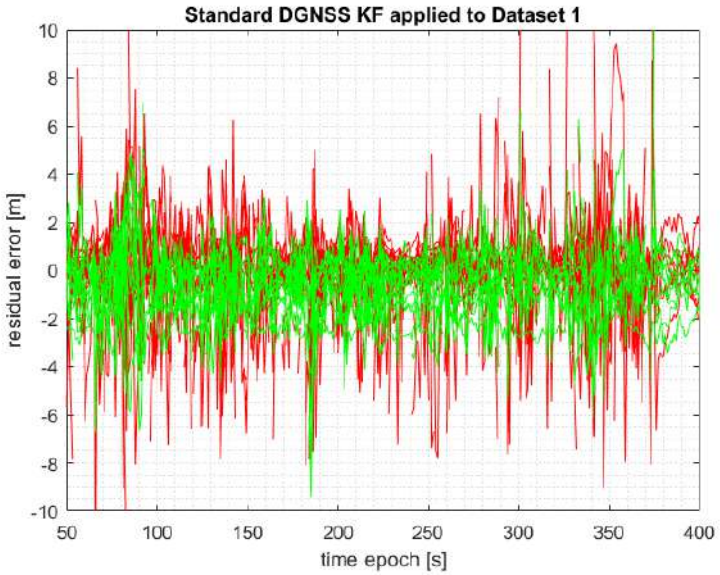

Figure 7-32 – Innovation residuals obtained for all satellite-in-view measurements applying the DGNSS Standard and TC EKF on Dataset 1. The red lines are the innovations obtained applying Standard EKF. The green lines are the innovations obtained applying TC EKF

Contrary to what has been observed for SA, for DGNSS a general improvement of the performance applying the EKF-TC is noted, for both the Data Collections. The improvement is between 15% and 30%. As expected, the temporal correlation model based on MN characterization is more reliable and effective on the DGNSS PVT solution since the MN errors are the main error components of the GNSS measurements.

Position Error Estimation RMSE [m]	**DGNSS**			
	Data Collection 1			
	Baseline	NLOS SE	IF	NLOS SE + IF
Standard	8.28	7.58	6.32	4.75
Time Differenced	6.91	5.50	6.71	3.51
Improvements [%]	**16.54**	**27.44**	**-**	**26.10**

Table 7-16 – Comparison between the DGNSS Standard EKF and EKF-TC, applied to Data collection 1

Position Error Estimation RMSE [m]	**DGNSS**			
	Data Collection 2			
	Baseline	NLOS SE	IF	NLOS SE + IF
Standard	9.62	7.85	8.95	5.68
Time Differenced	8.03	6.39	6.95	4.61
Improvements	**16.53**	**18.60**	**22.35**	**18.84**

[%]				

Table 7-17 – Comparison between the DGNSS Standard EKF and EKF-TC, applied to Data collection 2

7.3.4.3.3 Comparison with commercial PVT Estimators

This section compares the results of DGNSS EKF-TC with Baseline Measurement Model 1 followed by the NLO SE + IF Improvement Block, and the DGNSS commercial PVT estimators, presented in section 7.3.1.

The norm of the position error estimation and the corresponding RMSE of the DGNSS EKF-TC with Baseline Measurement Model 1 followed by the NLO SE + IF Improvement Block, of the DGNSS Inertial Explorer and of the U-blox M8T, applied to Data Collection 1, are portrayed in Figure 7-33.

The norm of the position error estimation and the corresponding RMSE of the DGNSS EKF-TC with Baseline Measurement Model 1 followed by the NLO SE + IF Improvement Block, of the DGNSS Inertial Explorer and of the U-blox M8T, applied to Data Collection 2, are portrayed in Figure 7-34.

- Regarding Data collection 1 (Figure 7-33):
  - The RMSE of the proposed solution is lower than the RMSE of the SA IE estimations: 3.51 m vs. 6.91 m;
  - The RMSE of the Standard EKF with Baseline Solution is 2m lower than the RMSE of the U-blox M8T estimations: 3.51 m vs. 6.73 m.
- Regarding Data collection 2 (Figure 7-34):
  - The RMSE of the Standard EKF with Baseline Solution is lower than the RMSE of the SA IE estimations: 4.61 m vs. 9.66 m;
  - The RMSE of the Standard EKF with Baseline Solution is 1m lower than the RMSE of the U-blox M8T estimations: 4.61 m vs. 5.73 m.

The results are summarized in Table 7-7.

In conclusion, the proposed DGNSS PVT estimator has better performance with respect to the DGNSS IE commercial software solution, and the SA U-blox M8T receiver solutions. The application of the Time Differenced technique and the MN temporal correlations provide a fundamental improvement on the performances of the proposed PVT estimator. Whilst it is true that the U-blox solution does not benefit from the differential corrections, it is expected that MP is the primary error contributor. There is therefore, a clear motivation to consider SBAS aiding of a low-cost receiver in partnership with the time-differenced EKF architecture and the modelling approach presented.

Position Estimation RMSE [m]	SA U-blox M8T	DGNSS Inertial Explorer	DGNSS Baseline +NLOS SE + IF
Data Collection 1	6.73	9.74	3.51
Data Collection 2	5.73	9.66	4.61

Table 7-18 – RMSE of the Proposed DGNSS EKF-TC with Baseline + Improvement Blocks, compared to existing PVT estimators

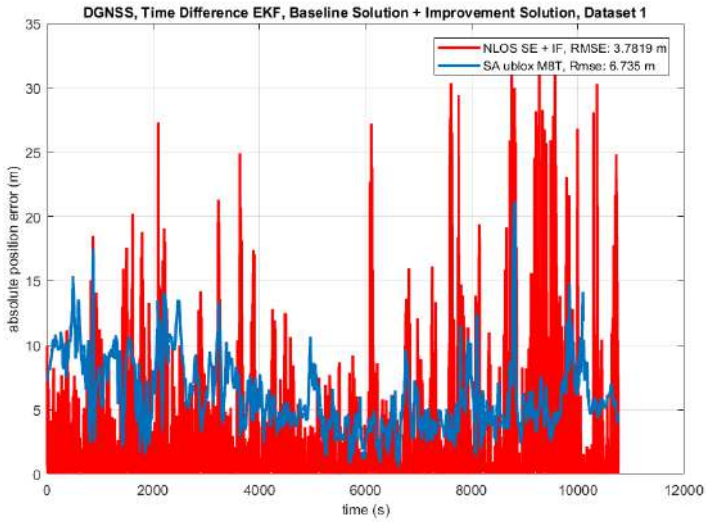

Figure 7-33 – Absolute Position estimation error with the corresponding RMSE: Dataset 1, DGNSS EKF-TC with Baseline Block and NLOS SE + IF (red line) vs. SA U-Blox M8T (blue line)

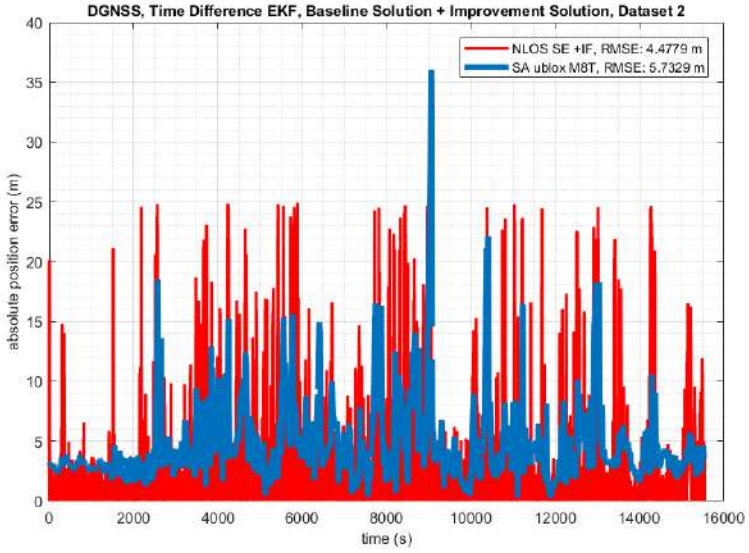

Figure 7-34 – Absolute Position estimation error with the corresponding RMSE: Dataset 2, DGNSS EKF-TC with Baseline Block and NLOS SE + IF (red line) vs. SA U-blox M8T (blue line)

7.3.4.3.4 Conclusions

In this section the performance of the DGNSS EKF-TC with Baseline Block and the Improvement Block have been illustrated and investigated.

The first goal of the section was the performances comparison between the DGNSS TD EKF estimator implementing the Baseline solution and the one implementing the Improvement Solution (section 7.3.4.2.1). The highest improvement is obtained by applying the NLOS SE + IF, while the lowest is obtained with the IF.

The second goal of the section was the performances comparison of the DGNSS TD EKF with the DGNSS Standard EKF. Contrarily to what has been observed for SA, for DGNSS it can be notice a general improvement of the performance applying the EKF-TC, for both the Data Collection under exam. The improvement is between 15% and 30%. As expected, the temporal correlation model based on MN characterization is more reliable and effective on the DGNSS PVT solution since the MN errors are the main error components of the GNSS measurements.

The third goal was the comparison of the performances between the DGNSS TD EKF and the other commercial PVT estimators (section 7.3.3.2.4). Some final considerations are summarized in section 7.3.3.2.5. The proposed DGNSS PVT estimator has better performance with respect to the DGNSS IE commercial software solution, and the SA U-blox M8T receiver solutions. The application of the Time Differenced technique and the MN temporal correlations provide a fundamental improvement on the performances of the proposed PVT estimator.

7.4 Conclusions

The results and conclusions obtained for the PSR/PSR-R MN error characterization, the LOS/NLOS empirical discrimination and temporal PSR/PSR-R MN error correlation characterization as a function of the receiver speed (Chapter 6) have been exploited to design a MN mitigation technique for a low-cost GNSS PVT estimator algorithm, applied in the urban environment.

The techniques identified as possible low-cost mitigation solutions to multipath degradation for the EKF algorithm include measurement weighting, measurement masking and decorrelation of the measurements (through for example a time difference architecture [8].

Two different EKF architectures have been proposed in the chapter:

The ***first EKF architecture***, called the Standard EKF based on MN statistics, enhances the benefits of the basic Weighting and Masking techniques using empirical MP error models and reduces their limitations, exploiting the knowledge of the *a priori* MN error distributions of the PSR and PSR-R measurements and LOS/NLOS reception state discrimination, using the methodology provided in Chapter 5. The proposed EKF architecture differs from the benchmark one by the implementation of:

- the Baseline Block which calculates the time-variant Measurement Error Covariance Matrix, as a function of the MN error statistics;
- the Improvement Block: applied before the Baseline Block which excludes the low-quality measurements, through the application of some Satellite Exclusion Techniques, exploiting a conditional threshold based on both LOS/NLOS C/N_0 discrimination threshold and the MN error statistics.

The ***second EKF architecture***, called the EKF Time Correlated and incorporating a Time-Differenced EKF also using on MN statistics. Contrary to the Standard EKF, it also exploits the models of MN error temporal correlations as a function of the receiver speed. The EKF design is based on the Time Differencedd EKF proposed in [1], [2].

Some conclusions regarding the ***first EKF architecture*** are given below:

The use of **clock tuning** in the Benchmark SA and DGNSS EKF both lead to a slight reduction of the RMSE, **around 10%**. Despite this change, clock tuning alone is ineffective against the largest error spikes. Secondly, the SA Standard EKF has been compared to the SA Benchmark EKF. The proposed Standard EKF, *improves* ***performance*** *with respect to the Benchmark solution*, with both configurations (**between 23% and 31%**). The SA Standard EKF with Baseline Solution, has **better** results with respect to **Inertial Explorer**, while the performance is **worse** than the **U-blox** solution, as described in section 7.3.3.2.4. Thirdly, the DGNSS Standard EKF has been compared to the DGNSS Benchmark EKF. The application of the proposed Standard EKF ***improves the performance*** *with respect to the Benchmark solution* (**between 38% and 46%**), greater than SA PVT estimator (**between 23% and 31%**). The DGNSS Standard EKF with Baseline Solution, is **comparable** to Inertial Explorer performance, while they are **worse** than SA U-blox solutions, 8.37 m against 6.73 m for data collection 1, 9.62 m against 5.73 m for data collection 2. In conclusion, the application of the Standard EKF with Baseline Block improves the performances of the PVT estimates, with respect to the basic EKF but **does not reach U-blox** proprietary performance levels.

The Improvement Block consists of the application of the NLOS Satellite Exclusion, and Satellite Measurement Selection based on innovations filtering (IF). The **optimal C/N0 threshold** was found to be $C/N_0 = \mathbf{35\ dB\text{-}Hz}$. The performance of the SA Standard EKF based on MN statistics, applying both Baseline and **Improvement** Blocks, have been compared to the SA Standard EKF with Baseline Block. The highest improvement is obtained by applying the NLOS SE + IF (**34.60%** for **Data Collection 1** and **39.08%** for the **Data Collection 2**). The SA Standard EKF with Baseline and Improvement Blocks has been compared to the SA Inertial Explorer and SA U-blox M8T error performances. The RMSE of the proposed EKF is still higher than the RMSE of the SA U-blox M8T receiver: **8.24 m vs. 6.73** for Data Collection 1, 8.90 vs. 5.73 for Data Collection 2.

The performance of the DGNSS Standard EKF applying the Baseline and Improvement Blocks (NLOS SE + IF) lead to an improvement of **42.62%** for **Data Collection 1** and **40.95%**, for **Data Collection 2**. The DGNSS Standard EKF with Baseline and Improvement Block have been compared to DGNSS Inertial Explorer and SA U-blox M8T solutions. The RMSE of the proposed EKF is **lower** than for the SA U-blox M8T the data collection 1, **4.75 m vs. 6.73** while they are comparable for the data collection 2, **5.68 m vs. 5.73 m**. The application of the

C/N0-based NLOS Satellite Exclusion followed by Innovation Filtering improves the performance of the PVT estimates. Performance is comparable to the proprietary U-blox M8T solution.

Some conclusions regarding the ***second EKF architecture*** are given below:

The Time Difference EKF algorithm employs the modelling of the temporal correlation as a function of speed performed in section 10.4.3.2. In the standalone case, only a small improvement is observed with respect to the Standard EKF. Therefore, the performances of the SA Time Difference EKF based on MN statistics, applying the Baseline Block and the Improvement Block, have been compared to the corresponding SA Standard EKF. The presence of the satellite clock, ionospheric, and tropospheric errors, which are characterized by a larger temporal correlation than the MN errors implies that the MN temporal correlation model is not suitable for SA measurements.

Contrary to what has been observed for SA, for DGNSS a **performance improvement** is observed applying the Time Difference EKF, for both Data Collections (**15%** and **30%.**). As expected, the temporal correlation model based on MN characterization is more reliable and effective on the DGNSS PVT solution since multipath and noise are the main sources of error.

8 Conclusions and Recommendations for Future Works

In Chapter 1, it was well **established** that there is an ongoing growth in GNSS applications in micromobility services, often employing the use of low-cost receiver technologies. Such applications operate frequently in the urban environment where, issues due to loss-of-tracking, multipath and Non-Line-of-Sight (NLOS) errors are common. The work in this thesis has **justified focusing** on low-cost solutions to mitigate these issues. Whilst it is true that fusing GNSS with an IMU is now a relatively low-cost solution, it adds complexity to the testing and research process and has thus been excluded from this study.

The solution proposed in this PhD thesis has consisted of three phases. Firstly, to provide a **methodology** to **isolate** the GNSS pseudorange and pseudorange rate errors in the **urban environment** as a result of **multipath** and thermal noise (MN). Secondly, to **statistically characterize** and **model** these errors. Thirdly, **to exploit** these **models** through **refined Kalman Filter architectures** to improve the positioning accuracy.

The study has focused on the GPS L1 C/A and Galileo E1 signals due their interoperable properties. The single frequency solution was chosen as the **lowest cost study case** whilst it is understood that dual-frequency solutions for micromobility are growing. The methodology may equally be applied in future to other signals and constellations. Both a classical and **time differenced** Extended Kalman filter architecture have been studied in both **standalone** and **DGNSS** modes. **Aiding** from freely available SBAS or ubiquitous low-cost **differential solutions** in future are likely to make the DGNSS model more accessible to micromobility applications.

This chapter summarises the main achievements of the PhD in the following section (8.1), followed by a summary of proposed future work in section (8.2).

8.1 Thesis Achievements

The introduction of Chapter 1 defined the scope of the application domain and the **high-level research problem** of addressing the **multipath and noise errors present in the urban environment**. Chapters 2 and 0 have summarised in detail the state-of-the-art relating to the problem and refined the research question to modelling the error models for aiding weighting and masking within innovated EKF architectures.

In Chapter 0 the **impact** of **multipath** phenomenon in **LOS** and **NLOS** reception state on the **FLL tracking process** has been **theoretically analyzed**. The **FLL tracking error** model in the steady-state regime was determined to be equal to the addition of the FLL discriminator bias plus the discriminator noise filtered by closed-loop transfer function. The final goal was to determine the **FLL tracking error PDF** due to the presence of multipath and thermal noise and to compare the result to empirical PDFs models obtained from collected data in chapter 6; the goal was achieved by determining specific **FLL tracking error PDFs** as a function of the carrier phase and Doppler frequency displacements and by averaging the specific PDFs by their probability of occurrence (carrier phase and Doppler frequency displacements PDFs).

Firstly, the **Doppler frequency displacement** was derived from a dynamic GNSS receiver moving through the urban canyon. The **LOS** and **NLOS Doppler frequency displacement PDFs** were found to be **symmetric** and **centered distributions**, with high concentrations of values around the 0 Hz frequency. **NLOS** Doppler frequency displacement PDF is **spread greater than** for **LOS** receiver state conditions.

Secondly, the **Cross-Product** (CP) discriminator **tracking error bias** in the steady-state regime depending on the Doppler frequency and on the carrier phase displacements was analyzed. The absolute value of the FLL tracking error bias for a **MLR = ½** is **never larger** than **20 Hz** and for a **MLR = ¼** is **never larger** than **12 Hz**. Thirdly, the **Cross-Product** (CP) discriminator **error noise PDF** was analyzed**.** The PDF was determined to be centered gaussian with a variance value depending on the **carrier phase and Doppler frequency displacements** as well

as $\boldsymbol{C/N_0}$**received signal** C/N_0. Irrespective of the C/N_0, the variance presents minima at multiples of the inverse of the correlation time and maxima at the Doppler frequency displacement values equally placed between two minima. Its **value goes** from **few Hz²** for 50 dB-Hz **to** about **80 Hz²** for 30 dB-Hz.

Finally, the **FLL tracking error PDF** in presence of multipath and thermal noise was derived. The PDF is **similar to** a **Gaussian PDF** but with a **higher concentration** of **values** around the **0 Hz frequency**. This concentration around the 0 Hz frequencies is probably due to the Doppler frequency displacement PDF (overweighting the discriminator noise Gaussian PDF). Finally, the derived FLL tracking error PDF is marginal for small error values even for low C/N_0, such as 30 dB-Hz.

In Chapter 5 a **methodology** for the **isolation** of the **multipath and noise** has been **successfully developed**. Certain difficulties have been **overcome** to achieve this, starting from the selection of a **differential metric**. This was **justified** by the fact that the low-cost user receiver in an urban environment has a multipath and noise error component which dominates the residual signal-in-space errors, residual atmospheric errors and reference station local errors. It was also **argued** that the alternative employing the levelled code-minus-carrier statistics is not suitable for NLOS error isolation. Particular **challenges** in this **development** were resolving the receiver clock, to avoid contamination from NLOS errors and resolving the inter-constellation processing bias.

A second thread of study in Chapter 5 addressed the possibility to **detect** (or **discriminate**) **NLOS signals**. The notion here was to use a fish-eye to provide a truth reference and led to the use of a C/N0 based mask to exclude measurements with elevated risk of being from NLOS receptions. The methodology was applied in Chapter 6 with the comprehensive data collection. This work **partially validated this approach**, although further study into refining both the truth and also the mask (i.e. incorporating other parameters) might be envisaged. A value of **35 dB-Hz was selected** as the **optimal** trade-off between reliable measurement exclusion and maintaining satellite geometry. Below **30 dB-Hz**, the empirical distributions were found to be non-zero mean, with inflated variances (**15-50m**) and non-Gaussian in shape. Above **40 dB-Hz**, the empirical distributions were found to be zero mean, with reasonable variances (between **1-4m**) and a Gaussian-like shape.

Also developed in Chapter 5 were methodologies to estimate the temporal correlation of multipath and noise errors. It was concluded that a one-size-fits-all approach to temporal correlation was not representative, and that **spatial correlation** should be characterised. Two **innovative techniques** were developed, and the **speed-dependent model selected** and applied.

Chapter 5 also described the steps taken in **characterization** and **modelling** of the **isolated multipath and noise errors**. Analysis was performed which concluded that $\boldsymbol{C/N_0}$ is the **preferred indicator** of strong multipath. Furthermore, the **ideal bin size** for the C/N_0 parameterisation was investigated. The **statistical properties** of the sample data were then determined in the Chapter 6 analysis; mean, std. dev., empirical PDF. In Chapter 6, **Gaussian error models** were derived from the raw models through **CDF overbounding at the 95% level**.

In Chapter 6, the multipath and noise **isolation**, **characterization** and **discrimination** methodologies were applied to a **substantial data collection** of **50 hours** obtained in Toulouse city centre.

The **GPS PSR MN** error model is characterized as follows. The **sample average** is around **0** for the $\boldsymbol{C/N_0 \geq 40}$ **dB-Hz**, between **0.01m and 5m** for $\boldsymbol{40 < C/N_0 < 35}$ **dB-Hz**, and between **5m and 40m** for the $\boldsymbol{C/N_0 < 35}$ **dB-Hz**. The **sample standard deviation** is around **0.9m and 4m** for the $\boldsymbol{C/N_0 \geq 40}$ **dB-Hz**, between **4m and 11m** for $\boldsymbol{40 < C/N_0 < 35}$ **dB-Hz**, and between **11m and 50m** for $\boldsymbol{C/N_0 < 35}$ **dB-Hz**. The PSR MN error PDFs are comparable to the theoretical assumptions derived in Chapter 0.

On the contrary, the **GPS PSR-R MN** error model is characterized a **sample mean** around **0m/s for all the** $\boldsymbol{C/N_0}$ values and a **sample standard deviation** progressively increasing as a function of the C/N_0 decrease: **from 0.06m/s for** $\boldsymbol{57.5 \leq C/N_0 < 60}$ **dB-Hz to 6.52m/s for** $\boldsymbol{12.5 \leq C/N_0 < 15}$ **dB-Hz**. The PSR-R MN error PDFs are comparable to the theoretical assumptions derived in Chapter 0.

The **Galileo PSR MN** error model is characterized as follows. The **sample mean** is around **1m** for $\boldsymbol{40 \leq C/N_0 < 35}$ **dB-Hz**, between **1m and 50m for the** $\boldsymbol{C/N_0 < 35}$ **dB-Hz**, but **always lower than** the corresponding value of **GPS MN model** in the same C/N_0 bin. The **sample standard deviation** is around **2m and 3m** for the $\boldsymbol{C/N_0 > 40}$ dB-Hz, between **3m and 6m** for $\boldsymbol{40 \leq C/N_0 < 35}$ **dB-Hz**, and between **5m and 50m** for $\boldsymbol{C/N_0 < 35}$ **dB-Hz**, but **always lower** than the corresponding value of **GPS MN model** in the same C/N_0 bin. The PSR MN error PDFs are comparable to the theoretical assumptions derived in Chapter 0.

The **Galileo PSR-R MN** error model is characterized by a **sample average** around **0m/s** for **all the C/N_0** values and a sample **standard deviation** between **0.08m/s for $50 \leq C/N_0 < 52.5$ dB-Hz** to **7m/s for $7.5 \leq C/N_0 < 10$ dB-Hz**. The PSR-R MN error PDFs are comparable to the theoretical assumptions derived in Chapter 4.

Correlation times for **pseudoranges** ranged from around **5s for static** and very low speed dynamics to around **1s for high-speed dynamics**. Correlation times for **pseudorange-rates** ranged from around **0.5s for static** and very low speed dynamics to around <**0.2s for high-speed dynamics**.

In Chapter 7, the modelling described in Chapter 5 and applied in Chapter 6 has been **exploited for improved positioning accuracy**. In particular a Standard EKF has been developed incorporating both measurement **de-weighting** and **exclusion** on the basis of the **empirical models**. In particular the **innovations filtering** used to aid measurement exclusion benefits from the empirical models for **multipath and thermal noise**.

Furthermore, a time-differenced EKF architecture has been **successfully implemented**. In order to perform this implementation, the time-correlation models developed and applied in Chapter 5 and Chapter 6 respectively, were required. This work has partially **validated** with **real-data** the **time-differenced EKF architecture** proposed in [1], [2]. Moreover, it required the use of an **innovative speed-dependent model** for the **temporal correlation**. This approach led to a significant improvement in positioning accuracy, particularly for the DGNSS solution and may be further improved as discussed in future work.

The final configuration of the proposed Standard EKF includes the use of the NLOS Satellite Exclusion and Innovation Filtering techniques.

Positioning performance of the tested solutions **surpassed** the performances of the benchmark EKF with an RMSE of 8.26m vs 18.29m and 4.75m vs 13.66m for the standard EKF standalone and DGNSS solutions respectively, and 7.93 m vs 18.29m and 9.33 m vs 13.66m for time-differenced EKF standalone and DGNSS solutions respectively.

Positioning performance of the tested solutions **surpassed** the commercial PVT solution of Inertial Explorer with an RMSE of 8.26 m vs. 24.44 m and 4.75 m vs. 9.75 m for the standard EKF standalone and DGNSS solutions respectively, and 7.93 m vs. 24.44 m and 3.51 m vs. 6.91 m for time-differenced EKF standalone and DGNSS solutions respectively.

Positioning performance of the tested solutions **do not surpass** the U-blox M8T performances with an RMSE of 8.26 m vs. 6.73 m for the standard EKF standalone and 7.93 m vs. 6.73 m for time-differenced EKF standalone and solutions.

Positioning performance of the tested solutions **surpassed** the U-blox M8T performances with an RMSE of 4.75 m vs. 6.75 m for the standard EKF DGNSS and 3.51 m vs. 6.73 m for time-differenced EKF standalone and solutions.

The results have shown that in the case of the standalone positioning system **comparable** performance to U-Blox is achieved in spite of not having access to internal processing information relating to clock behaviour and tracking indicators.

8.2 Recommendations for future work

According to the results presented in this PhD dissertation, several questions are raised and can be used by the reader as some recommendations for future works.

- Proposed MN isolation methodology from pseudorange and pseudorange-rate measurements

To be more effective, the isolation methodology could exploit the Doppler measurements to calculate the receiver clock drift and, consequently, to have a refinement of the receiver clock bias, allowing a more reliable receiver clock bias exclusion and, consequently, a more accurate MN error isolated error components.

The isolation methodology is applied to single-frequency GNSS measurements to fulfil the requirements of proposing a methodology for low-cost GNSS receiver. Nevertheless, nowadays, several low-cost receiver starts to be implemented with dual frequency signal processing modules. Therefore, an interesting improvement of this methodologies could be the extension to dual frequency pseudorange and pseudorange-rate measurements.

The effectiveness of the MN isolation methodologies resides in the possibility to access a large amount of data, used to characterize the statistical properties of the MN errors. Therefore, the data collected during this PhD work (around 50h of data) is just an initial work that must be extended with several data campaigns in order to improve the reliability of the statistical models.

Another suggestion is related to an improved solution to characterize the MN errors in urban environment. Even if the urban environment is complex to be modelled, is very diverse in terms of geometric components and dynamic elements making a precise characterization very complex, a possible improvement could be the characterization of MN errors for different urban environment sections, obtained individuating urban sections which have similar geometric properties.

Finally, in this PhD work it has been used only the Ublox M8T to characterize the MN error components. It is suggested to apply the investigations proposed in this dissertation using with different GNSS receivers.

- Proposed image processing LOS/NLOS classification used to define the empirical C/N_0 LOS/NLOS threshold

In this work a grey-scale color camera has been applied. However, several limitations, described in Chapter 5, prevents the image processing the be more accurate and to provide a refined empirical C/N_0 LOS/NLOS threshold estimation. Therefore, it is proposed to apply a different camera, i.e. with a full color camera it is possible to improve the sky area detection in the pictures.

- Proposed NLOS/LOS classification methodology

This dissertation proposed an empirical C/N_0 LOS/NLOS threshold to discriminate between the LOS and NLOS receiver reception states. However, the use of only C/N_0 observable is only indicative of the LOS/NLOS behavior. Therefore, a fundamental improvement should be the introduction of more observable parameters used together to obtain a more realistic LOS/NLOS discrimination. The application of elevation angle, azimuth angle and C/N_0 parameters could improve it a decisive manner.

- Proposed MN characterization methodology

The final MN characterization is obtained by applying a classification of the MN errors as a function of the relative C/N_0 and calculating the corresponding Probability density function, sample average and sample mean. Even in this case, a general improvement could be brought by the introduction of other classification parameters. For example, a MN error classification based on the relative C/N_0, elevation angle and azimuth angle could be more representative and may result in a refinement of the MN error characterization, continuing to be easy to exploit in a KF-based PVT solution.

- Proposed EKF-based PVT architecture

The application of a generic EKF state model represents a limitation of the performances of the proposed solutions. It is firstly envisaged to express the EKF state model in the right body frame. Since this work is mainly focused on the localization/navigation of vehicles for micromobility, an important improvement could be assessed by the refinement of the EKF state model with respect to the generic dynamics of a vehicle in an urban environment.

The clock tuning operation presented in this work is applied on a data collection conducted in the urban environment. The accuracy of the receiver clock EKF model, therefore, is impacted by the presence of the multipath error components. It is therefore proposed to the lecture to apply a clock tuning operation independently, with a data collection conducted in open-sky environment.

A low-cost alternative for the DGNSS positioning technique could be the application of SBAS corrections which are sent by internet connection to the GNSS receiver mounted on the vehicles.

The Time Difference EKF algorithm, proposed in this PhD work, avoid the correlation existing between measurement differences sharing a common epoch (i.e., not between differenced measurements separated by more than one epoch), by simply differencing applying a combination of a standard EKF update and a time-differenced EKF update are used. However, another possibility is to perform the state prediction over two epochs instead of using the standard EKF update. A comparison of the two approaches should be treated in future work.

- Other PVT architectures

Amore complex PVT solution will be implemented taking into account the non-Gaussianity of the pseudorange NLOS multipath error measurements, as the exploitation of the Particle Filter.

The application of low-cost IMU should allow to have slightly improvements of the PVT performances. Therefore, it is highly recommended to apply a GNSS-aided solution.

9 Bibliography

[1] M. G. Petovello, K. O'Keefe, G. Lachapelle, and M. E. Cannon, "Consideration of time-correlated errors in a Kalman filter applicable to GNSS," *J. Geod.*, vol. 83, no. 1, pp. 51–56, 2009.

[2] M. G. Petovello, K. O'Keefe, G. Lachapelle, and M. E. Cannon, "Erratum to: Consideration of time-correlated errors in a Kalman filter applicable to GNSS (J Geod, (2009), 83, (51-56), 10.1007/s00190-008-0231-z)," *J. Geod.*, vol. 85, no. 6, pp. 367–368, 2011.

[3] Víctor Moyano and Josep Laborda, "ARIADNA - D3.1 - The role and challenges of GNSS for Urban Mobility and Public Transport," no. 870264, pp. 1–39.

[4] Mike Horton and Jens Windau, "Catching a Ride: Improvements to Position Accuracy for eMobility Applications," *Insid. GNSS*, no. April, 2021.

[5] European Global Navigation Satellite Systems Agency, *GSA GNSS Market Report 2019*, no. 6. 2019.

[6] C. Xue, P. Psimoulis, Q. Zhang, and X. Meng, "Analysis of the performance of closely spaced low-cost multi-GNSS receivers," *Appl. Geomatics*, 2021.

[7] L. Biagi, F. Grec, and M. Negretti, "Low-cost GNSS receivers for local monitoring: Experimental simulation, and analysis of displacements," *Sensors (Switzerland)*, vol. 16, no. 12, 2016.

[8] A. Cina and M. Piras, "Performance of low-cost GNSS receiver for landslides monitoring: test and results," *Geomatics, Nat. Hazards Risk*, vol. 6, no. 5–7, pp. 497–514, 2015.

[9] G. W. Hein, "GNSS Interoperability: Achieving a Global System of Systems or "Does Everything Have to Be the Same?"," no. 57, pp. 57–60, 2006.

[10] GMV, "Principles of Interoperability among GNSS," 2011. [Online]. Available: https://gssc.esa.int/navipedia/index.php/Principles_of_Interoperability_among_GNSS#:~:text=In the GNSS context%2C interoperability,respect to the standalone system.

[11] International Civil Aviation Organisation, "Global Navigation Satellite System (GNSS) Manual," pp. 1–69, 2005.

[12] D.E. Kaplan and J.C. Hegarty, "Understanding GPS: Principles and Applications. Second edition," 2006.

[13] J. Subirana, J. Zornoza, and M. Hernández-Pajares, *Gnss Data Processing*, vol. II. 2013.

[14] P. Viswanath and M. Mathew, "Autonomous road vehicles localization using satellites , lane markings and vision," pp. 1–9, 2017.

[15] P. D. Groves, "Principles of GNSS, inertial, and multisensor integrated navigation systems, 2nd edition," *IEEE Aerosp. Electron. Syst. Mag.*, vol. 30, no. 2, pp. 26–27, 2015.

[16] F. DILSSNER, "GPS IIF-1 Satellite Antenna Phase Center and Attitude Modeling," *Insid. GNSS*, pp. 59–64, 2010.

[17] R. Gold, "Optimal Binary Sequences for Spread Spectrum Multiplexing," vol. 13, pp. 619–621, 1967.

[18] C. J. H. Elliott D. Kaplan, *Understanding GPS. Principles and applications*, vol. 59, no. 5. 1997.

[19] S. Gleason and D. Gebre-Egziabher, *GNSS applications and methods*. 2009.

[20] Enik Shytermeja, "Design and Performance of a GNSS Single-frequency Multi-constellation Vector Tracking Architecture for Urban Environments," 2017.

[21] GSA, "European GNSS (Galileo) Open Service, Signal In Space Interface Control Document," 2010.

[22] J.-A. Avila-Rodriguez *et al.*, "CBOC : an implementation of MBOC," 2014.

[23] O. Julien *et al.*, "1-bit processing of composite BOC (CBOC) signals," 2014.

[24] V. Heiries, D. Roviras, L. Ries, and V. Calmettes, "Analysis of non ambiguous BOC signal acquisition

performance," *Proc. 17th Int. Tech. Meet. Satell. Div. Inst. Navig. ION GNSS 2004*, pp. 2611–2622, 2004.

[25] M. Foucras, "Performance Analysis of Modernized GNSS Signal Acquisition," 2015.

[26] S. J. Sanz Subirana, J.M. Juan Zornoza and M. Hernández-Pajares, Technical University of Catalonia, "Ionospheric Delay," 2011. [Online]. Available: https://gssc.esa.int/navipedia/index.php/Ionospheric_Delay.

[27] R. D. J. Van Nee, "Multipath Effects on GPS Code Phase Measurements," vol. 39, no. 2, pp. 177–190, 1992.

[28] J. Marais, D. F. Nahimana, N. Viandier, and E. Duflos, "GNSS accuracy enhancement based on pseudo range error estimation in an urban propagation environment," *Expert Syst. Appl.*, vol. 40, no. 15, pp. 5956–5964, 2013.

[29] A. Lehner, "Technical Note on the Implementation of the Land Mobile Satellite Channel Model," pp. 1–25.

[30] D. Betaille, F. Peyret, M. Ortiz, S. Miquel, and L. Fontenay, "A new modeling based on urban trenches to improve GNSS positioning quality of service in cities," *IEEE Intell. Transp. Syst. Mag.*, vol. 5, no. 3, pp. 59–70, 2013.

[31] D. Bétaille, F. Peyret, M. Ortiz, S. Miquel, and F. Godan, "Improving Accuracy and Integrity with a Probabilistic Urban Trench Modeling," *Navig. J. Inst. Navig.*, vol. 63, no. 3, pp. 283–294, 2016.

[32] M. Bétaille, D.; Peyret, F.; Ortiz, "How to enhance accuracy and integrity of satellite positioning for mobility pricing in cities: The Urban Trench method," in *Proceedings of the Transport Research Arena 2014*.

[33] A. Steingass and A. Lehner, "Measuring the navigation multipath channel-a statistical analysis," *ION GPS 2004 Conf. Long Beach, Calif. …*, no. June, 2004.

[34] C. Ratti, S. Di Sabatino, and R. Britter, "Analysis of 3-d Urban Databases with Respect to Air Pollution Dispersion for a Number of European and American Cities," *Water, Air, Soil Pollut.*, 2002.

[35] D. Betaille, F. Peyret, M. Ortiz, S. Miquel, and L. Fontenay, "A new modeling based on urban trenches to improve GNSS positioning quality of service in cities," *IEEE Intell. Transp. Syst. Mag.*, vol. 5, no. 3, pp. 59–70, 2013.

[36] A. Lehner, A. Steingaß, and F. Schubert, "A location and movement dependent GNSS multipath error model for pedestrian applications."

[37] S. H. Kong, "Statistical analysis of urban GPS multipaths and pseudo-range measurement errors," *IEEE Trans. Aerosp. Electron. Syst.*, vol. 47, no. 2, pp. 1101–1113, 2011.

[38] B. W. Parkinson, *Progress in Astronautics and Aeronautics: Global Positioning System: Theory and Applications*, vol. 2. 1996.

[39] P. R. and S. H. J. K. Borre, D.M. Akos, N. Bertelsen, *A software-defined GPS and Galileo receiver: a single-frequency approach*. 2007.

[40] O. Julien, "Design of Galileo L1F Receiver Tracking Loops," *Thesis*, no. 20227, 2005.

[41] M. Irsigler and B. Eissfeller, "PLL Tracking Performance in the Presence of Oscillator Phase Noise," *GPS Solut.*, vol. 5, no. 4, pp. 45–57, 2002.

[42] E. Falletti, M. Pini, and L. Lo Presti, "Are C/N0 Algorithms Equivalent in All Situations?"

[43] M. Foucras, B. Ekambi, U. Ngayap, J. Y. Li, O. Julien, and C. Macabiau, "Performance study of FLL schemes for a successful acquisition-to-tracking transition," *Rec. - IEEE PLANS, Position Locat. Navig. Symp.*, pp. 529–540, 2014.

[44] S. A. Stephens and J. B. Thomas, "Controlled-Root Formulation for Digital Phase-Locked Loops," *IEEE Trans. Aerosp. Electron. Syst.*, vol. 31, no. 1, pp. 78–95, 1995.

[45] D. Salós, "Integrity monitoring applied to the reception of GNSS signals in urban environments," p. 250, 2012.

[46] M. Olynik, “Temporal Characteristics of GPS Error Sources and Their Impact on Relative Positioning,” no. January, pp. 28–30, 2002.

[47] B. Bidikar, G. Sasibhushana Rao, L. Ganesh, and M. Santosh Kumar, “Satellite Clock Error and Orbital Solution Error Estimation for Precise Navigation Applications,” *Positioning*, vol. 05, no. 01, pp. 22–26, 2014.

[48] M. G. Petovello, “UCGE Reports Real-Time Integration of a Tactical-Grade IMU and GPS for High-Accuracy Positioning and Navigation by,” no. 20173, 2003.

[49] A. GUILBERT, “OPTIMAL GPS/GALILEO GBAS METHODOLOGIES WITH AN APPLICATION TO TROPOSPHERE,” 2016.

[50] R. W. L. and P. A. A. M.S. Grewal, *Global positioning systems, inertial navigation, and integration*. 2007.

[51] J. J. Z. and M. H.-P. J. Sanz Subirana, “GPS Navigation Message,” 2011. [Online]. Available: https://gssc.esa.int/navipedia/index.php/GPS_Navigation_Message.

[52] J. J. Z. and M. H.-P. J. Sanz Subirana, “Galileo Navigation Message,” 2011. [Online]. Available: https://gssc.esa.int/navipedia/index.php/Galileo_Navigation_Message.

[53] G. Johnston, A. Riddell, and G. Hausler, *The International GNSS Service*. Springer Handbook of Global Navigation Satellite Systems (1st ed., pp. 967-982). Cham, Switzerland: Springer International Publishing., 2017.

[54] U. S. . Department Of Defense, “Global Positioning System Standard Positioning Service Performance Standard,” *Www.Gps.Gov*, no. 5th Edition, pp. 1–196, 2020.

[55] J.A. Klobuchar, “Ionospheric Time-Delay Algorithm for Single-Frequency GPS Users,” *IEEE Trans. Aerosp. Electron. Syst.*, pp. 325–331, 1987.

[56] G. Di Giovanni and S. Radicella, “An analytical model of the electron density profile in the ionosphere,” *Adv. Sp. Res.*, vol. 10, pp. 27–30, 1990.

[57] D. 301 RTCA, “MOPS for GNSS Airborne Active Antenna Equipment for the L1 Frequency Band,” 2006.

[58] R. F. Leandro, “PRECISE POINT POSITIONING WITH GPS A NEW APPROACH FOR POSITIONING , ATMOSPHERIC STUDIES , AND SIGNAL ANALYSIS A NEW APPROACH FOR POSITIONING ,” no. 267, 2009.

[59] S. Carcanague, “Low-cost GPS/GLONASS Precise Positioning Algorithm in Constrained Environment,” p. 200, 2013.

[60] U. DoD, “Global Positioning System Standard Positioning Service Performance Standard.” [Online]. Available: https://www.gps.gov/technical/ps/2008-SPS-performance-standard.pdf.

[61] J. Zhang, K. Zhang, R. Grenfell, and R. Deakin, “GPS Satellite Velocity and Acceleration Determination using the Broadcast Ephemeris,” *J. Navig.*, vol. 59, no. April 2016, p. 12, 2006.

[62] R. E. Kalman, “A new approach to linear filtering and prediction problems,” *J. Fluids Eng. Trans. ASME*, vol. 82, no. 1, pp. 35–45, 1960.

[63] D. Medina, K. Gibson, R. Ziebold, and P. Closas, “Determination of pseudorange error models and multipath characterization under signal-degraded scenarios,” *Proc. 31st Int. Tech. Meet. Satell. Div. Inst. Navig. ION GNSS+ 2018*, no. October, pp. 3446–3456, 2018.

[64] N. Zhu, D. Betaille, J. Marais, and M. Berbineau, “Extended Kalman Filter (EKF) Innovation-Based Integrity Monitoring Scheme with C / N0 Weighting,” no. 1, pp. 1–6.

[65] S. Carcanague, “Real-Time Geometry-Based Cycle Slip Resolution Technique for Single-Frequency PPP and RTK,” p. pp 1136-1148, 2012.

[66] A. Pirsiavash, A. Broumandan, G. Lachapelle, and K. Orkeefe, “Detection and De-weighting of Multipath-affected Measurements in a GPS/Galileo Combined Solution,” *Eur. Navig. Conf. ENC 2019*, no. April, 2019.

[67] P. D. Groves and Z. Jiang, “Height Aiding, C/N 0 Weighting and Consistency Checking for GNSS NLOS

and Multipath Mitigation in Urban Areas," *J. Navig.*, vol. 66, no. 05, pp. 653–669, 2013.

[68] Y. Wang, Y. Wang, L. Precise, A. Signal, and I. Inpt, "Localization Precise in Urban Area," 2020.

[69] P. D. Groves, *Principles of GNSS , Inertial , and Multisensor Integrated Systems*. 2008.

[70] E. Amani *et al.*, "GPS Multipath Induced Errors for the Vector Tracking Loop : Insight into Multipath Detection," 2017.

[71] Y. H. Chen, S. Lo, and D. Akos, "Direct Comparison of the Multipath Performance of L1 BOC and C/A using On-Air Galileo and QZSS Transmissions," no. 1.

[72] M. Fantino, G. Marucco, P. Mulassano, and M. Pini, "Performance analysis of MBOC, AltBOC and BOC modulations in terms of multipath effects on the carrier tracking loop within GNSS receivers," *Rec. - IEEE PLANS, Position Locat. Navig. Symp.*, pp. 369–376, 2008.

[73] G. Brodin and P. Daly, "GNSS code and carrier tracking in the presence of multipath," *Int. J. Satell. Commun.*, vol. 15, no. 1, pp. 25–34, 1997.

[74] J. Chen, L. Cheng, and M. Gan, "Modeling of GPS code and carrier tracking error in multipath," *Chinese J. Electron.*, vol. 21, no. 1, pp. 78–84, 2012.

[75] M. Irsigler, "Characterization of multipath phase rates in different multipath environments," *GPS Solut.*, vol. 14, no. 4, pp. 305–317, 2010.

[76] L. U. O. Yu, W. Yongqing, W. U. Siliang, and W. Pai, "Multipath effects on vector tracking algorithm for GNSS signal," vol. 57, no. October, pp. 1–13, 2014.

[77] M. S. Braasch, "ON THE CHARACTERIZATION OF MULTIPATH ERRORS IN SATELLITE-BASED PRECISION APPROACH AND LANDING SYSTEMS," 1992.

[78] C. Chang and J. Juang, "An Adaptive Multipath Mitigation Filter for GNSS Applications," vol. 2008, 2008.

[79] BENACHENHOU and SARI, "Multipath Mitigation in GPS/Galileo Receivers with Different Signal Processing Techniques," pp. 1–14, 2002.

[80] S. N. Sadrieh, A. Broumandan, and G. Lachapelle, "Doppler Characterization of a Mobile GNSS Receiver in Multipath Fading Channels," no. April 2012, pp. 477–494, 2019.

[81] T. Johnsen and K. E. Olsen, "Bi- and Multistatic Radar," vol. 1, no. c, pp. 1–34, 2006.

[82] A. Garcia-Pena, "Digital Receivers, Lecture ENAC," 2021.

[83] P. A. B. W. Parkinson, J. J. S. Jr and P. Enge, *The Global Positioning System: Theory and Applications*. 1996.

[84] K. Larson, D. Akos, and L. Marti, "Characterizing multipath from satellite navigation measurements in urban environments," *2008 5th IEEE Consum. Commun. Netw. Conf. CCNC 2008*, pp. 620–625, 2008.

[85] P. D. Groves, Z. Jiang, M. Rudi, and P. Strode, "A portfolio approach to NLOS and multipath mitigation in dense urban areas," *26th Int. Tech. Meet. Satell. Div. Inst. Navig. ION GNSS 2013*, vol. 4, no. September, pp. 3231–3247, 2013.

[86] N. Zhu, J. Marais, D. Betaille, and M. Berbineau, "GNSS Position Integrity in Urban Environments: A Review of Literature," *IEEE Trans. Intell. Transp. Syst.*, vol. 19, no. 9, pp. 2762–2778, 2018.

[87] M. Irsigler, G. W. Hein, and B. Eissfeller, "Multipath Performance Analysis for Future GNSS Signals."

[88] E. Shytermeja *et al.*, "Performance Comparison of a proposed Vector Tracking architecture versus the Scalar configuration for a L1 / E1 GPS / Galileo receiver Performance Comparison of a proposed Vector Tracking architecture versus the Scalar configuration for a L1 / E1 GPS / Ga," 2019.

[89] H. Pesonen, "Robust Estimation Techniques for GNSS Positioning," no. January 2007, 2007.

[90] C. Huang, A. F. Molisch, R. Wang, P. Tang, R. He, and Z. Zhong, "Angular information-based NLOS/LOS identification for vehicle to vehicle MIMO System," *2019 IEEE Int. Conf. Commun. Work. ICC Work.*

2019 - Proc., 2019.

[91] C. Groves, P.D.; Wang, L.; Adjrad, M.; Ellul, "GNSS Shadow Matching: The Challenges Ahead," in *Proceedings of the 28th International Technical Meeting of The Satellite Division of the Institute of Navigation (ION GNSS+ 2015)*, pp. 2421–2443.

[92] J. Marais, C. Meurie, D. Attia, Y. Ruichek, and A. Flancquart, "Toward accurate localization in guided transport: Combining GNSS data and imaging information," *Transp. Res. Part C Emerg. Technol.*, vol. 43, pp. 188–197, 2014.

[93] G. Obst, M.; Bauer, S.; Wanielik, "Urban multipath detection and mitigation with dynamic 3D maps for reliable land vehicle localization," in *Proceedings of the 2012 IEEE/ION Position Location and Navigation Symposium (PLANS)*, pp. 685–691.

[94] N. Suzuki, T., Kubo, "N-LOS GNSS signal detection using fish-eye camera for vehicle navigation in urban environments," *27th Int. Tech. Meet. Satell. Div. Inst. Navig. ION GNSS 2014*, vol. Volume 3, p. Pages 1897-1906.

[95] J. S. Sánchez *et al.*, "Use of a FishEye Camera for GNSS NLOS Exclusion and Characterization in Urban Environments To cite this version : HAL Id : hal-01271970 Use of a FishEye Camera for GNSS NLOS Exclusion and Characterization in Urban Environments," 2017.

[96] P. V. Gakne and M. Petovello, "Assessing image segmentation algorithms for sky identification in GNSS," *2015 Int. Conf. Indoor Position. Indoor Navig. IPIN 2015*, no. October, pp. 1–7, 2015.

[97] J. Y. Bourdeau, A.; Sahmoudi, M.; Tourneret, "Constructive use of GNSS NLOS-multipath: Augmenting the navigation Kalman filter with a 3D model of the environment," in *Proceedings of the 2012 15th International Conference on Information Fusion (FUSION)*, pp. 2271–2276.

[98] J. Y. Sahmoudi, M.; Bourdeau, A.; Tourneret, "Deep fusion of vector tracking GNSS receivers and a 3D city model for robust positioning in urban canyons with NLOS signals," in *Proceedings of the 2014 7th ESA Workshop on Satellite Navigation Technologies and European Workshop on GNSS Signals and Signal Processing (NAVITEC)*, pp. 1–7.

[99] D. Attia, "Segmentation D'images par Combinaison Adaptative Couleur-Texture et Classification de Pixels: Applications à la Caractérisation de L'environnement de Réception de Signaux GNSS," Université de Technologie de Belfort-Montbéliard Belfort, France, 2013.

[100] S. Tay and J. Marais, "Weighting models for GPS Pseudorange observations for land transportation in urban canyons," *6th Eur. Work. GNSS Signals Signal Process.*, 2014.

[101] E. R. Matera, A. Garcia-Pena, O. Julien, C. Milner, and B. Ekambi, "Characterization of line-of-sight and non-line-of-sight pseudorange multipath errors in urban environment for GPS and galileo," in *ION 2019 International Technical Meeting Proceedings*, 2019.

[102] E. R. Matera, A. Garcia-Pena, O. Julien, C. Milner, and B. Ekambi, "Characterization of line-of-sight and non-line-of-sight pseudorange multipath errors in urban environment for GPS and galileo," *ION 2019 Int. Tech. Meet. Proc.*, pp. 177–196, 2019.

[103] S. Kato, M. Kitamura, T. Suzuki, and Y. Amano, "NLOS satellite detection using a fish-eye camera for improving GNSS positioning accuracy in urban area," *J. Robot. Mechatronics*, vol. 28, no. 1, pp. 31–39, 2016.

[104] H. Bour, Y. El Merabet, Y. Ruichek, R. Messoussi, and I. Benmiloud, "An Efficient Sky Detection Algorithm From Fisheye Image Based on region classification and segment analysis," *Trans. Mach. Learn. Artif. Intell.*, vol. 5, no. 4, 2017.

[105] D. Scaramuzza *et al.*, "A Toolbox for Easily Calibrating Omnidirectional Cameras To cite this version : HAL Id : inria-00359941 A Toolbox for Easily Calibrating Omnidirectional Cameras," 2009.

[106] I. Nikiforov, "From the pseudo-range overbounding to the integrity risk overbounding," *Proc. Int. Tech. Symp. Navig. Timing*, pp. 1–12, 2017.

[107] C. Miller, K. O'Keefe, and Y. Gao, "Time Correlation in GNSS Positioning over Short Baselines," *J. Surv. Eng.*, vol. 138, no. 1, pp. 17–24, 2012.

[108] X. Niu *et al.*, “Using Allan variance to analyze the error characteristics of GNSS positioning,” *GPS Solut.*, vol. 18, no. 2, pp. 231–242, 2014.

[109] R. Odolinski, “Temporal correlation for network RTK positioning,” *GPS Solut.*, vol. 16, no. 2, pp. 147–155, 2012.

[110] K. Wang, Y. Li, and C. Rizos, “Practical approaches to Kalman filtering with time-correlated measurement errors,” *IEEE Trans. Aerosp. Electron. Syst.*, vol. 48, no. 2, pp. 1669–1681, 2012.

[111] J. Wang, C. Satirapod, and C. Rizos, “Stochastic assessment of GPS carrier phase measurements for precise static relative positioning,” *J. Geod.*, vol. 76, no. 2, pp. 95–104, 2002.

[112] A. El-Rabbany and A. Kleusberg, “Effect of temporal physical correlation on accuracy estimation in GPS relative positioning,” *J. Surv. Eng.*, vol. 129, no. 1, pp. 28–32, 2003.

[113] J. Howind, H. Kutterer, and B. Heck, “Impact of temporal correlations on GPS-derived relative point positions,” *J. Geod.*, vol. 73, no. 5, pp. 246–258, 1999.

[114] M. Olynik, M. G. Petovello, M. E. Cannon, and G. Lachapelle, “Temporal Variability of GPS Error Sources and Their Effect on Relative Positioning Accuracy,” *Inst. Navig. Natl. Tech. Meet.*, no. April 2015, pp. 1–12, 2002.

[115] B. Pervan, S. Khanafseh, and J. Patel, “Test statistic auto- and cross-correlation effects on monitor false alert and missed detection probabilities,” *Proc. 2017 Int. Tech. Meet. Inst. Navig. ITM 2017*, pp. 562–590, 2017.

[116] “Ublox EVK-M8T User Guide.” [Online]. Available: https://www.u-blox.com/sites/default/files/products/documents/EVK-M8T_UserGuide_%28UBX-14041540%29.pdf.

[117] “GNSS antennas - RF design considerations for u-blox GNSS receivers.” [Online]. Available: https://www.u-blox.com/en/docs/UBX-15030289.

[118] “Novatel Propak 6 User Manual.”

[119] “Tactical Grade, Low Noise IMU Delivers 3D Position, Velocity and Attitude Solution as Part of SPAN Technology.” [Online]. Available: https://hexagondownloads.blob.core.windows.net/public/Novatel/assets/Documents/Papers/IMU-LCI/IMU-LCI.pdf.

[120] A. El Idrissi, Y. El Merabet, Y. Ruichek, R. Touahni, and A. Sbihi, “A Multiple-Objects Recognition Method Based on Region Similarity Measures : Application to Roof Extraction from Orthophotoplans,” vol. 6, no. 11, 2015.

[121] “Fujistu FE185C046057 Lens Datasheet.” [Online]. Available: https://www.rmaelectronics.com/content/Fujinon-Lens-PDF/FE185C046057.pdf.

[122] “IDS UI-3240CP CMOS camera.”

[123] “TLSG GNSS reference station.” [Online]. Available: http://rgp.ign.fr/STATIONS/#TLSG.

[124] M. El-Diasty and S. Pagiatakis, “A rigorous temperature-dependent stochastic modelling and testing for MEMS-based inertial sensor errors,” *Sensors*, vol. 9, no. 11, pp. 8473–8489, 2009.

[125] European Commission, “EGNOS Service Definition Document Open Service,” pp. 1–40, 2009.

[126] “Novatel Inertial Explorer.” [Online]. Available: https://novatel.com/products/waypoint-post-processing-software/inertial-explorer.

[127] “U-Blox M8T-EVK.” [Online]. Available: https://www.u-blox.com/en/product/evk-8evk-m8.

[128] C. Gioia and D. Borio, “A statistical characterization of the Galileo-to-GPS inter-system bias,” *J. Geod.*, vol. 90, no. 11, pp. 1279–1291, 2016.

[129] P. Misra, *Global Positioning System, Signals, Measurements and Performance*. 2001.

10 Annex

10.1 Annex – GNSS Architecture

10.1.1 Coordinate Systems

The coordinate system determines the way one describes/observes the motion in each reference frame. Two types of coordinate systems are commonly used in navigation: the Cartesian system and the Polar system.

The 3D Cartesian coordinate system deals with an origin of the axes and 3 mutually perpendicular straight axes (Figure 10-1). A point is identified by the distance from the origin along the three different axes.

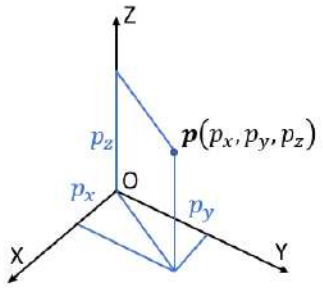

Figure 10-1 – Definition of Cartesian Coordinate System

The 3D Polar coordinate system involves the distance from the origin and two angles, as portrayed in Figure 10-2. The position of point $\boldsymbol{p}$ is described by

- the modulo of the vector $\boldsymbol{p}$ which is equal to the distance of the point from the origin (O);
- the horizontal azimuth angle measured on the x-y plane from the x-axis in the counter-clockwise direction, θ;
- the azimuth angle measured from the z-axis, φ.

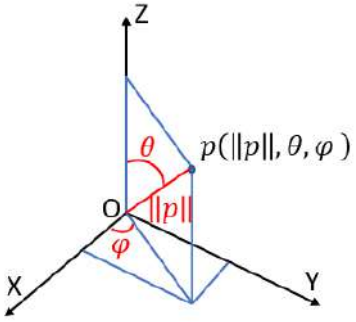

Figure 10-2 – Definition of Polar Coordinate System

The relationship between the spherical coordinates (p_x, p_y, p_z) and the Cartesian coordinates $(\|\boldsymbol{p}\|, \varphi, \theta)$ can be summarized as follows:

$$\|\boldsymbol{p}\| = \sqrt{p_x^2 + p_y^2 + p_z^2} \qquad 10\text{-}1$$

$$\varphi = \begin{cases} \tan^{-1}(p_y/p_x), & p_x > 0 \\ \tan^{-1}(p_y/p_x) + \pi, & p_x < 0, p_y > 0 \\ \tan^{-1}(p_y/p_x) - \pi, & p_x \geq 0, p_y < 0 \\ \pi/2, & p_x = 0, p_y > 0 \\ -\pi/2, & p_x = 0, p_y < 0 \end{cases}$$

$$\theta = \begin{cases} \tan^{-1}\left(\dfrac{\sqrt{p_x^2 + p_y^2}}{p_z}\right), & p_z > 0 \\ \tan^{-1}\left(\dfrac{\sqrt{p_x^2 + p_y^2}}{p_z}\right) + \pi, & p_z < 0 \\ \pi/2, & p_z = 0 \end{cases}$$

where $-\pi \leq \varphi < \pi$ and $0 \leq \theta \leq \pi$.

Or, viceversa:

$$\begin{aligned} p_x &= \|\boldsymbol{p}\| \sin\theta \cos\varphi \\ p_y &= \|\boldsymbol{p}\| \sin\theta \sin\varphi \\ p_z &= \|\boldsymbol{p}\| \cos\theta \end{aligned} \qquad 10\text{-}2$$

10.1.2 Elevation and Azimuth angles

The direction of a GNSS satellite from the receiver antenna is described by the elevation, φ, and azimuth, θ angles. To define these two parameters, a specific reference frame must be used. In this case the reference frame to be used is the local reference frame, defined with the origin in the phase centre of the receiver antenna. Indeed, these angles define the orientation of the LOS vector (vector of unitary magnitude) with respect to the north, east, and down axes of the local navigation frame, as shown in Figure 10-3.

Elevation and azimuth angles are obtained from the LOS vector in the local navigation frame, $\boldsymbol{u}^n = (u_N^n, u_E^n, u_D^n)$:

- The Azimuth angle, θ, is the angle between the user antenna and the transmitted signal in the horizontal plane, obtained projecting the Line of Sight in the horizonal plane.
- The Elevation angle, φ, is the angle between the user antenna and the transmitted signal in the vertical plane.

$$\begin{aligned} \theta &= -\arcsin(u_D^n) \\ \varphi &= \arctan2(u_E^n, u_N^n) \end{aligned} \qquad 10\text{-}3$$

where a four-quadrant arctangent function must be used. The reverse transformation is

$$\boldsymbol{u}^n = \begin{pmatrix} \cos\varphi \cos\theta \\ \cos\varphi \sin\theta \\ -\sin\varphi \end{pmatrix} \qquad 10\text{-}4$$

The local navigation frame line-of-sight vector is transformed to and from its ECEF and ECI-frame counterparts

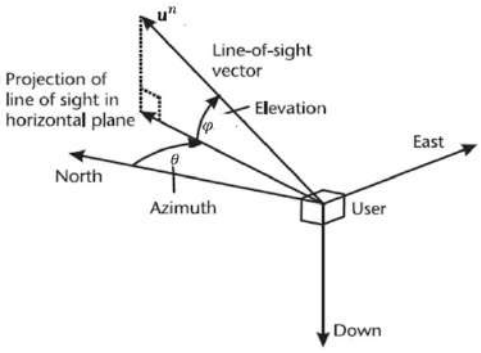

Figure 10-3 – Satellite elevation and azimuth [15]

10.2 Annex – GNSS Receiver Processing

10.2.1 Error Model

GNSS error components affect the transmitted signals which propagates through the transmission channel, section 2.4. When facing the GNSS error model, a fundamental assumption is usually made: the error sources can be allocated to individual satellite measurements and can be viewed as an equivalent error in the measurement values.

The overall error component is equal to the sum of independent error components:

$$\varepsilon_\rho(t) = \sum_{k=1}^{N} y_k(t) \tag{10-5}$$

Each error component defining 10-5 are defined by their statistical properties: each error component can be modelled as a random variable, $y_k(t)$ generated from a ergodic random process, Y, and characterized by a constant mean, μ_{y_k}, and a constant variance, $\sigma^2_{y_k}$, over time: even if the random variables under exam are not characterized by the stationary property, a simplification can be applied: the processing time can be divided in several temporal windows where the random variable are assumed characterized by the ergodicity property:

$$\begin{aligned} y_k &\sim \mathrm{Y}\left(\mu_{y_k}, \sigma^2_{y_k}\right) \\ \mu_{y_k} &= E\{y_k(t)\} \\ \sigma^2_{y_k} &= E\left\{\left[y_k(t) - \mu_{y_k}\right]^2\right\} = E\{[y_k(t)]^2\} - \mu^2_{y_k} \end{aligned} \tag{10-6}$$

Moreover, two important characteristics of the error components are the spatial and the temporal correlation. The temporal correlation identifies the dependency of the error component at a given time epoch from the error components of the previous time epochs. The greater is the correlation, the greater is this dependency. Similarly, spatial correlation identifies the mutual correlation of the same error component affecting two different users at the same time epoch.

Temporal correlations are deeply investigated, [46], [112] and exploited in the Navigation Solutions Estimation to determine more accurate solutions. Almost all the error components affecting the PSR measurements are temporally correlated. Spatial correlations regard in particular the environmental source of errors, such as ionosphere, troposphere and multipath, clock errors, satellite position errors, etc., which can affect in a similar way the PSR measurements in a specific geographic area. Spatial correlation of ionospheric and tropospheric errors have been investigated in several works, [48], [49], [59], while multipath space correlation it is a subject less covered in literature, given its great variability and complexity.

Temporal correlation models for the different error components could be generalized and approximated to the model described in the following paragraph. Spatial correlation is usually modelled as a function of the distance between the two receivers at the same time epoch, as described in [18]. Since this work focuses on the applications relative to a dynamic mass-market receiver, the spatial correlation of the error have sense only if combined to the temporal correlation.

The time correlation of a given random variable y generated from a wide sense stationary process Y, is characterized by the autocovariance function of y, C_y, and it is only dependent on the time lag $\tau = t_1 - t_2$ between the two realizations of the process used to calculate the autocovariance:

$$C_y(\tau) = E\{(y(t) - \mu_y)(y(t+\tau) - \mu_y)\} = E\{y(t)y(t+\tau)\} - \mu_y^2 \tag{10-7}$$

The autocovariance function for time uncorrelated process is equal to σ_y^2 when $\tau = 0$, whereas it is equal to zero in any other case:

$$C_y(\tau) = \begin{cases} \sigma_y^2, \tau = 0 \\ 0, \tau \neq 0 \end{cases} \tag{10-8}$$

The autocorrelation function for time correlated process, is an even decreasing function, with a maximum value equal to σ_y^2 when $\tau = 0$:

$$\left|C_y(\tau)\right| \leq C_y(0), \forall\, \tau \neq 0 \qquad 10\text{-}9$$

As already said, it can be assumed that the GNSS error random processes is characterized by the ergodicity property. With this assumption, 10-7 could be rewritten replacing ensemble average calculated over several realizations by the time average (or sample average) obtained from a specific set of observations $\boldsymbol{y}$, varying in time

$$\boldsymbol{y}(t) = [y(t+T), \dots, y(t), \dots, y(t-T)] \qquad 10\text{-}10$$

The autocovariance on a finite sequence of observations could be written as

$$C(\tau) = \lim_{T\to\infty} \frac{1}{2T} \int_{-T}^{T} \big(y(t) - \mu_y\big)\big(y(t+\tau) - \mu_y\big) dt \qquad 10\text{-}11$$

However, the autocovariance is calculated for a finite sequence of observations. Assume we have $2N+1$ observations,

$$\boldsymbol{y} = [y_{-N}, \dots, Y_0, \dots, Y_N] \qquad 10\text{-}12$$

The autocovariance on a finite sequence of observations could be written as

$$C[\tau] = \lim_{N\to\infty} \frac{1}{2N+1} \sum_{k=-N}^{N} \big(y_k - \mu_y\big)\big(y_{k+\tau} - \mu_y\big) \qquad 10\text{-}13$$

Usually, the autocovariance function of each error component is normalized in order to be easily compared, the normalization is obtained as follows,

$$R(\tau) = \frac{C(\tau)}{C(0)} = \frac{C(\tau)}{\sigma_y^2} \qquad 10\text{-}14$$

and it is called the autocorrelation function.

A common mathematic process used to fit the temporal correlation of the error sources [60], is called first order Gauss-Markov process,. The first-order Gauss-Markov (GM) process is a one-dimensional stochastic process, used to describe a sequence where the quantity varies with time as the sum of its previous value scaled by an exponential coefficient and a driving white noise sequence. The two processes are independents.

The time-correlated process, y, can be modelled in continuous time by a first order stochastic differential equation as follows:

$$\dot{y} = \alpha_{\tau_y} \cdot y + \varepsilon_y \qquad 10\text{-}15$$

where:

- y is the random process with zero mean and variance σ_y^2;
- $\dot{y}$ is the first-order derivative of y;
- α_{τ_y} is the time correlation factor, which defines the correlation between y and $\dot{y}$;
- τ_y is the correlation time;
- ε_y is the process noise with zero mean and variance $\sigma_{\varepsilon_y}^2$.

The stochastic differential equation describing a first-order Gauss-Markov (GM) process, y, is expressed in continuous time as follows: y is the GM random process with zero mean and variance σ_y^2;

$$\alpha_{\tau_y} = -\frac{1}{\tau_y} \qquad 10\text{-}16$$

where τ_y is called correlation time.

Moreover, the discrete time model of the GM random process is expressed as follows:

$$\alpha_{\tau_y} = e^{-\frac{T_s}{\tau_y}} \qquad 10\text{-}17$$

It can be stated that the effects of previous values on the value at the $k\text{-}th$ epoch decay exponentially, and it is inversely proportional to the correlation time. As a consequence, the process driven noise variance $\sigma^2_{w_{y,k}}$, at epoch k, is deduced from the global GM process using the following relation:

$$\sigma^2_{\varepsilon_{y,k}} = \sigma^2_{y_k} \cdot \left(1 - e^{-\frac{2T_S}{\tau_y}}\right) \qquad 10\text{-}18$$

It follows that the main parameters that are required for the full description of the GM process are the correlation time τ_y and the process driven noise variance $\sigma^2_{y_k}$. The autocorrelation function of the GM random process is expressed by:

$$R(\tau) = \frac{C(\tau)}{C(0)} = \frac{\sigma^2_{y_k} e^{-\frac{|\tau|}{\tau_y}}}{\sigma^2_{y_k}} \qquad 10\text{-}19$$

An illustration of 10-19 is depicted in Figure 10-4.

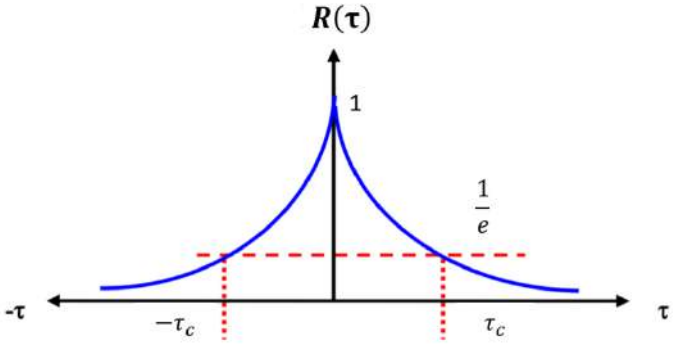

Figure 10-4 – Illustration of autocorrelation function modelled by first-order Gaussian Markov process [124]

Therefore, the overall PSR and PSR-R statistical error models could be described by the following parameters:

- the probability density function of the random process;
- the sample mean;
- the sample variance;
- the correlation time;

10.2.2 PVT Computational Steps

Basic PVTE methodologies applied to mass market receivers perform two fundamental operations:

- The first fundamental operation is defined by the mathematical model used to determine the navigation solution from the system of the measurements. The unknown parameters cannot be directly accessed due to the presence of the measurement error components. Therefore, an error minimization technique is implemented. The estimation is described in section 10.2.2.1.
- the second one is the linearisation of the measurement equation, section 10.2.2.2. Usual PVT resolution technique consists of linearising the PSR and PSR-R measurement equations and employing a numerical iterative solution. This is obtained by performing a Taylor expansion about an initial estimate of the state vector.

10.2.2.1 Error Minimization

The PVT estimator's purpose is to estimate the state vector, $\boldsymbol{x}$, knowing the observation vector, $\boldsymbol{z}$. Basic PVT estimator's methodology consist of the computation of the state vector, $\hat{\boldsymbol{x}}$, which minimizes the difference between the true measurements $\tilde{\boldsymbol{z}}$ and the predicted measurements $\hat{\boldsymbol{z}}$, usually called measurement residual vector, $d\boldsymbol{z}$:

$$d\boldsymbol{z} = \tilde{\boldsymbol{z}} - \hat{\boldsymbol{z}} = \tilde{\boldsymbol{z}} - \mathrm{h}(\boldsymbol{p}^i, \dot{\boldsymbol{p}}^i, \hat{\boldsymbol{x}}) \qquad 10\text{-}20$$

where $\hat{\boldsymbol{z}}$ is the predicted measurement obtained using the estimated state vector:

$$\hat{\boldsymbol{z}} = \mathrm{h}(\boldsymbol{p}^i, \dot{\boldsymbol{p}}^i, \hat{\boldsymbol{x}}) \tag{10-21}$$

A common criterion used in GNSS is the least square error minimization, which is defined by the condition

$$\hat{\boldsymbol{x}} \rightarrow \min\|d\boldsymbol{z}\|^2 = \min\left[\left(\sum_{i=1}^{N}(\tilde{\rho}^i - \hat{\rho}^i)^2\right), \left(\sum_{i=1}^{N}\left(\tilde{\dot{\rho}}^i - \hat{\dot{\rho}}^i\right)^2\right)\right] \tag{10-22}$$

The predicted measurement vector, is equal to:

$$\hat{\boldsymbol{z}} = \left[\hat{\rho}^1, \ldots, \hat{\rho}^{N_1+N_2} | \hat{\dot{\rho}}^1, \ldots, \hat{\dot{\rho}}^{N_1+N_2}\right] \tag{10-23}$$

where the predicted PSR provided by the PVTE for a given satellite i (from the GPS (N_1) and Galileo (N_2) satellites in-view) may be written as:

$$\begin{aligned} \hat{\rho}^i_{GPS} &= \hat{R}^i_{GPS} + \hat{b}_r, \qquad 1 < i \leq N_1 \\ \hat{\rho}^i_{GAL} &= \hat{R}^i_{GAL} + \hat{b}_r + \hat{\delta}, \quad N_1 + 1 < i \leq N_1 + N_2 \end{aligned} \tag{10-24}$$

with $\hat{R}^i = \sqrt{\left(\hat{p}^i_x - \hat{p}_{r,x}\right)^2 + \left(\hat{p}^i_y - \hat{p}_{r,y}\right)^2 + \left(\hat{p}^i_z - \hat{p}_{r,z}\right)^2}$ is the satellite to user effective distance.

- the estimated PSR-R provided by the PVTE for a given satellite i (from the GPS (N_1) and Galileo (N_2) satellites in-view) be written as:

$$\hat{\dot{\rho}}^i = \hat{\dot{R}}^i + \hat{\dot{b}}_r + \dot{\varepsilon} \tag{10-25}$$

with $\hat{\dot{R}}^i = \left(\hat{\dot{p}}^i_x - \hat{\dot{p}}_{r,x}\right)\hat{u}^i_x + \left(\hat{\dot{p}}^i_y - \hat{\dot{p}}_{r,y}\right)\hat{u}^i_y + \left(\hat{\dot{p}}^i_z - \hat{\dot{p}}_{r,z}\right)\hat{u}^i_z$ the satellite to user relative velocity.

The corrected and estimated observation vectors, $\tilde{\boldsymbol{z}}$, $\hat{\boldsymbol{z}}$, are composed of nonlinear equations. To simplify the PVT estimation methodology, a linearization process is applied to $\tilde{\boldsymbol{z}}$ and $\hat{\boldsymbol{z}}$.

10.2.2.2 Linearization

The linearization process consists of linearizing the measurement equations around a previous estimate of the state vector, initially at $\hat{\boldsymbol{x}}_0$, corresponding to an approximate position and velocity of the receiver. The initial estimates used to apply the linearization method is defined as follows:

$$\hat{\boldsymbol{x}}_0 = \left(\hat{\boldsymbol{p}}_{r,0}, \hat{\dot{\boldsymbol{p}}}_{r,0}, \hat{b}_0, \hat{\dot{b}}_0, \hat{\delta}_0\right) \tag{10-26}$$

The connection between the true states $\boldsymbol{x}$ and the initialization estimates $\hat{\boldsymbol{x}}_0$ is based on the following equations:

$$\boldsymbol{x} = \hat{\boldsymbol{x}}_0 + \delta\boldsymbol{x} \tag{10-27}$$

where $\delta\boldsymbol{x}$ is called state correction and is expressed as:

$$\delta\boldsymbol{x} = \left(\delta\boldsymbol{p}_r, \delta\dot{\boldsymbol{p}}_r, \delta b_r, \delta\dot{b}_r, \delta\delta\right) \tag{10-28}$$

where:

- $\boldsymbol{\delta p} = \left(\delta p_{r,x}, \delta p_{r,y}, \delta p_{r,z}\right)$, is the 3-D position correction along the three axes, respectively, which are applied to the initial estimates;
- $\boldsymbol{\delta\dot{p}} = \left(\delta\dot{p}_{r,x}, \delta\dot{p}_{r,y}, \delta\dot{p}_{r,z}\right)$ are the 3-D velocity correction along the three axes, respectively, which are applied to the initial estimates;
- δb, $\delta\dot{b}$, $\delta\delta$ are the clock bias and clock drift corrections which are applied to the initial estimates.

After linearization, the $\boldsymbol{\delta x}$ term contains the unknown parameters to be determined, and it is calculated by developing a system of linear equations for each locked satellite. The linearization approach consists of defining a linearized model of the PSR and PSR-R measurements around the initial guesses. Considering only the receiver clock error and the inter-constellation error, the corresponding PSR for each satellite i based on the initial estimates can be written as:

$$\tilde{\rho}^i = \hat{R}^i_0 + d\rho^i \tag{10-29}$$

where $\hat{R}^i_0$ is the estimated effective range obtained from the initialization state $\hat{\boldsymbol{x}}_{\rho,0}$, and $\delta\rho^i$ is the linear measurement correction term defined as:

$$d\rho^i = \delta R^i + \delta b + \delta\delta \tag{10-30}$$

obtained applying the 1st order Taylor series approximation, obtaining

$$\delta R^i = \frac{(p_{r,x,0} - p_x^i)}{R_0^i}\delta p_{r,x} + \frac{(p_{r,y,0} - p_y^i)}{R_0^i}\delta p_{r,y} + \frac{(p_{r,z,0} - p_z^i)}{R_0^i}\delta p_{r,z}$$
$$\delta R^i = -\hat{u}_{0,x}^i \delta p_{r,x} - \hat{u}_{0,y}^i \delta p_{r,y} - \hat{u}_{0,z}^i \delta p_{r,z} \quad \text{10-31}$$

with $\hat{\boldsymbol{u}}_0^i = \left(\hat{u}_{0,x}^i, \hat{u}_{0,y}^i, \hat{u}_{0,z}^i\right)$ the direction cosines or LOS projections from the initial receiver location (denoted as 0) to the satellite i, computed along the three ECEF axes.

Same approach can be used to linearize PSR-R measurements:

$$\dot{\rho}^i = \dot{R}_0^i + d\dot{\rho}^i = \dot{R}_0^i - \hat{u}_{0,x}^i \delta \dot{p}_{r,x} - \hat{u}_{0,y}^i \delta \dot{p}_{r,y} - \hat{u}_{0,z}^i \delta \dot{p}_{r,z} + \delta \dot{b}_r \quad \text{10-32}$$

where $\dot{R}_0^i$ is the estimated range-rate component obtained applying the initialization state $\hat{\boldsymbol{x}}_{\dot{\rho},0}$, and $\delta\dot{\rho}^i$ is the linear measurement correction term obtained applying the 1st order Taylor series approximation on the estimated distance.

The linear measurements vector, $d\boldsymbol{z}$, including also the overall error component, $\boldsymbol{\varepsilon}$, is finally written as follows:

$$d\boldsymbol{z} = \boldsymbol{H} \cdot \boldsymbol{\delta x} + \boldsymbol{\varepsilon} \quad \text{10-33}$$

where $\boldsymbol{H}$ is the so-called design matrix, that is used to relate the user states to the measurements. The dual-constellation design matrix is as follows:

$$\boldsymbol{H} = \begin{bmatrix}
-\hat{u}_{x,GPS}^1 & -\hat{u}_{y,GPS}^1 & -\hat{u}_{z,GPS}^1 & 0 & 0 & 0 & 1 & 0 & 0 \\
-\hat{u}_{x,GPS}^2 & -\hat{u}_{y,GPS}^2 & -\hat{u}_{z,GPS}^2 & 0 & 0 & 0 & 1 & 0 & 0 \\
\dots & \dots & \dots & \dots & \dots & \dots & \dots & \dots & \dots \\
-\hat{u}_{x,GPS}^{N_1} & -\hat{u}_{y,GPS}^{N_1} & -\hat{u}_{z,GPS}^{N_1} & 0 & 0 & 0 & 1 & 0 & 0 \\
-\hat{u}_{x,GAL}^{N_1+1} & -\hat{u}_{y,GAL}^{N_1+1} & -\hat{u}_{z,GAL}^{N_1+1} & 0 & 0 & 0 & 1 & 0 & 1 \\
-\hat{u}_{x,GAL}^{N_1+2} & -\hat{u}_{y,GAL}^{N_1+2} & -\hat{u}_{z,GAL}^{N_1+2} & 0 & 0 & 0 & 1 & 0 & 1 \\
\dots & \dots & \dots & \dots & \dots & \dots & \dots & \dots & \dots \\
-\hat{u}_{x,GAL}^{N_1+N_2} & -\hat{u}_{y,GAL}^{N_1+N_2} & -\hat{u}_{z,GAL}^{N_1+N_2} & 0 & 0 & 0 & 1 & 0 & 1 \\
0 & 0 & 0 & -\hat{u}_{x,GPS}^1 & -\hat{u}_{y,GPS}^1 & -\hat{u}_{z,GPS}^1 & 0 & 1 & 0 \\
0 & 0 & 0 & -\hat{u}_{x,GPS}^2 & -\hat{u}_{y,GPS}^2 & -\hat{u}_{z,GPS}^2 & 0 & 1 & 0 \\
\dots & \dots & \dots & \dots & \dots & \dots & \dots & \dots & \dots \\
0 & 0 & 0 & -\hat{u}_{x,GPS}^{N_1} & -\hat{u}_{y,GPS}^{N_1} & -\hat{u}_{z,GPS}^{N_1} & 0 & 1 & 0 \\
0 & 0 & 0 & -\hat{u}_{x,GAL}^{N_1+1} & -\hat{u}_{y,GAL}^{N_1+1} & -\hat{u}_{z,GAL}^{N_1+11} & 0 & 1 & 0 \\
0 & 0 & 0 & -\hat{u}_{x,GAL}^{N_1+2} & -\hat{u}_{y,GAL}^{N_1+2} & -\hat{u}_{z,GAL}^{N_1+2} & 0 & 1 & 0 \\
\dots & \dots & \dots & \dots & \dots & \dots & \dots & \dots & \dots \\
0 & 0 & 0 & -\hat{u}_{x,GAL}^{N_1+N_2} & -\hat{u}_{y,GAL}^{N_1+N_2} & -\hat{u}_{z,GAL}^{N_1+N_2} & 0 & 1 & 0
\end{bmatrix} \quad \text{10-34}$$

Taking into account the presence of N_1 GPS observables and N_2 Galileo observables, it could be stated that the measurement vector contains $N = N_1 + N_2$ pseudorange measurements and N pseudorange-rate measurements. The first N observables, (from 1 to N) are the PSR measurements, while from $N_1 + 1$ to $N_1 + N_2$ are the PSR-R observables.

The first N rows of the design matrix $\boldsymbol{H}$, relates the PSR measurements to the initialization user states:

- The columns 1 to 3 are the partial derivatives computed for the position terms of the state vector;
- The columns 4 to 6 are the partial derivatives computed for the velocity terms;
- The column 7 is the partial derivative computed for the clock bias term;
- The column 8 is the partial derivative computed for the clock drift term;
- The column 9 the partial derivative computed for the inter-constellation bias, is zero in correspondence of GPS observables and one in correspondence of Galileo observables.

Successively, the remaining N rows of the design matrix $\boldsymbol{H}$ relating the PSR-R measurements to the initialization user states using the h_2 function from

- The columns 1 to 3 are the partial derivatives computed for the position terms of the state vector;
- The columns 4 to 6 are the partial derivatives computed for the velocity terms;
- The column 7 is the partial derivative computed for the clock bias term;

- The column 8 is the partial derivative computed for the clock drift term;
- The column 9 the partial derivative computed for the inter-constellation bias.

10.2.3 Extended Kalman Filter (EKF)

The next subsections define the several aspects of the EKF navigation filter.

10.2.3.1 EKF State Model

In this subsection the EKF State Model is presented. The approach used in this work is the following: firstly, the state vector is modelled starting from the continuous-time navigation equations. Afterwards, the state vector is converted from continuous time to discrete time.

10.2.3.1.1 EKF State continuous-time model

The continuous-time EKF state model is based on the following equations:

- the position vector at time t, $\boldsymbol{p}(t)$, it depends on the position vector $\boldsymbol{p}(t-1)$, the speed vector $\dot{\boldsymbol{p}}(t-1)$, and the acceleration vector $\ddot{\boldsymbol{p}}(t-1)$, at time $t-1$. This is approximated as follows:
$$\boldsymbol{p}(t) = \boldsymbol{p}(t-1) + \dot{\boldsymbol{p}}(t-1)\Delta T + \frac{1}{2}\ddot{\boldsymbol{p}}(t-1)\Delta T^2 \quad 10\text{-}35$$
- the speed vector at time t, $\dot{\boldsymbol{p}}(t)$, depends on the speed vector $\dot{\boldsymbol{p}}(t-1)$, and the acceleration vector $\ddot{\boldsymbol{p}}(t-1)$, at time $t-1$. This is approximated as follows:
$$\dot{\boldsymbol{p}}(t) = \dot{\boldsymbol{p}}(t-1) + \ddot{\boldsymbol{p}}(t-1)\Delta T \quad 10\text{-}36$$
- the model of the acceleration vector at time t, $\ddot{\boldsymbol{p}}(t)$, it is modelled by a random acceleration process, usually white gaussian process, $\boldsymbol{\eta}_{\ddot{x}} = \boldsymbol{\eta}_a = (\eta_{a,x}, \eta_{a,y}, \eta_{a,z})$,
$$\ddot{\boldsymbol{p}}(t) = \boldsymbol{\eta}_{\ddot{p}} = (\eta_{\ddot{p},x}, \eta_{\ddot{p},y}, \eta_{\ddot{p},z}) \quad 10\text{-}37$$
- the clock bias at time t, $b(t)$, depends on the clock drift $\dot{b}(t-1)$ at time $t-1$,
$$b(t) = \dot{b}(t-1)\Delta T \quad 10\text{-}38$$
- the clock drift at time t, $\dot{b}(t)$, it is modelled by a random noise oscillator process, usually white gaussian process, $\eta_{\dot{b}} = \eta_{ck}$,
$$\dot{b}(t) = \eta_{\dot{b}} \quad 10\text{-}39$$
- the inter constellation clock bias at time t, $\delta(t)$, it is generated by a random noise process, usually white gaussian process, η_δ,
$$\delta(t) = \eta_\delta \quad 10\text{-}40$$

where $\Delta T = T_P$ is the period between two processed navigation solutions.

Therefore, the equations can be rearranged in matrix form,

$$\frac{d}{dt}\boldsymbol{x}(t) = \boldsymbol{F}(t)\boldsymbol{x}(t) + \boldsymbol{B}(t)\boldsymbol{w}(t)$$

$$\frac{d}{dt}\begin{bmatrix} p_{r,x} \\ p_{r,y} \\ p_{r,z} \\ \dot{p}_{r,x} \\ \dot{p}_{r,y} \\ \dot{p}_{r,z} \\ \ddot{p}_{r,x} \\ \ddot{p}_{r,y} \\ \ddot{p}_{r,z} \\ b_r \\ \dot{b}_r \\ \delta \end{bmatrix} = \begin{bmatrix} 0 & 0 & 0 & 1 & 0 & 0 & \frac{1}{2} & 0 & 0 & 0 & 0 & 0 \\ 0 & 0 & 0 & 0 & 1 & 0 & 0 & \frac{1}{2} & 0 & 0 & 0 & 0 \\ 0 & 0 & 0 & 0 & 0 & 1 & 0 & 0 & \frac{1}{2} & 0 & 0 & 0 \\ 0 & 0 & 0 & 0 & 0 & 0 & 1 & 0 & 0 & 0 & 0 & 0 \\ 0 & 0 & 0 & 0 & 0 & 0 & 0 & 1 & 0 & 0 & 0 & 0 \\ 0 & 0 & 0 & 0 & 0 & 0 & 0 & 0 & 1 & 0 & 0 & 0 \\ 0 & 0 & 0 & 0 & 0 & 0 & 0 & 0 & 0 & 0 & 0 & 0 \\ 0 & 0 & 0 & 0 & 0 & 0 & 0 & 0 & 0 & 0 & 0 & 0 \\ 0 & 0 & 0 & 0 & 0 & 0 & 0 & 0 & 0 & 1 & 0 & 0 \\ 0 & 0 & 0 & 0 & 0 & 0 & 0 & 0 & 0 & 0 & 0 & 0 \\ 0 & 0 & 0 & 0 & 0 & 0 & 0 & 0 & 0 & 0 & 0 & 0 \end{bmatrix} \cdot \begin{bmatrix} p_{r,x} \\ p_{r,y} \\ p_{r,z} \\ \dot{p}_{r,x} \\ \dot{p}_{r,y} \\ \dot{p}_{r,z} \\ \ddot{p}_{r,x} \\ \ddot{p}_{r,y} \\ \ddot{p}_{r,z} \\ b_r \\ \dot{b}_r \\ \delta \end{bmatrix} + \begin{bmatrix} 0 & 0 & 0 & 0 & 0 & 0 \\ 0 & 0 & 0 & 0 & 0 & 0 \\ 0 & 0 & 0 & 0 & 0 & 0 \\ 0 & 0 & 0 & 0 & 0 & 0 \\ 0 & 0 & 0 & 0 & 0 & 0 \\ 0 & 0 & 0 & 0 & 0 & 0 \\ 1 & 0 & 0 & 0 & 0 & 0 \\ 0 & 1 & 0 & 0 & 0 & 0 \\ 0 & 0 & 1 & 0 & 0 & 0 \\ 0 & 0 & 0 & 1 & 0 & 0 \\ 0 & 0 & 0 & 0 & 1 & 0 \\ 0 & 0 & 0 & 0 & 0 & 1 \end{bmatrix} \cdot \begin{bmatrix} w_{\ddot{x}} \\ w_{\ddot{y}} \\ w_{\ddot{z}} \\ w_b \\ w_{\dot{b}} \\ w_{\delta C} \end{bmatrix} \quad 10\text{-}41$$

where:

- $\frac{d}{dt}\boldsymbol{x}$ denotes the time derivation operation applied to the state vector;

- $\boldsymbol{F}$ represents the state transition matrix describing the user's platform and receiver's clock dynamics;
- $\boldsymbol{B}$ represents the colored noise transition matrix;
- $\boldsymbol{w}$ is the process noise vector representing the uncertainties affecting the system model, coming from the user's dynamics and the receiver oscillator;

The process noise vector $\boldsymbol{w}$, is considered as a White Gaussian Noise vector and the continuous-time covariance matrix $\boldsymbol{Q}$ is designed taking into account the user's dynamics sensitivity and the receiver's oscillator noise variance. The first is related to the uncertainty concerning the vehicle dynamics and including the velocity error variance terms along the three ECEF axes $\left(\sigma_{\dot{x}}^2, \sigma_{\dot{y}}^2, \sigma_{\dot{z}}^2\right)$; the second includes the oscillator's phase noise PSDs affecting the receiver clock biases denoted as σ_b^2 and the oscillator's frequency noise variance $\sigma_{\dot{b}}^2$ related to the user's clock drift.

The deviation of the state vector estimate from the true value of the state vector is equal to:

$$\delta \boldsymbol{x}_0 = x_0 - \hat{x}_0 \tag{10-42}$$

The error covariance matrix defines the expectation of the square of the deviation of the state vector estimate from the true value of the state vector:

$$\boldsymbol{P_0} = E\{\delta \boldsymbol{x}_0 \cdot \delta \boldsymbol{x}_0^T\} \tag{10-43}$$

The state covariance matrix is symmetric, and the diagonal elements are the variances of each state estimate, while their square roots are the standard deviations:

$$P_0 = \begin{pmatrix} \sigma_{p_{r,x,0}}^2 & 0 & 0 & 0 & 0 & 0 & 0 & 0 & 0 & 0 & 0 & 0 \\ 0 & \sigma_{p_{r,y,0}}^2 & 0 & 0 & 0 & 0 & 0 & 0 & 0 & 0 & 0 & 0 \\ 0 & 0 & \sigma_{p_{r,z,0}}^2 & 0 & 0 & 0 & 0 & 0 & 0 & 0 & 0 & 0 \\ 0 & 0 & 0 & \sigma_{\dot{p}_{r,x,0}}^2 & 0 & 0 & 0 & 0 & 0 & 0 & 0 & 0 \\ 0 & 0 & 0 & 0 & \sigma_{\dot{p}_{r,y,0}}^2 & 0 & 0 & 0 & 0 & 0 & 0 & 0 \\ 0 & 0 & 0 & 0 & 0 & \sigma_{\dot{p}_{r,z,0}}^2 & 0 & 0 & 0 & 0 & 0 & 0 \\ 0 & 0 & 0 & 0 & 0 & 0 & \sigma_{\ddot{p}_{r,x,0}}^2 & 0 & 0 & 0 & 0 & 0 \\ 0 & 0 & 0 & 0 & 0 & 0 & 0 & \sigma_{\ddot{p}_{r,y,0}}^2 & 0 & 0 & 0 & 0 \\ 0 & 0 & 0 & 0 & 0 & 0 & 0 & 0 & \sigma_{\ddot{p}_{r,z,0}}^2 & 0 & 0 & 0 \\ 0 & 0 & 0 & 0 & 0 & 0 & 0 & 0 & 0 & \sigma_{b_{r,0}}^2 & 0 & 0 \\ 0 & 0 & 0 & 0 & 0 & 0 & 0 & 0 & 0 & 0 & \sigma_{\dot{b}_{r,0}}^2 & 0 \\ 0 & 0 & 0 & 0 & 0 & 0 & 0 & 0 & 0 & 0 & 0 & \sigma_{\delta_0}^2 \end{pmatrix} \tag{10-44}$$

where:

- $\boldsymbol{\sigma}_{p_0}^2 = \left[\sigma_{p_{r,x,0}}^2, \sigma_{p_{r,y,0}}^2, \sigma_{p_{r,z,0}}^2\right]$ is the initial position error variance,
- $\boldsymbol{\sigma}_{\dot{p}_0}^2 = \left[\sigma_{\dot{p}_{r,x,0}}^2, \sigma_{\dot{p}_{r,y,0}}^2, \sigma_{\dot{p}_{r,z,0}}^2\right]$ is the initial speed error variance,
- $\boldsymbol{\sigma}_{a_0}^2 = \left[\sigma_{\ddot{p}_{r,x,0}}^2, \sigma_{\ddot{p}_{r,y,0}}^2, \sigma_{\ddot{p}_{r,z,0}}^2\right]$ is the initial acceleration error variance,
- $\sigma_{b_0}^2$ is the initial GPS clock bias error variance,
- $\sigma_{\dot{b}_0}^2$ is the initial GPS clock drift error variance,
- $\sigma_{\delta_0}^2$ is the initial GPS-to-Galileo inter-constellation bias error variance.

10.2.3.1.2 EKF State discrete-time model

The discrete EKF state model is obtained by applying the expectation operator $E\{\ldots\}$ on the state-space model of 10-41 yielding a differential equation equal to:

$$E\left\{\frac{d}{dt}\boldsymbol{x}(t)\right\} = \frac{d}{dt}\left(\overline{\boldsymbol{x}}(t)\right) = \boldsymbol{F}(t)\overline{\boldsymbol{x}}(t) \tag{10-45}$$

Solving 10-45 provides the state vector estimation at time t as a function of the state vector at time $t - \tau$ as [15]:

$$\overline{\boldsymbol{x}}(t) = \exp\left(\int_{t-\tau}^{t} \boldsymbol{F}(t)dt\right)\overline{\boldsymbol{x}}(t-\tau) \tag{10-46}$$

Calculating 10-46, it could be assumed that $\exp\left(\int_{t-\tau}^{t} \boldsymbol{F}(t)dt\right)$ could be simplified since the state transition matrix is constant in time, obtaining a discrete state transition matrix $\boldsymbol{\Phi}_l$ that is computed as:

$$\boldsymbol{\Phi}_l \approx \exp(\boldsymbol{F} \cdot \Delta T) \tag{10-47}$$

Where $\Delta T = lT_P - (l-1)T_P = t_l - t_{l-1}$ is the time step between two successive epochs. The matrix exponential $\exp(\boldsymbol{F} \cdot \Delta T)$, is calculated as the Taylor's power-series expansion of the continuous-time transition matrix $\boldsymbol{F}$ as:

$$\boldsymbol{\Phi}_l = \sum_{n=0}^{+\infty} \frac{\boldsymbol{F}_l^n \Delta T^n}{n!} = \boldsymbol{I} + \boldsymbol{F}_l \Delta T + \frac{1}{2}\boldsymbol{F}_l^2 \Delta T^2 + \frac{1}{6}\boldsymbol{F}_l^3 \Delta T^3 + \cdots \tag{10-48}$$

Due to GNSS EKF short propagation time ΔT, the power-series expansion is truncated in the first-order solution. Thus, the discrete transition matrix is given by:

$$\boldsymbol{\Phi}_l \approx \boldsymbol{I} + \boldsymbol{F}_l \Delta T \tag{10-49}$$

The final discrete state transition matrix is defined as follows:

$$\boldsymbol{\Phi}_l \approx \begin{bmatrix}
1 & 0 & 0 & \Delta T & 0 & 0 & \frac{\Delta T^2}{2} & 0 & 0 & 0 & 0 & 0 & 0 \\
0 & 1 & 0 & 0 & \Delta T & 0 & 0 & \frac{\Delta T^2}{2} & 0 & 0 & 0 & 0 & 0 \\
0 & 0 & 1 & 0 & 0 & \Delta T & 0 & 0 & \frac{\Delta T^2}{2} & 0 & 0 & 0 & 0 \\
0 & 0 & 0 & 1 & 0 & 0 & \Delta T & 0 & 0 & 0 & 0 & 0 & 0 \\
0 & 0 & 0 & 0 & 1 & 0 & 0 & \Delta T & 0 & 0 & 0 & 0 & 0 \\
0 & 0 & 0 & 0 & 0 & 1 & 0 & 0 & \Delta T & 0 & 0 & 0 & 0 \\
0 & 0 & 0 & 0 & 0 & 0 & 1 & 0 & 0 & 0 & 0 & 0 & 0 \\
0 & 0 & 0 & 0 & 0 & 0 & 0 & 1 & 0 & 0 & 0 & 0 & 0 \\
0 & 0 & 0 & 0 & 0 & 0 & 0 & 0 & 1 & 0 & 0 & 0 & 0 \\
0 & 0 & 0 & 0 & 0 & 0 & 0 & 0 & 0 & 1 & 0 & 0 & 0 \\
0 & 0 & 0 & 0 & 0 & 0 & 0 & 0 & 0 & 0 & 1 & \Delta T & 0 \\
0 & 0 & 0 & 0 & 0 & 0 & 0 & 0 & 0 & 0 & 0 & 1 & 0 \\
0 & 0 & 0 & 0 & 0 & 0 & 0 & 0 & 0 & 0 & 0 & 0 & 1
\end{bmatrix} \tag{10-50}$$

Therefore, the solution of the differential equation shown in 10-41 in discrete time at the successive time epoch t_l, can be written as:

$$\boldsymbol{x}(t_l) = \boldsymbol{\Phi}(t_l, t_{l-1})\boldsymbol{x}(t_l) + \int_{t_{l-1}}^{t_l} \boldsymbol{\Phi}(t_l, \tau)\boldsymbol{w}(\tau)d\tau \tag{10-51}$$

where the discrete white process noise sequence is represented by the integral relation $w_l = \int_{t_{l-1}}^{t_l} \boldsymbol{\Phi}(t_l, \tau)\boldsymbol{w}(\tau)d\tau$, whose covariance matrix is given as:

$$\boldsymbol{Q}_l = E\{\boldsymbol{w}_l \cdot \boldsymbol{w}_l^T\} = \int_{t_{l-1}}^{t_l} \boldsymbol{\Phi}(t_l, \tau)\boldsymbol{Q}(\tau)\boldsymbol{\Phi}^{\mathrm{T}}(t_l, \tau)d\tau \tag{10-52}$$

where $\boldsymbol{Q}$ is the continuous-time process noise covariance matrix, already presented in the previous chapter.

The process noise discretization for the position and velocity states along the X-axis is computed as:

$$\boldsymbol{Q}_{x,l} = \int_{t_{l-1}}^{t_l} \begin{bmatrix} 1 & \Delta T & \Delta T^2 \\ 0 & 1 & \Delta T \\ 0 & 0 & 1 \end{bmatrix} \cdot \begin{bmatrix} 0 & 0 & 0 \\ 0 & 0 & 0 \\ 0 & 0 & \sigma_{\ddot{p}_x}^2 \end{bmatrix} \cdot \begin{bmatrix} 1 & 0 & 0 \\ \Delta T & 1 & 0 \\ \Delta T^2 & \Delta T & 1 \end{bmatrix} d\tau = \sigma_{\ddot{p}_x}^2 \cdot \begin{bmatrix} \frac{\Delta T^5}{20} & \frac{\Delta T^4}{8} & \frac{\Delta T^3}{6} \\ \frac{\Delta T^4}{8} & \frac{\Delta T^3}{3} & \frac{\Delta T^2}{2} \\ \frac{\Delta T^3}{6} & \frac{\Delta T^2}{2} & \Delta T \end{bmatrix} \tag{10-53}$$

where $\begin{bmatrix} 1 & \Delta T & \Delta T^2 \\ 0 & 1 & \Delta T \\ 0 & 0 & 1 \end{bmatrix}$ is the discrete representation of the continuous time state transition sub-matrix.

The same is applied to obtain the discrete time process noise covariance matrixes for the Y- user's position projections:

$$\boldsymbol{Q}_{y,l} = \sigma_{\ddot{p}_y}^2 \cdot \begin{bmatrix} \frac{\Delta T^5}{20} & \frac{\Delta T^4}{8} & \frac{\Delta T^3}{6} \\ \frac{\Delta T^4}{8} & \frac{\Delta T^3}{3} & \frac{\Delta T^2}{2} \\ \frac{\Delta T^3}{6} & \frac{\Delta T^2}{2} & \Delta T \end{bmatrix} \quad 10\text{-}54$$

and Z- axis user's position projections

$$\boldsymbol{Q}_{z,l} = \sigma_{\ddot{p}_z}^2 \cdot \begin{bmatrix} \frac{\Delta T^5}{20} & \frac{\Delta T^4}{8} & \frac{\Delta T^3}{6} \\ \frac{\Delta T^4}{8} & \frac{\Delta T^3}{3} & \frac{\Delta T^2}{2} \\ \frac{\Delta T^3}{6} & \frac{\Delta T^2}{2} & \Delta T \end{bmatrix} \quad 10\text{-}55$$

where $\sigma_a^2 = \sigma_{\ddot{p}_x}^2 = \sigma_{\ddot{p}_y}^2 = \sigma_{\ddot{p}_z}^2$ is the acceleration PSD matrix resolved about the axes of ECEF frame, These depend on the dynamics of the application. A suitable value used for the data campaign under exam [15] is 1 $\mathrm{m^2 s^{-3}}$.

Applying the discretization process to the user's clock covariance states, the following relation is obtained:

$$\boldsymbol{Q}_{clk,l} = \int_{t_{l-1}}^{t_l} \begin{bmatrix} 1 & \Delta T \\ 0 & 1 \end{bmatrix} \cdot \begin{bmatrix} \sigma_b^2 & 0 \\ 0 & \sigma_{\dot{b}}^2 \end{bmatrix} \cdot \begin{bmatrix} 1 & 0 \\ \Delta T & 1 \end{bmatrix} d\tau = \begin{bmatrix} \sigma_b^2 \Delta T + \sigma_{\dot{b}}^2 \frac{\Delta T^3}{3} & \sigma_{\dot{b}}^2 \frac{\Delta T^2}{2} \\ \sigma_{\dot{b}}^2 \frac{\Delta T^2}{2} & \sigma_{\dot{b}}^2 \Delta T \end{bmatrix} \quad 10\text{-}56$$

where:

- σ_b^2 is the receiver clock phase-drift PSD, typical value for a TCXO is 0.01 $\mathrm{m^2}$ [15];
- $\sigma_{\dot{b}}^2$ is the receiver clock frequency-drift PSD, typical value for a TCXO is 0.04 $\mathrm{m^2}$ [15];

Combining the expressions in 10-53, 10-54, 10-55 and 10-56, the final discrete process noise covariance matrix is written as

$$\boldsymbol{Q}_l = \begin{pmatrix} \frac{1}{20}\sigma_a^2\Delta T^5 & 0 & 0 & \frac{1}{8}\sigma_a^2\Delta T^4 & 0 & 0 & \frac{1}{6}\sigma_a^2\Delta T^3 & 0 & 0 & 0 & 0 & 0 \\ 0 & \frac{1}{20}\sigma_a^2\Delta T^5 & 0 & 0 & \frac{1}{8}\sigma_a^2\Delta T^4 & 0 & 0 & \frac{1}{6}\sigma_a^2\Delta T^3 & 0 & 0 & 0 & 0 \\ 0 & 0 & \frac{1}{20}\sigma_a^2\Delta T^5 & 0 & 0 & \frac{1}{8}\sigma_a^2\Delta T^4 & 0 & 0 & \frac{1}{6}\sigma_a^2\Delta T^3 & 0 & 0 & 0 \\ \frac{1}{8}\sigma_a^2\Delta T^4 & 0 & 0 & \frac{1}{3}\sigma_a^2\Delta T^3 & 0 & 0 & \frac{1}{2}\sigma_a^2\Delta T^2 & 0 & 0 & 0 & 0 & 0 \\ 0 & \frac{1}{8}\sigma_a^2\Delta T^4 & 0 & 0 & \frac{1}{3}\sigma_a^2\Delta T^3 & 0 & 0 & \frac{1}{2}\sigma_a^2\Delta T^2 & 0 & 0 & 0 & 0 \\ 0 & 0 & \frac{1}{8}\sigma_a^2\Delta T^4 & 0 & 0 & \frac{1}{3}\sigma_a^2\Delta T^3 & 0 & 0 & \frac{1}{2}\sigma_a^2\Delta T^2 & 0 & 0 & 0 \\ \frac{1}{6}\sigma_a^2\Delta T^3 & 0 & 0 & \frac{1}{2}\sigma_a^2\Delta T^2 & 0 & 0 & \sigma_a^2\Delta T & 0 & 0 & 0 & 0 & 0 \\ 0 & \frac{1}{6}\sigma_a^2\Delta T^3 & 0 & 0 & \frac{1}{2}\sigma_a^2\Delta T^2 & 0 & 0 & \sigma_a^2\Delta T & 0 & 0 & 0 & 0 \\ 0 & 0 & \frac{1}{6}\sigma_a^2\Delta T^3 & 0 & 0 & \frac{1}{2}\sigma_a^2\Delta T^2 & 0 & 0 & \sigma_a^2\Delta T & 0 & 0 & 0 \\ 0 & 0 & 0 & 0 & 0 & 0 & 0 & 0 & 0 & \sigma_b^2\Delta T + \sigma_{\dot{b}}^2\frac{\Delta T^3}{3} & \sigma_{\dot{b}}^2\frac{\Delta T^2}{2} & 0 \\ 0 & 0 & 0 & 0 & 0 & 0 & 0 & 0 & 0 & \sigma_{\dot{b}}^2\frac{\Delta T^2}{2} & \sigma_b^2\Delta T & 0 \\ 0 & 0 & 0 & 0 & 0 & 0 & 0 & 0 & 0 & 0 & 0 & \sigma_{\delta C}^2\Delta T \end{pmatrix}$$

10-57

where:

- σ_a^2 is the acceleration noise process PSD;
- σ_b^2 is the clock bias noise process;
- $\sigma_{\dot{b}}^2$ is the clock drift noise process;
- $\sigma_{\delta C}^2$ is the inter-constellation GPS-to-Galileo PSD;
- ΔT is the time constant.

10.2.3.2 EKF Design Matrix

This section presents the EKF observation model, applied in the innovative PVTE estimator used in this work, section 3.2.3.2.1 and the EKF computational steps.

The EKF observation model is already described in the section describing the computational steps of the PVT estimator, section 3.2.3.2.2.2. Also, the predicted measurement vector $\hat{\boldsymbol{z}}$ is calculated as detailed in section 10.2.2.1, where the estimated state used to calculate $\hat{\boldsymbol{z}}$ is equal to the predicted state model obtained from the state prediction model.

The predicted measurement vector $\hat{\boldsymbol{z}}$ is used to compute the observation matrix $\boldsymbol{H}$:

$$\boldsymbol{H}_l = \begin{bmatrix} -\hat{u}_{x,GPS}^{1} & -\hat{u}_{y,GPS}^{1} & -\hat{u}_{z,GPS}^{1} & 0 & 0 & 0 & 0 & 0 & 0 & 1 & 0 & 0 \\ -\hat{u}_{x,GPS}^{2} & -\hat{u}_{y,GPS}^{2} & -\hat{u}_{z,GPS}^{2} & 0 & 0 & 0 & 0 & 0 & 0 & 1 & 0 & 0 \\ \dots & \dots & \dots & \dots & \dots & \dots & \dots & \dots & \dots & \dots & \dots & \dots \\ -\hat{u}_{x,GPS}^{N_1} & -\hat{u}_{y,GPS}^{N_1} & -\hat{u}_{z,GPS}^{N_1} & 0 & 0 & 0 & 0 & 0 & 0 & 1 & 0 & 0 \\ -\hat{u}_{x,GAL}^{N_1+1} & -\hat{u}_{y,GAL}^{N_1+1} & -\hat{u}_{z,GAL}^{N_1+1} & 0 & 0 & 0 & 0 & 0 & 0 & 1 & 0 & 1 \\ -\hat{u}_{x,GAL}^{N_1+2} & -\hat{u}_{y,GAL}^{N_1+2} & -\hat{u}_{z,GAL}^{N_1+2} & 0 & 0 & 0 & 0 & 0 & 0 & 1 & 0 & 1 \\ \dots & \dots & \dots & \dots & \dots & \dots & \dots & \dots & \dots & \dots & \dots & \dots \\ -\hat{u}_{x,GAL}^{N_1+N_2} & -\hat{u}_{y,GAL}^{N_1+N_2} & -\hat{u}_{z,GAL}^{N_1+N_2} & 0 & 0 & 0 & 0 & 0 & 0 & 1 & 0 & 1 \\ 0 & 0 & 0 & -\hat{u}_{x,GPS}^{1} & -\hat{u}_{y,GPS}^{1} & -\hat{u}_{z,GPS}^{1} & 0 & 0 & 0 & 0 & 1 & 0 \\ 0 & 0 & 0 & -\hat{u}_{x,GPS}^{2} & -\hat{u}_{y,GPS}^{2} & -\hat{u}_{z,GPS}^{2} & 0 & 0 & 0 & 0 & 1 & 0 \\ \dots & \dots & \dots & \dots & \dots & \dots & \dots & \dots & \dots & \dots & \dots & \dots \\ 0 & 0 & 0 & -\hat{u}_{x,GPS}^{N_1} & -\hat{u}_{y,GPS}^{N_1} & -\hat{u}_{z,GPS}^{N_1} & 0 & 0 & 0 & 0 & 1 & 0 \\ 0 & 0 & 0 & -\hat{u}_{x,GAL}^{N_1+1} & -\hat{u}_{y,GAL}^{N_1+1} & -\hat{u}_{z,GAL}^{N_1+11} & 0 & 0 & 0 & 0 & 1 & 0 \\ 0 & 0 & 0 & -\hat{u}_{x,GAL}^{N_1+2} & -\hat{u}_{y,GAL}^{N_1+2} & -\hat{u}_{z,GAL}^{N_1+2} & 0 & 0 & 0 & 0 & 1 & 0 \\ \dots & \dots & \dots & \dots & \dots & \dots & \dots & \dots & \dots & \dots & \dots & \dots \\ 0 & 0 & 0 & -\hat{u}_{x,GAL}^{N_1+N_2} & -\hat{u}_{y,GAL}^{N_1+N_2} & -\hat{u}_{z,GAL}^{N_1+N_2} & 0 & 0 & 0 & 0 & 1 & 0 \end{bmatrix} \quad 10\text{-}58$$

10.2.3.3 EKF innovated covariance matrix

The innovated covariance matrix at epoch l is equal to:

$$\boldsymbol{P}_{l|l} = E\{d\boldsymbol{x}_{l|l} \cdot d\boldsymbol{x}_{l|l}^{\boldsymbol{T}}\} \quad 10\text{-}59$$

The state covariance matrix is symmetric and the diagonal elements are the variances of each state estimate:

$$\boldsymbol{P}_{l|l} = \begin{pmatrix} \sigma_x^2[l] & 0 & 0 & 0 & 0 & 0 & 0 & 0 & 0 & 0 & 0 & 0 \\ 0 & \sigma_y^2[l] & 0 & 0 & 0 & 0 & 0 & 0 & 0 & 0 & 0 & 0 \\ 0 & 0 & \sigma_z^2[l] & 0 & 0 & 0 & 0 & 0 & 0 & 0 & 0 & 0 \\ 0 & 0 & 0 & \sigma_{\dot{x}}^2[l] & 0 & 0 & 0 & 0 & 0 & 0 & 0 & 0 \\ 0 & 0 & 0 & 0 & \sigma_{\dot{y}}^2[l] & 0 & 0 & 0 & 0 & 0 & 0 & 0 \\ 0 & 0 & 0 & 0 & 0 & \sigma_{\dot{z}}^2[l] & 0 & 0 & 0 & 0 & 0 & 0 \\ 0 & 0 & 0 & 0 & 0 & 0 & \sigma_{\ddot{x}}^2[l] & 0 & 0 & 0 & 0 & 0 \\ 0 & 0 & 0 & 0 & 0 & 0 & 0 & \sigma_{\ddot{y}}^2[l] & 0 & 0 & 0 & 0 \\ 0 & 0 & 0 & 0 & 0 & 0 & 0 & 0 & \sigma_{\ddot{z}}^2[l] & 0 & 0 & 0 \\ 0 & 0 & 0 & 0 & 0 & 0 & 0 & 0 & 0 & \sigma_{b,GPS}^2[l] & 0 & 0 \\ 0 & 0 & 0 & 0 & 0 & 0 & 0 & 0 & 0 & 0 & \sigma_{\dot{b},GPS}^2[l] & 0 \\ 0 & 0 & 0 & 0 & 0 & 0 & 0 & 0 & 0 & 0 & 0 & \sigma_{\delta C}^2[l] \end{pmatrix} \quad 10\text{-}60$$

where:

- $\sigma_r^2 = \left[\sigma_x^2,\ \sigma_y^2,\ \sigma_z^2\right]$ is the initial position error variance,
- $\sigma_v^2 = \left[\sigma_{\dot{x}}^2,\ \sigma_{\dot{y}}^2,\ \sigma_{\dot{z}}^2\right]$ is the initial speed error variance,
- $\sigma_a^2 = \left[\sigma_{\ddot{x}}^2,\ \sigma_{\ddot{y}}^2,\ \sigma_{\ddot{z}}^2\right]$ is the initial acceleration error variance,
- $\sigma_{b,GPS}^2$ is the initial GPS clock bias error variance,
- $\sigma_{\dot{b},GPS}^2$ is the initial GPS clock drift error variance,
- $\sigma_{\delta C}^2$ is the initial GPS-to-Galileo inter-constellation bias error variance.

10.2.3.4 EKF Operational steps

The detailed flowchart of the EKF estimation process is illustrated in Figure 10-5, where it can be noted that the EKF estimation equations fall in to two categories:

- State prediction block, composed of:
  - State prediction equations, performing the propagation in time of the state vector $\boldsymbol{x}_{l|l-1}$ and its covariance matrix $\boldsymbol{P}_{l|l-1}$ from the previous time epoch $(l-1)$ to the current one l;
  - Measurement prediction equations, $\hat{z}_l$ in the current epoch l, through the use of the predicted state, $\boldsymbol{x}_{l|l-1}$;
- Innovation block, composed by:
  - Measurement update (correction) equations, refining the a priori state vector and covariance matrix estimations $(\boldsymbol{x}_{l|l-1}, \boldsymbol{P}_{l|l-1})$ by feeding the current epoch measurements $(\boldsymbol{z}_l)$ into the filter and thus, obtaining the improved a posteriori estimate $(\boldsymbol{x}_{l|l}, \boldsymbol{P}_{l|l})$.

In this work the notation $\boldsymbol{x}_{m|n}$ represents the estimate of $\boldsymbol{x}$ at the epoch m given measurements from epoch n up to the current epoch m, where $n \leq m$. The same consideration holds also for the other vector and matrix terms.

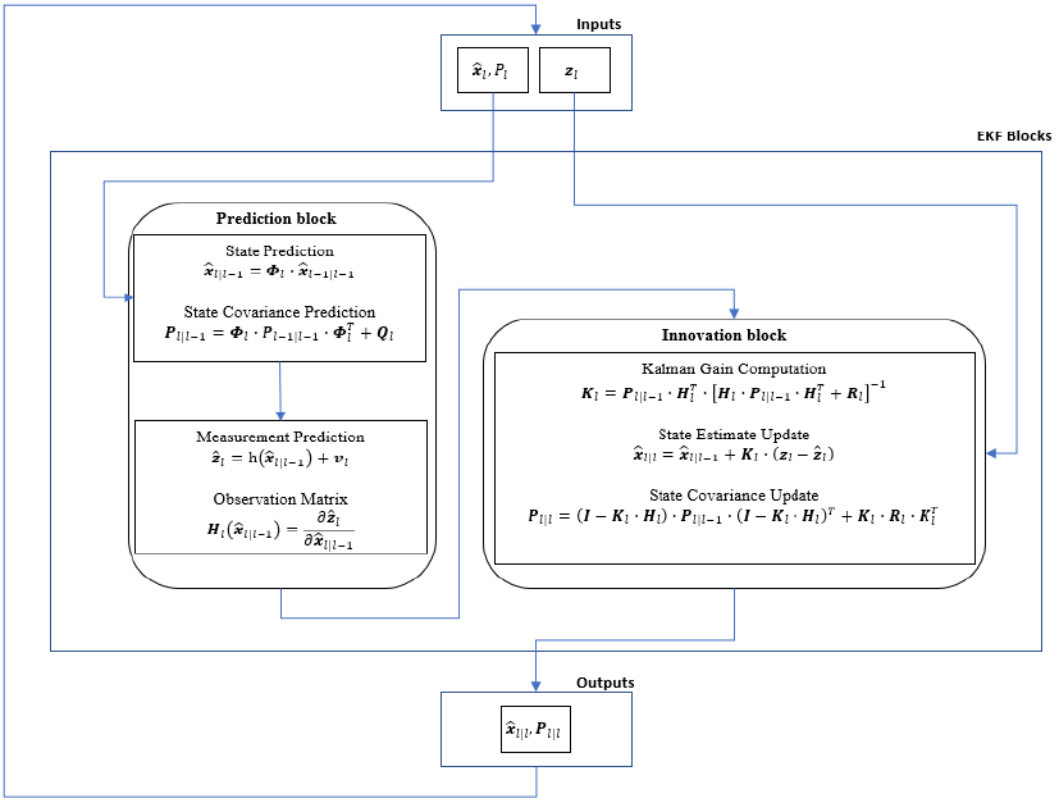

Figure 10-5 – The complete flowchart of the EKF recursive operation.

The first step of the EKF is the state vector initialization. As the name implies, the initial state is defined, denoted as $\boldsymbol{x}_0$. The deviation of the state vector estimate from the true value of the state vector is equal to:

$$\delta \boldsymbol{x}_0 = x_0 - \hat{x}_0 \tag{10-61}$$

The error covariance matrix defines the expectation of the square of the deviation of the state vector estimate from the true value of the state vector:

$$\boldsymbol{P}_0 = E\{\delta \boldsymbol{x}_0 \cdot \delta \boldsymbol{x}_0^T\} \tag{10-62}$$

The state covariance matrix is symmetric and the diagonal elements are the variances of each state estimate, while their square roots are the standard deviations. Detailed model is provided in Annex 10.2.2.

Afterwards, the computational steps that the EKF performs to obtain a navigation solution are described in the following. As already stated, the EKF basic stages are the state prediction and the measurement update stage. The

state prediction stage, in Figure 4-1, corresponds to the forward time projection of the state vector $\hat{\boldsymbol{x}}_{l|l-1}$ and state covariance matrix $P_{l|l-1}$. It is performed with two different actions:

1- State Prediction:

$$\hat{\boldsymbol{x}}_{l|l-1} = \boldsymbol{\Phi}_l \cdot \hat{\boldsymbol{x}}_{l-1|l-1} \quad 10\text{-}63$$

2- State matrix covariance prediction:

$$\boldsymbol{P}_{l|l-1} = \boldsymbol{\Phi}_l \cdot \boldsymbol{P}_{l-1|l-1} \cdot \boldsymbol{\Phi}_l^T + \boldsymbol{Q}_l \quad 10\text{-}64$$

Once the prediction is performed, the observables are used to generate a correction of the predicted estimations. The goal is to finally obtain a corrected state estimation and a corrected state covariance matrix.

The correction is an operation based on the difference between the predicted measurements, obtained using the predicted solutions and the real observables, weighted by a factor, called Kalman Gain, which is used to minimize the a posteriori state vector and its error covariance matrix. Intuitively, if the prediction is accurate, then there is little need to update it with the current measurement. On the contrary, worst prediction will need more corrections due to measurements. The Kalman gain is calculated as follows:

$$\boldsymbol{K}_l = \boldsymbol{P}_{l|l-1} \cdot \boldsymbol{H}_l^T \cdot \left[\boldsymbol{H}_l \cdot \boldsymbol{P}_{l|l-1} \cdot \boldsymbol{H}_l^T + \boldsymbol{R}_l\right]^{-1} \quad 10\text{-}65$$

The state vector estimate update $\hat{\boldsymbol{x}}_{l|l}$ is obtained using the following expression:

$$\hat{\boldsymbol{x}}_{l|l} = \hat{\boldsymbol{x}}_{l|l-1} + \boldsymbol{K}_l \cdot d\hat{\boldsymbol{z}}_l \quad 10\text{-}66$$

The state vector error covariance matrix update, is given by:

$$\boldsymbol{P}_{l|l} = (\boldsymbol{I} - \boldsymbol{K}_l \cdot \boldsymbol{H}_l) \cdot \boldsymbol{P}_{l|l-1} \quad 10\text{-}67$$

The innovated covariance matrix at epoch l is equal to:

$$\boldsymbol{P}_{l|l} = E\{d\boldsymbol{x}_{l|l} \cdot d\boldsymbol{x}_{l|l}^{\boldsymbol{T}}\} \quad 10\text{-}68$$

10.3 Annex – Multipath effects on the GNSS Receiver Tracking

This section contains the Annex developed for the Chapter 0. In the section 10.3.1, the mathematical model of the Atan 2 discriminator function in presence of composite signal affected by multipath, is developed. Finally, the mathematical model of the CP discriminator error variance, in presence of multipath and thermal noise, is illustrated in section 10.3.2.

10.3.1 MP Atan 2 Discriminator Function

The generic discriminator function can be written as follows:

$$D_{Atan2,k}(\varepsilon_{f,LOS}) = \frac{\text{atan2}\left(\frac{CROSS}{DOT}\right)}{2\pi T_I}$$

where:

$$DOT = I_{k-1}^P I_k^P + Q_{k-1}^P Q_k^P$$
$$CROSS = I_{k-1}^P Q_k^P - I_k^P Q_{k-1}^P$$

Firstly, it is calculated the DOT component

$$DOT = \left(\begin{array}{l} \frac{A_0}{2} R(\varepsilon_{\tau,LOS}) \,\text{sinc}(\pi \varepsilon_{f,LOS} T_I) \cos(\pi \varepsilon_{f,LOS} T_I + \varepsilon_{\varphi,LOS}) + \tilde{\alpha}_1 \frac{A_0}{2} R(\varepsilon_{\tau,MP}) \,\text{sinc}(\pi \varepsilon_{f,MP} T_I) \cos(\pi \varepsilon_{f,MP} T_I + \varepsilon_{\varphi,MP}) + \eta_{I,k-1}^P \\ \cdot \left[\frac{A_0}{2} R(\varepsilon_{\tau,LOS}) \,\text{sinc}(\pi \varepsilon_{f,LOS} T_I) \cos(3\pi \varepsilon_{f,LOS} T_I + \varepsilon_{\varphi,LOS}) + \tilde{\alpha}_1 \frac{A_0}{2} R(\varepsilon_{\tau,MP}) \,\text{sinc}(\pi \varepsilon_{f,MP} T_I) \cos(3\pi \varepsilon_{f,MP} T_I + \varepsilon_{\varphi,MP}) + \eta_{I,k}^P \right] \end{array} \right)$$

$$+\left(\begin{array}{c}\frac{A_0}{2}R(\varepsilon_{\tau,LOS})\,\mathrm{sinc}(\pi\varepsilon_{f,LOS}T_I)\sin(\pi\varepsilon_{f,LOS}T_I+\varepsilon_{\varphi,LOS})+\tilde{\alpha}_1\frac{A_0}{2}R(\varepsilon_{\tau,MP})\,\mathrm{sinc}(\pi\varepsilon_{f,MP}T_I)\sin(\pi\varepsilon_{f,MP}T_I+\varepsilon_{\varphi,MP})+\eta^P_{Q,k-1}\\ \cdot\left[\frac{A_0}{2}R(\varepsilon_{\tau,LOS})\,\mathrm{sinc}(\pi\varepsilon_{f,LOS}T_I)\sin(3\pi\varepsilon_{f,LOS}T_I+\varepsilon_{\varphi,LOS})+\tilde{\alpha}_1\frac{A_0}{2}R(\varepsilon_{\tau,MP})\,\mathrm{sinc}(\pi\varepsilon_{f,MP}T_I)\sin(3\pi\varepsilon_{f,MP}T_I+\varepsilon_{\varphi,LOS})+\eta^P_{Q,k}\right]\end{array}\right)=$$

$$=\left[\begin{array}{c}\left(\frac{A_0}{2}R(\varepsilon_{\tau,LOS})\,\mathrm{sinc}(\pi\varepsilon_{f,LOS}T_I)\cos(\pi\varepsilon_{f,LOS}T_I+\varepsilon_{\varphi,LOS})\cdot\frac{A_0}{2}R(\varepsilon_{\tau,LOS})\,\mathrm{sinc}(\pi\varepsilon_{f,LOS}T_I)\cos(3\pi\varepsilon_{f,LOS}T_I+\varepsilon_{\varphi,LOS})\right)+\\ \left(\frac{A_0}{2}R(\varepsilon_{\tau,LOS})\,\mathrm{sinc}(\pi\varepsilon_{f,LOS}T_I)\cos(\pi\varepsilon_{f,LOS}T_I+\varepsilon_{\varphi,LOS})\cdot\tilde{\alpha}_1\frac{A_0}{2}R(\varepsilon_{\tau,MP})\,\mathrm{sinc}(\pi\varepsilon_{f,MP}T_I)\cos(3\pi\varepsilon_{f,MP}T_I+\varepsilon_{\varphi,MP})\right)+\\ \left(\frac{A_0}{2}R(\varepsilon_{\tau,LOS})\,\mathrm{sinc}(\pi\varepsilon_{f,LOS}T_I)\cos(\pi\varepsilon_{f,LOS}T_I+\varepsilon_{\varphi,LOS})\cdot\eta^P_{I,k}\right)+\\ \left(\tilde{\alpha}_1\frac{A_0}{2}R(\varepsilon_{\tau,MP})\,\mathrm{sinc}(\pi\varepsilon_{f,MP}T_I)\cos(\pi\varepsilon_{f,MP}T_I+\varepsilon_{\varphi,MP})\cdot\frac{A_0}{2}R(\varepsilon_{\tau,LOS})\,\mathrm{sinc}(\pi\varepsilon_{f,LOS}T_I)\cos(3\pi\varepsilon_{f,LOS}T_I+\varepsilon_{\varphi,LOS})\right)+\\ \left(\tilde{\alpha}_1\frac{A_0}{2}R(\varepsilon_{\tau,MP})\,\mathrm{sinc}(\pi\varepsilon_{f,MP}T_I)\cos(\pi\varepsilon_{f,MP}T_I+\varepsilon_{\varphi,MP})\cdot\tilde{\alpha}_1\frac{A_0}{2}R(\varepsilon_{\tau,MP})\,\mathrm{sinc}(\pi\varepsilon_{f,MP}T_I)\cos(3\pi\varepsilon_{f,MP}T_I+\varepsilon_{\varphi,MP})\right)+\\ \left(\tilde{\alpha}_1\frac{A_0}{2}R(\varepsilon_{\tau,MP})\,\mathrm{sinc}(\pi\varepsilon_{f,MP}T_I)\cos(\pi\varepsilon_{f,MP}T_I+\varepsilon_{\varphi,MP})\cdot\eta^P_{I,k}\right)+\\ \left(\eta^P_{I,k-1}\cdot\frac{A_0}{2}R(\varepsilon_{\tau,LOS})\,\mathrm{sinc}(\pi\varepsilon_{f,LOS}T_I)\cos(3\pi\varepsilon_{f,LOS}T_I+\varepsilon_{\varphi,LOS})\right)+\\ \left(\eta^P_{I,k-1}\cdot\tilde{\alpha}_1\frac{A_0}{2}R(\varepsilon_{\tau,MP})\,\mathrm{sinc}(\pi\varepsilon_{f,MP}T_I)\cos(3\pi\varepsilon_{f,MP}T_I+\varepsilon_{\varphi,MP})\right)+\\ \left(\eta^P_{I,k-1}\cdot\eta^P_{I,k}\right)+\end{array}\right]+$$

$$\left[\begin{array}{c}\left(\frac{A_0}{2}R(\varepsilon_{\tau,LOS})\,\mathrm{sinc}(\pi\varepsilon_{f,LOS}T_I)\sin(\pi\varepsilon_{f,LOS}T_I+\varepsilon_{\varphi,LOS})\cdot\frac{A_0}{2}R(\varepsilon_{\tau,LOS})\,\mathrm{sinc}(\pi\varepsilon_{f,LOS}T_I)\sin(3\pi\varepsilon_{f,LOS}T_I+\varepsilon_{\varphi,LOS})\right)+\\ \left(\frac{A_0}{2}R(\varepsilon_{\tau,LOS})\,\mathrm{sinc}(\pi\varepsilon_{f,LOS}T_I)\sin(\pi\varepsilon_{f,LOS}T_I+\varepsilon_{\varphi,LOS})\cdot\tilde{\alpha}_1\frac{A_0}{2}R(\varepsilon_{\tau,MP})\,\mathrm{sinc}(\pi\varepsilon_{f,MP}T_I)\sin(3\pi\varepsilon_{f,MP}T_I+\varepsilon_{\varphi,MP})\right)+\\ \left(\frac{A_0}{2}R(\varepsilon_{\tau,LOS})\,\mathrm{sinc}(\pi\varepsilon_{f,LOS}T_I)\sin(\pi\varepsilon_{f,LOS}T_I+\varepsilon_{\varphi,LOS})\cdot\eta^P_{Q,k}\right)+\\ \left(\tilde{\alpha}_1\frac{A_0}{2}R(\varepsilon_{\tau,MP})\,\mathrm{sinc}(\pi\varepsilon_{f,MP}T_I)\sin(\pi\varepsilon_{f,MP}T_I+\varepsilon_{\varphi,MP})\cdot\frac{A_0}{2}R(\varepsilon_{\tau,LOS})\,\mathrm{sinc}(\pi\varepsilon_{f,LOS}T_I)\sin(3\pi\varepsilon_{f,LOS}T_I+\varepsilon_{\varphi,LOS})\right)+\\ \left(\tilde{\alpha}_1\frac{A_0}{2}R(\varepsilon_{\tau,MP})\,\mathrm{sinc}(\pi\varepsilon_{f,MP}T_I)\sin(\pi\varepsilon_{f,MP}T_I+\varepsilon_{\varphi,MP})\cdot\tilde{\alpha}_1\frac{A_0}{2}R(\varepsilon_{\tau,MP})\,\mathrm{sinc}(\pi\varepsilon_{f,MP}T_I)\sin(3\pi\varepsilon_{f,MP}T_I+\varepsilon_{\varphi,MP})\right)+\\ \left(\tilde{\alpha}_1\frac{A_0}{2}R(\varepsilon_{\tau,MP})\,\mathrm{sinc}(\pi\varepsilon_{f,MP}T_I)\sin(\pi\varepsilon_{f,MP}T_I+\varepsilon_{\varphi,MP})\cdot\eta^P_{Q,k}\right)+\\ \left(\eta^P_{Q,k-1}\cdot\frac{A_0}{2}R(\varepsilon_{\tau,LOS})\,\mathrm{sinc}(\pi\varepsilon_{f,LOS}T_I)\sin(3\pi\varepsilon_{f,LOS}T_I+\varepsilon_{\varphi,LOS})\right)+\\ \left(\eta^P_{Q,k-1}\cdot\tilde{\alpha}_1\frac{A_0}{2}R(\varepsilon_{\tau,MP})\,\mathrm{sinc}(\pi\varepsilon_{f,MP}T_I)\sin(3\pi\varepsilon_{f,MP}T_I+\varepsilon_{\varphi,MP})\right)+\\ \left(\eta^P_{Q,k-1}\cdot\eta^P_{Q,k}\right)+\end{array}\right]= \quad 10\text{-}69$$

The common variables can be grouped as follows:

$$DOT=\left[\begin{array}{c}\left(\frac{A_0^2}{4}R^2(\varepsilon_{\tau,LOS})\,\mathrm{sinc}^2(\pi\varepsilon_{f,LOS}T_I)\cos(\pi\varepsilon_{f,LOS}T_I+\varepsilon_{\varphi,LOS})\cdot\cos(3\pi\varepsilon_{f,LOS}T_I+\varepsilon_{\varphi,LOS})\right)+\\ \left(\tilde{\alpha}_1\frac{A_0^2}{4}R(\varepsilon_{\tau,LOS})R(\varepsilon_{\tau,MP})\,\mathrm{sinc}(\pi\varepsilon_{f,LOS}T_I)\,\mathrm{sinc}(\pi\varepsilon_{f,MP}T_I)\cos(\pi\varepsilon_{f,LOS}T_I+\varepsilon_{\varphi,LOS})\cdot\cos(3\pi\varepsilon_{f,MP}T_I+\varepsilon_{\varphi,MP})\right)+\\ \left(\frac{A_0}{2}R(\varepsilon_{\tau,LOS})\,\mathrm{sinc}(\pi\varepsilon_{f,LOS}T_I)\cos(\pi\varepsilon_{f,LOS}T_I+\varepsilon_{\varphi,LOS})\cdot\eta^P_{I,k}\right)+\\ \left(\tilde{\alpha}_1\frac{A_0^2}{4}R(\varepsilon_{\tau,MP})R(\varepsilon_{\tau,LOS})\,\mathrm{sinc}(\pi\varepsilon_{f,MP}T_I)\,\mathrm{sinc}(\pi\varepsilon_{f,LOS}T_I)\cos(\pi\varepsilon_{f,MP}T_I+\varepsilon_{\varphi,MP})\cdot\cos(3\pi\varepsilon_{f,LOS}T_I+\varepsilon_{\varphi,LOS})\right)+\\ \left(\tilde{\alpha}_1^2\frac{A_0^2}{4}R^2(\varepsilon_{\tau,MP})\,\mathrm{sinc}^2(\pi\varepsilon_{f,MP}T_I)\cos(\pi\varepsilon_{f,MP}T_I+\varepsilon_{\varphi,MP})\cdot\cos(3\pi\varepsilon_{f,MP}T_I+\varepsilon_{\varphi,MP})\right)+\\ \left(\tilde{\alpha}_1\frac{A_0}{2}R(\varepsilon_{\tau,MP})\,\mathrm{sinc}(\pi\varepsilon_{f,MP}T_I)\cos(\pi\varepsilon_{f,MP}T_I+\varepsilon_{\varphi,MP})\cdot\eta^P_{I,k}\right)+\\ \left(\eta^P_{I,k-1}\cdot\frac{A_0}{2}R(\varepsilon_{\tau,LOS})\,\mathrm{sinc}(\pi\varepsilon_{f,LOS}T_I)\cos(3\pi\varepsilon_{f,LOS}T_I+\varepsilon_{\varphi,LOS})\right)+\\ \left(\eta^P_{I,k-1}\cdot\tilde{\alpha}_1\frac{A_0}{2}R(\varepsilon_{\tau,MP})\,\mathrm{sinc}(\pi\varepsilon_{f,MP}T_I)\cos(3\pi\varepsilon_{f,MP}T_I+\varepsilon_{\varphi,MP})\right)+\\ \left(\eta^P_{I,k-1}\cdot\eta^P_{I,k}\right)+\end{array}\right]+$$

$$\left[\begin{array}{c}\left(\frac{A_0^2}{4}R^2(\varepsilon_{\tau,LOS})\,\mathrm{sinc}^2(\pi\varepsilon_{f,LOS}T_I)\sin(\pi\varepsilon_{f,LOS}T_I+\varepsilon_{\varphi,LOS})\cdot\sin(3\pi\varepsilon_{f,LOS}T_I+\varepsilon_{\varphi,LOS})\right)+\\ \left(\tilde{\alpha}_1\frac{A_0^2}{4}R(\varepsilon_{\tau,LOS})R(\varepsilon_{\tau,MP})\,\mathrm{sinc}(\pi\varepsilon_{f,LOS}T_I)\,\mathrm{sinc}(\pi\varepsilon_{f,MP}T_I)\sin(\pi\varepsilon_{f,LOS}T_I+\varepsilon_{\varphi,LOS})\cdot\sin(3\pi\varepsilon_{f,MP}T_I+\varepsilon_{\varphi,MP})\right)+\\ \left(\frac{A_0}{2}R(\varepsilon_{\tau,LOS})\,\mathrm{sinc}(\pi\varepsilon_{f,LOS}T_I)\sin(\pi\varepsilon_{f,LOS}T_I+\varepsilon_{\varphi,LOS})\cdot\eta_{Q,k}^P\right)+\\ \left(\tilde{\alpha}_1\frac{A_0^2}{4}R(\varepsilon_{\tau,MP})R(\varepsilon_{\tau,LOS})\,\mathrm{sinc}(\pi\varepsilon_{f,MP}T_I)\,\mathrm{sinc}(\pi\varepsilon_{f,LOS}T_I)\sin(\pi\varepsilon_{f,MP}T_I+\varepsilon_{\varphi,MP})\cdot\sin(3\pi\varepsilon_{f,LOS}T_I+\varepsilon_{\varphi,LOS})\right)+\\ \left(\tilde{\alpha}_1^2\frac{A_0^2}{4}R^2(\varepsilon_{\tau,MP})\,\mathrm{sinc}^2(\pi\varepsilon_{f,MP}T_I)\sin(\pi\varepsilon_{f,MP}T_I+\varepsilon_{\varphi,MP})\cdot\sin(3\pi\varepsilon_{f,MP}T_I+\varepsilon_{\varphi,MP})\right)+\\ \left(\tilde{\alpha}_1\frac{A_0}{2}R(\varepsilon_{\tau,MP})\,\mathrm{sinc}(\pi\varepsilon_{f,MP}T_I)\sin(\pi\varepsilon_{f,MP}T_I+\varepsilon_{\varphi,MP})\cdot\eta_{Q,k}^P\right)+\\ \left(\eta_{Q,k-1}^P\cdot\frac{A_0}{2}R(\varepsilon_{\tau,LOS})\,\mathrm{sinc}(\pi\varepsilon_{f,LOS}T_I)\sin(3\pi\varepsilon_{f,LOS}T_I+\varepsilon_{\varphi,LOS})\right)+\\ \left(\eta_{Q,k-1}^P\cdot\tilde{\alpha}_1\frac{A_0}{2}R(\varepsilon_{\tau,MP})\,\mathrm{sinc}(\pi\varepsilon_{f,MP}T_I)\sin(3\pi\varepsilon_{f,MP}T_I+\varepsilon_{\varphi,MP})\right)+\\ \left(\eta_{Q,k-1}^P\cdot\eta_{Q,k}^P\right)+\end{array}\right] \quad 10\text{-}70$$

Defining:

$$\begin{gathered}\varepsilon_{\varphi_{0,k-1}}=\pi\varepsilon_{f,LOS}T_I+\varepsilon_{\varphi,LOS}\\ \varepsilon_{\varphi_{0,k}}=3\pi\varepsilon_{f,LOS}T_I+\varepsilon_{\varphi,LOS}\\ \varepsilon_{\varphi_{1,k-1}}=\pi\varepsilon_{f,MP}T_I+\varepsilon_{\varphi,MP}\\ \varepsilon_{\varphi_{1,k}}=3\pi\varepsilon_{f,MP}T_I+\varepsilon_{\varphi,MP}\end{gathered} \quad 10\text{-}71$$

Substituting 10-71 in the equation 10-70 it is obtained:

$$\begin{gathered}\frac{A_0^2}{4}R^2(\varepsilon_{\tau,LOS})\,\mathrm{sinc}^2(\pi\varepsilon_{f,LOS}T_I)\left(\cos(\varepsilon_{\varphi_{0,k-1}})\cdot\cos(\varepsilon_{\varphi_{0,k}})+\sin(\varepsilon_{\varphi_{0,k-1}})\cdot\sin(\varepsilon_{\varphi_{0,k}})\right)+\\ \tilde{\alpha}_1\frac{A_0^2}{4}R(\varepsilon_{\tau,LOS})R(\varepsilon_{\tau,MP})\,\mathrm{sinc}(\pi\varepsilon_{f,LOS}T_I)\,\mathrm{sinc}(\pi\varepsilon_{f,MP}T_I)\left(\left(\cos(\varepsilon_{\varphi_{0,k-1}})\cdot\cos(\varepsilon_{\varphi_{1,k}})\right)+\left(\cos(\varepsilon_{\varphi_{1,k-1}})\cdot\cos(\varepsilon_{\varphi_{0,k}})\right)+\left(\sin(\varepsilon_{\varphi_{0,k-1}})\cdot\sin(\varepsilon_{\varphi_{1,k}})\right)+\left(\sin(\varepsilon_{\varphi_{1,k-1}})\cdot\sin(\varepsilon_{\varphi_{0,k}})\right)\right)\\ +\frac{A_0}{2}R(\varepsilon_{\tau,LOS})\,\mathrm{sinc}(\pi\varepsilon_{f,LOS}T_I)\left(\left(\cos(\varepsilon_{\varphi_{0,k-1}})\cdot\eta_{I,k}^P\right)+\left(\cos(\varepsilon_{\varphi_{0,k}})\cdot\eta_{I,k-1}^P\right)+\left(\sin(\varepsilon_{\varphi_{0,k-1}})\cdot\eta_{Q,k}^P\right)+\left(\sin(\varepsilon_{\varphi_{0,k}})\cdot\eta_{Q,k-1}^P\right)\right)\\ +\tilde{\alpha}_1^2\frac{A_0^2}{4}R^2(\varepsilon_{\tau,MP})\,\mathrm{sinc}^2(\pi\varepsilon_{f,MP}T_I)\left(\cos(\varepsilon_{\varphi_{1,k-1}})\cdot\cos(\varepsilon_{\varphi_{1,k}})+\sin(\varepsilon_{\varphi_{1,k-1}})\cdot\sin(\varepsilon_{\varphi_{1,k}})\right)\\ +\tilde{\alpha}_1\frac{A_0}{2}R(\varepsilon_{\tau,MP})\,\mathrm{sinc}(\pi\varepsilon_{f,MP}T_I)\left(\left(\cos(\varepsilon_{\varphi_{1,k-1}})\cdot\eta_{I,k}^P\right)+\left(\cos(\varepsilon_{\varphi_{1,k}})\cdot\eta_{I,k-1}^P\right)+\left(\sin(\varepsilon_{\varphi_{1,k-1}})\cdot\eta_{Q,k}^P\right)+\left(\sin(\varepsilon_{\varphi_{1,k}})\cdot\eta_{Q,k-1}^P\right)\right)\\ +\left(\eta_{I,k-1}^P\cdot\eta_{I,k}^P\right)+\left(\eta_{Q,k-1}^P\cdot\eta_{Q,k}^P\right)\end{gathered} \quad 10\text{-}72$$

Finally, applying the trigonometric identities to 10-72:

$$DOT=\left[\begin{array}{c}X\left(\cos(\varepsilon_{\varphi_{0,k}}-\varepsilon_{\varphi_{0,k-1}})\right)+\\ Y\left(\cos(\varepsilon_{\varphi_{1,k}}-\varepsilon_{\varphi_{0,k-1}})+\cos(\varepsilon_{\varphi_{0,k}}-\varepsilon_{\varphi_{1,k-1}})\right)\\ +W\left(\left(\cos(\varepsilon_{\varphi_{0,k-1}})\cdot\eta_{I,k}^P\right)+\left(\cos(\varepsilon_{\varphi_{0,k}})\cdot\eta_{I,k-1}^P\right)+\left(\sin(\varepsilon_{\varphi_{0,k-1}})\cdot\eta_{Q,k}^P\right)+\left(\sin(\varepsilon_{\varphi_{0,k}})\cdot\eta_{Q,k-1}^P\right)\right)\\ +Z\left(\cos(\varepsilon_{\varphi_{1,k}}-\varepsilon_{\varphi_{1,k-1}})\right)\\ +R\left(\left(\cos(\varepsilon_{\varphi_{1,k-1}})\cdot\eta_{I,k}^P\right)+\left(\cos(\varepsilon_{\varphi_{1,k}})\cdot\eta_{I,k-1}^P\right)+\left(\sin(\varepsilon_{\varphi_{1,k-1}})\cdot\eta_{Q,k}^P\right)+\left(\sin(\varepsilon_{\varphi_{1,k}})\cdot\eta_{Q,k-1}^P\right)\right)\\ +\left(\eta_{I,k-1}^P\cdot\eta_{I,k}^P\right)+\left(\eta_{Q,k-1}^P\cdot\eta_{Q,k}^P\right)\end{array}\right]$$

$$\begin{gathered}X=\frac{A_0^2}{4}R^2(\varepsilon_{\tau,LOS})\,\mathrm{sinc}^2(\pi\varepsilon_{f,LOS}T_I)\\ Y=\frac{A_0}{2}R(\varepsilon_{\tau,LOS})\,\mathrm{sinc}(\pi\varepsilon_{f,LOS}T_I)\,\tilde{\alpha}_1\frac{A_0}{2}R(\varepsilon_{\tau,MP})\,\mathrm{sinc}(\pi\varepsilon_{f,MP}T_I)\\ Z=\tilde{\alpha}_1^2\frac{A_0^2}{4}R^2(\varepsilon_{\tau,MP})\,\mathrm{sinc}^2(\pi\varepsilon_{f,MP}T_I)\\ W=\frac{A_0}{2}R(\varepsilon_{\tau,LOS})\,\mathrm{sinc}(\pi\varepsilon_{f,LOS}T_I)\\ R=\tilde{\alpha}_1\frac{A_0}{2}R(\varepsilon_{\tau,MP})\,\mathrm{sinc}(\pi\varepsilon_{f,MP}T_I)\\ \varepsilon_{\varphi_{0,k}}-\varepsilon_{\varphi_{0,k-1}}=3\pi\varepsilon_{f,LOS}T_I+\varepsilon_{\varphi,LOS}-(\pi\varepsilon_{f,LOS}T_I+\varepsilon_{\varphi,LOS})=2\pi(\varepsilon_{f,LOS})T_I\\ \varepsilon_{\varphi_{1,k}}-\varepsilon_{\varphi_{0,k-1}}=3\pi\varepsilon_{f,MP}T_I+\varepsilon_{\varphi,MP}-(\pi\varepsilon_{f,MP}T_I+\varepsilon_{\varphi,MP})=2\pi(f_{LOS}-f_L)T_I+3\pi\Delta DT_I+\Delta\varphi\\ \varepsilon_{\varphi_{0,k}}-\varepsilon_{\varphi_{1,k-1}}=3\pi\varepsilon_{f,LOS}T_I+\varepsilon_{\varphi,LOS}-(\pi\varepsilon_{f,MP}T_I+\varepsilon_{\varphi,MP})=2\pi(\varepsilon_{f,LOS})T_I-\pi\Delta DT_I-\Delta\varphi\\ \varepsilon_{\varphi_{1,k}}-\varepsilon_{\varphi_{1,k-1}}=3\pi\varepsilon_{f,MP}T_I+\varepsilon_{\varphi,MP}-(\pi\varepsilon_{f,MP}T_I+\varepsilon_{\varphi,MP})=2\pi(\varepsilon_{f,LOS}+\Delta D)T_I=2\pi(\varepsilon_{f,LOS})T_I+2\pi\Delta DT_I\end{gathered}$$

Similarly, the Cross component is calculated as follows:

$$CROSS = I_{k-1}^{P} Q_{k}^{P} - I_{k}^{P} Q_{k-1}^{P} =$$

$$\begin{pmatrix} \frac{A_0}{2} R(\varepsilon_{\tau,LOS}) \operatorname{sinc}(\pi \varepsilon_{f,LOS} T_I) \cos(\pi \varepsilon_{f,LOS} T_I + \varepsilon_{\varphi,LOS}) + \tilde{\alpha}_1 \frac{A_0}{2} R(\varepsilon_{\tau,MP}) \operatorname{sinc}(\pi \varepsilon_{f,MP} T_I) \cos(\pi \varepsilon_{f,MP} T_I + \varepsilon_{\varphi,MP}) + \eta_{I,k-1}^{P} \\ \left[\frac{A_0}{2} R(\varepsilon_{\tau,LOS}) \operatorname{sinc}(\pi \varepsilon_{f,LOS} T_I) \sin(3\pi \varepsilon_{f,LOS} T_I + \varepsilon_{\varphi,LOS}) + \tilde{\alpha}_1 \frac{A_0}{2} R(\varepsilon_{\tau,MP}) \operatorname{sinc}(\pi \varepsilon_{f,MP} T_I) \sin(3\pi \varepsilon_{f,MP} T_I + \varepsilon_{\varphi,LOS}) + \eta_{Q,k}^{P} \right] \end{pmatrix}$$

$$- \begin{pmatrix} \frac{A_0}{2} R(\varepsilon_{\tau,LOS}) \operatorname{sinc}(\pi \varepsilon_{f,LOS} T_I) \cos(3\pi \varepsilon_{f,LOS} T_I + \varepsilon_{\varphi,LOS}) + \tilde{\alpha}_1 \frac{A_0}{2} R(\varepsilon_{\tau,MP}) \operatorname{sinc}(\pi \varepsilon_{f,MP} T_I) \cos(3\pi \varepsilon_{f,MP} T_I + \varepsilon_{\varphi,MP}) + \eta_{I,k}^{P} \\ \left[\frac{A_0}{2} R(\varepsilon_{\tau,LOS}) \operatorname{sinc}(\pi \varepsilon_{f,LOS} T_I) \sin(\pi \varepsilon_{f,LOS} T_I + \varepsilon_{\varphi,LOS}) + \tilde{\alpha}_1 \frac{A_0}{2} R(\varepsilon_{\tau,MP}) \operatorname{sinc}(\pi \varepsilon_{f,MP} T_I) \sin(\pi \varepsilon_{f,MP} T_I + \varepsilon_{\varphi,MP}) + \eta_{Q,k-1}^{P} \right] \end{pmatrix} =$$

$$\begin{bmatrix} \frac{A_0}{2} R(\varepsilon_{\tau,LOS}) \operatorname{sinc}(\pi \varepsilon_{f,LOS} T_I) \cos(\pi \varepsilon_{f,LOS} T_I + \varepsilon_{\varphi,LOS}) \cdot \frac{A_0}{2} R(\varepsilon_{\tau,LOS}) \operatorname{sinc}(\pi \varepsilon_{f,LOS} T_I) \sin(3\pi \varepsilon_{f,LOS} T_I + \varepsilon_{\varphi,LOS}) \\ + \frac{A_0}{2} R(\varepsilon_{\tau,LOS}) \operatorname{sinc}(\pi \varepsilon_{f,LOS} T_I) \cos(\pi \varepsilon_{f,LOS} T_I + \varepsilon_{\varphi,LOS}) \cdot \tilde{\alpha}_1 \frac{A_0}{2} R(\varepsilon_{\tau,MP}) \operatorname{sinc}(\pi \varepsilon_{f,MP} T_I) \sin(3\pi \varepsilon_{f,MP} T_I + \varepsilon_{\varphi,LOS}) \\ + \frac{A_0}{2} R(\varepsilon_{\tau,LOS}) \operatorname{sinc}(\pi \varepsilon_{f,LOS} T_I) \cos(\pi \varepsilon_{f,LOS} T_I + \varepsilon_{\varphi,LOS}) \cdot \eta_{Q,k}^{P} \\ + \tilde{\alpha}_1 \frac{A_0}{2} R(\varepsilon_{\tau,MP}) \operatorname{sinc}(\pi \varepsilon_{f,MP} T_I) \cos(\pi \varepsilon_{f,MP} T_I + \varepsilon_{\varphi,MP}) \cdot \frac{A_0}{2} R(\varepsilon_{\tau,LOS}) \operatorname{sinc}(\pi \varepsilon_{f,LOS} T_I) \sin(3\pi \varepsilon_{f,LOS} T_I + \varepsilon_{\varphi,LOS}) \\ + \tilde{\alpha}_1 \frac{A_0}{2} R(\varepsilon_{\tau,MP}) \operatorname{sinc}(\pi \varepsilon_{f,MP} T_I) \cos(\pi \varepsilon_{f,MP} T_I + \varepsilon_{\varphi,MP}) \cdot \tilde{\alpha}_1 \frac{A_0}{2} R(\varepsilon_{\tau,MP}) \operatorname{sinc}(\pi \varepsilon_{f,MP} T_I) \sin(3\pi \varepsilon_{f,MP} T_I + \varepsilon_{\varphi,LOS}) \\ + \tilde{\alpha}_1 \frac{A_0}{2} R(\varepsilon_{\tau,MP}) \operatorname{sinc}(\pi \varepsilon_{f,MP} T_I) \cos(\pi \varepsilon_{f,MP} T_I + \varepsilon_{\varphi,MP}) \cdot \eta_{Q,k}^{P} \\ + \eta_{I,k-1}^{P} \cdot \frac{A_0}{2} R(\varepsilon_{\tau,LOS}) \operatorname{sinc}(\pi \varepsilon_{f,LOS} T_I) \sin(3\pi \varepsilon_{f,LOS} T_I + \varepsilon_{\varphi,LOS}) \\ + \eta_{I,k-1}^{P} \cdot \tilde{\alpha}_1 \frac{A_0}{2} R(\varepsilon_{\tau,MP}) \operatorname{sinc}(\pi \varepsilon_{f,MP} T_I) \sin(3\pi \varepsilon_{f,LOS} T_I + \varepsilon_{\varphi,LOS}) \\ + \eta_{I,k-1}^{P} \cdot \eta_{Q,k}^{P} \end{bmatrix} -$$

$$\begin{bmatrix} \frac{A_0}{2} R(\varepsilon_{\tau,LOS}) \operatorname{sinc}(\pi \varepsilon_{f,LOS} T_I) \cos(3\pi \varepsilon_{f,LOS} T_I + \varepsilon_{\varphi,LOS}) \cdot \frac{A_0}{2} R(\varepsilon_{\tau,LOS}) \operatorname{sinc}(\pi \varepsilon_{f,LOS} T_I) \sin(\pi \varepsilon_{f,LOS} T_I + \varepsilon_{\varphi,LOS}) \\ + \frac{A_0}{2} R(\varepsilon_{\tau,LOS}) \operatorname{sinc}(\pi \varepsilon_{f,LOS} T_I) \cos(3\pi \varepsilon_{f,LOS} T_I + \varepsilon_{\varphi,LOS}) \cdot \tilde{\alpha}_1 \frac{A_0}{2} R(\varepsilon_{\tau,MP}) \operatorname{sinc}(\pi \varepsilon_{f,MP} T_I) \sin(\pi \varepsilon_{f,MP} T_I + \varepsilon_{\varphi,MP}) \\ + \frac{A_0}{2} R(\varepsilon_{\tau,LOS}) \operatorname{sinc}(\pi \varepsilon_{f,LOS} T_I) \cos(3\pi \varepsilon_{f,LOS} T_I + \varepsilon_{\varphi,LOS}) \cdot \eta_{Q,k-1}^{P} \\ + \tilde{\alpha}_1 \frac{A_0}{2} R(\varepsilon_{\tau,MP}) \operatorname{sinc}(\pi \varepsilon_{f,MP} T_I) \cos(3\pi \varepsilon_{f,MP} T_I + \varepsilon_{\varphi,MP}) \cdot \frac{A_0}{2} R(\varepsilon_{\tau,LOS}) \operatorname{sinc}(\pi \varepsilon_{f,LOS} T_I) \sin(\pi \varepsilon_{f,LOS} T_I + \varepsilon_{\varphi,LOS}) \\ + \tilde{\alpha}_1 \frac{A_0}{2} R(\varepsilon_{\tau,MP}) \operatorname{sinc}(\pi \varepsilon_{f,MP} T_I) \cos(3\pi \varepsilon_{f,MP} T_I + \varepsilon_{\varphi,MP}) \cdot \tilde{\alpha}_1 \frac{A_0}{2} R(\varepsilon_{\tau,MP}) \operatorname{sinc}(\pi \varepsilon_{f,MP} T_I) \sin(\pi \varepsilon_{f,MP} T_I + \varepsilon_{\varphi,MP}) \\ + \tilde{\alpha}_1 \frac{A_0}{2} R(\varepsilon_{\tau,MP}) \operatorname{sinc}(\pi \varepsilon_{f,MP} T_I) \cos(3\pi \varepsilon_{f,MP} T_I + \varepsilon_{\varphi,MP}) \cdot \eta_{Q,k-1}^{P} \\ + \eta_{I,k}^{P} \cdot \frac{A_0}{2} R(\varepsilon_{\tau,LOS}) \operatorname{sinc}(\pi \varepsilon_{f,LOS} T_I) \sin(\pi \varepsilon_{f,LOS} T_I + \varepsilon_{\varphi,LOS}) \\ + \eta_{I,k}^{P} \cdot \tilde{\alpha}_1 \frac{A_0}{2} R(\varepsilon_{\tau,MP}) \operatorname{sinc}(\pi \varepsilon_{f,MP} T_I) \sin(\pi \varepsilon_{f,MP} T_I + \varepsilon_{\varphi,MP}) \\ + \eta_{I,k}^{P} \cdot \eta_{Q,k-1}^{P} \end{bmatrix} =$$

$$\begin{bmatrix} \frac{A_0^2}{4} R^2(\varepsilon_{\tau,LOS}) \operatorname{sinc}^2(\pi \varepsilon_{f,LOS} T_I) \cos(\pi \varepsilon_{f,LOS} T_I + \varepsilon_{\varphi,LOS}) \cdot \sin(3\pi \varepsilon_{f,LOS} T_I + \varepsilon_{\varphi,LOS}) \\ + \frac{A_0}{2} R(\varepsilon_{\tau,LOS}) \operatorname{sinc}(\pi \varepsilon_{f,LOS} T_I) \tilde{\alpha}_1 \frac{A_0}{2} R(\varepsilon_{\tau,MP}) \operatorname{sinc}(\pi \varepsilon_{f,MP} T_I) \cos(\pi \varepsilon_{f,LOS} T_I + \varepsilon_{\varphi,LOS}) \cdot \sin(3\pi \varepsilon_{f,MP} T_I + \varepsilon_{\varphi,LOS}) \\ + \frac{A_0}{2} R(\varepsilon_{\tau,LOS}) \operatorname{sinc}(\pi \varepsilon_{f,LOS} T_I) \cos(\pi \varepsilon_{f,LOS} T_I + \varepsilon_{\varphi,LOS}) \cdot \eta_{Q,k}^{P} \\ + \tilde{\alpha}_1 \frac{A_0}{2} R(\varepsilon_{\tau,MP}) \operatorname{sinc}(\pi \varepsilon_{f,MP} T_I) \frac{A_0}{2} R(\varepsilon_{\tau,LOS}) \operatorname{sinc}(\pi \varepsilon_{f,LOS} T_I) \cos(\pi \varepsilon_{f,MP} T_I + \varepsilon_{\varphi,MP}) \cdot \sin(3\pi \varepsilon_{f,LOS} T_I + \varepsilon_{\varphi,LOS}) \\ + \tilde{\alpha}_1^2 \frac{A_0^2}{4} R^2(\varepsilon_{\tau,MP}) \operatorname{sinc}^2(\pi \varepsilon_{f,MP} T_I) \cos(\pi \varepsilon_{f,MP} T_I + \varepsilon_{\varphi,MP}) \cdot \sin(3\pi \varepsilon_{f,MP} T_I + \varepsilon_{\varphi,LOS}) \\ + \tilde{\alpha}_1 \frac{A_0}{2} R(\varepsilon_{\tau,MP}) \operatorname{sinc}(\pi \varepsilon_{f,MP} T_I) \cos(\pi \varepsilon_{f,MP} T_I + \varepsilon_{\varphi,MP}) \cdot \eta_{Q,k}^{P} \\ + \eta_{I,k-1}^{P} \cdot \frac{A_0}{2} R(\varepsilon_{\tau,LOS}) \operatorname{sinc}(\pi \varepsilon_{f,LOS} T_I) \sin(3\pi \varepsilon_{f,LOS} T_I + \varepsilon_{\varphi,LOS}) \\ + \eta_{I,k-1}^{P} \cdot \tilde{\alpha}_1 \frac{A_0}{2} R(\varepsilon_{\tau,MP}) \operatorname{sinc}(\pi \varepsilon_{f,MP} T_I) \sin(3\pi \varepsilon_{f,LOS} T_I + \varepsilon_{\varphi,LOS}) \\ + \eta_{I,k-1}^{P} \cdot \eta_{Q,k}^{P} \end{bmatrix}$$

$$\begin{bmatrix} \frac{A_0^2}{4}R^2(\varepsilon_{\tau,LOS})\,\mathrm{sinc}^2(\pi\varepsilon_{f,LOS}T_I)\cos(3\pi\varepsilon_{f,LOS}T_I+\varepsilon_{\varphi,LOS})\cdot\sin(\pi\varepsilon_{f,LOS}T_I+\varepsilon_{\varphi,LOS}) \\ +\frac{A_0}{2}R(\varepsilon_{\tau,LOS})\,\mathrm{sinc}(\pi\varepsilon_{f,LOS}T_I)\,\tilde{\alpha}_1\frac{A_0}{2}R(\varepsilon_{\tau,MP})\,\mathrm{sinc}(\pi\varepsilon_{f,MP}T_I)\cos(3\pi\varepsilon_{f,LOS}T_I+\varepsilon_{\varphi,LOS})\cdot\sin(\pi\varepsilon_{f,MP}T_I+\varepsilon_{\varphi,MP}) \\ +\frac{A_0}{2}R(\varepsilon_{\tau,LOS})\,\mathrm{sinc}(\pi\varepsilon_{f,LOS}T_I)\cos(3\pi\varepsilon_{f,LOS}T_I+\varepsilon_{\varphi,LOS})\cdot\eta_{Q,k-1}^P \\ +\tilde{\alpha}_1\frac{A_0}{2}R(\varepsilon_{\tau,MP})\,\mathrm{sinc}(\pi\varepsilon_{f,MP}T_I)\frac{A_0}{2}R(\varepsilon_{\tau,LOS})\,\mathrm{sinc}(\pi\varepsilon_{f,LOS}T_I)\sin(3\pi\varepsilon_{f,MP}T_I+\varepsilon_{\varphi,MP})\cdot\sin(\pi\varepsilon_{f,LOS}T_I+\varepsilon_{\varphi,LOS}) \\ +\tilde{\alpha}_1^2\frac{A_0^2}{4}R^2(\varepsilon_{\tau,MP})\,\mathrm{sinc}^2(\pi\varepsilon_{f,MP}T_I)\sin(3\pi\varepsilon_{f,MP}T_I+\varepsilon_{\varphi,MP})\cdot\sin(\pi\varepsilon_{f,MP}T_I+\varepsilon_{\varphi,MP}) \\ +\tilde{\alpha}_1\frac{A_0}{2}R(\varepsilon_{\tau,MP})\,\mathrm{sinc}(\pi\varepsilon_{f,MP}T_I)\sin(3\pi\varepsilon_{f,MP}T_I+\varepsilon_{\varphi,MP})\cdot\eta_{Q,k-1}^P \\ +\eta_{I,k}^P\cdot\frac{A_0}{2}R(\varepsilon_{\tau,LOS})\,\mathrm{sinc}(\pi\varepsilon_{f,LOS}T_I)\sin(\pi\varepsilon_{f,LOS}T_I+\varepsilon_{\varphi,LOS}) \\ +\eta_{I,k}^P\cdot\tilde{\alpha}_1\frac{A_0}{2}R(\varepsilon_{\tau,MP})\,\mathrm{sinc}(\pi\varepsilon_{f,MP}T_I)\sin(\pi\varepsilon_{f,MP}T_I+\varepsilon_{\varphi,MP}) \\ +\eta_{I,k}^P\cdot\eta_{Q,k-1}^P \end{bmatrix} \quad 10\text{-}73$$

Finally, 10-73 is written as:

$$CROSS=\begin{bmatrix} Y\left(\sin\left(\varepsilon_{\varphi_{0,k}}-\varepsilon_{\varphi_{1,k-1}}\right)+\sin\left(\varepsilon_{\varphi_{1,k}}-\varepsilon_{\varphi_{0,k-1}}\right)\right) \\ +Z\left(\sin\left(\varepsilon_{\varphi_{1,k}}-\varepsilon_{\varphi_{1,k-1}}\right)\right) \\ +W\left(\left(\cos\left(\varepsilon_{\varphi_{0,k-1}}\right)\cdot\eta_{Q,k}^P\right)+\left(\sin\left(\varepsilon_{\varphi_{0,k}}\right)\cdot\eta_{I,k-1}^P\right)-\left(\cos\left(\varepsilon_{\varphi_{0,k}}\right)\cdot\eta_{Q,k-1}^P\right)-\left(\sin\left(\varepsilon_{\varphi_{0,k-1}}\right)\cdot\eta_{I,k}^P\right)\right) \\ +R\left(\left(\cos\left(\varepsilon_{\varphi_{1,k-1}}\right)\cdot\eta_{Q,k}^P\right)+\left(\sin\left(\varepsilon_{\varphi_{1,k}}\right)\cdot\eta_{I,k-1}^P\right)-\left(\sin\left(\varepsilon_{\varphi_{1,k}}\right)\cdot\eta_{Q,k-1}^P\right)+\left(\sin\left(\varepsilon_{\varphi_{1,k-1}}\right)\cdot\eta_{I,k}^P\right)\right) \\ +\eta_{I,k-1}^P\cdot\eta_{Q,k}^P-\eta_{I,k}^P\cdot\eta_{Q,k-1}^P \end{bmatrix}=$$

$$X=\frac{A_0^2}{4}R^2(\varepsilon_{\tau,LOS})\,\mathrm{sinc}^2(\pi\varepsilon_{f,LOS}T_I)$$

$$Y=\frac{A_0}{2}R(\varepsilon_{\tau,LOS})\,\mathrm{sinc}(\pi\varepsilon_{f,LOS}T_I)\,\tilde{\alpha}_1\frac{A_0}{2}R(\varepsilon_{\tau,MP})\,\mathrm{sinc}(\pi\varepsilon_{f,MP}T_I)$$

$$Z=\tilde{\alpha}_1^2\frac{A_0^2}{4}R^2(\varepsilon_{\tau,MP})\,\mathrm{sinc}^2(\pi\varepsilon_{f,MP}T_I)$$

$$W=\frac{A_0}{2}R(\varepsilon_{\tau,LOS})\,\mathrm{sinc}(\pi\varepsilon_{f,LOS}T_I)$$

$$R=\tilde{\alpha}_1\frac{A_0}{2}R(\varepsilon_{\tau,MP})\,\mathrm{sinc}(\pi\varepsilon_{f,MP}T_I)$$

10.3.2 CP discriminator error Variance, in presence of multipath and thermal noise

The expectation of the CP discriminator has the same expression for the case where no multipath was present if expressed as a function of the correlator outputs:

$$E\{D_{CP,k}\}=E\{S_{I,k-1}^P S_{Q,k}^P\}-E\{S_{I,k}^P S_{Q,k-1}^P\}=E\{S_{I,k-1}^P S_{Q,k}^P-S_{I,k}^P S_{Q,k-1}^P\} \quad 10\text{-}74$$

As defined in 4-55, the variance of the discriminator output is identified by

$$\sigma^2\{D_{CP,k}\}=X\cdot\sigma^2+2\sigma^4 \quad 10\text{-}75$$

where:

$$\begin{aligned} X\cdot\sigma^2&=\sigma^2\left(S_{I,k}^P\right)^2+\sigma^2\left(S_{Q,k-1}^P\right)^2+\sigma^2\left(S_{I,k-1}^P\right)^2+\sigma^2\left(S_{Q,k}^P\right)^2= \\ &=\sigma^2\left[\left(S_{I,k}^P\right)^2+\left(S_{Q,k}^P\right)^2+\left(S_{I,k-1}^P\right)^2+\left(S_{Q,k-1}^P\right)^2\right] \end{aligned} \quad 10\text{-}76$$

In the presence of multipath it can be further derived using the notation proposed in equation 4-10,

$$\begin{aligned} \left(S_{I,k}^P\right)^2&=\left(S_{I,0,k}^P+S_{I,0,k}^P\right)^2=\left(\left(S_{I,0,k}^P\right)^2+\left(S_{I,1,k}^P\right)^2+2S_{I,0,k}^P S_{I,1,k}^P\right) \\ &=A_L^2\cos(L,k)^2+A_M^2\cos(M,k)^2+2A_LA_M\cos(L,k)\cos(M,k) \\ \left(S_{Q,k}^P\right)^2&=\left(S_{Q,0,k}^P+S_{Q,1,k}^P\right)^2=\left(\left(S_{Q,0,k}^P\right)^2+\left(S_{Q,1,k}^P\right)^2+2S_{Q,0,k}^P S_{Q,1,k}^P\right) \\ &=A_L^2\,sin(L,k)^2+A_M^2\,sin(M,k)^2+2A_LA_M\,sin(L,k)\,sin(M,k) \end{aligned} \quad 10\text{-}77$$

$$\left(S_{I,k-1}^P\right)^2=A_L^2\,cos(L,k-1)^2+A_M^2\,cos(M,k-1)^2+2A_LA_M\,cos(L,k-1)\,cos(M,k-1)$$

$$\left(S_{Q,k-1}^{P}\right)^2 = A_L^2\,sin(L,k-1)^2 + A_M^2\,sin(M,k-1)^2 + 2A_LA_M\,sin(L,k-1)\,sin(M,k-1)$$

$$\left(S_{I,k}^{P}\right)^2 + \left(S_{Q,k}^{P}\right)^2 = A_L^2 + A_M^2 + 2A_LA_M[cos(3\pi(-\Delta D)T_I - \Delta\varphi)]$$

$$\left(S_{I,k-1}^{P}\right)^2 + \left(S_{Q,k-1}^{P}\right)^2 = A_L^2 + A_M^2 + 2A_LA_M[cos(\pi(-\Delta D)T_I - \Delta\varphi)]$$

Therefore, developing the previous equation, it is obtained

$$\begin{gathered}
X\cdot\sigma^2 = \\
= \sigma^2\left[A_L^2 + A_M^2 + 2A_LA_M[cos(3\pi(-\Delta D)T_I - \Delta\varphi)] + A_L^2 + A_M^2 + 2A_LA_M[cos(\pi(-\Delta D)T_I - \Delta\varphi)]\right] = \\
= \sigma^2\left[2A_L^2 + 2A_M^2 + 2A_LA_M[cos(3\pi(-\Delta D)T_I - \Delta\varphi) + cos(\pi(-\Delta D)T_I - \Delta\varphi)]\right] = \\
= \sigma^2\begin{bmatrix} 2\frac{C}{2}sinc^2(\pi\varepsilon_{f,LOS}T_I) + 2\frac{\tilde{\alpha}_1^2 C}{2}sinc^2(\pi(\varepsilon_{f,LOS}+\Delta D)T_I) \\ +2\frac{A_0}{2}\frac{\tilde{\alpha}_1 A_0}{2}sinc(\pi\varepsilon_{f,LOS}T_I)\,sinc(\pi(\varepsilon_{f,LOS}+\Delta D)T_I)\,[cos(3\pi(-\Delta D)T_I - \Delta\varphi) + cos(\pi(-\Delta D)T_I - \Delta\varphi)] \end{bmatrix} = \\
= \sigma^2\begin{bmatrix} C\,sinc^2(\pi\varepsilon_{f,LOS}T_I) + \tilde{\alpha}_1^2 C\,sinc^2(\pi(\varepsilon_{f,LOS}+\Delta D)T_I) \\ +\tilde{\alpha}_1 C\,sinc(\pi\varepsilon_{f,LOS}T_I)\,sinc(\pi(\varepsilon_{f,LOS}+\Delta D)T_I)\,[cos(3\pi(-\Delta D)T_I - \Delta\varphi) + cos(\pi(-\Delta D)T_I - \Delta\varphi)] \end{bmatrix} = \\
= \sigma^2\begin{bmatrix} C\,sinc^2(\pi\varepsilon_{f,LOS}T_I) + \tilde{\alpha}_1^2 C\,sinc^2(\pi(\varepsilon_{f,LOS}+\Delta D)T_I) \\ +\tilde{\alpha}_1 C\,sinc(\pi\varepsilon_{f,LOS}T_I)\,sinc(\pi(\varepsilon_{f,LOS}+\Delta D)T_I)\,[cos(3\pi(-\Delta D)T_I - \Delta\varphi) + cos(\pi(-\Delta D)T_I - \Delta\varphi)] \end{bmatrix} = \\
= \sigma^2 C\begin{bmatrix} sinc^2(\pi\varepsilon_{f,LOS}T_I) + \tilde{\alpha}_1^2\,sinc^2(\pi(\varepsilon_{f,LOS}+\Delta D)T_I) \\ +\tilde{\alpha}_1\,sinc(\pi\varepsilon_{f,LOS}T_I)\,sinc(\pi(\varepsilon_{f,LOS}+\Delta D)T_I)\,[cos(3\pi(-\Delta D)T_I - \Delta\varphi) + cos(\pi(-\Delta D)T_I - \Delta\varphi)] \end{bmatrix}
\end{gathered} \tag{10-78}$$

denoting:

$$\begin{gathered}
C = \frac{A_0^2}{2} \\
A_L^2 = \frac{C}{2}sinc^2(\pi\varepsilon_{f,LOS}T_I), \\
A_M^2 = \frac{\tilde{\alpha}_1^2 C}{2}sinc^2(\pi(\varepsilon_{f,LOS}+\Delta D)T_I)
\end{gathered} \tag{10-79}$$

the normalized Cross-Product discriminator error variance is computed as follows:

$$\begin{gathered}
\sigma^2(\widetilde{D}_{CP,k}) = \sigma_{FLL,k}^2 = \\
= \frac{\sigma^2 C\begin{bmatrix} sinc^2(\pi\varepsilon_{f,LOS}T_I) + \tilde{\alpha}_1^2\,sinc^2(\pi(\varepsilon_{f,LOS}+\Delta D)T_I) + \tilde{\alpha}_1\,sinc(\pi\varepsilon_{f,LOS}T_I)\,sinc(\pi(\varepsilon_{f,LOS}+\Delta D)T_I) \\ [cos(3\pi(-\Delta D)T_I - \Delta\varphi) + cos(\pi(-\Delta D)T_I - \Delta\varphi)] \end{bmatrix} + 2\sigma^4}{4\pi^2 T_I^2\left(\left(S_{I,k-1}^{P}\right)^2 + \left(S_{Q,k-1}^{P}\right)^2\right)^2}
\end{gathered} \tag{10-80}$$

where:

$$\left(S_{I,k-1}^{P}\right)^2 + \left(S_{Q,k-1}^{P}\right)^2 = C\begin{bmatrix} \frac{1}{2}\mathrm{sinc}^2(\pi\varepsilon_{f,LOS}T_I) + \frac{\tilde{\alpha}_1^2}{2}\mathrm{sinc}^2(\pi(\varepsilon_{f,LOS}+\Delta D)T_I) \\ +\tilde{\alpha}_1\,\mathrm{sinc}(\pi\varepsilon_{f,LOS}T_I)\mathrm{sinc}(\pi(\varepsilon_{f,LOS}+\Delta D)T_I)[\cos(\pi(-\Delta D)T_I - \Delta\varphi)] \end{bmatrix}$$

The theoretical FLL discriminator output error variance in presence of Multipath, expressed in Hz^2, is given by:

$$\begin{gathered}
\sigma_{FLL,k}^2 = \\
= \frac{\begin{bmatrix} sinc^2(\pi\varepsilon_{f,LOS}T_I) + \tilde{\alpha}_1^2\,sinc^2(\pi(\varepsilon_{f,LOS}+\Delta D)T_I) + \tilde{\alpha}_1\,sinc(\pi\varepsilon_{f,LOS}T_I)\,sinc(\pi(\varepsilon_{f,LOS}+\Delta D)T_I) \\ [cos(3\pi(-\Delta D)T_I - \Delta\varphi) + cos(\pi(-\Delta D)T_I - \Delta\varphi)] \end{bmatrix} + \frac{1}{2T_I\frac{C}{N_0}}}{16\pi^2 T_I^3\frac{C}{N_0}\begin{bmatrix} \frac{1}{2}\mathrm{sinc}^2(\pi\varepsilon_{f,LOS}T_I) + \frac{\tilde{\alpha}_1^2}{2}\mathrm{sinc}^2(\pi(\varepsilon_{f,LOS}+\Delta D)T_I) \\ +\tilde{\alpha}_1\,\mathrm{sinc}(\pi\varepsilon_{f,LOS}T_I)\mathrm{sinc}(\pi(\varepsilon_{f,LOS}+\Delta D)T_I)[\cos(\pi(-\Delta D)T_I - \Delta\varphi)] \end{bmatrix}^2}
\end{gathered} \tag{10-81}$$

10.3.3 Equation of Generic open loop variance model of the FLL CP Discriminator developed

The variance of the discriminator error is computed based on the following relation [129]

$$var(D_{CP,k}) = E\{{D_{CP,k}}^2\} - \left(E\{D_{CP,k}\}\right)^2 \tag{10-82}$$

where the second term, $\left(E\{D_{CP,k}\}\right)^2$ is equal to $E\{S_{I,k-1}^{P}S_{Q,k}^{P} - S_{I,k}^{P}S_{Q,k-1}^{P}\}^2$.

Therefore, the first term, $E\{{D_{CP,k}}^2\}$ has to be computed as:

$$E\{D_{CP,k}{}^2\} = E\left\{\left(I_{k-1}^P\right)^2\left(Q_k^P\right)^2\right\} - 2E\{I_{k-1}^P I_k^P Q_{k-1}^P Q_k^P\} + E\left\{\left(I_k^P\right)^2\left(Q_{k-1}^P\right)^2\right\} \quad 10\text{-}83$$

The first component of 10-83 is equal to:

$$E\left\{\left(I_{k-1}^P\right)^2\left(Q_k^P\right)^2\right\} = \left(S_{I,k-1}^P\right)^2\left(S_{Q,k}^P\right)^2 + \sigma^2\left(S_{I,k-1}^P\right)^2 + \sigma^2\left(S_{Q,k}^P\right)^2 + 2\sigma^4 \quad 10\text{-}84$$

The second component of 10-83 is equal to:

$$E\{I_{k-1}^P I_k^P Q_{k-1}^P Q_k^P\} = S_{I,k-1}^P S_{I,k}^P S_{Q,k-1}^P S_{Q,k}^P + S_{I,k-1}^P S_{I,k}^P \sigma^2 + S_{Q,k-1}^P S_{Q,k}^P \sigma^2 + \sigma^4 \quad 10\text{-}85$$

The third component of 10-83 is represented by:

$$E\left\{\left(I_k^P\right)^2\left(Q_{k-1}^P\right)^2\right\} = \left(S_{I,k}^P\right)^2\left(S_{Q,k-1}^P\right)^2 + \sigma^2\left(S_{I,k}^P\right)^2 + \sigma^2\left(S_{Q,k-1}^P\right)^2 + 2\sigma^4 \quad 10\text{-}86$$

Finally, the first term of 4-53 is thus equal to:

$$E\{D_{CP,k}{}^2\} = E\{S_{I,k-1}^P S_{Q,k}^P - S_{I,k}^P S_{Q,k-1}^P\}^2 + \sigma^2\left(\left(S_{I,k-1}^P\right)^2 + \left(S_{Q,k}^P\right)^2 + \left(S_{I,k}^P\right)^2 + \left(S_{Q,k-1}^P\right)^2\right) + 2\sigma^4 \quad 10\text{-}87$$

where σ^2 is the AWGN noise variance.

The equation 10-82 can be finally written as:

$$\begin{aligned} var(D_{CP,k}) = {} & E\{S_{I,k-1}^P S_{Q,k}^P - S_{I,k}^P S_{Q,k-1}^P\}^2 + \sigma^2\left(\left(S_{I,k-1}^P\right)^2 + \left(S_{Q,k}^P\right)^2 + \left(S_{I,k}^P\right)^2 + \left(S_{Q,k-1}^P\right)^2\right) \\ & + 2\sigma^4 - E\{S_{I,k-1}^P S_{Q,k}^P - S_{I,k}^P S_{Q,k-1}^P\}^2 = \\ & = \sigma^2\left(\left(S_{I,k-1}^P\right)^2 + \left(S_{Q,k}^P\right)^2 + \left(S_{I,k}^P\right)^2 + \left(S_{Q,k-1}^P\right)^2\right) + 2\sigma^4 \end{aligned} \quad 10\text{-}88$$

10.4 Annex – Multipath Characterization Results

10.4.1 C/N_0 vs elevation angle characterization accuracy applied to Data Collection 1

GPS L1 C/A and Galileo E1 OS joint constellations satellites measurements in Figure 10-6. In Figure 10-6 the satellite C/N_0 as a function to the satellite elevation angle during the data campaign is provided. From this Figure, it can be observed that for low elevation angle values, the C/N_0 has a large variation which goes from 10 dB-Hz to 45 dB-Hz (vertical axis): a lot of possible C/N_0 situations/received signal conditions, even quite high C/N_0 values, are present. On the contrary, for low C/N_0 values, the elevation angle values are less spread and more concentrated in the low values (horizontal axis).

Some preliminary considerations can be formulated on the comparison between the multipath plus noise error models as a function of the C/N_0 and satellite elevation angle, by exploiting Table 6-7 and Table 6-9. It can be observed that the MN error component mean values are higher for low C/N_0 values than they are for low satellite elevation angle values. This suggests that the MN isolation methodology is a valid technique able to characterize the PSR and PSR-R Multipath and thermal noise residual errors, in urban environment.

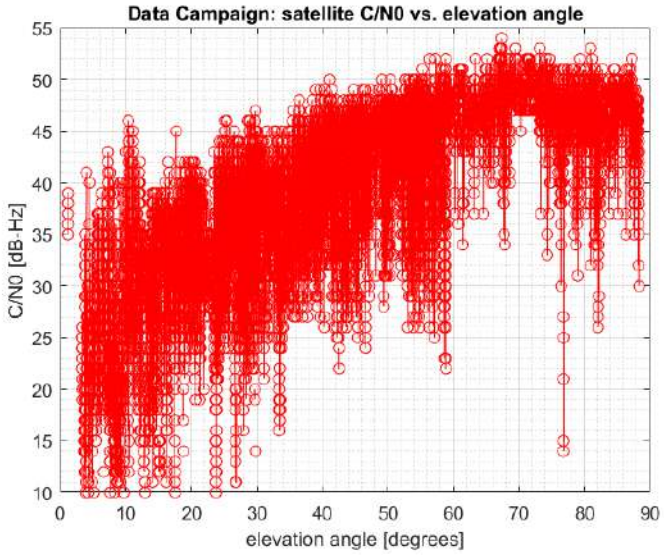

Figure 10-6 – Satellite C/N_0 in function of the elevation angles

10.4.2 Statistics of the discarded data

In this section are showed the number of the samples of the original dataset, collected in different C/N_0 bins of 5 dB-Hz and the number of samples after the application of the image processing algorithm. The data are collected in Table 10-1. The last column shows the percentage of discarded data due to the image processing application.

C/N_0 bins [dB-Hz]	Original N samples	N samples After Image Proc.	% Discarded samples
0 – 5	0	0	-
5 – 10	83	48	**42.16%**
10 – 15	1880	1654	**12.02%**
15 – 20	10328	10188	**1.35%**
20 – 25	28434	22125	**22.18%**
25 – 30	49895	39537	**20.75%**
30 – 35	61304	55226	**9.91%**
35 – 40	93082	71317	**23.38%**
40 – 45	150694	134688	**10.62%**
45 – 50	149910	133075	**11.23%**
50 – 55	40441	30284	**25.11%**
55-60	23	21	**8.69%**
TOT	586074	498163	**14.99%**

Table 10-1 – PSR MN Samples before Image processing and after Image processing, per different C/N_0 bins

The total discarded data due to the application of the image processing block in this specific case is roughly the 15% of the total number of samples. Therefore, to efficiently apply this methodology is highly recommended

- to perform a large data campaign;
- to have a very stable connection between the camera and the PC collecting the pictures;
- to reduce the exposition of the camera to strong lights which can blind the lens and consequently capture a “black” picture;
- to perform the data campaign in a cloudy day, when the sky is uniformly covered by the clouds, which avoid the presence of artifacts due to single clouds or sunlight in the picture.

10.4.3 Extended Results Dataset n. 3

In this section the complete results of PSR and PSR-R MN error model and the corresponding Gaussian overbounding CDFs are illustrated. In details, Section 10.4.3.1 is devoted to the PSR MN error model characterization and Section 10.4.3.2 to the PSR-R MN error statistics.

10.4.3.1 Pseudorange MN Residual Error characterization and overbounding

10.4.3.1.1 Dual constellation

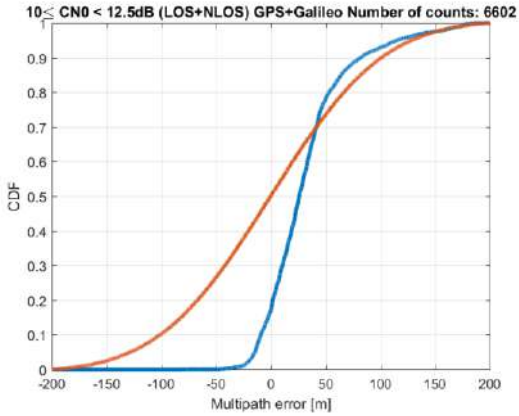

Figure 10-7 – Dual constellation PSR MN error CDFs for 10 dB-Hz $\leq C/N_0 <$ 12.5 dB-Hz. In blue: original PSR MN error CDF. In red: Gaussian overbounding CDF

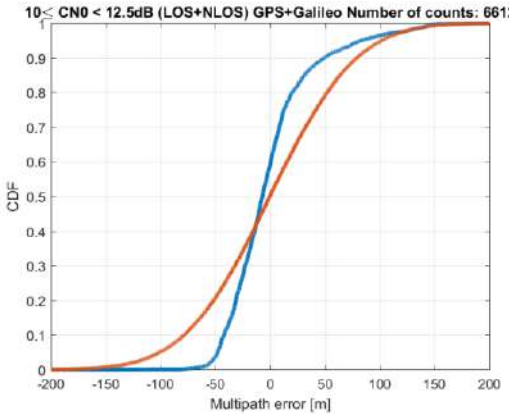

Figure 10-8 – Dual constellation PSR MN error CDFs for 10 dB-Hz $\leq C/N_0 <$ 12.5 dB-Hz. In blue: original PSR MN error CDF after mean removal application. In red: Gaussian overbounding CDF

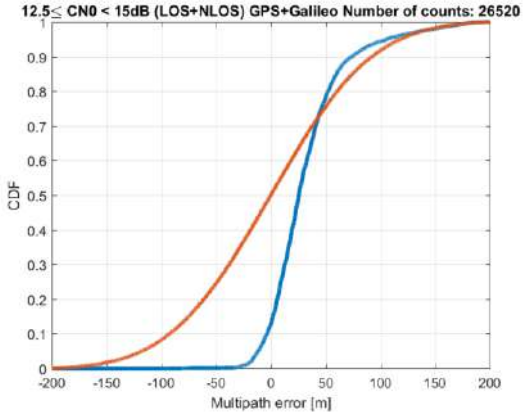

Figure 10-9 – Dual constellation PSR MN error CDFs for 12.5 dB-Hz $\leq C/N_0 <$ 15 dB-Hz. In blue: original PSR MN error CDF. In red: Gaussian overbounding CDF

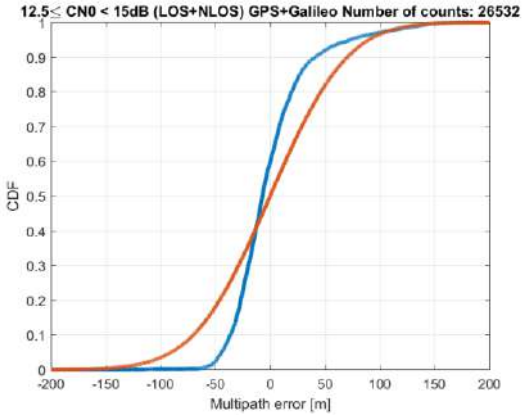

Figure 10-10 – Dual constellation PSR MN error CDFs for 12.5 dB-Hz $\leq C/N_0 <$ 15 dB-Hz. In blue: original PSR MN error CDF after mean removal application. In red: Gaussian overbounding CDF

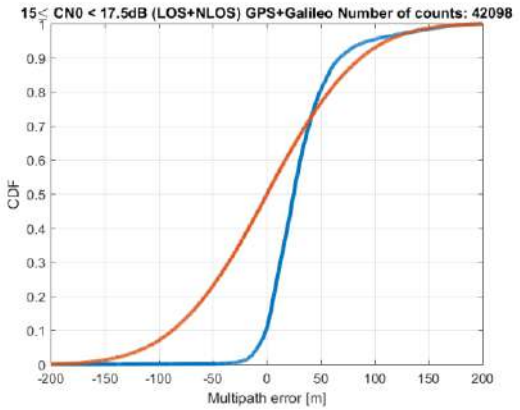

Figure 10-11 – Dual constellation PSR MN error CDFs for 15 dB-Hz $\leq C/N_0 <$ 17.5 dB-Hz. In blue: original PSR MN error CDF. In red: Gaussian overbounding CDF

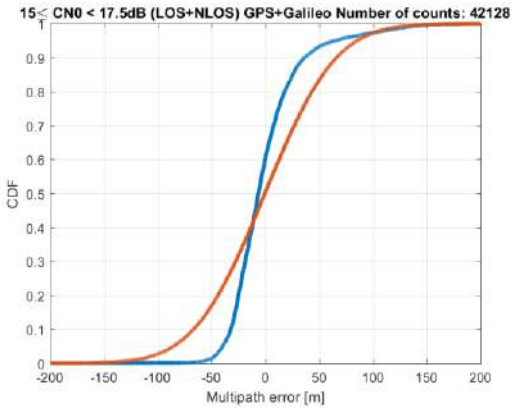

Figure 10-12 – Dual constellation PSR MN error CDFs for 15 dB-Hz $\leq C/N_0 <$ 17.5 dB-Hz. In blue: original PSR MN error CDF after mean removal application. In red: Gaussian overbounding CDF

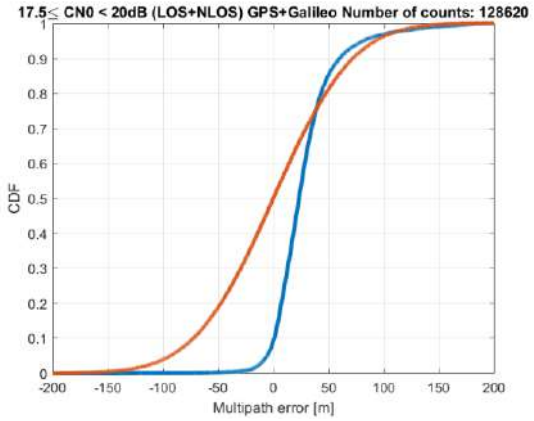

Figure 10-13 – Dual constellation PSR MN error CDFs for 17.5 dB-Hz $\leq C/N_0 <$ 20 dB-Hz. In blue: original PSR MN error CDF. In red: Gaussian overbounding CDF

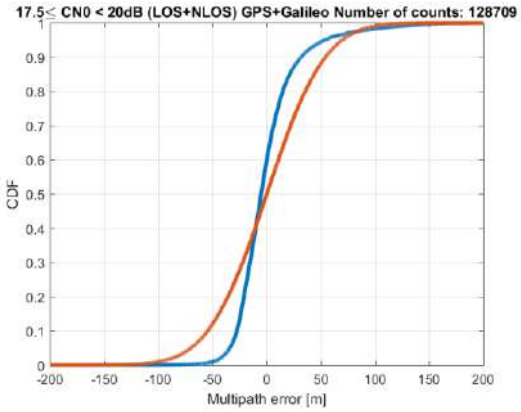

Figure 10-14Dual constellation PSR MN error CDFs for 17.5 dB-Hz $\leq C/N_0 <$ 20 dB-Hz. In blue: original PSR MN error CDF after mean removal application. In red: Gaussian overbounding CDF

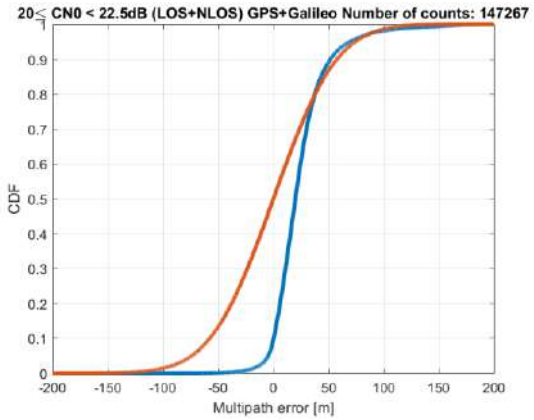

Figure 10-15 – Dual constellation PSR MN error CDFs for 20 dB-Hz $\leq C/N_0 <$ 22.5 dB-Hz. In blue: original PSR MN error CDF. In red: Gaussian overbounding CDF

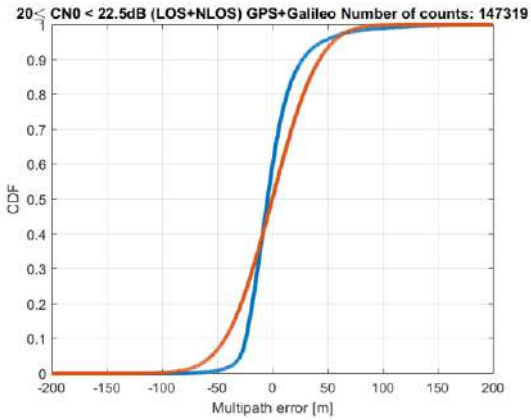

Figure 10-16 – Dual constellation PSR MN error CDFs for 20 dB-Hz $\leq C/N_0 <$ 22.5 dB-Hz. In blue: original PSR MN error CDF after mean removal application. In red: Gaussian overbounding CDF

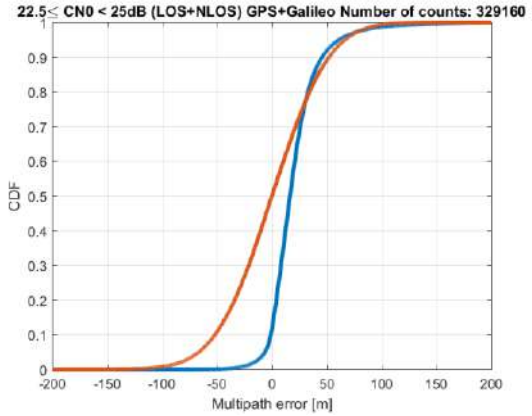

Figure 10-17 – Dual constellation PSR MN error CDFs for 22.5 dB-Hz $\leq C/N_0 <$ 25 dB-Hz. In blue: original PSR MN error CDF. In red: Gaussian overbounding CDF

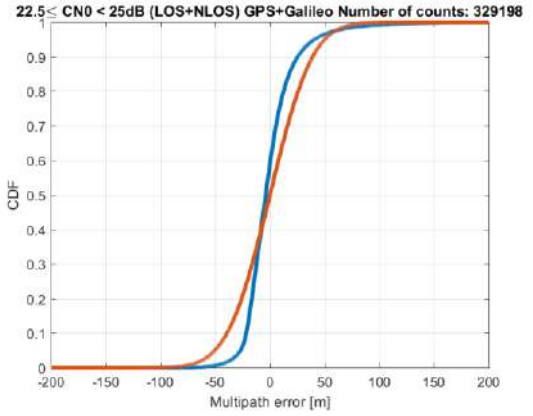

Figure 10-18 – Dual constellation PSR MN error CDFs for 22.5 dB-Hz $\leq C/N_0 <$ 25 dB-Hz. In blue: original PSR MN error CDF after mean removal application. In red: Gaussian overbounding CDF

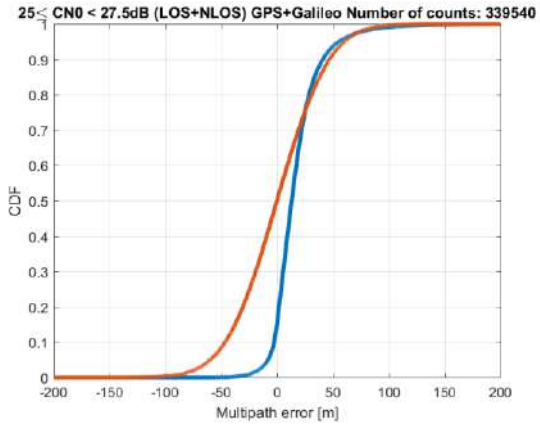

Figure 10-19 – Dual constellation PSR MN error CDFs for 25 dB-Hz $\leq C/N_0 <$ 27.5 dB-Hz. In blue: original PSR MN error CDF. In red: Gaussian overbounding CDF

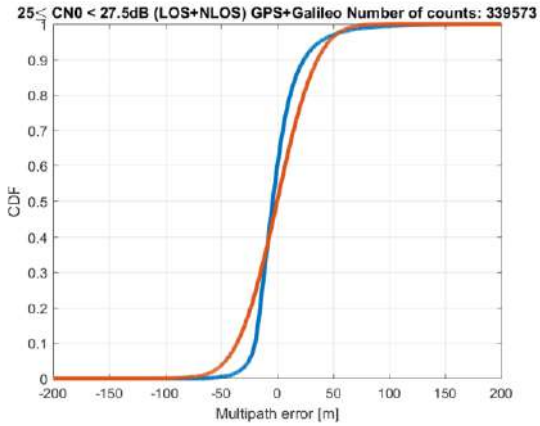

Figure 10-20 – Dual constellation PSR MN error CDFs for 25 dB-Hz $\leq C/N_0 <$ 27.5 dB-Hz. In blue: original PSR MN error CDF after mean removal application. In red: Gaussian overbounding CDF

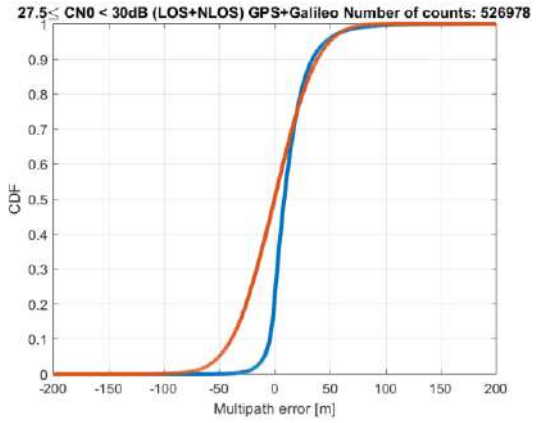

Figure 10-21 – Dual constellation PSR MN error CDFs for 27.5 dB-Hz $\leq C/N_0 <$ 30 dB-Hz. In blue: original PSR MN error CDF. In red: Gaussian overbounding CDF

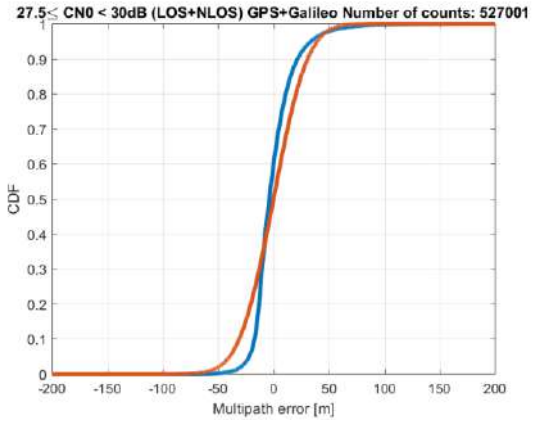

Figure 10-22 – Dual constellation PSR MN error CDFs for 27.5 dB-Hz $\leq C/N_0 <$ 30 dB-Hz. In blue: original PSR MN error CDF after mean removal application. In red: Gaussian overbounding CDF

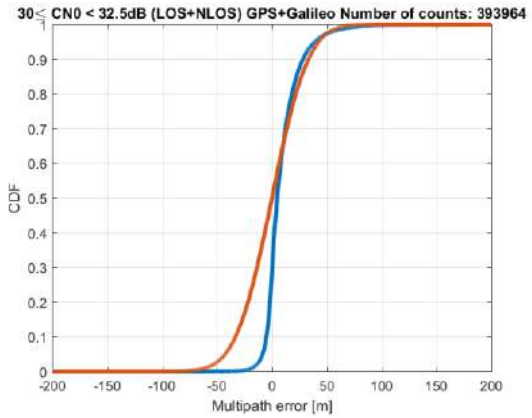

Figure 10-23 – Dual constellation PSR MN error CDFs for 30 dB-Hz $\leq C/N_0 <$ 32.5 dB-Hz. In blue: original PSR MN error CDF. In red: Gaussian overbounding CDF

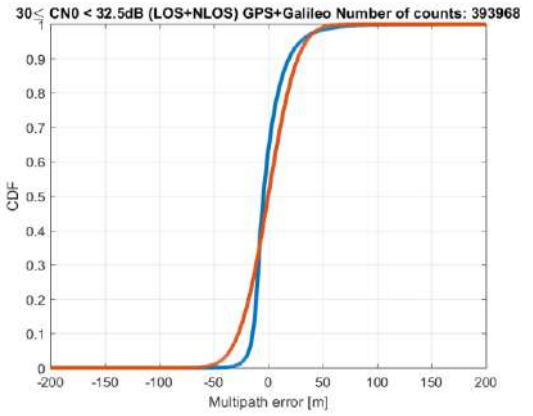

Figure 10-24 – Dual constellation PSR MN error CDFs for 30 dB-Hz $\leq C/N_0 <$ 32.5 dB-Hz. In blue: original PSR MN error CDF after mean removal application. In red: Gaussian overbounding CDF

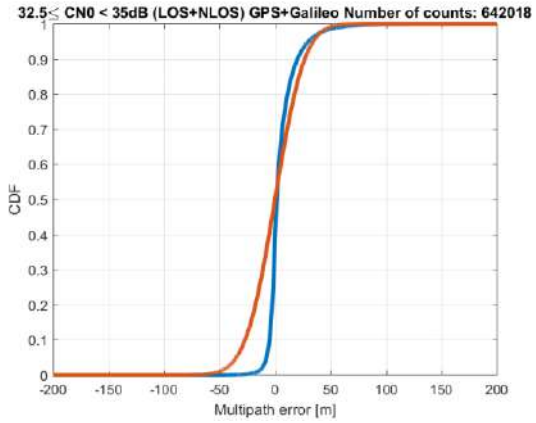

Figure 10-25 – Dual constellation PSR MN error CDFs for 32.5 dB-Hz $\leq C/N_0 <$ 35 dB-Hz. In blue: original PSR MN error CDF. In red: Gaussian overbounding CDF

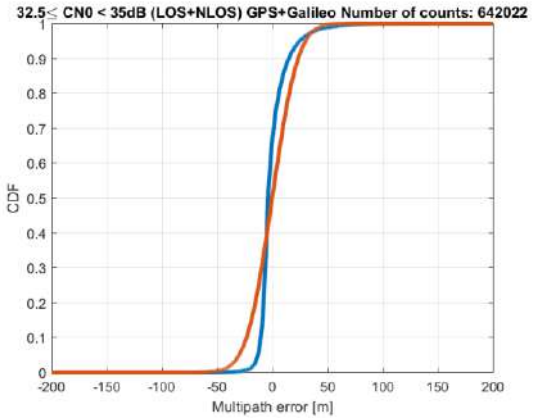

Figure 10-26 – Dual constellation PSR MN error CDFs for 32.5 dB-Hz $\leq C/N_0 <$ 35 dB-Hz. In blue: original PSR MN error CDF after mean removal application. In red: Gaussian overbounding CDF

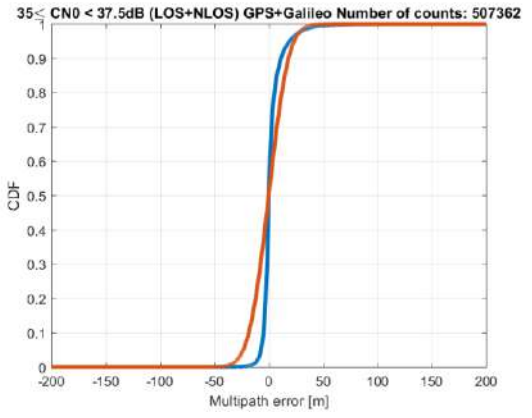

Figure 10-27 – Dual constellation PSR MN error CDFs for 35 dB-Hz $\leq C/N_0 <$ 37.5 dB-Hz. In blue:

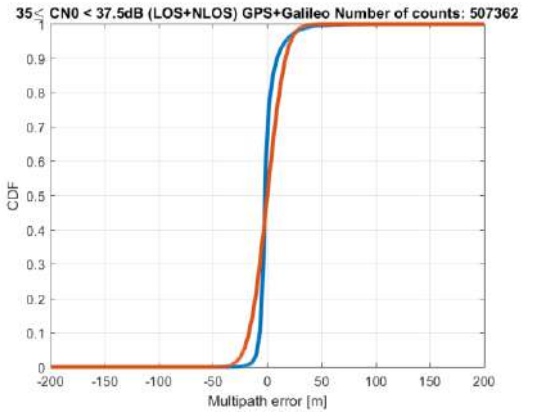

Figure 10-28 – Dual constellation PSR MN error CDFs for 35 dB-Hz $\leq C/N_0 <$ 37.5 dB-Hz. In blue:

original PSR MN error CDF. In red: Gaussian overbounding CDF

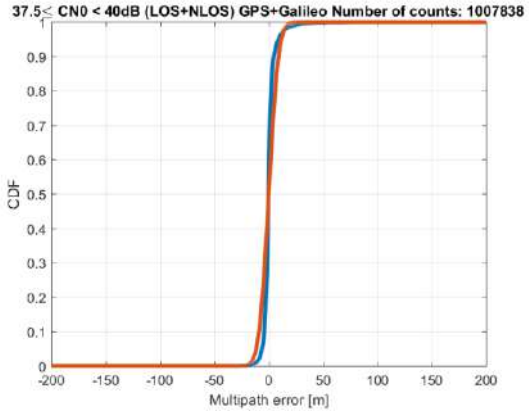

Figure 10-29 – Dual constellation PSR MN error CDFs for 37.5 dB-Hz $\leq C/N_0 <$ 40 dB-Hz. In blue: original PSR MN error CDF. In red: Gaussian overbounding CDF

original PSR MN error CDF after mean removal application. In red: Gaussian overbounding CDF

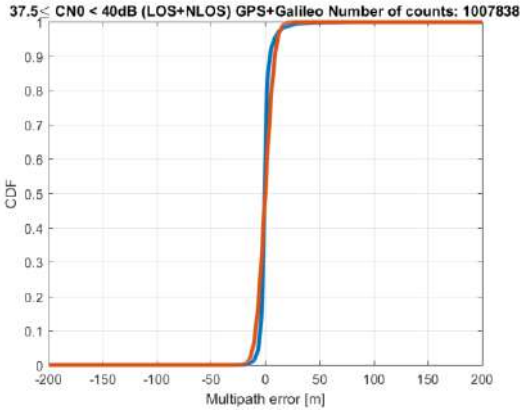

Figure 10-30 – Dual constellation PSR MN error CDFs for 37.5 dB-Hz $\leq C/N_0 <$ 40 dB-Hz. In blue: original PSR MN error CDF after mean removal application. In red: Gaussian overbounding CDF

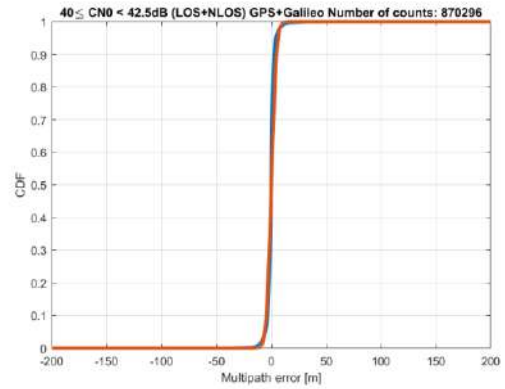

Figure 10-31 – Dual constellation PSR MN error CDFs for 40 dB-Hz $\leq C/N_0 <$ 42.5 dB-Hz. In blue: original PSR MN error CDF. In red: Gaussian overbounding CDF

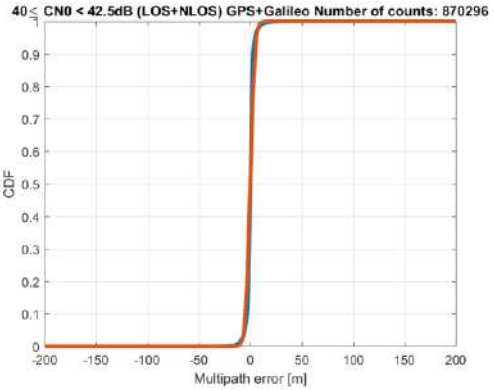

Figure 10-32 – Dual constellation PSR MN error CDFs for 40 dB-Hz $\leq C/N_0 <$ 42.5 dB-Hz. In blue: original PSR MN error CDF after mean removal application. In red: Gaussian overbounding CDF

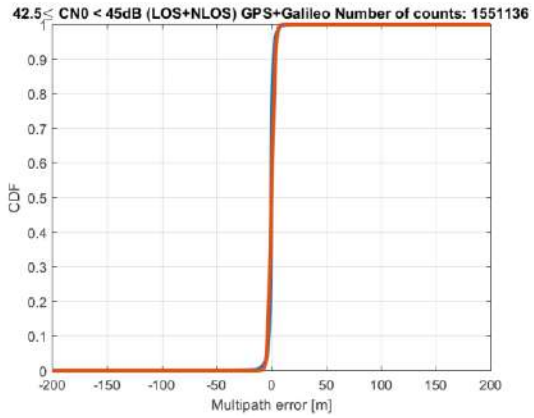

Figure 10-33 – Dual constellation PSR MN error CDFs for 42.5 dB-Hz $\leq C/N_0 <$ 45 dB-Hz. In blue: original PSR MN error CDF. In red: Gaussian overbounding CDF

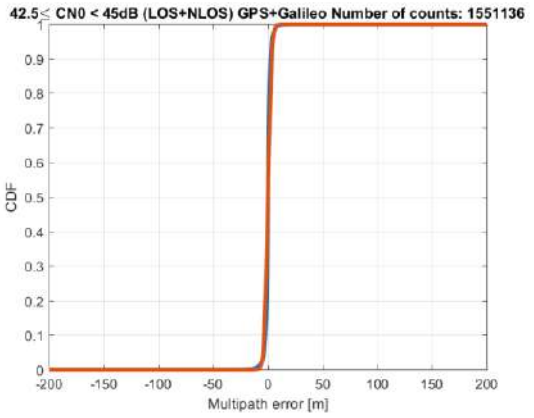

Figure 10-34 – Dual constellation PSR MN error CDFs for 42.5 dB-Hz $\leq C/N_0 <$ 45 dB-Hz. In blue: original PSR MN error CDF after mean removal application. In red: Gaussian overbounding CDF

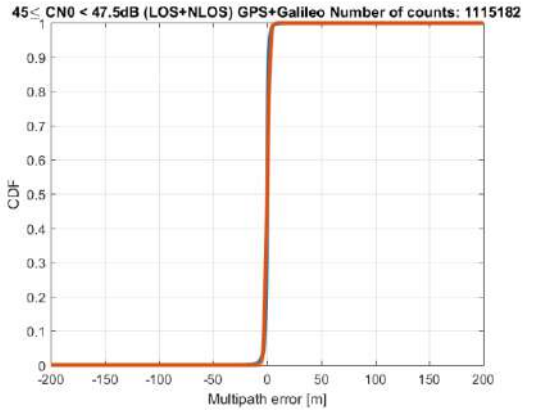

Figure 10-35 – Dual constellation PSR MN error CDFs for 45 dB-Hz $\leq C/N_0 <$ 47.5 dB-Hz. In blue: original PSR MN error CDF. In red: Gaussian overbounding CDF

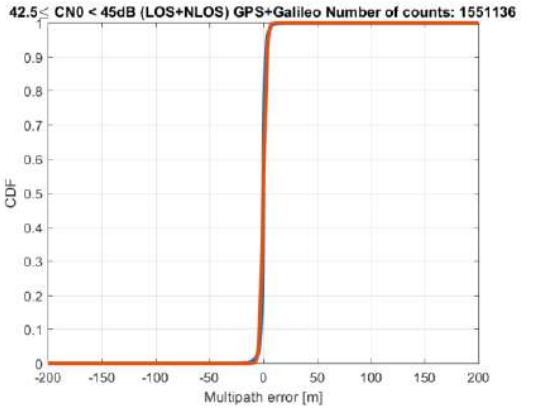

Figure 10-36 – Dual constellation PSR MN error CDFs for 45 dB-Hz $\leq C/N_0 <$ 47.5 dB-Hz. In blue: original PSR MN error CDF after mean removal application. In red: Gaussian overbounding CDF

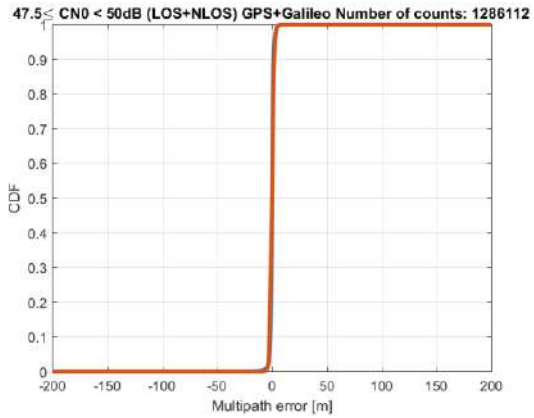

Figure 10-37 – Dual constellation PSR MN error CDFs for 47.5 dB-Hz $\leq C/N_0 <$ 50 dB-Hz. In blue: original PSR MN error CDF. In red: Gaussian overbounding CDF

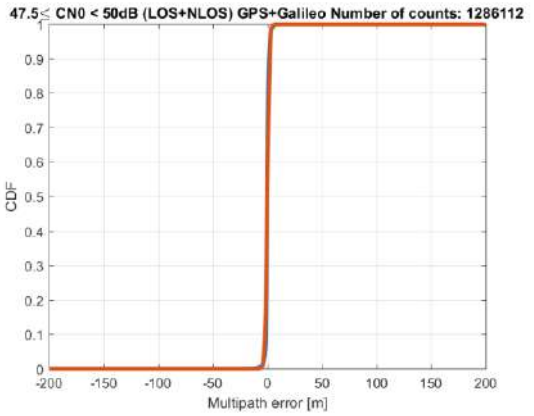

Figure 10-38 – Dual constellation PSR MN error CDFs for 47.5 dB-Hz $\leq C/N_0 <$ 50 dB-Hz. In blue: original PSR MN error CDF after mean removal application. In red: Gaussian overbounding CDF

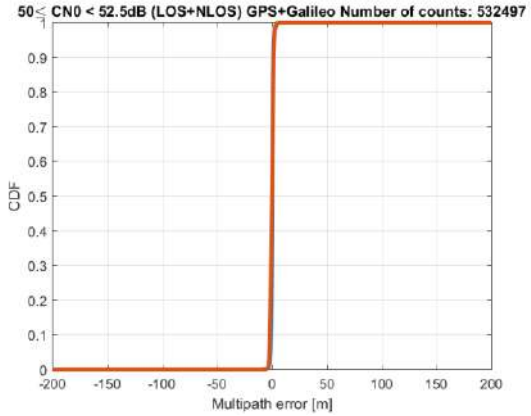

Figure 10-39 – Dual constellation PSR MN error CDFs for 50 dB-Hz $\leq C/N_0 <$ 52.5 dB-Hz. In blue: original PSR MN error CDF. In red: Gaussian overbounding CDF

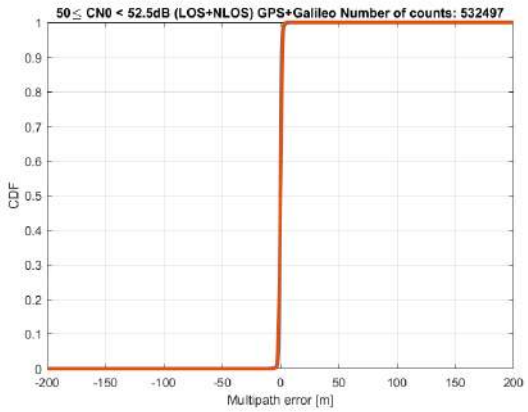

Figure 10-40 – Dual constellation PSR MN error CDFs for 50 dB-Hz $\leq C/N_0 <$ 52.5 dB-Hz. In blue: original PSR MN error CDF after mean removal application. In red: Gaussian overbounding CDF

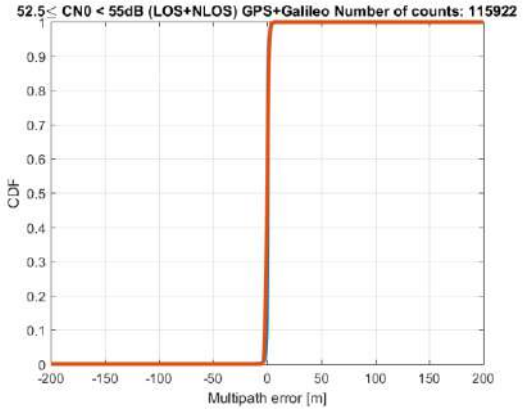

Figure 10-41 – Dual constellation PSR MN error CDFs for 52.5 dB-Hz $\leq C/N_0 <$ 55 dB-Hz. In blue: original PSR MN error CDF. In red: Gaussian overbounding CDF

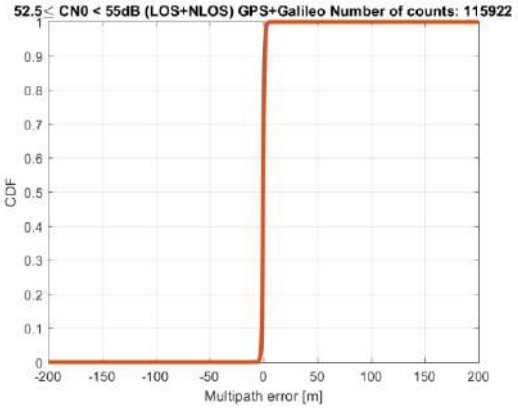

Figure 10-42 – Dual constellation PSR MN error CDFs for 52.5 dB-Hz $\leq C/N_0 <$ 55 dB-Hz. In blue: original PSR MN error CDF after mean removal application. In red: Gaussian overbounding CDF

10.4.3.1.2 GPS L1 C/A

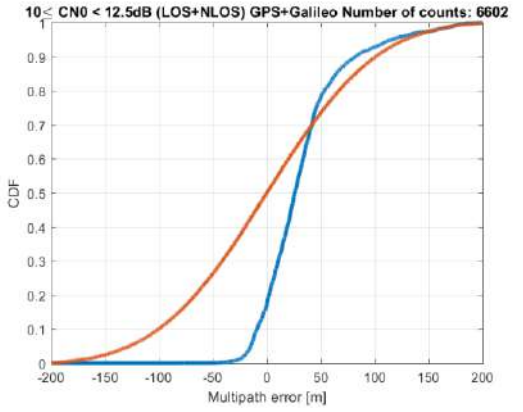

Figure 10-43 – GPS PSR MN error CDFs for 10 dB-Hz $\leq C/N_0 <$ 12.5 dB-Hz. In blue: original PSR MN error CDF. In red: Gaussian overbounding CDF

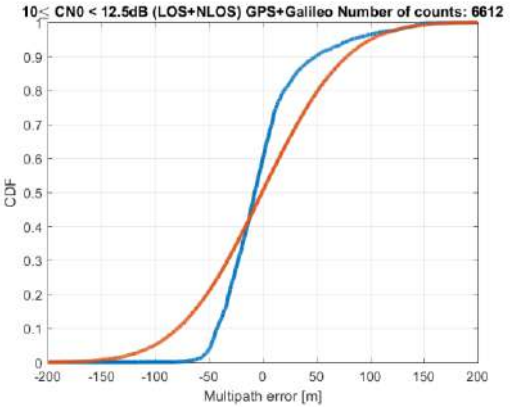

Figure 10-44 – GPS PSR MN error CDFs for 10 dB-Hz $\leq C/N_0 <$ 12.5 dB-Hz. In blue: original PSR MN error CDF after mean removal application. In red: Gaussian overbounding CDF

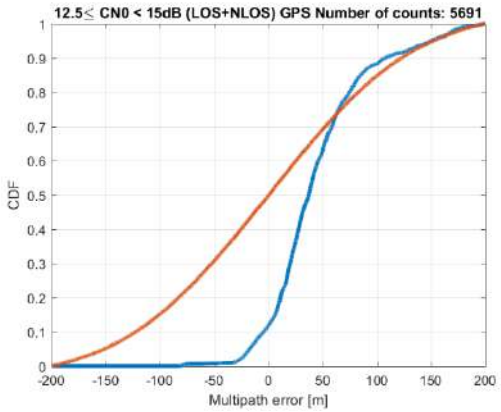

Figure 10-45 – GPS PSR MN error CDFs for 12.5 dB-Hz $\leq C/N_0 <$ 15 dB-Hz. In blue: original PSR MN error CDF. In red: Gaussian overbounding CDF

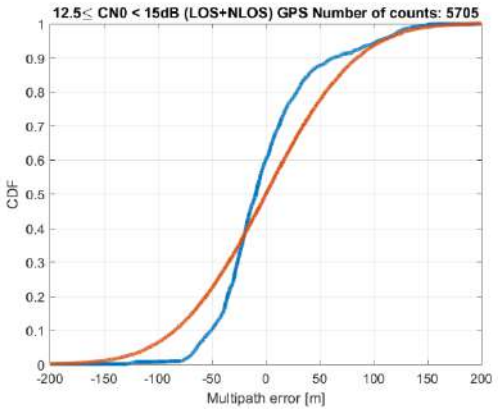

Figure 10-46 – GPS PSR MN error CDFs for 12.5 dB-Hz $\leq C/N_0 <$ 15 dB-Hz. In blue: original PSR MN error CDF after mean removal application. In red: Gaussian overbounding CDF

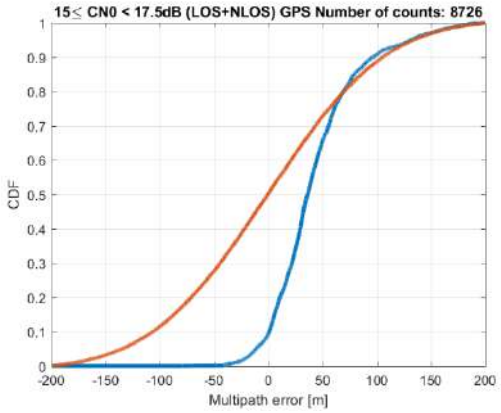

Figure 10-47 – GPS PSR MN error CDFs for 15 dB-Hz $\leq C/N_0 <$ 17.5 dB-Hz. In blue: original PSR MN error CDF. In red: Gaussian overbounding CDF

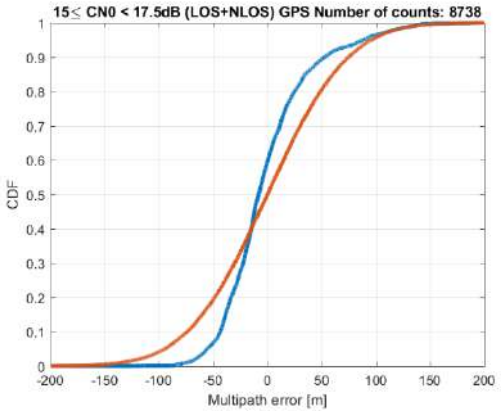

Figure 10-48 – GPS PSR MN error CDFs for 15 dB-Hz $\leq C/N_0 <$ 17.5 dB-Hz. In blue: original PSR MN error CDF after mean removal application. In red: Gaussian overbounding CDF

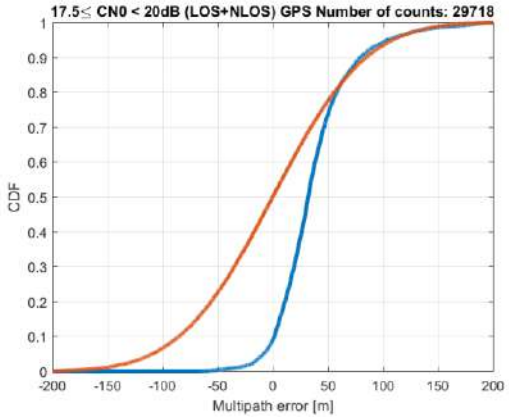

Figure 10-49 – GPS PSR MN error CDFs for 17.5 dB-Hz $\leq C/N_0 <$ 20 dB-Hz. In blue: original PSR MN error CDF. In red: Gaussian overbounding CDF

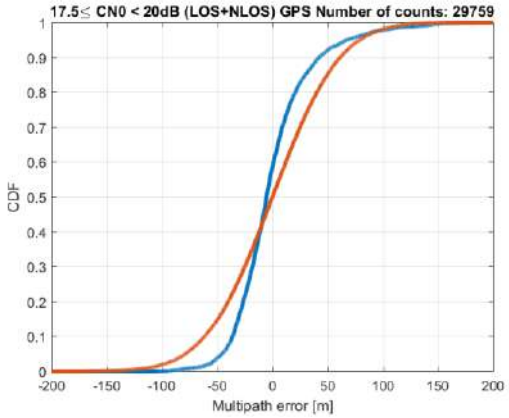

Figure 10-50 – GPS PSR MN error CDFs for 17.5 dB-Hz $\leq C/N_0 <$ 20 dB-Hz. In blue: original PSR MN error CDF after mean removal application. In red: Gaussian overbounding CDF

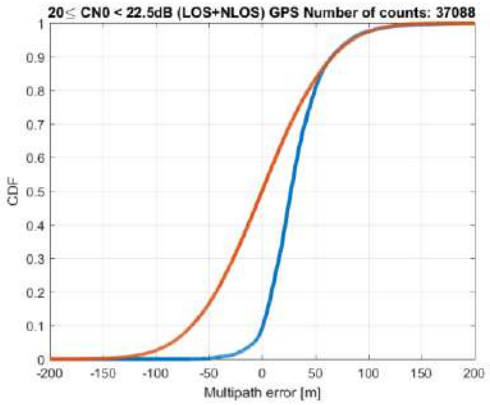

Figure 10-51 – GPS PSR MN error CDFs for 20 dB-Hz $\leq C/N_0 <$ 22.5 dB-Hz. In blue: original PSR MN error CDF. In red: Gaussian overbounding CDF

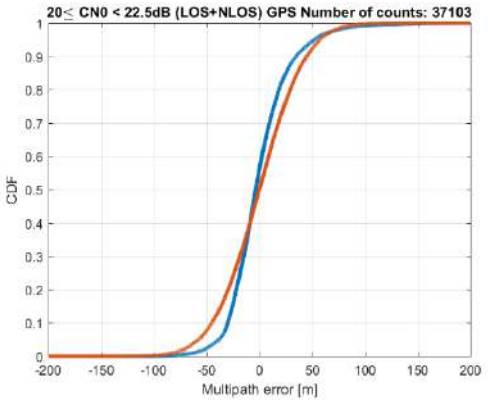

Figure 10-52 – GPS PSR MN error CDFs for 20 dB-Hz $\leq C/N_0 <$ 22.5 dB-Hz. In blue: original PSR MN error CDF after mean removal application. In red: Gaussian overbounding CDF

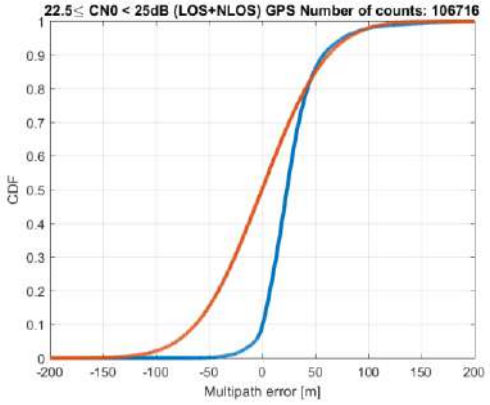

Figure 10-53 – GPS PSR MN error CDFs for 22.5 dB-Hz $\leq C/N_0 <$ 25 dB-Hz. In blue: original PSR MN error CDF. In red: Gaussian overbounding CDF

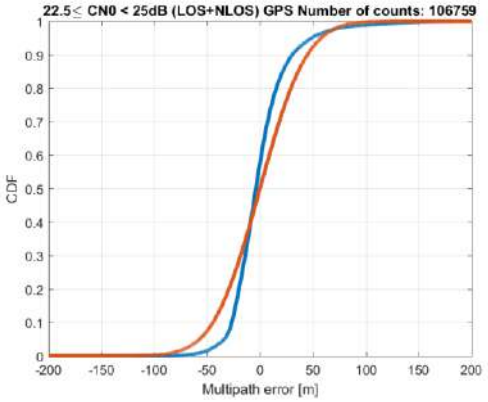

Figure 10-54 – GPS PSR MN error CDFs for 22.5 dB-Hz $\leq C/N_0 <$ 25 dB-Hz. In blue: original PSR MN error CDF after mean removal application. In red: Gaussian overbounding CDF

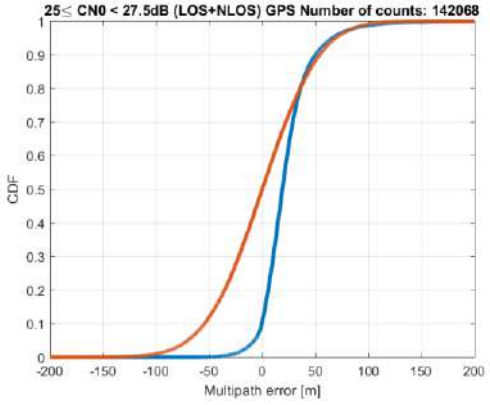

Figure 10-55 – GPS PSR MN error CDFs for 25 dB-Hz $\leq C/N_0 <$ 27.5 dB-Hz. In blue: original PSR MN error CDF. In red: Gaussian overbounding CDF

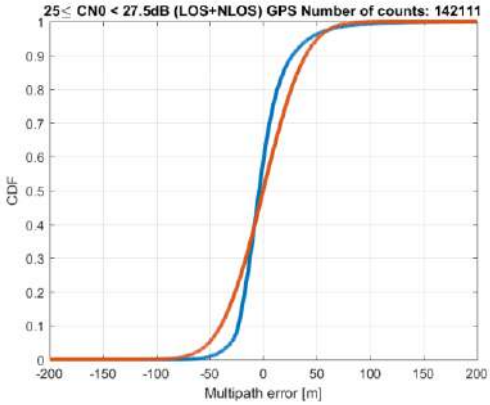

Figure 10-56 – GPS PSR MN error CDFs for 25 dB-Hz $\leq C/N_0 <$ 27.5 dB-Hz. In blue: original PSR MN error CDF after mean removal application. In red: Gaussian overbounding CDF

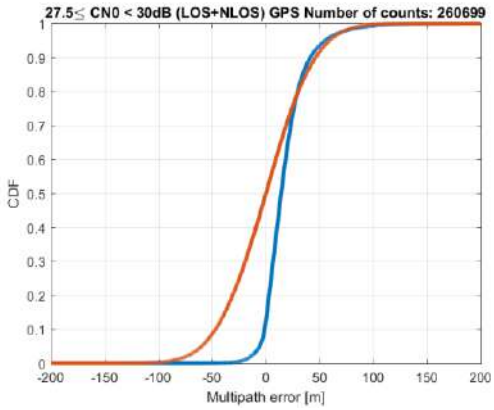

Figure 10-57 – GPS PSR MN error CDFs for 27.5 dB-Hz $\leq C/N_0 <$ 30 dB-Hz. In blue: original PSR MN error CDF. In red: Gaussian overbounding CDF

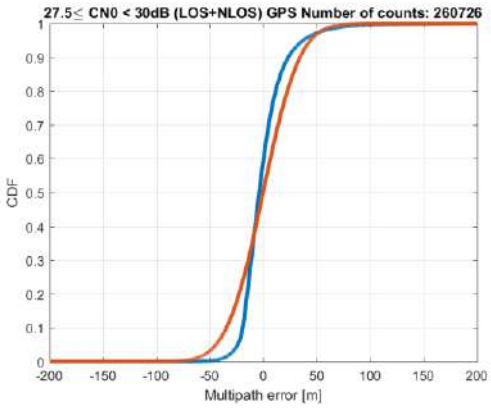

Figure 10-58 – GPS PSR MN error CDFs for 27.5 dB-Hz $\leq C/N_0 <$ 30 dB-Hz. In blue: original PSR MN error CDF after mean removal application. In red: Gaussian overbounding CDF

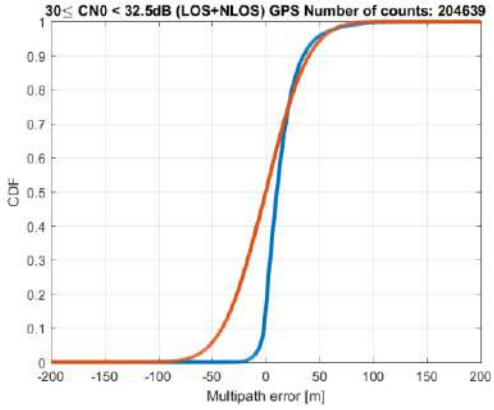

Figure 10-59 – GPS PSR MN error CDFs for 30 dB-Hz $\leq C/N_0 <$ 32.5 dB-Hz. In blue: original PSR MN error CDF. In red: Gaussian overbounding CDF

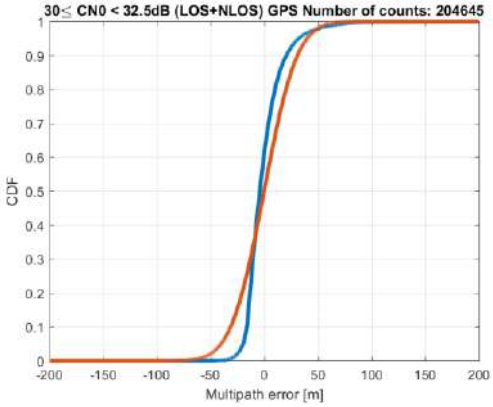

Figure 10-60 – GPS PSR MN error CDFs for 30 dB-Hz $\leq C/N_0 <$ 32.5 dB-Hz. In blue: original PSR MN error CDF after mean removal application. In red: Gaussian overbounding CDF

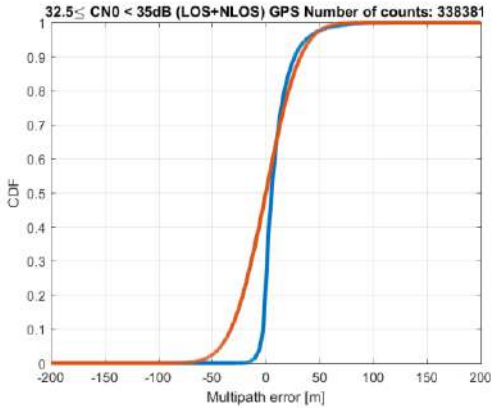

Figure 10-61 – GPS PSR MN error CDFs for 32.5 dB-Hz $\leq C/N_0 <$ 35 dB-Hz. In blue: original PSR MN error CDF. In red: Gaussian overbounding CDF

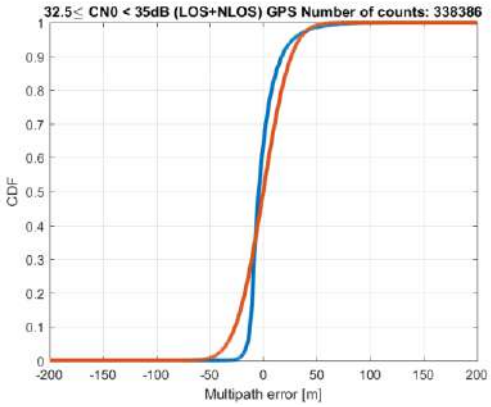

Figure 10-62 – GPS PSR MN error CDFs for 32.5 dB-Hz $\leq C/N_0 <$ 35 dB-Hz. In blue: original PSR MN error CDF after mean removal application. In red: Gaussian overbounding CDF

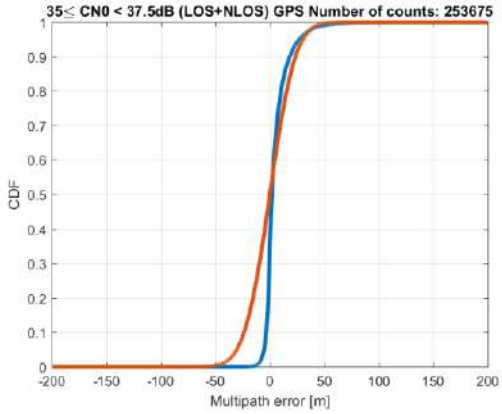

Figure 10-63 – GPS PSR MN error CDFs for 35 dB-Hz $\leq C/N_0 <$ 37.5 dB-Hz. In blue: original PSR MN error CDF. In red: Gaussian overbounding CDF

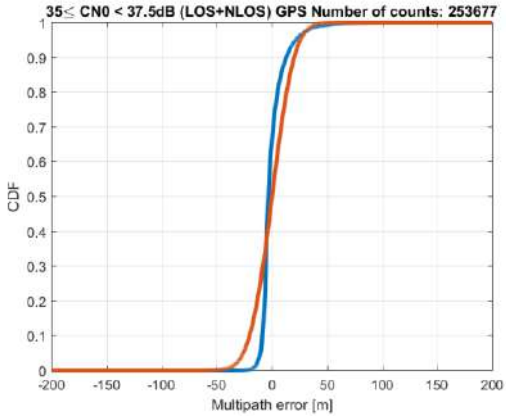

Figure 10-64 – GPS PSR MN error CDFs for 35 dB-Hz $\leq C/N_0 <$ 37.5 dB-Hz. In blue: original PSR MN error CDF after mean removal application. In red: Gaussian overbounding CDF

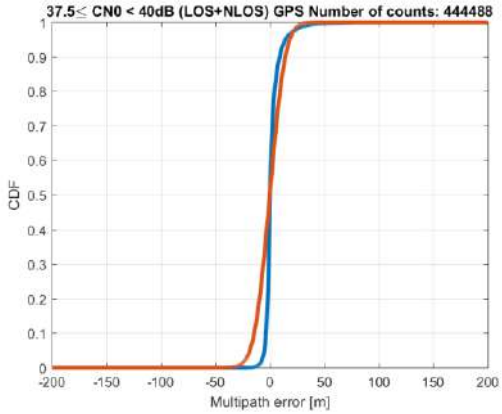

Figure 10-65 – GPS PSR MN error CDFs for 37.5 dB-Hz $\leq C/N_0 <$ 40 dB-Hz. In blue: original PSR MN error CDF. In red: Gaussian overbounding CDF

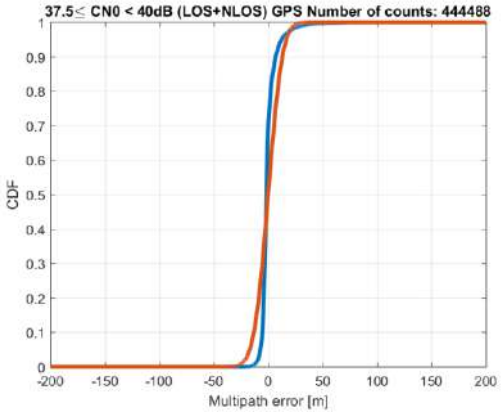

Figure 10-66 – GPS PSR MN error CDFs for 37.5 dB-Hz $\leq C/N_0 <$ 40 dB-Hz. In blue: original PSR MN error CDF after mean removal application. In red: Gaussian overbounding CDF

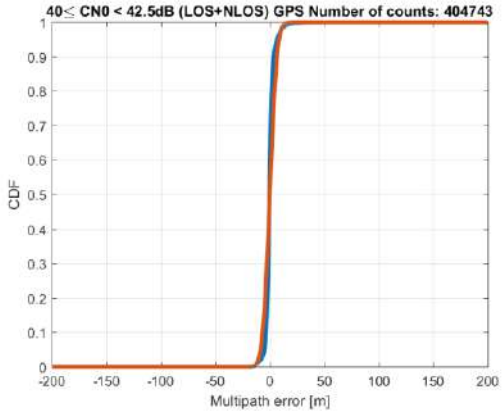

Figure 10-67GPS PSR MN error CDFs for 40 dB-Hz $\leq C/N_0 <$ 42.5 dB-Hz. In blue: original PSR MN error CDF. In red: Gaussian overbounding CDF

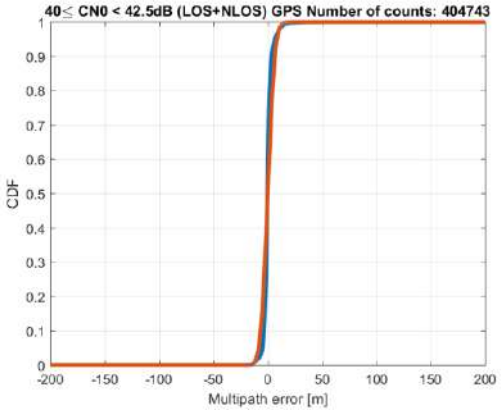

Figure 10-68 – GPS PSR MN error CDFs for 40 dB-Hz $\leq C/N_0 <$ 42.5 dB-Hz. In blue: original PSR MN error CDF after mean removal application. In red: Gaussian overbounding CDF

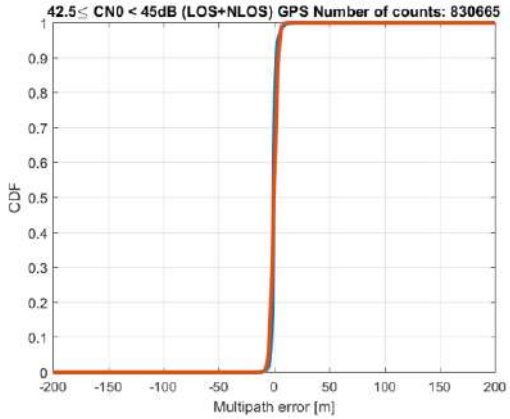

Figure 10-69 – GPS PSR MN error CDFs for 42.5 dB-Hz $\leq C/N_0 <$ 45 dB-Hz. In blue: original PSR MN error CDF. In red: Gaussian overbounding CDF

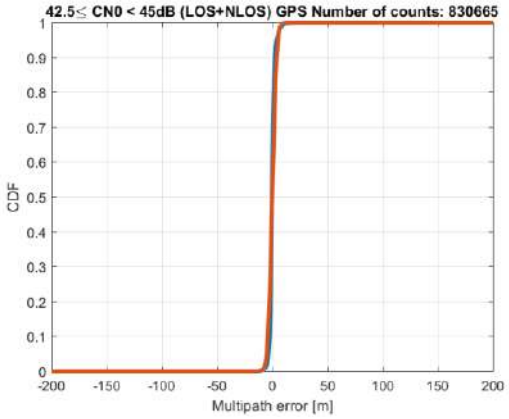

Figure 10-70 – GPS PSR MN error CDFs for 42.5 dB-Hz $\leq C/N_0 <$ 45 dB-Hz. In blue: original PSR MN error CDF after mean removal application. In red: Gaussian overbounding CDF

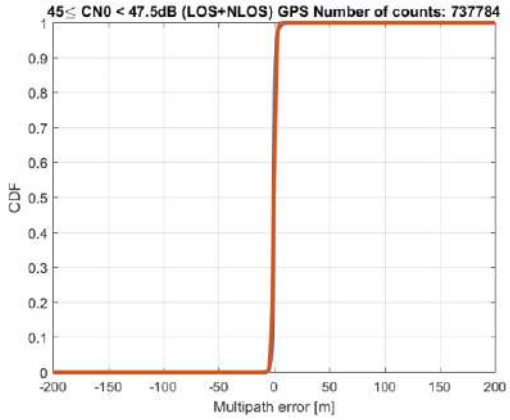

Figure 10-71 – GPS PSR MN error CDFs for 45 dB-Hz $\leq C/N_0 <$ 47.5 dB-Hz. In blue: original PSR MN error CDF. In red: Gaussian overbounding CDF

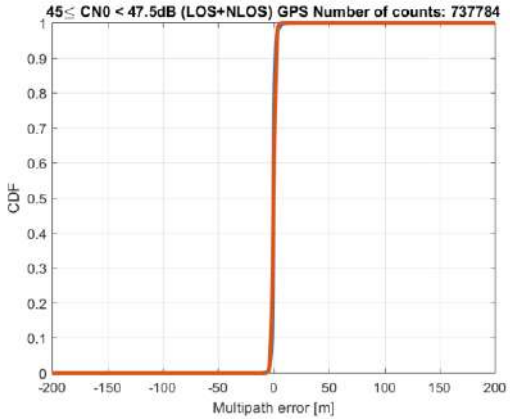

Figure 10-72 – GPS PSR MN error CDFs for 42.5 dB-Hz $\leq C/N_0 <$ 45 dB-Hz. In blue: original PSR MN error CDF after mean removal application. In red: Gaussian overbounding CDF

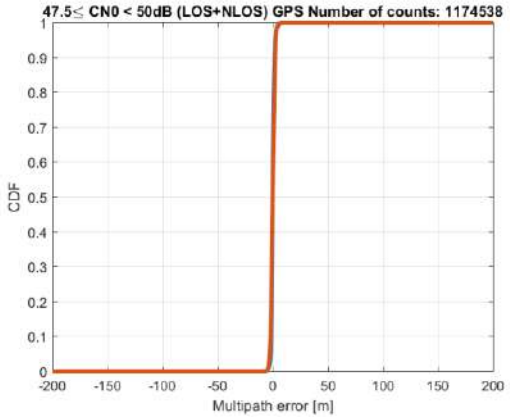

Figure 10-73 – GPS PSR MN error CDFs for 47.5 dB-Hz $\leq C/N_0 <$ 50 dB-Hz. In blue: original PSR MN error CDF. In red: Gaussian overbounding CDF

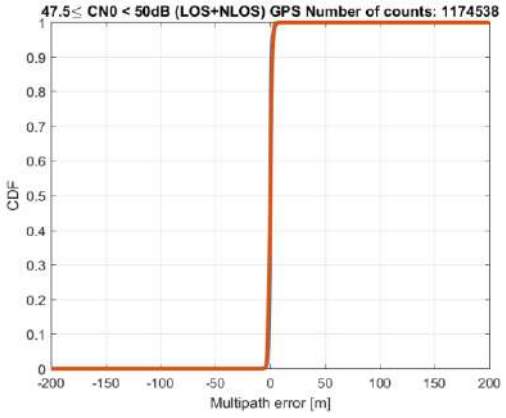

Figure 10-74 – GPS PSR MN error CDFs for 47.5 dB-Hz $\leq C/N_0 <$ 50 dB-Hz. In blue: original PSR

MN error CDF after mean removal application. In red: Gaussian overbounding CDF

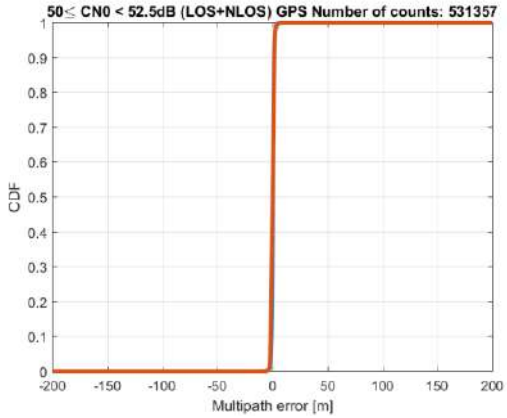

Figure 10-75 – GPS PSR MN error CDFs for 50 dB-Hz $\leq C/N_0 <$ 52.5 dB-Hz. In blue: original PSR MN error CDF. In red: Gaussian overbounding CDF

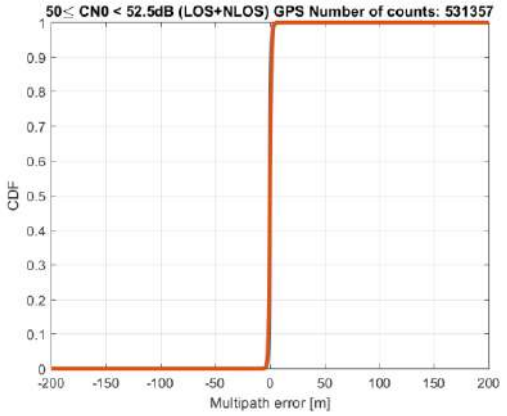

Figure 10-76 – GPS PSR MN error CDFs for 50 dB-Hz $\leq C/N_0 <$ 52.5 dB-Hz. In blue: original PSR MN error CDF after mean removal application. In red: Gaussian overbounding CDF

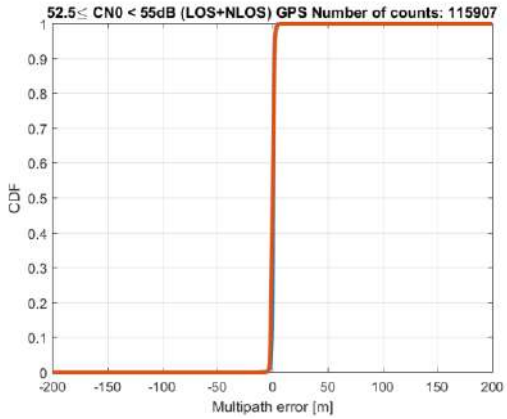

Figure 10-77 – GPS PSR MN error CDFs for 52.5 dB-Hz $\leq C/N_0 <$ 55 dB-Hz. In blue: original PSR MN error CDF. In red: Gaussian overbounding CDF

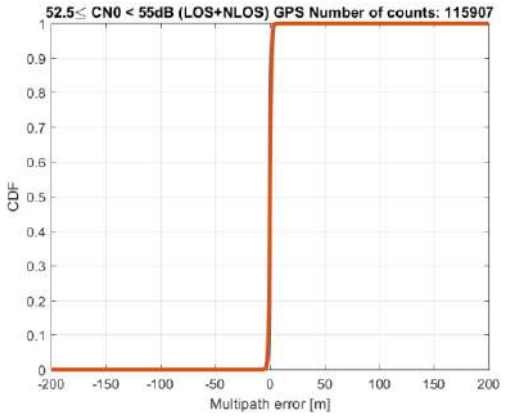

Figure 10-78 – GPS PSR MN error CDFs for 52.5 dB-Hz $\leq C/N_0 <$ 55 dB-Hz. In blue: original PSR MN error CDF after mean removal application. In red: Gaussian overbounding CDF

10.4.3.1.3 Galileo E1 OS

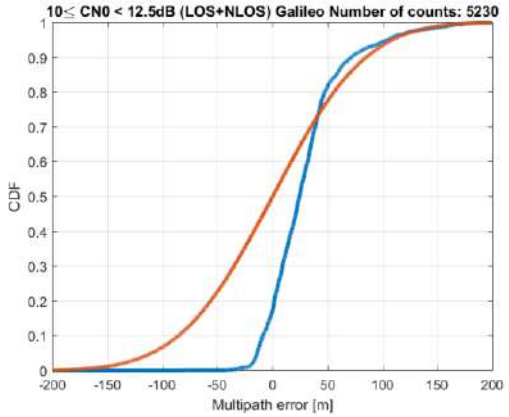

Figure 10-79 – GAL PSR MN error CDFs for 10 dB-Hz $\leq C/N_0 <$ 12.5 dB-Hz. In blue: original PSR MN error CDF. In red: Gaussian overbounding CDF

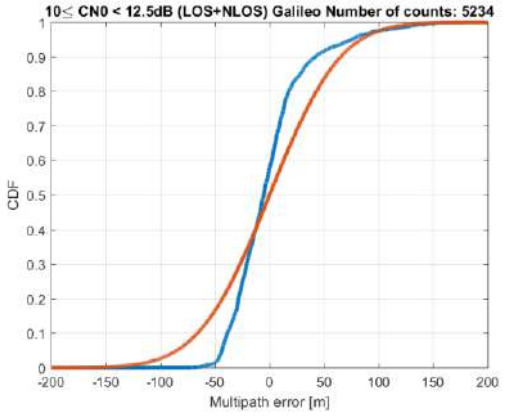

Figure 10-80 – GAL PSR MN error CDFs for 10 dB-Hz $\leq C/N_0 <$ 12.5 dB-Hz. In blue: original PSR MN error CDF after mean removal application. In red: Gaussian overbounding CDF

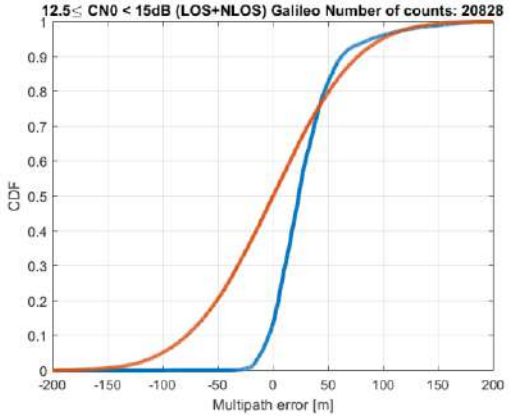

Figure 10-81 – GAL PSR MN error CDFs for 12.5 dB-Hz $\leq C/N_0 <$ 15 dB-Hz. In blue: original PSR MN error CDF. In red: Gaussian overbounding CDF

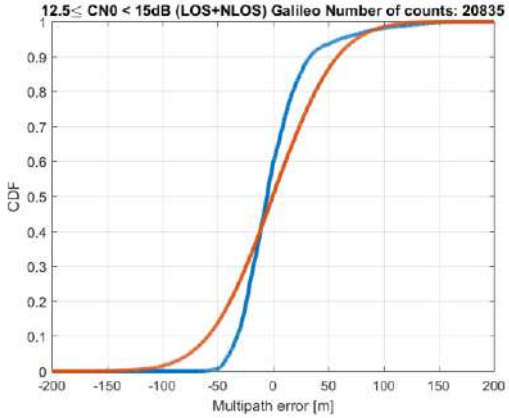

Figure 10-82 – GAL PSR MN error CDFs for 12.5 dB-Hz $\leq C/N_0 <$ 15 dB-Hz. In blue: original PSR MN error CDF after mean removal application. In red: Gaussian overbounding CDF

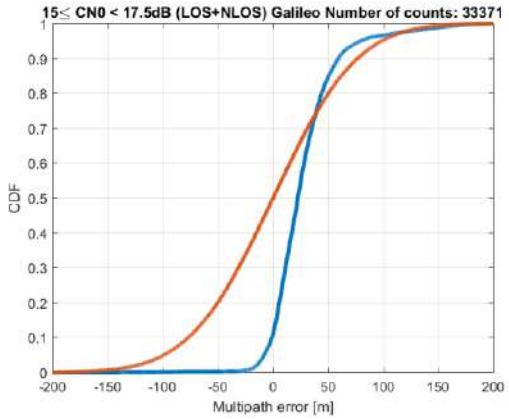

Figure 10-83 – GAL PSR MN error CDFs for 15 dB-Hz $\leq C/N_0 <$ 17.5 dB-Hz. In blue: original PSR MN error CDF. In red: Gaussian overbounding CDF

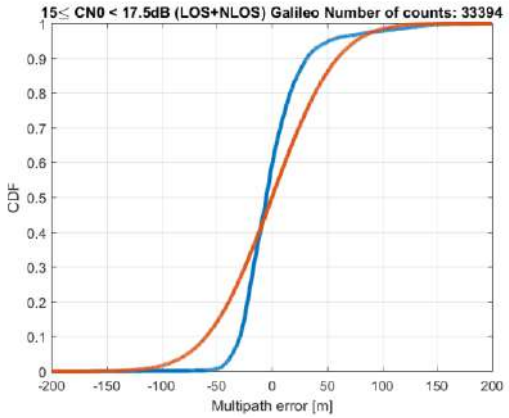

Figure 10-84 – GAL PSR MN error CDFs for 15 dB-Hz $\leq C/N_0 <$ 17.5 dB-Hz. In blue: original PSR MN error CDF after mean removal application. In red: Gaussian overbounding CDF

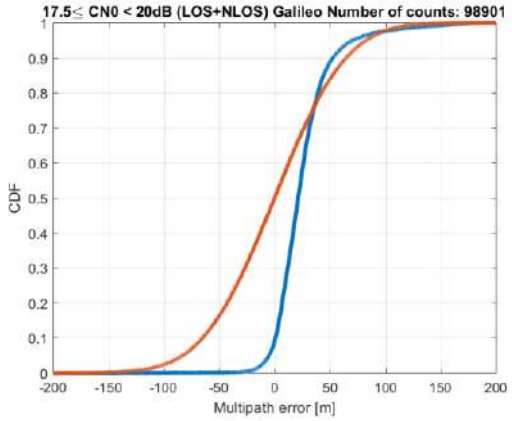

Figure 10-85 – GAL PSR MN error CDFs for 17.5 dB-Hz $\leq C/N_0 <$ 20 dB-Hz. In blue: original PSR MN error CDF. In red: Gaussian overbounding CDF

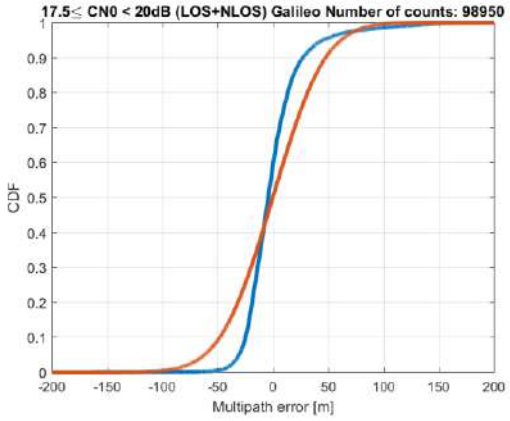

Figure 10-86 – GAL PSR MN error CDFs for 17.5 dB-Hz $\leq C/N_0 <$ 20 dB-Hz. In blue: original PSR MN error CDF after mean removal application. In red: Gaussian overbounding CDF

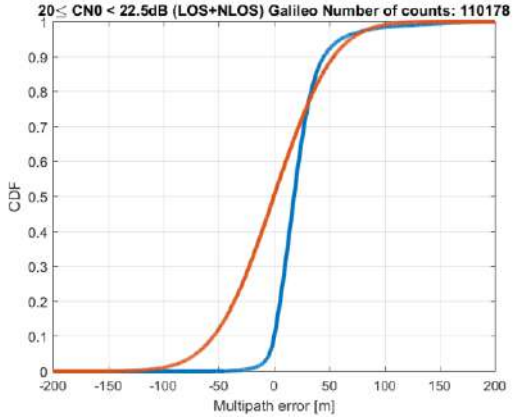

Figure 10-87 – GAL PSR MN error CDFs for 20 dB-Hz $\leq C/N_0 <$ 22.5 dB-Hz. In blue: original PSR MN error CDF. In red: Gaussian overbounding CDF

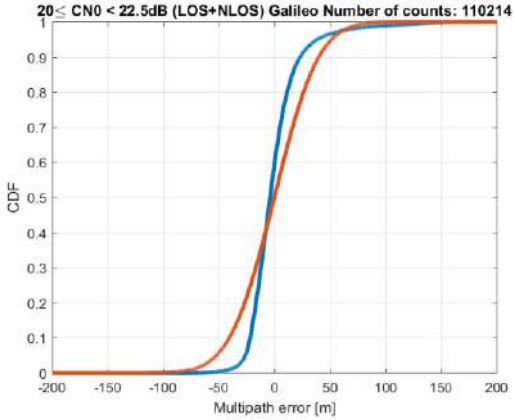

Figure 10-88 – GAL PSR MN error CDFs for 20 dB-Hz $\leq C/N_0 <$ 22.5 dB-Hz. In blue: original PSR MN error CDF after mean removal application. In red: Gaussian overbounding CDF

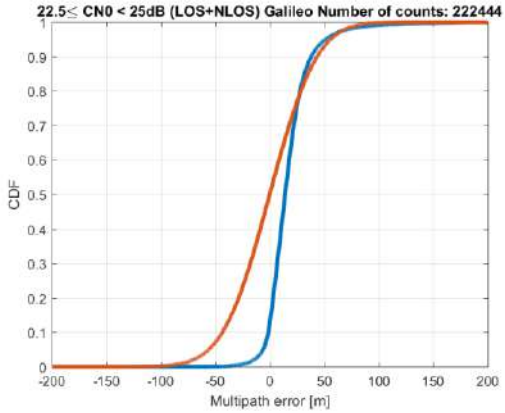

Figure 10-89 – GAL PSR MN error CDFs for 22.5 dB-Hz $\leq C/N_0 <$ 25 dB-Hz. In blue: original PSR MN error CDF. In red: Gaussian overbounding CDF

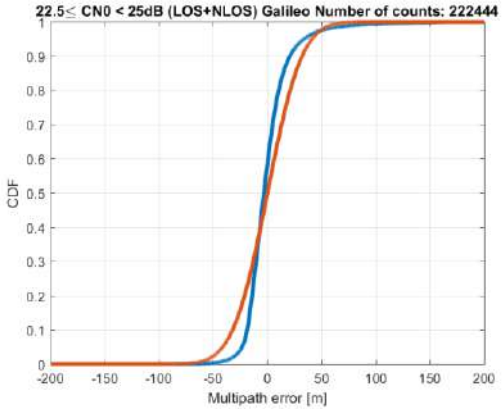

Figure 10-90 – GAL PSR MN error CDFs for 22.5 dB-Hz $\leq C/N_0 <$ 25 dB-Hz. In blue: original PSR MN error CDF after mean removal application. In red: Gaussian overbounding CDF

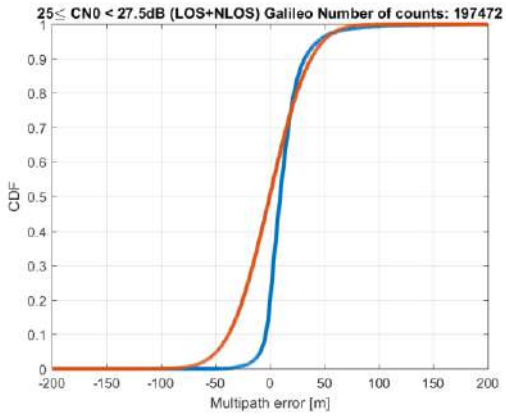

Figure 10-91 – GAL PSR MN error CDFs for 25 dB-Hz $\leq C/N_0 <$ 27.5 dB-Hz. In blue: original PSR MN error CDF. In red: Gaussian overbounding CDF

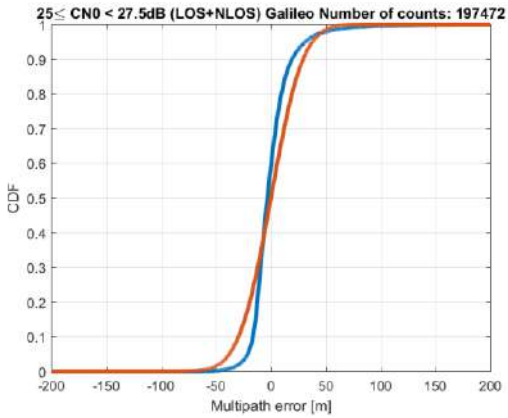

Figure 10-92 – GAL PSR MN error CDFs for 25 dB-Hz $\leq C/N_0 <$ 27.5 dB-Hz. In blue: original PSR MN error CDF after mean removal application. In red: Gaussian overbounding CDF

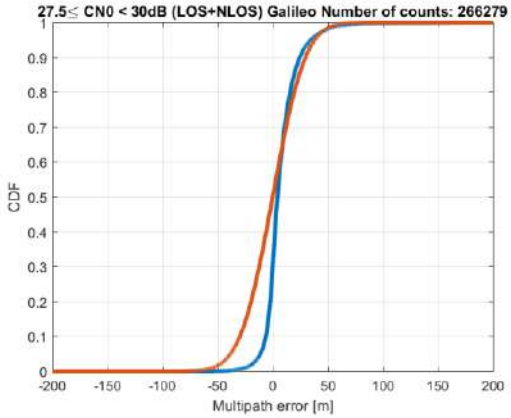

Figure 10-93 – GAL PSR MN error CDFs for 27.5 dB-Hz $\leq C/N_0 <$ 30 dB-Hz. In blue: original PSR MN error CDF. In red: Gaussian overbounding CDF

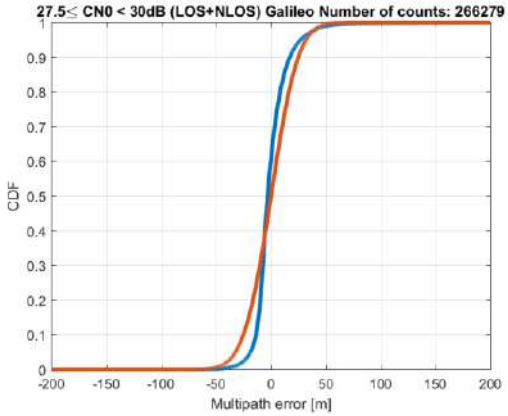

Figure 10-94 – GAL PSR MN error CDFs for 27.5 dB-Hz $\leq C/N_0 <$ 30 dB-Hz. In blue: original PSR MN error CDF after mean removal application. In red: Gaussian overbounding CDF

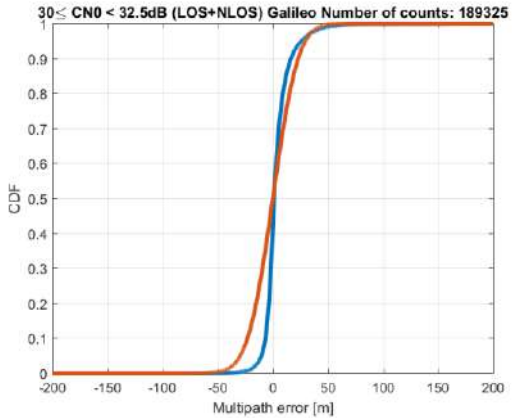

Figure 10-95 – GAL PSR MN error CDFs for 30 dB-Hz $\leq C/N_0 <$ 32.5 dB-Hz. In blue: original PSR MN error CDF. In red: Gaussian overbounding CDF

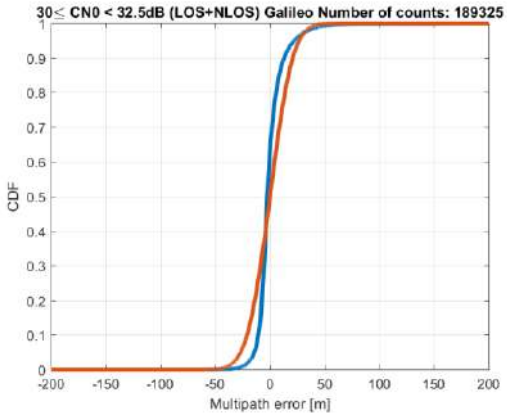

Figure 10-96 – GAL PSR MN error CDFs for 30 dB-Hz $\leq C/N_0 <$ 32.5 dB-Hz. In blue: original PSR MN error CDF after mean removal application. In red: Gaussian overbounding CDF

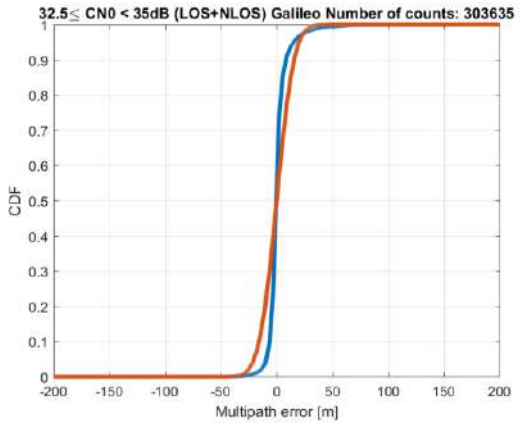

Figure 10-97 – GAL PSR MN error CDFs for 32.5 dB-Hz $\leq C/N_0 <$ 35 dB-Hz. In blue: original PSR MN error CDF. In red: Gaussian overbounding CDF

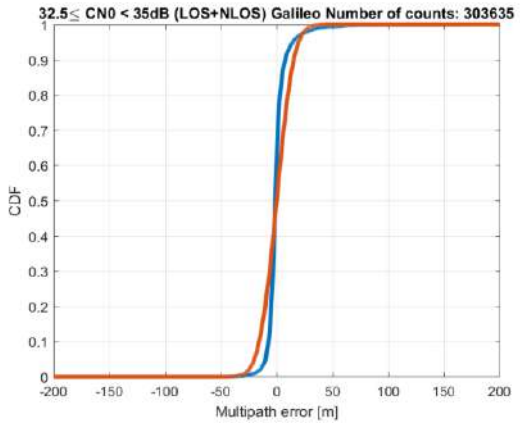

Figure 10-98 – GAL PSR MN error CDFs for 32.5 dB-Hz $\leq C/N_0 <$ 35 dB-Hz. In blue: original PSR MN error CDF after mean removal application. In red: Gaussian overbounding CDF

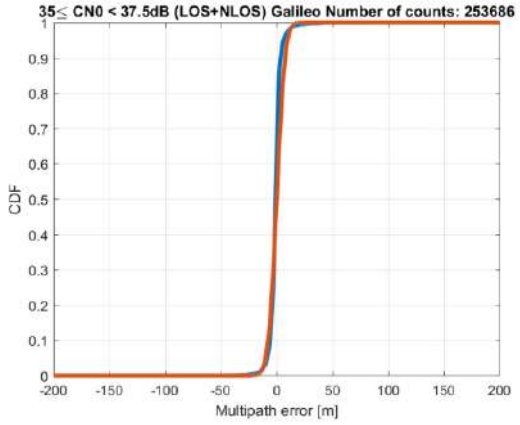

Figure 10-99 – GAL PSR MN error CDFs for 32.5 dB-Hz $\leq C/N_0 <$ 35 dB-Hz. In blue: original PSR MN error CDF. In red: Gaussian overbounding CDF

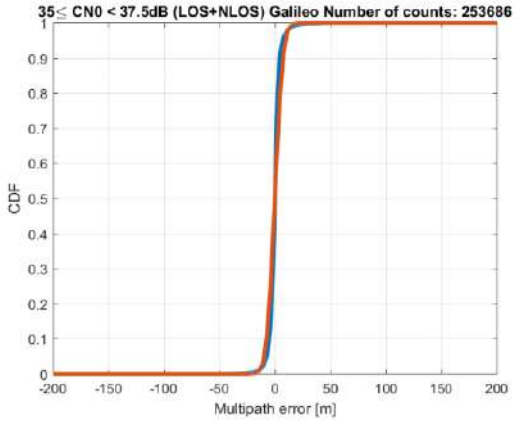

Figure 10-100 – GAL PSR MN error CDFs for 32.5 dB-Hz $\leq C/N_0 <$ 35 dB-Hz. In blue: original PSR MN error CDF after mean removal application. In red: Gaussian overbounding CDF

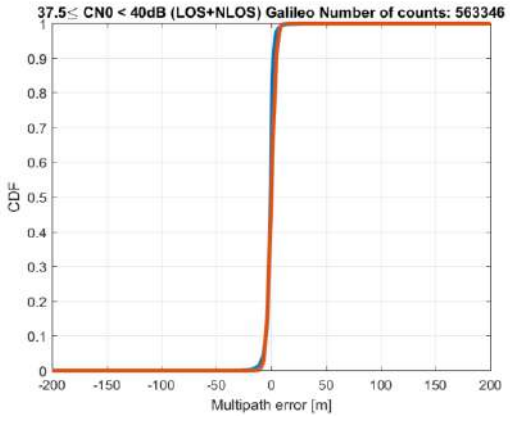

Figure 10-101 – GAL PSR MN error CDFs for 37.5 dB-Hz $\leq C/N_0 <$ 40 dB-Hz. In blue: original PSR MN error CDF. In red: Gaussian overbounding CDF

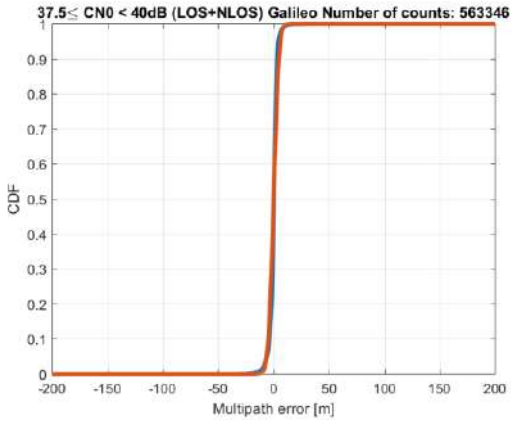

Figure 10-102 – GAL PSR MN error CDFs for 37.5 dB-Hz $\leq C/N_0 <$ 40 dB-Hz. In blue: original PSR MN error CDF after mean removal application. In red: Gaussian overbounding CDF

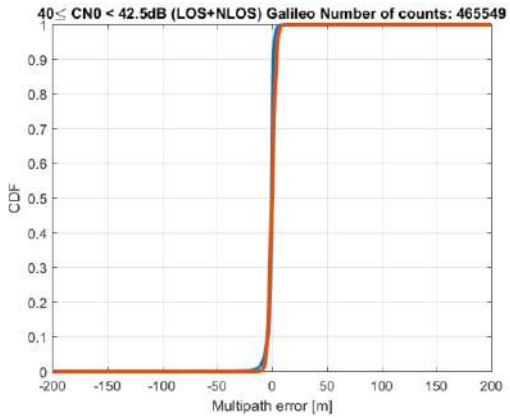

Figure 10-103 – GAL PSR MN error CDFs for 37.5 dB-Hz $\leq C/N_0 <$ 40 dB-Hz. In blue: original PSR MN error CDF. In red: Gaussian overbounding CDF

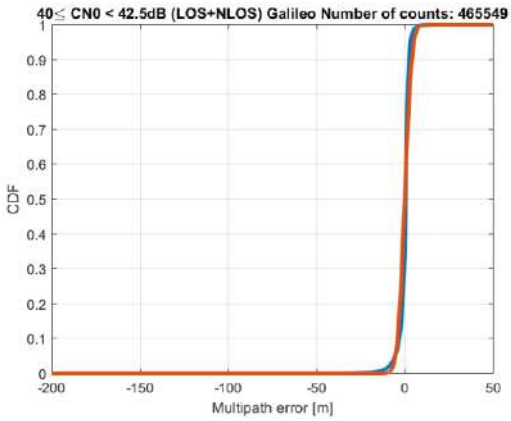

Figure 10-104 – GAL PSR MN error CDFs for 37.5 dB-Hz $\leq C/N_0 <$ 40 dB-Hz. In blue: original PSR MN error CDF after mean removal application. In red: Gaussian overbounding CDF

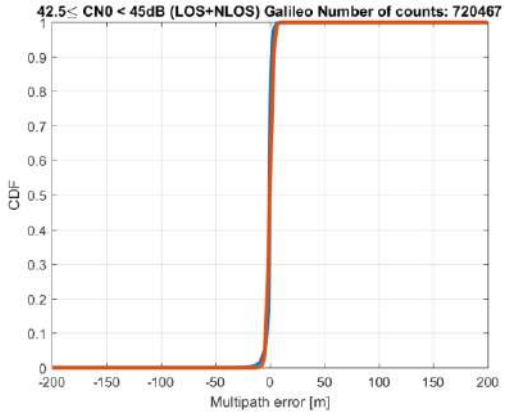

Figure 10-105 – GAL PSR MN error CDFs for 42.5 dB-Hz $\leq C/N_0 <$ 45 dB-Hz. In blue: original PSR MN error CDF. In red: Gaussian overbounding CDF

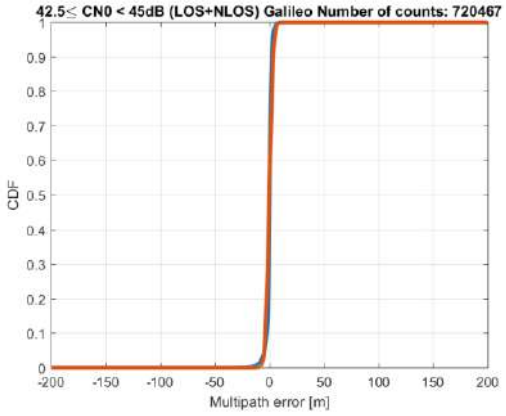

Figure 10-106 – GAL PSR MN error CDFs for 42.5 dB-Hz $\leq C/N_0 <$ 45 dB-Hz. In blue: original PSR MN error CDF after mean removal application. In red: Gaussian overbounding CDF

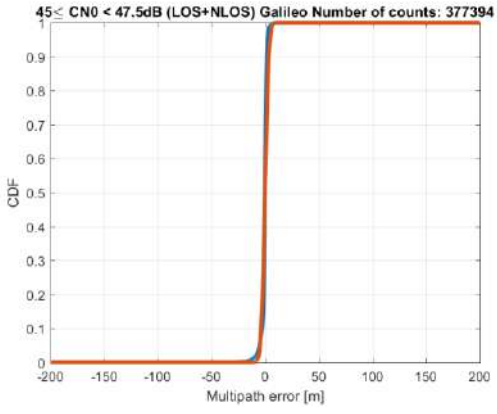

Figure 10-107 – GAL PSR MN error CDFs for 45 dB-Hz $\leq C/N_0 <$ 47.5 dB-Hz. In blue: original PSR MN error CDF. In red: Gaussian overbounding CDF

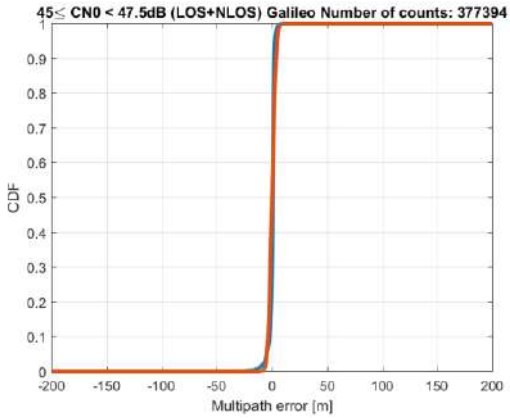

Figure 10-108 – GAL PSR MN error CDFs for 45 dB-Hz $\leq C/N_0 <$ 47.5 dB-Hz. In blue: original PSR MN error CDF after mean removal application. In red: Gaussian overbounding CDF

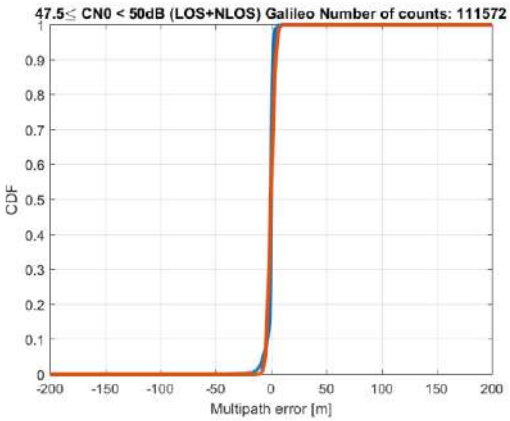

Figure 10-109 – GAL PSR MN error CDFs for 47.5 dB-Hz $\leq C/N_0 <$ 50 dB-Hz. In blue: original PSR MN error CDF. In red: Gaussian overbounding CDF

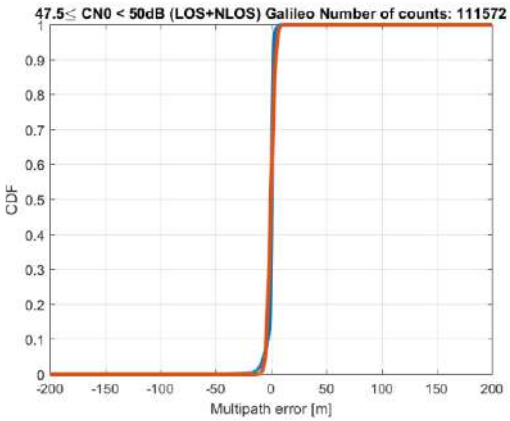

Figure 10-110 – GAL PSR MN error CDFs for 47.5 dB-Hz $\leq C/N_0 <$ 50 dB-Hz. In blue: original PSR MN error CDF after mean removal application. In red: Gaussian overbounding CDF

10.4.3.2 PSR-R MN Residual Error characterization and overbounding

10.4.3.2.1 Dual constellation

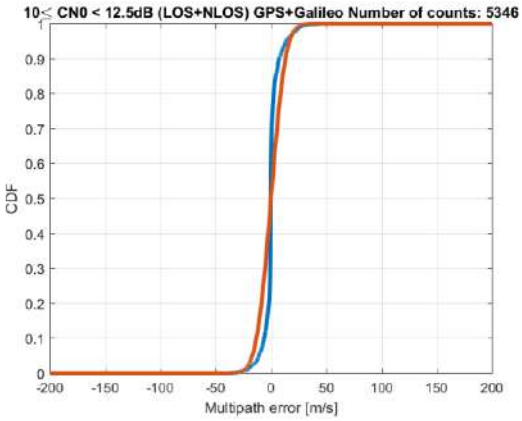

Figure 10-111 – Dual constellation PSR-R MN error CDFs for 10 dB-Hz $\leq C/N_0 <$ 12.5 dB-Hz. In blue: original PSR-R MN error CDF. In red: Gaussian overbounding CDF

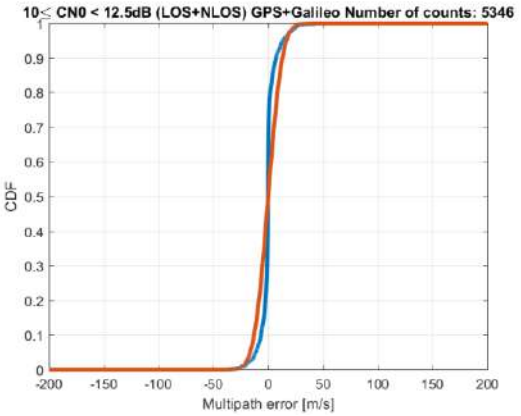

Figure 10-112 – Dual constellation PSR-R MN error CDFs for 10 dB-Hz $\leq C/N_0 <$ 12.5 dB-Hz. In blue: original PSR-R MN error CDF after mean removal application. In red: Gaussian overbounding CDF

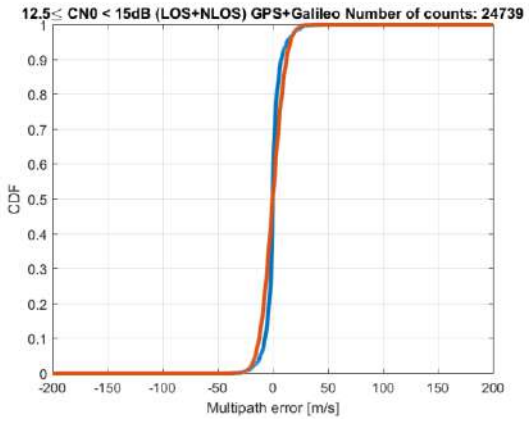

Figure 10-113 – Dual constellation PSR-R MN error CDFs for 12.5 dB-Hz $\leq C/N_0 <$ 15 dB-Hz. In blue: original PSR-R MN error CDF. In red: Gaussian overbounding CDF

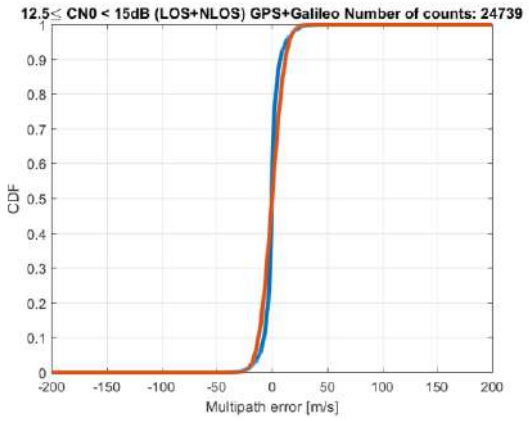

Figure 10-114 – Dual constellation PSR-R MN error CDFs for 12.5 dB-Hz $\leq C/N_0 <$ 15 dB-Hz. In blue: original PSR-R MN error CDF after mean removal application. In red: Gaussian overbounding CDF

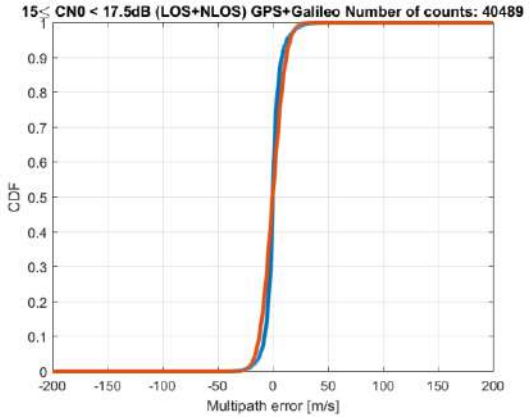

Figure 10-115 – Dual constellation PSR-R MN error CDFs for 15 dB-Hz $\leq C/N_0 <$ 17.5 dB-Hz. In blue: original PSR-R MN error CDF. In red: Gaussian overbounding CDF

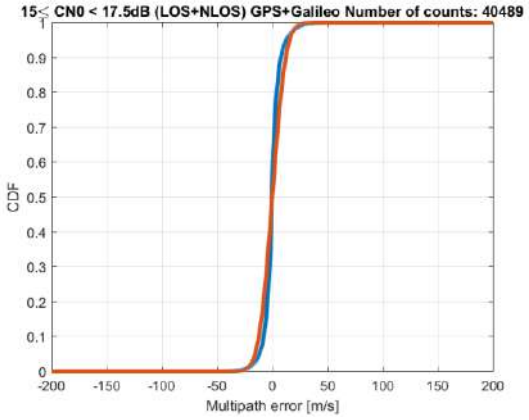

Figure 10-116 – Dual constellation PSR-R MN error CDFs for 15 dB-Hz $\leq C/N_0 <$ 17.5 dB-Hz. In blue: original PSR-R MN error CDF after mean removal application. In red: Gaussian overbounding CDF

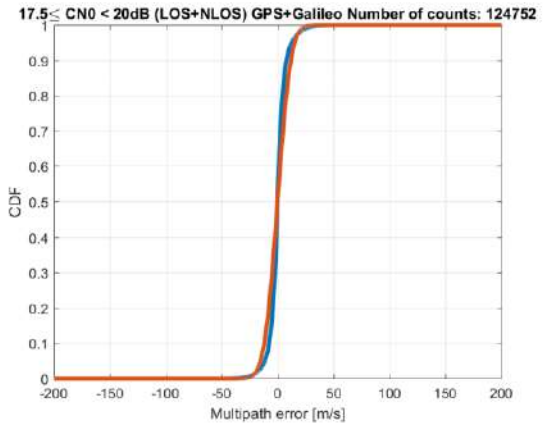

Figure 10-117 – Dual constellation PSR-R MN error CDFs for 17.5 dB-Hz $\leq C/N_0 <$ 20 dB-Hz. In blue: original PSR-R MN error CDF. In red: Gaussian overbounding CDF

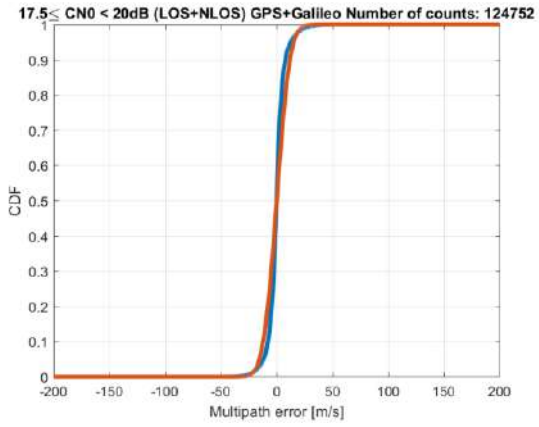

Figure 10-118 – Dual constellation PSR-R MN error CDFs for 17.5 dB-Hz $\leq C/N_0 <$ 20 dB-Hz. In blue: original PSR-R MN error CDF after mean removal application. In red: Gaussian overbounding CDF

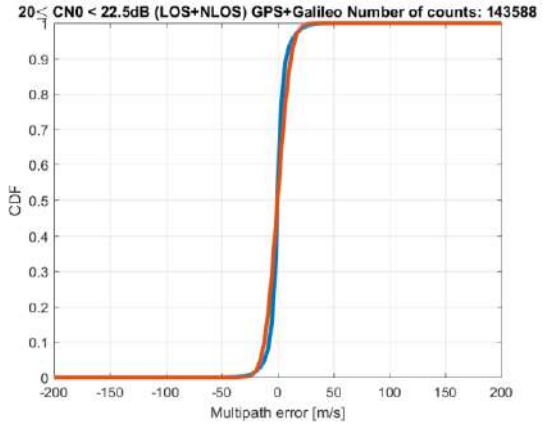

Figure 10-119 – Dual constellation PSR-R MN error CDFs for 20 dB-Hz $\leq C/N_0 <$ 22.5 dB-Hz. In blue: original PSR-R MN error CDF. In red: Gaussian overbounding CDF

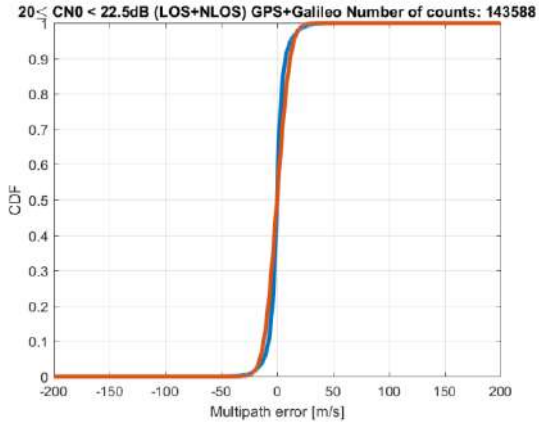

Figure 10-120 – Dual constellation PSR-R MN error CDFs for 20 dB-Hz $\leq C/N_0 <$ 22.5 dB-Hz. In blue: original PSR-R MN error CDF after mean removal application. In red: Gaussian overbounding CDF

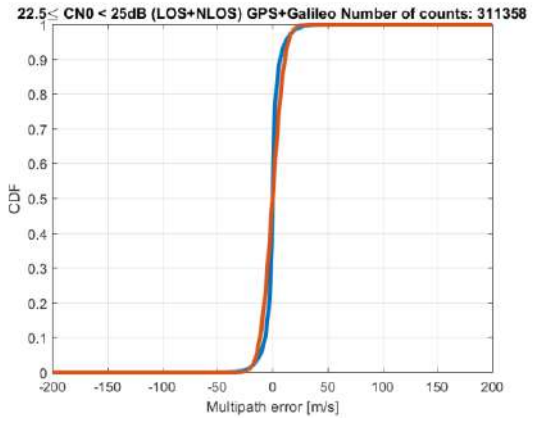

Figure 10-121 – Dual constellation PSR-R MN error CDFs for 22.5 dB-Hz $\leq C/N_0 <$ 25 dB-Hz. In blue: original PSR-R MN error CDF. In red: Gaussian overbounding CDF

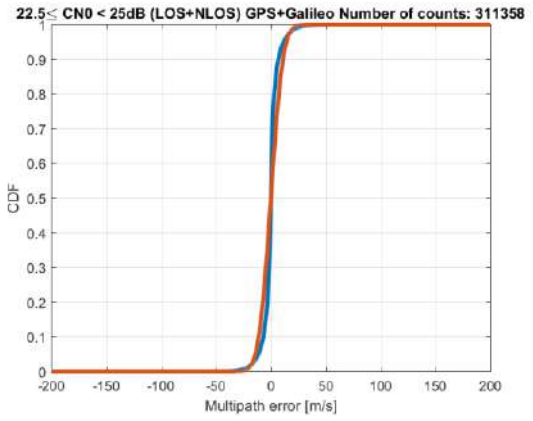

Figure 10-122 – Dual constellation PSR-R MN error CDFs for 22.5 dB-Hz $\leq C/N_0 <$ 25 dB-Hz. In blue: original PSR-R MN error CDF after mean removal application. In red: Gaussian overbounding CDF

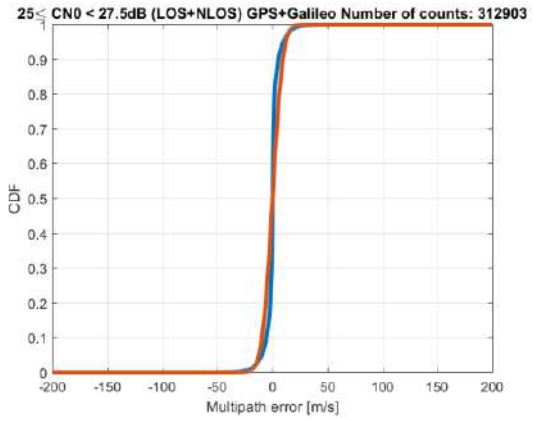

Figure 10-123 – Dual constellation PSR-R MN error CDFs for 25 dB-Hz $\leq C/N_0 <$ 27.5 dB-Hz. In blue: original PSR-R MN error CDF. In red: Gaussian overbounding CDF

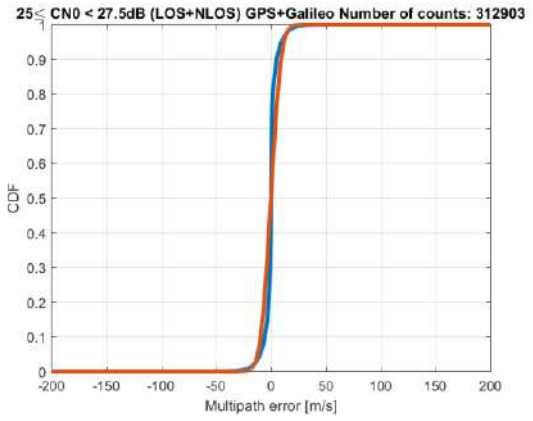

Figure 10-124 – Dual constellation PSR-R MN error CDFs for 25 dB-Hz $\leq C/N_0 <$ 27.5 dB-Hz. In blue: original PSR-R MN error CDF after mean removal application. In red: Gaussian overbounding CDF

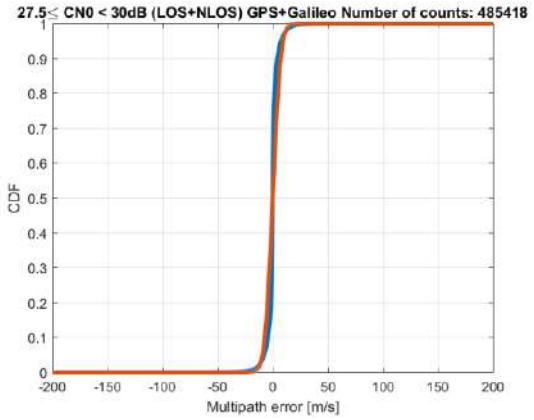

Figure 10-125 – Dual constellation PSR-R MN error CDFs for 27.5 dB-Hz $\leq C/N_0 <$ 30 dB-Hz. In blue:

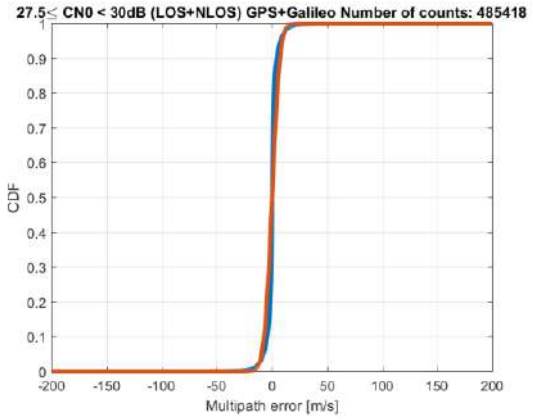

Figure 10-126 – Dual constellation PSR-R MN error CDFs for 27.5 dB-Hz $\leq C/N_0 <$ 30 dB-Hz. In blue:

original PSR-R MN error CDF. In red: Gaussian overbounding CDF

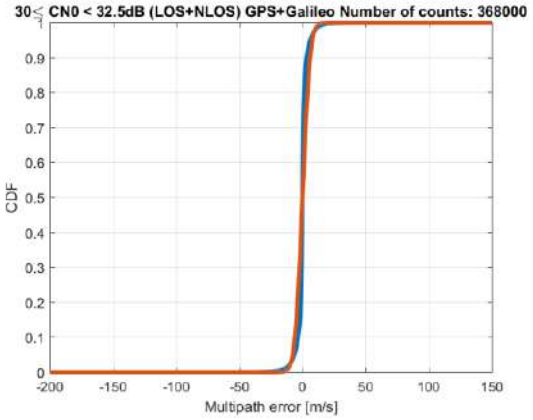

Figure 10-127 – Dual constellation PSR-R MN error CDFs for 30 dB-Hz $\leq C/N_0 <$ 32.5 dB-Hz. In blue: original PSR-R MN error CDF. In red: Gaussian overbounding CDF

original PSR-R MN error CDF after mean removal application. In red: Gaussian overbounding CDF

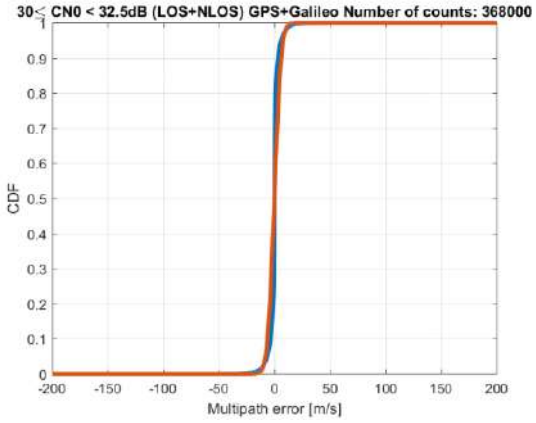

Figure 10-128 – Dual constellation PSR-R MN error CDFs for 30 dB-Hz $\leq C/N_0 <$ 32.5 dB-Hz. In blue: original PSR-R MN error CDF after mean removal application. In red: Gaussian overbounding CDF

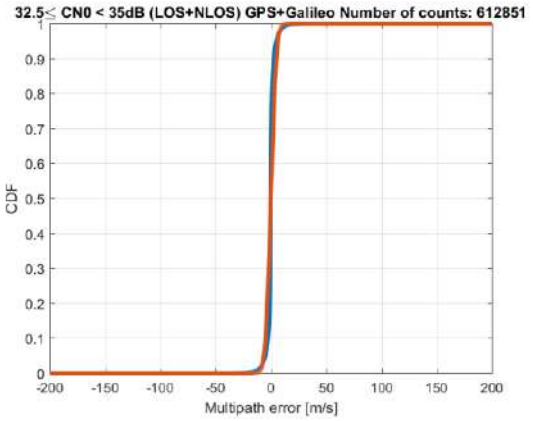

Figure 10-129 – Dual constellation PSR-R MN error CDFs for 32.5 dB-Hz $\leq C/N_0 <$ 35 dB-Hz. In blue: original PSR-R MN error CDF. In red: Gaussian overbounding CDF

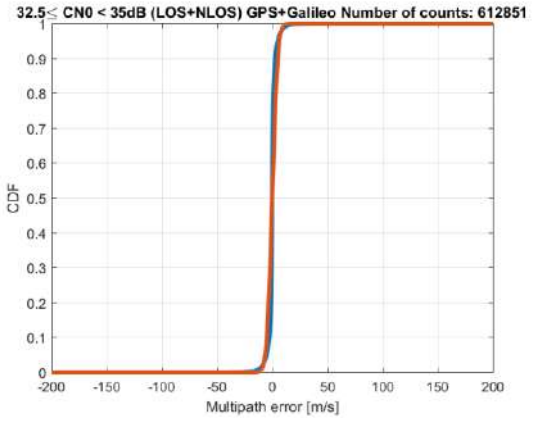

Figure 10-130 – Dual constellation PSR-R MN error CDFs for 32.5 dB-Hz $\leq C/N_0 <$ 35 dB-Hz. In blue: original PSR-R MN error CDF after mean removal application. In red: Gaussian overbounding CDF

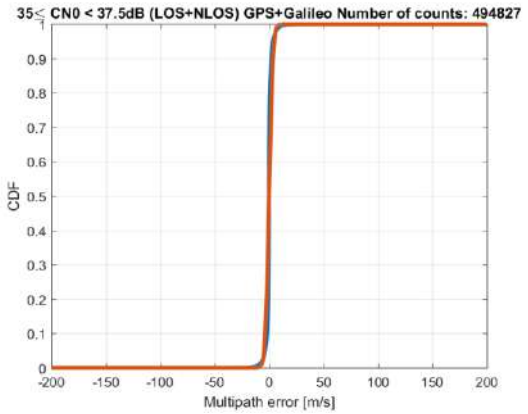

Figure 10-131 – Dual constellation PSR-R MN error CDFs for 35 dB-Hz $\leq C/N_0 <$ 37.5 dB-Hz. In blue: original PSR-R MN error CDF. In red: Gaussian overbounding CDF

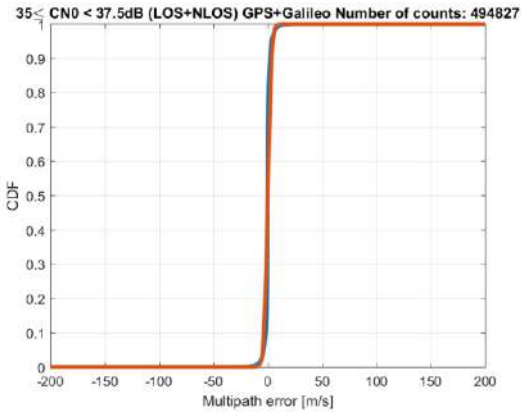

Figure 10-132 – Dual constellation PSR-R MN error CDFs for 35 dB-Hz $\leq C/N_0 <$ 37.5 dB-Hz. In blue: original PSR-R MN error CDF after mean removal application. In red: Gaussian overbounding CDF

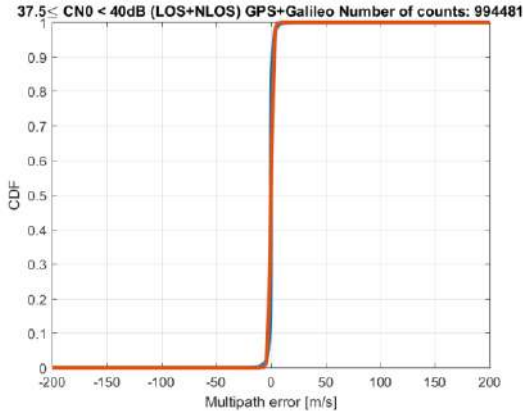

Figure 10-133 – Dual constellation PSR-R MN error CDFs for 37.5 dB-Hz $\leq C/N_0 <$ 40 dB-Hz. In blue: original PSR-R MN error CDF. In red: Gaussian overbounding CDF

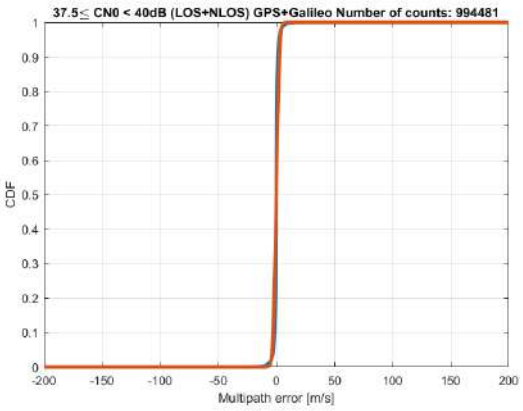

Figure 10-134 – Dual constellation PSR-R MN error CDFs for 37.5 dB-Hz $\leq C/N_0 <$ 40 dB-Hz. In blue: original PSR-R MN error CDF after mean removal application. In red: Gaussian overbounding CDF

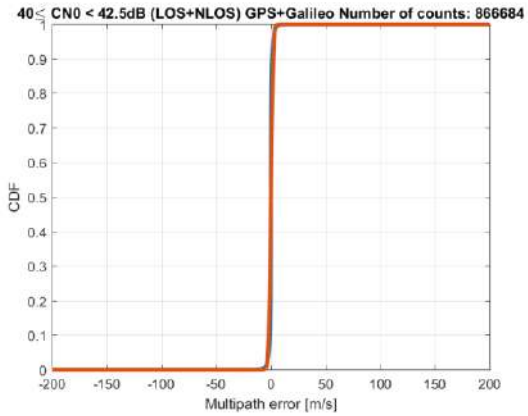

Figure 10-135 – Dual constellation PSR-R MN error CDFs for 40 dB-Hz $\leq C/N_0 <$ 42.5 dB-Hz. In blue: original PSR-R MN error CDF. In red: Gaussian overbounding CDF

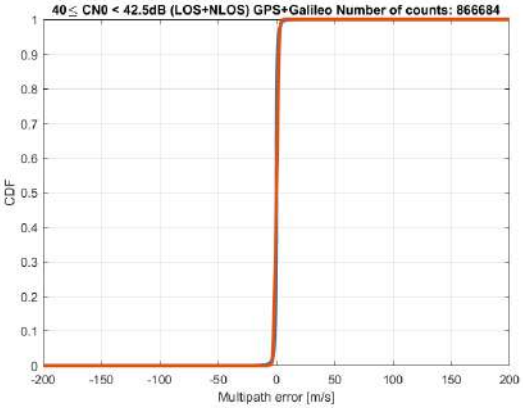

Figure 10-136 – Dual constellation PSR-R MN error CDFs for 40 dB-Hz $\leq C/N_0 <$ 42.5 dB-Hz. In blue: original PSR-R MN error CDF after mean removal application. In red: Gaussian overbounding CDF

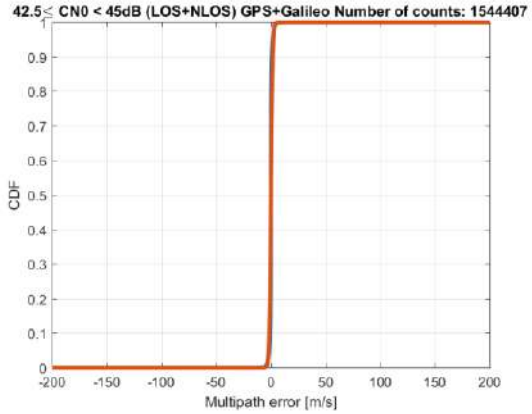

Figure 10-137 – Dual constellation PSR-R MN error CDFs for 42.5 dB-Hz $\leq C/N_0 <$ 45 dB-Hz. In blue: original PSR-R MN error CDF. In red: Gaussian overbounding CDF

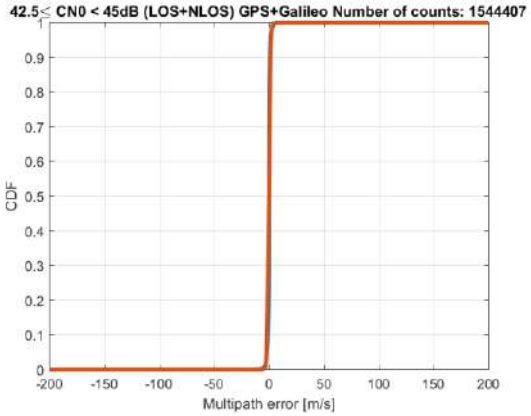

Figure 10-138 – Dual constellation PSR-R MN error CDFs for 42.5 dB-Hz $\leq C/N_0 <$ 45 dB-Hz. In blue: original PSR-R MN error CDF after mean removal application. In red: Gaussian overbounding CDF

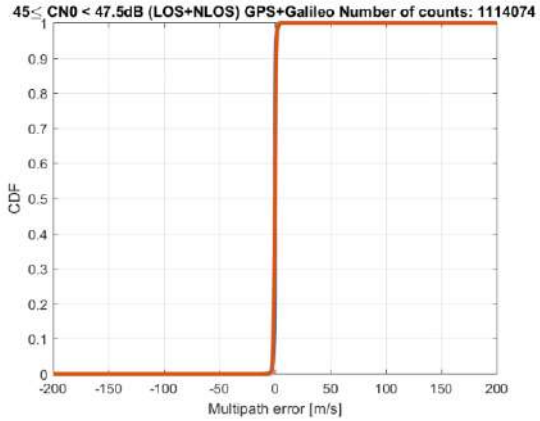

Figure 10-139 – Dual constellation PSR-R MN error CDFs for 45 dB-Hz $C/N_0 <$ 47.5 dB-Hz. In blue: original PSR-R MN error CDF. In red: Gaussian overbounding CDF

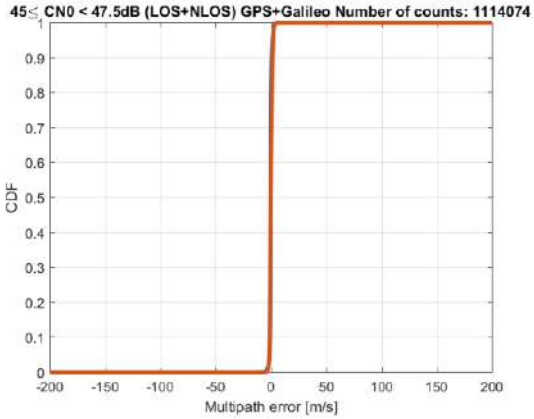

Figure 10-140 – Dual constellation PSR-R MN error CDFs for 45 dB-Hz $C/N_0 <$ 47.5 dB-Hz. In blue: original PSR-R MN error CDF after mean removal application. In red: Gaussian overbounding CDF

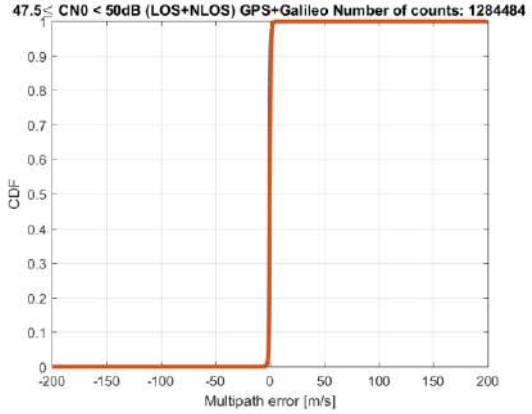

Figure 10-141 – Dual constellation PSR-R MN error CDFs for 47.5 dB-Hz $C/N_0 <$ 50 dB-Hz. In blue: original PSR-R MN error CDF. In red: Gaussian overbounding CDF

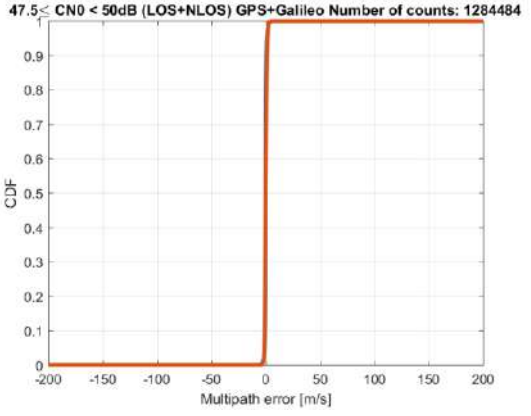

Figure 10-142 – Dual constellation PSR-R MN error CDFs for 47.5 dB-Hz $C/N_0 <$ 50 dB-Hz. In blue: original PSR-R MN error CDF after mean removal application. In red: Gaussian overbounding CDF

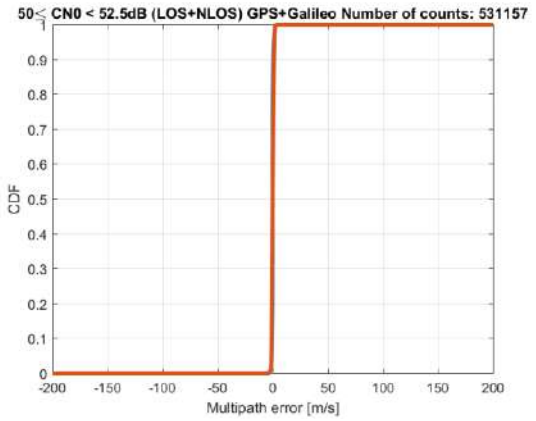

Figure 10-143 – Dual constellation PSR-R MN error CDFs for 50 dB-Hz $C/N_0 < 52.5$ dB-Hz. In blue: original PSR-R MN error CDF. In red: Gaussian overbounding CDF

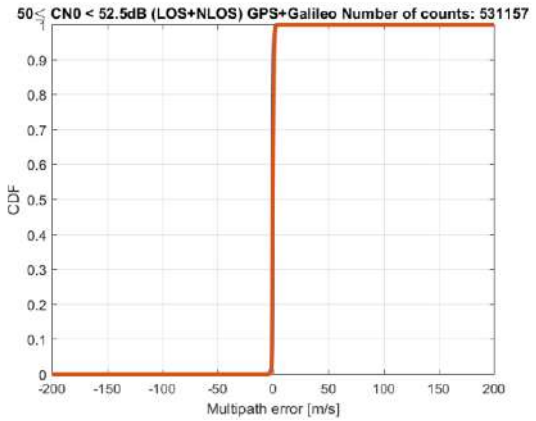

Figure 10-144 – Dual constellation PSR-R MN error CDFs for 50 dB-Hz $C/N_0 < 52.5$ dB-Hz. In blue: original PSR-R MN error CDF after mean removal application. In red: Gaussian overbounding CDF

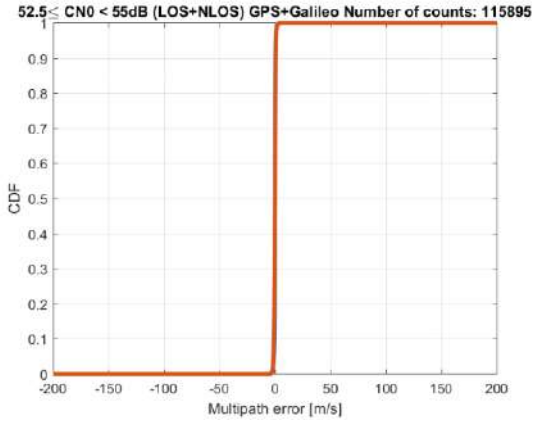

Figure 10-145 – Dual constellation PSR-R MN error CDFs for 52.5 dB-Hz $C/N_0 < 55$ dB-Hz. In blue: original PSR-R MN error CDF. In red: Gaussian overbounding CDF

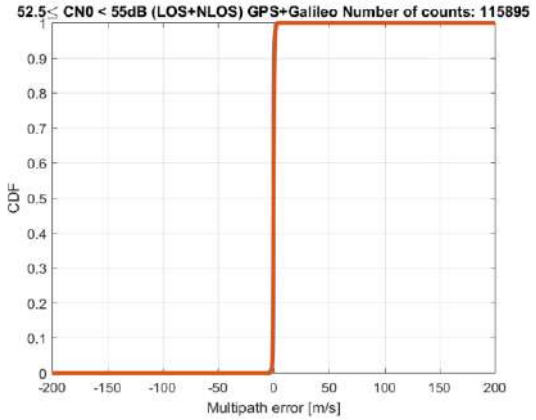

Figure 10-146 – Dual constellation PSR-R MN error CDFs for 52.5 dB-Hz $C/N_0 < 55$ dB-Hz. In blue: original PSR-R MN error CDF after mean removal application. In red: Gaussian overbounding CDF

10.4.3.2.2 GPS L1 C/A

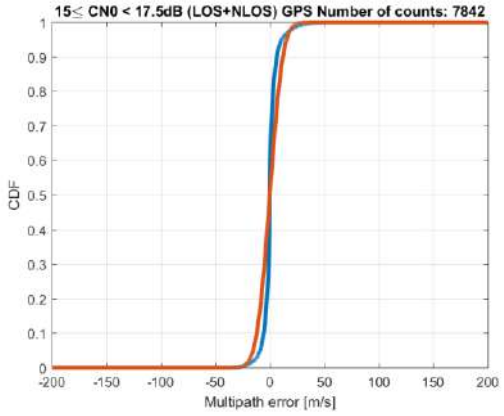

Figure 10-147 – GPS PSR-R MN error CDFs for 15 dB-Hz $\leq C/N_0 < 17.5$ dB-Hz. In blue: original PSR-

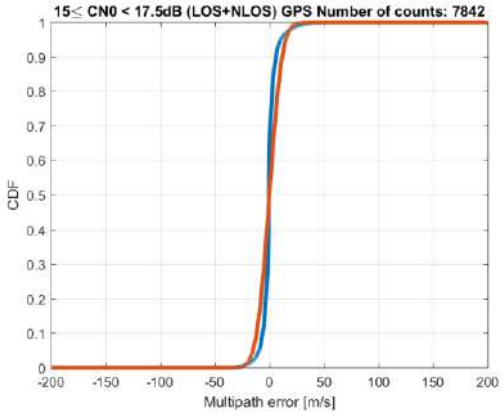

Figure 10-148 – GPS PSR-R MN error CDFs for 15 dB-Hz $\leq C/N_0 < 17.5$ dB-Hz. In blue: original PSR-

R MN error CDF. In red: Gaussian overbounding CDF

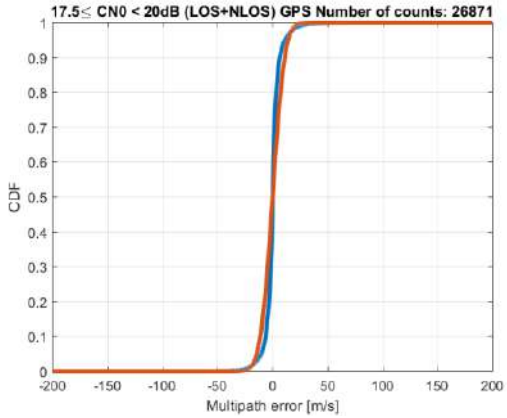

Figure 10-149 – GPS PSR-R MN error CDFs for 17.5 dB-Hz $\leq C/N_0 <$ 20 dB-Hz. In blue: original PSR-R MN error CDF. In red: Gaussian overbounding CDF

R MN error CDF after mean removal application. In red: Gaussian overbounding CDF

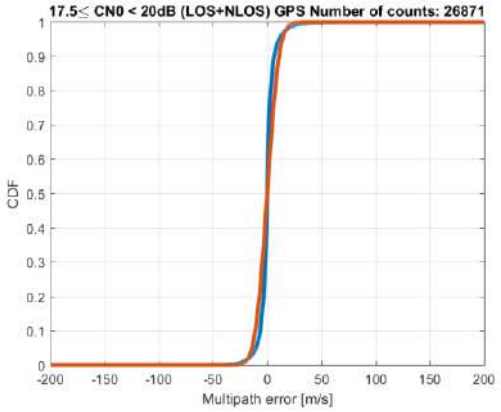

Figure 10-150 – GPS PSR-R MN error CDFs for 17.5 dB-Hz $\leq C/N_0 <$ 20 dB-Hz. In blue: original PSR-R MN error CDF after mean removal application. In red: Gaussian overbounding CDF

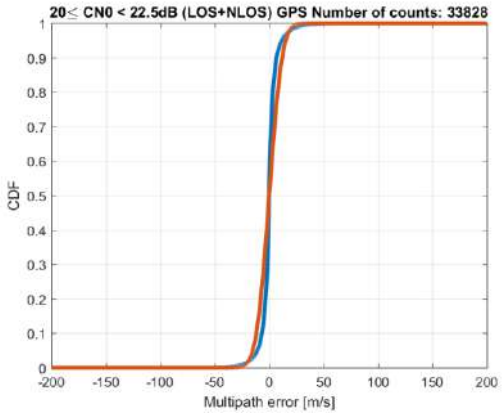

Figure 10-151 – GPS PSR-R MN error CDFs for 20 dB-Hz $\leq C/N_0 <$ 22.5 dB-Hz. In blue: original PSR-R MN error CDF. In red: Gaussian overbounding CDF

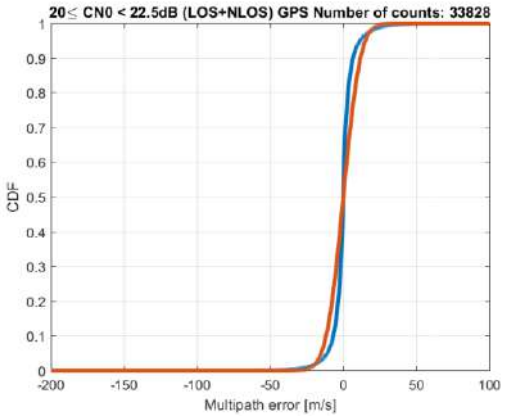

Figure 10-152 – GPS PSR-R MN error CDFs for 20 dB-Hz $\leq C/N_0 <$ 22.5 dB-Hz. In blue: original PSR-R MN error CDF after mean removal application. In red: Gaussian overbounding CDF

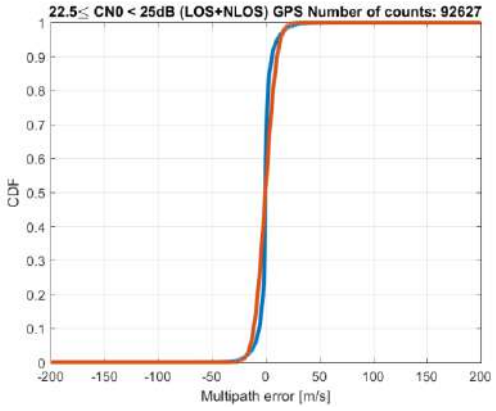

Figure 10-153 – GPS PSR-R MN error CDFs for 22.5 dB-Hz $\leq C/N_0 <$ 25 dB-Hz. In blue: original PSR-R MN error CDF. In red: Gaussian overbounding CDF

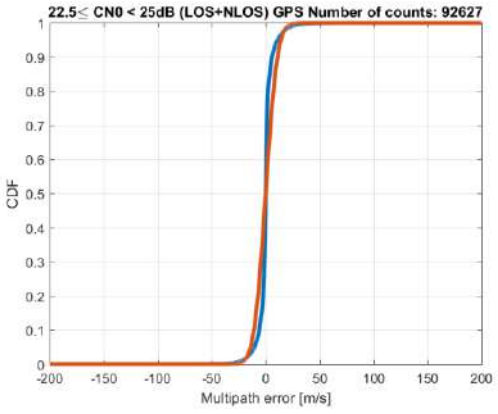

Figure 10-154 – GPS PSR-R MN error CDFs for 22.5 dB-Hz $\leq C/N_0 <$ 25 dB-Hz. In blue: original PSR-R MN error CDF after mean removal application. In red: Gaussian overbounding CDF

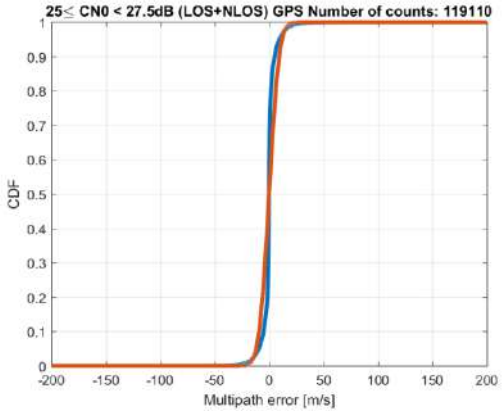

Figure 10-155

GPS PSR-R MN error CDFs for 25 dB-Hz $\leq C/N_0 <$ 27.5 dB-Hz. In blue: original PSR-R MN error CDF. In red: Gaussian overbounding CDF

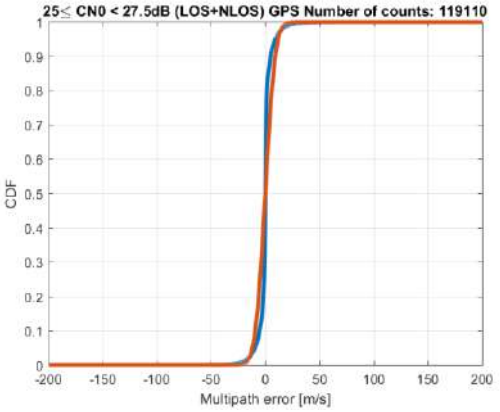

Figure 10-156

GPS PSR-R MN error CDFs for 25 dB-Hz $\leq C/N_0 <$ 27.5 dB-Hz. In blue: original PSR-R MN error CDF after mean removal application. In red: Gaussian overbounding CDF

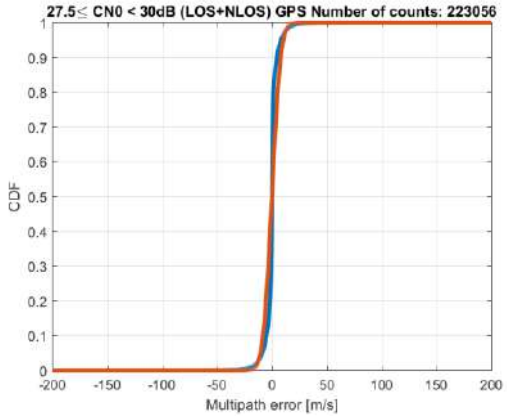

Figure 10-157 – GPS PSR-R MN error CDFs for 27.5 dB-Hz $\leq C/N_0 <$ 30 dB-Hz. In blue: original PSR-R MN error CDF. In red: Gaussian overbounding CDF

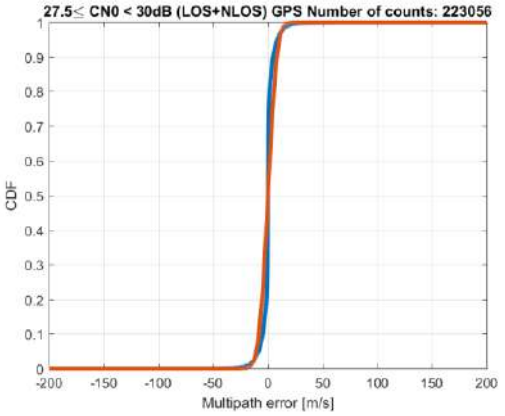

Figure 10-158 – GPS PSR-R MN error CDFs for 27.5 dB-Hz $\leq C/N_0 <$ 30 dB-Hz. In blue: original PSR-R MN error CDF after mean removal application. In red: Gaussian overbounding CDF

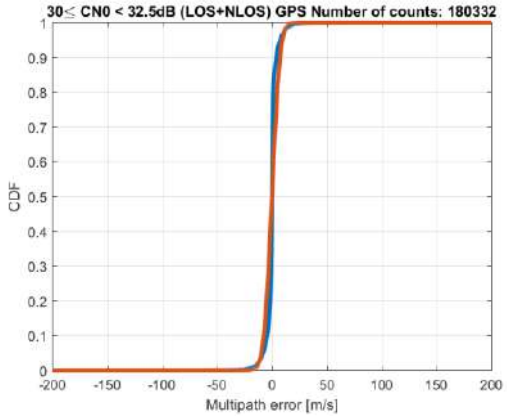

Figure 10-159 – GPS PSR-R MN error CDFs for 30 dB-Hz $\leq C/N_0 <$ 32.5 dB-Hz. In blue: original PSR-R MN error CDF. In red: Gaussian overbounding CDF

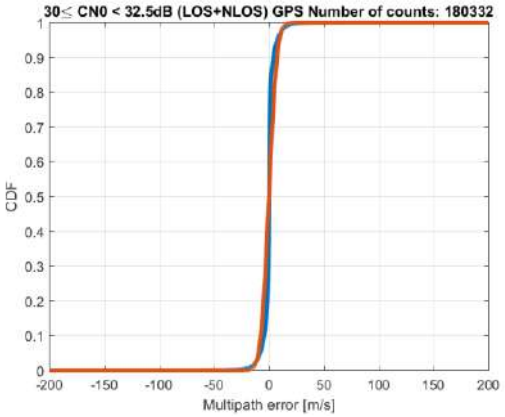

Figure 10-160 – GPS PSR-R MN error CDFs for 30 dB-Hz $\leq C/N_0 <$ 32.5 dB-Hz. In blue: original PSR-R MN error CDF after mean removal application. In red: Gaussian overbounding CDF

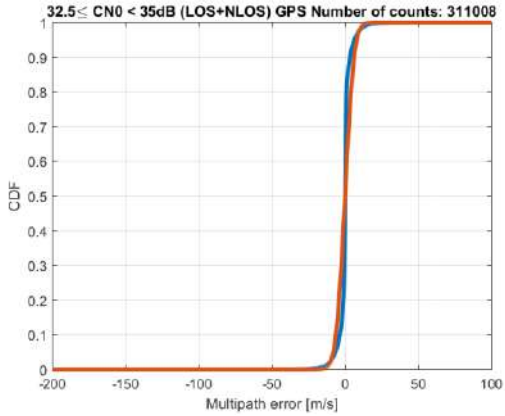

Figure 10-161 – GPS PSR-R MN error CDFs for 32.5 dB-Hz $\leq C/N_0 <$ 35 dB-Hz. In blue: original PSR-R MN error CDF. In red: Gaussian overbounding CDF

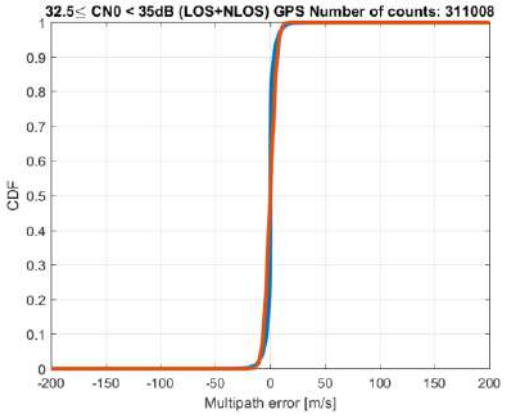

Figure 10-162 – GPS PSR-R MN error CDFs for 32.5 dB-Hz $\leq C/N_0 <$ 35 dB-Hz. In blue: original PSR-R MN error CDF after mean removal application. In red: Gaussian overbounding CDF

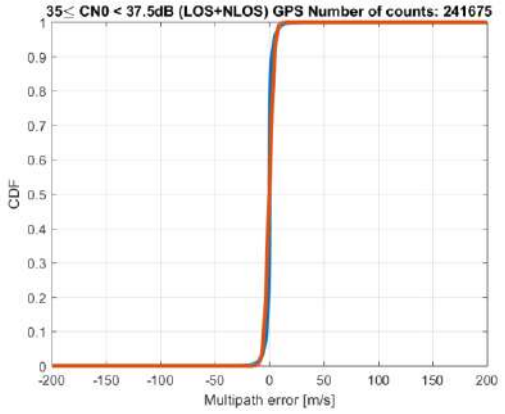

Figure 10-163 – GPS PSR-R MN error CDFs for 35 dB-Hz $\leq C/N_0 <$ 37.5 dB-Hz. In blue: original PSR-R MN error CDF. In red: Gaussian overbounding CDF

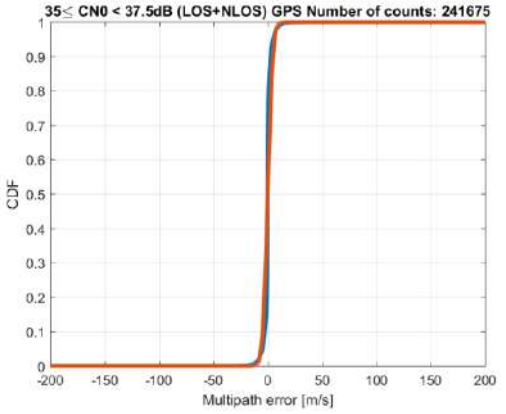

Figure 10-164 – GPS PSR-R MN error CDFs for 35 dB-Hz $\leq C/N_0 <$ 37.5 dB-Hz. In blue: original PSR-R MN error CDF after mean removal application. In red: Gaussian overbounding CDF

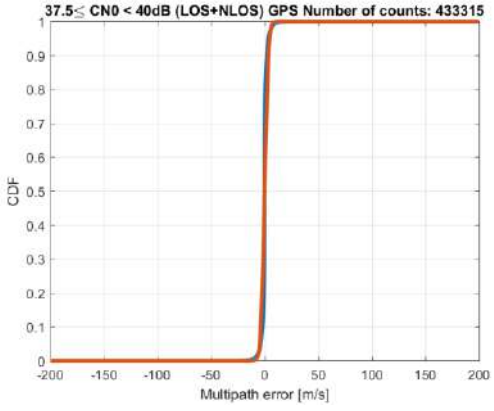

Figure 10-165 – GPS PSR-R MN error CDFs for 37.5 dB-Hz $\leq C/N_0 <$ 40 dB-Hz. In blue: original PSR-R MN error CDF. In red: Gaussian overbounding CDF

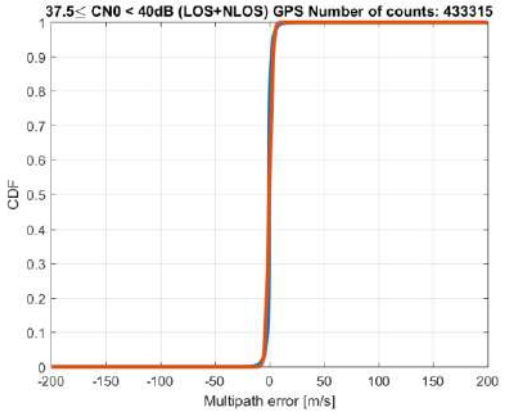

Figure 10-166 – GPS PSR-R MN error CDFs for 37.5 dB-Hz $\leq C/N_0 <$ 40 dB-Hz. In blue: original PSR-R MN error CDF after mean removal application. In red: Gaussian overbounding CDF

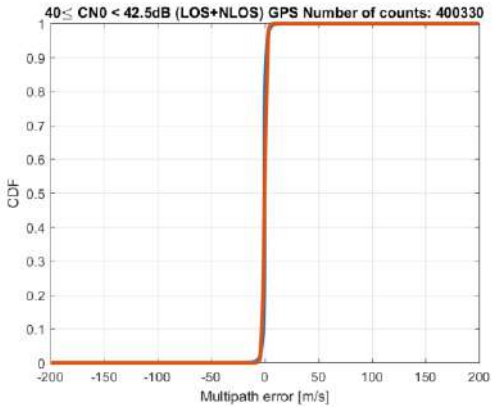

Figure 10-167 – GPS PSR-R MN error CDFs for 40 dB-Hz $\leq C/N_0 <$ 42.5 dB-Hz. In blue: original PSR-R MN error CDF. In red: Gaussian overbounding CDF

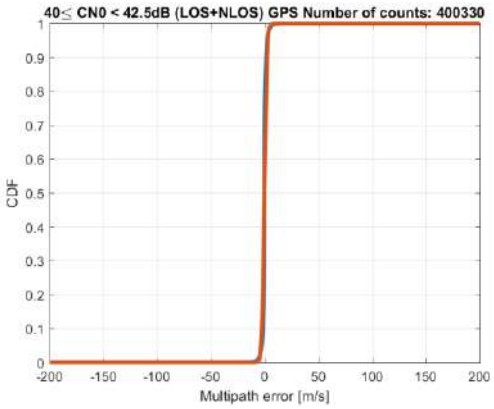

Figure 10-168 – GPS PSR-R MN error CDFs for 40 dB-Hz $\leq C/N_0 <$ 42.5 dB-Hz. In blue: original PSR-R MN error CDF after mean removal application. In red: Gaussian overbounding CDF

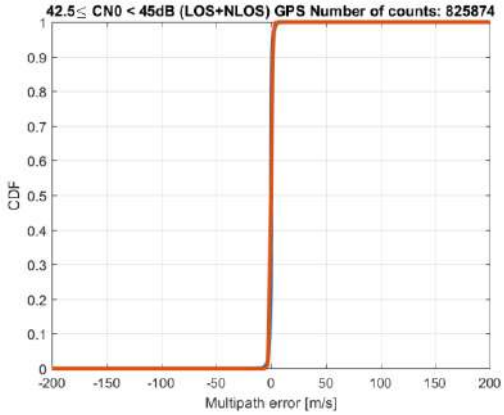

Figure 10-169 – GPS PSR-R MN error CDFs for 42.5 dB-Hz $\leq C/N_0 <$ 45 dB-Hz. In blue: original PSR-R MN error CDF. In red: Gaussian overbounding CDF

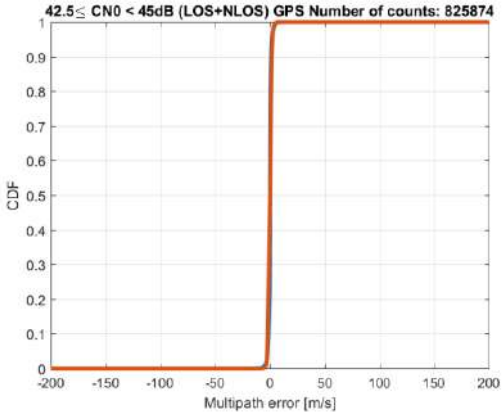

Figure 10-170 – GPS PSR-R MN error CDFs for 42.5 dB-Hz $\leq C/N_0 <$ 45 dB-Hz. In blue: original PSR-R MN error CDF after mean removal application. In red: Gaussian overbounding CDF

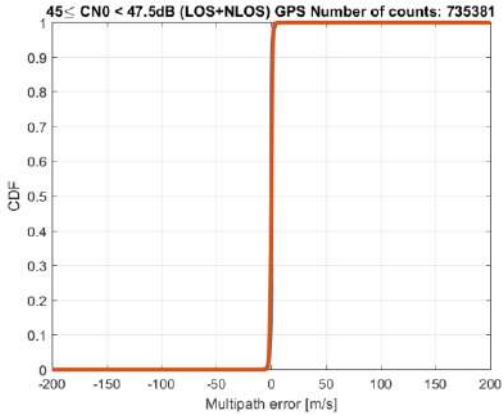

Figure 10-171 – GPS PSR-R MN error CDFs for 45 dB-Hz $\leq C/N_0 <$ 47 dB-Hz. In blue: original PSR-R MN error CDF. In red: Gaussian overbounding CDF

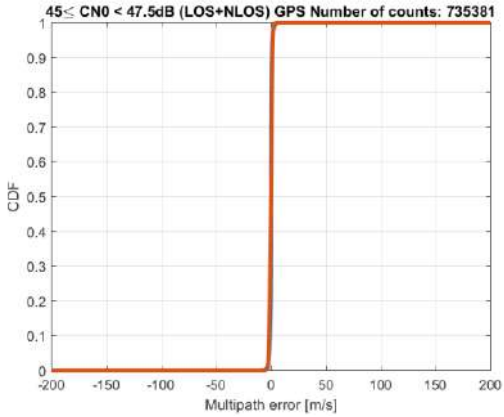

Figure 10-172 – GPS PSR-R MN error CDFs for 45 dB-Hz $\leq C/N_0 <$ 47 dB-Hz. In blue: original PSR-R MN error CDF after mean removal application. In red: Gaussian overbounding CDF

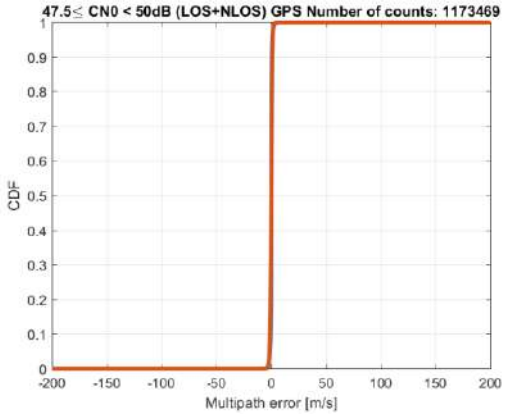

Figure 10-173 – GPS PSR-R MN error CDFs for 47.5 dB-Hz $\leq C/N_0 <$ 50 dB-Hz. In blue: original PSR-R MN error CDF. In red: Gaussian overbounding CDF

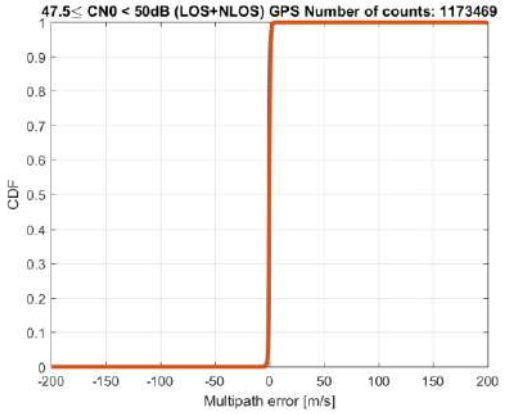

Figure 10-174 – GPS PSR-R MN error CDFs for 47.5 dB-Hz $\leq C/N_0 <$ 50 dB-Hz. In blue: original PSR-R MN error CDF after mean removal application. In red: Gaussian overbounding CDF

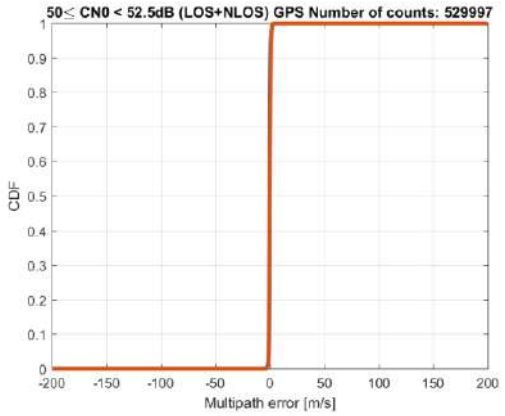

Figure 10-175 – GPS PSR-R MN error CDFs for 50 dB-Hz $\leq C/N_0 <$ 52.5 dB-Hz. In blue: original PSR-R MN error CDF. In red: Gaussian overbounding CDF

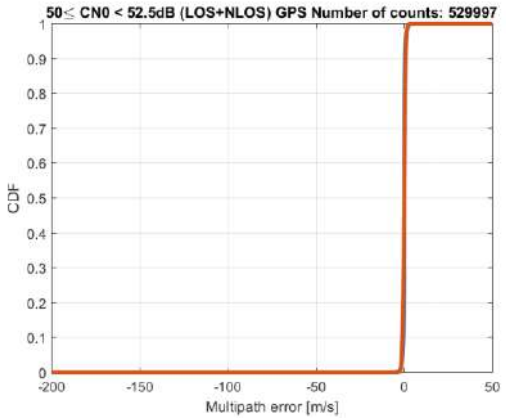

Figure 10-176 – GPS PSR-R MN error CDFs for 50 dB-Hz $\leq C/N_0 <$ 52.5 dB-Hz. In blue: original PSR-R MN error CDF after mean removal application. In red: Gaussian overbounding CDF

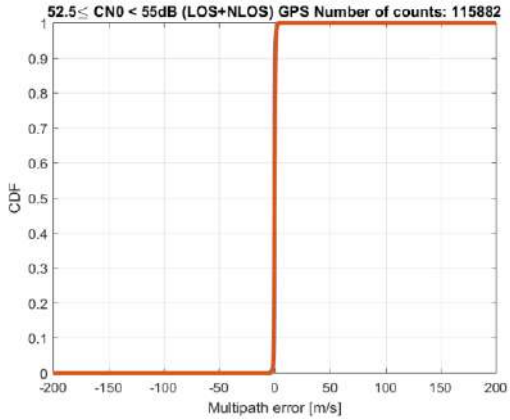

Figure 10-177 – GPS PSR-R MN error CDFs for 52.5 dB-Hz $\leq C/N_0 <$ 55 dB-Hz. In blue: original PSR-R MN error CDF. In red: Gaussian overbounding CDF

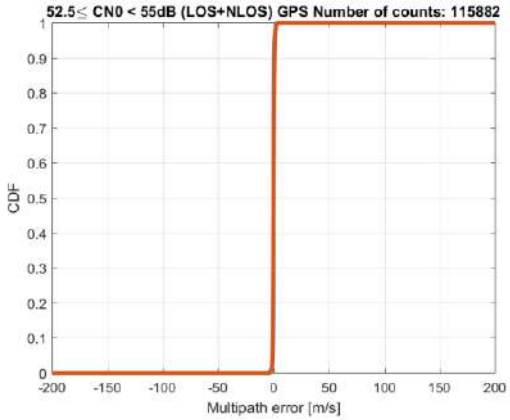

Figure 10-178 – GPS PSR-R MN error CDFs for 52.5 dB-Hz $\leq C/N_0 <$ 55 dB-Hz. In blue: original PSR-R MN error CDF after mean removal application. In red: Gaussian overbounding CDF

10.4.3.2.3 Galileo E1 OS

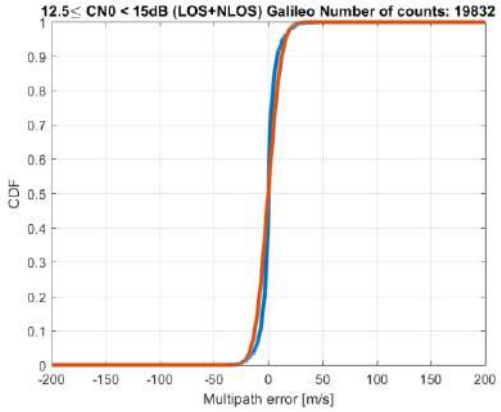

Figure 10-179 – GAL PSR-R MN error CDFs for 12.5 dB-Hz $\leq C/N_0 <$ 15 dB-Hz. In blue: original PSR-R MN error CDF. In red: Gaussian overbounding CDF

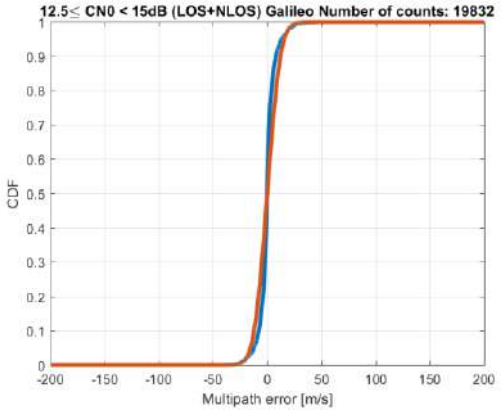

Figure 10-180 – GAL PSR-R MN error CDFs for 12.5 dB-Hz $\leq C/N_0 <$ 15 dB-Hz. In blue: original PSR-R MN error CDF after mean removal application. In red: Gaussian overbounding CDF

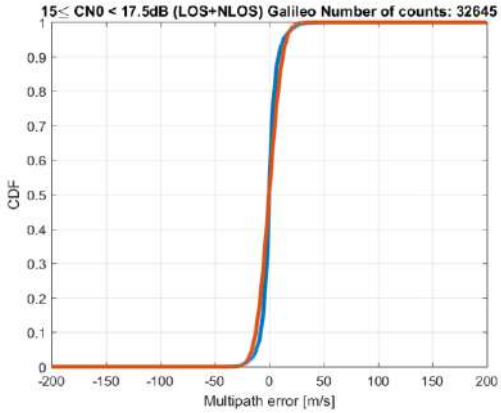

Figure 10-181 – GAL PSR-R MN error CDFs for 15 dB-Hz $\leq C/N_0 <$ 17.5 dB-Hz. In blue: original PSR-R MN error CDF. In red: Gaussian overbounding CDF

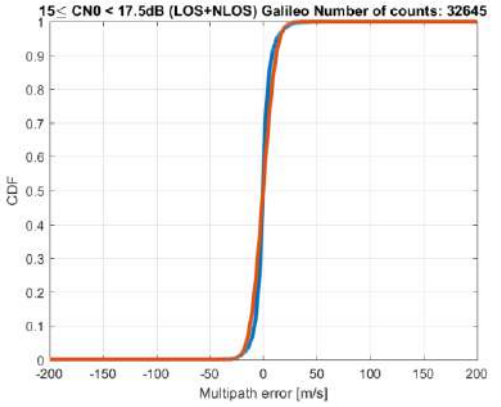

Figure 10-182 – GAL PSR-R MN error CDFs for 15 dB-Hz $\leq C/N_0 <$ 17.5 dB-Hz. In blue: original PSR-R MN error CDF after mean removal application. In red: Gaussian overbounding CDF

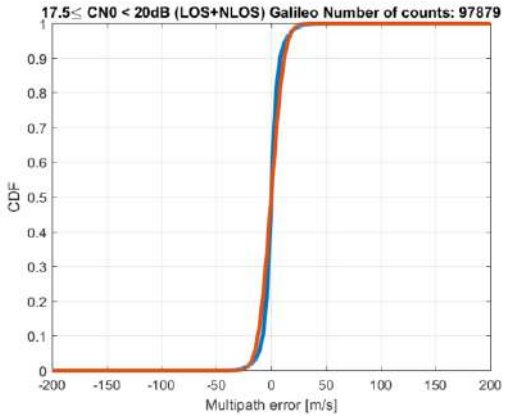

Figure 10-183 – GAL PSR-R MN error CDFs for 17.5 dB-Hz $\leq C/N_0 <$ 20 dB-Hz. In blue: original PSR-R MN error CDF. In red: Gaussian overbounding CDF

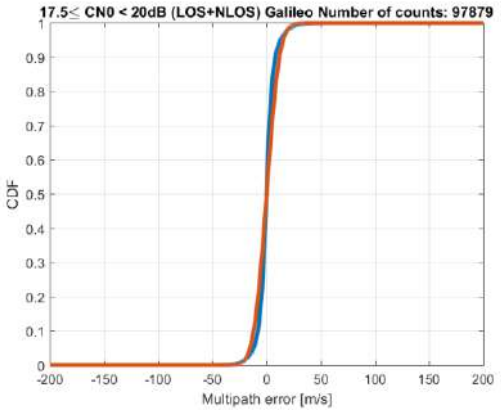

Figure 10-184 – GAL PSR-R MN error CDFs for 17.5 dB-Hz $\leq C/N_0 <$ 20 dB-Hz. In blue: original PSR-R MN error CDF after mean removal application. In red: Gaussian overbounding CDF

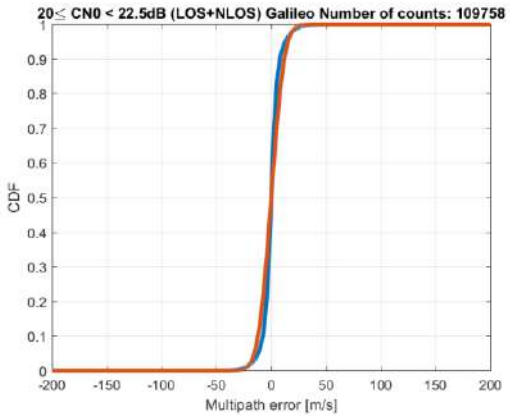

Figure 10-185 – GAL PSR-R MN error CDFs for 17.5 dB-Hz $\leq C/N_0 <$ 20 dB-Hz. In blue: original PSR-R MN error CDF. In red: Gaussian overbounding CDF

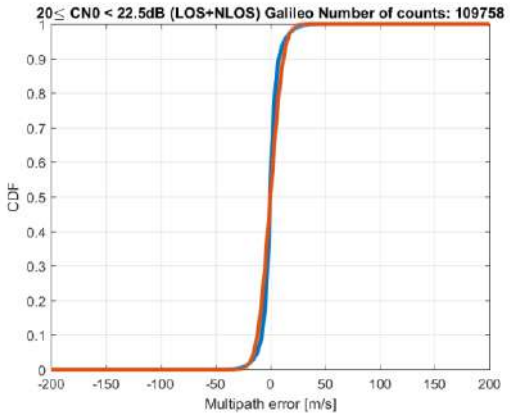

Figure 10-186 – GAL PSR-R MN error CDFs for 17.5 dB-Hz $\leq C/N_0 <$ 20 dB-Hz. In blue: original PSR-R MN error CDF after mean removal application. In red: Gaussian overbounding CDF

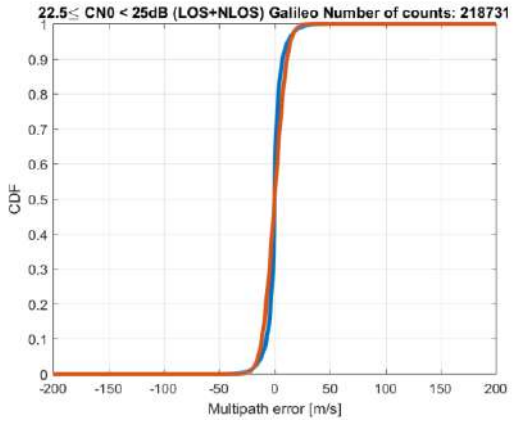

Figure 10-187 – GAL PSR-R MN error CDFs for 22.5 dB-Hz $\leq C/N_0 <$ 25 dB-Hz. In blue: original PSR-R MN error CDF. In red: Gaussian overbounding CDF

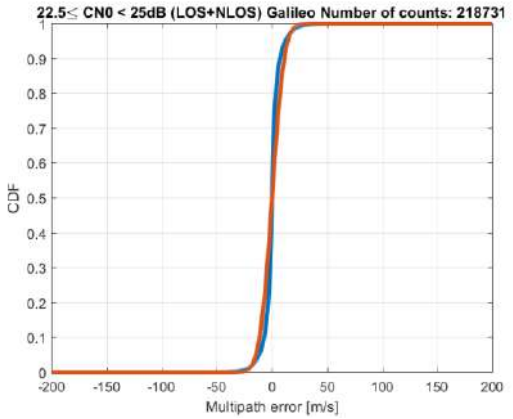

Figure 10-188 – GAL PSR-R MN error CDFs for 22.5 dB-Hz $\leq C/N_0 <$ 25 dB-Hz. In blue: original PSR-R MN error CDF after mean removal application. In red: Gaussian overbounding CDF

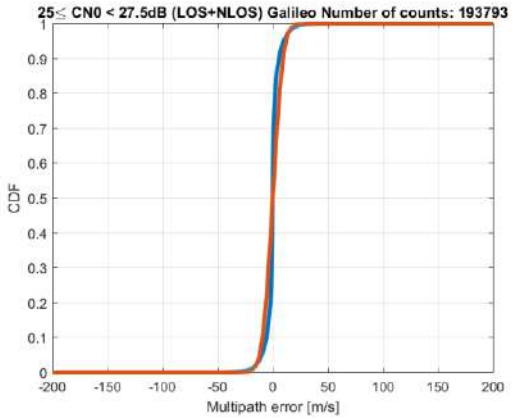

Figure 10-189 – GAL PSR-R MN error CDFs for 25 dB-Hz $\leq C/N_0 <$ 27.5 dB-Hz. In blue: original PSR-R MN error CDF. In red: Gaussian overbounding CDF

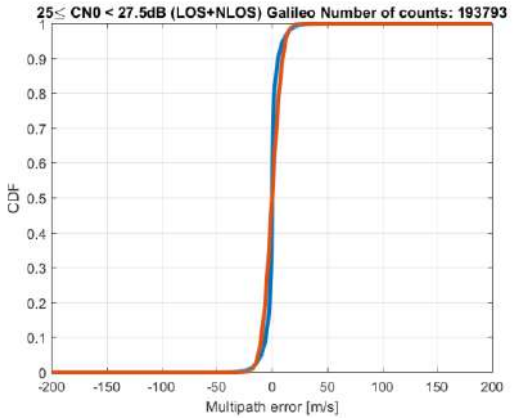

Figure 10-190 – GAL PSR-R MN error CDFs for 25 dB-Hz $\leq C/N_0 <$ 27.5 dB-Hz. In blue: original PSR-R MN error CDF after mean removal application. In red: Gaussian overbounding CDF

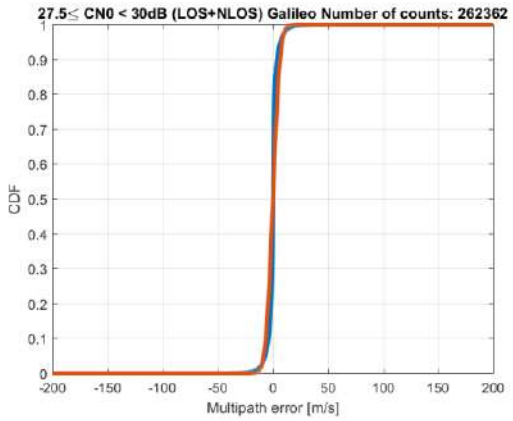

Figure 10-191 – GAL PSR-R MN error CDFs for 27.5 dB-Hz $\leq C/N_0 <$ 30 dB-Hz. In blue: original PSR-R MN error CDF. In red: Gaussian overbounding CDF

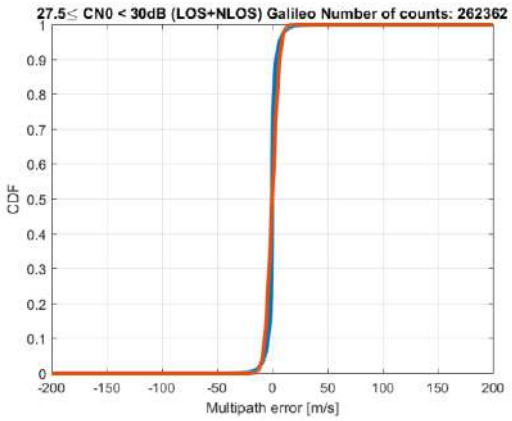

Figure 10-192 – GAL PSR-R MN error CDFs for 27.5 dB-Hz $\leq C/N_0 <$ 30 dB-Hz. In blue: original PSR-R MN error CDF after mean removal application. In red: Gaussian overbounding CDF

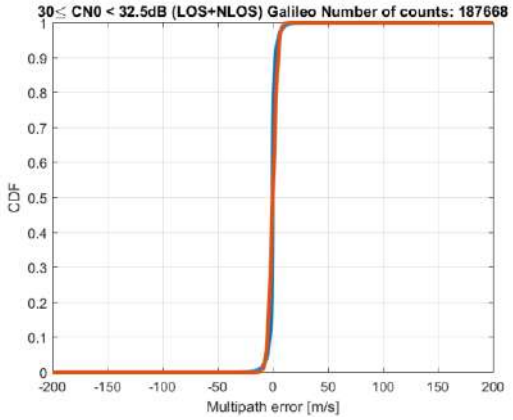

Figure 10-193 – GAL PSR-R MN error CDFs for 30 dB-Hz $\leq C/N_0 <$ 32.5 dB-Hz. In blue: original PSR-R MN error CDF. In red: Gaussian overbounding CDF

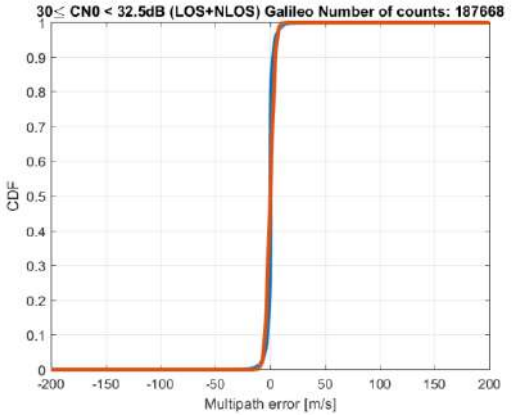

Figure 10-194 – GAL PSR-R MN error CDFs for 30 dB-Hz $\leq C/N_0 <$ 32.5 dB-Hz. In blue: original PSR-R MN error CDF after mean removal application. In red: Gaussian overbounding CDF

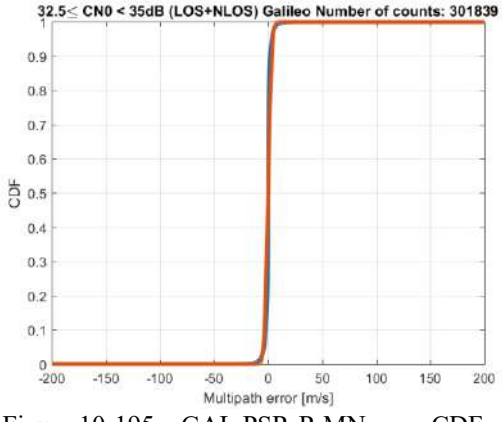

Figure 10-195 – GAL PSR-R MN error CDFs for 32.5 dB-Hz $\leq C/N_0 <$ 35 dB-Hz. In blue: original PSR-R MN error CDF. In red: Gaussian overbounding CDF

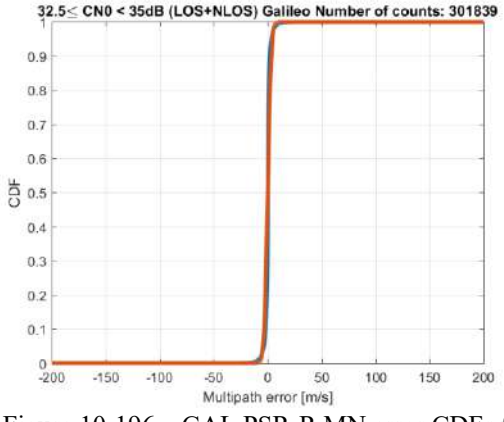

Figure 10-196 – GAL PSR-R MN error CDFs for 32.5 dB-Hz $\leq C/N_0 <$ 35 dB-Hz. In blue: original PSR-R MN error CDF after mean removal application. In red: Gaussian overbounding CDF

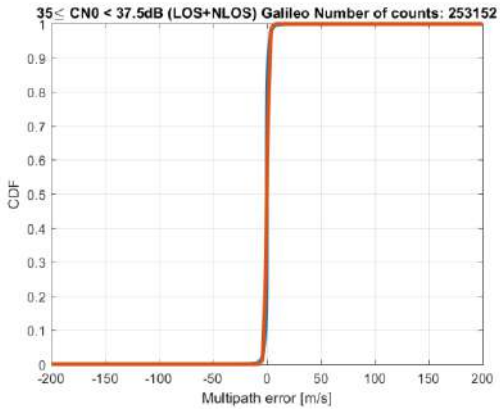

Figure 10-197 – GAL PSR-R MN error CDFs for 32.5 dB-Hz $\leq C/N_0 <$ 35 dB-Hz. In blue: original PSR-R MN error CDF. In red: Gaussian overbounding CDF

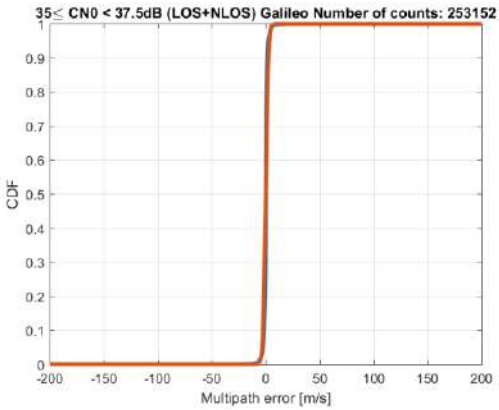

Figure 10-198 – GAL PSR-R MN error CDFs for 32.5 dB-Hz $\leq C/N_0 <$ 35 dB-Hz. In blue: original PSR-R MN error CDF after mean removal application. In red: Gaussian overbounding CDF

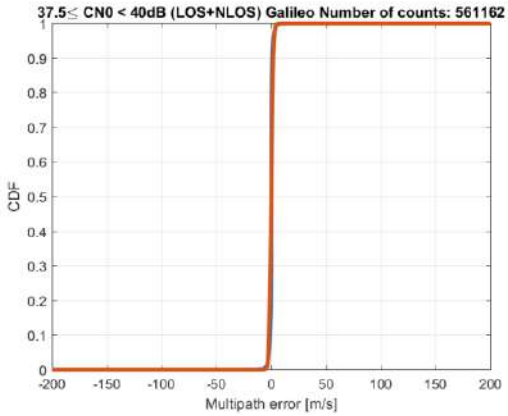

Figure 10-199 – GAL PSR-R MN error CDFs for 37.5 dB-Hz $\leq C/N_0 <$ 40 dB-Hz. In blue: original PSR-R MN error CDF. In red: Gaussian overbounding CDF

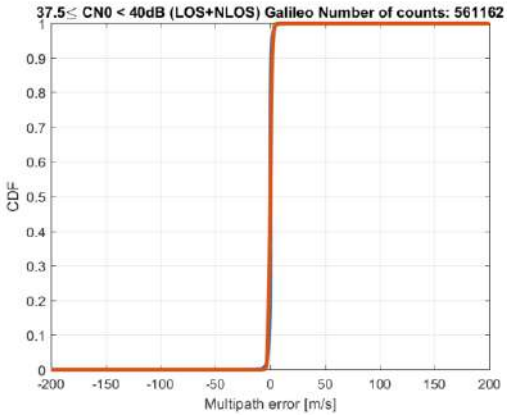

Figure 10-200 – GAL PSR-R MN error CDFs for 37.5 dB-Hz $\leq C/N_0 <$ 40 dB-Hz. In blue: original PSR-R MN error CDF after mean removal application. In red: Gaussian overbounding CDF

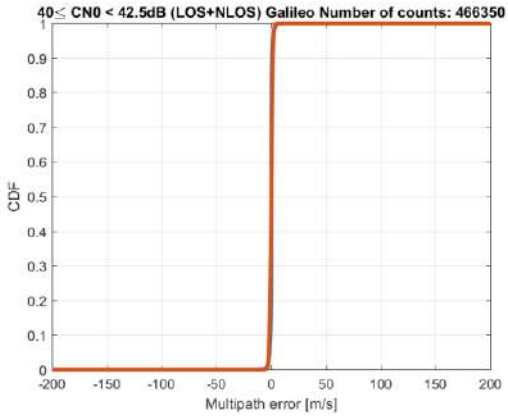

Figure 10-201 – GAL PSR-R MN error CDFs for 40 dB-Hz $\leq C/N_0 <$ 42.5 dB-Hz. In blue: original PSR-R MN error CDF. In red: Gaussian overbounding CDF

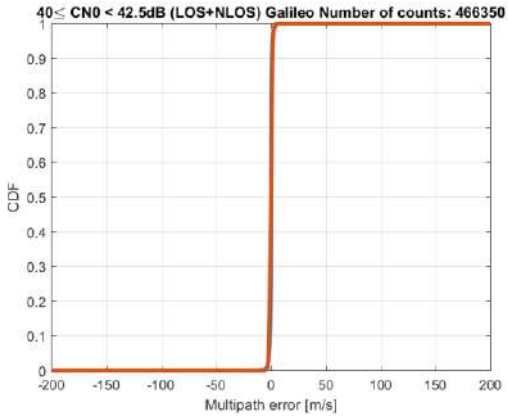

Figure 10-202 – GAL PSR-R MN error CDFs for 37.5 dB-Hz $\leq C/N_0 <$ 40 dB-Hz. In blue: original PSR-R MN error CDF after mean removal application. In red: Gaussian overbounding CDF

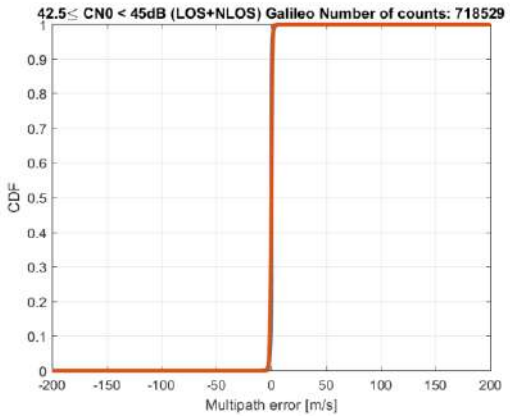

Figure 10-203 – GAL PSR-R MN error CDFs for 42.5 dB-Hz $\leq C/N_0 <$ 45 dB-Hz. In blue: original PSR-R MN error CDF. In red: Gaussian overbounding CDF

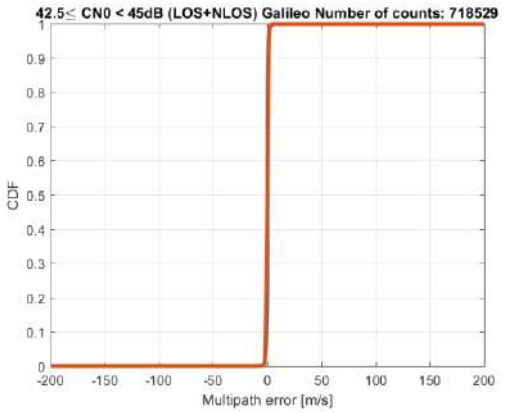

Figure 10-204 – GAL PSR-R MN error CDFs for 42.5 dB-Hz $\leq C/N_0 <$ 45 dB-Hz. In blue: original PSR-R MN error CDF after mean removal application. In red: Gaussian overbounding CDF

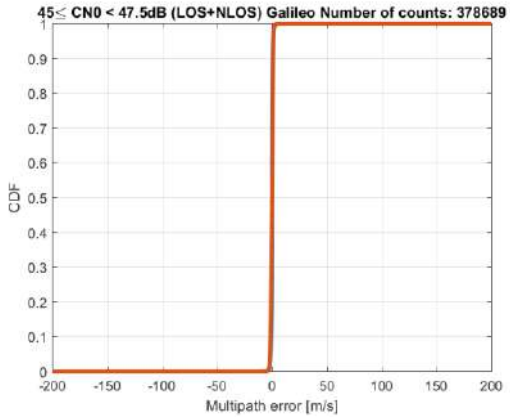

Figure 10-205 – GAL PSR-R MN error CDFs for 45 dB-Hz $\leq C/N_0 <$ 47.5 dB-Hz. In blue: original PSR-R MN error CDF. In red: Gaussian overbounding CDF

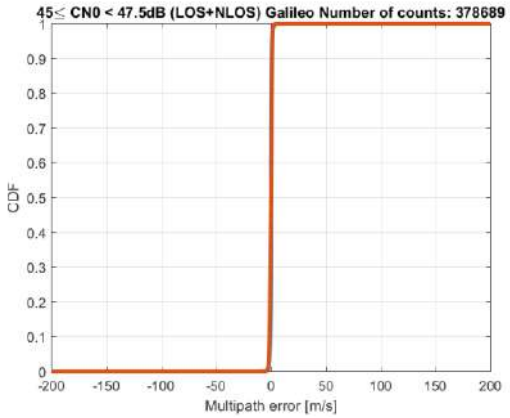

Figure 10-206 – GAL PSR-R MN error CDFs for 45 dB-Hz $\leq C/N_0 <$ 47.5 dB-Hz. In blue: original PSR-R MN error CDF after mean removal application. In red: Gaussian overbounding CDF

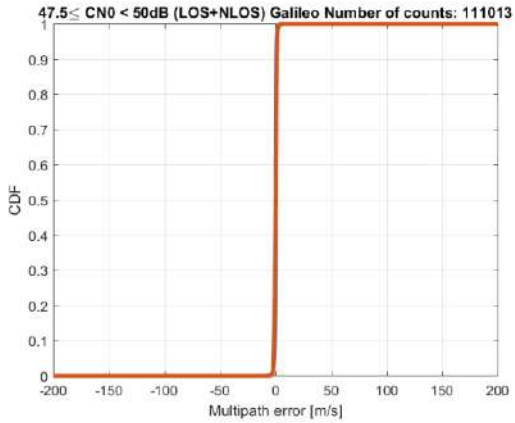

Figure 10-207 – GAL PSR-R MN error CDFs for 47.5 dB-Hz $\leq C/N_0 <$ 50 dB-Hz. In blue: original PSR-R MN error CDF. In red: Gaussian overbounding CDF

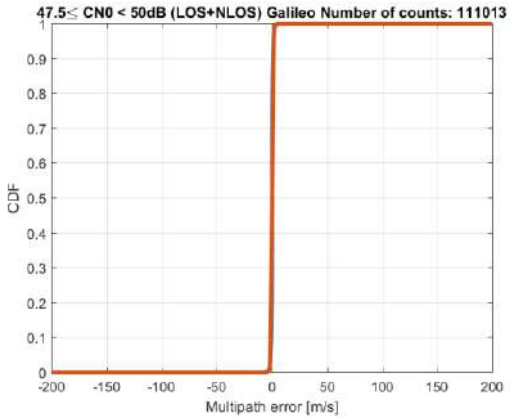

Figure 10-208 – GAL PSR-R MN error CDFs for 47.5 dB-Hz $\leq C/N_0 <$ 50 dB-Hz. In blue: original PSR-R MN error CDF after mean removal application. In red: Gaussian overbounding CDF

10.5 Annex – Proposed EKF Algorithm

10.5.1 Innovation vector of Standard and TC Kalman Filters obtained from Dataset 1

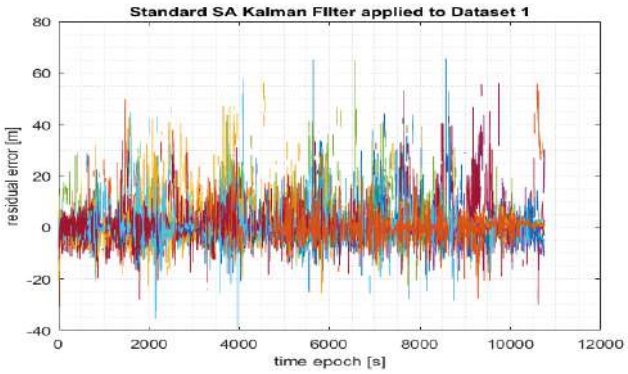

Figure 10-209 – Innovation residuals obtained for all satellite-in-view measurements applying the Stand Alone Standard EKF on Dataset 1

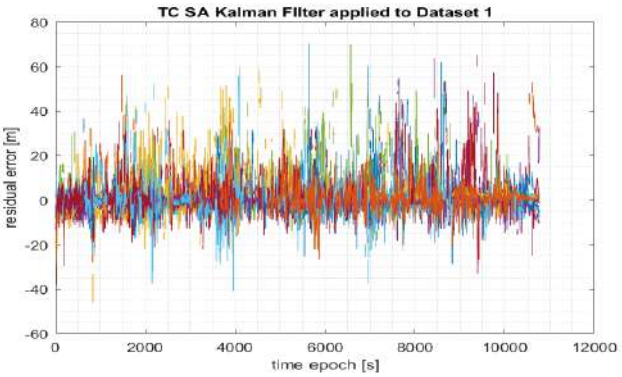

Figure 10-210 – Innovation residuals obtained for all satellite-in-view measurements applying the Stand Alone TC EKF on Dataset 1

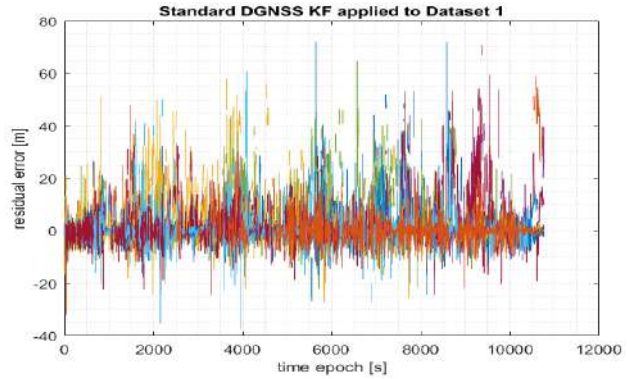

Figure 10-211 – Innovation residuals obtained for all satellite-in-view measurements applying the DGNSS Standard EKF on Dataset 1

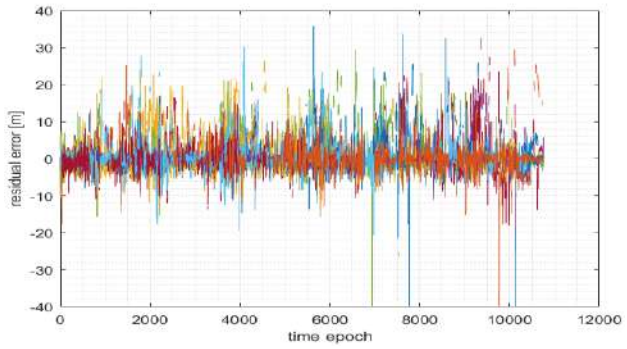

Figure 10-212 – Innovation residuals obtained for all satellite-in-view measurements applying the DGNSS TC EKF on Dataset 1

10.5.2 Results of proposed PVT estimators applied to Data Collection 2

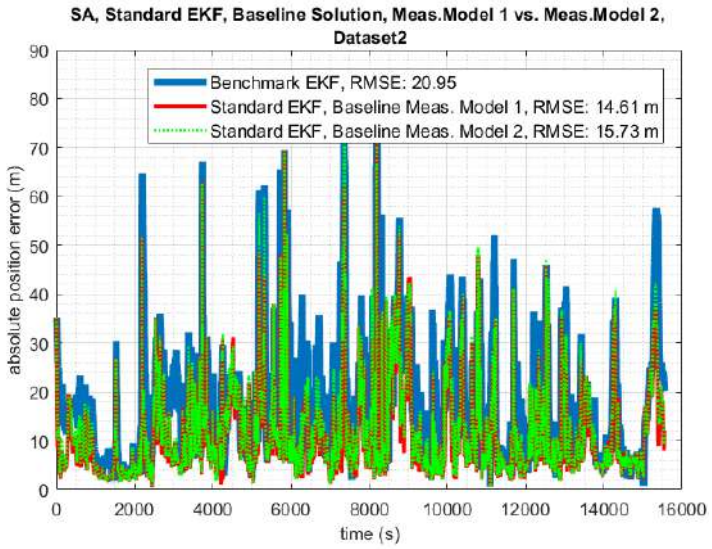

Figure 10-213 – Absolute Position estimation error with the corresponding RMSE: Dataset 2, SA Benchmark EKF (blue line) vs. Standard EKF with Baseline Block Measurement Model 1 (red line) vs. Measurement Model 2 (green line)

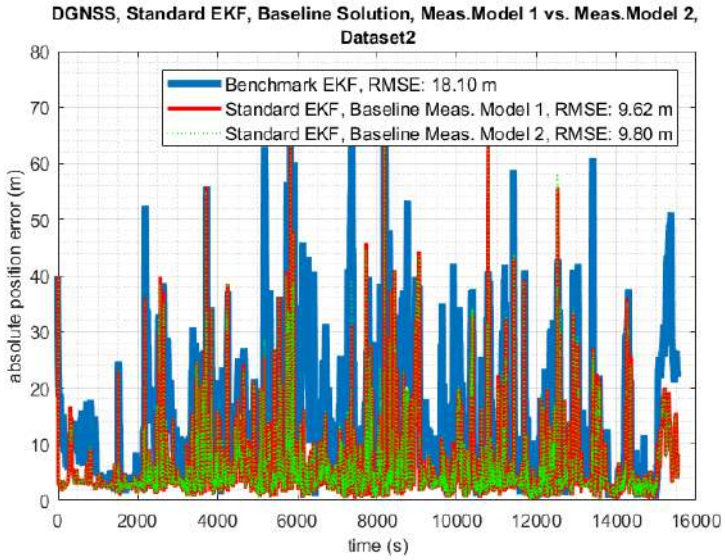

Figure 10-214 – Absolute Position estimation error with the corresponding RMSE: Dataset 2, DGNSS Benchmark EKF (blue line) vs. Standard EKF with Baseline Block Measurement Model 1 (red line) vs. Measurement Model 2 (green line)

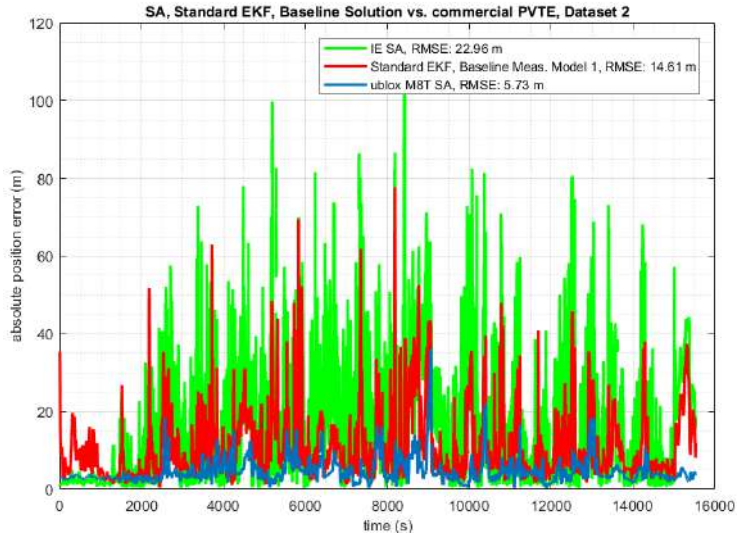

Figure 10-215 – Absolute Position estimation error with the corresponding RMSE: Dataset 2, SA Standard EKF with Baseline Measurement Model 1 (red line) vs. SA Inertial explorer (geen line) vs. SA U-blox M8T (bleu line)

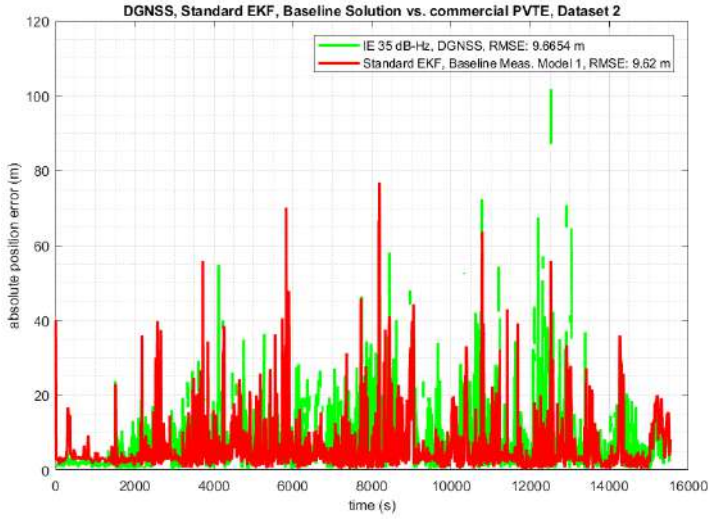

Figure 10-216 – Absolute Position estimation error with the corresponding RMSE: Dataset 2, DGNSS Standard EKF with Baseline Measurement Model 1 (red line) vs. DGNSS Inertial explorer (green line)

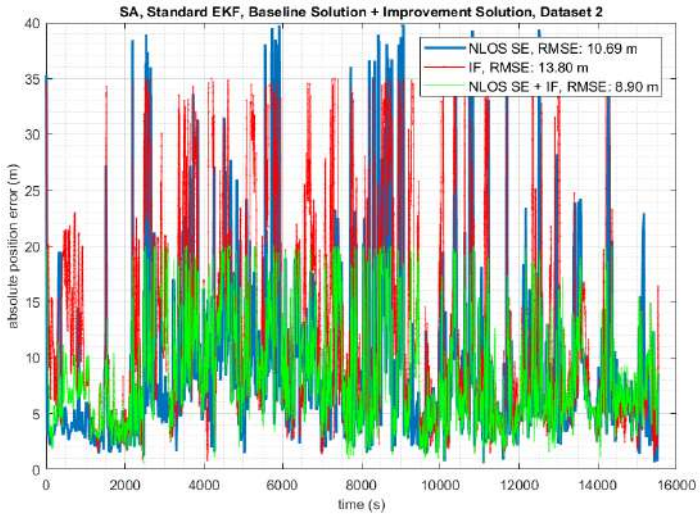

Figure 10-217 – Absolute Position estimation error with the corresponding RMSE: Dataset 2, SA Standard EKF with Improvement Block: NLOS SE (blue line) vs. IF (red line) vs. NLOS SE + IF (green line)

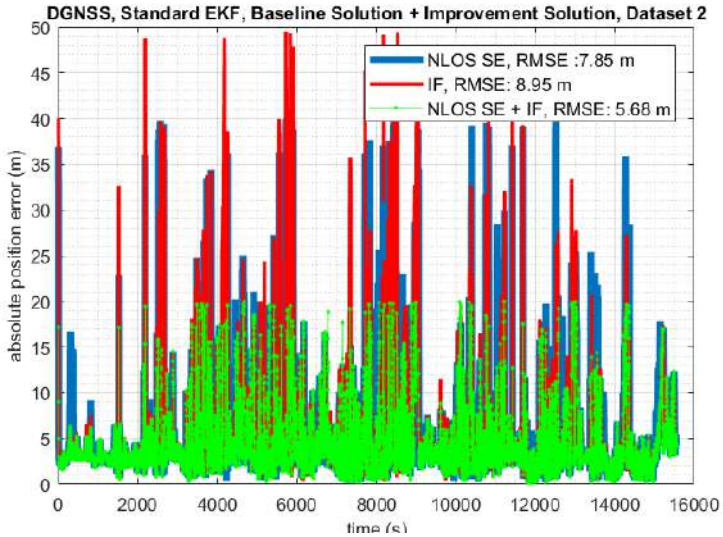

Figure 10-218 – Absolute Position estimation error with the corresponding RMSE: Dataset 2, DGNSS Standard EKF with Improvement Block: NLOS SE (blue line) vs. IF (red line) vs. NLOS SE + IF (green line)